Geographia Technica



Technical Geography
an International Journal for the Progress of Scientific Geography

Volume 21, Geographia Technica No. 1/2026

www.technicalgeography.org

Cluj University Press

Editorial Board

Okke **Batelaan**, Flinders University Adelaide, Australia
Yazidhi **Bamutaze**, Makerere University, Kampala, Uganda
Valerio **Baiocchi**, Sapienza University of Rome, Italy
Gabriela **Biali**, "Gh. Asachi" University of Iasi, Romania
Habib **Ben Boubaker**, University of Manouba, Tunisia
Gino **Dardanelli**, University of Palermo, Italy
Qingyun **Du**, Wuhan University, China
Renata **Dulias**, University of Silesia, Poland
Massimiliano **Fazzini**, University of Ferrara, Italy
Muhammad **Helmi,** Diponegoro University, Indonesia
Edward **Jackiewicz**, California State University, Northridge CA, USA
Shadrack **Kithiia**, University of Nairobi, Kenya
Jaromir **Kolejka**, Masaryk University Brno, Czech Republic
Jelena **Kovačević-Majkić,** Geographical Institute "Jovan Cvijić", Belgrade, Serbia
František **Križan**, Comenius University in Bratislava, Slovakia
Muh Aris **Marfai**, Universitas Gadjah Mada, Yogyakarta, Indonesia
Béla **Márkus**, University of West Hungary Szekesfehervar, Hungary
Jean-Luc **Mercier**, Université de Strasbourg, France
Yuri Sandoval **Montes,** Universidad Mayor de San Andrés, La Paz, Bolivia
Igor **Patrakeyev**, Kyiv University of Construction and Architecture, Ukraine
Cristian Valeriu **Patriche**, Romanian Academy, Iasi, Romania
Dušan **Petrovič**, University of Lujubjana, Slovenia
Claudia **Pipitone,** National Institute of Geophysics and Volcanology, Naples, Italy
Hervé **Quénol**, Université de Rennes 2 et CNRS, France
Sanda **Roșca**, Babes-Bolyai University of Cluj-Napoca, Romania
José J. de **Sanjosé Blasco**, University of Extremadura, Spain
Lucian **Sfîcă,** "Al.I.Cuza" University of Iasi, Romania
Richard R. **Shaker**, Reyson University, Toronto, Canada
Sarintip **Tantanee**, Naresuan University, Phitsanulok, Thailand
Gábor **Timár**, Eötvös University Budapest, Hungary
Kinga **Temerdek-Ivan**, Babes-Bolyai University of Cluj-Napoca, Romania
Yuri **Tuchkovenko**, Odessa State Environmental University, Ukraine
Kamila **Turečková,** Silesian University in Opava, Czech Republic
Eugen **Ursu**, Université de Bordeaux, France
Changshan **Wu**, University of Wisconsin-Milwaukee, USA
Chong-yu **Xu**, University of Oslo, Norway

Editor-in-chief

Ionel **Haidu**, University of Lorraine, France

Editorial Secretary

Marcel Mateescu, Airbus Group Toulouse, France
George Costea, Yardi Systemes, Cluj-Napoca, Romania

Online Publishing

Magyari-Sáska Zsolt, "Babes-Bolyai" University of Cluj-Napoca, Romania

Geographia Technica



Technical Geography

an International Journal for the Progress of Scientific Geography

2026 – No. 1

Cluj University Press

ISSN: 1842 - 5135 (Printed version)
ISSN: 2065 - 4421 (Online version)

© 2026. All rights reserved. No part of this publication may be reproduced or transmitted in any form or by any means, electronic or mechanical, including photocopy, recording or any information storage and retrieval system, without permission from the editor.

Babeș-Bolyai University
Cluj University Press
Director: Codruța Săcelean
Str. Hașdeu nr. 51
400371 Cluj-Napoca, România
Tel./fax: (+40)-264-597.401
E-mail: editura@editura.ubbcluj.ro
http://www.editura.ubbcluj.ro/

Asociatia Geographia Technica
2, Prunilor Street
400334 Cluj-Napoca, România
Tel. +40 744 238093
editorial-secretary@technicalgeography.org
http://technicalgeography.org/

Cluj University Press and Asociatia Geographia Technica
assume no responsibility for material, manuscript, photographs or artwork.

C o n t e n t

Geographia Technica

Volume 21, Issue 1, winter 2026

An International Journal of Technical Geography

ISSN 2065-4421 (Online); ISSN 1842-5135 (printed)

CHANGES IN CHLOROPHYLL-A CONCENTRATION AS AN INDICATOR OF PRIMARY PRODUCTIVITY IN WATERS BEFORE AND AFTER SEA FENCING ON THE COAST OF TANGERANG, INDONESIA

Najwa ELZAHRA, Luthfi ANZANI, Yulius YULIUS, Muhammad RAMDHAN, Dini PURBANI, Aprizon PUTRA, Taslim ARIFIN, Hadiwijaya L. SALIM, Anang D. PURWANTO, Joko PRIHANTONO, Rinny RAHMANIA, Sri Endah PURNAMANINGTYAS & Herlina Ika RATNAWATI 1

DOI: 10.21163/GT_2026.211.01

A COMPARATIVE STUDY OF HILLSLOPE AND SLOPE SEGMENT APPROACHES IN A SEMI-DISTRIBUTED INFLOW PREDICTION MODEL

Thattanaporn KHOMSRI, Chatchai TANTASIRIN & Venus TUANKRUA 16

DOI: 10.21163/GT_2026.211.02

URBAN LATENT TRANSITION INDEX (ULTI): MAPPING VACANT LAND TRANSFORMATION POTENTIAL IN THE GUATEMALA CITY METROPOLITAN AREA

Jose Luis ARGUETA MAYORGA, Mayra Virginia CARVAJAL CASTILLO, Mayra Virginia CASTILLO MONTES & Walter Arnoldo BARDALES ESPINOZA 31

DOI: 10.21163/GT_2026.211.03

REMOTE SENSING OF RESERVOIR WATER QUALITY: MODELLING OPTICALLY SENSITIVE AND NON-SENSITIVE PARAMETERS WITH LANDSAT

Suraj PAWAR, Rushikesh KULKARNI, Kanchan KHARE & Humera KHANUM 46

DOI: 10.21163/GT_2026.211.05

MULTISPECTRAL IMAGING FOR RICE HEALTH IN FERTILE ALLUVIAL PLAIN OF SOUTHEASTERN FLANK MERAPI VOLCANO

Aditya SAPUTRA, Danardono DANARDONO, Afif Ari WIBOWO, Christopher GOMEZ, Dedi SURACHMAN, Said Willya PUTRA & Ridwan HAFIDZIN 61

DOI : 10.21163/GT_2026.211.06

A GEOSPATIAL ASSESSMENT OF SHORELINE DYNAMICS AND COASTAL VULNERABILITY INDUCED BY THE SEMARANG–DEMAK SEA-TOLL ROAD INFRASTRUCTURE IN CENTRAL JAVA, INDONESIA
Indra HERMAWAN, Sutrisno ANGGORO, Suradi Wijaya SAPUTRA, Agus SUHERMAN, Wisnu Arya GEMILANG & Ulung Jantama WISHA 80
DOI : 10.21163/GT_2026.211.07

DEFORESTATION AND COASTAL EROSION IN ALBANIA ASSESSED BY REMOTE SENSING
Medjon HYSENAJ & Dritan RUSTJA 95
DOI: 10.21163/GT_2026.211.08

GEOSPATIAL IDENTIFICATION OF SOIL EROSION HOTSPOTS EXACERBATING THE CATASTROPHIC FLASH FLOOD IN BALI, INDONESIA
Ni Made TRIGUNASIH, Moh SAIFULLOH, I Nyoman SUNARTA, Ida Bagus Putu BHAYUNAGIRI & Zulkarnain ZULKARNAIN 105
DOI: 10.21163/GT_2026.211.09

SUB-HOURLY PRECIPITATION EXTREMES IN ROMANIA AND THEIR LONG-TERM TEMPORAL TREND
Adrian IRAȘOC, Nicoleta IONAC, Andreea BETERINGHE & Alexandru DUMITRESCU 127
DOI: 10.21163/GT_2026.211.10

SPEI-BASED DROUGHT PROJECTIONS FOR UGANDA UNDER CLIMATE CHANGE SCENARIOS USING THE CANESM5 CMIP6 MODEL
Obed BYAMUKAMA, Ronald SSEMBAJWE, Mihai VODA & Brian Odhiambo AYUGI 145
DOI : 10.21163/GT_2026.211.11

SOME CHARACTERISTICS OF CONVECTIVE PHENOMENA IN THE AREA OF "MIHAIL KOGĂLNICEANU" INTERNATIONAL AIRPORT CONSTANȚA, IN THE PERIOD 2003 – 2022
Andreea BETERINGHE, Adrian IRAȘOC & Nicoleta IONAC 166
DOI: 10.21163/GT_2026.211.12

GIS-BASED SPATIAL BIAS ADJUSTMENT OF RADAR-DERIVED RAINFALL ESTIMATES DURING STORM DISSIPATION IN CENTRAL THAILAND
Apichaya KANGERD & Nattapon MAHAVIK 186
DOI: 10.21163/GT_2026.211.13

DRIVERS OF ELEVATED CHLOROPHYLL-A IN LUMAJANG WATERS: A COMPARATIVE ANALYSIS OF UPWELLING AND TERRESTRIAL RUNOFF MECHANISMS
Bayu MUNANDAR, Adzkia Noerma ARIFA, Annisa Aulia LUKMAN, Anindya WIRASATRIYA & Yusuf Jati WIJAYA 205
DOI: 10.21163/GT_2026.211.14

CLIMATIC TRENDS AND CLASSIFICATION SHIFTS IN THE MAT RIVER BASIN IN ALBANIA, BASED ON THE KÖPPEN- GEIGER AND KÖPPEN-TREWARTHA CLIMATE CLASSIFICATION

Albana HASIMI, Elvin ÇOMO, Gazmir ÇELA, Entela VAKO, Amarildo SHALLAS, Mirela DVORANI, Anira GJONI & Blerina PAPAJANI .. 218
DOI: 10.21163/GT_2026.211.15

URBAN WATER SUPPLY AND DEMAND ASSESSMENT UNDER SOCIOECONOMIC SITUATION OF CHANCHO TOWN, CENTRAL ETHIOPIA, USING WEAP MODEL

Merry Amensisa TOLA, Tamru Tesseme ARAGAW & Mihai VODA 228
DOI: 10.21163/GT_2026.211.16

EXTRACTING THE SPACE-BORNE RADAR BACKSCATTERING RESPONSES OF DIFFERENT ROCK UNITS FOR GEOLOGICALLY MAPPING TAFILALET REGION IN MOROCCO

Naoual El HAMMOUCH, Fatima El HAMMICHI, Hassan TABYAOUI, Ahmed GABER, Magaly KOCH & Mohammed MOURJANE 254
DOI: 10.21163/GT_2026.211.17

ADVANCING LOW-COST MANGROVE ECOSYSTEM MAPPING: PRECISION VALIDATION OF IPHONE 12 PRO LIDAR FOR DTM GENERATION ACROSS CANOPY DENSITY GRADIENT

Sigit Bayhu IRYANTHONY, Anindya WIRASATRIYA, Rudhi PRIBADI & Pujiono Wahyu PURNOMO 271
DOI: 10.21163/GT_2026.211.18

ASSESSMENT AND CHARACTERIZATION OF WATER QUALITY AND POLLUTION IN THE COASTAL ENVIRONMENT OF PEKALONGAN, CENTRAL JAVA, INDONESIA

Muhammad ZAINURI, Anindita Rahma CANDRASEKAR, Kunarso KUNARSO, Baskoro ROCHADDI, Lilin BUDIATI, Salma Ayu SASMITA, Asshifa Poetri FEBRIYANTI & Anik SUSILOWATI 288
DOI: 10.21163/GT_2026.211.19

DEVELOPMENT OF FLOOD RISK MAPS USING AN INTEGRATED HYDRODYNAMIC MODEL AND FAHP IN THE LOWER NAM PHONG BASIN, THAILAND

Chalermchai PAWATTANA, Phaisarn JEEFOO, Chaiwiwat VANSAROCHANA & Satit POOPIWKHAM 306
DOI: 10.21163/GT_2026.211.20

RIVERBED DYNAMICS OF SUCEAVA RIVER AT THE TRANSITION BETWEEN THE CARPATHIANS AND THE EASTERN LOWLANDS

Diana ISTRATE, Domenic Raul BECICA, Mihai BARBACARIU, Ionela GRĂDINARU & Marcel MÎNDRESCU 323
DOI: 10.21163/GT_2026.211.21

CHANGES IN CHLOROPHYLL-A CONCENTRATION AS AN INDICATOR OF PRIMARY PRODUCTIVITY IN WATERS BEFORE AND AFTER SEA FENCING ON THE COAST OF TANGERANG, INDONESIA

Najwa ELZAHRA [1], Luthfi ANZANI [1], Yulius YULIUS [2*], Muhammad RAMDHAN [3], Dini PURBANI [2], Aprizon PUTRA [2], Taslim ARIFIN [2], Hadiwijaya L. SALIM [2], Anang D. PURWANTO [2], Joko PRIHANTONO [2], Rinny RAHMANIA[2], Sri Endah PURNAMANINGTYAS [2], Herlina Ika RATNAWATI [2]

DOI: 10.21163/GT_2026.211.01

ABSTRACT

Coastal eutrophication is an escalating concern in Indonesian estuaries, driven by anthropogenic pressures and physical interventions such as sea fencing. This study analyses the spatial and temporal changes in Chlorophyll-a (Chl-a) concentrations and Net Primary Productivity (NPP) in the coastal waters of Kronjo, Tangerang Regency, before (2020) and after (2024) the installation of illegal sea fences. High-resolution (3 m) PlanetScope satellite imagery was processed using the Normalised Difference Chlorophyll Index (NDCI) and subsequently modelled into NPP using the Vertically Generalised Productivity Model (VGPM), incorporating supporting data such as Photosynthetically Active Radiation (PAR), Sea Surface Temperature (SST), and Euphotic Zone Depth (Zeu). Despite an increase in localised maximum values, the results revealed a slight decrease in mean Chl-a concentrations from 6.12 to 5.89 mg/m^3. The spatial distribution of NPP became more homogenised, with high-value areas becoming more spatially constrained. A robust Pearson correlation ($r = 0.99$; $p < 0.001$) between Chl-a and NPP confirms the reliability of NDCI for capturing primary productivity dynamics. This study demonstrates the efficacy of high-resolution remote sensing in evaluating the ecological impacts of coastal physical structures and informing spatially explicit management strategies. This is the first high-resolution remote sensing study assessing Southeast Asia's pre- and post-se fencing impacts, highlighting the critical need for integrated spatial monitoring in tropical estuarine ecosystems.

Key-words: *Chlorophyll-a; Estuarine monitoring; PlanetScope; Primary productivity; Sea fence.*

1. INTRODUCTION

Indonesia is an archipelagic country with a maritime area of over 6.4 million km² and a coastline of approximately 108,000 km (Yanuar et al., 2023). Its coastal regions are central to a country's development and ecological resilience. Approximately 22% of Indonesia's population resides in coastal regions and relies on fishing, trade, tourism, and maritime transport activities for livelihoods (Jamal, 2019). These activities make the coast a national economic hub and increase pressure on the coastal environment.

---

[1]*Indonesia University of Education (UPI), Bandung-West Java, Indonesia. (NE) najwaelzr26@upi.edu; (LA) luthfi_anzani@upi.edu*

[2]*National Research and Innovation Agency (BRIN), Bogor-West Java, Indonesia. (YY) yuli058@brin.go.id; (DP) dini017@brin.go.id, (AP) apri024@brin.go.id; (TA) tasl003@brin.go.id; (HLS) hadi026@brin.go.id; (ADP) anan009@brin.go.id; (JP) joko.prihantono@brin.go.id; (RR) rinny.rahmania@brin.go.id; (SEP) srie005@brin.go.id; (HIR) herl010@brin.go.id*

[3]*National Research and Innovation Agency (BRIN), Bandung-West Java, Indonesia. (MR) muha307@brin.go.id*

[*]*Corresponding author email: yuli058@brin.go.id*

One coastal region that reflects the complexity of interactions between oceanographic processes and anthropogenic pressures is the Kronjo estuary on the northern coast of Tangerang Regency, Banten Province, Indonesia. This area is influenced by the flow of the Cidurian River and its tributaries (Kali Malang-Muara Selasih and Cipasilian), as well as by micro-tidal dynamics and land runoff (Laksana, 2011; Fadlillah et al., 2018).

In recent decades, this area has experienced significant water quality degradation due to domestic industrial waste, reclamation, and infrastructure development, triggering local eutrophication (Wijayanti et al., 2022). The main parameters for evaluating the quality of aquatic ecosystems are Chlorophyll-a (Chl-a) concentration and Net Primary Productivity (NPP) (Fan et al., 2023). Chl-a is the primary photosynthetic pigment in phytoplankton, which is highly sensitive to light, nutrients, and water turbidity variations. In the tropical coastal waters of Indonesia, Chl-a has been shown to have a robust correlation with marine primary productivity, with a coefficient of determination $R^2 \geq 0.9$ (Arridhaty Akita et al., 2023; Nuzapril et al., 2019). Local studies in the Karimun Jawa Islands, Lake Lait, and Tangkil Island support these findings, with R^2 values up to 0.99 (Nuzapril et al., 2017; Fitra et al., 2013; Fathia et al., 2021).

The latest physical stress has emerged on the coast of Tangerang Regency since 2021, namely massive unauthorised sea fencing constructed using bamboo. These structures can modify tidal currents, trap sediments, and reduce water transparency, suppressing phytoplankton biomass and primary productivity. A similar phenomenon has been reported in Jinmeng Bay, China, where a land reclamation project involving the creation of artificial islands has led to a 35% increase in water residence time, a decrease in nutrient diffusion capacity, and an increased risk of eutrophication and algal blooms (Kuang et al., 2024). Studies in the Malacca Strait also showed a decrease in Chl-a concentrations from 7-9 mg/L to 5-7 mg/L after reclamation, with a significant correlation to changes in Total Suspended Solids (TSS), Sea Surface Temperature (SST), and tidal currents (Abdullah & Dusuki, 2018). Additionally, the spatial-temporal distribution of Chl-a in the Pearl River Estuary is significantly influenced by anthropogenic activities and changes in water dynamics (Fan et al., 2023).

Through the Ministry of Marine Affairs and Fisheries or KKP (2025), the Indonesian government has also stated that sea fencing can seriously threaten the balance of marine ecosystems. However, there are no high-resolution quantitative spatial-temporal studies explicitly comparing ecosystem conditions before and after the installation of coastal physical structures such as sea fences in Indonesia. Direct monitoring in shallow and muddy waters, such as Kronjo, often faces access and cost limitations. Therefore, remote sensing can effectively and efficiently monitor spatial-temporal changes (Yulius et al., 2021). Satellite imagery such as the Moderate Resolution Imaging Spectroradiometer (MODIS) or Sentinel-2 has been widely used, but its low resolution makes it unsuitable for monitoring local changes on a metre scale. PlanetScope, satellite imagery with a spatial resolution of 3 metres and daily recording frequency, can detect subtle spatial dynamics in narrow areas such as Kronjo. The Normalised Difference Chlorophyll Index (NDCI) algorithm, which utilises the red (665 nm) and red-edge (708 nm) bands, has proven accurate for estimating Chl-a in turbid and shallow waters (Mishra & Mishra, 2012). In a study by Wasehun et al. (2025), PlanetScope was superior in capturing fine spatial dynamics in small water bodies and producing relatively high Chl-a estimation accuracy values ($R^2 = 0.71$). This supports the use of PlanetScope imagery in studies of narrow areas such as Kronjo Sub-district.

To support a more comprehensive assessment of ecosystem productivity, NDCI can be integrated with parameters such as Photosynthetically Active Radiation (PAR) and SST in the Vertically Generalised Productivity Model (VGPM) to obtain NPP values (Behrenfeld & Falkowski, 1997). Similar studies in tropical regions show that NPP and Chl-a follow the same seasonal patterns and are strongly influenced by environmental variability, including The El Niño-Southern Oscillation (ENSO) effects, seasonal changes, and human interventions (Dewi et al., 2018; Marpaung et al., 2022; Nugraheni et al., 2014). This study aims to analyse the spatial and temporal changes in Chl-a and NPP concentrations in Kronjo waters before (2020) and after (2024) the installation of sea fences. In addition, this study will evaluate the impact of sea fencing on Chl-a dynamics by combining the NDCI algorithm and the VGPM model based on PlanetScope imagery. This study is expected to fill the gap

in study on the physical effects of sea fences on tropical waters and offer a spatially detailed approach that can be used to support coastal management policies and serve as a reference for similar studies in Southeast Asia.

2. STUDY AREA

Kronjo Sub-district is one of the coastal regions in Tangerang Regency, Banten Province, Indonesia, located on the northern coast of Java Island and directly bordering the Java Sea. Geographically, Kronjo Sub-district is located at approximately 6° 03′37″ South Latitude and 106° 25′27″ East Longitude and has a relatively long coastline with waters dominated by river estuaries and estuary areas. This area is a transitional zone between fluvial and marine systems, influenced by micro-tidal fluctuations, dominant west-to-east coastal currents, and nutrient inputs from the mainland, particularly from the Cidurian, Cipasilian, and Cimanceuri rivers. Its coastal geomorphological characteristics include swampy land, ponds, and secondary mangrove vegetation, making the region highly sensitive to natural and anthropogenic environmental changes. Starting in 2021, physical intervention in sea fence construction using bamboo structures and nets has occurred at several coastal locations in Kronjo. These structures were built without hydrodynamic studies or official permits and have been reported to harm the coastal ecosystem. A spatial overview of the study location is shown in **figure 1**, which shows the river flow system and the location of the sea fences on the coast of Kronjo Kronjo Sub-district.

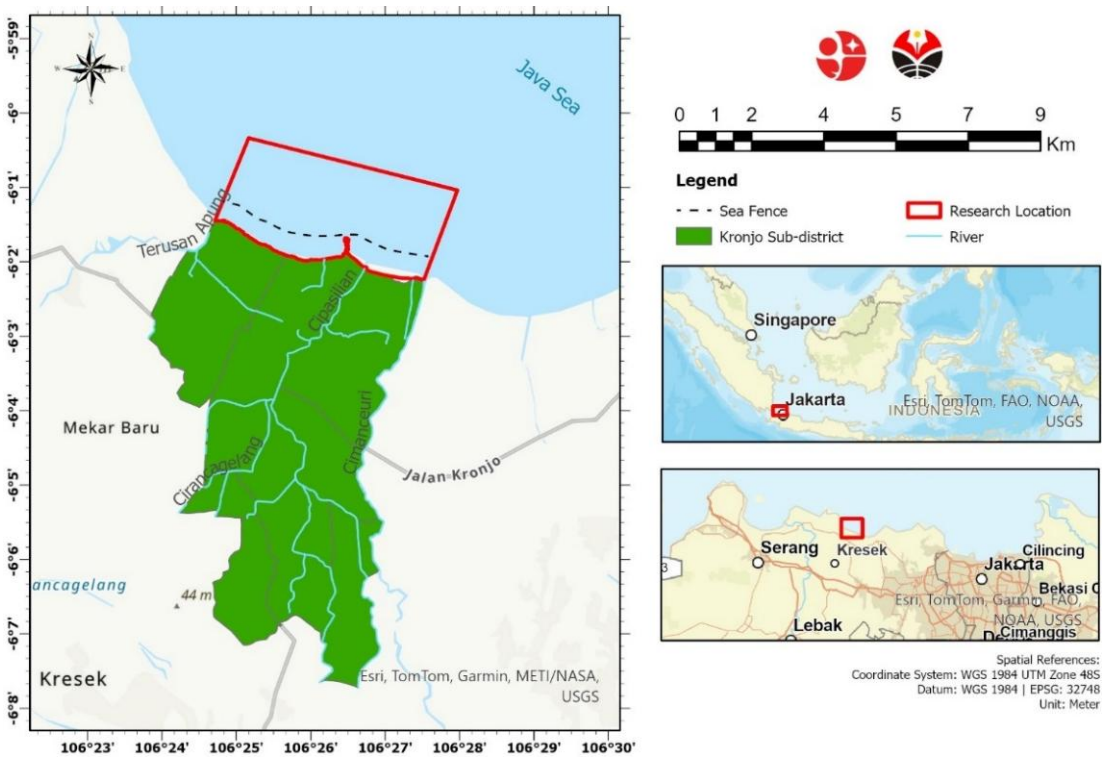


Fig. 1. Map of the study area.

3. DATA AND METHODS

This study method began with problem identification, followed by data collection that included PlanetScope satellite imagery, PAR, and SST. PlanetScope imagery was processed to calculate the Normalised Difference Water Index (NDWI) to separate water areas, which were then used in NDCI

calculations and Chl-a estimates. The Chl-a, PAR, and SST parameters are then entered into the VGPM to calculate NPP. The estimated NPP and Chl-a results are analysed using Pearson's correlation to evaluate the relationship between variables. The final stage of the study is interpreting the correlation results and spatial distribution to understand the dynamics of primary productivity changes in the study area. The study workflow is shown in **figure 2** below.

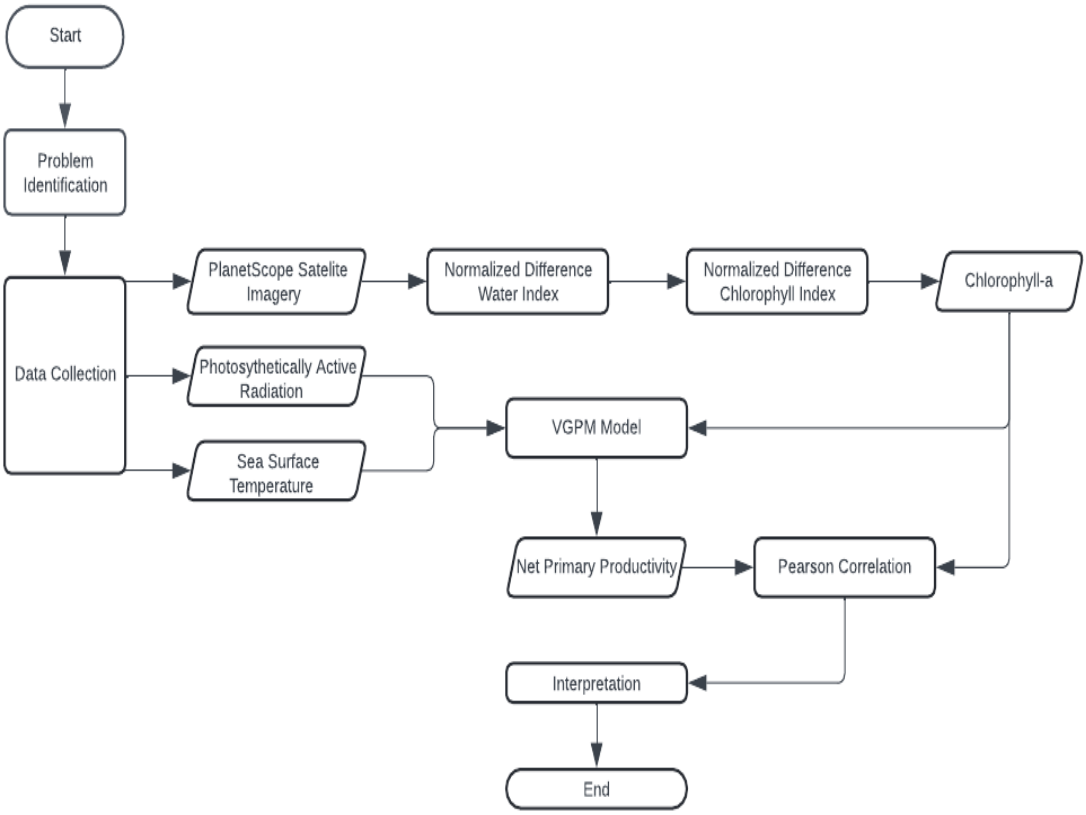


Fig. 2. Flowchart.

3.1. Data

This study utilises PlanetScope satellite imagery of the Analytic MS_SR 8-band type, which has undergone atmospheric correction (Surface Reflectance). The imagery has a spatial resolution of 3 m, with additional information including sun elevation angle, off-nadir angle, and cloud cover percentage. The dataset used covers two observation periods June 20, 2020 (pre-fencing) and October 26, 2024 (post-fencing), with a cloud cover criterion of <10%. Each image covers eight spectral channels, with the bands used in the analysis having the following criteria. More details can be seen in **table 1** below.

Table 1.

PlanetScope spectral channels and their use in analysis.

Band	Spectral Name	Wavelength (nm)	Function
B4	Green	~550	NDWI, Zeu
B6	Red	~665	NDCI
B7	Red edge	~705	NDCI
B8	Near Infrared (NIR)	~865	NDCI, Shadow

Source : https://developers.planet.com/docs/apis/data/sensors/

The following supporting data was used (in **table 2**).

Table 2.

Supporting data for NPP.

Parameters	Data Source	Spatial Resolution	Temporal Resolution
PAR	MODIS-Aqua L3 PAR	4 km	Daily
SST	MODIS-Aqua L3 SST	4 km	Daily
Precipitation	CHIRPS v2.1	0.05° (~5 km)	Daily

3.2. Methods

This study uses a quantitative approach based on remote sensing to identify and compare spatial and temporal changes in water physical-chemical parameters, particularly Chl-a and NPP, before and after the installation of marine fencing on the Kronjo coast, Tangerang Regency. The analysis was carried out through the following series of processes.

3.2.1. Pre-processing and Masking

The image used is PlanetScope AnalyticMS_SR, which is at the Surface Reflectance (SR) level, so no additional atmospheric correction is required. Before calculating the index, cloud, shadow, and water masking is performed to ensure that only undisturbed water areas are analysed.

- Cloud Masking: Clouds generally have very high reflectance in the visible channel, especially in the green and red channels. Based on the harmonised PlanetScope SR usage documentation for analysis purposes. The 2500 DN threshold corresponds to a reflectance of approximately 0.25 (on a scale of 0–10,000), indicating thick clouds with high reflectance. This threshold minimises the misclassification of very bright pixels as clouds, the following empirical thresholds are used.

$$Green > 2500 \text{ and } Red > 2500$$

- Shadows (from both clouds and topographic surfaces) exhibit very low reflectance values in the visible and NIR channels. The 500 Digital Number (DN) threshold on a 0–10,000 scale corresponds to a reflectance value of approximately 0.05, which aligns with the characteristics of dark areas. This technique is commonly used in shadow masking algorithms for high-resolution imagery such as Landsat/Sentinel (e.g., Fmask) and has been adapted for PlanetScope SR. Following the cloud and shadow masking procedures, only water pixels that were completely free from contamination were retained. As a result, the final region of interest (ROI) selected for the Chl-a and NPP analysis consisted entirely of clear-sky and non-shadowed areas. Therefore, 100% of the analysed area was classified as valid, ensuring high spatial integrity and reliability in the results. Therefore, pixels are classified as part of a shadow if.

$$Green > 500 \text{ and } NIR > 500$$

- Water Masking: The masking of water areas was carried out using the Normalised Difference Water Index (NDWI) (McFeeters, 1996), which is a remote sensing technique developed by McFeeters (1996) to detect and separate water features from land and terrestrial vegetation. This index is handy in identifying water bodies in satellite images because it utilises the difference in reflectance characteristics between the green and near-infrared (NIR) channels. Water typically has low reflectance to NIR light and high reflectance to green light, while vegetation and dry soil show the opposite pattern. NDWI values greater than zero (NDWI > 0) are interpreted as water bodies, and these pixels are then used for NDCI-based Chl-a index calculations. The NDWI equation used refers to the formula from McFeeters (1996).

$$NDWI = \frac{Green - NIR}{Green + NIR}$$

where: Green = Band 4; and NIR = Band 8.

3.2.2. Indeks NDCI

NDCI has been recognised as one of the most efficient and practical methods for estimating Chl-a concentrations in various water bodies. Numerous studies have documented its practical application in Case II waters (An Ru et al., 2013), coastal estuaries (Mishra et al., 2014), and bay areas (Manuel & Blanco, 2023). Compared to other methods, NDCI offers ease of application, estimation accuracy, and flexibility in cross-platform remote sensing use (An Ru et al., 2013). Furthermore, several studies have shown a strong correlation between NDCI values and in situ measured Chl-a concentrations, with reported determination coefficients (R^2) ranging from 0.74 to 0.96 (Mishra et al., 2014; Manuel & Blanco, 2023). This indicates the consistency of NDCI in describing the spatial and temporal variability of primary productivity in water bodies. NDCI is calculated based on the formulation introduced by Mishra & Mishra (2012) as follows.

$$NDCI = \frac{R_{red-edge} - R_{red}}{R_{red-edge} + R_{red}}$$

where: $R_{red-edge}$ = Band 7; and R_{red} = Band 6.

The NDCI values obtained were then converted to Chl-a (mg/m³) using the equation from the Mishra & Mishra (2012) study, which is widely applied in tropical regions:

$$Chl\text{-}a = a \times e^{b.NDCI}$$

where: NDCI = Calculated from the Red Edge (708 nm) and Red (665 nm) channels; Chl- a = Chl-a concentration (mg/m³); a = Scale constant (intercept) from regression results; b = Slope coefficient from regression results; and e = Euler's number, the basis of natural logarithms.

This model is widely used in tropical regions because it has been tested under high nutrient and light fluctuations and turbidity conditions. This algorithm was applied to high-resolution imagery in the study by Saulquin et al. (2019). It showed spatial consistency with in situ data, making it ideal for monitoring coastal waters in developing regions. The following **table 3** shown the classification of Chl-a concentrations based on NDCI values for ecological interpretation.

Table 3.

Classification of Chl-a values based on the NDCI index.

NDCI Range	Chl-a Range (mg/m³)
< -0	< 7.5
-0.1 to 0	7.5 - 16
0 to 0.1	16 - 25
0.1 to 0.2	25 - 33
0.2 to 0.4	33 - 50
0.4 to 0.5	> 50
0.5 to 1	Severe bloom

Source: Mishra & Mishra (2012).

The application of NDCI in this study enabled the identification of productive and eutrophic zones and the detection of possible ecological disturbances caused by human interventions such as marine fencing. The strong correlation between NDCI and Chl-a, which has been proven in various studies, makes this method valid for assessing changes in water quality spatially and temporally.

3.2.3. NPP

NPP can be estimated using the VGPM global scale model with remote sensing satellite image data inputs (Behrenfeld & Falkowski, 1997; Marpaung et al., 2022). This model calculates NPP (in units of mg C/m²/day) based on Chl-a concentration, PAR, Zeu, and maximum daily phytoplankton productivity P_b^{opt}, which is controlled by SST, using the following equation.

$$NPP = 0.66125 \times P_b^{opt} \times \left(\frac{E_{PAR}}{E_{PAR} + 4.1}\right) \times C_{sat} \times Z_{eu}$$

where: P_b^{opt} = Optimal productivity parameters, depending on temperature; C_{sat} = Chl-a concentration (mg/m³); E_{PAR} = Photosynthetic active radiation intensity (Einstein/m²/day); Z_{eu} = Depth of the Euphotic zone (m).

3.2.4. Pearson Correlation

To assess the relationship between Chl-a concentration and NPP, Pearson's correlation analysis (r) was performed, assuming a normal distribution and a linear relationship between variables. The analysis was conducted on paired samples for 2020 and 2024, using data from raster to sampling points obtained from the NDWI masking process. The correlation was considered strong if $r > 0.8$, and statistical significance was determined with $p < 0.05$. This analysis refers to the classical statistical method by Pearson (1896), which has been revisited and widely used in modern oceanography and ecology study (Marpaung et al., 2022). Pearson's correlation (r) was calculated using the formula.

$$r = \frac{r\sum xy - \sum x \sum y}{\sqrt{[n\sum x^2 - (\sum x)^2][n\sum y^2 - (\sum y)^2]}}$$

where: x = Chl-a (mg/m³); y = NPP mg C/m²/day; and n = Sample size.

Pearson's correlation is used to evaluate the extent to which two variables are related. A Pearson correlation value (r) close to +1 or -1 indicates a robust linear relationship with a positive or negative direction. If the r value is positive ($r > 0$), then the relationship between the variables is unidirectional, and the higher the value, the stronger the relationship. Conversely, $r < 0$ indicates an inverse relationship but is still strong. If the r value approaches zero, the relationship between the variables is considered weak or statistically insignificant (Walpole, 2012; Sambah et al., 2020). Generally, an r value > 0.8 is categorised as a strong correlation, with a significance level accepted if $p < 0.05$. This approach follows Pearson (1896), which is still widely applied in spatial relationship analysis in modern oceanography and ecology.

4. RESULTS

4.1. Spatial changes in NDCI

The spatial distribution of NDCI values as a bio-optical indicator of Chl-a shows striking spatial-temporal variations between the two observation periods. In 2020 (pre-fencing), the maximum NDCI value was 0.245, with a fairly widespread distribution of positive values in the eastern and central coastal regions. This indicates a high abundance of phytoplankton, particularly in the nutrient-rich estuary of the Cidurian River, which receives significant terrestrial runoff. Conversely, in 2024 (post-fencing), the maximum NDCI value was 0.428, but areas with negative NDCI values (< 0) expanded significantly, particularly in regions bounded by the sea fence. The distribution map of NDCI values can be seen in **figure 3** below. These findings indicate decreased primary productivity homogeneity and local accumulation of Chl-a in enclosed areas due to nutrient circulation and distribution disruption. Activities around the coast, such as reclamation and especially the construction of sea fences, contribute to changes in the distribution and concentration of Chl-a in the water. The interpretation of the values occurring before and after the construction of the sea wall can be seen in **table 4** below and in **table 5,** the comparison of Chl-a before and after sea walling.

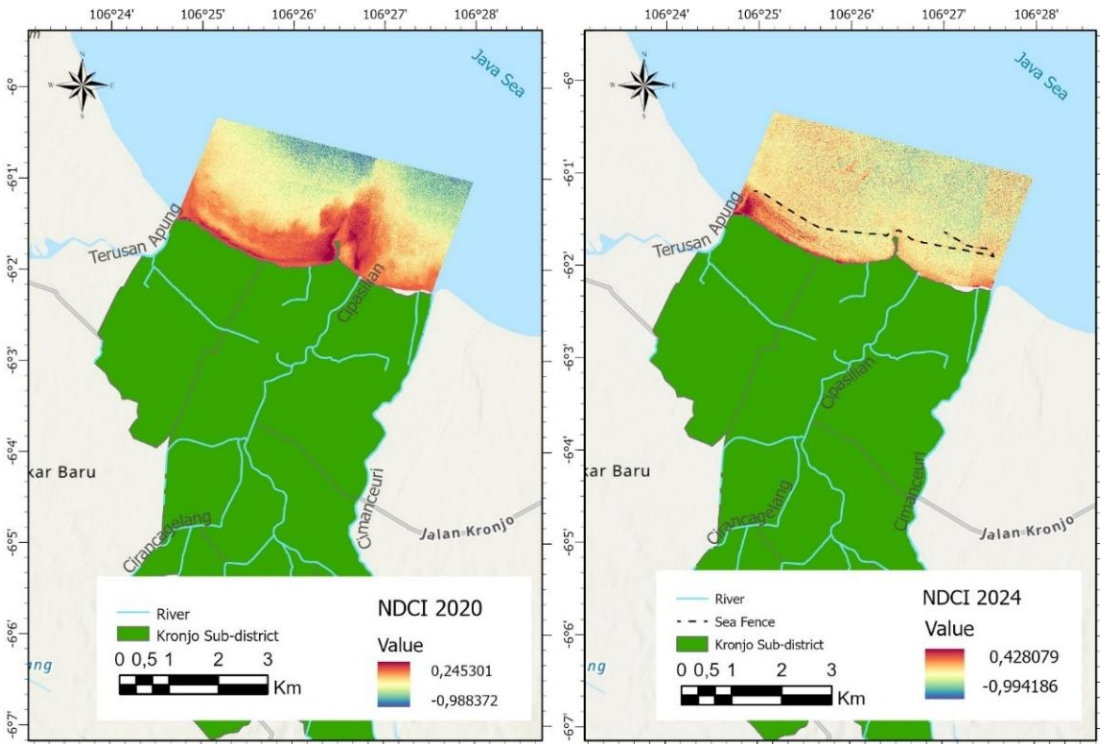


Fig. 3. Spatial distribution map of NDCI values in June 2020 (pre-fencing) and October 2024 (post-fencing).

Table 4.

Comparison of NDCI values before and after sea fencing.

Year	Min	Max	Mean	STD
2020	-0.988	0.245	-0.169	0.140
2024	-0.994	0.428	-0.155	0.086

Source: Data analysis, 2025.

4.2. Spatial changes in Chl-a

As the primary pigment for photosynthesis in phytoplankton, Chl-a reflects the dynamics of water fertility. In 2020, the maximum value was 30.16 mg/m³ with an average of 6.12 mg/m³. By 2024, the maximum value increased to 65.47 mg/m³, but the average decreased to 5.89 mg/m³. The distribution map of Chl-a can be seen in **figure 4** below.

Similar to what happened with NDCI values, the increase in maximum Chl-a values was not accompanied by an increase in the average area of this area, reflecting the presence of local eutrophication due to water stagnation. The area enclosed by the sea fence became a place accumulating nutrients and Chl-a, but overall productivity actually decreased. These findings support studies by Mishra & Mishra (2012); Manuel & Blanco (2023), which state that Chl-a is a sensitive indicator of physical disturbances and water dynamics.

Table 5.

Comparison of Chl-a before and after sea walling.

Year	Min	Max	Mean	STD
2020	0.16	30.16	6.12	3.40
2024	0.15	65.47	5.89	2.29

Source: Data analysis, 2025.

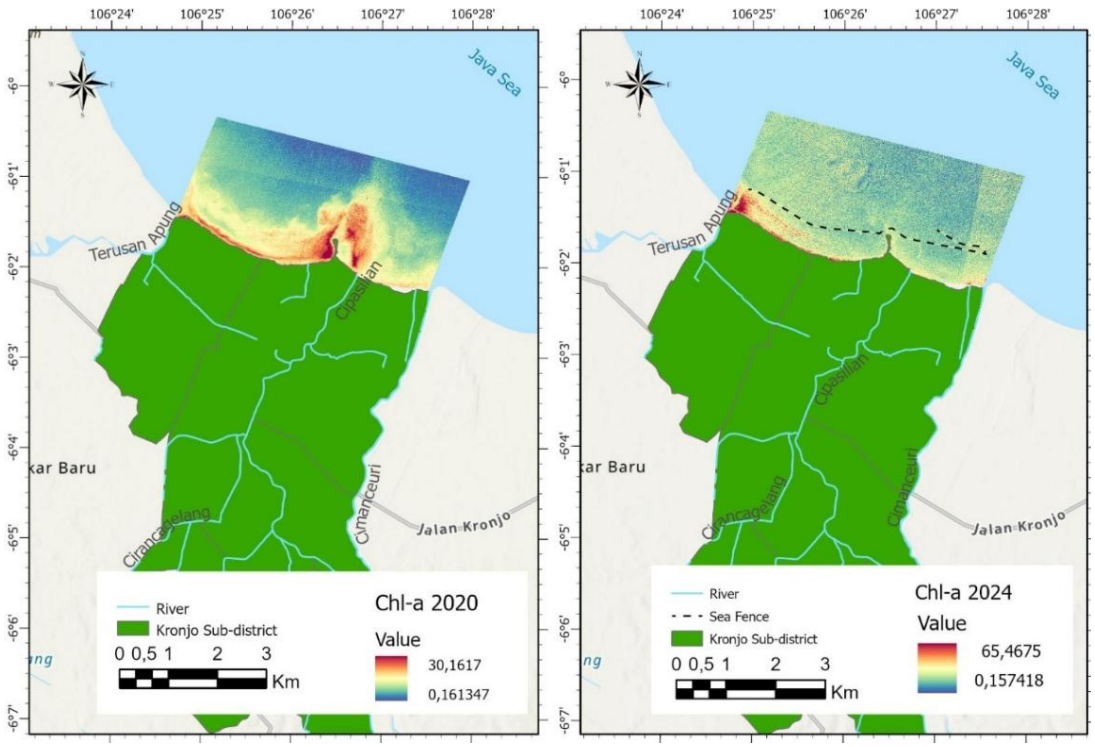


Fig. 4. Spatial distribution map of Chl-a in June 2020 (pre-fencing) and October 2024 (post-fencing).

4.3. Estimation and Distribution of NPP

NPP, estimated using the VGPM, which integrates Chl-a concentration, Euphotic Zeu, PAR, and SST, shows a spatial pattern consistent with the distribution of Chl-a. In 2020 (before the installation of the sea fence), NPP ranged from 3.23 to 64.82 mg C/m²/day, with an average of 26.91 mg C/m²/day. In 2024 (after the installation of the sea fence), the range increased to 3.17 to 96.63 mg C/m²/day, although the average decreased slightly to 26.80 mg C/m²/day. Maps of the spatial distribution of these values are shown in **figure 5** below.

As shown in **table 6**, although the average values appear relatively stable in both periods, the spatial distribution of NPP shows clear homogenisation. High-productivity zones have become increasingly fragmented and localised, reflecting the spatial patterns observed in the NDCI and Chl-a maps. This indicates that the presence of the sea fence has disrupted nutrient circulation and vertical mixing, causing primary productivity to concentrate in limited and stagnant zones. These findings align with previous studies highlighting the sensitivity of NPP to bio-optical and physical parameters of the water column.

Table 6.

Comparison of NPP before and after sea walling.

Year	Min	Max	Mean	STD
2020	3,23	64,82	26,91	5,31
2024	3,17	96,63	26,80	5,32

Source: Data analysis, 2025.

According to the trophic classifications proposed by Vollenweider (1968) and Rodhe (1969), as cited in Kumar et al. (2023), oligotrophic waters are defined as having daily NPP values of 65-300 mg C/m² and 30-100 mg C/m², respectively. With average values of less than 27 mg C/m²/day recorded in 2020 and 2024, the waters of Kronjo fall well below both thresholds, particularly even below Rodhe's lower limit.

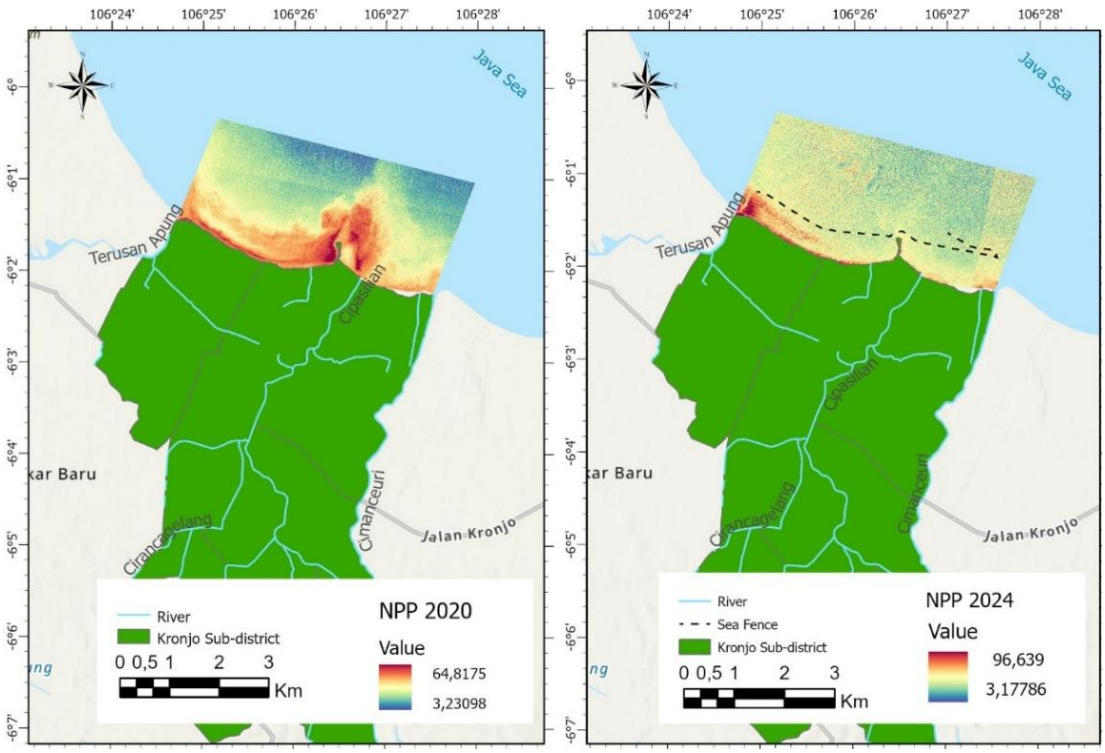


Fig. 5. Spatial distribution map of NPP in June 2020 (pre-fencing) and October 2024 (post-fencing).

This places the study area in a severely nutrient-deficient state, indicating a very low level of primary productivity. These results confirm that the Kronjo coastal waters are not only outside the productive range of typical oligotrophic systems but may represent an ultra-oligotrophic condition, which is ecologically concerning for a tropical coastal zone. The disruption in hydrodynamics caused by the sea fence, combined with limited land-based nutrient inputs, has likely constrained phytoplankton growth and reduced overall ecosystem function in the area.

4.4. The effect of rainfall on water dynamics

Precipitation is one of the main climatological factors affecting primary productivity in coastal regions, particularly through runoff mechanisms that carry nutrients from land to water. Based on CHIRPS (Climate Hazards Group InfraRed Precipitation with Station) data, monthly rainfall in the study area was recorded at 84.17 mm in June 2020 and 46.67 mm in October 2024 (**figure 6**). Although there was no rainfall on the main observation dates (20 June 2020 and 26 October 2024), the high monthly precipitation accumulation still significantly impacted water fertility dynamics.

During June 2020, relatively high rainfall likely contributed to increased runoff from the Cidurian River, its tributaries, and adjacent irrigation networks along the Kronjo coastline. This runoff may have introduced dissolved nutrients such as nitrogen and phosphate into the coastal waters, potentially supporting phytoplankton growth. According to Suardiani et al. (2018), rainfall in tropical coastal regions can increase phytoplankton biomass by supplying land-derived nutrients. In this period, the average Chl-a concentration reached 6.12 mg/m^3, accompanied by a uniform spatial distribution of NPP across the estuarine zone. Comparable responses to precipitation have been documented elsewhere. Prabuwono et al. (2023) observed that heightened runoff in the southern Red Sea was associated with increased Chl-a concentrations exceeding 1.3 mg/m^3, while Herdianti et al. (2023) emphasised the role of seasonal precipitation variability in modulating Chl-a and NPP in tropical shallow coastal systems.

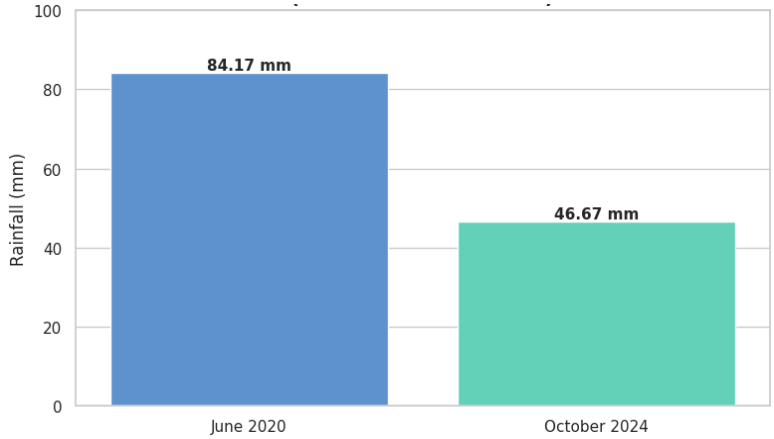


Fig. 6. Monthly rainfall graph in June 2020 and October 2024.

In contrast, October 2024 was characterised by a significant decline in monthly rainfall-nearly 50% lower than in June 2020, coinciding with a sea fence structure that physically restricted water circulation and vertical mixing. Although localised Chl-a maxima reached 65.47 mg/m^3, the overall average concentration declined to 5.89 mg/m^3, and NPP distribution became more spatially confined. These observations indicate the emergence of localised eutrophication, likely driven by the reduced exchange of nutrients in semi-enclosed areas.

Overall, the results suggest that the productive conditions observed in 2020 were shaped by a combination of hydrological and physical factors, including nutrient delivery and water circulation. In the case of Kronjo' s coastal waters, monthly rainfall should be considered a contributing driver of nutrient dynamics, particularly when interpreted alongside anthropogenic modifications and hydrodynamic constraints.

4.5. Relationship between Chl-a concentration and NPP

Pearson's correlation analysis between Chl-a concentration and NPP values showed a robust and statistically significant relationship in both years of observation. The correlation test results are shown in **figure 7** below.

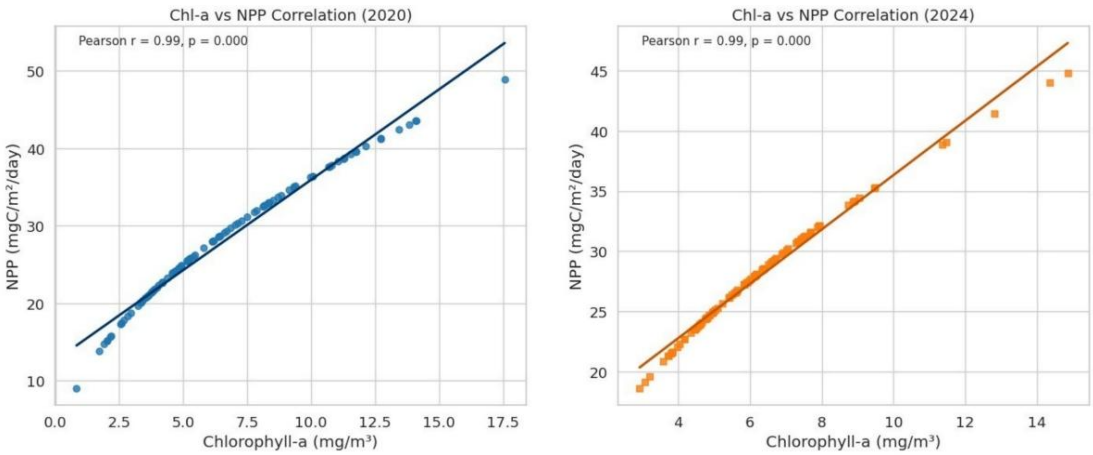


Fig. 7. The linear relationship between Chl-a and NPP in 2020 and 2024.

In 2020, the Pearson correlation between Chl-a and NPP reached r = 0.99 with a significance value of p = 0.000, indicating an almost perfect linear relationship. This reflects that variations in Chl-a concentration explain almost all variations in NPP values in conditions before marine fencing. Most data points show a consistent positive trend, indicating that increases in phytoplankton biomass directly enhance primary productivity in the water. In 2024, a similar relationship remained strong, with a value of r = 0.99 and p = 0.000. Although the correlation remained high, the distribution of points tended to be more concentrated in the Chl-a range of 5-10 mg/m³, with a few outliers at high values. This indicates that despite the implementation of marine fencing and changes in the spatial pattern of Chl-a, the functional relationship between phytoplankton biomass and productivity remains intact. However, the spatial homogenisation of NPP (discussed in Section 3.3) suggests that productivity contributions tend to be more locally concentrated post-fencing (not spatially extensive).

These findings reinforce previous study results that Chl-a is a strong indicator for estimating primary productivity in tropical coastal waters (Behrenfeld & Falkowski, 1997; Werdell et al., 2013). The strong correlation likewise reflects the reliability of the NDCI algorithm in conjunction with the VGPM method in consistently capturing ecosystem responses to physical alterations resulting from human activities. Ecologically, this strong correlation underscores the central role of phytoplankton as primary producers in the marine food chain and as early indicators of changes in water health (Bedford et al., 2018). Therefore, fluctuations in Chl-a, as observed before and after the installation of the sea fence, can serve as a key parameter for monitoring anthropogenic impacts on tropical coastal ecosystems.

While the strong correlation between Chl-a and NPP reinforces the reliability of the remote sensing approach, it is important to acknowledge the limitations associated with the absence of in-situ validation. The estimation of Chl-a using the NDCI may be subject to uncertainties caused by several factors, including high turbidity, suspended sediments, atmospheric correction residuals, and shallow water effects common in estuarine environments. These uncertainties can lead to under- or overestimation of Chl-a concentrations, which, when used as input in the VGPM model, may propagate and influence the derived NPP values. Therefore, although the spatial trends and correlations remain consistent, the absolute accuracy of productivity estimates should be interpreted with caution. Incorporating ground-truth data in future studies would enhance model robustness and strengthen the interpretation of remote sensing-derived productivity assessments.

5. CONCLUSION

The findings of this study indicate that the level of primary productivity in the coastal waters of the Kronjo Sub-district is extremely low, falling below the oligotrophic threshold. This reflects limited water fertility and an imbalance within the local ecosystem. The low average values of NPP, along with the narrowing spatial distribution of chl-a, suggest restricted nutrient supply and disrupted phytoplankton dynamics, which play a key role as primary producers in the marine food web. The installation of these fences appears to impede the natural mixing of water masses, thereby intensifying stagnation and promoting the build-up of nutrients in confined zones-conditions which may give rise to localised eutrophication. This situation is further aggravated by a decline in rainfall, resulting in diminished terrestrial runoff that would otherwise serve as a key source of nutrients.

In light of these findings, it is strongly recommended that all sea fence structures, particularly those located in estuarine areas critical for nutrient exchange, be urgently reviewed and dismantled to restore ecological connectivity and natural hydrodynamic flow. Such interventions are essential for supporting primary productivity and preventing further degradation of estuarine ecosystems. Beyond these site-specific recommendations, this study highlights broader implications for coastal spatial governance in Indonesia.

The results underscore the importance of integrating high-resolution ecological monitoring into the enforcement of spatial regulations, such as the Regional Spatial Plan or RTRW and Coastal and Small Islands Zoning Plan or RZWP3K. Although these planning instruments are formally established, they often lack effective enforcement, allowing unregulated physical structures to persist

in ecologically sensitive zones. Strengthening monitoring systems and enforcement mechanisms is therefore critical to ensuring that future coastal development aligns with ecosystem resilience and long-term sustainability goals.

This study successfully achieved its objective of identifying changes in Chl-a concentrations and primary productivity before and after the construction of sea fences and assessing the impact on ecosystem balance. The integration of high-resolution satellite imagery, the NDCI, and the VGPM has proven to effectively detect ecological changes spatially and temporally. It holds potential as a long-term monitoring tool for other tropical coastal regions. Nonetheless, the study was constrained by the absence of in-situ validation data. Future study should incorporate synchronous field-based measurements to enhance the accuracy and robustness of remote sensing-based primary productivity assessments in coastal environments.

ACKNOWLEDGEMENTS

We would like to express our sincere gratitude to the The Freedom to Learn – Independent Campus Program (MBKM), the National Research and Innovation Agency or BRIN, and the Marine Information System Study Program, Indonesia University of Education or UPI. Their support and collaboration have been invaluable in the successful completion of this study. The authors also to thank Planet Labs PBC for providing the high-resolution PlanetScope imagery under a student license through the Planet Education and Research Program.

REFERENCES

Abdullah, A. L., & Dusuki, M. S. A. (2018). Coastal reclamation influence on biological status of coastal waters in Northern Straits of Malacca. *International Journal of Latest Research in Science and Technology, 7*(6), 16-19. doi:10.29111/ijlrst-2018-10959

An Ru., Liu, Y., Qu, C., Zhang, Y., & Wang, Y. (2013). Estimation of chlorophyll-a concentration of case II waters from hyperspectral remote sensing data in NDCI method. *Journal of Lake Sciences, 25*(3), 437-444. (in Chinese with English abstract). doi:10.18307/2013.0319

Ar-ridhaty Akita, E., Gaol, J. L., & Amri, K. (2023). Model Maximum Entropy Untuk Prediksi Daerah Penangkapan Ikan Pelagis Kecil Di Laut Jawa. *Jurnal Ilmu dan Teknologi Kelautan Tropis, 14*(3), 449-461. https://doi.org/10.29244/jitkt.v14i3.45164

Bedford, J., Johns, D. G., Greenstreet, S. P. R., & McQuatters-Gollop, A. (2018). Plankton as prevailing conditions: A surveillance role for plankton indicators within the Marine Strategy Framework Directive. *Marine Policy*. https://doi.org/10.1016/j.marpol.2017.12.021

Behrenfeld, M. J., & Falkowski, P. G. (1997). A consumer's guide to phytoplankton primary productivity models. *Limnology and Oceanography*, *42*(7), 1479-1491. https://doi.org/10.4319/lo.1997.42.7.1479

Dewi, N. N., Kamal, M., Wardiatno, Y., & Rozi. (2018). The exploration of trophic structure modeling using mass balance Ecopath model of Tangerang coastal waters. *IOP Conference Series: Earth and Environmental Science, 137*(1). https://doi.org/10.1088/1755-1315/137/1/012044

Fadlillah, L. N., Sunarto, Widyastuti, M., & Marfai, M. A. (2018). The impact of human activities in the Wulan Delta Estuary, Indonesia. *IOP Conference Series: Earth and Environmental Science, 148*(1). https://doi.org/10.1088/1755-1315/148/1/012032

Fan, W., Xu, Z., Dong, Q., Chen, W., & Cai, Y. (2023). Remote sensing-based spatiotemporal variation and driving factor assessment of chlorophyll-a concentrations in China's Pearl River Estuary. *Frontiers in Marine Science*, *10*, 122. https://doi.org/10.3389/fmars.2023.1226234

Fathia, D. (2021) Analisis produktivitas primer berdasarkan pengukuran kelimpahan fitoplankton dan konsentrasi klorofil-a di perairan Pulau Tangkil, Lampung. Undergraduate thesis. Jurusan Ilmu Kelautan, Fakultas Matematika dan Ilmu Pengetahuan Alam, Universitas Sriwijaya. [Online] Available from: http://repository.unsri.ac.id/ [Accessed: 20 May 2025].

Fitra, F., Zakaria, I. J., & Syamsuardi. (2013). Produktivitas primer fitoplankton di Teluk Bungus. *Biologika, 2*(1), 59-66.

Herdianti, T. P., Yulius., Agus, S. B., Arifin, T., Putra, A., Prihantono, J., Heriati, A., Hartati, S. T., Akhwady, R., Suryono, D. D., Rahmania, R., Ramdhan, M., Hilmawan, A., Ningsih, A., Sadad, S., Mudjijono, M., & Asyiri, A. (2025). Habitat assessment of whale sharks (Rhincodon typus) in Saleh Bay, Indonesia: Linking chlorophyll-a and sea surface temperature using Aqua MODIS data. *Geographia Technica, 20*(2), 52-64. https://doi.org/10.21163/GT_2025.202.04

Jamal, F. (2019). Peran Pemerintah Daerah Dalam Pengelolaan Wilayah Pesisir. Rechtsregel: *Jurnal Ilmu Hukum, 2*(1). https://doi.org/10.32493/rjih.v2i1.2981

Kuang, C., Wang, D., Wang, G., Liu, J., Han, X., & Li, Y. (2024). Impact of reclamation projects on water quality in Jinmeng Bay, China. *Estuarine, Coastal and Shelf Science*. https://doi.org/10.1016/j.ecss.2024.108719

Kumar, R., Kumar, V., Meena, R. C., Meena, P. D., & Kumar, A. (2023). Knowledge mining for the differentiation pattern with respect to the productivity and trophic status of some selected lakes of Western Himalayas. *Frontiers in Environmental Science*, 11, 1009942. https://doi.org/10.3389/fenvs.2023.1009942

Laksana, I. W. (2011) *Analisis pengelolaan wilayah pesisir di Kecamatan Kronjo Kabupaten Tangerang*. Undergraduate thesis. Fakultas Ilmu Sosial dan Ilmu Politik, Universitas Sultan Ageng Tirtayasa. [Online] Available from: http://repositori.untirta.ac.id/ [Accessed: 18th April 2025].

Manuel, A., & Blanco, A. C. (2023). Transformation of the Normalized Difference Chlorophyll Index To Retrieve Chlorophyll-a Concentrations in Manila Bay. International Archives of the Photogrammetry, *Remote Sensing and Spatial Information Sciences*, 217-221. https://doi.org/10.5194/isprs-archives-XLVIII-4-W6-2022-217-2023

Marpaung, S., Prayogo, T., Yati, E., Dwi Purwanto, A., Nandika, M. R., Dirgahayu Domiri, D., & Kushardono, D. (2022). Analisis Karakteristik Net Primary Productivity Dan Klorofil-a Di Laut Banda dan Sekitarnya. *Jurnal Ilmu dan Teknologi Kelautan Tropis, 14*(1), 31-46. https://doi.org/10.29244/jitkt.v14i1.36757

McFeeters, S. K. (1996). The use of the Normalized Difference Water Index (NDWI) in the delineation of open water features. *International Journal of Remote Sensing, 17*(7), 1425-1432. https://doi.org/10.1080/01431169608948714

Mishra, D. R., Schaeffer, B. A., & Keith, D. (2014). Performance evaluation of normalized difference chlorophyll index in northern Gulf of Mexico estuaries using the Hyperspectral Imager for the Coastal Ocean. *GIScience and Remote Sensing, 51*(2), 175-198. https://doi.org/10.1080/15481603.2014.895581

Mishra, S., & Mishra, D. R. (2012). Normalized difference chlorophyll index: A novel model for remote estimation of chlorophyll-a concentration in turbid productive waters. *Remote Sensing of Environment, 117*, 394-406. https://doi.org/10.1016/j.rse.2011.10.016

Nugraheni, D. D., Zainuri, M., & Afi Ati, R. N. (2014). Studi Tentang Variabilitas Klorofil-a dan Net Primary Productivity di Perairan Morosari, Kecamatan Sayung, Demak. *Journal of Oceanography, 3*(4), 519 – 527. Retrieved from: https://ejournal3.undip.ac.id/index.php/joce/article/view/6905

Nuzapril, M., Susilo, S. B., & Panjaitan, J. P. (2017). Hubungan antara konsentrasi klorofil-a dengan tingkat produktivitas primer menggunakan citra satelit Landsat-8. *Jurnal Teknologi Perikanan dan Kelautan*, 8(1), 105-114. https://doi.org/10.24319/jtpk.8.105-114

Nuzapril, M., Susilo, S. B., & Panjaitan, J. P. (2019). Sebaran produktivitas primer kaitannya dengan kondisi kualitas air di perairan Karimun Jawa. *Jurnal Segara, 15*(1), 9-17. https://doi.org/10.15578/segara.v15i1.7559

Pearson, K. (1896). VII. Mathematical contributions to the theory of evolution.—III. Regression, heredity, and panmixia. *Philosophical Transactions of the Royal Society of London. Series A, containing papers of a mathematical or physical character*, (187), 253-318.

Prabuwono, A. S., Kunarso, K., Wirasatriya, A., & Antoni, S. (2023). Investigation of chlorophyll-a variability in Red Sea using satellite-based meteorology and oceanography data. *Geographia Technica, 18*(2), 238-248. https://doi.org/10.21163/GT_2023.182.18

Sambah, A. B., Oktavia, T. D., Kusuma, D. W., Iranawati, F., Hidayati, N., & Wijaya, A. (2020). Oceanographic variability and its influence on pelagic fish catch in the Bali Strait. *Berkala Penelitian Hayati, 26*(1), 8-16. https://doi.org/10.23869/bphjbr.26.1.20202

Saulquin, B., Gohin, F., & Fanton d'Andon, O. (2019). Interpolated fields of satellite-derived multi algorithm chlorophyll-a estimates at global and European scales in the frame of the European Copernicus-Marine Environment Monitoring Service. *Journal of Operational Oceanography, 12*(1), 47-57. https://doi.org/10.1080/1755876X.2018.1552358

Suardiani, N. K., Arthana, I. W., & Kartika, G. R. A. (2018). Produktivitas Primer Fitoplankton pada Daerah Penangkapan Ikan di Taman Wisata Alam Danau Buyan, Buleleng, Bali. *Current Trends in Aquatic Science, 1*(1), 8. https://doi.org/10.24843/ctas.2018.v01.i01.p02

Walpole, R. E., Myers, R. H., Myers, S. L. & Ye, K. E. (2011). *Probability and Statistics for Engineers and Scientists. 9th ed. [Online] Boston, Pearson Education*. Available from: https://spada.uns.ac.id/pluginfile.php/221008/mod_resource/content/1/ProbabilityStatistics_for_Engineers Scientists(9th_Edition)_Walpole.pdf [Accessed 16th June 2025].

Wasehun, E. T., Beni, L. H., Di Vittorio, C. A., Zarzar, C. M., & Young, K. R. L. (2025). Comparative analysis of Sentinel-2 and PlanetScope imagery for chlorophyll-a prediction using machine learning models. *Ecological Informatics, 85*, 102988. https://doi.org/10.1016/j.ecoinf.2024.102988

Werdell, P. J., Franz, B. A., Bailey, S. W., Feldman, G. C., Boss, E., Brando, V. E., Dowell, M., Hirata, T., Lavender, S. J., Lee, Z., Loisel, H., Maritorena, S., Mélin, F., Moore, T. S., Smyth, T. J., Antoine, D., Devred, E., Fanton d'Andon, O. H., & Mangin, A. (2013). Generalized ocean color inversion model for retrieving marine inherent optical properties. *Applied Optics, 52*(10), 2019-2037. https://doi.org/10.1364/AO.52.002019

Wijayanti, T. I., Mitasari, W., Nday, S. U., & Subandrio, A. (2022). Valuasi Lingkungan Melalui Contingent Valuation Methode (CVM) dalam Revitalisasi Waduk Rowo Jombor Klaten. *Jurnal Pembangunan Wilayah Dan Kota, 18*(3), 283-295. https://doi.org/10.14710/pwk.v18i3.36930

Yanuar., Ibnusina, F., Hutahaean, A. A., Doktoralina, C. M., Caniago, A., Alisafira, S., Rumingkang, N. S., Sa'badini, S. A., Mangkurat, R. S. B., Kholil, & Prasetyo, T. (2023). *Menuju Puncak Pengintegrasian Rencana Tata Ruang Darat dan Laut*. 1-90.

Yulius., Aidina, V., Ramdhan, M., & Daulat, A. (2021). Fishing Ground Mapping Based on Chlorophyll-A Distribution Using Aqua Modis Satellite Imagery in The Fisheries Management Area (FMA) 712. *E3S Web of Conferences, 324*, 10-12. https://doi.org/10.1051/e3sconf/202132401007

A COMPARATIVE STUDY OF HILLSLOPE AND SLOPE SEGMENT APPROACHES IN A SEMI-DISTRIBUTED INFLOW PREDICTION MODEL

Thattanaporn KHOMSRI [1*], ***Chatchai TANTASIRIN*** [1], ***Venus TUANKRUA*** [1].

DOI: 10.21163/ GT_2026.211.02

ABSTRACT

Accurate inflow prediction models are essential decision-support tools for effective reservoir management and optimal water resource utilization. Among semi-distributed hydrological models, the hillslope-based approach has traditionally offered the finest spatial resolution. However, this study explores the integration of a higher-resolution spatial discretization method—slope segments—originally introduced by Tantasirin et al. (2016) for soil erosion modeling, into inflow prediction modeling for reservoir systems in the Lam Phra Phloeng watershed, Thailand. The Lam Phra Phloeng watershed was subdivided into 4,839 hillslope units and 54,378 slope segments. Compared to hillslopes, slope segments provided more homogeneous spatial units, reducing internal variability in land use and soil properties. This refinement allowed for more representative Curve Number (CN) values, enhancing the accuracy of runoff estimation using the SCS-CN method. Model performance was evaluated using three metrics—Percentage Error in Peak Flow (PEPF), Root Mean Square Error (RMSE), and Nash–Sutcliffe Efficiency (NSE)—during the validation years 2015, 2019, and 2020. The slope segment-based model consistently outperformed the hillslope-based model. For example, PEPF values were significantly lower (0.18%, 0.18%, and 2.02% vs. 1.25%, 1.47%, and 7.01%), RMSE values were reduced (0.61, 1.23, and 4.32 MCM vs. 0.66, 1.50, and 4.48 MCM), and NSE values were higher (0.94, 0.36, and 0.44 vs. 0.90, 0.30, and 0.40). These results demonstrate that slope segment-based spatial subdivision enhances the predictive performance of inflow models and offers a promising approach for improving hydrological modeling in reservoir systems. Future applications in diverse watersheds could further validate its utility for water resource planning and management.

Key-words: *SCS-CN model; Spatial discretization; Slope segment delineation; Reservoir inflow prediction*

1. INTRODUCTION

Reservoirs are typically formed by constructing dams across streams, with their primary function being the regulation of natural streamflow. This regulation is achieved by storing excess water during wet seasons and releasing it during dry periods to mitigate low river flows. Accurate inflow forecasting is particularly critical during the rainy season, as it directly informs reservoir drainage planning and operational decision-making. A wide range of inflow prediction models are employed as decision-support tools in reservoir management. These models are generally classified based on their spatial representation into three categories: lumped, semi-distributed, and distributed models.

Semi-distributed hydrological models rely on spatial discretization schemes to represent heterogeneity in land use, soils, and topography. Different schemes have been proposed, including sub-catchments, hydrological response units (HRUs), representative elementary areas (REA), geomorphological units, and hillslopes. Each has advantages and weaknesses: sub-catchments reduce computational time but may obscure variability; HRUs capture heterogeneity but are often not spatially explicit; REAs aim for optimal process homogeneity at a given scale; while hillslopes provide finer spatial representation but can still encompass diverse soils and land uses.

---

[1]*Faculty of Forest, Department of Conservation, Kasetsart University, Thailand. *Corresponding author (TK) janjao.geo@gmail.com; (CT) fforcct@ku.ac.th; (VT) ffor.venus@gmail.com.*

The scale of these units directly influences runoff timing, volume predictions, and water balance estimates (Beven, 1993; Reggani et al., 1998; Vannametee et al., 2012, 2013).

While finer units can preserve spatial heterogeneity, they also increase the number of modeling elements, raising challenges of parameterization and computation. Semi-distributed models therefore aim to identify an optimal spatial scale that balances realism with efficiency. Hillslopes are widely used but may remain too coarse for representing local hydrological processes. In response, Tantasirin et al. (2016) introduced slope segments, which subdivide hillslopes into smaller, hydrologically connected planes delineated by stream links and contour lines. These units are more homogeneous in soil and land use properties, and are directly connected to local drainage networks.

Based on this background, we hypothesize that slope segment discretization will improve inflow prediction compared to traditional hillslope units. Specifically, slope segments reduce aggregation errors in land use–soil combinations, yield more representative Curve Number (CN) values, and better capture flow connectivity along hillslopes. At the same time, the scale remains compatible with semi-distributed modeling frameworks, avoiding the parameter burden of fully distributed models. This study evaluates the performance of slope segments against hillslopes to test this hypothesis.

In Thailand, the most commonly used lumped model is the Artificial Neural Network (ANN) model (Suiadee &Tingsanchali,2007; Chiamsathit,2016; Ngamsanroaj et al.,2019; Amnatsan,2021). Distributed models such as the HO8 (Kompor,2021) and wflow_sbm (Wannasin et al.,2021) have also been applied, while the Soil and Water Assessment Tool (SWAT) (Phomcha et al.,2021) serves as a representative semi-distributed model.

Lumped models treat each sub-basin as a single, homogeneous unit. While this approach simplifies computation and enables faster forecasts, it also generalizes spatial variability—such as rainfall-runoff dynamics—across the entire sub-basin. This can lead to parameter inaccuracies and reduced predictive performance. In contrast, distributed models incorporate detailed spatial data, including soil properties, vegetation, and land use, and divide the basin into fine-resolution grids. These models simulate water flow across cells, enabling runoff estimation at ungauged locations and assessments of water quality and land-use impacts (Smith et al.,2004) However, their high computational demands and long processing times can be limiting factors (Ejaz et al.,2022).

Semi-distributed models offer a compromise between these two approaches. They provide a more realistic representation of spatial heterogeneity than lumped models while requiring less computational power than fully distributed models (Tantasirin et al.,2016). These models typically use spatial units such as hydrological response units (HRUs), irregular grids, or hillslopes. Among these, hillslope-based models represent the finest level of spatial subdivision currently used in many semi-distributed frameworks (Flugel,1995). Hillslopes are key hydrological units that channel water to river networks via surface and subsurface pathways (Lapides et al.,2022), and are often divided into three zones: left, right, and top slopes (Fan et al.,2019).

Despite their finer resolution, hillslopes can still encompass large and heterogeneous areas. The size of these computational units significantly influences hydrological responses (Zehe et al.,2014). Larger units may obscure spatial variability, leading to less accurate parameterization and reduced model fidelity (Hutchinson, 1988; Kienzle, 2003; Jha, 2004; Rouhani, 2009). To address this, Tantasirin et al. (2016) introduced a method for subdividing hillslopes into smaller, more homogeneous units called slope segments, initially for soil erosion modeling. However, this finer-scale spatial discretization has not yet been adopted in semi-distributed inflow prediction models.

This study aims to incorporate slope segment-based spatial subdivision into inflow prediction modeling for reservoirs and to evaluate its performance relative to traditional hillslope-based models. By comparing the predictive accuracy of these two approaches, the study seeks to determine whether slope segment discretization can enhance model performance. Improved inflow forecasting has the potential to significantly strengthen reservoir water resource management, particularly in the face of increasing challenges posed by land-use changes and climate variability. Ultimately, more accurate modeling will support more efficient and equitable water allocation across the watershed.

2. MATERIALS AND METHODS

2.1. Automated drainage network extraction

The automated drainage network extraction method proposed by Tantasirin et al. (2016) was adopted, integrating spatial hydrological analysis with Digital Elevation Model (DEM) processing. A 10-m resolution DEM was generated using the ANUDEM algorithm (Hutchinson, 1988; Hutchinson, 1989), followed by hydrological preprocessing to correct topographic depressions ("sinks") using the efficient sink-filling method of Wang & Liu (2006). Flow direction and accumulation were computed using the Rho8 algorithm (Fairfield & Leymarie, 1991), and the Lam Phra Phloeng Dam outlet was designated as the watershed outlet. The Drainage Area Threshold (DAT), which determines stream initiation points, was defined to balance hydrological detail with computational efficiency.

Hydrological and spatial datasets used in this study were compiled from official government agencies (**Table 1**). Rainfall data were obtained from the Thai Meteorological Department (TMD) and the Royal Irrigation Department (RID), while streamflow and reservoir inflow records were provided by RID. Contour maps were sourced from the Royal Thai Survey Department (RTSD) and subsequently converted into a DEM, while land use/cover and soil datasets were supplied by the Land Development Department (LDD). These datasets form the basis for model input, calibration, and validation.

Table 1.

Summary of datasets used in this study.

Dataset	Variable(s)	Source	Units	Resolution	Period
Rainfall gauges	Daily (mm)	TMD & RID	Station points	Daily	2010–2023
Streamflow	Q (m^3/s)	RID	Station points	Daily	2010–2023
Inflow	MCM	RID	Station points	Daily	2010–2023
Contour	Elevation (m)	RTSD	Shapefile	-	2023
DEM	Elevation (m)	Generated from contour data	Raster	10*10 m	2023
Land use/cover	LULC classes	LDD	Shapefile	-	2011,2015,2019
Soil	HSG / texture	LDD	Shapefile	-	2023

2.2. Determination of the Optimal Drainage Area Threshold (DAT)

To identify the optimal DAT, the Number of Error Stream Cells (NESC) method was applied by Tantasirin et al. (2016). Stream networks were extracted using DAT values ranging from 10,000 to 500,000 m^2. The optimal threshold was determined using the Power Rule derivative, identifying the point where error reduction plateaued. The selected DAT of 450,000 m^2 (4,453 cells) minimized spatial errors and was used for subsequent watershed segmentation.

2.3. Slope Segment-Based Spatial Delineation

Following stream extraction, the watershed was subdivided into hydrological units using a hillslope-based approach (Lapides et al., 2022) dividing each sub-watershed into left, right, and upper hillslopes. These hillslopes were further refined into slope segments using Tantasirin's method.

Stream links were extended and segmented at 100-meter intervals, with adjacent land areas defined as slope planes. These were then subdivided along contour lines to form slope segments—smaller, more homogeneous units that enhance spatial resolution. The delineation was implemented using a custom-developed script (**Fig. 1**). To achieve finer spatial resolution, each hillslope unit was further subdivided using the slope segment method introduced by Tantasirin. This method begins by extending the stream links within each hillslope unit. These extended stream links are then segmented at 100-meter intervals, producing a series of stream segments. The land area adjacent to each stream segment is defined as a slope plane. Each slope plane is subsequently subdivided based on contour lines derived from elevation data, resulting in smaller and more homogeneous spatial units known as slope segments (**Fig. 2**). This hierarchical delineation process enhances the spatial granularity of the model, allowing for more accurate representation of hydrological processes. The final delineation of slope segments was implemented using a custom-developed script.

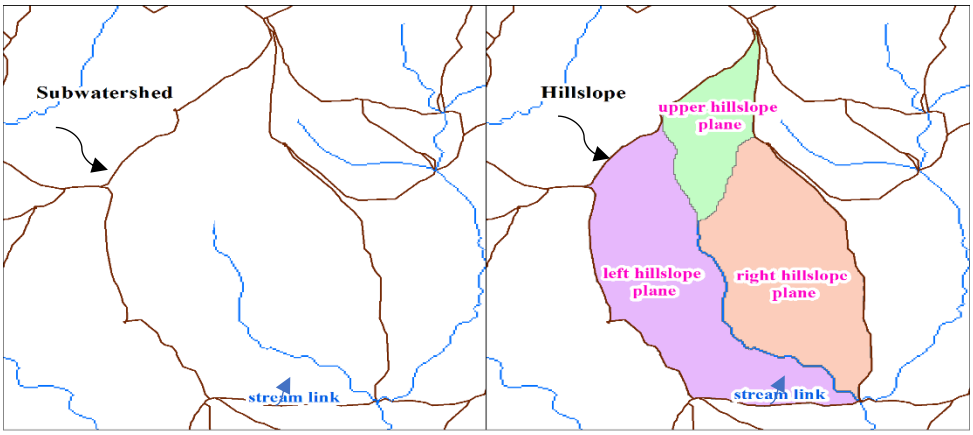


Fig. 1. Sub-watershed delineation and corresponding hillslope units within the Lam Phra Phloeng watershed, illustrating the spatial hierarchy used in the semi-distributed hydrological model.

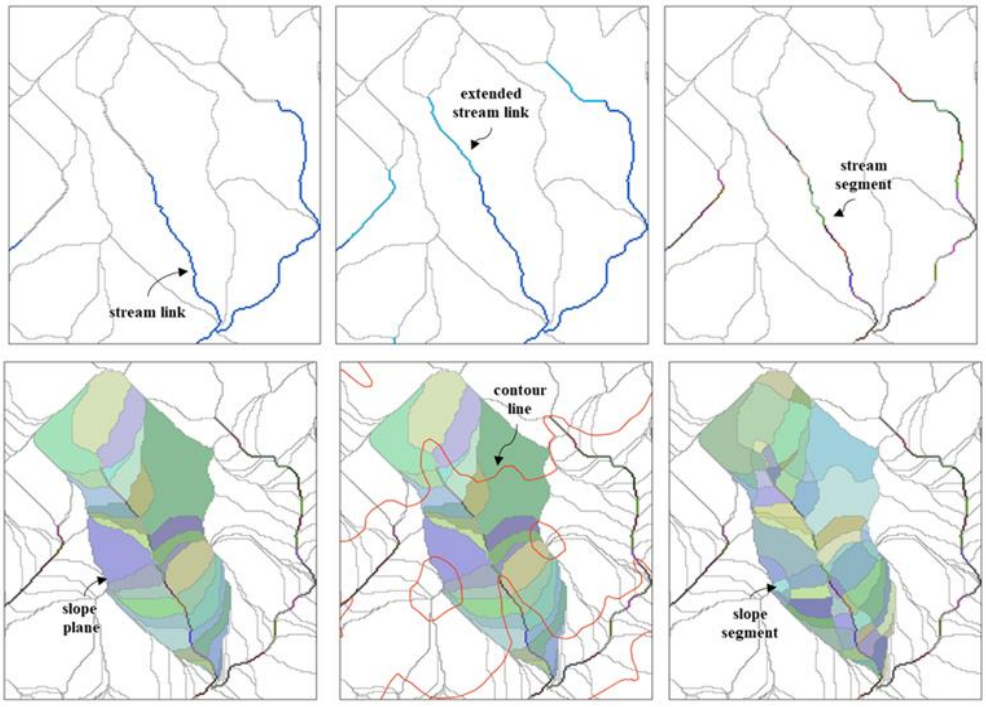


Fig. 2. Procedure for refining hillslope boundaries to smaller, more hydrologically representative units, adapted from Tantasirin, aimed at improving spatial resolution and runoff response accuracy in watershed modeling.

2.4. Reservoir Inflow Modeling

2.4.1. SCS–Curve Number Implementation and Inflow Modeling

The SCS–Curve Number (SCS–CN) method was applied to estimate surface runoff into the Lam Phra Phloeng Reservoir, Thailand. This empirical method is widely used in data-scarce regions due to its simplicity and minimal input requirements (Soil Conservation Service, 1986). It has also been successfully applied in hillslope runoff estimation and spatial runoff modeling in Europe (Crăciun et al., 2007; Crăciun et al., 2009; Haidu & Ivan, 2016; Haidu et al., 2017) and Asia (Tripathi et al., 2006; Lian et al., 2020; Ngamsanroaj & Tamee, 2019).

2.4.2. CN Assignment and Antecedent Moisture Adjustment

Curve Number (CN) values were assigned to each spatial unit based on hydrologic soil group (HSG), land use (LU), and antecedent moisture condition (AMC). AMC adjustment followed USDA (2004) guidelines, using 5-day cumulative rainfall thresholds: CN I: < 35 mm and CN III: > 75 mm

This dynamic adjustment allows the model to account for soil wetness between storm events, improving runoff estimation accuracy (Crăciun et al., 2007). The distribution of HSG–LU combinations across hillslope and slope segment units is summarized in **Table 3** and **Fig. 6**, showing that slope segments preserve greater spatial heterogeneity than hillslopes.

2.4.3. Runoff Calculation

Daily runoff depth for each unit was computed using a custom Python script, implementing the standard SCS–CN equation:

$$Q = \frac{(P-0.2S)^2}{P+0.8S} 3^{f_0 rP} > 0.2S \quad (1)$$

$$S = \frac{254000}{CN} - 245 \quad (2)$$

where: Q = direct runoff (mm); P = total rainfall (mm); S = potential maximum retention after runoff begins (mm); CN = curve number adjusted for AMC.

2.4.4. Routing to the Reservoir

Runoff depth (mm) was converted to volume by multiplying by the unit area (m²). Volumes from all units were routed downstream via the *D8 flow direction network* derived from the DEM. Daily inflow to the reservoir pour point was obtained by summing contributions from all upstream units. Channel hydraulics were not explicitly simulated, consistent with a semi-distributed modeling approach.

2.4.5. Performance Metrics

Model performance was evaluated using three metrics:

$$RMSE = \sqrt{\left(\frac{1}{n}\sum_{t=1}^{n}(Q_t^{sim} - Q_t^{obs}\right)^2} \quad (3)$$

$$NSE = 1 - \frac{\sum_{t=1}^{n}(Q_t^{sim} - Q_t^{obs})^2}{\sum_{t=1}^{n}(Q_t^{obs} - Q_t^{-obs})^2} \quad (4)$$

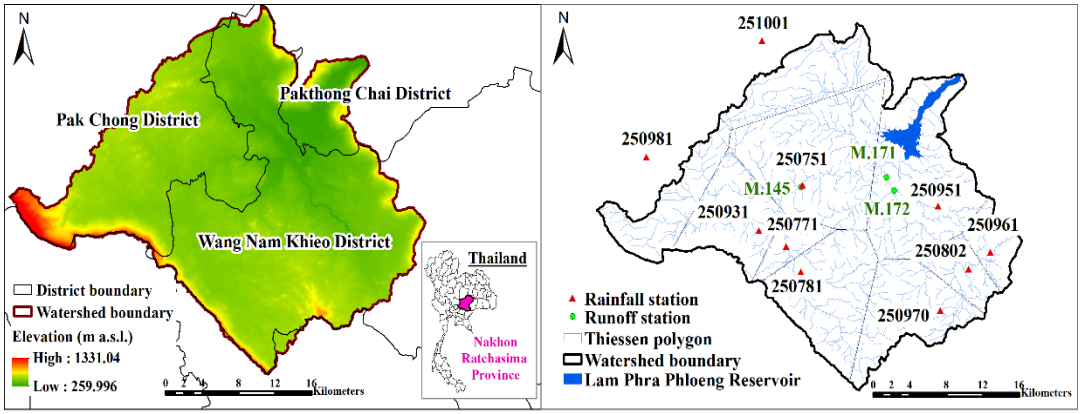
$$PEPF = 100 * \frac{\left(Q_{peak}^{\{sim\}} - Q_{peak}^{\{obs\}}\right)}{Q_{peak}^{\{obs\}}} \quad (5)$$

where: Q^{Sim} and Q^{Obs} are simulated and observed reservoir inflows at time t; Q^{Obs} is the mean observed inflow.

These metrics allow evaluation of both overall hydrograph similarity (RMSE, NSE) and peak flow prediction accuracy (PEPF) (**Fig. 9**).

2.5. Rainfall-Runoff Data Preparation

Hydrological data from 2012–2023 were used, including daily runoff from Stations M.145 and M.171, and inflow data for the Lam Phra Phloeng Reservoir, all sourced from the Royal Irrigation Department (RID). Rainfall data from 10-gauge stations were evaluated for consistency using the Double Mass Curve (DMC) method (Searcy & Hardison,1960), with R^2 used to assess reliability. To account for climate variability, years were categorized by ENSO phase: La Niña: 2013, 2020; Neutral: 2012, 2015, 2018, 2021–2023; El Niño: 2014, 2016, 2017, 2019 Average rainfall was estimated using the Thiessen Polygon method (Arianti et al.,2018) (**Fig. 3**).

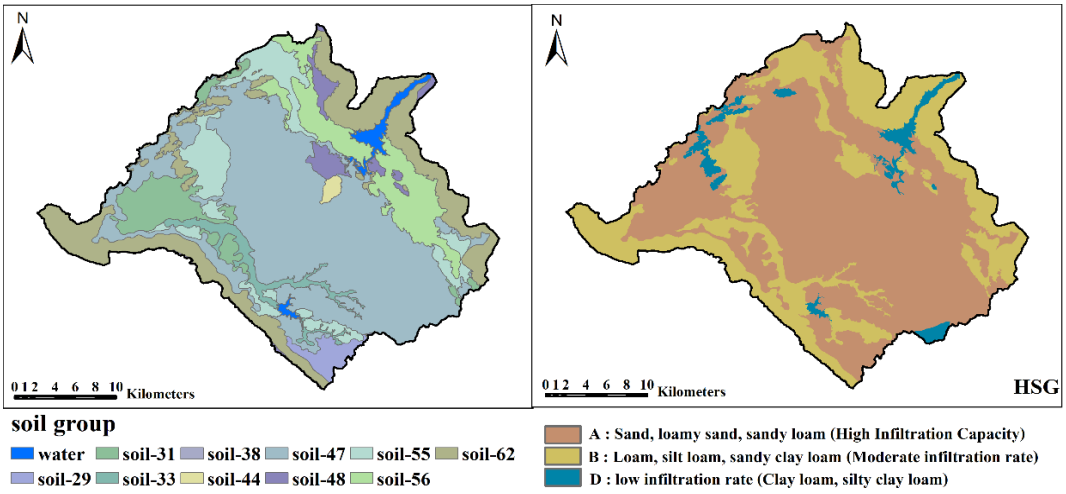


(a) (b)

Fig. 3. Study area and DEM (a); Rainfall and Runoff station in The Lam Phra Phloeng watershed (b).

2.6. Determination of Curve Number (CN)

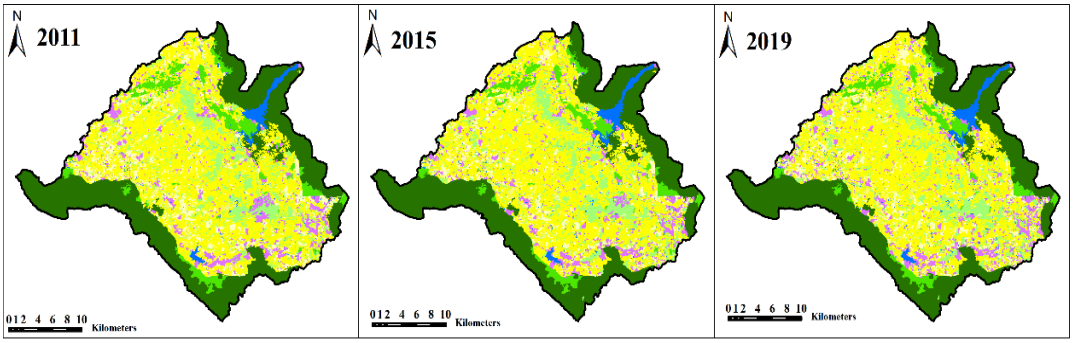
CN values were derived from HSG and land use data provided by the Land Development Department of Thailand. HSGs were classified following Thephasit and Kriangsiri (Thephasit & Kriengsiri, 2001) into: Group A (high infiltration capacity): Soil Groups 29, 31, 38, 44, 47, 56 Group B (moderately high infiltration capacity): Soil Groups 33, 48, 55, 62 and Group D (low infiltration capacity): Water bodies. These classifications are illustrated in **Fig. 4**.



(a) (b)

Fig. 4. Classification derived from 15 soil groups in the Lam Phra Phloeng watershed (a); categorized into Groups A, B, and D based on infiltration capacity (b).

Land use was reclassified into nine categories (e.g., evergreen forest (For_evg), deciduous forest (For_dec), forest plantation (For_plant), rehabilitation forest (For_rehab): includes degraded forests, grasslands, shrublands, and wetlands , paddy fields (A_pad), field crops (A_crp), perennial plantations (A_tree), urban areas (Urb) and water bodies (Wat) and matched to rainfall-runoff years (e.g., 2011 land use for 2012–2013). To ensure temporal consistency with rainfall-runoff datasets, land use data (**Fig. 5**) were matched to the corresponding years: 2011 land use for 2012–2013 (La Niña and Neutral years); 2015 land use for 2014–2015 (El Niño and La Niña years); 2019 land use for 2018–2019 (Neutral and El Niño years). Spatial layers (hillslopes/slope segments, rainfall, HSG, land use) were integrated using raster union and zonal statistics to assign dominant attributes. CN values were then assigned using USDA (2004) (**Table 2** and **Fig. 6**).



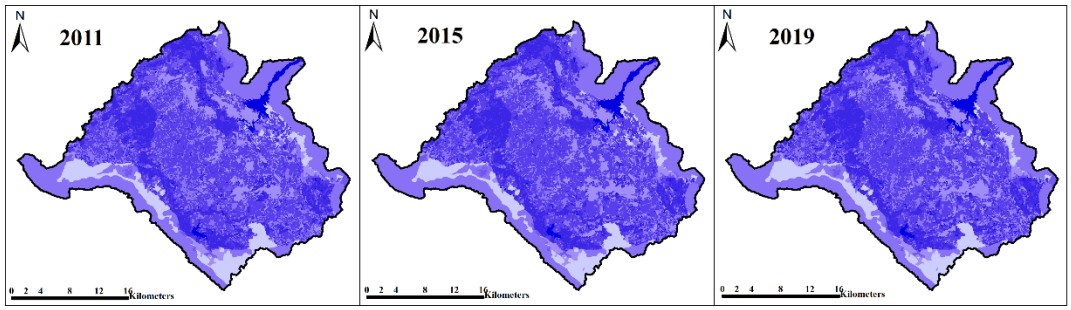
(a) (b) (c)

Fig. 5. Reclassified land use categories in the Lam Phra Phloeng watershed, grouped into nine hydrologically relevant classes for Curve Number assignment: 2011 (a); 2015 (b); 2019 (c).

Table 2.

Initial CN values.

Land Use	HSG		
	A	B	D
For_evg	33.08	57.75	60.00
For_dec	36.75	63.00	76.65
For_plant	42.00	69.30	78.75
For_rehab	47.25	73.50	80.85
A_pad	63.00	84.00	87.15
A_crp	74.09	85.00	89.00
A_tree	52.50	78.75	84.00
Urb	89.25	89.25	89.25
Wat	100.00	100.00	100.00



(a) (b) (c)

Fig. 6. Initial Curve Number (CN) values assigned to each spatial unit based on the intersection of land use and Hydrologic Soil Group (HSG) data, following USDA standard guidelines: 2011 (a), 2015 (b), 2019 (c).

2.7. Model calibration and validation

Given the sensitivity of the SCS-CN method to land use and Hydrologic Soil Group (HSG), a detailed analysis of Curve Number (CN) distribution was conducted for the calibration and validation years. Across the 2011, 2015, and 2019 land use datasets, the dominant types were field crops (A_crp), evergreen forest (For_evg), and rehabilitation forest (For_rehab), with A_crp showing a notable increase over time. The most extensive CN–HSG combinations were: AA_crp: 43.33% (hillslopes), 36.83% (slope segments) and BFor_evg, BA_crp, and AFor_evg followed in area coverage.

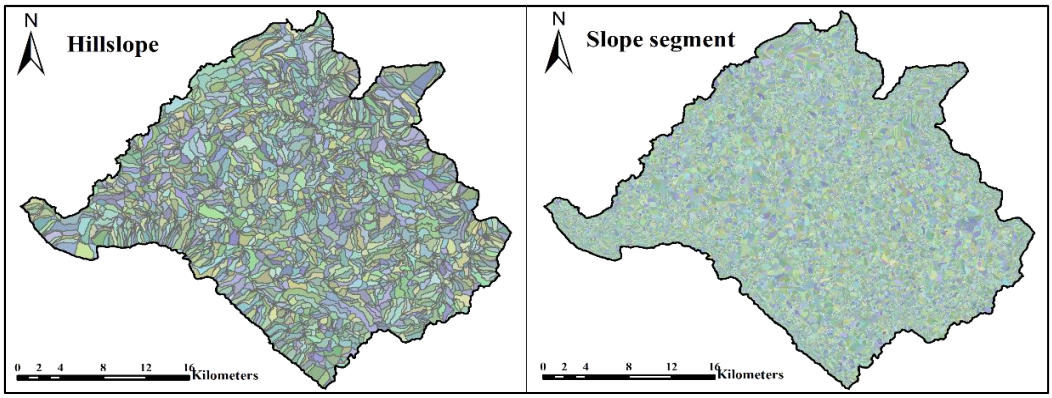
Sensitivity analysis revealed that AA_crp had the greatest influence on runoff predictions, significantly affecting PEPF, NSE, and RMSE. Calibration used data from 2012–2014 (La Niña, Neutral, El Niño), while validation applied 2015, 2019, and 2020 datasets. CN values for AA_crp were fine-tuned using a trial-and-error approach in the developed scripts. Model performance was assessed using: PEPF: Peak flow error (%), with values near zero indicating accuracy (Zhang et al., 2013; Kocyigit et al., 2017; Wang et al., 2025); RMSE: Measures average prediction error; values <50% of the observed standard deviation are acceptable (Sing et al., 2004); NSE: Indicates model efficiency (Nash & Sutcliffe, 1970; Waseem al., 2017).

3. RESULTS AND DISCUSSION

3.1. Watershed Subdivision into Hillslopes and Slope Segments

3.1.1. Number of Spatial Units

The Lam Phra Phloeng watershed was initially subdivided into 4,839 hillslope units and 54,378 slope segment units (**Fig. 7**). To improve computational efficiency and ensure timely forecasting, spatial units smaller than 0.1 km² (for hillslopes) and 0.03 km² (for slope segments) were excluded. This resulted in 1,738 hillslope units, covering 97.0% of the watershed area, and a slope segment model retaining 96.9% of the area. Model testing confirmed that excluding the smallest 3% of the area had no significant impact on performance metrics (PEPF, RMSE, NSE), while reducing simulation time by approximately 15 minutes per cycle.



(a) (b)

Fig. 7. Spatial delineation of the Lam Phra Phloeng watershed into hydrological modeling units: Hillslope units (a), Slope segment units (b).

3.1.2. Hydrologic Soil Group (HSG) and Land Use (LU) Distribution

As shown in **Table 3**, the distribution of HSGs remained relatively stable across the original, hillslope, and slope segment models. Group A soils dominated, accounting for over 63% in all cases. However, land use distributions varied significantly. For example, in 2011: A_crp (field crops) increased from 39.26% in the original data to 51.32% in the hillslope model and 45.65% in the slope segment model. For rehab (rehabilitation forest) decreased from 10.23% to 4.55% (hillslope) and 6.74% (slope segment). Urban areas (Urb) and water bodies (Wat) also showed reduced representation in both models. This pattern was consistent across 2015 and 2019, with A_crp consistently increasing in both models, especially in the hillslope-based approach. These changes reflect how spatial aggregation can influence land use representation; a phenomenon also observed in other studies. For instance, in the Makiogawa River Basin (Japan), varying cell sizes led to different estimates of dominant land cover (Fong & Kawata, 2019). Similarly, Gebrie and Ludwig found that subbasin resolution affected land use proportions in the Blue Nile Basin Gebre & Ludwig, 2014).

Table 3.

Land use (LU) and Hydrologic Soil Group (HSG–LU) distributions calculated by zonal statistics.

Year	Dataset	For_evg	For_rehab	A_crp	A_tree	Urb	Wat	Other	Sum (%)
2011	Original	27.02	10.23	39.26	9.61	6.03	2.01	5.84	100
	Hillslope	29.11	4.55	51.32	4.65	3.86	1.1	5.41	100
	Slope seg	26.41	6.74	45.65	8.29	5.27	1.79	5.85	100
2015	Original	26.86	11.3	40.87	7.03	6.14	2.25	5.55	100
	Hillslope	28.63	5.95	53.18	2.6	3.35	1.19	5.1	100
	Slope seg	26.24	8.18	47.16	5.76	5.16	1.94	5.56	100
2019	Original	26.49	11.17	40.01	8.03	6.8	2.33	5.17	100
	Hillslope	28.45	5.77	52.82	3.04	4.09	1.16	4.67	100
	Slope seg	25.14	5.85	46.39	6.57	0.51	1.79	13.75	100

Percentages in each scenario (Original, Hillslope, Slope segment) sum ≈100%. Small differences (<±0.5%) are due to dominant-class assignment within units and area thresholds.

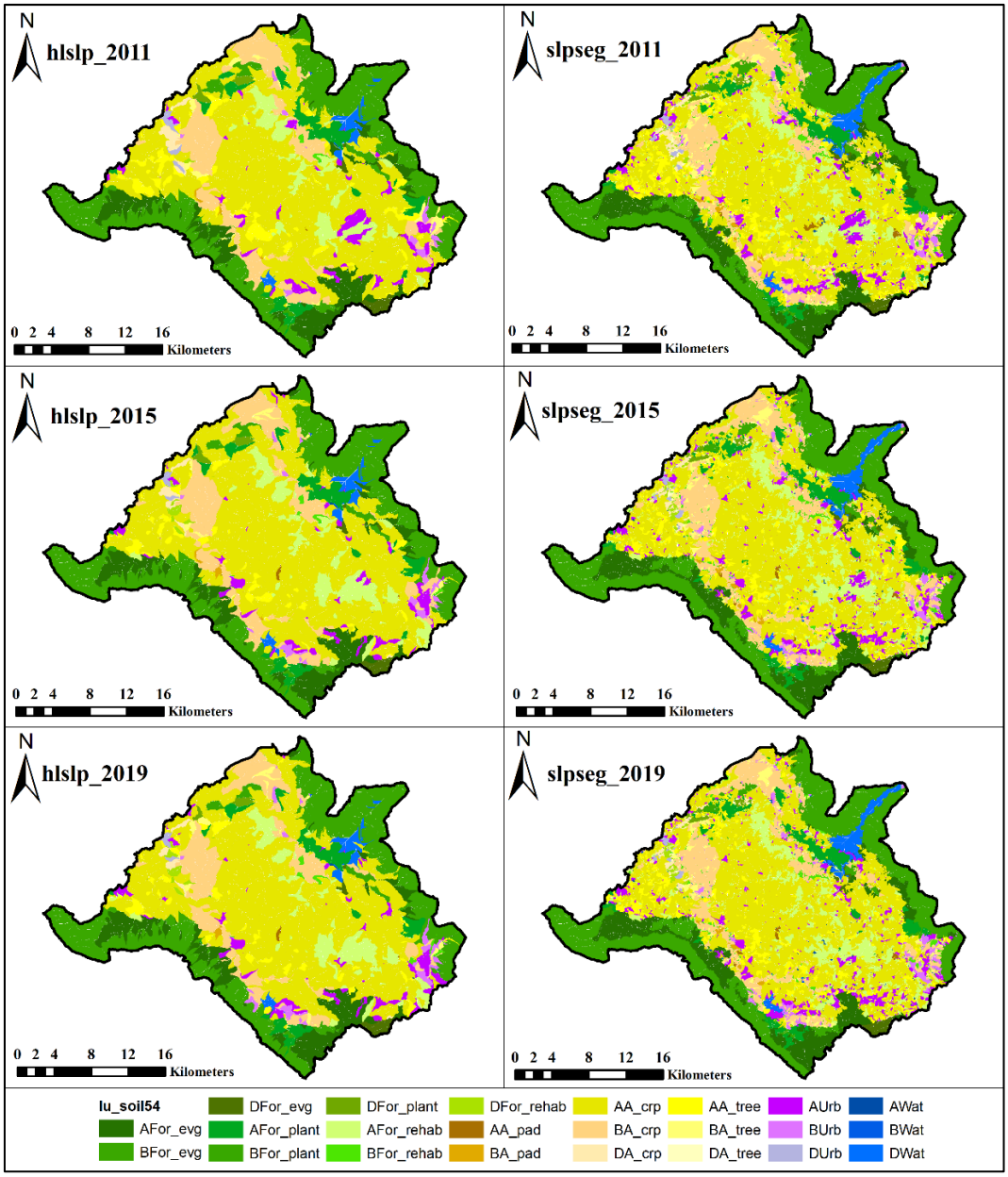
3.1.3. HSG–LU Combinations and Spatial Heterogeneity

The integration of HSG and LU data revealed further differences between the two models. As shown in **Table 4** and **Fig. 8**, the most dominant combination was AA_crp (Group A soil + field crops), which increased from 30.94% in the original data to 41.04% in the hillslope model and 36.34% in the slope segment model for 2011. Similar trends were observed in 2015 and 2019.

Table 4.

Distribution (%) of combined Hydrologic Soil Group and Land Use (HSG–LU) classifications.

Group	2011			2015			2019		
	orig	hlslp	slpseg	orig	hlslp	slpseg	orig	hlslp	slpseg
AFor_evg	7.80	7.73	7.71	7.67	7.32	7.58	7.43	7.16	7.37
AFor_dec	0.00	0.00	0.00	0.02	0.00	0.01	0.02	0.00	0.00
AFor_plant	3.45	3.54	3.49	3.28	3.24	3.38	3.00	3.01	3.17
AFor_rehab	8.59	4.34	5.96	9.49	5.37	7.10	9.28	5.04	7.00
AA_pad	0.27	0.02	0.21	0.20	0.07	0.16	0.20	0.06	0.17
AA_crp	30.94	41.04	36.34	32.09	43.03	37.39	31.53	42.91	36.77
AA_tree	7.35	3.80	6.32	5.38	2.11	4.41	6.16	2.36	5.10
AUrb	4.49	2.88	3.96	4.54	2.30	3.75	5.00	2.77	4.14
BFor_evg	18.56	20.71	18.06	18.53	20.67	18.04	18.43	20.68	17.86
BFor_dec	0.05	0.00	0.06	0.05	0.00	0.06	0.05	0.00	0.01
BFor_plant	1.53	1.36	1.53	1.46	1.24	1.42	1.43	1.22	1.37
BFor_rehab	1.44	0.17	0.64	1.49	0.25	0.78	1.55	0.35	0.87
BA_pad	0.22	0.10	0.24	0.22	0.15	0.22	0.19	0.08	0.18
BA_crp	7.81	9.66	8.83	8.24	9.69	9.28	7.93	9.51	9.12
BA_tree	2.03	0.83	1.78	1.50	0.50	1.23	1.71	0.68	1.36
BUrb	1.21	0.60	1.00	1.33	0.83	1.12	1.54	1.11	1.38
DFor_evg	0.65	0.66	0.64	0.65	0.65	0.63	0.63	0.61	0.60
DFor_dec	0.00	0.00	0.00	0.00	0.00	0.00	0.00	0.00	0.05
DFor_plant	0.31	0.40	0.33	0.30	0.40	0.31	0.30	0.30	0.30
DFor_rehab	0.19	0.04	0.15	0.32	0.33	0.30	0.33	0.39	0.34
DA_pad	0.00	0.00	0.00	0.00	0.00	0.00	0.00	0.00	0.00
DA_crp	0.51	0.62	0.48	0.55	0.46	0.49	0.56	0.40	0.51
DA_tree	0.23	0.01	0.19	0.15	0.00	0.12	0.17	0.00	0.11
DUrb	0.33	0.39	0.31	0.27	0.21	0.29	0.26	0.21	0.28



(a) (b)

Fig. 8. Distribution of Hydrologic Soil Groups (HSG) and Land Use (LU) types across different spatial discretizationsHillslope units (hlslp) (a); Slope segment units (slpeg) (b).

Other combinations, such as BFor_evg and BA_crp, also showed variation between models. The slope segment model generally preserved more heterogeneity due to its finer spatial resolution. For example, in a large hillslope unit containing multiple HSGs and LU types, area-weighted averaging was used to assign a single representative classification. In contrast, slope segments—being smaller—often retained distinct classifications, such as BA_crp instead of AA_crp, which can lead to higher predicted runoff due to higher CN values. This example illustrates how discretizing hillslopes into slope segments enhances spatial heterogeneity, improving the model's ability to represent variations in land use and soil properties, which are critical for accurate runoff prediction.

3.2. Comparison of Inflow Prediction Accuracy

3.2.1. Influence of CN Values on Runoff Prediction

Across all six years of simulation, both the hillslope and slope segment methods demonstrated that increasing the Curve Number (CN) led to higher total runoff volumes. This is expected, as higher CN values indicate reduced rainfall retention capacity, resulting in more surface runoff. The optimal CNII value for the AA_crp (Group A soil + field crops) combination was determined to be 81.5, compared to the USDA (2004) handbook value of 74.9. This 10% increase aligns with findings from Wang et al. (2025) and Lian et al. (2020), who also reported that CN values often need to be adjusted upward from USDA recommendations to improve model accuracy. Lian et al. found CN values up to 33% higher than USDA tables. Using slope segments improves land use–HSG homogeneity, which reduces CN averaging errors. This leads to more realistic initial abstraction and effective rainfall, and better peak timing through routing along locally connected planes.

3.2.2. Model Accuracy: Calibration and Validation

To complement the annual hydrograph comparisons, we conducted an event-based evaluation across the validation years. Rainfall–runoff events were extracted using a threshold of daily rainfall ≥10 mm, and corresponding peak inflows were identified. For each event, Percentage Error in Peak Flow (PEPF), Root Mean Square Error (RMSE), and Nash–Sutcliffe Efficiency (NSE) were computed for both hillslope and slope segment models. **Table 5** summarizes the average and variability (mean ± SD) of event-based metrics. Across all events, the slope segment model consistently achieved lower PEPF, smaller RMSE, and higher NSE than the hillslope model. Model performance was evaluated using PEPF, RMSE, and NSE metrics. The slope segment method consistently outperformed the hillslope method during both calibration and validation phases (**Table 5, Fig. 9**). However, in 2020, both models showed unsatisfactory accuracy. This was attributed to a mismatch in rainfall distribution: while 2013 (calibration year) experienced widespread rainfall, 2020 (validation year) saw heavy rainfall only in the upper and middle watershed. This spatial inconsistency led to inaccurate peak flow predictions. As shown in **Table 5**, heterogeneity preservation was enhanced, which links directly to improved performance metrics such as PEPF and NSE. Event-based evaluation across all validation years (2012–2015, 2019–2020) is summarized in the table. Slope segment units consistently outperform hillslope units, with higher PEPF and NSE and lower RMSE, particularly in years with heterogeneous land use–soil distributions. This suggests that finer representation of local connectivity and CN assignment improves peak discharge timing and overall simulation accuracy (Moriasi et al., 2007; Vannametee et al., 2013).

Table 5.

Event-based performance comparison of hillslope and slope segment units across calibration and validation years.

Period	Unit type	Number of events	PEPF (%)	RMSE (m^3/s)	NSE
Calibration	Hillslope	3	3.93 ± 3.03	2.97 ± 1.06	0.68 ± 0.05
	Slope segment	3	0.34 ± 1.04	2.71 ± 1.16	0.79 ± 0.03
Validation	Hillslope	3	3.91 ± 3.21	2.21 ± 2.00	0.53 ± 0.31
	Slope segment	3	0.79 ± 0.99	2.05 ± 1.56	0.59 ± 0.31

Values are mean ± standard deviation (SD) across multiple rainfall–runoff events. PEPF: peak error in peak flow (%), RMSE: root mean square error (m^3/s), NSE: Nash–Sutcliffe efficiency.

3.2.3. Case Study: 2019 Validation Challenges

In 2019, model accuracy was again unsatisfactory. Although rainfall occurred between September 20–25, the observed inflow did not match the expected hydrograph. Two possible causes were identified: Rainfall was concentrated in the upper watershed, differing from the 2014 calibration year. Inflow data from the Royal Irrigation Department, derived using a water balance method, may have contained inaccuracies. The lower model performance during the 2019 and 2020 events can be attributed to several factors: spatial mismatch of rainfall, inflow estimation uncertainties, and limits

in calibration transfer. While ENSO phases may contribute, the limited number of events precludes strong inference.

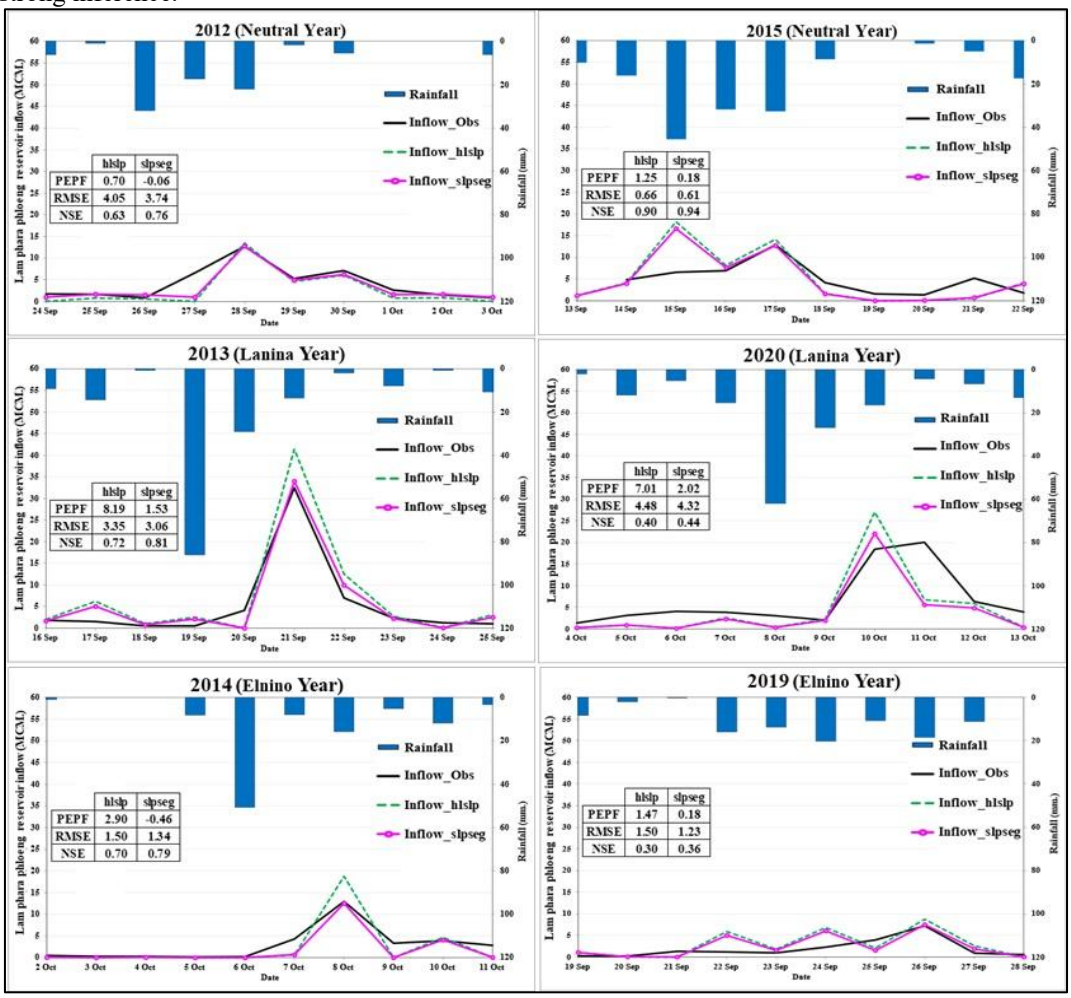


Fig. 9. Performance comparison of reservoir inflow prediction models using hillslope and slope segment methods.

3.2.4. Impact of Spatial Resolution on Model Performance

Subdividing the watershed into smaller slope segments increased spatial heterogeneity, allowing for more homogeneous units in terms of land use, soil group, and rainfall. This improved the representativeness of model parameters and enhanced prediction accuracy. For instance, within the same year, the slope segment model consistently produced lower PEPF values, indicating better alignment with observed peak inflows. This supports findings from Norris and Haan (1993), Kalin et al. (2003), Tripathi et al. (2006), who reported that finer spatial resolution improves peak inflow prediction—critical for reservoir management during the rainy season. Our slope segment method, relying on DEM-derived connectivity and standard CN values, is expected to transfer well to similar data contexts. Testing in contrasting physiography is suggested as future work.

3.2.5. Comparative Performance Metrics

RMSE: Lower in the slope segment model, indicating smaller deviations from observed inflows. NSE: Higher in the slope segment model, suggesting better overall prediction of total inflow volume. These results are consistent with studies by Bingner et al.,1997, Jha et al. (2004), and Rouhani et al. (2009), which found that models with larger sub-areas tend to overestimate total runoff volumes.

3.2.6. Summary on the comparison

The SCS CN method proved effective for inflow prediction in the Lam Phra Phloeng Reservoir. However, the slope segment-based model demonstrated superior accuracy compared to the hillslope-based model, particularly in representing spatial variability and predicting peak and total inflows. The event-based analysis further supports this conclusion, showing that improvements with slope segments were statistically significant across multiple rainfall events, not just isolated years. This strengthens confidence that the method enhances inflow prediction under a range of hydrological conditions.

4. CONCLUSIONS

The results demonstrate that slope segment discretization improved inflow prediction compared to hillslope units across all metrics. The main reason lies in the preservation of land use–soil heterogeneity at smaller scales. As shown in Table 3, slope segments retained distinct combinations (e.g., BA_crp) that were averaged out in hillslopes, leading to more representative CN values. This reduced aggregation error in estimating initial abstraction and effective rainfall, directly improving peak flow predictions. In addition, slope segments are delineated along local drainage links and contours, which enhances flow connectivity and the representation of hillslope hydrological processes. This explains why the slope segment model produced more realistic hydrograph shapes, with improved peak timing and magnitude. Similar findings have been reported in studies on the effect of grid size on runoff predictions (e.g., Hessel, 2005).

Although slope segments increased the number of modeling units, the computational burden remained acceptable within the semi-distributed framework. This suggests that slope segments may represent an optimal compromise scale: fine enough to capture local processes, but still efficient compared to fully distributed models. Years such as 2019 and 2020 showed weaker performance. While spatially uneven rainfall distribution likely played a role, other factors may also have contributed, including inflow data uncertainty and the transferability of calibrated CN parameters. We therefore refrain from attributing performance differences solely to ENSO phases, and suggest further testing with multi-year hydrographs. Overall, slope segments improve model fidelity by reducing spatial averaging errors, enhancing connectivity, and better representing heterogeneity in runoff generation. This supports our initial hypothesis and indicates strong potential for transferring the method to other watersheds with complex terrain and land-use mosaics.

REFERENCES

Amnatsan, S. (2021) Inflow forecasting of Bhavanisagar Reservoir using Artificial Neural Network (ANN). *Sustainable Practices and Innovations in Civil Engineering*, **79**, 119–131. https://doi.org/10.1007/978-981-15-5101-7_12

Arianti, I., Soemarno, Hasyim, A. W. & Sulistyono, R. (2018) Rainfall estimation by using Thiessen polygons, inverse distance weighted, spline, and kriging methods: A case study in Pontianak, West Kalimantan. *International Journal of Education and Research*, **6**, 301-310. https://ijern.com/journal/2018/November-2018/25.pdf

Beven, K. (1993) Prophecy, reality and uncertainty in distributed hydrological modelling. Advances in Water Resources, 16(1), 41–51. https://doi.org/10.1016/0309-1708(93)90028-E

Bingner, R., Garbrecht, J., Arnold, J. & Srinivasan, R. (1997) Effect of Watershed Subdivision on Simulation Runoff and Fine Sediment Yield. *Transactions of the ASAE*. **40**(5): 1329-1335. https://doi.org/10.13031/2013.21391

Chiamsathit, C. (2016). Optimisation of hedging-integrated rule curves for reservoir operation. PhD dissertation, Heriot-Watt University. https://www.ros.hw.ac.uk/bitstream/handle/10399/3168/ChiamsathitC_0616_egis.pdf?isAllowed=y&sequence=1

Crăciun, A.I., Haidu, I. & Bilaşco, Şt. (2007). The SCS-CN model assisted by G.I.S.– alternative estimation of the hydric runoff in real time. *Geographia Technica*, **2**(1), 1–7. https://technicalgeography.org/pdf/1_2007/gt_1_2007.pdf

Crăciun, A.I., Haidu, I., Magyari-Sáska, Zs. & Imbroane, A.I. (2009). Estimation of Runoff Coefficient According to Soil Moisture Using GIS Technique. *Geographia Technica*, **4**(2), 1–10. https://technicalgeography.org/pdf/2_2009/gt_2_2009.pdf

Ejaz, F., Wohling, T., Hoge, M. & Nowak, W. (2022) Lumped geohydrological modelling for long-term predictions of groundwater storage and depletion. *Journal of Hydrology*, 606. https://doi.org/10.1016/j.jhydrol.2021.127347

Fairfield, J. & Leymarie, P. (1991) Drainage networks from grid digital elevation models. *Water Resources Research*, 27, 709-717. https://doi.org/10.1029/90WR02658

Fan, Y., Clark, M., Lawrence, D. M., Swenson, S., Band, L. E., Brantley, S. L. & Yamazaki, D. (2019) Hillslope Hydrology in Global Change Research and Earth System Modeling. *Water Resources Research*, 1737-1772. https://doi.org/10.1029/2018WR023903

Flugel, W.A. (1995) Delineating hydrological response units by geographical information system analyses for regional hydrological modelling using PRMS/MMS in the drainage basin of the River Brol, Germany. *Hydrological Processes*, **9**, 423-436. https://doi.org/10.1002/hyp.3360090313

Fong, A. & Kawata, Y. (2019) Assessing the Influence of Cell Size on Flood Modelling by the PWRI-DH Model Using IFAS. *Journal of Disaster Research*, 14, 188-197.

Haidu, I. & Ivan, K. (2016). Urban runoff pathways and surface water volumes evolution. Case study: Bordeaux 1984–2014, France. (Évolution du ruissellement et du volume d'eau ruisselé en surface urbaine. Étude de cas : Bordeaux 1984-2014, France). *La Houille Blanche*, **5**, 51–56. https://doi.org/10.1051/lhb/2016050

Haidu, I., Batelaan, O., Crăciun, A.I. & Domnița, M. (2017). GIS module for the estimation of the hillslope torrential peak flow. *Environmental Engineering and Management Journal*, **16**(5), 1137–1144. https://eemj.eu/index.php/EEMJ/article/view/3269

Hessel, R., (2005), Effects of grid cell size and time step length on simulation results of the Limburg soil erosion model (LISEM), Journal Hydrological Processes. 19, 3037–3049. https://doi.org/10.1002/hyp.5815

Hutchinson, M.F. (1988) Calculation of Hydrologically Sound Digital Elevation Models. In *Third International Symposium on Spatial Data Handling*, August 17-19, 1988, Sydney, 117-133. https://www.researchgate.net/publication/242529374_Calculation_of_Hydrologically_Sound_Digital_Elevation_Models

Hutchinson, M.F. (1989) A new procedure for Gridding Elevation and Stream Line Data with Automatic Removal of Spurious Pits. *Journal of Hydrology*, **106**(3-4), 211-232. https://doi.org.10.1016/0022-1694(89)90073-5

Jha, P., Gassman, M. & Secchi, S. (2004) Effect of Watershed Subdivision on SWAT Flow, Sediment, and Nutrient Predictions. *Journal of the American Water Resources Association*, 811-825. https://doi.org/10.1111/j.1752-1688.2004.tb04460.x

Kalin, L. & Hantush, M.M. (2003) Assessment of Two Physically-Based Watershed Models Based on Their Performances of Simulating Water and Sediment Movement. In Proceedings, *First Interagency Conference on Research in the Watersheds*, Benson, AZ, October 27 - 30, 2003. USDA Agricultural Research Service, Washington, DC, 316-322. https://www.tucson.ars.ag.gov/icrw/Proceedings/Kalin.pdf

Kienzle, S. (2003) The Effect of DEM Raster Resolution on First Order, Second Order and Compound Terrain Derivatives. *Transactions in GIS*, 8, 83-111. https://doi.org/10.1111/j.1467-9671.2004.00169.x

Kocyigit, M.B., Akay, H. & Yanmaz, A.M. (2017) Effect of watershed partitioning on hydrologic parameters and estimation of hydrograph of an ungauged basin: a case study in Gokirmak and Kocanaz, Turkey. *Arab J Geosci* **10**, 331 (2017). https://doi.org/10.1007/s12517-017-3132-8

Kompor, W. (2021) Use of seasonal streamflow forecast to support reservoir operation for flood mitigation in the Chao Phraya River basin. PhD dissertation, Tokyo Institute of Technology.

Lapides, D., Sytsma, A., Neil, G., Djokic, D., Nichols, M. & Thompson, S. (2022) Arc Hydro Hillslope and Critical Duration: New tools for hillslope-scale runoff analysis. *Environmental Modelling and Software*, 153. https://doi.org/10.1016/j.envsoft.2022.105408

Lian, H., Yen, H. Huang, J.C., Feng, Q., Qin, L., Bashir, M.A., Wu, S., Zhu, X., Luo, J., Di,H., Lei, Q. & Liu, H. (2020) CN-China: Revised runoff curve number by using rainfall-runoff events data in China. *Water Research*, 177. https://doi.org/10.1016/j.watres.2020.115767

Moriasi, D.N., Arnold, J.G., Van Liew, M.W., Bingner, R.L., Harmel, R.D. & Veith, T.L. (2007) Model evaluation guidelines for systematic quantification of accuracy in watershed simulations, *Transactions of the ASABE*, 50(3), pp. 885–900. https://doi.org/10.13031/2013.23153

Nash, J.E. & Sutcliffe, J.V. (1970) River flow forecasting through conceptual models: Part I. A discussion of principles. *Journal of Hydrology*, 10, 282–290. https://doi.org/10.1016/0022-1694(70)90255-6

Ngamsanroaj, Y. Tamee, K. (2019) Improved Model using Estimate Error for Daily Reservoir Inflow Forecasting. https://doi.org/10.37936/ecti-cit.2019132.198508

ECTI Transactions on Computer and Information Technology, 13(2), 170-177.

Phomcha, P. (2021) Suitability of SWAT Model for Simulating of Monthly Streamflow in Lam Sonthi Watershed. *Journal of Industrial Technology*, 7(2), 49-56. https://ph01.tci-thaijo.org/index.php/jit_journal/article/view/3555

Reggiani, P., Sivapalan, M. & Majid Hassanizadeh, S. (1998) A unifying framework for watershed thermodynamics: balance equations for mass, momentum, energy and entropy, and the second law of thermodynamics. Advances in Water Resources, 22(4), 367–398. https://doi.org/10.1016/S0309-1708(98)00012-8

Rouhani, H., Willems, H. & Feyen, J. (2009) Effect of Watershed Delineation and Areal Rainfall Distribution on Runoff Prediction Using the SWAT Model. *Hydrology Research*, 40(6), 505-519. https://doi.org/10.2166/nh.2009.042

Searcy, J. K. & Hardison, C. H. (1960) Double Mass Curves. Manual of hydrology: Part 1. General Surface Water Techniques. US Geological Survey, Water-Supply Paper. https://www.scirp.org/reference/referencespapers?referenceid=396974

Sing, J., Knapp, H.V., Arnold, J. & Misganaw, D. (2004) Hydrologic Modeling of the Iroquois River Watershed Using HSPF and SWAT. Illionois State Water Survey. Champaign, IL, 8. https://www.isws.illinois.edu/pubdoc/cr/iswscr2004-08.pdf

Smith, M.B., Seo, D.J., Koren, V.I., Reed, S.M., Zhang, Z., Duan, Q., Moreda, F. & Cong, S. (2004) The distributed model intercomparison project (DMIP): motivation and experiment design. Journal of Hydrology, **298**(1-4), 4–26. https://doi.org/10.1016/j.jhydrol.2004.03.040

Soil Conservation Service. (1986) Urban Hydrology for Small Watersheds. Technical Release No.55. U.S. Department of Agriculture, Washington, D.C. https://www.hydrocad.net/tr-55.htm

Suiadee, W. & Tingsanchali, T. (2007) A combined simulation–genetic algorithm optimization model for optimal rule curves of a reservoir: a case study of the Nam Oon Irrigation Project, Thailand. *Hydrological Processes*, **21**(23), 3211–3225. https://doi.org/10.1002/hyp.6528

Tantasirin, C., Nagai, M., Tipdecho T. & Tripathi, N.K. (2016) Reducing hillslope size in digital elevation models at various scales and the effects on slope gradient estimation. *Geocarto International*, **31**(2), 140-157. https://doi.org/10.1080/10106049.2015.1004133

Tripathi, M., Rghuwanshi, N. & Rao, G. (2006) Effect of Watershed Subdivision on Simulation of Water Balance Components. *Hydrological Processes*, **20**(5), 1137-1156. https://doi.org/10.1002/hyp.5927

United States Department of Agriculture, Natural Resources Conservation Service. (2004) National Engineering Handbook, Part 630 Hydrology. https://directives.nrcs.usda.gov/sites/default/files2/1712930634/Part%20630%20-%20Hydrology.pdf

Vannametee, E., Karssenberg, D. & Bierkens, M.F.P. (2012) Towards closure relations in the Representative Elementary Watershed (REW) framework containing observable parameters: Relations for Hortonian overland flow. *Advances in Water Resources*, **43**, 52–66. https://doi.org/10.1016/j.advwatres.2012.03.029

Vannametee, E., Karssenberg, D., Hendriks, M.R. & Bierkens, M.F.P. (2013) Hortonian runoff closure relations for geomorphologic response units: evaluation against field data. *Hydrology and Earth System Sciences*, **17**(7), 2981–3004. https://doi.org/10.5194/hess-17-2981-2013

Wang, X. & Liu, J. (2006) An efficient method for identifying and filling surface depressions in digital elevation models for hydrologic analysis and modelling. International Journal of Geographical Information Science, 20(2), 193–213. https://doi.org/10.1080/13658810500433453

Wang, M., Shi, W., Zhao, Y., Yu, J., Chen, T., Bao, J., Song, W. & Chen, H. (2025) A modified curve number method for runoff prediction of different soil types in China. *Catena*, 254. https://doi.org/10.1016/j.catena.2025.108957

Wannasin, C., Brauer, C.C., Uijlenhoet, R., Verseveld, W.J. & Weerts, A.H. (2021) Daily flow simulation in Thailand Part I: Testing a distributed hydrological model with seamless parameter maps based on global data. *Journal of Hydrology*, **34**. https://doi.org/10.1016/j.ejrh.2021.100794

Zehe, E., Ehret, U., Pfister, L., Blume, T., Schroder, B., Westhoff, M. & Kleidon, A. (2014) HESS Opinions: From response units to functional units: a thermodynamic reinterpretation of the HRU concept to link spatial organization and functioning of intermediate scale catchments. *Hydrol Earth Syst Sci*, **18**(11), 4635–4655. https://doi.org/10.5194/hess-18-4635-2014

Zhang, H.L., Wang, Y.J., Wang, Y.Q., Li, D.X. & Wang X.K. (2013) The effect of watershed scale on HEC–HMS calibrated parameters: A case study in the Clear Creek watershed in Iowa, US. *Hydrol Earth Syst Sci*, **17**(7), 2735–2745. https://doi.org/10.5194/hess-17-2735-2013

URBAN LATENT TRANSITION INDEX (ULTI): MAPPING VACANT LAND TRANSFORMATION POTENTIAL IN THE GUATEMALA CITY METROPOLITAN AREA

Jose Luis ARGUETA MAYORGA [1*], ***Mayra Virginia CARVAJAL CASTILLO*** [1], ***Mayra Virginia CASTILLO MONTES*** [1], ***Walter Arnoldo BARDALES ESPINOZA*** [1]

DOI: 10.21163/GT_2026.211.03

ABSTRACT

The Urban Latent Transition Index (ULTI) is a novel spatial tool designed to identify and classify vacant land within the Guatemala City Metropolitan Area based on their potential for urban transformation. Moving beyond traditional approaches that often prioritize central areas, ULTI incorporates accessibility, land price, land cover, and traffic intensity into a composite index, applying K-Means clustering to reveal spatial patterns of latent transition. The results demonstrate that while central zones with higher land value and greater connectivity exhibit strong transformation potential, several peripheral areas also emerge as active transition zones with distinct behavioral profiles. This differentiation underscores the heterogeneous nature of urban change across the metropolitan landscape. By capturing these varied dynamics, ULTI redefines urban vacancy as a latent opportunity for sustainable and inclusive planning; especially in fragmented contexts of developing countries where data infrastructure is limited.

Key-words**:** *Urban Transformation; Vacant Land; Latent Transition Index (ULTI); Spatial Analysis; Geostatistics.*

1. INTRODUCTION

Urban transition refers to the dynamic processes of spatial change that transform intermediate areas between urban and rural zones, shaped by market pressures, accessibility, connectivity, and territorial appropriation. Unlike static approaches that classify land as either urban or non-urban, this notion acknowledges functional, institutional, and ecological instability that gives rise to hybrid landscapes in constant reconfiguration (Hölscher & Frantzeskaki, 2021; Watson, 2009). In such spaces, transition is not only physical but also political and social, as it responds to both capital-driven logic and informal urbanization processes. In the case of Latin America, and particularly Guatemala, these transitions often occur without formal planning, making them difficult to detect through conventional methods.

Within this framework, the notion of urban latency provides a forward-looking interpretation of territory. As Németh and Langhorst (2014) and O'Callaghan (2024) explain, latency does not imply an absence of use but rather an embedded potential: a state of anticipation in which certain conditions accumulate and may trigger transformation. This perspective is particularly relevant for vacant land, which can generate negative impacts while also containing opportunities for future development. Research highlights that vacant parcels can reduce property values, fragment communities, and delay service provision (Inostroza, 2017; Kim & Newman, 2021; Lee & Newman, 2019; Newman & Lee, 2019), as well as negatively influence neighborhood property values and create localized disamenities (Noh et al., 2021). At the same time, indicators such as land price, proximity to the urban core, traffic intensity, and land cover composition act as indirect signals of predisposition to urban change (Lee & Newman, 2017; Song et al., 2020), positioning vacancy not merely as a void but as a latent element within broader urban transformation dynamics (Rahman et al., 2020).

---

[1] *Unidad de Modelación Matemática e Investigación, Facultad de Ingeniería, Universidad de San Carlos de Guatemala.* [*]*Corresponding author (JLAM) jlargueta02@ingenieria.usac.edu.gt; (MVCC) 2050848420101@ingenieria.usac.edu.gt; (MVCM) 1901275620101@ingenieria.usac.edu.gt; (WABE) 1974958690501@ingenieria.usac.edu.gt.*

Nevertheless, existing indices often leave gaps in identifying where transition pressure is most acute. For example, indices such as the Urban Liveability Index (Higgs et al., 2019) evaluate quality-of-life outcomes but do not address transformation feasibility. Likewise, while theoretical work by Hölscher and Frantzeskaki (2021) emphasizes adaptive governance, it lacks operational tools for detecting sites of transition. In Global South contexts such as Guatemala, limited availability of regulatory and zoning data further complicates this task, reflecting structural challenges shaped by informality and fragmented institutional arrangements. Building on these gaps, the present research introduces the Urban Latent Transition Index (ULTI) as a novel methodological contribution to the study of spatial transformation in metropolitan areas, particularly within developing-country contexts. Unlike traditional approaches that rely on isolated indicators such as distance to the city center or land price (Baba & Asami, 2017; Lee & Newman, 2017; Yamazaki, 2001), ULTI integrates multiple spatial, economic, and infrastructural dimensions into a unified and scalable framework, consistent with recent calls for comprehensive and context-sensitive analytical tools (Naghibi, 2024; O'Callaghan, 2024). One of its core innovations is the combination of diverse indicators such as accessibility measures (distance to the city center and travel time), land market dynamics (price per square meter), traffic intensity (flows of light and heavy vehicles), and land use composition (forest, crops, pasture, water) into a single analytical model. These variables collectively provide a holistic representation of the pressures and opportunities shaping transition readiness.

A further methodological strength of ULTI lies in its continuous scoring system. Rather than relying on binary or categorical classifications, the index assigns normalized values ranging from zero to one, which facilitates nuanced spatial comparisons and prioritization of sites according to relative transformation potential. The use of Min–Max normalization ensures comparability among heterogeneous variables (measured in different units such as quetzales, kilometers, minutes, vehicle counts, and percentages) and prevents variables with large ranges, such as traffic flows, from dominating the analysis. This design enhances interpretability, supports longitudinal monitoring, and is compatible with spatial clustering. Indeed, the integration of K-Means clustering strengthens the analytical framework by grouping vacant land into zones of similar transformation potential. These spatially explicit typologies, built on geographic coordinates and ULTI scores, can be visualized against development patterns, while distance buffers and geospatial overlays enhance the identification of transition gradients and potential priority zones.

The objective of this research is to construct and apply the Urban Latent Transition Index (ULTI) as a spatial analytical tool that integrates variables related to accessibility, land use morphology, traffic intensity, and land market value. The purpose is to identify, classify, and evaluate vacant land in the Guatemalan City Metropolitan Area according to its potential for urban transformation, and to interpret spatial patterns that reflect varying levels of transition readiness. The hypothesis guiding this study is that vacant land with shorter travel times, higher land prices, lower ecological constraints, and greater traffic intensity presents significantly higher latent transition potential than lands located in peripheral or environmentally constrained areas, as measured by the ULTI score.

2. STUDY AREA

This study is grounded in the context of the Guatemala City Metropolitan Area (GCMA), functionally defined by Carvajal and Argueta (2025). The GCMA is a rapidly expanding Latin American region that faces spatial and institutional challenges shaped by limited coordination, unequal infrastructure provision, widespread informal urbanization, and ecological constraints such as ravines and steep slopes. Despite these limitations, it remains Guatemala's principal urban center, concentrating over four million inhabitants and serving as the nation's political, economic, and cultural core. Vacant land is here defined as urban or peri-urban parcels that are unbuilt, abandoned, or used only for temporary functions such as informal parking or open storage, without permanent residential, commercial, or institutional uses. Lands were considered if they exceeded 200 m², following thresholds commonly applied in land vacancy studies (Yamazaki, 2001; Song et al., 2020). This definition excludes greenfield agricultural areas in continuous production but incorporates land

that, due to location and context, demonstrates latent potential for urban transition. While anchored to the GCMA boundary, the analysis also considers adjacent areas when their proximity and linkages suggest metropolitan relevance.

3. DATA AND METHODS

3.1. Methodology

To develop the Urban Latent Transition Index (ULTI), we constructed a comprehensive dataset of vacant land within the Guatemala City Metropolitan Area. The primary data on vacant land was collected directly by the authors through field surveys and georeferenced mapping campaigns (2023–2025). Complementary variables were obtained from the following sources: (i) land price data compiled from real estate companies, appraisal reports, and market platforms operating in Guatemala (2023–2025); (ii) distance to the urban center and travel time estimated using the Google Maps API (2024–2025), which captured both Euclidean distances and network-based accessibility; (iii) traffic intensity data (light and heavy vehicles) provided by the Unidad de Conservación Vial and the Ministry of Communications, Infrastructure and Housing (CIV, 2024), which report traffic volumes along metropolitan road corridors; (iv) land cover classifications (forest, crops, grasslands, and water) processed from Landsat 8 Operational Land Imager (OLI) imagery supplied by the United States Geological Survey (USGS, May 2023); and (v) administrative boundaries and base maps adapted from Carvajal and Argueta (2025). Each land was georeferenced using the WGS 1984 coordinate system, enabling spatial analysis, clustering, and visualization.

Fig. 1 displays a geospatial map showing the distribution of vacant land within the Guatemala City Metropolitan Area. Each black dot represents a registered vacant land, revealing a high concentration across the urban and peri-urban zones that span multiple municipalities in the departments of Guatemala, Sacatepéquez, and parts of El Progreso, Escuintla, and Santa Rosa. The clustering pattern highlights areas with significant land availability or vacant land within the metropolitan fabric.

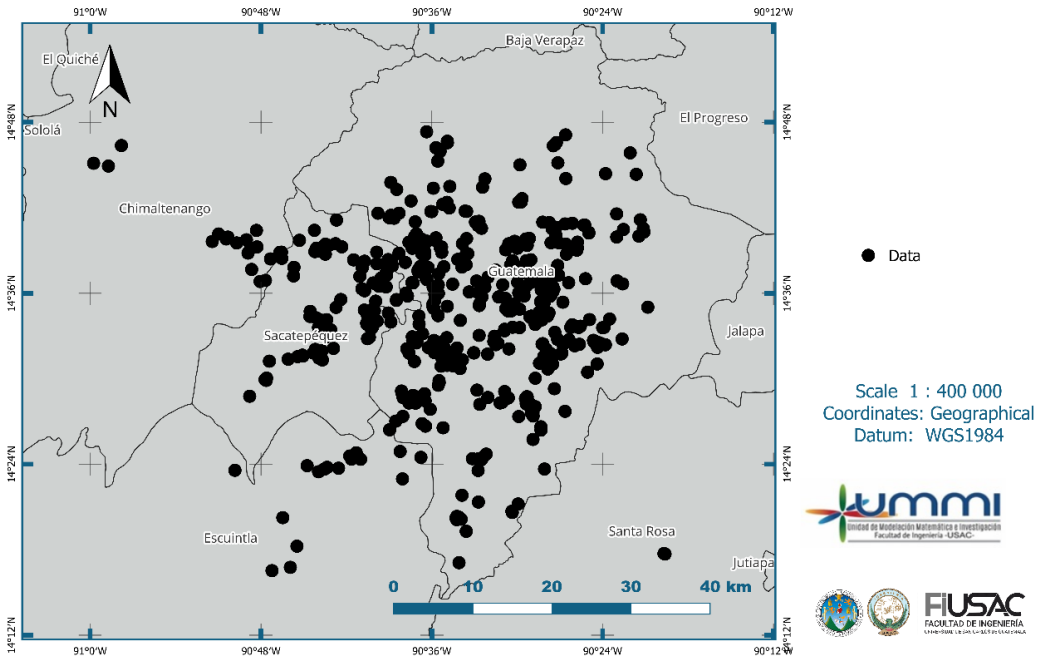


Fig. 1. Spatial Distribution of Data Collection Points in the Guatemala City Metropolitan Area.
Data source: Own field survey and database of vacant land collected by the authors (2023–2025).

Within the Guatemala City Metropolitan Area, **Fig. 2** shows the spatial distribution of vacant land using concentric rings extending from the urban core, delineating zones at 5, 10, 15, 20, and 25 kilometers. This visualization emphasizes the transitional urban peripheral zone, located roughly between 10 and 20 kilometers from the center, where development dynamics are most pronounced.

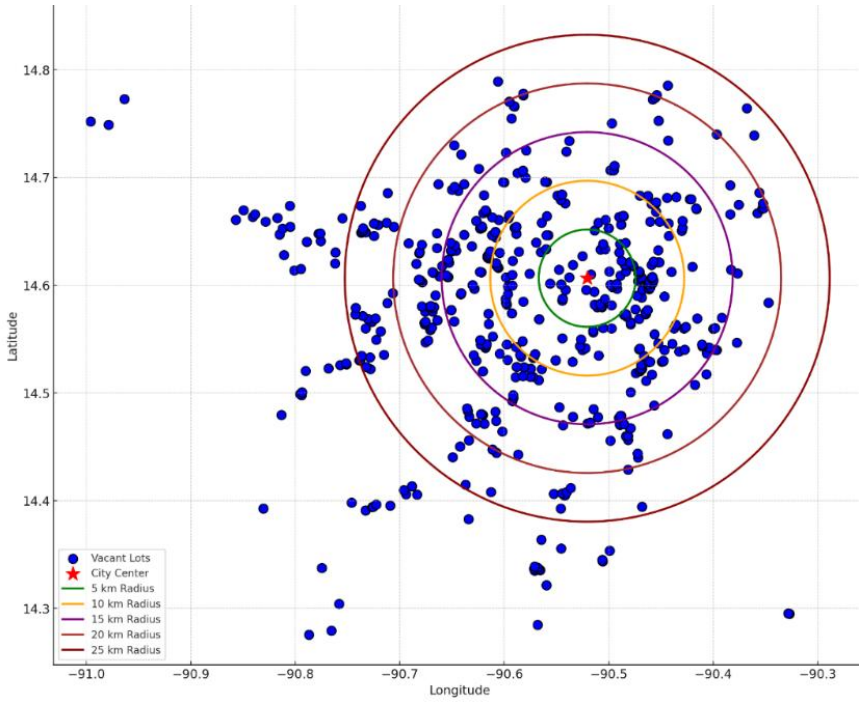


Fig. 2. Spatial Distribution of Vacant Land Around Guatemala City Center with Distance-Based Influence Zones. *Data source: Authors' own field survey and georeferenced database of vacant land (2023–2025)*

To reflect the intensity of urban activity, we included traffic volume data, distinguishing between light and heavy vehicle flows at nearby transport corridors. This indicator serves as a proxy for commercial activity, accessibility, and infrastructure demand. In parallel, we incorporated land cover classifications (forest, crops, grasslands, water) by processing Landsat 8 imagery (USGS, May 2023) through supervised classification techniques. Each land was georeferenced using latitude and longitude coordinates, enabling spatial analysis, clustering, and visualization.

ULTI was designed as a composite spatial index that quantifies latent pressure for urban transformation. It integrates indicators related to urban flow, proximity to the metropolitan core, market signals, and ecological resistance. Specifically, parcels with high traffic volumes, shorter travel distances, elevated land prices, and lower percentages of forest and pasture were assigned higher scores. Because these indicators are measured in heterogeneous units—such as quetzales per square meter, kilometers, minutes, vehicle counts, and percentages—it was necessary to apply a normalization procedure to ensure comparability and balanced influence across variables.

To normalized, the Min–Max normalization (Ahmad et al., 2014) was used, which rescales each variable X to a standardized range between 0 and 1 according to the expression:

$$X' = \frac{X - X_{min}}{X_{max} - X_{min}}$$

where X' is the normalized value, X is the original observation, and X_{min} and X_{max} are the minimum and maximum values of the variable within the dataset.

This transformation preserves the relative distances between observations and maintains the original distribution shape, unlike other methods (e.g., z-scores) that assume normality. By constraining all indicators to the same scale, Min–Max normalization avoids the problem of dominance by variables with large numerical ranges (e.g., traffic counts in thousands versus percentages of land cover). This approach ensures: (i) direct comparability across spatial, market, and environmental indicators; (ii) interpretability of ULTI values as degrees of transformation potential, ranging from 0 to 1; and (iii) balanced contributions in the clustering algorithm, given that K-Means relies on Euclidean distances.

To interpret the spatial distribution of transformation potential, we applied a K-Means clustering algorithm that used both geospatial coordinates and ULTI scores. This method enabled us to group parcels with similar characteristics into distinct transformation typologies. We initially classified the study area into three general clusters (central, transitional, and peripheral) and then refined the analysis into a five-cluster model to capture finer-grained variations. These clusters reveal spatial patterns and allow for the identification of high-priority zones for urban reinvestment or policy attention.

The results were visualized using Python libraries (GeoPandas, Matplotlib**)**. We generated thematic maps displaying spatial clusters, distance rings from the urban core, and convex hulls enclosing cluster boundaries. Additionally, land price gradients were mapped to detect economic patterns associated with transformation potential. These visual tools make the complex relationships in the data more interpretable and actionable for urban planners, policymakers, and stakeholders.

3.2. Theorizing the Variables of the Urban Latent Transition Index (ULTI)

The ULTI is grounded in theoretical recognition that vacant land can act as indicators of urban transformation. Rather than seeing vacancy solely as a sign of decline, ULTI interprets these spaces as thresholds of change. This approach reflects current urban studies literature, which frames vacancy as a condition with latent potential for regeneration and reintegration into the urban fabric (Németh & Langhorst, 2014; O'Callaghan, 2024).

1. Accessibility and Distance Variables: Travel Time and Distance to Center Travel time and distance to the urban core are key indicators of spatial centrality and accessibility. These measures affect land desirability and are often correlated with transformation potential. Lee and Newman (2017) argue that central areas are more likely to attract investment and redevelopment. Similarly, Baba and Asami (2017) and Yamazaki (2001) emphasize that areas close to dense urban centers often experience stronger economic activity and land value appreciation. Accessibility also reflects infrastructure provision and connectivity, both of which are vital for transformation, particularly in peri-urban areas (Naghibi, 2024).
2. Land Use and Morphological Structure: Crops, Forest, Pasture, Water Land cover types serve as indicators of a parcel's environmental function and development constraints. The ULTI includes variables such as forest, crops, pasture, and water to assess ecological resistance or capacity for transformation. Naghibi (2024) note that land cover is a proxy for environmental resilience, and areas with significant forest or water presence may face restrictions despite their locational advantages. Meanwhile, Lee et al (2018) argue that morphology plays a key role in shaping urban expansion trajectories.
3. Traffic Intensity and Urban Flow Traffic data provides insight into the functional role of each area within the urban system. High traffic volumes indicate vibrant activity and accessibility, signaling readiness for land use intensification. As Higgs et al (2019) and O'Callaghan (2024) explain, traffic corridors are often aligned with commercial growth. In areas where formal planning data is scarce, traffic flow serves as an indirect but valuable proxy for spatial transformation. Owusu-Ansah (2018) also highlights how traffic patterns often reflect informal dynamics and bottom-up urbanization processes.
4. Land Price: Speculative and Institutional Value Land price represents both market perception and institutional interest. In contexts with limited planning data, price acts as a synthetic

indicator capturing economic anticipation and development constraints. Lee and Newman (2019) and Yamazaki (2001) suggest that land prices reflect accessibility, desirability, and speculative expectations. O'Callaghan (2024) further points out that in fragmented governance systems, market signals may precede formal policy action, making price data a critical tool for early-stage identification of transformative zones.

The variables incorporated (**Table 1**) into the Urban Latent Transition Index (ULTI) reflect a multidimensional framework for assessing the transformation potential of vacant land. Land price serves as a proxy for speculative demand and urban integration prospects, supported by Song et al (2020) and Yamazaki (2001). Distance to the urban center and travel time capture both static and dynamic dimensions of accessibility, essential for understanding spatial centrality and infrastructure reach, as emphasized by Baba and Asami (2017) and Lee et al (2018). Traffic intensity further enriches this dimension by indicating functional pressure and mobility relevance (Higgs et al, 2019; O'Callaghan, 2024). Environmental constraints are integrated through forest cover and land use typologies such as crops, pasture, and water bodies, which differentiate ecological resilience and productive underutilization (Naghibi, 2024; Rahman et al, 2020).

Table 1.

Empirical Foundations of the Urban Latent Transition Index (ULTI): Variable Selection and Supporting Studies.

Variable	Role in ULTI	Data Source	Justifying Literature
Land Price (per m²)	Serves as a proxy for market demand, perceived land utility, and speculative or institutional value. Higher prices often anticipate future urban integration.	Compiled from real estate companies, appraisal reports, and market platforms (2023–2025).	Yamazaki (2001) links land price to transformation triggers; Song et al. (2020) identifies speculation and insufficient investment as drivers of vacant land.
Distance to Urban Center	Indicates spatial centrality. Proximity to city centers correlates with access to services and infrastructure, increasing likelihood of development.	Calculated from parcel coordinates using Google Maps API (2024–2025).	Baba & Asami (2017); Lee & Newman (2017); Naghibi (2024) support centrality as a key transformation factor.
Travel Time	Adds a dynamic layer to accessibility by considering network and congestion effects beyond physical distance.	Estimated using Google Maps API travel time data (2024–2025).	Lee et al. (2018) use travel time as a critical metric of accessibility and land development viability.
Traffic Intensity	Reflects functional intensity of urban space. Heavy and light traffic volumes serve as proxies for mobility demand and infrastructural relevance.	*Unidad de Conservación Vial* and Ministry of Communications, Infrastructure and Housing (CIV, 2024).	Higgs et al. (2019); O'Callaghan (2024); Owusu-Ansah (2018) argue that traffic density can highlight emerging zones of pressure and informal expansion.
Forest Cover (%)	Signals ecological resilience or environmental constraint. High values indicate protected or less suitable areas for urban development.	Processed from Landsat 8 OLI imagery (USGS, May 2023).	Naghibi(2024); Rahman et al. (2020) link forest coverage to transformation resistance and legal-environmental buffers.
Crops, Pasture, Water (%)	Identify existing land uses with varied transformation potential. Crop and pasture areas may reflect productive rural zones or land banking. Water is a strong spatial constraint.	Processed from Landsat 8 OLI imagery (USGS, May 2023).	Song et al. (2020) treats vacant land as agricultural land as latent vacancy; Naghibi (2024) assess such cover types in urban expansion modeling.
Geographic Coordinates	Used for spatial clustering, mapping, and interpolation of ULTI scores. They do not influence transition directly but enable geographical modeling.	Authors' field survey and georeferenced database of vacant land (2023–2025).	Higgs et al. (2019); Lee et al. (2018) geocode parcels for spatial segmentation in clustering-based typologies.

Data Source: Own elaboration based on reviewed literature and the authors' integrated dataset (2023–2025).

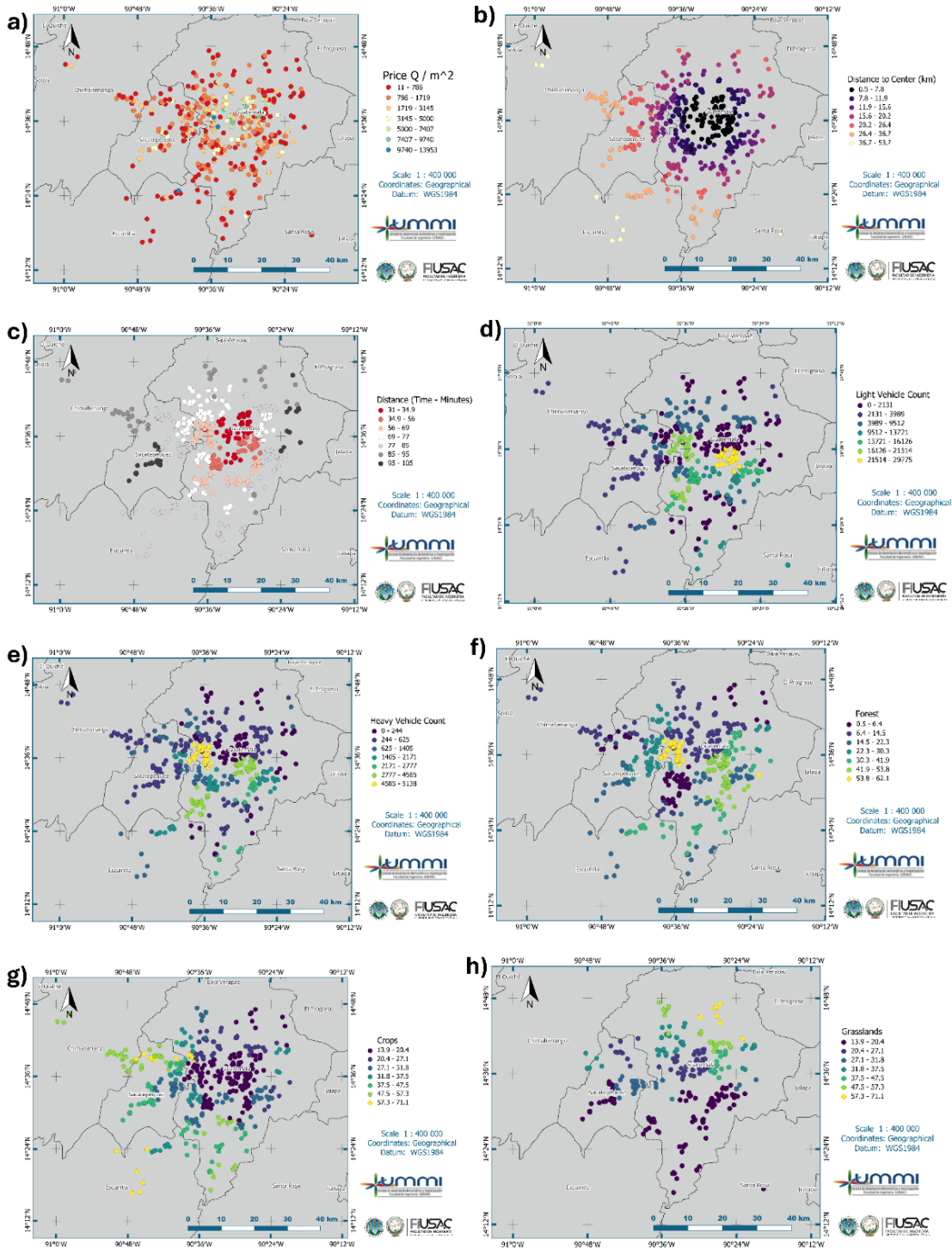


Fig. 3. Spatial Distribution of Key Variables for the Urban Latent Transition Index (ULTI) in the Guatemala City Metropolitan Area. a) land price (in Quetzales), b) distance to the center (in kilometers), c) distance to the center (in minutes), d) light vehicle trips to the center, e) heavy vehicle trips to the center, f) area of forest cover, g) area of crop cover, and h) area of grassland cover.
Data source: Authors' elaboration based on data described in Methods.

Lastly, geographic coordinates support spatial clustering and mapping without directly affecting transition probabilities, enabling the spatial modeling backbone of the ULTI approach (Higgs et al, 2019; Lee et al, 2018). Our findings also support broader methodological arguments that composite indices provide a robust way to integrate heterogeneous urban variables into a single framework (Rahman & Szabó, 2022), especially in data-scarce contexts.

This set of maps (**Fig. 3**) illustrates the spatial distribution of key variables used to calculate the Urban Latent Transition Index (ULTI) within the Guatemala City Metropolitan Area, integrating economic, accessibility, mobility, and land-use dimensions. Variables such as land price, distance to the center (both in kilometers and minutes), and vehicle counts (light and heavy) reflect urban intensity and connectivity, while the presence of forest, crops, and grasslands indicates environmental and rural land-use contexts. The combined analysis of these layers allows the identification of zones with latent potential for urban transformation, particularly those that balance high accessibility and mobility with lower land values and compatible land cover types, offering a comprehensive view of areas likely to experience spatial transitions.

4. RESULTS

Fig. 4 presents the distribution of ULTI scores for vacant land in the Guatemala City Metropolitan Area, ranging from 0 to 1. Higher values, represented by lighter tones, are concentrated in the central and eastern sectors, reflecting zones with stronger transformation potential. In contrast, lower values, indicated by darker tones, predominate in peripheral areas, where transition conditions are comparatively weaker. This spatial variation provides a quantitative representation of differentiated transformation potential across the metropolitan area.

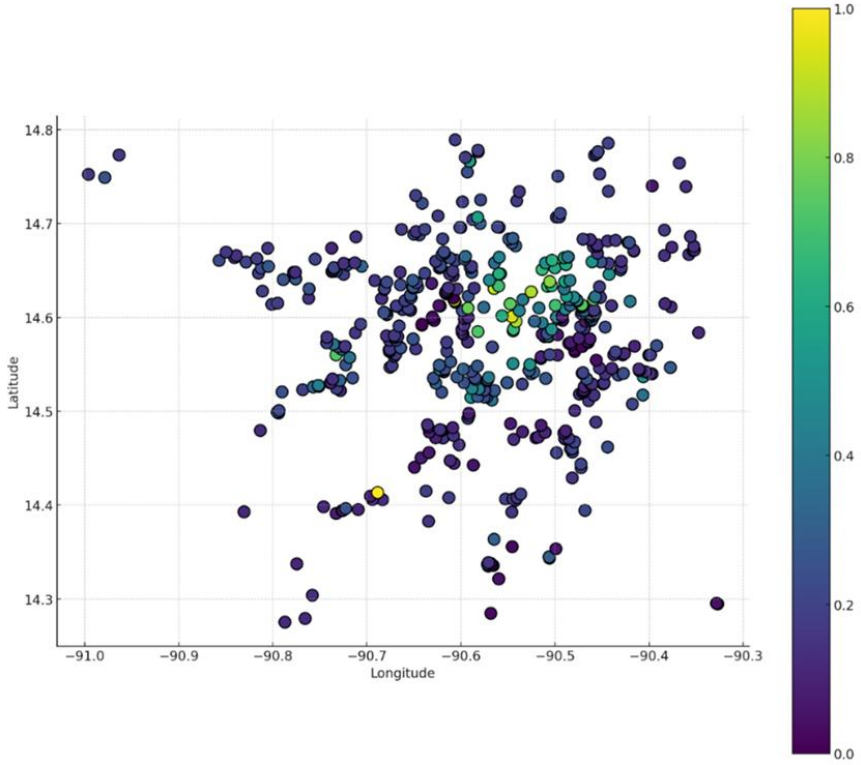


Fig. 4. Spatial Distribution of Vacant Land Classified by Urban Latent Transition Index (ULTI) Scores in the Guatemala City Metropolitan Area.

Data source: Own elaboration based on the variables considered (land price, distance to urban center, travel time, traffic intensity, forest cover, crops, and grasslands).

Fig. 5 presents a reclassification of vacant land into three latent transition categories: low, medium, and high potential. This categorization sharpens the differentiation of spatial patterns by consolidating the underlying variability into interpretable zones. Parcels with high transition potential are concentrated in the central and northeastern sectors of the metropolitan area, where accessibility, land value, and urban activity converge. By contrast, low-potential parcels extend outward into peri-urban and rural zones, reflecting areas where ecological constraints and limited infrastructure reduce the likelihood of transformation. The medium-potential category forms intermediate bands between these extremes, capturing transitional conditions that may evolve under favorable planning or investment strategies.

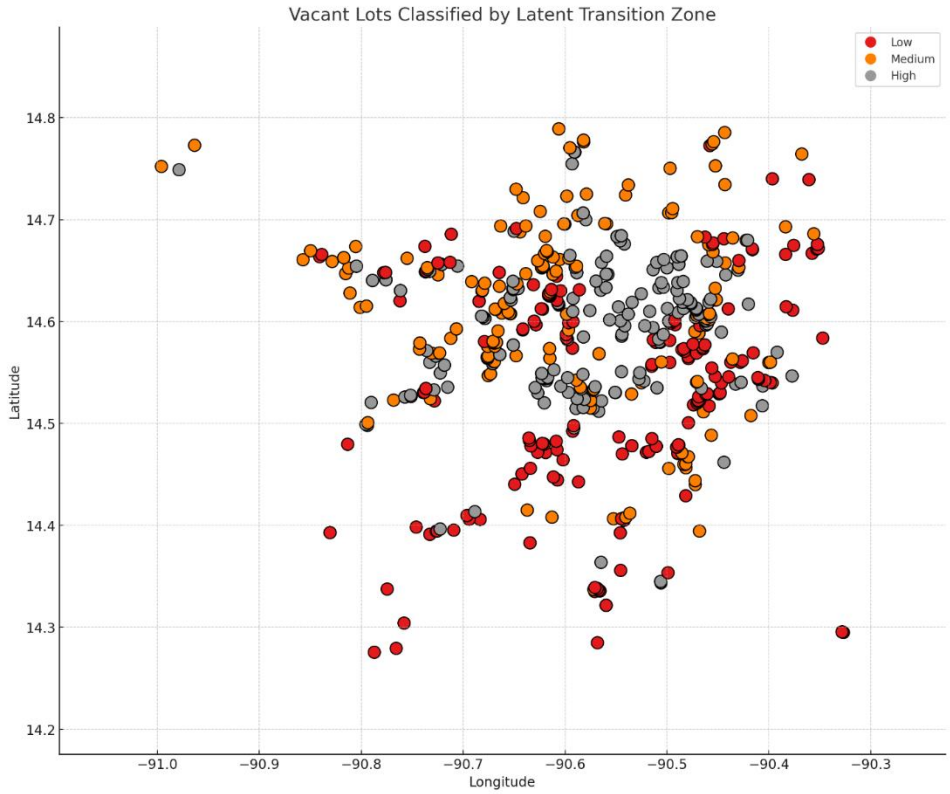


Fig. 5. Classification of Vacant Land by Latent Transition Zones in the Guatemala City Metropolitan Area. *Data source: Own elaboration based on the variables considered (land price, distance to urban center, travel time, traffic intensity, forest cover, crops, and grasslands).*

Each cluster reflects a specific combination of variables including accessibility, land value, traffic intensity, and land cover. Cluster 2 (orange) predominates in the southern and peripheral areas, which are characterized by limited connectivity and reduced readiness for transformation. In contrast, Clusters 4 (red) and 5 (purple) are concentrated in the central and northeastern sectors, where stronger urban pressures suggest higher latent transition potential. Clusters 1 (green) and 3 (blue) appear as transitional bands around core activity centers, representing intermediate conditions. This classification demonstrates differentiated spatial typologies and provides a systematic basis for identifying where transformation processes are more likely to occur and what type of intervention may be required in each case.

Fig. 6 presents the spatial cluster analysis of vacant land in the Guatemala City Metropolitan Area, organized into five transition groups. The convex hull boundaries delineate the spatial extent of each cluster and illustrate zones that share similar transition characteristics. The clusters, represented in green, orange, blue, red, and purple, capture distinct patterns of transformation potential derived from land price, accessibility, ecological constraints, and traffic intensity.

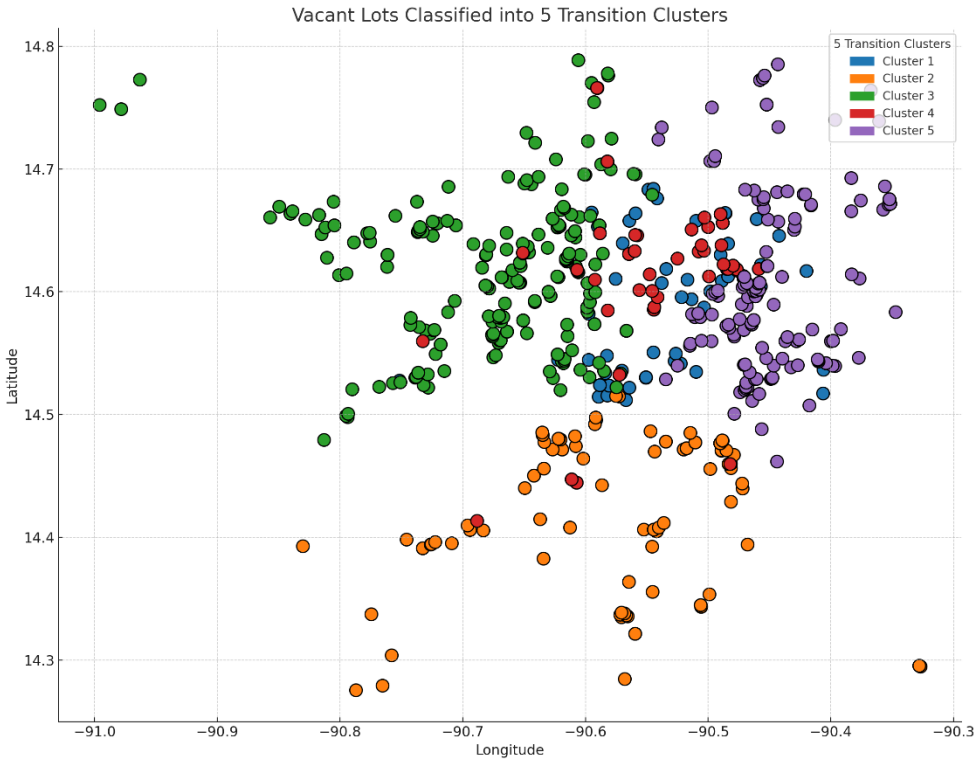


Fig. 6. Vacant Land Classified into Five Spatial Transition Clusters in the Guatemala City Metropolitan Area. *Data source: Own elaboration based on the variables considered (land price, distance to urban center, travel time, traffic intensity, forest cover, crops, and grasslands).*

Cluster 1 (green) extends across the northwest, encompassing dispersed rural and semi-urban parcels with limited integration. Cluster 2 (orange) is more clearly defined in the southern sector, where peripheral conditions constrain transformation readiness. In contrast, Clusters 3 (blue), 4 (red), and 5 (purple) are concentrated in central and northeastern areas, forming compact zones influenced by stronger urban activity and higher transition potential. These patterns reveal how vacant land follows differentiated trajectories of change across the metropolitan area. Beyond their descriptive value, the clusters provide a framework for interpreting the drivers of spatial transformation, thereby setting the basis for the discussion of how land-use dynamics, accessibility, and ecological constraints interact to shape urban transition pathways.

5. DISCUSSION

The convex hull boundaries of the five clustered transition zones, derived from the spatial analysis of vacant land in the Guatemala City Metropolitan Area, are presented in **Fig. 7**. Panel (a) shows the classification of vacant land into five clusters, each enclosed by convex hull perimeters. Panel (b) abstracts these results into aggregated polygons that emphasize the territorial extent of each cluster. Together, these visualizations reveal not only the discrete geography of each group but also the relational dynamics that emerge where clusters intersect.

A notable feature of this visualization is the overlapping areas among clusters, particularly near the urban center. Rather than interpreting these overlaps as classification ambiguities, they can be understood as transition interfaces that reveal hybrid conditions where multiple urban, environmental, and market dynamics converge. These areas differ both from the consolidated core and the homogeneous peripheries, functioning instead as spaces of uncertainty.

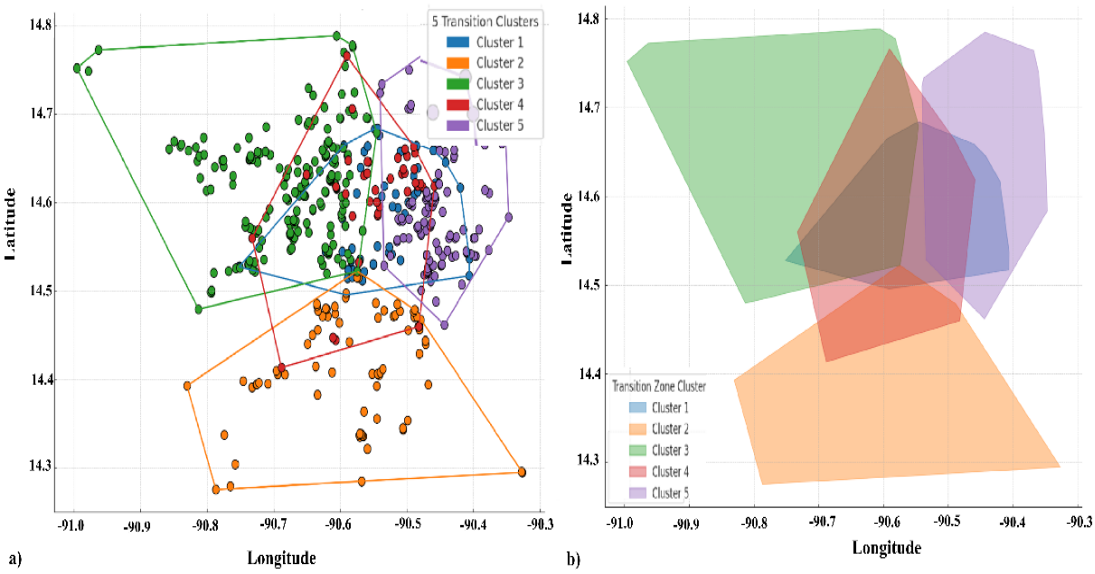


Fig. 7. (a) Vacant land classified into five transition clusters with colored convex hull boundaries, showing the distribution of parcels according to accessibility, land price, traffic intensity, and land cover. (b) Aggregated convex hull polygons representing the spatial extent of each cluster, highlighting overlapping and peripheral zones that define broader transition regions.

Source: Own elaboration based on land price, distance to urban center, travel time, traffic intensity, and land cover variables (forest, crops, and grasslands).

Their recognition introduces a novel perspective to the ULTI framework, suggesting that overlaps themselves constitute distinct transition areas requiring tailored planning approaches.

Table 2 highlights how the interaction of clusters generates distinct spatial interfaces that reveal the tensions of urban transition in the GCMA. Core–Intermediate overlaps illustrate zones where the metropolitan core expands into adjacent intermediate areas, where high land values and accessibility dominate but ecological or infrastructural limits prevent uniform consolidation. These areas point to opportunities for targeted densification if mobility networks and basic services are reinforced. In contrast, Intermediate–Peripheral overlaps capture the expansion frontiers of the city, where semi-urban and rural uses coexist under growing development pressure. These areas embody the dilemma of metropolitan growth, since strategies must carefully balance ecological conservation with controlled expansion to avoid unchecked sprawl.

Table 2.

Typology of Transition Overlap Areas in the Guatemala City Metropolitan Area.

Transition Type	Cluster Interaction	Key Characteristics	Planning Implications
Core–Intermediate Overlap	Cluster 3 with Clusters 0 and 2	High land values, strong accessibility, moderate ecological or infrastructural constraints	Suitable for managed densification and reinforcement of services and mobility networks
Intermediate–Peripheral Overlap	Clusters 0 or 2 with Clusters 1 and 4	Mix of rural and semi-urban uses, moderate accessibility, ecological presence, rising urban pressure	Require balanced strategies between conservation and controlled expansion
Multi-Cluster Intersection	Central overlaps of 3+ clusters	Hybrid environments with competing pressures (accessibility, market demand, ecological restrictions)	Represent critical transition corridors; demand flexible and adaptive planning tools

Data Source: Own elaboration.

Finally, the multi-cluster intersections reveal complex urban corridors where three or more clusters converge. Rather than simple overlaps, these are hybrid spaces shaped simultaneously by accessibility, market demand, and environmental constraints, making them critical arenas for adaptive and flexible planning.

Together, the three categories in **Table 2** show how cluster interactions mark not only geographical overlaps but also the strategic challenges for steering metropolitan transformation. This interpretation underscores that vacant land dynamics in the metropolitan area cannot be reduced to discrete clusters alone. By incorporating the notion of overlaps as transition interfaces, the analysis highlights relational geographies that extend beyond administrative divisions and introduces a critical dimension for urban policy: whether planning interventions reinforce consolidated cores, mediate contested intermediate belts, or adapt to the complexities of hybrid overlap zones.

The classification of vacant land into five transition clusters reveals a diverse spatial and functional landscape across the Guatemala City Metropolitan Area (**Table 3**). Cluster 3 stands out with the highest land price (Q 6,497/m²), short travel time (46.65 minutes), and proximity to the urban core (7.54 km). These attributes, combined with moderate traffic intensity and low ecological resistance, yield the highest ULTI score (0.67), positioning this cluster as the primary candidate for reinvestment and densification.

Table 3.

Descriptive Statistics of Transition Clusters and Key Variables for the Urban Latent Transition Index (ULTI).

Variable	Cluster 0	Cluster 1	Cluster 2	Cluster 3	Cluster 4
Price (Q/m²)	2,998.53	753.41	1,207.95	6,497.01	1,019.46
Distance to Center (km)	7.94	23.27	17.62	7.54	121.59
Travel Time (min)	56.35	75.51	78.46	46.65	71.89
Light Vehicle Count	9,008.74	8,444.57	7,549.63	3,222.29	13,796.73
Heavy Vehicle Count	1,202.11	1,949.37	1,428.49	645.95	2,006.49
Forest (%)	19.61	26.27	24.47	16.71	34.72
Crops (%)	21.66	43.74	38.09	18.36	22.09
Grasslands (%)	21.86	14.50	17.72	20.71	27.97
ULTI (Scaled)	0.38	0.13	0.19	0.67	0.15
Notable Traits	Balanced zone, moderate price, central	Distant, lowest price, high % crops	Mid-periphery, moderate crops/pasture	Urban core, very high price, fast access	Rural outlier, long distance from center

Data Source: Own elaboration based on ULTI clustering calculus (2025).

At the other extreme, Clusters 1 and 4 represent peripheral or rural zones with very low land values (Q 753 and Q 1,019/m², respectively) and long distances from the center (23.27 km and 121.59 km). Despite relatively high traffic volumes, likely associated with industrial or corridor functions, their ecological constraints and limited centrality result in very low ULTI values (0.13 and 0.15). Cluster 2, located in the mid-periphery, exhibits moderate land prices (Q 1,207/m²), longer travel times, and a high presence of crops and pastures. Its ULTI value (0.19) indicates only limited potential for transition under current conditions.

Cluster 0 occupies an intermediate position with moderate prices (Q 2,998/m²), relatively central location (7.94 km), and high traffic volumes. Its mixed land cover and somewhat high travel time (56.35 minutes) constrain its potential, reflected in a moderate ULTI score (0.38).

Overall, the cluster typology reveals a clear gradient of vacant land dynamics. Cluster 3, as the urban core, concentrates the strongest development pressures, while Clusters 1 and 4 highlight peripheral or rural contexts with minimal readiness for transformation. Cluster 0 shows potential consolidation zones if infrastructural bottlenecks are addressed, and Cluster 2 represents transitional

lands where rural and urban dynamics overlap. These findings confirm that spatial centrality, land market value, and ecological resistance are decisive variables shaping the likelihood of urban transformation.

This gradient is not unique to Guatemala. Comparable patterns have been documented across the Global South, where high-value, well-connected cores concentrate reinvestment, while peripheral lands remain ecologically constrained or dominated by informal uses. Inostroza (2017) highlights similar dynamics in Latin America, where informal urbanization often emerges in peri-urban zones despite low market value and high ecological sensitivity. Watson (2009) describes parallel tensions in African cities, where centrality and infrastructure access accelerate selective reinvestment while peripheral landscapes are marginalized by regulatory and institutional gaps. Likewise, Song et al. (2020), Lee & Newman (2017) and Lee & Newman (2019) emphasize that vacancy in the Global South frequently embodies both market anticipation and structural exclusion, producing a duality of constraint like that observed in Guatemala City Metropolitan Area. By situating the ULTI results within this comparative context, the analysis reinforces its broader relevance and underscores how metropolitan transitions in the Global South are shaped by uneven accessibility, ecological resistance, and fragmented governance.

6. CONCLUSIONS

The findings of this study confirm and extend key arguments in the existing literature regarding urban transformation, particularly in the context of vacancy and land use dynamics. Previous research has emphasized the importance of accessibility, market value, and infrastructure in determining urban transition potential. For example, Baba and Asami (2017) and Lee and Newman (2017) showed that proximity to central urban areas and high land prices are often correlated with redevelopment and reinvestment. This aligns closely with our results, which demonstrate that the most transformation-ready clusters in the Guatemala City Metropolitan Area are those with shorter travel times, central locations, and elevated land prices. However, while studies like Higgs et al (2019) and Saeed et al (2022) relied heavily on structured urban environments with formal planning mechanisms, the present research demonstrates that a composite index like ULTI can still function effectively in fragmented and informally governed settings. By spatially identifying these opportunities, this study operationalizes that conceptual shift and offers a practical approach to capturing transitional urban dynamics in cities with complex growth patterns and limited institutional coordination.

This research set out to construct and apply the Urban Latent Transition Index (ULTI) to assess the potential of vacant land to undergo urban transformation in the Guatemala City Metropolitan Area. By combining variables related to accessibility, land value, traffic flow, and ecological composition, the ULTI offers a comprehensive way to understand which areas are more likely to transition into active urban use. The findings support the initial hypothesis: vacant land that is closer to the city center, has higher land prices, lower ecological constraints, and more intense vehicle traffic tend to show a much greater potential for transformation.

One of the key contributions of this study is the ability of ULTI to offer detailed spatial insights in a context where formal urban planning tools and consistent datasets are limited. While many urban models have been developed for cities in the Global North or in data-rich Asian regions, this study demonstrates that meaningful urban analysis can still be achieved in places like Guatemala, where informal processes shape much of the city's growth. The results confirm what the literature has suggested: land value, accessibility, and infrastructure demand are strong indicators of where transformation pressure is building. At the same time, this research brings new clarity by organizing this information into clear spatial patterns using clustering techniques.

Theoretical contributions from authors such as Lee and Newman (2019), Németh & Langhorst (2014), O'Callaghan (2024), emphasize that vacant land is not simply leftover or failed space. This study aligns with that view and moves it forward by providing a way to identify and classify these opportunities in practical terms.

Using geospatial tools and data analysis, ULTI helps visualize the city's hidden potential and guides attention to where intervention or investment might make the most difference.

The Urban Latent Transition Index offers a valuable step toward more informed and adaptive urban planning. It helps bridge the gap between academic insight and real-world decision-making, especially in settings where cities grow faster than institutions can plan. ULTI not only highlights where transformation is likely to occur but also offers a replicable framework for understanding urban change in other cities facing similar challenges.

REFERENCES

Ahmad, S. M. T., Haque, S., & Khan, P. S. (2014). Privacy preserving in data mining by normalization. *International Journal of Computer Applications*, *96*(6). http://dx.doi.org/10.5120/16797-6509

Baba, H., & Asami, Y. (2017). Regional differences in the socio-economic and built-environment factors of vacant house ratio as a key indicator for spatial urban shrinkage. *Urban and Regional Planning Review, 4*, 251–267. http://dx.doi.org/10.14398/urpr.4.251

Carvajal, M. & Argueta, J. (2025). A Real-Time, Multi-Method Approach to Functional Metropolitan Delimitation: The Case of Guatemala City. *International Journal of Humanities and Social Science Invention (IJHSSI)*, 14 (4), 39-51. https://doi.org/10.35629/7722-14043951

Higgs, C., Badland, H., Simons, K., Knibbs, L. D., & Giles-Corti, B. (2019). The Urban Liveability Index: Developing a policy-relevant urban liveability composite measure and evaluating associations with transport mode choice. *International Journal of Health Geographics, 18*(1), 1–25. https://doi.org/10.1186/s12942-019-0178-8

Hölscher, K., & Frantzeskaki, N. (2021). Perspectives on urban transformation research: Transformations in, of, and by cities. *Urban Transformations, 3*(1), 1–14. https://doi.org/10.1186/s42854-021-00019-z

Inostroza, L. (2017). Informal urban development in Latin America: Understanding the regional dynamics of vacant land. *Land Use Policy*, 65, 1–12. https://doi.org/10.1016/j.landusepol.2017.03.026

Kim, G., & Newman, G. (2021). Land vacancy and sustainability: A review of the literature and conceptual framework. *Journal of Planning Literature*, 36(3), 313–328. https://doi.org/10.1177/08854122211003590

Lee, J., & Newman, G. (2017). Forecasting urban vacancy dynamics in a shrinking city: A land transformation model. *ISPRS International Journal of Geo-Information*, 6(4), 124. https://doi.org/10.3390/ijgi6040124

Lee, J., Newman, G., & Park, Y. (2018). A comparison of vacancy dynamics between growing and shrinking cities using the land transformation model. *Sustainability, 10*(5), 1513. https://doi.org/10.3390/su10051513

Lee, R. J., & Newman, G. (2019). A classification scheme for vacant urban lands: Integrating duration, land characteristics, and survival rates. *Journal of Land Use Science, 14*(4–6), 306–319. https://doi.org/10.1080/1747423X.2019.1706655

Naghibi, M. (2024). Rethinking small vacant lands in urban resilience: Decoding cognitive and emotional responses to cityscapes. *Cities*, 151, 105167. https://doi.org/10.1016/j.cities.2024.105167

Németh, J., & Langhorst, J. (2014). Rethinking urban transformation: Temporary uses for vacant land. *Cities, 40*, 143–150. https://doi.org/10.1016/j.cities.2013.04.007

Newman, G., & Lee, J. (2019). Urban vacancy and the shrinking city: Trends and policies in the US and abroad. *Cities*, 82, 13–22. https://doi.org/10.1016/j.cities.2018.12.005

Noh, Y., Newman, G., & Lee, R. J. (2021). Urban decline and residential preference: The effect of vacant lots on housing premiums. *Environment and Planning B: Urban Analytics and City Science, 48*(6), 1667–1683. https://doi.org/10.1177/2399808320933906

O'Callaghan, C. (2024). Rethinking vacancy within the urbanization process: Towards a new research agenda. *Urban Geography, 45*(5), 863–882. https://doi.org/10.1080/02723638.2023.2233862

Owusu-Ansah, A. (2018). *Construction and application of property price indices*. Routledge. https://doi.org/10.1201/9781315102085

Rahman, M. F., Murukannaiah, P., & Sharma, N. (2020). Predicting the influence of urban vacant lots on neighborhood property values. In: CEUR Workshop Proceedings, 2557, 1–16. [Online]. Available from: http://ceur-ws.org/Vol-2557/[Accessed 25 February 2025].

Rahman, M. M., & Szabó, G. (2022). A novel composite index to measure environmental benefits in urban land use optimization problems. *ISPRS International Journal of Geo-Information, 11*(4), 220. https://doi.org/10.3390/ijgi11040220

Saeed, U., Ahmad, S. R., Mohey-ud-din, G., Butt, H. J., & Ashraf, U. (2022). An integrated approach for developing an urban livability composite index—A cities' ranking road map to achieve urban sustainability. *Sustainability, 14*(14), 8755. https://doi.org/10.3390/su14148755

Song, X., Wen, M., Shen, Y., Feng, Q., Xiang, J., Zhang, W., ... & Wu, Z. (2020). Urban vacant land in growing urbanization: An international review. *Journal of Geographical Sciences, 30*, 669–687. https://doi.org/10.1007/s11442-020-1749-0

Watson, V. (2009). The planned city sweeps the poor away: Urban planning and 21st century urbanization. *Progress in Planning*, 72(3), 151–193. https://doi.org/10.1016/j.progress.2009.06.002

Yamazaki, R. (2001). Empirical testing of real option pricing models using Land Price Index in Japan. *Journal of Property Investment & Finance, 19*(1), 53–72. https://doi.org/10.1108/14635780110365361

REMOTE SENSING OF RESERVOIR WATER QUALITY: MODELLING OPTICALLY SENSITIVE AND NON-SENSITIVE PARAMETERS WITH LANDSAT

Suraj PAWAR [1], ***Rushikesh KULKARNI*** [1*], ***Kanchan KHARE*** [2] ***and Humera KHANUM*** [1]

DOI: 10.21163/GT_2026.211.05

ABSTRACT

This study integrated in situ water quality measurements with Landsat 8 Operational Land Imager (OLI) data to assess the water quality of the Khadakwasala Reservoir in Pune, India. Stepwise regression analysis was applied to develop models correlating Landsat-derived spectral indices with key water quality parameters, including turbidity, chlorophyll-a, dissolved oxygen (DO), biochemical oxygen demand (BOD), and chemical oxygen demand (COD). The models achieved predictive accuracy with R2 values of 0.85 for turbidity, 0.90 for chlorophyll-a, 0.65 for DO, 0.64 for BOD, and 0.84 for COD. Turbidity was identified as a key predictor for the non-sensitive parameters (DO, BOD, COD). These models provide a scalable method for monitoring water quality, facilitating broader spatial assessments using satellite data. The dataset supports the reuse of remote sensing data for water quality management and environmental monitoring. The distributed images of water quality parameters can be obtained at the repository address mentioned in the data availability section.

Key-words: *Water Quality Assessment; Remote Sensing of Lakes; Landsat 8/9 OLI; Surface Water Quality Parameters; Stepwise Regression Model; Chlorophyll, Turbidity; Khadakwasla Reservoir*

1. INTRODUCTION

Access to clean and safe water is of paramount importance for human health and ecological integrity. Surface water bodies, including reservoirs, are vital freshwater resources, but their quality is increasingly threatened by anthropogenic activities and natural processes (Akhtar et al., 2021). Monitoring and evaluation of water quality parameters is necessary to Effective water resource management.

Traditional water quality monitoring approaches often rely on in situ sampling and laboratory analysis, which can be time consuming, expensive, and spatially limited (Palmer et al., 2015; Olmanson et al., 2015; Chang et al., 2014). Remote sensing techniques, employing satellite imagery, offer a spatially comprehensive and cost-effective alternative for assessing water quality parameters over large geographical areas, (Olmanson et al., 2015; Chang et al., 2014. Landsat satellites, with their long-term data archives and moderate spatial resolution, have proven invaluable for monitoring inland water bodies (Vakili & Amanollahi, 2020; Wang et al., 2019).

The cornerstone of water quality recovery relies on establishing correlations between the concentrations of water components and the scattered signals - in particular, the radiance emitted by the water as observed by sensors, (Kirk, 2010). Models for retrieval can be built based on the relationship of underlying optical properties (IOPs) to remote sensing reflectance, because IOPs are unique optical properties of water that are independent of external conditions and depend entirely on the composition of the water body. Consequently, it becomes feasible to directly retrieve water quality parameters such as Chlorophyll-a (Chl), suspended matter (SM), and colored dissolved organic matter (CDOM), (Palmer et al., 2015; Wang et al., 2017; Li et al., 2018).

---

[1] *Symbiosis Institute of Technology, Symbiosis International University, 412115 Pune, Maharashtra, India; suraj.pawar.phd2024@sitpune.edu.in (SP); *corresponding author rushikeshk@sitpune.edu.in (RK); humera.khanum@sitpune.edu.in (HK).*

[2] *Sevavardhini, Water Resource Department, Pune Division, 411030 Pune, Maharashtra, India, kanchankhare@sevavardhini.org (KK).*

Water constituents devoid of optical activity like Total Nitrogen (TN), Total Phosphorus (TP), Chemical Oxygen Demand (COD), and Dissolved Oxygen (DO), which lack direct optical characteristics, can be approached either by exploring interrelationships between various substances in water or by deploying Artificial Intelligence (AI) techniques, (Sun et al., 2014; Sharaf El Din et al., 2017).

This study focused on a conventional regression-based approach to link optically sensitive parameters (turbidity, chlorophyll a) with non-optically sensitive parameters (DO, BOD, COD). While several recent works have highlighted the potential of artificial intelligence (AI) frameworks for indirect estimation of non-optically sensitive parameters, such approaches often face data limitations and require large, diverse training sets that were not available for the Khadakwasla case study. Therefore, instead of AI-driven models, our study demonstrates how statistically robust relationships can be derived between optically sensitive parameters and optically non-sensitive parameters to predict. This approach is particularly advantageous in data-limited settings, as it avoids the overfitting risks and transferability issues often associated with AI models.

However, quantifying a wide range of water quality parameters is challenging, particularly when calculating water-leaving reflectance due to the complex interactions of radiation among the atmosphere, water surface, and water body across various wavelengths. Generally, remote sensing-based water quality retrieval methods can be classified into empirical, physical, semi-empirical, and intelligent models, with AI methods standing out as a distinct empirical approach that uses statistical techniques (Palmer et al., 2015; Wang & Yang, 2019). Many reviews have highlighted the major advancements in water quality retrieval using remote sensing, especially focusing on different retrieval methods and the use of multi-source remote sensing data (Palmer et al., 2015; Chang et al., 2014; Wang et al., 2019; Chen et al., 2013; Kuhwald & Oppelt, 2016; Sagan et al., 2020; Chawla et al., 2020).

This study aims to examine the Khadakwasla Reservoir water quality. The reservoir serves as a primary drinking and farming water source in Pune, Maharashtra, which is found in India. The study has combined the in situ physical measurements of water quality parameters from Landsat 8 Operational Land Imager (OLI) surface reflectance data to acquire a wide-ranging knowledge about the lake's status on water quality. Furthermore, this integration leverages the strengths of both methods, resulting in a more comprehensive assessment with improved spatial accuracy.

This project involves the estimation of quality parameters of water such as chlorophyll (Chl), chemical oxygen demand (COD), turbidity (Tur), bio chemical oxygen demand (BOD), and dissolved oxygen (DO) based on sampling points of choice of the reservoir. The main task of the investigation is to use the pre-processed Landsat 8 Operational Land Imager (OLI) surface reflectance data to estimate the parameters of surface water quality (SWQP). Analytical approaches aimed at the statistical testing the relationship between the in-situ water quality measurements and the corresponding Landsat 8 OLI surface reflectance values will be the regression analytical methods.
The data obtained as a result will be aimed at providing a methodology to identify water quality in Khadakwasla Reservoir through the combination of in-situ measurements and remote sensing observations. The developed statistical association among parameters of in-situ water quality and those provided by the Landsat 8 OLI spectral reflectances make it possible to form the predictive models which will be able to approximate the spectra of water quality parameters in different across the reservoir sectors. Such a strategy is likely to work together with effective water resource management methods.

2. STUDY AREA AND METHODOLOGY

2.1. Study area

The Khadakwasala Reservoir is selected as a study area in this study due to easy accessibility for in-situ water sampling for testing water quality and wide spatial coverage (**Fig. 1**). As per the Water Resource Department data, the surface area of the reservoirs varies from ~ 8.5 Sq.km to ~12.0 Sq.km corresponding to the seasonal variation. This spatial extent is enough to use the high and moderate resolution satellite for analysis. The Pune metropolitan city and its surrounding areas primarily depend on the Khadakwasla reservoir for their water needs.

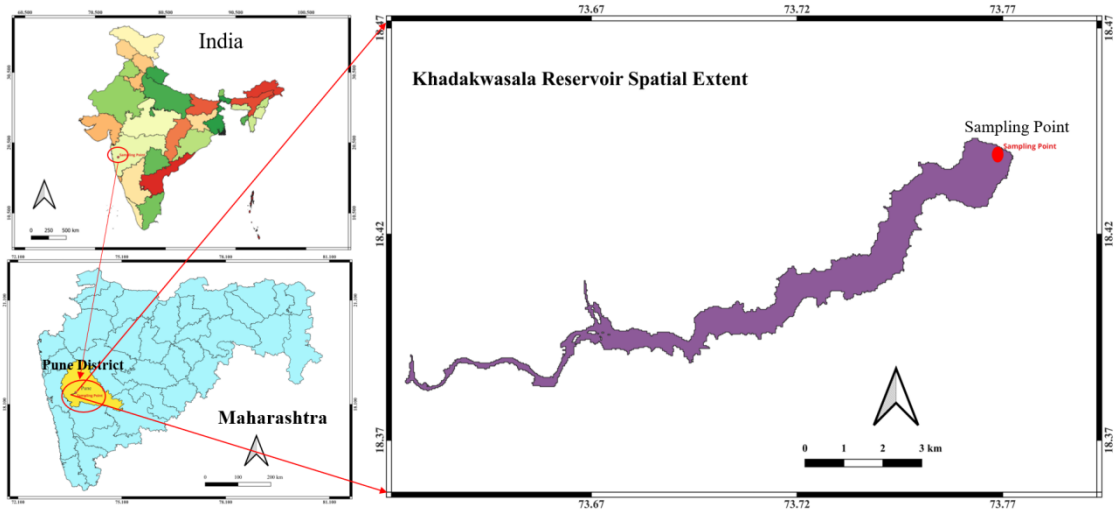


Fig. 1. Location of the Study Area: Khadakwasala Reservoir (Sampling Location :18.4390 N / 73.7720 E).

It is a source of water for domestic needs, agricultural needs, industrial needs, and hydroelectric power generation. For these reasons, understanding Khadakwasala's storage potential becomes integral to managing water resources within the locality. The Khadakwasala Reservoir was built in 1879 near Pune. Maharashtra, India, primarily to meet Pune's drinking water source and irrigation needs. It is located on the Mutha River and holds an approximate storage capacity of 2.46 million cubic meters.

2.2. Methodology

The methodology presented in the flowchart (**Fig. 2**) describes an integrated approach combining remote sensing and in-situ data for the prediction of surface water quality parameters (SWQPs). This process involves the use of Landsat 8/9 imagery along with physical water quality measurements. Satellite data goes through pre-processing steps, including geometric, radiometric, and atmospheric corrections, as well as masking of water bodies to obtain the reflectance of the upper atmosphere (ToA). Concurrently, in-situ measurements are gathered from the Khadakwasla Dam through physical sampling and laboratory analysis to determine values for turbidity (Tur), chlorophyll-a (Chl), dissolved oxygen (DO), biochemical oxygen demand (BOD), and chemical oxygen demand (COD).

The relationship between spectral data and SWQPs is established using stepwise regression, a statistical method that adds or removes predictor variables in an iterative manner based on their significance. At each step, the p-value of the independent variable is evaluated and only the value that is less than the specified threshold is retained in the model. This helps identify the most relevant spectral bands or indices that contribute significantly to the prediction of each water quality parameter, improving the accuracy and interpretation of the model. The SWQP's are divided into optically sensitive (Tur, Chl) and non-sensitive (DO, BOD, COD) groups, followed by training (75%) and testing (25%) datasets. The derived models are verified through accuracy analysis using test data.

2.3. Data Acquisition

2.3.1. Landsat OLI Images

The images of Landsat 8/9 OLI were accessed from the Earth Explorer platform *(http://earthexplorer.usgs.gov)* operated by the United States Geological Survey (USGS). The Landsat imagery for the Khadakwasala Reservoir was selected based on the specific path 147 and row 47 criteria. This led to a collection of 23 cloud-free Landsat OLI 8/9 images, which were used for the analysis. The downloaded images covered the period from 20th October 2022 to 22nd April 2023.

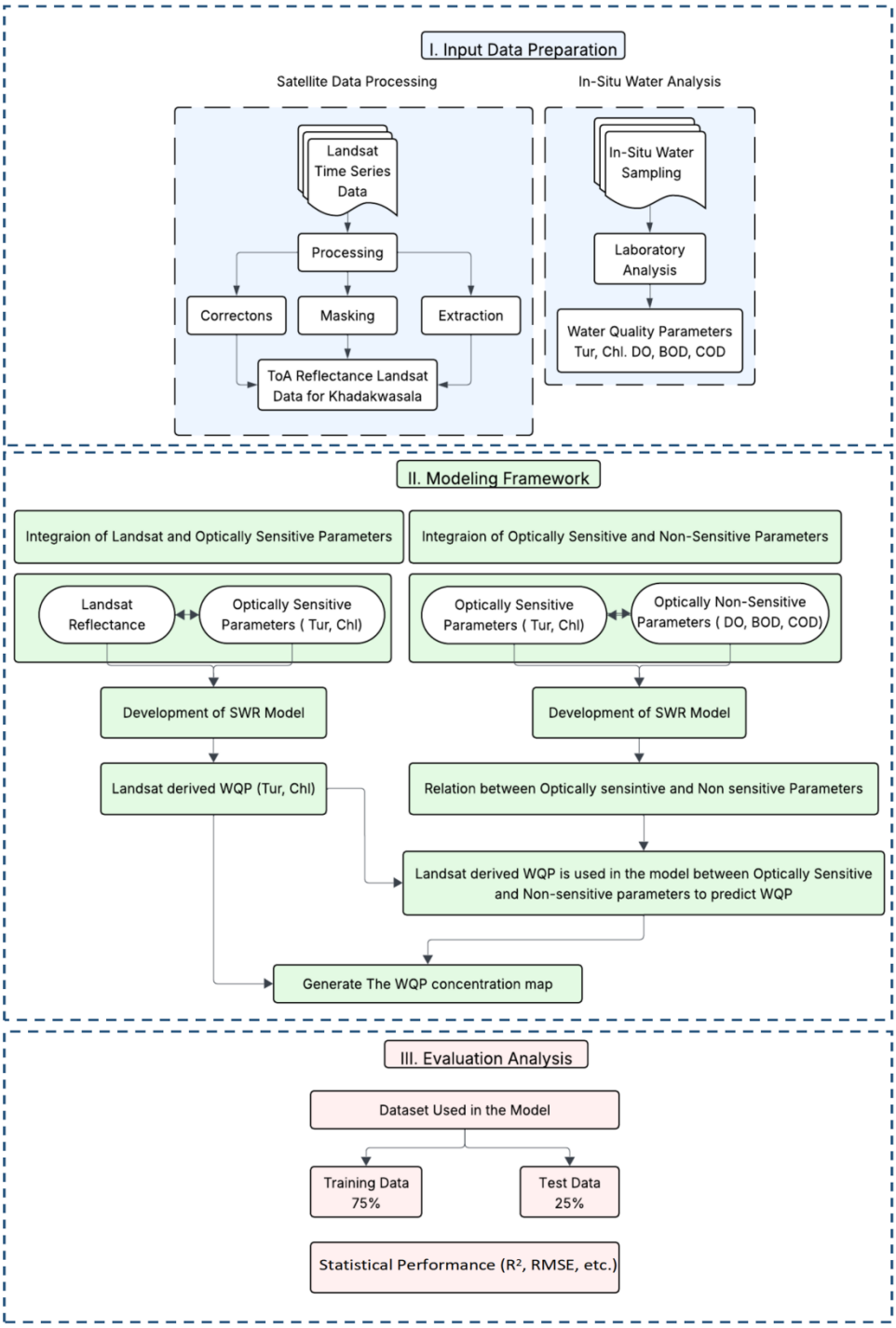


Fig. 2. Methodology Workflow for estimation of water quality parameters from Landsat 8/9 OLI using SWR.

2.3.2. Data Pre-processing

The first step in the methodology is data acquisition, which includes two types of data: in-situ water quality parameters and satellite imagery. The in-situ water quality data was specifically collected on dates when corresponding Landsat 8/9 OLI images were available to maintain data

consistency. The next process is the image processing of raw images for further analysis. The Landsat images are processed to reduce the interference caused by the atmosphere and sensors, allowing for accurate interpretation and analysis of water quality parameters. The image processing involves radiometric corrections, geometrical corrections, atmospheric corrections, and Dark Object Subtraction.

2.3.3. In-situ water quality parameter data

Physical water samples from the Khadakwasala Reservoir were collected at coordinates 18.4390 N and 73.7720 E. Sampling was conducted from October 20, 2022, to April 22, 2023, aligning with the satellite imagery acquisition period. These samples were analysed for various water quality parameters, including Chl, Turbidity, DO, BOD, and COD. Turbidity was measured on-site using a standard turbidity meter, while the other parameters were tested in the laboratory following the American Public Health Association (APHA) standards.

To ensure consistency and minimize contamination from surface debris and atmospheric effects, all measurements were taken at a depth of 0.25 meters. The clean, sterile, and non-reactive polyethylene bottles were used for collecting water samples. After collection, the samples were placed in an ice container and transported to the laboratory within the holding time specified by APHA guidelines.

2.3.4. Analytical Methods

The analysis of the sampled water was carried out following the Standard Methods outlined by APHA. DO levels were quantified utilizing the Winkler titration method and measured in milligrams per liter (mg/L). BOD was determined using the 5-day BOD test, which measures the amount of oxygen consumed by microorganisms during the aerobic breakdown of organic material. These concentrations were reported as milligram per liter (mg/liter). The chemical oxygen demand (COD) was measured using the closed reflux titrimetry which is used to measure the oxygen equivalent that is needed to completely oxidize all the organic and inorganic matter that exists in the aqueous sample and the reflux reaction result is expressed in mg/L. The level of chlorophyll which is a measure of the phytoplankton biomass was determined using a pigment extraction technique. The obtained figures were recorded in micrograms per liter (µg/L). Turbidity used as a surrogate of suspended solids was estimated with the help of a nephelometric turbidity unit (NTU) meter. The device measures the light scattering of suspended particles hence recording an indirect measure of turbidity on the NTU.

2.4. Stepwise Regression Technique

Stepwise regression (SWR) is one of the statistical methods where the influential predictor variables in a set of candidates are given sequentially, to form a strong predictive model. The Akaike Information Criterion (AIC) is an indispensable factor in model selection which gives a balance between the accuracy of prediction and the complexity of the model, thus alleviating the problem of overfitting. SWR makes use of forward selection and backward elimination steps which is driven by AIC. In the case of optical sensitive parameters, Landsat spectral bands and spectral ratios are considered as the independent variables and turbidity and chlorophyll concentrations are the dependent variables. In contrast, the chlorophyll and turbidity are taken as independent variables in optically non-sensitive parameters, whereas, the dissolved oxygen, biochemical oxygen demand, and chemical oxygen demand are dependent variables. The procedure chooses the variable that produces least AIC which makes it the most applicable predictor and includes it in the model. k suing the models, k -fold cross- validation was used to test the validity and reliability of the models. The best SWR was chosen based on maximization of adjusted R^2, minimum root-mean-square error (RMSE), mean absolute error (MAE) among another basis such as the AIC criterion.

2.4.1. Relationship of Landsat with optically sensitive water quality parameter

This research used SWR to find out the relations between surface reflectance measured using Landsat and in-situ of water quality factors, that is, turbidity (Tur) and chlorophyll-a concentration (Chl), in which the first five reflection bands and several band combinations as independent variables.

The combinations used in the model were (Band 3 / Band 2), (Band 2 + Band 3), (Band 3 + Band 4), and (Band 2 / Band 1). The model uses established research from the literature to select specific

bands and combinations for estimating water quality parameters like Tur and Chl, with in-situ measurements as dependent variables.

The selection of band combinations in this study was not arbitrary but guided by established findings in remote sensing of inland waters. Band ratios such as B3/B2 (green/blue) and B2/B1 (blue/coastal aerosol) are widely reported as effective indicators of turbidity and total suspended solids (TSS), since shorter wavelengths are strongly scattered by suspended particles, while green reflectance is more stable under varying concentrations. Similarly, combinations involving B3 and B4 (green + red) are sensitive to chlorophyll-a because of the strong absorption of red light by chlorophyll pigments and the differential scattering in the green band. The additive indices (e.g., B2 + B3) exploit the complementary absorption and scattering properties of blue and green bands, which enhance sensitivity to phytoplankton biomass and light attenuation. Accordingly, the combinations tested in this study—(B3/B2), (B2 + B3), (B3 + B4), and (B2/B1)—were adopted from prior literature demonstrating their utility in estimating optically active parameters like chlorophyll-a and turbidity in reservoirs and lakes (Vakili & Amanollahi, 2020; Kirk, 2010; Chen et al., 2013; Sagan et al., 2020). These indices were therefore incorporated into the stepwise regression framework to ensure comparability with earlier studies and to leverage their proven biophysical sensitivity, rather than being developed empirically from scratch. This approach both strengthens model interpretability and ensures consistency with established remote sensing methodologies.

2.4.2. Relationship of Landsat with optically non-sensitive water quality parameters

The first step in our analysis is to establish a correlation between the optically sensitive parameters, derived from Landsat, and the optically non-sensitive parameters. We treat the optically sensitive parameters as independent variables and the non-sensitive parameters as dependent variables. Using the relationships from the previous step, we derive the optically sensitive parameters from Landsat data, allowing us to estimate the optically non-sensitive parameters despite their lack of direct correlation with Landsat reflectance.

3. DATA RECORD

This data record provides a distinctive evaluation of the surface water quality of the Khadakwasala reservoir by utilizing two separate datasets: physically sampled and measured surface water quality data, and water quality data obtained from Landsat 8 and 9 OLI. Landsat 8/9 OLI-derived data is assessed by integrating physical measurements with top-of-atmospheric reflectance, enabling a thorough spatial analysis of water quality parameters.

3.1. Data Record

In-situ water quality data for the Khadakwasala Reservoir, including measurements of DO, BOD, COD, Chl, and Tur, were collected from October 2022 to April 2023 (**Table 1**). Chl serves as a vital indicator of phytoplankton density and productivity in aquatic ecosystems, reflecting oligotrophic to mesotrophic states. Reduced Chl concentrations signify limited algal blooms, thereby maintaining water quality and ecological equilibrium. Turbidity, a factor influencing light penetration and habitat quality, varies from 1.82 to 3.42 NTU, signifying clear water conditions. DO concentrations ranging from 7.48 to 7.84 mg/l signify optimal conditions for aquatic organisms. The BOD values fluctuate between 3.70 and 4.25 mg/l, signifying heightened organic pollution. The COD values span from 14.99 to 24.25 mg/l, signifying the existence and concentration of various pollutants, including those resistant to microbial degradation. Consistent monitoring of BOD facilitates the comprehension of the impacts of activities on water quality and the identification of trends in organic matter accumulation. Elevated COD levels may signify sources of non-biodegradable pollutants.

The temporal trends of the water quality data set show seasonal variation following precipitation, temperature fluctuation, and human activities. Higher levels of COD and BOD may occur during periods of increased runoff, while temperature stratification during different months or years can lead to varying DO levels. Throughout the period, the Khadakwasala Reservoir maintained quality levels that are safe enough to support life in the water bodies without showing any sign of intense pollution or eutrophication.

Table 1.

In-situ SWQPs measured at Khadakwasala reservoir.

Date	DO (mg/L)	BOD (mg/L)	COD (mg/L)	Chl (ug/L)	Tur (NTU)
20-10-2022	7.68	3.97	16.61	0.15	2.03
28-10-2022	7.76	3.93	24.25	0.14	1.87
05-11-2022	7.84	4.04	17.99	0.18	1.82
13-11-2022	7.70	3.84	18.91	0.14	2.06
21-11-2022	7.67	3.92	20.88	0.15	2.10
29-11-2022	7.65	3.83	21.09	0.15	2.07
07-12-2022	7.73	3.93	17.15	0.16	1.91
23-12-2022	7.70	3.79	21.30	0.15	2.09
31-12-2022	7.67	3.97	20.16	0.15	2.04
08-01-2023	7.67	4.25	23.43	0.15	1.86
16-01-2023	7.59	3.83	19.86	0.15	2.06
24-01-2023	7.76	3.97	18.10	0.15	1.99
01-02-2023	7.68	3.87	16.60	0.17	2.07
09-02-2023	7.61	3.80	17.59	0.15	2.15
17-02-2023	7.48	3.80	15.11	0.15	2.21
25-02-2023	7.51	3.73	14.99	0.16	2.19
05-03-2023	7.57	3.90	17.70	0.19	1.95
13-03-2023	7.61	3.70	16.20	0.21	2.12
21-03-2023	7.50	3.70	15.90	0.22	3.42
29-03-2023	7.59	4.00	19.00	0.17	2.06
06-04-2023	7.48	3.90	17.40	0.21	2.32
14-04-2023	7.58	3.80	17.70	0.20	2.08
22-04-2023	7.75	4.00	16.20	0.22	1.85

3.2. Landsat 8 OLI-derived Water Quality Data

Landsat 8 OLI-derived data were utilized to assess SWQPs in the Khadakwasala Reservoir. A total of 24 samples were collected during the Landsat satellite pass from October 20, 2022, to April 22, 2023, corresponding to the post-monsoon through pre-monsoon dry period in Pune. The sample from March 21, 2023, was excluded from the analysis due to cloud cover, which compromised the accuracy of the Landsat image for estimating surface water quality parameters. Thus, the analysis was performed on the 23 remaining samples. Consequently, the regression models are calibrated for dry-season conditions and should be applied to monsoon periods only with caution, ideally following season-specific validation or recalibration.

The differentiation between optically sensitive (Tur and Chl) and optically non-sensitive (DO, COD, and BOD) parameters underscores the distinct approaches required for their estimation from remote sensing data. The optically sensitive parameters were directly estimated from the spectral data due to their strong correlation with surface reflectance. In contrast, the optically non-sensitive parameters, although not directly retrievable, were modeled using indirect approaches that leverage the relationship with the optically sensitive parameters.

3.2.1. Landsat-derived Turbidity

The Tur concentration in the Khadakwasla Reservoir was estimated using a SWR analysis. The SWR analysis identified the band ratio of B2 (blue) to B1 (coastal aerosol) as the most significant variable for predicting turbidity concentration. The results of the multiple linear regression model using the selected variables are shown in **Table 2**. The resulting regression equation for Tur concentration is given by Eq. (1):

$$Turbidity = 1.01 \times \frac{B2}{B1} + 1.02 \quad (1)$$

This equation indicates that the ratio of reflectance between the B2 and B1 bands is a strong predictor of turbidity concentration, explaining 84.5% of the variance in the measured turbidity values ($R^2 = 0.85$). The model's statistical significance is reinforced by an F-statistic of 76.04 and a p-value below 0.05, signifying a highly significant correlation between the predictor variable and turbidity concentration.

The regression coefficients, comprising the constant term (1.02) and the coefficient for the (B2/B1) band ratio (1.01), were determined to be statistically significant at the 0.05 level. The t-values (8.76 and 8.72) and their corresponding p-values (both below 0.05) confirm the strength of these coefficients. The 95% confidence intervals for the coefficients ([0.02, 0.98] for both) further substantiate their reliability and the robustness of the predictive relationship.

The results validate that the (B2/B1) band ratio is a robust and statistically significant predictor of turbidity concentration (see **Fig. 3a**) in the Khadakwasala Reservoir, illustrating the efficacy of remote sensing methodologies for water quality evaluation.

3.2.2. Landsat-derived Chlorophyll

The Chl data for the Khadakwasala Reservoir, derived from Landsat 8 OLI, were acquired via a SWR analysis. This analy sis identified six principal spectral variables as significant predictors of Chl concentration: B3/B2, B4, B3+B4, B2, B5, and B2+B3. The results of the multiple linear regression model using the selected variables are shown in **Table 2**. The regression model is represented by the subsequent (Eq. 2):

$$Chlorophyll = -0.16 \times \left(\frac{B3}{B2}\right) - 0.96 \times B4 + 1.54 \times (B3 + B4) - 2.12 \times B2 - 0.49 \times B5 + 0.37 \times B2 + 0.31 \quad (2)$$

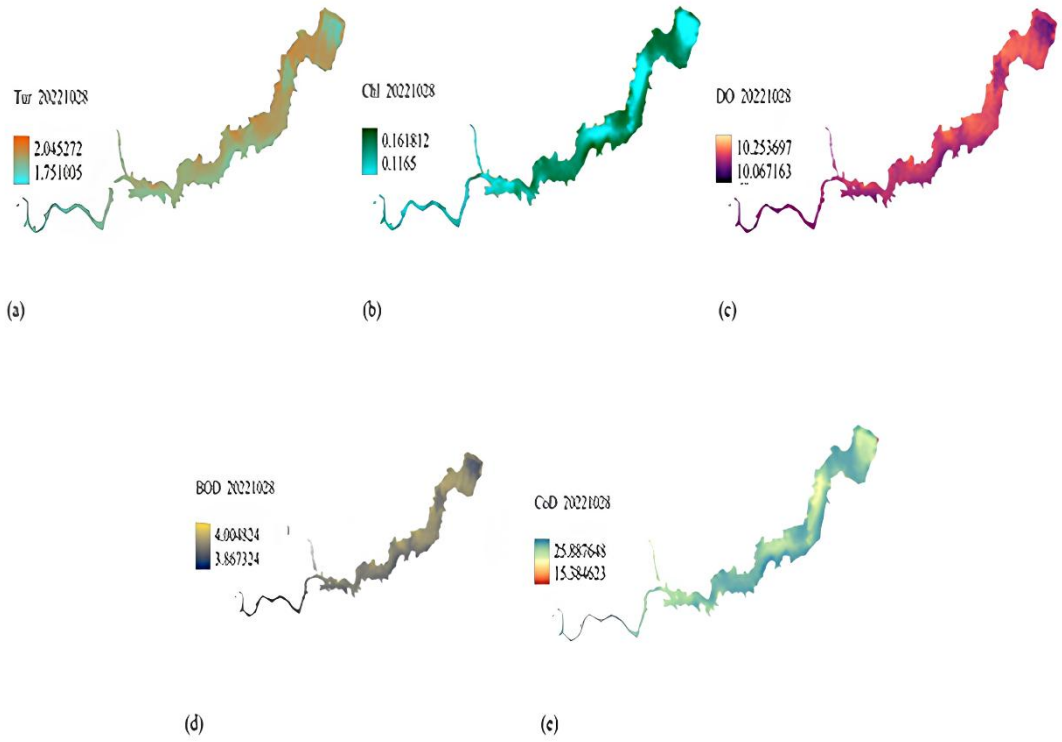


Fig. 3. Sample images of the Spatial variability of water quality parameters concentration across Khadakwasala reservoir sampled on 28-10-2022: (a) Turbidity (NTU); (b) Chlorophyll a, (µg/L); (c) DO (mg/L); (d) BOD (mg/L); (e) COD (mg/L).

This model achieved a R^2 value of 0.90, indicating that 89.6% of the variability in chlorophyll concentration can be explained by the selected spectral predictors. The adjusted R^2 of 0.85 demonstrates the model's robustness, accounting for the number of predictors while maintaining a high level of explanatory power. The F-statistic of 17.31 and the associated p-value less than 0.05 confirm the statistical significance of the model, underscoring the effectiveness of the selected spectral bands and ratios in predicting chlorophyll concentration.

The strong predictive capability of the SWR model, as evidenced by the high R^2 value, emphasizes the utility of Landsat 8 OLI spectral data in assessing Chl concentrations in surface water at Khadakwasala Reservoir. The identified relationships align with known optical properties of Chl and suspended matter, where the B2 and B3 bands are sensitive to Chl due to their response to specific light absorption and scattering characteristics. The Landsat 8 OLI-derived Chl data contribute valuable insights into the spatial and temporal distribution of chlorophyll concentration in the Khadakwasala Reservoir (refer to **Fig. 3b**), offering a reliable tool for water quality monitoring and management.

3.2.3. Landsat-derived DO

The SWR analysis used to estimate DO concentration identified turbidity as the sole predictor. The results of the multiple linear regression model using the selected variables are shown in **Table 2**. The linear regression model developed is described by the following equation (Eq.3):

$$DO = -0.63 \times Tur + 8.96 \quad (3)$$

The R^2 value of this model was 0.65 which shows that 64.9percent of the variance of dissolved oxygen concentration can be explained by the level of turbidity. The adjusted R 2 of 0.62, has validated the fact that the model still has a fairly adequate explanatory power whilst still taking into consideration the number of the predictors used. Statistical significance of the model is further confirmed by this F statistic that equals 25.89 and p value below, 0.005 and shows that turbidity is the significant predictor of dissolved oxygen concentration (refer **Fig. 3c**). The coefficient for Tur in the regression model is -0.63, with a p-value less than 0.001, demonstrating that Tur has a statistically significant negative effect on DO concentration. This negative relationship implies that as Tur increases, the DO concentration decreases. This is an ecologically sound trend in the sense that increased turbidity reduces light penetration into the water column thus repressing the photosynthetic mechanism of aquatic plants and algae of the water column, which eventually leads to low oxygen generation.

3.2.4. Landsat-derived BOD

The stepwise regression analysis for estimating BOD concentration identified turbidity as the only significant predictor. The results of the multiple linear regression model using the selected variables are shown in **Table 2**. The linear regression model is described by the following equation (Eq.4):

$$BOD = -0.87 \times Tur + 5.67 \quad (4)$$

This model attained a R^2 value of 0.64, signifying that 64.4% of the variability in BOD concentration is explicable by turbidity levels. The adjusted R^2 value of 0.62 indicates that the model possesses a substantial degree of explanatory power, considering the number of predictors employed. The F-statistic of 25.30 and the corresponding p-value below 0.05 establish the statistical significance of the model, signifying that turbidity is a significant predictor of BOD concentration. The coefficient for turbidity in the regression model is -0.869, with a p-value less than 0.001, demonstrating that turbidity has a statistically significant negative effect on BOD concentration. This negative relationship implies that as turbidity increases, BOD concentration decreases. This inverse relationship may be explained by the fact that higher turbidity levels can lead to reduced light

penetration in the water column, which may limit primary productivity and reduce the availability of organic matter for microbial decomposition, ultimately resulting in lower BOD concentrations (refer Fig. 3d).

The significant relationship between Tur and BOD concentration underscores the utility of remote sensing data, particularly Landsat 8 OLI-derived Tur, in estimating BOD in surface waters. While Tur alone was identified as a significant predictor, the complexity of BOD dynamics suggests that additional optically sensitive parameters or more advanced modelling approaches could further enhance the predictive accuracy of the model.

3.2.5. Landsat-derived COD

The stepwise regression analysis identified Tur and Chl as significant predictors of COD concentration. The results of the multiple linear regression model using the selected variables are shown in **Table 2**. The resulting linear regression model is described by the following equation (Eq.5):

$$COD = -233.18 \times Chl - 17.16 \times Tur + 89.44 \quad (5)$$

This model achieved R^2 value of 0.84, indicating that 83.5% of the variability in COD concentration can be explained by turbidity and chlorophyll levels. The adjusted R^2 value of 0.81 confirms that the model retains a high level of explanatory power while accounting for the number of predictors used. The F-statistic of 32.79 and the associated p-value less than 0.05 validate the statistical significance of the model, highlighting that Tur and Chl are meaningful predictors of COD concentration (refer **Fig. 3e**).

The regression coefficients for Chl (-233.18) and Tur (-17.16) are both negative, with p-values less than 0.001, indicating their statistically significant contributions to the model. The negative coefficients suggest that as chlorophyll and turbidity increase, COD concentration decreases. This inverse relationship can be attributed to the fact that higher Chl concentrations are indicative of increased photosynthetic activity, which can enhance oxygen production and thus reduce COD levels. Additionally, higher Tur levels may correspond with an abundance of suspended particles that limit light penetration, potentially decreasing the availability of organic matter and, consequently, COD concentrations. Identifying TUR and CHL as significant predictors emphasizes the utility of Landsat-derived data for assessing COD concentrations in surface waters. This approach allows for indirect estimation of COD, which is challenging to measure directly through remote sensing due to its optical insensitivity.

Table 2.
Ordinary Least Squares result obtained by SWR analysis between Landsat spectral reflectance bands and SWQPs at Khadakwasala.

SWQPs	Selected Features	R^2	Adj. R^2	F-Statistics	p-value
Turbidity	'B2 / B1'	0.85	0.83	76.04	< 0.05
Chlorophyll	'B3/B2', 'B4', 'B3+B4', 'B2', 'B5', 'B2+B3'	0.90	0.85	17.31	< 0.05
DO	'Turbidity'	0.65	0.62	24.89	< 0.05
BOD	'Turbidity'	0.65	0.62	25.30	< 0.05
COD	'Chlorophyll', 'Turbidity'	0.84	0.81	23.45	< 0.05

4. TECHNICAL VALIDATION

The Water quality parameters of Khadakwasla reservoir were estimated using Landsat-based SWR models and validated using a training dataset of 17 records and a testing dataset of six records. The models were assessed for predictive efficacy using metrics like R2, RMSE, and p-values to determine the correlation between predictor variables and water quality parameters.

4.1. Model Validation Results

Model of Turbidity. The Turbidity model had an R^2 of 0.62, which means that almost 62% of the observed turbidity data variability is captured by the model. An RMSE of 0.07 indicates the average deviation between predicted and observed turbidity values, indicating moderate levels of predictive precision (ref. **Fig. 4a**).

Model of Chlorophyll. The Chl model had an R^2 equal to 0.65, indicating that approximately 64.84% of the chlorophyll variability was explained by the model. The RMSE of 0.0095 indicates the average difference between actual chlorophyll values and their respective predicted values.There is a strong p-value for the model's significance of 0.001 or less, (ref. **Fig. 4b**).

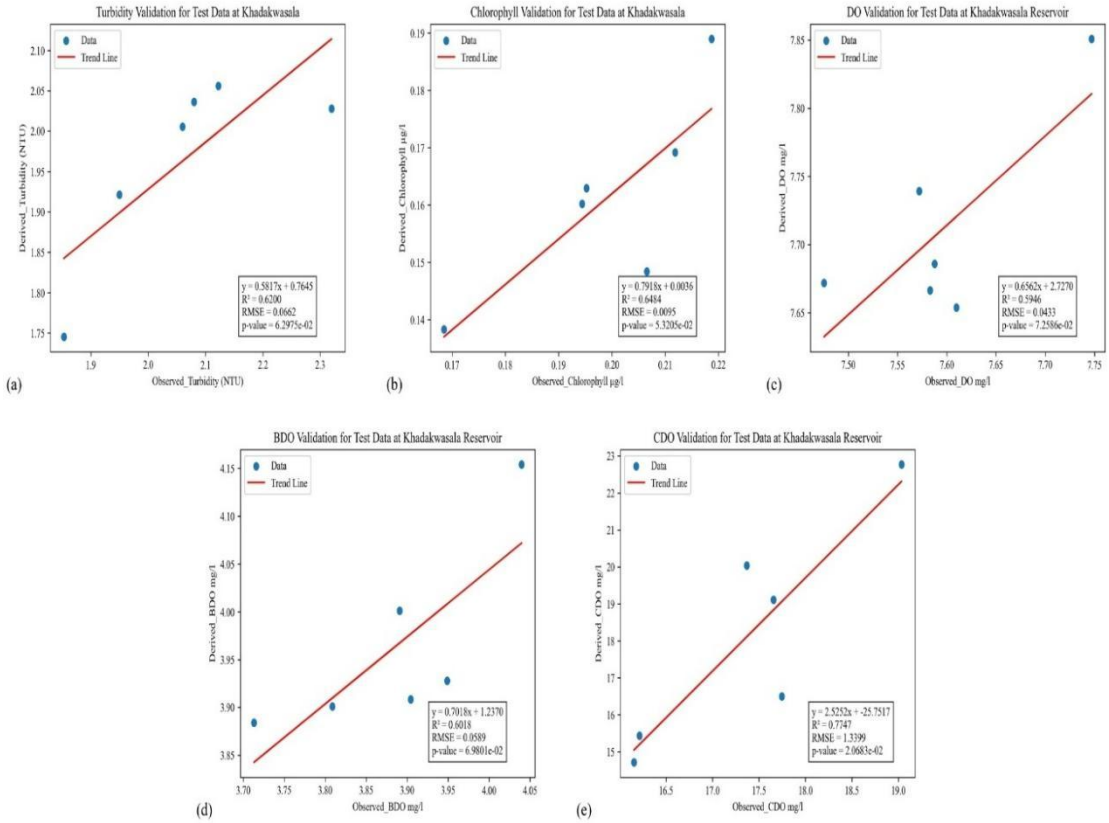


Fig. 4. Test-set validation of stepwise-regression models for Landsat 8/9 OLI water-quality retrievals sampled on 28-10-2022 (Observed vs Modelled), Khadakwasala Reservoir: Turbidity, Chlorophyll a, Dissolved Oxygen, Biochemical Oxygen Demand and Chemical Oxygen Deman.

Model of Dissolved Oxygen. The Dissolved Oxygen (DO) model attained a R^2 score of 0.60 for the observed DO data, where about 59.46% variance could be explained. Low RMSE values (0.043) signify that predictive accuracy is not very high in the case of DO concentration. The statistical validity of this model has been attested by the p-value being less than 0.001 (ref. **Fig. 4c**).

Model of Biological Oxygen Demand. The Biological Oxygen Demand (BOD) model displayed an R^2 value equal to 0.60, implying that it covers approximately 60.18% of all BOD data variances. RMSE was estimated at 0.06, thus showing an average difference between the projected and actual BOD values. A P-value less than 0.001 confirms the significance of the relation between turbidity and BOD (ref. **Fig. 4d**).

Model of Chemical Oxygen Demand. In the COD model, an R^2 of 0.78 was obtained, indicating that the model could justify almost 77.47% of COD variability. A RMSE of 1.34 is used as an average

comprehension between the estimated and actual values of COD. A P-value below 0.001 for this model also adds strength to its predictivity (ref. **Fig. 4e**).

The models exhibited statistically significant correlations (p-value < 0.001) between the predictor variables and the corresponding water quality parameters; however, the R^2 values suggest a moderate degree of predictive accuracy. The validation outcomes of the Landsat-derived SWR models for Khadakwasala Reservoir demonstrate a moderate degree of precision in assessing water quality parameters. The moderate R^2 for DO and BOD (≈0.60–0.65) reflects on certain limitations induced in predicting non-optical water quality parameters from optically sensitive parameters. In this study, turbidity was the only retained predictor for both DO and BOD, while other external parameters (e.g., temperature, microbial activity, etc.) are not considered in the model which could be one reason for moderate accuracy.

The limited dataset comprising 23 samples (17 for training and 6 for testing), all collected from a single surface location (0.25 m), restricts the ability to map both horizontal and vertical concentration variations Although field work was aligned with satellite passes, short-term variability and residual correction uncertainties (radiometric/atmospheric) introduce additional noise in reflectance–chemistry relationships. These factors together account for the observed R^2 while the fits remain statistically robust; denser, multi-site/depth sampling and added covariates are expected to narrow uncertainties in future work.

Improving model performance can be achieved by rectifying the constraints of the training dataset, integrating supplementary data points, and investigating alternative modeling methodologies. Such enhancements will ultimately support more accurate and reliable estimation of surface water quality parameters using remote sensing data, contributing to better water resource management and environmental monitoring efforts.

The influence of seasonal variability, especially significant events like monsoons, on water quality parameters and subsequently on model performance, is a critical consideration. Seasonal changes, particularly monsoon events, can drastically alter the physical, chemical, and biological characteristics of a water body. Increased rainfall during monsoons typically leads to higher runoff from the surrounding catchment area, introducing larger quantities of suspended sediments, organic matter, and nutrients into the reservoir. This influx can lead to significant increases in turbidity, total suspended solids, and potentially influence chlorophyll concentrations due to nutrient enrichment. The models developed in this study were calibrated on data from a specific period specially during non-monsoon period, and their performance may vary when applied to different seasons with distinct environmental conditions. Models developed using limited, localized datasets tend to lack generalizability across different seasons.

5. CONCLUSIONS

This study successfully integrates In situ water quality measurements have been integrated with Landsat 8/9 Operational Land Imager (OLI) data for assessing water quality in the Khadakwasala Reservoir, Pune, India. Using stepwise regression analysis, predictive models have been developed that relate Landsat-derived spectral indices to key parameters, including turbidity, chlorophyll-a, dissolved oxygen (DO), biochemical oxygen demand (BOD), and chemical oxygen demand (COD). The models demonstrated predictive accuracies with R2 values of 0.85 for turbidity, 0.90 for chlorophyll-a, 0.65 for DO, 0.64 for BOD, and 0.84 for COD, confirming the feasibility of using remote sensing for water quality assessment.

These results highlight the utility of satellite imagery, particularly Landsat 8/9 data, for monitoring water quality over large geographic areas, providing an efficient and cost-effective alternative to traditional in situ monitoring methods. This study do not observe the major fluctuation in the water quality in both dataset in-situ and by Landsat. This means the 8 days revisit temporal resolution monitoring frequency of alternate Landsat 8 and 9 does not affect lake and reservoir monitoring. However, it may make the issue of concern in case of rivers. Furthermore, turbidity was found to be a significant predictor for several non-optically sensitive parameters (DO, BOD, COD),

enhancing the robustness of the models. This study provides a scalable method for routine water quality monitoring that can be applied to other water bodies with similar environmental conditions.

The Integrating remote sensing data with physical water quality measurements presents a comprehensive approach to effective water resources management. This approach not only aids in the monitoring and management of water bodies like the Khadakwasala Reservoir but also holds promise for broader applications in environmental monitoring, supporting the sustainable management of water resources across regions. Future research could focus on increasing the accuracy of the models by incorporating additional data sources or exploring advanced machine learning techniques to improve the predictive ability for water quality parameters. Also, we recommend to consider other water quality parameters like temperature, CDOM, Secchi Depth etc. for betterment and improvement of the model.

ANNEX CONTAINING DATA AVAILABILITY

A1) In-situ Water Quality Data

The surface water quality parameters data, including Tur, Chl, DO, BOD, and COD for the Khadakwasala Reservoir in Pune, is available for public access. This dataset can be freely downloaded and used from the Zenodo Open Access Repository at https://zenodo.org/records/10901935 , (Kulkarni & Khare, 2024a ; Kulkarni & Khare, 2024b). The data is hosted at Zenodo and is licensed for open access, ensuring its availability for researchers and practitioners interested in water quality assessment and related studies.

A2) Landsat 8/9 OLI Derived Water Quality Data

The publicly available dataset "Water Quality Parameters for Khadakwasala Dam derived using Landsat 8 OLI Surface Reflectance" (Mendeley Data, v1; DOI: 10.17632/nwp835npgk.1) provides GeoTIFF raster layers for chlorophyll-a, turbidity, COD, BOD, and DO derived from Landsat-8 OLI surface-reflectance bands and band ratios for 20 Oct 2022–22 Apr 2023 (post-monsoon to pre-monsoon period). The accompanying description details the regression equations used to produce the layers (OACs from reflectance; NOACs from turbidity/chlorophyll), the file naming convention (Parameter_YYYYMMDD_Khadakwasala.tiff), and a caution that the relationships are site-specific. The dataset is released under CC BY 4.0, enabling reuse with attribution. All image data generated in this study are stored in the Mendeley Data repository and can be accessed via the following DOI: https://data.mendeley.com/datasets/nwp835npgk/1. This dataset is publicly available without any access restrictions, for distribution and reproduction in any medium, provided the original work is properly cited.

A3) Code availability

The Python code used for the generation and processing of datasets in this study is available at https://github.com/rpkulkarni/stepwise-regression-SWQP-khadakwasala.git. This repository contains the exact version of the code used in the study, along with the relevant documentation. The primary dependencies for this code include Python 3.8, along with libraries such as NumPy (v1.21.0), Pandas (v1.3.0), and Scikit-learn (v0.24.2). The specific variables and parameters used for dataset generation and processing are documented within the repository's README file. Access to the code is unrestricted and available for public use.

ACKNOWLEDGEMENTS

We thank the Water Resources Department, Government of Maharashtra, Pune Division, for granting access to collect the water samples from the Khadakwasala Reservoir and providing assistance for the same. We also thank the Staff of the Civil Engineering Department, Symbiosis Institute of Technology, for supporting us in conducting the experiments in the laboratory.

REFERENCES

Akhtar, N., Ishak, M. I. S., Bhawani, S. A., & Umar, K. (2021). Various natural and anthropogenic factors responsible for water quality degradation: A review. Water, 13(19), 2660. https://doi.org/10.3390/w13192660

Chang, N.-B., Imen, S., & Vannah, B. (2014). Remote sensing for monitoring surface water quality status and ecosystem state in relation to the nutrient cycle: A 40-year perspective. *Critical Reviews in Environmental Science and Technology, 44*(19), 2209-2250. https://doi.org/10.1080/10643389.2013.829981

Chawla, I., Karthikeyan, L., & Mishra, A. K. (2020). A review of remote sensing applications for water security: Quantity, quality, and extremes. *Journal of Hydrology, 585*, 124826. https://doi.org/10.1016/j.jhydrol.2020.124826

Chen, J., Zhang, M., Cui, T., & Wen, Z. (2013). A review of some important technical problems in respect of satellite remote sensing of chlorophyll-a concentration in coastal waters. *IEEE Journal of Selected Topics in Applied Earth Observations and Remote Sensing, 6*(5), 2275–2289. https://doi.org/10.1109/JSTARS.2013.2242845

Kirk, J. T. O. (2010). Light and photosynthesis in aquatic ecosystems (3rd ed.). Cambridge University Press. https://doi.org/10.1017/CBO9781139168212

Kuhwald, K., & Oppelt, N. (2016). Remote sensing for lake research and monitoring – Recent advances. *Ecological Indicators, 64*, 105–122. https://doi.org/10.1016/j.ecolind.2015.12.009

Kulkarni, R., & Khare, K. (2024). Water quality parameters for Khadakwasala Dam derived using Landsat 8 OLI surface reflectance [Data set]. *Mendeley Data, V1*. https://data.mendeley.com/datasets/nwp835npgk/1

Kulkarni, R., & Khare, K. (2024). Surface water quality parameters data of Khadakwasala Reservoir Pune, India [Data set]. *Zenodo*. https://zenodo.org/records/10901935

Li, J., et al. (2018). Spatio-temporal variations of CDOM in shallow inland waters from a semi-analytical inversion of Landsat-8. *Remote Sensing of Environment, 218*, 189–200. https://doi.org/10.1016/j.rse.2018.09.014

Olmanson, L. G., Brezonik, P. L., & Bauer, M. E. (2015). Remote sensing for regional lake water quality assessment: Capabilities and limitations of current and upcoming satellite systems. In *Advances in Watershed Science and Assessment* (Vol. 33, pp. 111–140). Springer. https://doi.org/10.1007/978-3-319-14212-8_5

Palmer, S. C. J., Kutser, T., & Hunter, P. D. (2015). Remote sensing of inland waters: Challenges, progress and future directions. *Remote Sensing of Environment, 157*, 1–8. https://doi.org/10.1016/j.rse.2014.09.021

Sagan, V., et al. (2020). Monitoring inland water quality using remote sensing: Potential and limitations of spectral indices, bio-optical simulations, machine learning, and cloud computing. *Earth-Science Reviews, 205*, 103187. https://doi.org/10.1016/j.earscirev.2020.103187

Sharaf El Din, E., Zhang, Y., & Anctil, F. (2017). Mapping concentrations of surface water quality parameters using a novel remote sensing and artificial intelligence framework. *International Journal of Remote Sensing, 38*(4), 1023–1042. https://doi.org/10.1080/01431161.2016.1275056

Sun, D., Qiu, Z., Shi, K., & Gao, S. (2014). Detection of total phosphorus concentrations of turbid inland waters using a remote sensing method. *Water, Air, & Soil Pollution, 225*(3), 1953. https://doi.org/10.1007/s11270-014-1953-6

Vakili, T., & Amanollahi, J. (2020). Determination of optically inactive water quality variables using Landsat 8 data: A case study in Geshlagh reservoir affected by agricultural land use. *Journal of Cleaner Production, 247*, 119134. https://doi.org/10.1016/j.jclepro.2019.119134

Wang, C., et al. (2017). The spatial and temporal variation of total suspended solid concentration in Pearl River Estuary during 1987–2015 based on remote sensing. *Science of the Total Environment, 618–619*, 1125–1138. https://doi.org/10.1016/j.scitotenv.2017.09.196

Wang, S., et al. (2019). High spatial resolution monitoring of land surface energy, water, and CO_2 fluxes from an unmanned aerial system. *Remote Sensing of Environment, 229*, 14–31. https://doi.org/10.1016/j.rse.2019.03.040

Wang, X., & Yang, W. (2019). Water quality monitoring and evaluation using remote-sensing techniques in China: A systematic review. *Ecosystem Health and Sustainability, 5*(1), 1571443. https://doi.org/10.1080/20964129.2019.1571443

MULTISPECTRAL IMAGING FOR RICE HEALTH IN FERTILE ALLUVIAL PLAIN OF SOUTHEASTERN FLANK MERAPI VOLCANO

Aditya SAPUTRA[1], *Danardono DANARDONO*[1], *Afif Ari WIBOWO*[1], *Christopher GOMEZ*[2], *Dedi SURACHMAN*[3], *Said Willya PUTRA*[4] *and Ridwan HAFIDZIN*[4]

DOI: 10.21163/ GT_2026.211.06

ABSTRACT

Food security is a pressing issue in Indonesia, where challenges in land suitability and crop productivity are exacerbated by rice diseases and pests. This study aims to detect and analyze rice diseases and pests in southeastern Mount Merapi, Klaten Regency, using UAV technology to support sustainable agriculture. The research establishes an integrated framework for precision agriculture by combining a region Land Potency Index (LPI) with UAV-based multispectral monitoring to address these challenges. The LPI, assessing slope, lithology, soil, water, and hazard exposure, strategically identified the central zone of Klaten Regency as the area with the highest agricultural potential, thereby optimizing the focus for subsequent detailed analysis. Within these high-potential zones, UAV-derived vegetation indices (NDVI and NDCI) served as effective early-warning indicators. The analysis revealed a clear distinction where healthy rice plants consistently exhibited NDVI > 0.6 and NDCI > 0.5, while significant clusters fell below these thresholds. Crucially, field validation confirmed that these low-value clusters were predominantly associated with leaf blast disease, demonstrating the method's efficacy in pinpointing specific physiological stress. The widespread prevalence of blast in high-potential areas underscores a direct and significant threat to regional yield. Therefore, this study demonstrates that the integration of LPI for targeting and UAVs for diagnosis provides a scalable, data-driven workflow. The findings highlight the critical need for management strategies that leverage this early detection capability to implement timely interventions, such as the use of resistant varieties and balanced fertilization, thereby enhancing the sustainability and resilience of rice production systems in Indonesia and similar agro-ecological contexts.

Keywords: *Multispectral drone; LPI; NDVI; NDCI; Leaf blast.*

1. INTRODUCTION

Food security is a pressing global issue that affects developed countries, developing countries, and even the very poor nations (Fada et al., 2024; Sundram and Brennan, 2024) Similarly, in Indonesia, with its diverse geography and rapidly growing population, the country faces significant challenges in ensuring a stable and sustainable food supply. Key factors in addressing these challenges include land availability and suitability, agricultural commodities and productivity, as well as food accessibility (Sundram and Brennan, 2024). The proper selection of land for agricultural effectiveness and productivity is crucial. Although Indonesia's tropical climate offers advantages for agriculture, its diverse topography requires appropriate agricultural techniques for optimal utilization (Pereponove et al., 2023; Hariyanto et al., 2025; Atapattu et al., 2025). In addition, the diversity of landforms, which are the surface manifestations. of morphological units, materials, and geomorphic processes that form or transform them over time, results in varied land resources (Migoń and Jancewicz, 2024; Jawabreh et al., 2025).

---

[1]*Faculty of Geography, Universitas Muhammadiyah Surakarta, Indonesia:* [*]*Corresponding author as105@ums.ac.id (AS); dan115@ums.ac.id (DD); aaw346@ums.ac.id (AAW)*

[2]*Graduate School of Maritime Science, Kobe University, Japan: christophergomez@bear.kobe-u.ac.jp (CG)*

[3]*The Regional Development, Planning and Research Agency of Tegal Regency, Slawi, Indonesia: dedi.surachman@sdm.tegalkab.go.id (DS)*

[4]*Land and Resource Laboratory, Universitas Muhammadiyah Surakarta, Indonesia: ridwan.hafidzin@gmail.com (RH)*

There are two main factors causing crop losses in all regions, namely “rice diseases and pests” and “outdated equipment” (Yuan et al., 2024; Junaid and Gokce, 2025). Diseases and pests in rice agriculture have long been a concern, and they have recently gained more attention due to their increasing frequency and severity caused by climate change (Karmakar et al., 2022; Oraon et al., 2024). Rising temperatures lead to changes in the behaviour of pests and pathogens, affecting their ability to damage rice crops. Various strategies have been previously implemented to protect rice crops from diseases and pests. Integrated Pest Management (IPM) is the most ideal approach to curb the rapid increase in rice diseases and pests due to climate change, having shifted toward more sustainable and environmentally friendly method by reducing reliance of chemical pesticides (Tiwari, 2024; Abdollahzadeh and Sharifzadeh, 2024). However, its adoption in developing countries like Indonesia is hindered by financial constraints, high initial costs, and the inherent complexity and labor-intensive nature to IPM strategies compared to traditional methods. Currently, advanced technology can be used to improve the quality of agricultural yields without human presence, including disease and pest prevention (Ma et al., 2024). Remote sensing has become a powerful tool for identifying and monitoring plant diseases and pests to improve agricultural productivity. Many academics have achieved satisfactory results in mapping disease damage using satellite imagery (Ma et al., 2024; Dolatabadian et al., 2025). However, Technological solutions often face scalability issues, for instance, smart farming applications are typically limited to small areas, while satellite imagery can be constrained by its spatial and temporal resolution, leading to mismatches between field data and image pixels.

Rapid advances in remote sensing, supported by wider access to multispectral imagery and improved image processing algorithms, are enabling more complex applications in environmental monitoring and surveying, including agriculture sector (Fakriyah et al., 2023; Sabir et al., 2024; Wang et al., 2025; Nguyen et al., 2025). Remote sensing technology and Unmanned Aerial Vehicles (UAVs) offers innovative solutions in agricultural management.

Remote sensing has capability to extract spatial data rapidly over wider area. Thus, the Land Potency Index (LPI) can be generated and used for the preliminary identification of ideal agricultural land. The LPI Integrates six critical physical parameters-slope, lithology, soil type, surface water, ground water, and hazard exposure to systematically identify and map high potential agricultural zones. Meanwhile, multispectral drones provide significant advantages for monitoring rice pests and diseases. Their ability to capture images in various wavelengths beyond the visible spectrum enables early detection of plant health issues that are invisible to the naked eye. This enhanced detection capability results in more accurate assessments of pest manifestations and disease symptoms. In addition, drones can cover large areas quickly and efficiently, providing comprehensive data across vast rice fields that are difficult to inspect manually. Rapid analysis and timely decision-making can help control pest and disease outbreaks before they spread widely. The objective of this study is to identify and analyse rice diseases and pests on the southeastern flank of Mount Merapi, Klaten Regency, Central Java-a key rice producing region on a fertile alluvial plain where protecting yields is crucial for maintaining national food security.

2. STUDY AREA

Klaten Regency, located in Central Java, Indonesia, is strategically situated between two major urban centers—Yogyakarta to the west and Surakarta (Solo) to the east—making it an important transitional zone for economic, cultural, and transportation linkages in the region. Geographically, it lies between the volcanic highlands of Mount Merapi in the northwest and the extensive lowlands in the southeast. Elevation varies considerably, from over 1,000 meters above sea level on the steep volcanic slopes to less than 100 meters in the flat eastern plains. This elevational gradient produces a distinct topographic transition from rugged mountainous terrain to gently undulating hills and broad alluvial plains. Geologically, Klaten is dominated by Quaternary volcanic deposits from Merapi, including volcanic breccia, tuff, and andesite lava, which contribute to the region’s high soil fertility (Saputra et al., 2020). The uplands are characterized by Andisols with high porosity and excellent

water retention, well-suited for horticulture and perennial crops. In the lowlands, Inceptisols and Alfisols provide favorable conditions for intensive irrigated rice cultivation. The region's hydrology is shaped by river systems and irrigation channels descending from the volcanic slopes toward the plains, ensuring a reliable water supply for agriculture. These diverse physical characteristics, combined with its strategic location, make Klaten a vital agricultural and socio-economic hub in Central Java. The overview of the study area is illustrated in **figure 1**.

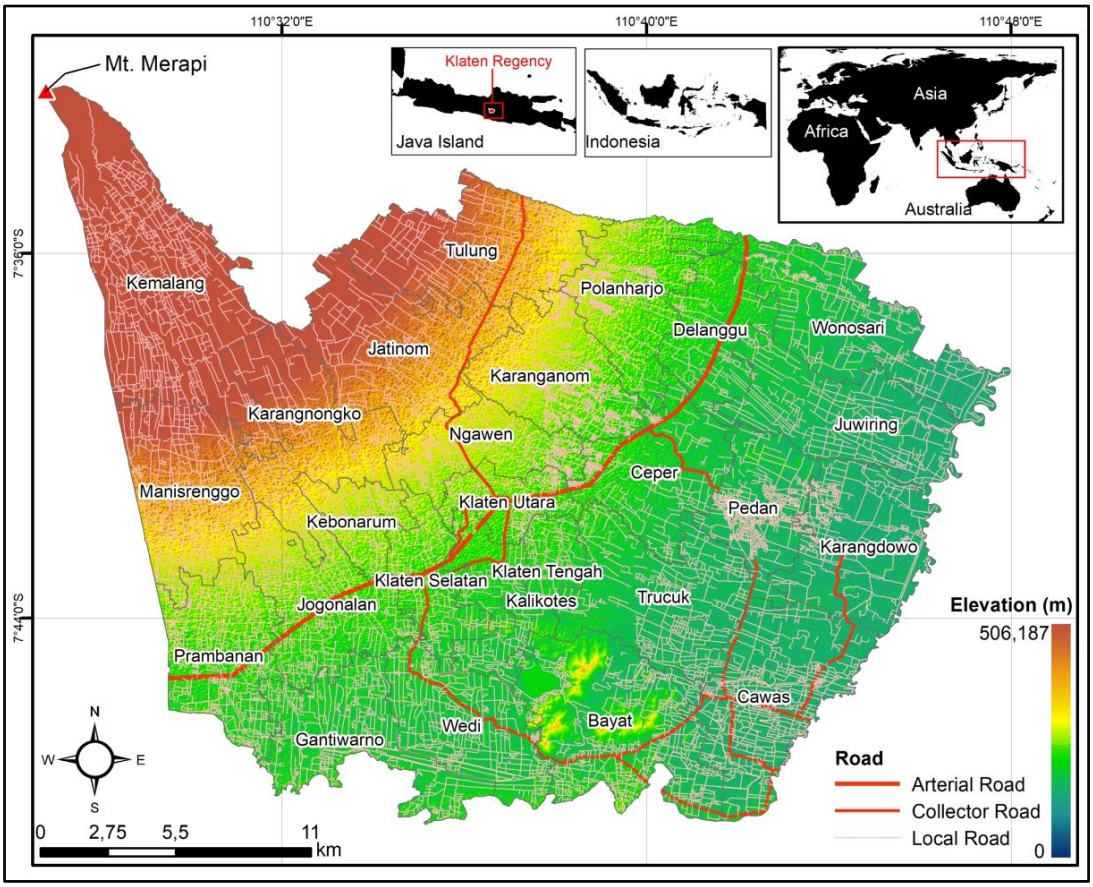


Fig. 1. Overview of Klaten Regency.

3. DATA AND METHODS

3.1. Rice Field Selection

Preliminary analysis was conducted to select the field of rice crop. The specific rice crop field was selected by using Land Potency Index (LPI). LPI was conducted in entire area of Klaten regency to identify which land has high LPI and low LPI. High LPI indicate that the land has high potency for agriculture activity, vice versa, the low LPI indicates that the land has low potency for agricultural activity due to particular factors. At least 6 parameters were used in this analysis to generate the LPI in entire Klaten Regency such as slope, lithology, soil type, surface water, ground water, and hazard condition in this case the volcano and flood hazards). The summary of the data used for extract the LPI in the study area can be seen in **table 1**.

Further analysis was conducted by applying the drone multispectral survey to obtain the level of healthiness of rice plant in study area. The high LPI area was analysed by using NDVI from multispectral drone. Additionally, physiology observation of rice plant was also conducted to identify type of disease and pets that might be found in observed paddy field.

Table 1.

The data used.

No	Data	Format Data	Scale	Source and year Provided
1	Geospatial data	Shp (vector)	1:25.000	Indonesia Geospasial Information Agency, 2010
2	Topography data	Shp (vector)	1:25.000	Indonesia Geospasial Information Agency, 2010
3	Indonesian DEM	Raster	8.3 m (Spatial Resolution)	Indonesia Geospasial Information Agency, 2022
4	Disaster data at regency level	Tabular	Regency Level	BPDP Klaten Regency, 2024

3.2. Land Potency Index (LPI)

Land potency index (LPI) was used to decide which paddy field will be observed further by using multispectral drone. LPI was obtained by overlaying 6 parameters such as slope, lithology, soil, surface water, groundwater, and hazards exposure. The general formula of LPI can be seen as follow:

$$\mathrm{LPI} = (\mathrm{R} + \mathrm{L} + \mathrm{H}) \times B \quad (1)$$

where:

LPI -Land Potency Index;
R -Slope;
L -Lithology;
H -Hydrology (Groundwater and Surface Water Condition)
B -Hazards exposure

The slope was generated from Indonesia Digital Elevation Model of known as DEMNAS. DEMNAS is an integrated elevation dataset, synthesized from multiple sources including IFSAR (5m resolution), TERRASAR-X (5m resolution), and ALOS PALSAR (11.25 m resolution). By amalgamating these diverse data sources, DEMNAS achieves a spatial resolution of 0.27 arc-seconds or approximately 8.3 m (Susetyo, 2023). The lithology of Klaten Regency was mainly extracted from the Geological Map of Yogyakarta and Surakarta Scale 1:100,000. The previous research results such as (Saputra et al., 2020) also used to obtain mode detail information of geology.

Regarding the hydrological aspect, two key factors are considered: surface water potential and groundwater potential. Surface water potential is assessed based on the abundance of surface water sources — such as rivers, lakes, and reservoirs — within a given area and the feasibility of irrigation development. Groundwater potential, conversely, is evaluated based on aquifer productivity, with data sourced from the groundwater basins of the Klaten region. Areas characterized by a high abundance of surface water, high feasibility for irrigation, high groundwater productivity, and extensive aquifer distribution are considered to have high land potential.

From a disaster aspect, volcanic activity, landslides, earthquakes, and floods were considered in determining the Land Potency Index (LPI) for Klaten Regency, given the historical occurrence of these four hazards in the region. Volcanic hazards were excluded from the overlay process because the entire Klaten area exhibits a uniform ground shaking potential, characterized by low to moderate Peak Ground Acceleration (PGA). Regarding flood susceptibility, areas prone to flooding are predominantly located in the southern part of the regency, adjacent to the rivers that form the border between Klaten Regency and Gunungkidul Regency in the Special Region of Yogyakarta.

The results of the Land Potential Index (LPI) assessment using the formula will produce a value that determines the potential of a particular land area based on the weight of each parameter. The values obtained through the calculation are classified into several land potential classes, each with different value ranges. The land potential index classes are divided into five categories as shown in **table 2** below.

Table 2.

Land Potency Index (LPI) Class.

No	Class	LPI Class	LPI Value
1	I	Very High	32-40
2	II	High	24-31.9
3	III	Medium	16-23.9
4	IV	Low	8-15.9
5	V	Very Low	0-7.9

3.3. UAV Data Acquisition and Image Analysis

The multispectral drone mapping was conducted in rice fields with high LPI values to prioritize monitoring of high-yield potential areas. The Area of Interest (AoI) was selected based on safe flying zones, accessibility for ground validation, and a uniform late vegetative-early generative crop stage to ensure spectral variations reflected plant health. The flight mission was planned and executed using GSPRO software. In GSPRO, a double-grid (nadir) flight pattern was configured with 80% front overlap and 70% side overlap to ensure comprehensive coverage and robust data for photogrammetric processing. The mission was flown at an altitude of 80 meters AGL, achieving a ground sampling distance (GSD) of approximately 4.23 cm/pixel, a resolution sufficient for detecting intra-canopy stress. Manual pilot control, when necessary, was conducted using DJI Fly software.

Flight parameters such as altitude, overlap, and route must be set using flight planning software to ensure comprehensive coverage and high resolution. The UAV platform used was a DJI P4 Multispectral RTK, which features an integrated multispectral imaging system. This system is equipped with an integrated sunlight sensor that records solar irradiance during flight. This system captures synchronized imagery in five discrete bands: Blue (450 nm ± 16 nm FWHM), Green (560 nm ± 16 nm FWHM), Red (650 nm ± 16 nm FWHM), Red Edge (730 nm ± 16 nm FWHM), and Near-Infrared (840 nm ± 26 nm FWHM). All flights were conducted under stable, clear-sky conditions to minimize variations in illumination

Ground Control Points (GCPs) must be placed throughout the field, with their precise coordinates recorded using high-precision GPS to improve georeferencing accuracy. A network of five (5) GCPs, constructed from high-contrast material, were distributed across the AOI's perimeter and center. Their coordinates were surveyed using a Real-Time Kinematic (RTK) GPS receiver (DRTK2) with a horizontal accuracy of ±1 cm + 1 ppm and a vertical accuracy of ±1.5 cm + 1 ppm. This high-precision ground truthing is essential to correct for geometric distortions in the model and achieve a absolute spatial accuracy of under 5 cm RMSE, ensuring that identified stress zones can be reliably relocated in the field.

Finally, a thorough pre-flight check of the drone must be conducted, including checking battery levels, propeller conditions, and camera functionality, as well as ensuring all software systems are working properly and there is sufficient data storage (Saputra et al., 2022). The captured multispectral imagery was processed using a standard SfM photogrammetry workflow in DJI GS PRO. The Radiometric calibration was performed to convert the raw digital numbers (DN) to reflectance values using the sunlight data. The captured multispectral imagery and the concurrent solar irradiance data from the drone's sunlight sensor were processed in Agisoft Metashape Pro 2.2.2. The 'Sun Sensor Calibration' tool was activated, which uses the irradiance data to normalize the imagery for variations in sunlight intensity, generating a calibrated surface reflectance orthomosaic for each band. This process is a core function of the integrated DJI system for achieving accurate spectral measurements without a ground reflectance panel. The key computational steps included: (1) Initial Processing for feature point matching and generation of a sparse point cloud; (2) Point Cloud Densification to create a 3D model of the terrain and canopy; and (3) Digital Surface Model (DSM) and Orthomosaic Generation. The final outputs, the 5-band orthomosaic and the DSM, were then exported for spectral

analysis in a GIS environment, where pixel-based calculations for NDVI and NDCI were performed using their standard formula**.** Normalized Difference Vegetation Index (NDVI) and Normalized Difference Chlorophyll Index (NDCI) was calculated as:

$$NDVI = \left(\frac{NIR-Red}{NIR+Red}\right) \quad (2)$$

$$NDCI = \left(\frac{Red_Edge-Red}{Red_Edge+Red}\right) \quad (3)$$

Addressing each of these elements carefully will lay the foundation for an effective and accurate mapping operation. In general, the workflow of this stage of research can be seen in **figure 2** below.

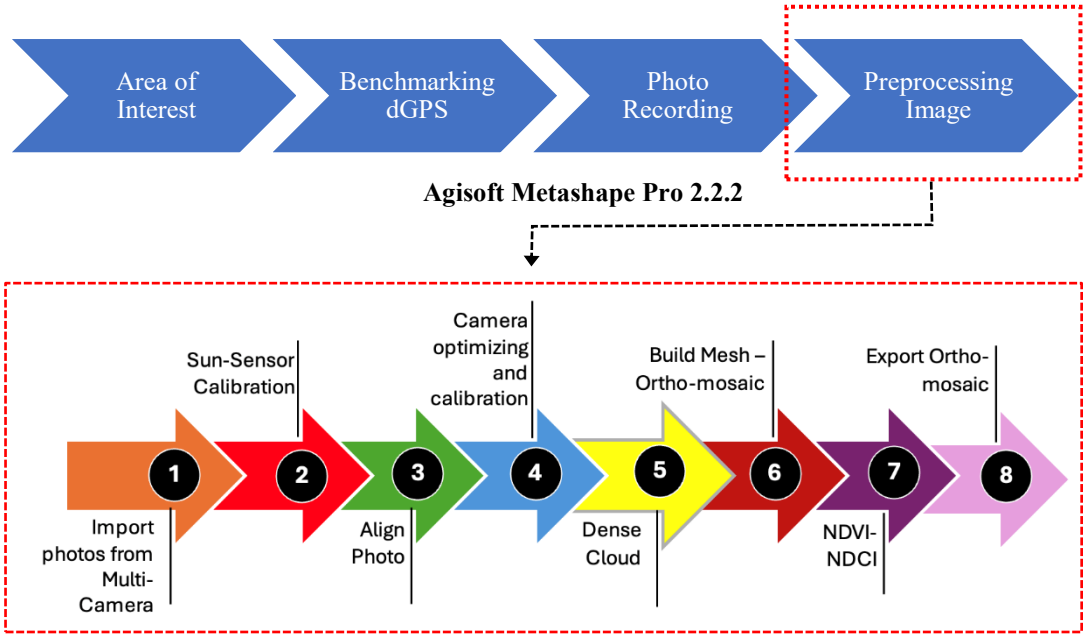


Fig. 2. The multispectral drone mapping and image analysis work flow.

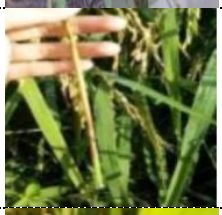
3.3. Field Observation

The field observation was conducted to obtain the ground truth data. The colour stratification from the preliminary NDVI and NDCI map was used to design the sample. The field survey will be conducted using a modified version of disease identification through physiological symptoms in rice plants based on colour stratification. Disease diagnosis through physiological symptoms will be identified based on the symptoms presented in **table 3**. At least 50 georeferenced sampling ponts (N=50) were randomly selected, ensuring a representative spatial distribution across the entire field. The sampling unit was an individual rice plant at the specified location.

At each sampling point, the designated rice plant was visually assessed for symptoms of Leaf Blast. The assessment was based on the presence of characteristic lesion as described in Table 3 (Masnilah et al., 2020). A binary scoring system (0/1) was used. Score 1 (Diseased) was assigned if one or more typical Leaf Blast lesions such as spindle-shaped, with grey centers and brown/necrotic margins were observed on any leaf of plant. Meanwhile, score 0 was assigned if no Leaf Blast lesions were observed on any leaf, and the plant exhibited vigorous growth without signs of chlorosis or necrosis attributable to blast.

Table 3.

Symptoms and diagnosis of rice plants affected by viruses and pests.

No	Disease	Symptoms	Pathogen Diagnosis	Example
1	Leaf Blight (Masnilah et al., 2020)	Leaves become gray or grayish. Disease progression causes the leaves to dry and curl along the midrib	*Xanthomonas campestris* pv. oryzae	
2	Leaf Blast (Masnilah et al., 2020)	A sharp spot appears at the tip of the leaf, with brown edges and a grayish or white center. The spot continues to develop, surrounded by a pale yellow area.".	Magnaporthe *oryzae*	
3	Leaf Spot (Rahmawati et al., 2017)	Dark brown spots appear on the leaves, with lighter brown edges. The rice grains turn yellow, and some of them become black.	*Fusarium sp.*	
4	Sheath Blight (Rahmawati et al., 2017)	The rice plant sheath becomes rotten with elongated lesions, yellow to light brown in color, and the base of the sheath turns greenish	*Rhizoctonia sp.*	
5	Narrow Brown Leaf Spot (Rahmawati et al., 2017)	Numerous small brown spots appear on a single leaf, with dark brown centers and lighter brown edges.	*Cercospora oryzae*	
6	Grain Rot (Widarti et al., 2020)	The rice grains turn dark brown, become soft and hollow, while the edges of the leaves turn reddish, surrounded by a yellowish rot-like color	*Burkholderia glumae*	

4. RESULTS

4.1. The Land Potential Index (LPI)

The Land Potential Index (LPI) is one of the analytical tools widely used in agriculture to assess land potential. Naturally, land with a high LPI (LPI ≥ 24) has great potential if optimized for agricultural activities. Conversely, land with a very low LPI (0–7.9) has limited potential for agricultural use due to several limiting factors. In general, the Land Potential Index (LPI) is composed of several parameters, including slope, lithology, soil type, hydrology, and hazards condition.

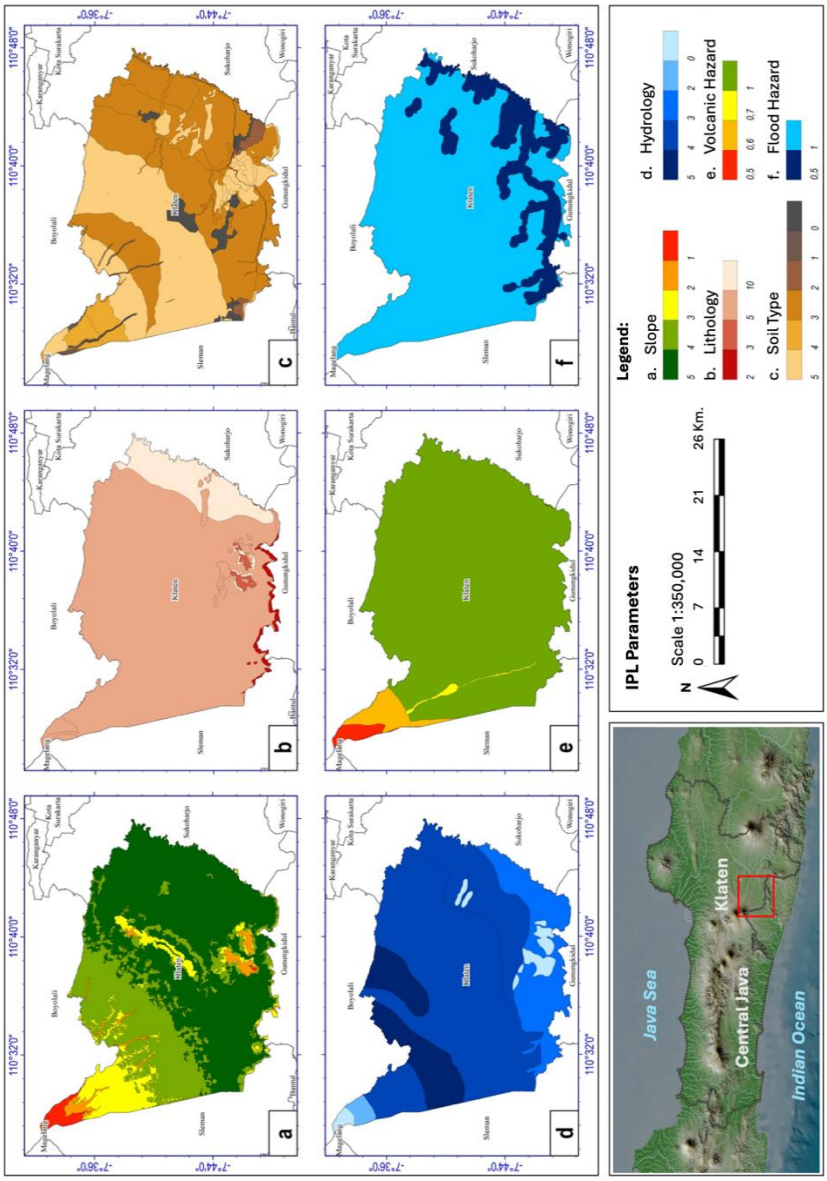


Fig. 3. The results of each parameter in term of LPI.

Gently sloping (0–5%) receives the highest score in the LPI assessment, as do alluvium-colluvium lithology, brown alluvial and Mediterranean soils, abundant surface water, highly productive groundwater, and areas free from natural hazards. The following presents the assessment results of each parameter in relation to land potential index.

Klaten Regency is predominantly characterized by an LPI slope score of 5, corresponding to slope class I with a gradient of 0–5% (flat to gently sloping). These flat-to-gently sloping areas are located in the central part of Klaten Regency, with geomorphology ranging from the volcanic foot plains of Mount Merapi to intensive alluvial plains. Steep to very steep slopes (slope > 45%) are found in the northern part of Klaten Regency, which is the cone of Mount Merapi. This area has an LPI slope score of 1. Moderately steep slopes are located in the northern and central-southern parts of Klaten Regency, namely on the upper slopes of Mount Merapi (north) and the Bayat sub-district area in the south.

Based on lithological aspects, Klaten Regency is mostly composed of volcanic rocks associated with Mount Merapi in the north. Additionally, there is a complex formation of rocks in Bayat Sub-district consisting of claystone sediments and metamorphic rocks. Alluvium and colluvium deposits are found along the narrow plains in the southern part of Klaten Regency, bordering the Baturagung Hills. The lithology or surface geology score classification of Klaten Regency can be seen in **figure 3.**

In the LPI (Land Potential Index) assessment, the soil aspect being evaluated is its texture, which refers to the ratio of sand, silt, and clay. Fine soil textures indicate that the soil is a result of denudational processes that have been accumulated and deposited. These denudational materials typically produce fine-textured deposits with high clay content. However, soils with high clay content are generally less favourable for agriculture. Similarly, soils with overly coarse textures are also less suitable for farming, as sandy soils have large pores and are unable to retain groundwater effectively. The LPI soil parameter scores for Klaten Regency can be seen in the following figure. Based on the LPI soil type scores, the highest scoring soil texture (score 5) is found in brown alluvial and Mediterranean soils, which have medium soil textures. These soil types are distributed in the central part of Klaten Regency and parts of the southern region.

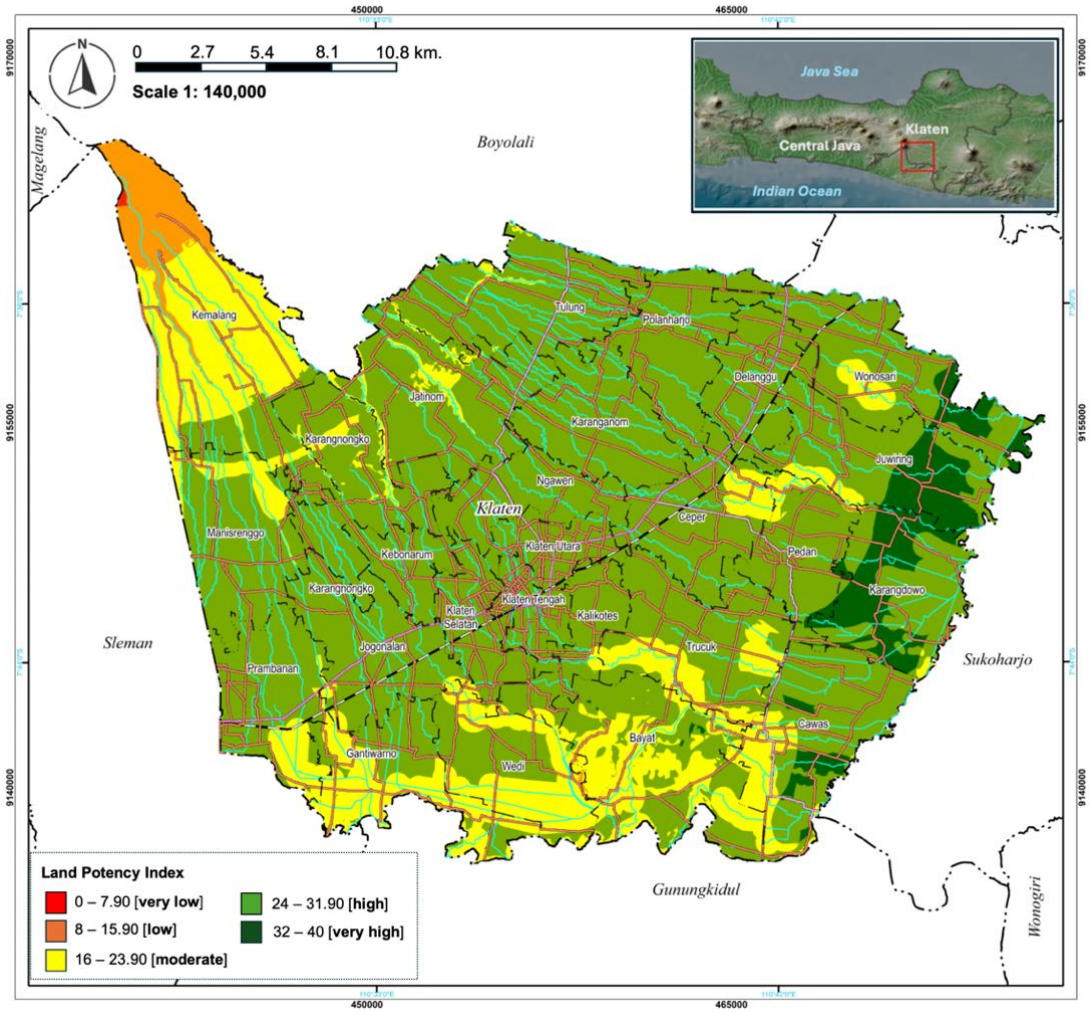


Fig. 4. LPI of Klaten Regency.

In relation to the hydrological aspect, two elements are considered: surface water potential and groundwater potential. Surface water potential is assessed based on the availability of surface water sources (rivers, lakes, and reservoirs) and the feasibility of developing irrigation. Groundwater potential is assessed based on groundwater productivity derived from the groundwater basin in the Klaten area. Characteristics that support high land potential include areas with abundant surface water resources, strong irrigation potential, and high groundwater productivity with wide distribution. The results of the hydrological assessment for LPI can be seen in **figure 3**. In terms of disaster aspects, volcanic eruptions, landslides, earthquakes, and floods are considered in determining the Land Potential Index (LPI) in Klaten Regency, as all four types of disasters have occurred in the area. Volcanic disasters were excluded during the overlay process because all areas of Klaten have similar ground acceleration (PGA) values, ranging from low to moderate. The disaster scores can be seen in **figure 3**. Areas prone to volcanic hazards are located in the northern part of Klaten Regency. These areas fall within Volcanic Hazard Zones 1 and 2. Meanwhile, the southern part of the region is prone to landslides. The central part of Klaten Regency, shown in green, is considered free from both volcanic and landslide hazards. Regarding flood hazards, flood-prone areas are located in the southern region, particularly around rivers that form the boundary between Klaten Regency and Gunungkidul Regency, in the Special Region of Yogyakarta Province.

Based on the overlay results using the formula described in Equation 1, the resulting Land Potential Index can be seen in **figure 4**. Based on the LPI Results, the drone mapping was conducted in the area which has LPI value very high in eastern part of Klaten Regency.

4.2. Multispectral drone results (NDVI and NDCI)

Multispectral drone mapping was conducted over three paddy field blocks selected specifically for their very high LPI classification, uniform late vegetative growth stage, and operational feasibility (safe flying zones, accessibility). This strategic selection ensured that spectral variations were primarily linked to plant health rather than underlying land constraints or phenological differences. The resulting NDVI and NDCI maps revealed distinct health patterns, with healthy rice exhibiting values >0.6 and >0.5, respectively, while lower values indicated stress, corroborated by field observations of leaf blast disease.

At least three blocks of paddy field were mapped by using multispectral drone and observed further in the field. Those three blocks (**Fig. 6, Fig. 7 and Fig. 8**) are belonged to very high LPI and cultivated as rice field. Based on the multispectral sensor, the drone mapping produce RGB orthophoto, Normalised Difference Vegetation Index (NDVI) and Normalised Difference Chlorophyl Index (NDCI). The Normalized Difference Vegetation Index (NDVI) is a widely used remote sensing indicator to assess vegetation health, including rice crops. In rice fields, high NDVI values (typically > 0.6) indicate dense, healthy, and photosynthetically active crops, while lower NDVI values suggest stress, disease, pest infestation, or poor growth due to insufficient nutrients or water (Liu et al., 2024; Safitri et al., 2024; Munandar et al., 2025)

The Normalized Difference Chlorophyll Index (NDCI) is a vegetation index specifically designed to estimate chlorophyll content, especially in aquatic or semi-aquatic vegetation like rice in paddy fields. This index is particularly sensitive to chlorophyll-a concentration, making it useful in monitoring crop vigour, nutrient status, and early signs of physiological stress. In rice crop health analysis, NDCI helps identify variations in chlorophyll levels that may result from nutrient deficiencies, diseases, or other stressors before these issues become visible. Compared to NDVI, NDCI can offer more nuanced insights into plant physiological conditions, especially in high-biomass or water-saturated environments (Li et al., 2024; Chen et al., 2024).

Based on the NDVI and NDCI of the observed paddy field. The NDVI of three paddy field ranging from 0-0.95.5. The lower the NDVI refers to the denser of rice crops while the lower value refers to the less dense of rice field. Several factor can affect the results of NDVI and such as, the different of plant, different rice crops ages, and land use change. In the observed rice field, low NDVI values were found due to those three factors. West Klaten famous by the extensive fertile agriculture area. Some of farmers also plant horticultural crops such vegetable, fruit, and ornament plants. Some

of theme use plastic mulch, which is widely used in horticulture to cover the soil surface for various benefits like moisture retention, weed suppression, temperature regulation, and improved crop quality. This area will likely result in relatively low NDVI values.

Different crop ages significantly influence NDVI values due to changes in plant structure, leaf area, and chlorophyll content throughout the growth cycle. In the early stages, crops are small with limited green biomass, resulting in low NDVI values. As the crops mature, the canopy becomes denser and chlorophyll levels increase, leading to higher NDVI values that reflect vigorous photosynthetic activity. However, during the senescence or harvesting phase, NDVI values decline again as leaves yellow, biomass reduces, and photosynthesis slows. Therefore, NDVI serves as a useful indicator to distinguish crop development stages and assess crop health over time.

There were two types of observed rice plant growth stages, vegetative ages (less than 45 days) and reproduction ages (between 45-70 days) (**Fig. 5**). Field observation and sampling was strategically restricted to a specific window of the crop cycle: from the late vegetative stage to the early generative stage in order to minimize the confounding effect of plant phenology on spectral indices. This ensured that the observed variations in NDVI and NDCI were more likely attributable to health status rather than the natural spectral differences between very young or senescing plants.

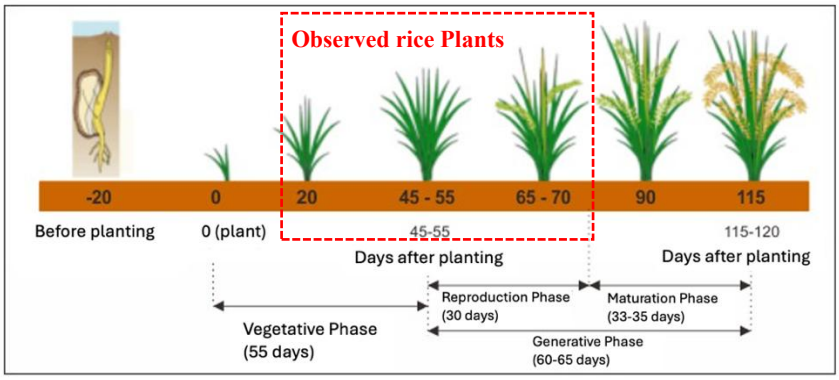


Fig. 5. Two types of rice plant phase observed in the field.

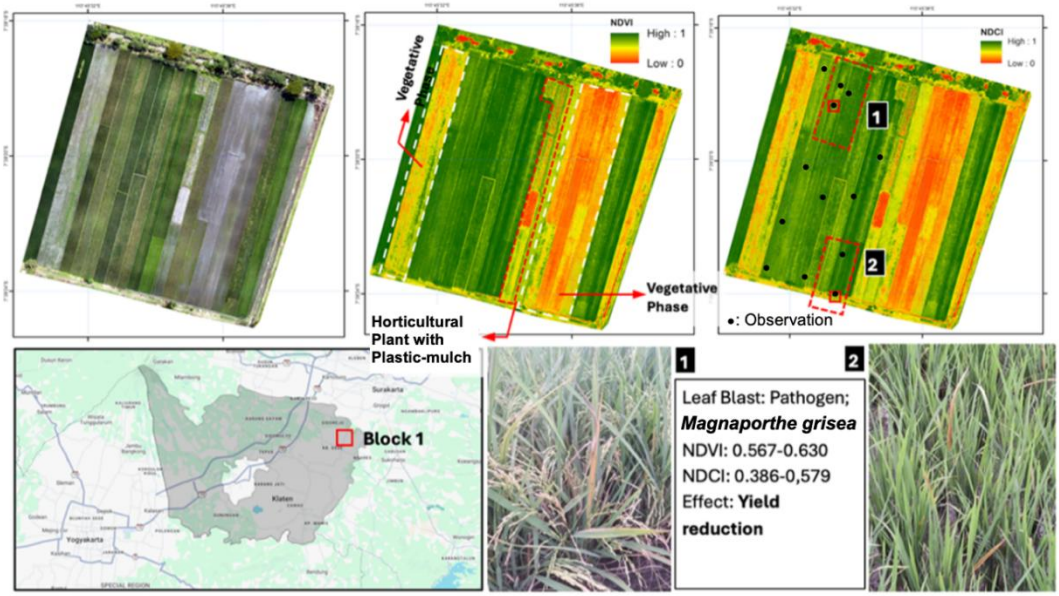


Fig. 6. The Multispectral drone results in Block 1.

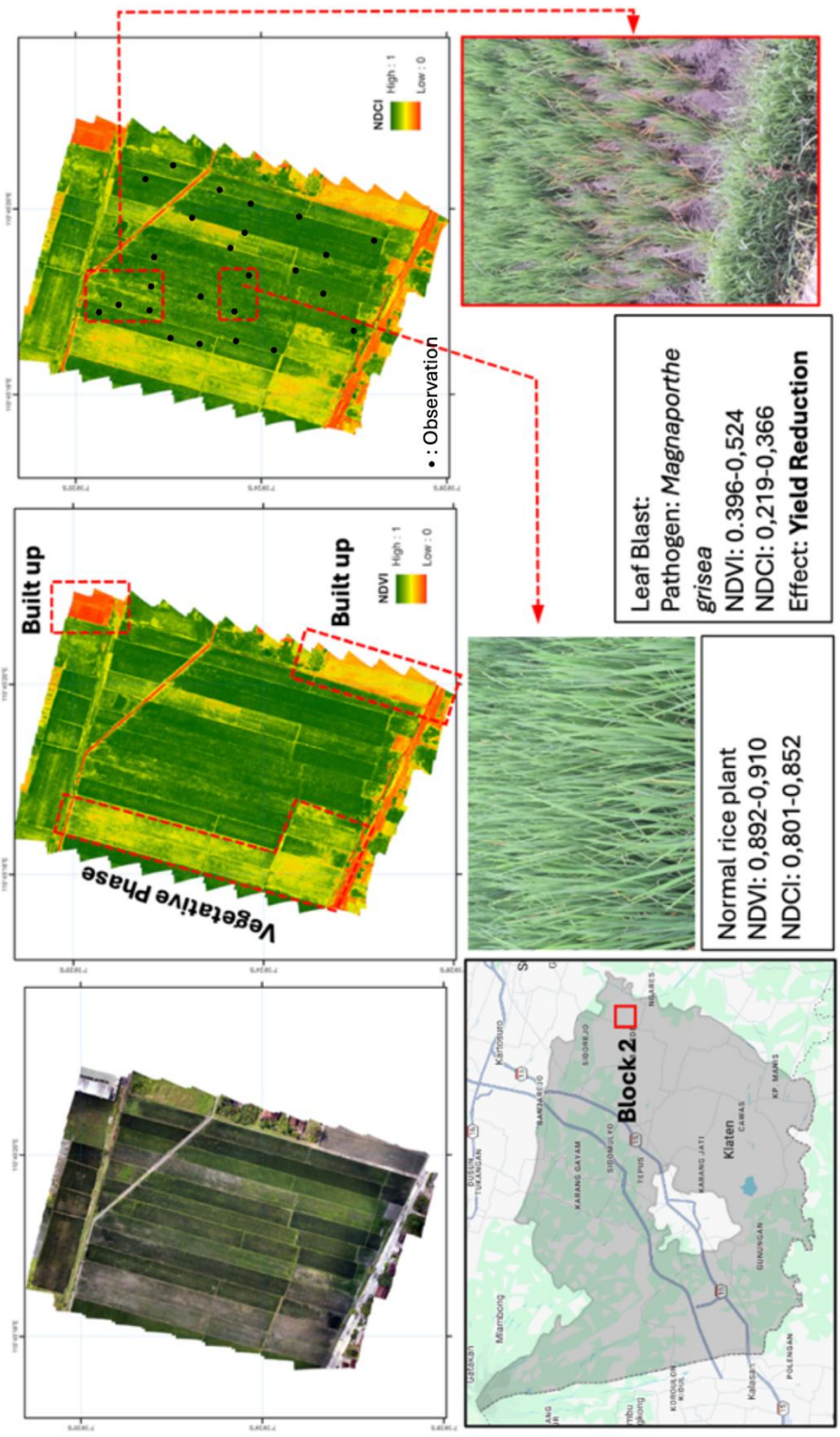


Fig 7. The Multispectral drone results in Block 2.

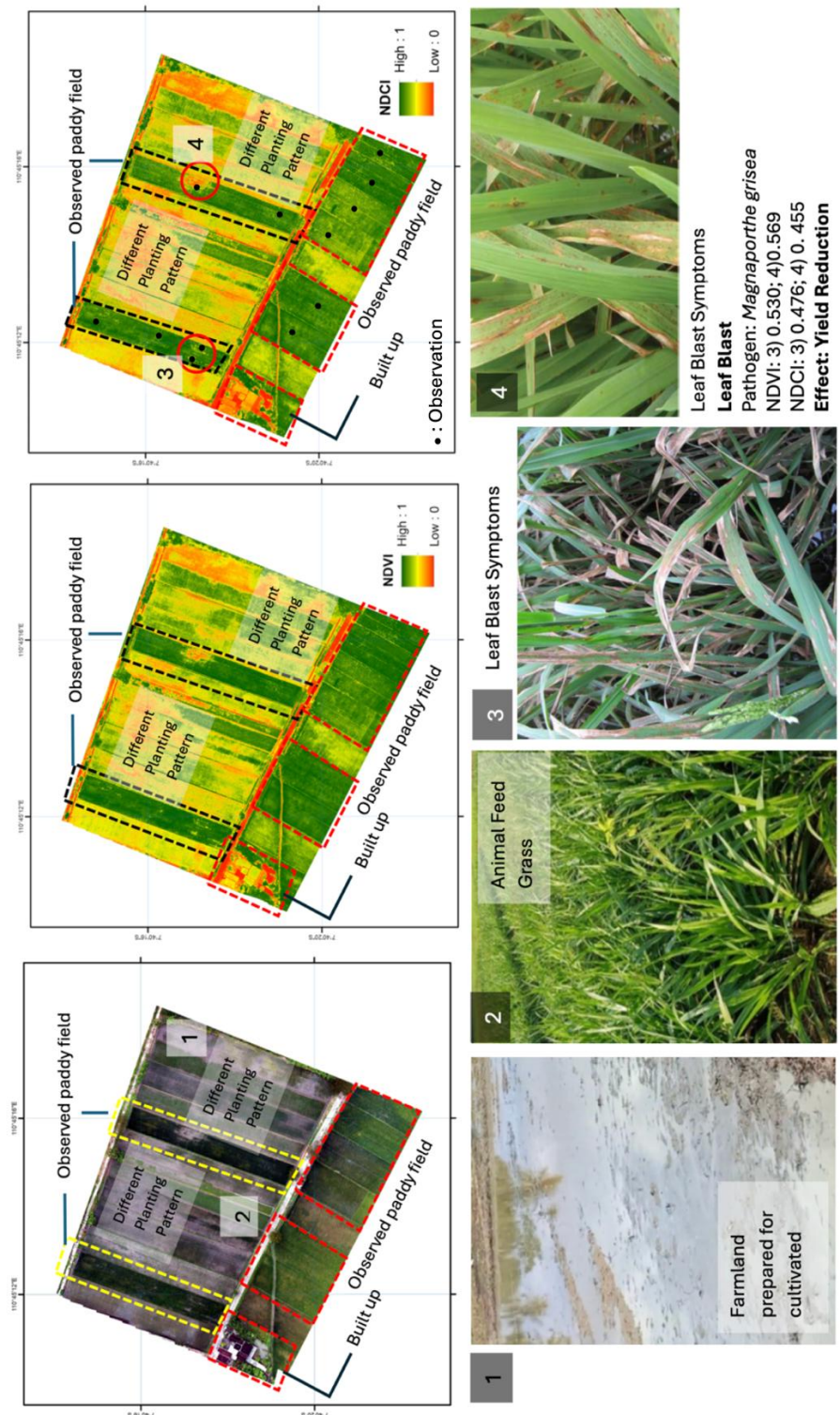


Fig. 8. The Multispectral drone results in Block 3.

Similar to NDVI, NDCI results can indicate the healthiness of rice plants. Low NDCI values, on the other hand, often point to stressed or aging crops, potentially caused by nutrient deficiencies, water stress, disease, or natural senescence. These areas may correspond with sections of the field showing poor growth or yellowing leaves. It is also possible that non-vegetated areas (e.g., bare soil, plastic mulch, or recently harvested plots) contribute to low NDCI readings. Therefore, analysing spatial patterns of NDCI across the field allows researchers to identify zones requiring further investigation or intervention, aiding in precision agriculture and crop health monitoring.

5. DISCUSSIONS

The results of this research demonstrate a clear distinction in vegetation index values between healthy and potentially diseased rice crops. Healthy rice plants generally recorded NDVI values above 0.6 and NDCI values above 0.5, reflecting vigorous growth, high chlorophyll concentration, and optimal physiological function. In contrast, certain spatial clusters exhibited NDVI values below 0.6 and NDCI values below 0.5, indicative of reduced chlorophyll content and possible physiological stress. Such reductions are commonly associated with early stages of disease, nutrient deficiency, or water stress. However, variations in NDVI may also be influenced by differences in rice growth stages across the study area. Younger rice plants in the early vegetative phase typically exhibit lower NDVI values due to incomplete canopy cover and less developed leaf area, while mature plants in the reproductive or grain-filling phases tend to reach higher NDVI values as chlorophyll concentration and biomass peak. Conversely, NDVI naturally declines in the late maturation stage as senescence begins and chlorophyll content decreases. Therefore, careful interpretation of NDVI results requires considering the crop calendar and planting synchrony to distinguish between stress-induced reductions and normal phenological variations.

A binary logistic regression was conducted to predict Leaf Blast (0/1) based on NDVI and NDCI. The model was trained on 50 observations. The model achieved an accuracy of 94.0% and an AUC of 0.976. McFadden's pseudo-R^2 was 0.676, indicating a strong relationship between the predictor and outcome (**Table 4**). The regression equation is provided as follow:

$$Logit\ (p) = 18.7398 - 5.4808\ \times NDVI - 26.0514 \times NDCI \quad (4)$$

where:

$$logit\ (p) = ln\left(\frac{p}{1-p}\right) \quad (5)$$

P is the probability of Leaf Blast = 1

Table 4.

Statistical model summary.

Statistic	Value
Pseudo R^2	0.6763
Log Likelihood	-10.58
AIC	27.15
BIC	32.89

The coefficient for NDVI (-5.4808) was not statistically significant (p = 0.245), suggesting that there is not enough evidence to conclude that NDVI is associated with Leaf Blast (**Table 5**). The coefficient for NDCI (-26.0514) was statistically significant (p = 0.008), indicating that for each one-unit increase in NDCI, the odds of Leaf Blast = 1 decrease by a factor of 0.000 (odds ratio). This means the probability of Leaf Blast = 1 decreases as NDCI increases. The intercept (18.7398) was statistically significant (p = 0.003). It represents the log odds when all predictors are 0, which corresponds to a probability of 1.000 for Leaf Blast = 1.

Table 5.

Regression Coefficient.

Variable	Coefficient	Std Error	z-value	p-value	Odds Ratio
(Intercept)	18.7398	6.3646	2.9444	0.0032	137598386.2298
NDVI	-5.4808	4.7163	-1.1621	0.2452	0.0042
NDCI	-26.0514	9.7987	-2.6587	0.0078	0.0000

At the standard threshold of 0.5, the model correctly classified 94% of cases (**Table 6**).

Table 6.

Classification Results.

Metric	Value
Accuracy	94.00%
Sensitivity (True Positive Rate)	88.89%
Specificity (True Negative Rate)	96.88%
AUC (Area Under ROC Curve)	0.9757

The area under ROC curve (AUC) of 0.976 suggests excellent discriminative ability (**Fig. 9**).

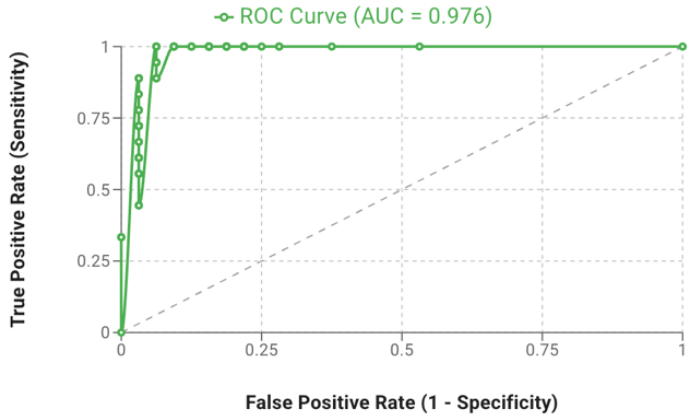


Fig. 9. ROC Curve.

Meanwhile the probability curve of each independent variable can be seen in **figure 10**. For multiple predictors, the probability depends on the combination of all predictor value.

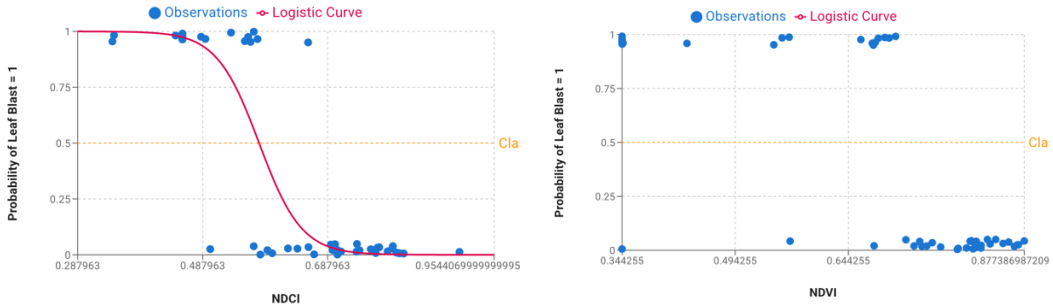


Fig. 10. (Left) Probability curve of NDCI; (Right) NDVI.

Field observations confirmed that leaf blast disease was prevalent across all paddy blocks, with visual symptoms such as elongated spindle-shaped lesions, chlorosis, and necrosis aligning closely with areas of low NDVI and NDCI values. The disease's widespread distribution suggests conducive environmental conditions—high humidity, warm temperatures, and frequent rainfall—which are characteristic of the study area during the growing season. In severe outbreaks, leaf blast can cause up to 50% yield reduction, primarily by reducing leaf area available for photosynthesis, shortening the tillering phase, and impairing panicle development (Asibi et al., 2019; Conde et al., 2025; Khadka et al., 2025; Younas et al., 2024). These physiological disruptions result in fewer spikelet's, lighter grains, and ultimately lower harvest weight. The spatial pattern analysis further supports the capability of NDVI and NDCI as effective early warning indicators. Both indices are sensitive to changes in leaf pigment concentration and canopy structure, allowing detection of sub-visual symptoms before they become apparent to the naked eye. This early detection is critical because timely intervention—within days rather than weeks—can significantly reduce the spread and severity of the disease.

The study's approach, which integrates UAV-based multispectral with targeted field validation, aligns with growing trend in precision agriculture yet offer specific advantages. Unlike satellite-based studies which can be constrained by cloud cover and fixed revisit schedules (Inoue, 2020; Phang et al., 2023), UAVs Provide on-demand, high-resolution data crucial for capturing the fine-scale heterogeneity of smallholder farms. Our findings are consistent with Mandal et al. (2022) who also reported strong correlations between NDVI dan blast incidence. However, our work specifically highlights the NDCI's sensitivity to the physiological stress caused by blast, potentially offering a more direct measure of photosynthetic apparatus health that the structural focus of NDVI. A key limitation, however, is the operational scope. While highly effective for village or sub-district level monitoring, scaling this method to a provincial or national level would be logistically and computationally challenging with UAV technology. A promising hybrid solution for larger-scale monitoring would be to use satellite imagery for broad surveillance, deploying UAVs for high-resolution follow-up in areas flagged as anomalous

The identification of zones with low NDCI values should trigger a precise and integrated management response. Specific treatments for these areas must be informed by on-ground diagnosis but primarily include: (1) the immediate application of systemic fungicides effective against *Magnaporthe oryzae* (e.g., containing tricyclazole or azoxystrobin) to curb fungal growth [Cite a fungicide efficacy study]; (2) a review of nitrogen fertilization practices, as excess nitrogen exacerbates blast susceptibility, suggesting a shift to split or controlled-release applications [Cite a study on N and blast]; and (3) ensuring proper water management to avoid prolonged leaf wetness, potentially by implementing alternate wetting and drying irrigation. To mitigate the risks posed by leaf blast disease in the long term, a broader integrated management approach is essential. The use of resistant rice varieties should be prioritized to reduce vulnerability to Magnaporthe oryzae infection. Proper planting spacing is critical to improve air circulation within the canopy, thereby lowering humidity levels that favor disease development. Timely and targeted fungicide applications, guided by the early detection protocol established here, can suppress pathogen spread while minimizing excessive chemical use. Effective field drainage systems should be maintained to prevent prolonged leaf wetness, which supports fungal proliferation. Additionally, balanced fertilization based on soil nutrient assessments is necessary. By combining these preventive measures with regular UAV or satellite-based monitoring and on-ground validation, farmers can implement a precision agriculture strategy that minimizes yield losses and sustains long-term productivity (Zhao et al., 2024).

6. CONCLUSIONS

This study established an integrated framework for agricultural assessment in Klaten Regency by combining a regional Land Potency Index (LPI) with field-scale UAV monitoring. The LPI, which synthesizes biophysical parameters, confirmed the central zone as highly suitable for agriculture due to its flat topography and abundant water resources, while the northern and southern regions were

constrained by steep slopes and natural hazards. Within these high-potential areas, UAV-based analysis revealed that healthy rice plants exhibit NDVI > 0.6 and NDCI > 0.5, whereas lower values correlated strongly with field-verified leaf blast disease, a major threat to yields. While effective for local monitoring, the UAV-based approach faces scalability limitations. Future efforts should therefore focus on developing a hybrid system using satellites for broad surveillance and UAVs for targeted diagnosis. Feature work will also aim to scale this approach by including a wider range of LPI classes and phenological stages to build a more comprehensive and robust model. Ultimately, translating these findings into practical tools for farmers will be crucial to enhance sustainable crop management and food security beyond the study area.

.

ACKNOWLEDGEMENT

This research was supported by funding from RISETMU 2024 (No. **2120/I.3/D/2024)**. The authors would also like to express sincere gratitude to the Land and Resource Laboratory, Faculty of Geography, Universitas Muhammadiyah Surakarta, for providing technical assistance, facilities, and access to field equipment that significantly contributed to the successful completion of this study.

REFERENCES

Abdollahzadeh, G., & Sharifzadeh, M. S. (2024). Perceived advantages and disadvantages of IPM practices among Iranian rice farmers. *International Journal of Pest Management*, 1–14. https://doi.org/10.1080/09670874.2024.2369552

Atapattu, A. J., Nuwarapaksha, T. D., Udumann, S. S., & Dissanayaka, N. S. (2025). Integrated farming systems: a holistic approach to sustainable agriculture. In *Agricultural diversification for sustainable food production* (pp. 89-127). Singapore: Springer Nature Singapore. Doi: 10.1007/978-981-97-7517-0_4

Chen, B., Su, Q., Li, Y., Chen, R., Yang, W., & Huang, C. (2025). Field Rice Growth Monitoring and Fertilization Management Based on UAV Spectral and Deep Image Feature Fusion. *Agronomy*, *15*(4), 886. doi.org/10.3390/agronomy15040886

Conde, S., Catarino, S., Ferreira, S., Temudo, M. P., & Monteiro, F. (2025). Rice Pests and Diseases Around the World: Literature-Based Assessment with Emphasis on Africa and Asia. *Agriculture*, *15*(7), 667. https://doi.org/10.3390/agriculture15070667

Dolatabadian, A., Neik, T. X., Danilevicz, M. F., Upadhyaya, S. R., Batley, J., & Edwards, D. (2025). Image-based crop disease detection using machine learning. *Plant Pathology*, *74*(1), 18-38. doi.org/10.1111/ppa.14006

Fadah, I., Lutfy, C., & Amruhu, A. (2024). Analysis of rice trade and food security in Southeast Asian countries. *KnE Social Sciences*, 641-653. 10.18502/kss.v9i21.16772

Fakriyah, V.N., Anggani, N.L., Kiat, U.E.I., Khikmah, F., Arroyan, W.A., Rizki, M.F. (2023). Integrated Use of Optical and Radar Data for Cropland Mapping Over The Mountain Slope Area in Boyolali, Indonesia. Geographia Technica, 18 (1), 108-122. DOI: 10.21163/GT_2023.181.08

Hariyanto, W., Basuki, S., Utomo, B., Wijayanti, F., Martino, M., Gunawan, T., & Erwinsyah, R. G. (2025). Farmer adaptation and mitigation in saving Indonesia's agriculture in the face of climate change: a scope review. *Climate Change and Social Responsibility*, 269-301. https://doi.org/10.1108/S2043-052320250000025014

Inoue, Y. (2020). Satellite-and drone-based remote sensing of crops and soils for smart farming–a review. *Soil Science and Plant Nutrition*, *66*(6), 798-810.

Jawabreh, O., Fahmawee, E. A. D. A., Ansari, R. W. A., Mahmoud, R., & Nassar, U. A. (2025). Geomorphological structure of landform characteristics as a reference for development recommendations in Wadi Rum protected area. *Geojournal of Tourism and Geosites*, *58*(1), 433-445. Doi: 10.30892/gtg.58140-1425

Junaid, M. D., & Gokce, A. F. (2024). Global agricultural losses and their causes. *Bulletin of Biological and Allied Sciences Research*, *2024*(1), 66-66. https://doi.org/10.54112/bbasr.v2024i1.66

Khadka, R. B., Manandhar, H. K., Shrestha, S., Acharya, B., Sharma, P., Baidya, S., Luu, V.C., & Joshi, K. D. (2025). Defending rice crop from blast disease in the context of climate change for food security in Nepal: A Review. *Frontiers in Plant Science*, *16*, 1511945. https://doi.org/10.3389/fpls.2025.1511945

Karmakar, S., Das, P., Panda, D., Xie, K., Baig, M. J., Molla, K. A. (2022). A detailed landscape of crispr-cas-mediated plant disease and pest management. *Plant Sci*. 323, 111376. Doi: 10.1016/j.plantsci.2022.111376

Li, W., He, J., Yu, M., Su, X., Wang, X., Zheng, H., Yao, X., Cheng, T., Zhu, Y., Cao, W., & Tian, Y. (2024). Multi-source remote sensing data-driven estimation of rice grain starch accumulation: Leveraging matter accumulation and translocation characteristics. IEEE Transactions on Geoscience and Remote Sensing. Doi: 10.1109/TGRS.2024.3500000

Liu, Z., Ju, H., Ma, Q., Sun, C., Lv, Y., Liu, K., Wu, T., & Cheng, M. (2024). Rice yield estimation using multi-temporal remote sensing data and machine learning: a case study of Jiangsu, China. Agriculture, 14(4), 638. https://doi.org/10.3390/agriculture14040638

Ma, H., Zhang, J., Huang, W., Ruan, C., Chen, D., Zhang, H., Zhou, X. and Gui, Z. (2024), Monitoring yellow rust progression during spring critical wheat growth periods using multi-temporal Sentinel-2 imagery. Pest Manag Sci. https://doi.org/10.1002/ps.8336

Mandal, N., Adak, S., Das, D.K., Sahoo, R.N., Kumar, A., Viswanathan, C., Mukherjee, J., Rajashekara, H., Gakhar, S. 2022. Assessment of Rice Blast Disease using Hyperspectral Vegetation Indices. Journal of Agricultural Physics, Vol 22 (10 pp. 89-98.

Masnilah, R., Wahyuni, W. S., Majid, A., Addy, H. S., & Wafa, A. (2020). Insidensi dan keparahan penyakit penting tanaman padi di Kabupaten Jember. *Agritrop: Jurnal Ilmu-Ilmu Pertanian (Journal of Agricultural Science)*, *18*(1), 1-12. https://doi.org/10.32528/agritrop.v18i1.3103

Migoń, P., & Jancewicz, K. (2024). Geomorphological diversity of Poland—Major controls and main geomorphological regions. In *Landscapes and Landforms of Poland* (pp. 53-89). Cham: Springer International Publishing. https://doi.org/10.1007/978-3-031-45762-3_4

Munandar, S., Saputra, A., Dirgahayu, D. (2025). Identification planting index of rice using landsat and entinel 2 time series images with geo-biophysics parameters as classification model base using Google Earth Engine (Study area: Serang Regency, Banten)." IOP Conference Series: Earth and Environmental Science. Vol. 1438. No. 1. Doi: 10.1088/1755-1315/1438/1/012088

Nguyen, Q-H., Du, Q.V.V., Pham, V.T., Vuong, H.N., Nguyen, V.H., Sang, T.V., Petrisor, A-I. (2025). Banana Reigns Wilt Based on Machine Learning and UAV-Based Multispectral Imagery. Geographia Technica, 20 (1). 329-345. DOI: 10.21163/GT_2025.201.22

Oraon, S., Padamini, R., Shahni, Y.S., Das, N., Sinha, D., Sujatha, G. S., Singh, O.B., Karanwal, K. (2024). Impact of Emerging Pathogens in Crop Production. *Microbiology Research Journal International*, 34 (7): 80-92. https://doi.org/10.9734/mrji/2024/v34i71460.

Phang, S. K., Chiang, T. H. A., Happonen, A., & Chang, M. M. L. (2023). From satellite to UAV-based remote sensing: A review on precision agriculture. *Ieee*, *11*, 127057-127076. Sabir, R. M., Mehmood, K., Sarwar, A., Safdar, M., Muhammad, N. E., Gul, N., ... & Akram, H. M. B. (2024). Remote sensing and precision agriculture: a sustainable future. In *Transforming agricultural management for a sustainable future: climate change and machine learning perspectives* (pp. 75-103). Cham: Springer Nature Switzerland. https://doi.org/10.1007/978-3-031-63430-7_4

Rachmawati, D., Maryani, & Masruroh, U. (2017). Effect of Rice Husk Ash on Physiological Responses of Rice (Oryza sativa L.)'Cempo Merah'and 'Segreng'Under Drought Conditions. In *Proceeding of the 1st International Conference on Tropical Agriculture* (pp. 63-71). Cham: Springer International Publishing.

Safitri, I., Yanti, D., & Irsyad, F. (2024). Analysis of Rice Plant Age Based on NDVI Value Using MODIS Imagery (Case Study of Koto Tangah District, Padang City). In IOP Conference Series: Earth and Environmental Science, Vol. 1426, No. 1, p. 012018). IOP Publishing. DOI: 10.1088/1755-1315/1426/1/012018

Saputra, A., Gomez, C., Delikostidis, I., Zawar-Reza, P., Hadmoko, D. S., & Sartohadi, J. (2020). Preliminary identification of earthquake triggered multi-hazard and risk in Pleret Sub-District (Yogyakarta, Indonesia). *Geo-spatial Information Science*, *24*(2), 256-278. https://doi.org/10.1080/10095020.2020.1801335

Saputra, A., Sigit, A.A., Priyana, Y., Abror, A.M., Sari., A.N.L., Nursetyani, O. (2022). A Low-Cost Drone Mapping and Simple Participatory GIS to Support The Urban Flood Modelling. Geographia Technica, 17 (2), 35-46. DOI: 10.21163/GT_ 2022.172.04.

Sharma, S. (2023). Cultivating Sustainable Solutions: Integrated Pest Management (IPM) For Safer and Greener Agronomy. *Corporate Sustainable Management Journal*, 1(2): 103-108. DOI: http://doi.org/10.26480/csmj.02.2023.103.108

Sundram, P., & Brennan, C. S. (2024). Triumphs, trials and tomorrow in food security: an ASEAN outlook. *International Journal of Food Science and Technology*, *59*(4), 2079-2087. https://doi.org/10.1111/ijfs.16899

Susetyo, D. B. (2023). Vertical accuracy assessment of various open-source DEM data: DEMNAS, SRTM-1, and ASTER GDEM. *Geodesy and Cartography*, *49*(4), 209–215. https://doi.org/10.3846/gac.2023.18168

Tiwari, A.K. (2024) IPM Essentials: Combining Biology, Ecology, and Agriculture for Sustainable Pest Control. *Journal of Advances in Biology & Biotechnology*, 27 (2). pp. 39-47. ISSN 2394-1081

Wang, X., Zeng, H., Yang, X., Shu, J., Wu, Q., Que, Y., Yang, X., Yi, X., Khalil, I., Zomaya, A. Y. (2025). Remote sensing revolutionizing agriculture: Toward a new frontier. *Future Generation Computer Systems*, 107691. https://doi.org/10.1016/j.future.2024.107691

Widarti, A., Giyanto, G., and Mutaqin, K.H. (2020). Incidence of Bacterial Grain Rot Disease, Identification, and Diversity of Burkolderia glumae in Some Rice Varieties in West Java. Jurnal Fitopatologi Indonesia, 16 (1), 9-20. https://doi.org/10.14692/jfi.16.1.9-20

Younas, M. U., Ahmad, I., Qasim, M., Ijaz, Z., Rajput, N., Parveen Memon, S., Zaman, W.U., Jiang, X., Zhang, Y., & Zuo, S. (2024). Progress in the management of rice blast disease: The role of avirulence and resistance genes through gene-for-gene interactions. *Agronomy*, *14*(1), 163. https://doi.org/10.3390/agronomy14010163

Yuan, X., Li, S., Chen, J., Yu, H., Yang, T., Wang, C., Huang, S., Chen, H., Ao, X. (2024). Impacts of global climate change on agricultural production: a comprehensive review. *Agronomy*, *14*(7), 1360. https://doi.org/10.3390/agronomy14071360

Zhao, D., Cao, Y., Li, J., Cao, Q., Li, J., Guo, F., Feng, S., & Xu, T. (2024). Early detection of rice leaf blast disease using unmanned aerial vehicle remote sensing: a novel approach integrating a new spectral vegetation index and machine learning. *Agronomy*, *14*(3), 602. https://doi.org/10.3390/agronomy14030602

A GEOSPATIAL ASSESSMENT OF SHORELINE DYNAMICS AND COASTAL VULNERABILITY INDUCED BY THE SEMARANG–DEMAK SEA-TOLL ROAD INFRASTRUCTURE IN CENTRAL JAVA, INDONESIA

Indra HERMAWAN[1], Sutrisno ANGGORO[2], Suradi Wijaya SAPUTRA[3], Agus SUHERMAN[1], Wisnu Arya GEMILANG[4] and Ulung Jantama WISHA[3]

DOI: 10.21163/GT_2026.211.07

ABSTRACT

The Semarang–Demak sea-toll road, a national strategic project in Central Java, Indonesia, was designed to enhance connectivity while simultaneously serving as a sea dike to mitigate tidal flooding and erosion. However, its construction within a subsiding and geomorphologically dynamic coastal environment raises concerns about long-term sustainability. This study assesses coastline change and coastal vulnerability after the toll road development using a GIS-based Digital Shoreline Analysis System (DSAS) and Coastal Vulnerability Index (CVI) frameworks that integrate nine geologic and oceanographic parameters. Results indicate pronounced spatial heterogeneity: North Semarang and Genuk exhibited high accretion rates (31.54 m/year and 51.64 m/year, respectively), whereas Sayung experienced extreme erosion, with retreat rates up to 654.09 m/year. CVI analysis revealed that 38.01% of the coastline falls under high vulnerability, particularly in the Sayung District, determined by factors such as sea-level rise, land subsidence (up to 8 cm/year), and extensive land use changes. The findings demonstrate that while the toll road enhances short-term protection and connectivity, it also intensifies long-term risks by disrupting sediment dynamics and degrading coastal ecosystems. Therefore, adaptive and ecosystem-based management is crucial to align infrastructure development with environmental resilience in rapidly subsiding deltaic regions.

Keywords: *Coastal vulnerability; Shoreline change; Land subsidence; Semarang–Demak Toll Road; Indonesia*

1. INTRODUCTION

Coastal zones, typically characterized by dense populations and vibrant economic activities, are inherently vulnerable to a range of natural and anthropogenic hazards, including flooding, coastal storms, sea-level rise (SLR), and erosion. Consequently, coastal vulnerability assessments have attracted substantial scholarly and policy attention (Dada et al., 2024; Kantamaneni et al., 2018; Tanim et al., 2022). Globally, shorelines exhibit diverse geomorphological characteristics that influence the development of trade, fisheries, maritime transport, tourism, and other coastal industries, thereby making significant contributions to national economies (De Vivo et al., 2022; Magnan et al., 2022). Coastal regions are home to approximately 40% of the world's population, and this proportion is projected to increase in the coming decades, intensifying pressures on coastal systems.

[1]*Department of Aquatic Resource Management, Faculty of Fisheries and Marine Science, Diponegoro University, Indonesia, indrakemenko@gmail.com (IH), Lpgsuherman2@gmail.com (AS)*
[2]*Study Program of Aquatic Resource Management and Environmental Sciences, School of Postgraduate Program, Diponegoro University, Indonesia, sutrisnoanggoro52@gmail.com (SA)*
[3]*Department of Capture Fisheries, Faculty of Fisheries and Marine Science, Diponegoro University, Indonesia, suradi@lecturer.undip.ac.id (SWS)*
[4]*Center for Marine and Fisheries Training, Ministry of Marine Affairs and Fisheries, Indonesia, wisnu.gemilang@yahoo.co.id (WAG)*
[5]*Research Center for Oceanography, National Research and Innovation Agency (BRIN), Indonesia, ulung.jantama.wisha@brin.go.id (UJW)*

The northern coast of Java, Indonesia, is of particular strategic importance due to its economic potential. Much of the coastline is of low relief and rich in both surface and groundwater resources, making it attractive for urban development. The region supports a wide range of socioeconomic functions, including industrial zones, government offices, seaports, marine tourism, fisheries, agriculture, settlements, mining, and public services such as roads, schools, hospitals, and markets (Solihuddin et al., 2021). However, as in many developing nations, low resilience and limited adaptive capacity within socio-ecological systems leave coastal communities, representing more than one-third of the global population, highly vulnerable to environmental change (Chai & Wu, 2023; Gu, 2019).

Climate change exacerbates these vulnerabilities by driving atmospheric warming and accelerating SLR, which in turn increases the frequency and severity of coastal flooding and erosion. In the Semarang–Demak coastal region of Central Java, tidal flooding (locally known as *rob*) and shoreline erosion are particularly acute, with the area experiencing the highest erosion rates in the province. Coastal flooding occurs regardless of rainfall events, with inundation depths ranging from 20 to 75 cm, largely driven by SLR and rapid coastal development (Salim et al., 2023). Sayung District, for instance, has experienced shoreline retreat rates of 0.6–1.15 m/year, categorizing it as a high-risk area (Rudiarto et al., 2020).

A major national strategic infrastructure project, the Semarang–Demak Toll Road, has been initiated to enhance regional mobility and logistics while also serving as a sea dike to mitigate tidal flooding and coastal erosion. This 27-km road traverses an area experiencing significant land subsidence (Chotimah et al., 2022), caused by geological cycles, continuous groundwater extraction, and the cumulative loading of urban infrastructure. While the toll road offers potential flood protection benefits, its construction in a subsiding and highly dynamic coastal environment raises questions regarding its long-term effectiveness and sustainability.

Globally, low-lying deltaic coasts represent some of the most vulnerable environments due to the combined pressures of SLR, land subsidence, and intensive human activity. The north coast of Java provides a quintessential example of these challenges, sharing similar characteristics with other subsiding megadeltas such as the Ganges–Brahmaputra, Mekong, and Mississippi, where rapid urban expansion coincides with geomorphological instability (Anderson et al., 2021; Dinh et al., 2012; Haque et al., 2024). Within this context, the Semarang–Demak region illustrates how coastal vulnerability intersects with infrastructure development, particularly through large-scale, dual-function projects such as toll roads that simultaneously act as sea dikes. Although the Coastal Vulnerability Index (CVI) has been widely applied to assess natural hazards and ecosystem sensitivity, few studies have employed it to evaluate the sustainability of infrastructure-based coastal defenses in subsiding deltaic environments. This study addresses this gap by integrating the CVI with the Digital Shoreline Analysis System (DSAS), extending conventional applications from general hazard assessment toward the quantitative evaluation of shoreline response and infrastructure effectiveness. This coupling enables a spatially explicit appraisal of how large-scale coastal structures influence sediment dynamics and ecosystem vulnerability. It is hypothesized that the sea-toll road induces a more stable coastline behind the structure, however, it causes exacerbated coastal erosion and vulnerability in the Sayung District as a result of hydrodynamic regime and sediment dynamic changes in the surrounding structures.

The findings of this study will provide a spatially explicit understanding of vulnerability patterns in the Semarang–Demak coastal zone, highlight priority areas for adaptive management, and offer insights into the integration of coastal protection measures within large-scale infrastructure planning. These outcomes will be relevant not only for Indonesia but also for other subsiding coastal megadeltas worldwide facing similar climate and development pressures.

2. STUDY AREA

The northern coastline of Java is underpinned by a diverse and relatively young geological framework, predominantly composed of unconsolidated and loosely compacted materials. These deposits include young volcanic products, extensive alluvial sediments, and coastal deposits that are highly susceptible to erosion and subsidence (Solihuddin et al., 2021). The Quaternary strata in this

area are largely made up of tuffaceous claystone, sand, silt, and clay, reflecting the combined influence of volcanic activity, fluvial processes, and marine sedimentation over the past several thousand years.

The Semarang–Demak Toll Road Project has emerged as a major National Strategic Project aimed at improving transportation efficiency and economic connectivity in Central Java. Spanning approximately 27 km, the toll road is designed to link industrial zones, ports, and key urban centers in Demak (**Fig. 1**), thereby facilitating the movement of goods and people while alleviating chronic traffic congestion. Beyond its transportation role, the project incorporates critical flood mitigation infrastructure, functioning as an integrated coastal defense system that combines a sea embankment, a polder network, and an upgraded drainage system to manage recurrent tidal inundation (Pamungkas, 2021).

Construction activities commenced in late 2019, with partial sections, particularly a 16 km stretch, temporarily opened during peak holiday travel periods to relieve traffic bottlenecks. Despite its potential socioeconomic benefits, the project has raised notable environmental concerns. The development is expected to result in the clearance of approximately 46 hectares of mangrove forest within the coastal zones of Semarang and Demak (Solahudin et al., 2024).

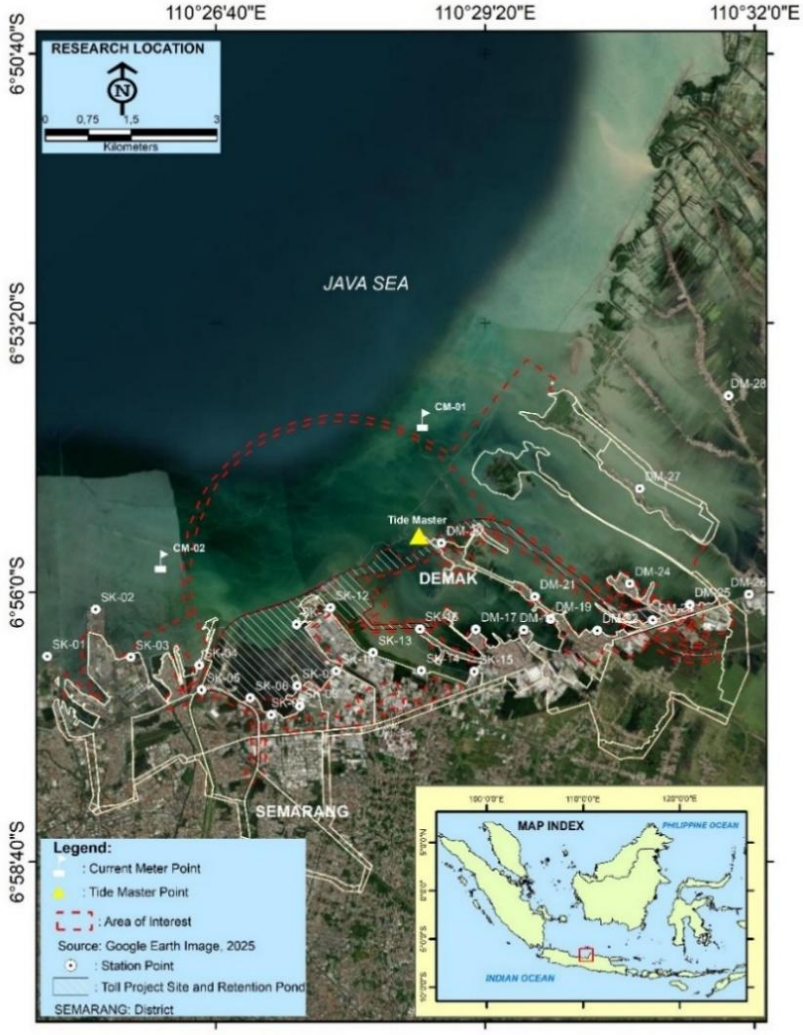


Fig. 1. Location of the Semarang–Demak sea-toll road development, field survey location, and *in situ* observation points.

3. DATA AND METHODS

3.1. Data acquisition

The Coastal Vulnerability Index (CVI) parameters used in this study comprise coastal relief, geomorphology, mean tidal range, shoreline change rate, relative sea-level change, mean wave height, slope, land subsidence, and land use. These parameters were chosen to capture the combined influence of geomorphology, hydrodynamics, relative SLR, and socio-economic exposure, factors that are particularly critical in low-lying, subsiding deltaic settings in the Semarang–Demak region. Data were obtained from multiple sources, including satellite imagery, digital elevation models (DEMs), tide gauge records, satellite altimetry, reanalysis datasets, and field surveys. The complete list of parameters, their sources, spatial/temporal coverage, and processing methods are summarized in **table 1**.

Table 1.

Data sources, resolution, and processing methods for CVI parameters

Parameter	Data source	Spatial resolution/coverage	Temporal coverage	Processing method
Coastal relief	SRTM DEM (USGS)	30 m	2000	Extracted coastal elevation profiles using GIS; reprojected to WGS 84 / UTM Zone 49S
Geomorphology	Sentinel-2 MSI (ESA); Field survey	10 m	2025	Visual interpretation and supervised classification; verified through ground-truthing
Mean tidal range	Tide gauge data (BIG); Tidal harmonic constituents	Point-based	2010-2025	Harmonic analysis and averaging of spring-neap cycles
Shoreline change rate	Landsat 5 TM, Landsat 7 ETM+, Landsat 8 OLI, Sentinel-2 MSI; DSAS v5.1	30 m (Landsat), 10 m (Sentinel-2)	1995-2025	Multi-temporal shoreline extraction and rate computation (EPR, LRR)
Relative sea-level change	AVISO+, Copernicus Marine Service (satellite altimetry); Local tide gauges	0.25^{o} (altimetry)	1993-2025	Combined mean sea-level trends with local vertical land motion
Mean wave height	ECMWF ERA5 reanalysis	0.25^{o}	1993-2025	Hourly data averaged to represent long-term wave climate
Slope	SRTM DEM (USGS)	30 m	2000	Derived nearshore slope using GIS terrain analysis tools
Land subsidence	Sentinel-1A/B (ESA) InSAR	20 m	2016-2021	InSAR time-series analysis using SNAP v12.0.0 & StaMPS v4.1 to estimate vertical displacement
Land use	Sentinel-2 MSI (ESA); ATR/BPN official maps	10 m	2025	Supervised classification validated with official land-use data and field checks

3.2. Digital shoreline analysis system (DSAS)

In this study, shoreline change analysis was conducted using the Digital Shoreline Analysis System (DSAS), a freely available add-in developed by the U.S. Geological Survey (USGS) for ArcGIS and QGIS platforms (Himmelstoss et al., 2021). DSAS enables the calculation of shoreline change rates by applying various statistical methods to multiple historical shoreline positions. Among these, the Linear Regression Rate (LRR) method was selected as it is widely regarded as one of the most robust approaches for estimating long-term shoreline change trends, particularly in large-scale coastal studies (Abdul Rahim et al., 2024; Nerves et al., 2024). The LRR method determines the slope of the best-fit line through all available shoreline positions along each transect, providing a statistically reliable rate of change. For this study, a reference baseline was established offshore, parallel to the general orientation of the coast. From this baseline, transects were automatically generated at 10 m intervals and oriented perpendicular to the shoreline. Historical shoreline vectors from different years were then compiled and processed within the DSAS framework to derive both net shoreline movement (NSM) and rate of change statistics. The NSM represents the total distance between the oldest and most recent shoreline positions, while the LRR expresses this movement as an annual rate by dividing the NSM by the elapsed time between the earliest and latest observations.

To ensure the reliability of the shoreline positions, uncertainty handling was explicitly incorporated in the analysis. The primary shoreline proxy used was the High-Water Level (HWL), extracted from atmospherically corrected multispectral satellite imagery. Tidal-stage normalization was performed using coincident tidal records to reduce temporal discrepancies among image acquisition dates. The total positional uncertainty (U_t) of each shoreline was estimated as the root sum of squares of image georeferencing error, spatial resolution, digitizing error, and tidal correction error. These cumulative uncertainties were integrated into DSAS to generate 95% confidence intervals for the calculated LRR values, ensuring statistically defensible estimates of shoreline change rates.

Shoreline datasets for this analysis were extracted from remote sensing imagery for four temporal snapshots (**Tab. 1**). This temporal resolution enables the assessment of both short-term variability and long-term trends, offering critical insights into the interplay between shoreline dynamics and coastal land-use transformations, as further examined in this study through supervised classification–based geospatial analysis.

3.3. Costal vulnerability index (CVI) assessment

Coastal vulnerability mapping and assessment in this study were conducted using the Smartline methodology formulated by Sharples et al. (2009). This framework consists of three principal stages: (1) Indicative Mapping, which identifies coastal areas according to their geological and geomorphological characteristics, representing the fundamental determinants of vulnerability; (2) Regional Assessment, which integrates geomorphic coastal types with additional variables influencing vulnerability, including climate, wave regime, tidal range, and vertical tectonic movements; and (3) Site-specific Assessment, which examines in detail all geological, geomorphological, topographic, oceanographic, and climatic factors that influence the coastal system.

The parameters applied in this approach were not confined to observations and measurements taken parallel to the coastline but also extended to areas oriented perpendicular to the shore. All three Smartline mapping stages were implemented in this study with several modifications to the observed parameters, as summarized in **table 2**. The selection of the nine CVI parameters (coastal relief, geomorphology, mean tidal range, shoreline change rate (DSAS), relative sea-level change, mean wave height, slope, land subsidence, and land use) was guided by their direct relevance to the geomorphological instability and anthropogenic pressures characteristic of deltaic, subsiding environments. These parameters were subsequently processed and interpreted to produce a coastal vulnerability map classified into five categories: very low, low, moderate, high, and very high vulnerability. Since the original Smartline methodology does not provide a detailed quantitative procedure for generating vulnerability maps, the classification in this study was calculated using the Coastal Vulnerability Index (CVI) developed by Gornitz et al. (1992). The CVI calculation was performed after all parameters were first grouped into value intervals ranging from 1 to 5, where a

value of 1 indicates that the corresponding parameter is considered to have minimal susceptibility to coastal hazards. The CVI was then calculated as the geometric mean of the ranked variables, following the formula:

$$CVI = \sqrt[n]{a_1 x a_2 x a_3 x \dots x a_n} \quad (1)$$

where a_1–a_n represent the rank values of the n selected parameters.

Equal weighting was assigned to all parameters to avoid subjective bias, though their relative influence was subsequently evaluated through a sensitivity analysis. This analysis examined the degree to which high-variance parameters, particularly land subsidence and shoreline change rate, dominated the composite CVI outcome. Results indicated that while subsidence exerted a significant local influence, the overall vulnerability pattern remained consistent across parameter weighting scenarios, demonstrating the model's stability.

Table 2.

Summary of indicative mapping parameter's scoring

Parameter	Very low (1)	Low (2)	Moderate (3)	High (4)	Very high (5)	References
Coastal relief (m)	> 30	21 – 30	11 – 20	6 – 10	0 – 5	(Shaw et al., 1998; Gornitz et al., 1991)
Geomorphology	Rocky, cliffed coasts, Fiords, Fiards; Plutonic, Volcanic, High-medium grade metamorphics	Medium cliffs, Indented coasts; Low grade metamorphics, Sand-stones and conglomerates, Metamorphic rocks	Low cliffs, Glacial drift, Alluvial plains; Most sedimentary rocks	Cobble beaches, Estuary Lagoon; Coarse, poorly sorted, unconsolidated sediments	Barrier beaches, Sand beaches, Salt marsh, Mud flats, Deltas, Mangroves, Coral reefs; Fine, consolidated sediment, Ice	(Gornitz et al., 1991)
Mean tidal range (m)	> 6.0	4.1 – 6.0	2.0 – 4.0	1.0 – 1.9	< 1.0	(Gornitz et al., 1991)
Shoreline change rate (m/year)	> 2.0	1.0 – 2.0	(-1.0)– (+1.0)	(-1.0) – (-2.0)	< -2.0	(Hammar-Klose et al., 2003; Gornitz et al., 1991)
Relative sea-level change (mm/year)	<-1.21	(-1.21) – (+0.1)	0.1 – 1.24	1.24 – 1.36	> 1.36	(Hammar-Klose et al., 2003)
Mean wave height (m)	< 1.1	1.1 – 2.0	2.0 – 2.25	2.25 – 2.6	> 2.60	(Hammar-Klose et al., 2003)
Slope (°)	> 10	7.5 – 10	5 – 7.5	2.5 – 5	≤ 2.5	(Reeder, et al. 2012)
Land subsidence (mm/year)	< -1.0	(-1.0) – (+1.0)	1.0 – 2.0	2.1 – 4.0	> 4.0	(Gornitz & White, 1992)
Land use	Dry land	Farm, Bush land	Vacant land with farm area	Sand area, Mangrove, plantation area	Building, Beach, Ponds degrade mangrove, Swamp, Aquaculture	(Romadhona, et al. 2020)

The final CVI values were classified into five vulnerability categories: very low, low, moderate, high, and very high, using natural breaks in the data distribution. Integrating the Smartline spatial framework with the quantitative CVI approach provided both geomorphological context and numerical precision, thereby enhancing the robustness, comparability, and reproducibility of the coastal vulnerability assessment. The spatial analysis framework in this study is illustrated in **figure 2.**

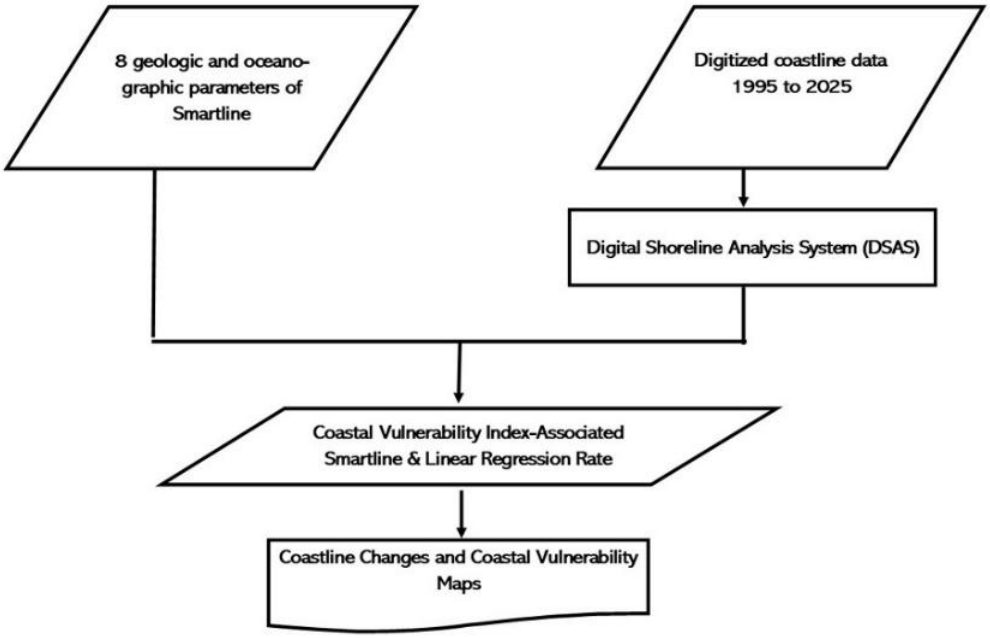


Fig. 2. Research framework of spatial analyses.

4. RESULTS AND DISCUSSIONS

4.1. Coastline change after the development of Semarang–Demak Sea-toll Road

The spatial distribution of shoreline change severity in the Semarang–Demak coastal zone is illustrated in **figure 3**. In the western sector, North Semarang was dominated by accretionary processes, ranging from moderate to severe accretion, with no significant erosion detected, indicating a relatively stable to advancing shoreline influenced by sediment deposition from local riverine inputs and coastal currents. Adjacent to this, Gayamsari exhibited a mixed shoreline change regime, where pockets of moderate accretion coexisted with severe erosion zones, suggesting localized erosional pressures likely driven by anthropogenic modification and changes in nearshore hydrodynamics.

Genuk recorded the most extensive accretion in the study area, encompassing severe to very severe accretion zones and contributing 60.1% of the total measured accretion, although certain segments experienced severe erosion, pointing to high sediment deposition rates counterbalanced by localized erosional forces. In stark contrast, the easternmost sector, Sayung, was overwhelmingly dominated by very severe erosion, accounting for 82.4% of the total very severe erosion recorded, with no evidence of accretion. The DSAS analysis identified the most extreme shoreline retreat in Sayung, reaching rates of 654.09 m/year between 2015 and 2021, underscoring the severe vulnerability of this area to coastal hazards (**Tab. 3**).

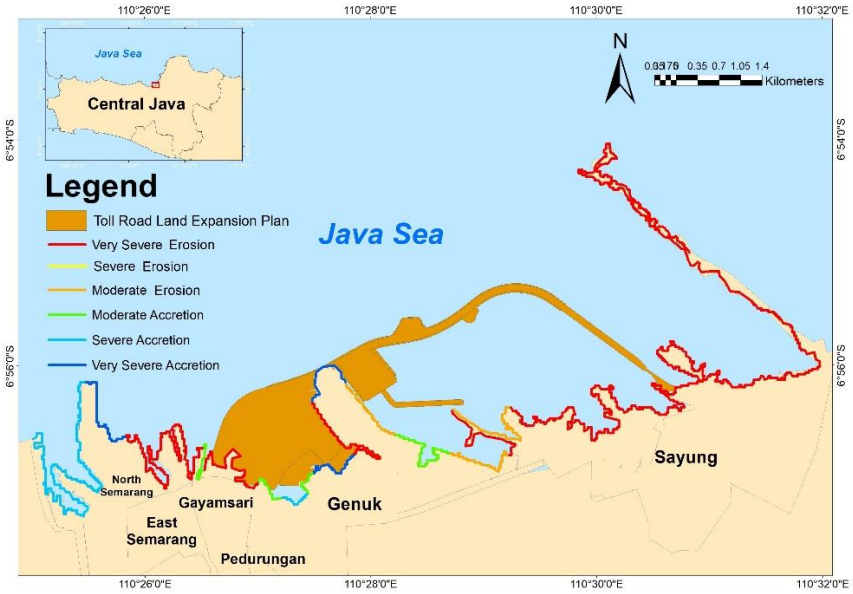


Fig. 3. Erosion and accretion status in the study area after the development of Semarang–Demak sea-toll road.

Table 3.

Summary of Coastline changes in the study area.

Zone	Erosion rate	Accretion rate	Category
North Semarang	-	31.54 m/year	Accretion
Gayamsari	18.01 m/year	2.75 m/year	Erosion
Genuk	55.65 m/year	51.64 m/year	Erosion-accretion
Sayung	654.09 m/year	-	Extreme erosion

4.2. Indicative mapping for CVI assessment

The indicative mapping of coastal vulnerability along the Semarang–Demak shoreline reveals pronounced spatial heterogeneity across the assessed parameters (**Fig. 4**). The coastal areas of Semarang City and Demak Regency are characterized by low relief and abundant water resources, both surface and groundwater, which historically made them favorable for urban development. The study area is also defined as a muddy coast. During low tide, the intertidal mudflats are exposed up to ±2 km seaward, forming extensive tidal mudflat morphology. The geological condition of the study area is largely categorized as alluvial plains, except in Gayamsari District, which is classified as mudflats.

The observed tidal range along the coast varies between 2.5 m and 2.8 m, with the highest values recorded in Sayung District. The result also indicates that the rate of SLR in the study area ranges between 8 and 25 mm/year, making the study area categorized as a very high vulnerability (Figure 3). The highest rates (20–25 mm/year) are concentrated in Genuk and North Semarang Districts, while the lowest rates (8–10 mm/year) are found in parts of Sayung.

Analysis of shoreline change between 2015 and 2025 along the Semarang–Demak coast reveals five categories: severe accretion (13.0%), very severe accretion (5.4%), moderate accretion (19.4%), very severe erosion (54.4%), and moderate erosion (7.7%) (**Fig. 3**). On the other hand, based on measurements in the study area, subsidence rates are categorized into three groups: 70–100 mm/year

(31.9%), 50–70 mm/year (5.4%), and 60–80 mm/year (62.7%), with the latter dominating, particularly in Sayung and Genuk.

Land use patterns introduce additional complexity. Areas dominated by urban development and aquaculture ponds exhibit moderate to high vulnerability (81.5%), while some segments classified as low vulnerability (18.5%) correspond to remnant mangrove belts and green buffer zones, which still provide limited protection against coastal hazards.

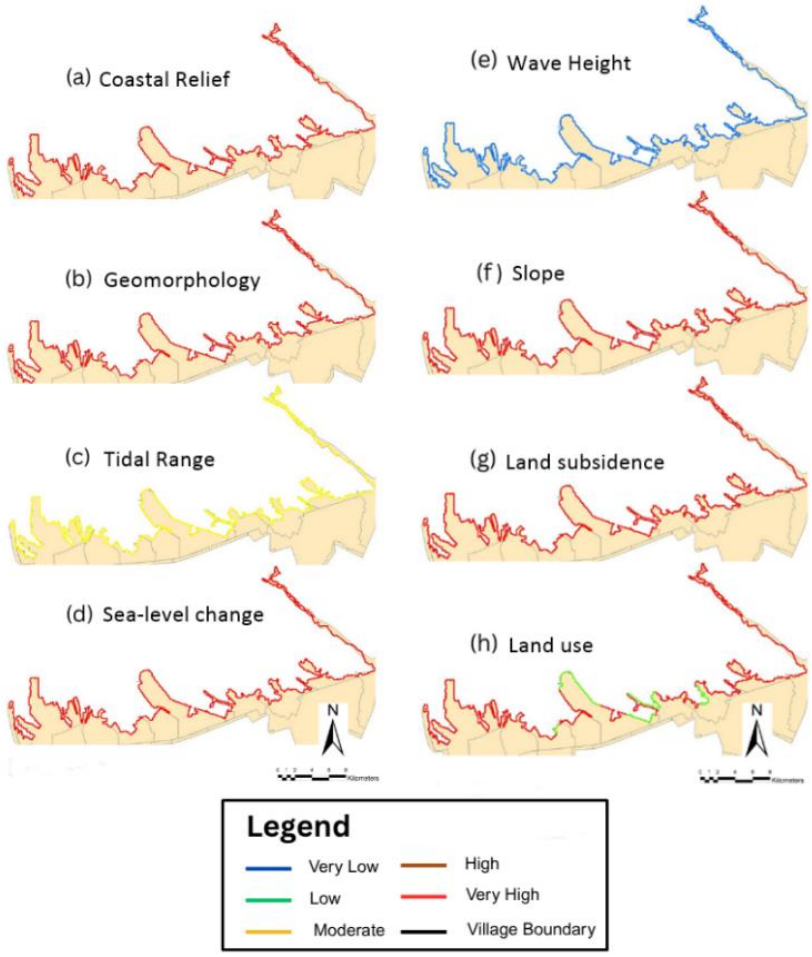


Fig. 4. The results of indicating mapping for CVI assessment, coastal relief (a), geomorphology (b), tidal range (c), sea-level change (d), wave height (e), slope (f), land subsidence (g), and land use (h).

4.3. Coastal vulnerability after the development of Semarang–Demak Sea-toll Road

The Coastal Vulnerability Index (CVI) analysis along the Semarang–Demak coastline after the development of the toll road revealed significant spatial variation across districts (**Fig. 5** and **Tab. 4**). In North Semarang, the coast is relatively less exposed, with only 2.2% categorized as highly vulnerable and 8.2% classified as low vulnerability. In Gayamsari, vulnerability increases slightly, with 4.4% of the coastline falling under high vulnerability and 2.0% under low vulnerability. A more complex distribution was observed in Genuk, where 8.9% of the shoreline is highly vulnerable, 11.9% moderately vulnerable, and 9.5% classified as low vulnerability.

By contrast, Sayung district exhibits the highest degree of coastal vulnerability, with 48.9% of its shoreline categorized as highly vulnerable and 4.0% as moderately vulnerable (**Tab. 4**), making it

the most critical hotspot along the study area. Overall, the CVI results highlight that coastal vulnerability increases eastward, with Sayung as the most threatened region compared to North Semarang, Gayamsari, and Genuk.

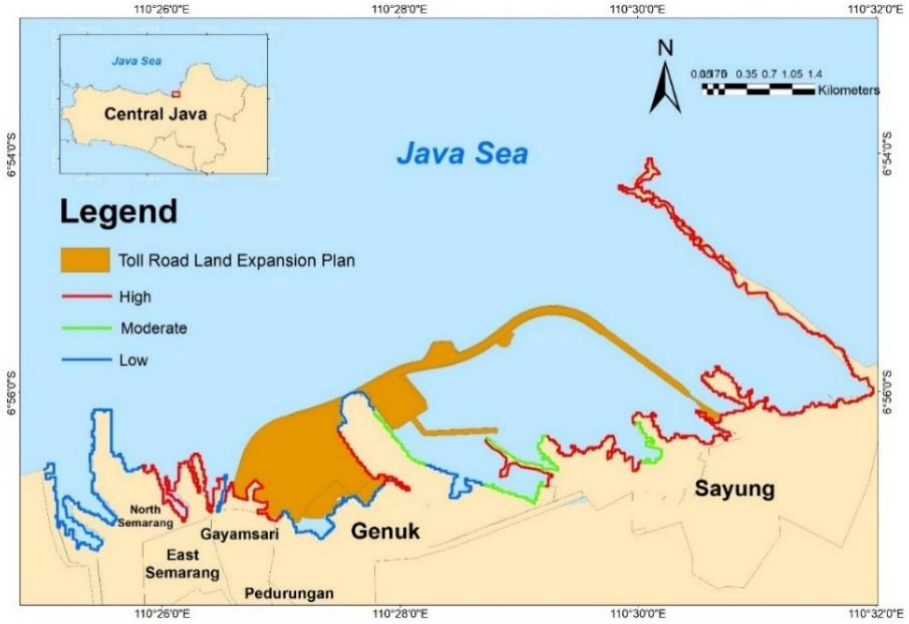


Fig. 5. Coastal vulnerability classification in the Semarang–Demak coastline after the development of sea-toll road.

Table 4.
Summary of CVI classification in each district impacted by the sea-toll road development.

District	Category	CVI percentage (%)
North Semarang	High vulnerability	2.2
	Low vulnerability	8.2
Gayamsari	High vulnerability	4.4
	Low vulnerability	2.0
Genuk	High vulnerability	8.9
	Moderate vulnerability	11.9
	Low vulnerability	9.5
Sayung	High vulnerability	48.9
	Moderate vulnerability	4.0

5. DISCUSSION

5.1. Sea-toll road impacts on coastal vulnerability

The Semarang–Demak sea-toll road represents a flagship example of dual-function infrastructure, designed simultaneously as a transport corridor and a coastal defense system. While such projects are promoted as strategic responses to the challenges of tidal flooding and transport connectivity in Java's northern corridor (Wibowo et al., 2023), their long-term impacts on shoreline stability and socio-ecological systems are highly complex.

DSAS analysis highlights strikingly uneven outcomes: North Semarang experienced net accretion (31.54 m/year) and Genuk recorded even higher rates of accretion (51.64 m/year), whereas Sayung underwent extreme erosion of up to 654.09 m/year with no evidence of compensatory accretion. These results indicate that the construction of the toll road and associated sea dike likely affected littoral drift patterns and altered sediment transport dynamics, contributing to localized areas of accretion and erosion toward the eastern part of the coastline.

Field evidence and local reports reinforce these findings. Fishers have noted declining catches as aquaculture ponds have been transformed into open sea, while tidal flooding has intensified due to the impermeability of road surfaces and inadequate drainage design (Jamaludin & Mahdi, 2025; Aditiya & Ito, 2023).

Such impacts demonstrate that while the toll road has delivered short-term benefits by reducing tidal flooding in selected areas, its construction has simultaneously heightened long-term vulnerability in others, particularly in Sayung. Moreover, mangrove removal for infrastructure expansion has reduced natural shoreline protection, further amplifying erosion and wave exposure. These dynamics underscore the paradox of hard-engineering interventions: they offer immediate socio-economic benefits but can destabilize coastal systems in ways that ultimately undermine resilience.

5.2. Natural vs. anthropogenic drivers of shoreline change

The vulnerability of the Semarang–Demak coast cannot be understood without considering the interaction between natural coastal processes and human-induced pressures. From a natural perspective, the region's coastal relief is dominated by very low elevations (0–5 m) and flat slopes averaging 0.22°, making the coastline highly susceptible to inundation and storm surge intrusion (Handiani, 2019; Solihuddin et al., 2021). Geologically, the northern coast of Java is composed primarily of unconsolidated alluvial and lahar deposits, intersected by river systems draining into the Java Sea, which renders the area morphologically unstable (Handiani, 2019; Sagala et al., 2024). Geomorphological diversity includes sandy, muddy, coral, and deltaic coasts (Solihuddin et al., 2021), yet the study area is dominated by muddy tidal flats and degraded mangrove zones, both of which are highly vulnerable to erosion.

The tidal regime is characterized by mixed tides with diurnal dominance, and the mean tidal range falls into the mesotidal category, contributing to sediment redistribution but not providing the stabilizing effect of macrotidal environments (Handiani, 2019). Although wave energy is relatively low, the combination of flat relief and estuarine tidal dynamics contributes to shoreline instability. Meanwhile, long-term SLR, combined with local tectonic and anthropogenic subsidence, drives very high vulnerability scores across most of the coastline. Indeed, land subsidence is among the most critical anthropogenic drivers, with Semarang and Demak experiencing rates of up to 8 cm/year due to excessive groundwater extraction (Sidiq et al., 2021). Subsidence amplifies relative SLR and leads directly to tidal inundation, shoreline retreat, and land loss (Prasetyo et al., 2019; Sarah et al., 2022). In addition to the SLR factor, this study applied the relative sea-level change classification developed by Hammar-Klose et al. (2003). Since sea-level projections in areas near the equatorial region are generally higher than those in the northern hemisphere (Wisha et al., 2025), the threshold used to classify vulnerability levels based on this factor should be higher than that applied to the east coast of the United States. Consequently, the resulting scores indicate a very high level of vulnerability in the study area, even though SLR remains a significant and ongoing issue affecting the northern coast of Java.

On the other hand, land-use changes and rapid urbanization further exacerbate vulnerability. Industrial zones dominate North Semarang and Genuk, while settlements expand across Sayung despite recurring tidal flooding (Solahudin et al., 2024).

The loss of natural buffers through mangrove clearing and conversion of ponds for industry and settlements has removed critical ecosystem services, intensifying exposure to flooding and erosion. CVI assessments confirm that SLR, land subsidence, and geomorphological setting exert the greatest

influence on overall vulnerability (Mujabar & Chandrasekar, 2013). Thus, the interaction of natural drivers with anthropogenic stressors results in a compound risk scenario where infrastructure like the sea-toll road operates within a highly unstable deltaic system.

5.3. Implications for resilience and sustainability

The Semarang–Demak case highlights a broader paradox in deltaic adaptation: infrastructure-led interventions are often pursued as urgent responses to coastal hazards, yet their long-term effectiveness is constrained by geomorphological instability and human-induced pressures. The CVI results, showing that 38% of sites fall into the high vulnerability category, emphasize the fragility of the system even after the toll road was constructed. Rather than reducing risk, the project has in some cases shifted or intensified it, raising questions about its long-term sustainability. The coastal transformation along the Semarang–Demak corridor has also produced profound socio-economic and governance implications. Recurrent tidal flooding and shoreline retreat have displaced communities, disrupted aquaculture livelihoods, and reduced agricultural productivity, particularly in Sayung.

These findings align with global concerns over infrastructure-led adaptation in megadeltas, where subsidence, SLR, and erosion converge to undermine conventional engineering solutions (Han et al., 2022). The Semarang–Demak toll road demonstrates how such projects may provide immediate socio-economic and transport benefits but at the expense of ecological integrity and livelihood security. Sustainable resilience strategies must therefore integrate ecosystem-based approaches such as mangrove restoration, sediment management, and living shorelines, which can complement hard infrastructure by enhancing natural defenses (Nurhidayah et al., 2022). Furthermore, adaptive governance frameworks are essential, ensuring that coastal management integrates scientific modeling, geospatial monitoring, and local knowledge to adjust interventions as risks evolve.

Ultimately, the resilience of the Semarang–Demak coast depends not solely on the performance of a single project but on broader strategies that balance development and ecological protection. Without such integration, the sea-toll road risks entrenching a cycle of dependency on increasingly costly engineering solutions, while leaving local communities and ecosystems more vulnerable to the accelerating impacts of climate change and subsidence.

6. CONCLUSIONS

The Semarang–Demak coast is highly vulnerable due to its low-lying alluvial plains, muddy tidal flats, and unstable geomorphology. Shoreline change is spatially uneven, with extreme erosion in Sayung and localized accretion in Genuk and North Semarang, reflecting the combined influence of natural processes and anthropogenic pressures, including the Semarang–Demak Toll Road. Relative SLR, rapid land subsidence, and intensive land use further heighten risks to communities, infrastructure, and ecosystems. CVI results confirm that much of the coastline is in the high-vulnerability category, where socio-economic exposure compounds physical hazards. While the toll road offers short-term transport and flood protection benefits, its long-term effectiveness is uncertain. Building resilience will require integrated, ecosystem-based strategies that restore natural defenses, manage sediment dynamics, and embed adaptive planning into coastal development

ACKNOWLEDGMENT

We would like to express our sincere gratitude to the Department of Aquatic Resource Management, Diponegoro University, for their continuous support throughout the course of this study. We also extend our appreciation to the local government authorities and community members for their invaluable assistance and cooperation during the field survey.

REFERENCES

Abdul Rahim, H., Azizan, N. N., Mohd, F. A., Adnan, N. A., Razali, R., & Ariffin, E. helmy. (2024). Assessment of shoreline changes at Northern Selangor Coast, Malaysia using Digital Shoreline Analysis System (DSAS). *Journal of Advanced Geospatial Science & Technology, 4*(2), 79–103. https://doi.org/10.11113/jagst.v4n2.97

Aditiya, A., & Ito, T. (2023). Present-day land subsidence over Semarang revealed by time series InSAR new small baseline subset technique. *International Journal of Applied Earth Observation and Geoinformation, 125*, 103579. https://doi.org/10.1016/j.jag.2023.103579

Anderson, C. C., Renaud, F. G., Hagenlocher, M., & Day, J. W. (2021). Assessing multi-hazard vulnerability and dynamic coastal flood risk in the Mississippi Delta: The Global Delta Risk Index as a social-ecological systems approach. *Water*, *13*(4), 577. https://doi.org/10.3390/w13040577

Chai, J., & Wu, H.-Z. (2023). Prevention/mitigation of natural disasters in urban areas. *Smart Construction and Sustainable Cities, 1*(1), 1–16. https://doi.org/10.1007/s44268-023-00002-6

Chotimah, S. N., Prasetyo, Y., Firdaus, H. S., & Harintaka, H. (2022). Analysis of land subsidence using Sentinel-1A Imagery with the DInSAR Method from 2019 to 2021 (Case study: Semarang–Demak Toll Road construction). *Elipsoida : Jurnal Geodesi Dan Geomatika, 5*(2), 53–60. (In Indonesian). https://doi.org/10.14710/elipsoida.2022.16744

Dada, O. A., Almar, R., & Morand, P. (2024). Coastal vulnerability assessment of the West African coast to flooding and erosion. *Scientific Reports, 14*(1), 1–15. https://doi.org/10.1038/s41598-023-48612-5

De Vivo, C., Ellena, M., Capozzi, V., Budillon, G., & Mercogliano, P. (2022). Risk assessment framework for Mediterranean airports: a focus on extreme temperatures and precipitations and sea level rise. *Natural Hazards, 111*(1), 547–566. https://doi.org/10.1007/s11069-021-05066-0

Dinh, Q., Balica, S., Popescu, I., & Jonoski, A. (2012). Climate change impact on flood hazard, vulnerability and risk of the Long Xuyen Quadrangle in the Mekong Delta. *International journal of river basin management*, *10*(1), 103-120. https://doi.org/10.1080/15715124.2012.663383

Gu, D. (2019). *Exposure and vulnerability to natural disasters for world's cities*. United Nations, Department of Economics and Social Affairs, Population Division, Technical Paper No. 4., pp. 1–43. Retrieved from https://www.un.org/en/development/desa/population/publications/pdf/technical/TP2019-4.pdf

Gornitz, V. M., White, T. W., & Daniels, R. C. (1991). *A coastal hazards data base for the US East Coast*. Oak Ridge National Laboratory, United States: Environmental Sciences Division. https://doi.org/10.3334/CDIAC/coastalndp043

Gornitz, V. M., & White, T. W. (1992). *A Coastal Hazards Data Base for the US East Coast (1992)(NDP-043a)*. Environmental System Science Data Infrastructure for a Virtual Ecosystem (ESS-DIVE)(United States). https://doi.org/10.3334/CDIAC/ssr.ndp043a

Hammar-Klose, E. S., Pendleton, E. A., Thieler, E. R., Williams, S. J., & Norton, G. A. (2003). Coastal vulnerability assessment of Cape Cod National Seashore (CACO) to sea-level rise. *US Geological Survey, Open File Report*, 02-233. https://doi.org/10.3133/ofr02233

Han, W., Zhang, L., Meehl, G. A., Kido, S., Tozuka, T., Li, Y., McPhaden, M. J., Hu, A., Cazenave, A., Rosenbloom, N., Strand, G., West, B. J., & Xing, W. (2022). Sea level extremes and compounding marine heatwaves in coastal Indonesia. *Nature Communications, 13*(1), 1–12. https://doi.org/10.1038/s41467-022-34003-3

Handiani, D. N. (2019). Study of coastal vulnerability to sea level rise in Subang Regency-West Java. *Jurnal Kelautan Nasional, 14*(3), 145–154. (In Indonesian). https://doi.org/10.15578/jkn.v14i3.7583

Haque, M. M., Haque, M., & Ghosh, M. K. (2024). The coastal dynamics of the Central Ganges–Brahmaputra–Meghna Delta Coast, Bangladesh: implications for coastal development and sustainability. *Journal of Coastal Conservation*, *28*(1), 29. https://doi.org/10.1007/s11852-024-01032-7

Himmelstoss, E. A., Henderson, R. E., Kratzmann, M. G., & Farris, A. S. (2021). *Digital Shoreline Analysis System (DSAS) Version 5.1 User Guide: U.S. Geological Survey Open-File Report 2021–1091*. U.S. Geological Survey, (2021–1091), 104 pp. https://doi.org/10.3133/ofr20211091

Jamaludin, H., & Mahdi, Z. (2025). Community resistance to development of the Semarang–Demak Sea Embankment Toll Road. *The Journal of Academic Science, 2*(4), 1046–1065. https://doi.org/10.59613/3gqcpc82

Kantamaneni, K., Phillips, M., Thomas, T., & Jenkins, R. (2018). Assessing coastal vulnerability: Development of a combined physical and economic index. *Ocean and Coastal Management, 158*, 164–175. https://doi.org/10.1016/j.ocecoaman.2018.03.039

Magnan, A. K., Oppenheimer, M., Garschagen, M., Buchanan, M. K., Duvat, V. K. E., Forbes, D. L., Ford, J. D., Lambert, E., Petzold, J., Renaud, F. G., Sebesvari, Z., van de Wal, R. S. W., Hinkel, J., & Pörtner, H. (2022). Sea level rise risks and societal adaptation benefits in low-lying coastal areas. *Scientific Reports, 12*(1), 1–22. https://doi.org/10.1038/s41598-022-14303-w

Mujabar, S., & Chandrasekar, N. (2013). Coastal erosion hazard and vulnerability assessment for southern coastal Tamil Nadu of India by using remote sensing and GIS. *Natural Hazards, 69*, 1295–1314. https://doi.org/10.1007/s11069-011-9962-x

Nerves, A., Rivera, F. D., Blanco, A., Tirol, Y., & Nadaoka, K. (2024). Shoreline change analysis in New Washington, Aklan using Digital Shoreline Analysis System (DSAS). *ISPRS Annals of the Photogrammetry, Remote Sensing and Spatial Information Sciences, 10*(5), 111–117. https://doi.org/10.5194/isprs-annals-X-5-2024-111-2024

Nurhidayah, L., Davies, P., Alam, S., Saintilan, N., & Triyanti, A. (2022). Responding to sea level rise: challenges and opportunities to govern coastal adaptation strategies in Indonesia. *Maritime Studies, 21*(3), 339–352. https://doi.org/10.1007/s40152-022-00274-1

Pamungkas, G. B. (2021). The land acquisition of inundated land for the Toll Road Project of Semarang–Demak Sea Embankment. *The Indonesian Journal of Planning and Development*, *6*(2), 48-55. https://doi.org/10.14710/ijpd.6.2.48-55

Prasetyo, Y., Bashit, N., Sasmito, B., & Setianingsih, W. (2019). Impact of land subsidence and sea level rise influence shoreline change in the coastal area of Demak. *IOP Conference Series: Earth and Environmental Science, 280*(1). https://doi.org/10.1088/1755-1315/280/1/012006

Reeder, L. A., Rick, T. C., & Erlandson, J. M. (2012). Our disappearing past: a GIS analysis of the vulnerability of coastal archaeological resources in California's Santa Barbara Channel region. *Journal of Coastal Conservation*, *16*(2), 187-197. https://doi.org/10.1007/s11852-010-0131-2

Romadhona, S., Mutmainnah, L., Wibowo, C., & Setiawati, T. C. (2020). Assessment of Coastal Vulnerability Index on potential agricultural land-CVI, Banyuwangi Regency. In *E3S Web of Conferences* (Vol. 142, p. 01002). EDP Sciences. https://doi.org/10.1051/e3sconf/202014201002

Rudiarto, I., Rengganis, H., Sarasadi, A., & Caesar, E. (2020). The effectiveness of strategy adaptations on tidal flood in the coastal areas of Sayung, Demak, Central Java, Indonesia. *IOP Conference Series: Earth and Environmental Science, 448*(1). https://doi.org/10.1088/1755-1315/448/1/012090

Sagala, P. M., Bhomia, R. K., & Murdiyarso, D. (2024). Assessment of coastal vulnerability to support mangrove restoration in the northern coast of Java, Indonesia. *Regional Studies in Marine Science, 70*, 103383. https://doi.org/10.1016/j.rsma.2024.103383

Salim, M. A., Wahyudi, S. I., & Wibowo, K. (2023). Analysis of Factors Influencing Coastal Flood Vulnerability (A Study on the Northern Coast of Central Java). *Proceedings Series on Social Sciences & Humanities, 6*, 20–27. (In Indonesian). https://doi.org/10.30595/pspfs.v6i.847

Sarah, D., Mulyono, A., Satriyo, N. A., Soebowo, E., & Wirabuana, T. (2022). Towards sustainable land subsidence mitigation in Semarang and Demak, Central Java: Analysis using DPSIR Framework. *Journal of Water and Land Development,* (55), 150–165. https://doi.org/10.24425/jwld.2022.142317

Sharples, C., Mount, R., Pedersen, T., Lacey, M., Newton, J., Jaskierniak, D., & Wallace, L. (2009). *The Australian coastal smartline geomorphic and stability map version 1: project report*. Tasmania.

Shaw, J., Taylor, R. B., Forbes, D. L., Ruz, M. H., & Solomon, S. (1998). *Sensitivity of the coasts of Canada to sea-level rise* (Vol. 505, pp. 1-7). Ottawa: Geological Survey of Canada.

Sidiq, T. P., Gumilar, I., Meilano, I., Abidin, H. Z., Andreas, H., & Permana, A. (2021). Land subsidence of Java North Coast observed by SAR Interferometry. *IOP Conference Series: Earth and Environmental Science, 873*(1). https://doi.org/10.1088/1755-1315/873/1/012078

Solahudin, D. S., Satria, B. A., & Jannah, N. T. (2024). DPSIR analysis of the Semarang–Demak Toll Road development and its impacts on the coastal mangrove ecosystem. *Syntax Literate*, *9*(8), 4218-4233. (In Indonesian). https://doi.org/10.36418/syntax-literate.v9i8.16000

Solihuddin, T., Husrin, S., Salim, H. L., Kepel, T. L., Mustikasari, E., Heriati, A., Ati, R. N. A., Purbani, D., Indiasari, V. Y., & Berliana, B. (2021, May). Coastal erosion on the north coast of Java: adaptation strategies and coastal management. In *IOP Conference Series: Earth and Environmental Science* (Vol. 777, No. 1, p. 012035). IOP Publishing. https://doi.org/10.1088/1755-1315/777/1/012035

Tanim, A. H., Goharian, E., & Moradkhani, H. (2022). Integrated socio-environmental vulnerability assessment of coastal hazards using data-driven and multi-criteria analysis approaches. *Scientific Reports, 12*(1), 1–28. https://doi.org/10.1038/s41598-022-15237-z

Wibowo, A. H., Hartopo, H., & Apriyanto, T. (2023). Analysis of N-SPT data on the Semarang–Demak Toll Road Section II (Sta. 10+690 to 27+000). *Rang Teknik Journal, 6*(2), 242–250. (In Indonesian). https://doi.org/10.31869/rtj.v6i2.4208

Wisha, U. J., Wijaya, Y. J., & Hisaki, Y. (2025). Effects of sea-level rise on tidal bore characteristics and sediment dynamics in the Kampar Estuary, Indonesia. *Regional Studies in Marine Science*, 104426. https://doi.org/10.1016/j.rsma.2025.104426

DEFORESTATION AND COASTAL EROSION IN ALBANIA ASSESSED BY REMOTE SENSING

Medjon HYSENAJ [1*] ***and Dritan RUSTJA*** [1]

DOI: 10.21163/GT_2026.211.08

ABSTRACT

This study investigates forest loss and coastal erosion in Albania between 2000 and 2025 using satellite-based remote sensing methods. Landsat time-series data and the Google Earth Engine platform were applied to detect vegetation decline, tree cover loss, and shoreline changes across different segments of the Albanian coastline. While several coastal areas were analyzed, the research concentrated on two representative zones the central coast around Golem beach and the northern coastal wetland of Viluni Lagoon where shoreline retreat and land-use pressure are most evident. In parallel, large-scale deforestation was examined across the country, with a focus on northern Albania, where forest loss has been particularly intense in mountainous regions. Results indicate widespread forest degradation combined with erosion-driven land loss along exposed coastal stretches. These findings highlight the urgency of adopting sustainable forest management and integrated coastal protection strategies to mitigate ongoing environmental degradation in Albania.

Keywords: *Deforestation; Coastal erosion; Remote sensing; Google Earth Engine; Landsat imagery; NDVI; MNDWI.*

1. INTRODUCTION

Forests and coastal ecosystems represent some of the most valuable natural resources in Albania, providing biodiversity, regulating climate, protecting soils, and supporting rural livelihoods. However, in recent decades the country has faced accelerating environmental pressures, notably deforestation, unsustainable land use, and shoreline retreat. These processes have reshaped the landscape and raised urgent concerns about ecological stability, human well-being, and the long-term sustainability of natural resources.

Monitoring such changes is often challenging due to the lack of consistent field data across long time periods. In this context, satellite remote sensing has become an essential tool for detecting, quantifying, and visualizing environmental change. Medium-resolution datasets such as Landsat imagery provide continuous coverage from the early 2000s to the present, making it possible to assess long-term deforestation patterns as well as shoreline dynamics. In particular, vegetation indices such as the Normalized Difference Vegetation Index (NDVI) are widely used to measure vegetation health and extent, while the Modified Normalized Difference Water Index (MNDWI) is effective in mapping water boundaries and shoreline change.

In addition to anthropogenic drivers such as deforestation and land-use change, natural disturbances also contribute significantly to forest dynamics. Windthrows, in particular, represent a major source of forest loss and structural change across Europe. Recent large-scale analyses have provided spatially explicit databases of such wind disturbances over the continent (Forzieri et al., 2020). Regional studies in the Vosges Mountains have demonstrated the potential of low-cost remote sensing methods for detecting scattered windthrow events (Haidu et al., 2019), while investigations in the Apuseni Mountains have clarified the synoptic meteorological processes leading to such extreme wind episodes (Furtuna et al., 2018). Incorporating these perspectives highlights the need to interpret vegetation decline as a result of both natural and anthropogenic processes when assessing forest change in Albania.

[1]*Dept. of Geography, Universiteti i Shkodrës "Luigj Gurakuqi", Albania,* [*]*Corresponding author medjon.hysenaj@unishk.edu.al (MH); dritan.rustja@unishk.edu.al (DR).*

This study applies these methods to examine two critical dimensions of environmental change in Albania between 2000 and 2025: deforestation and forest degradation, using Landsat-based NDVI composites to map vegetation cover change and coastal erosion and shoreline advance, with a focus on areas such as Golem and Viluni Lagoon, applying MNDWI to highlight water encroachment into land.

The analysis was conducted using the Google Earth Engine (GEE) platform, which enables access to multi-decadal satellite archives and cloud-based processing at the scale of an entire country. By combining satellite imagery, pixel-based indices, and change detection techniques, this work provides an updated picture of Albania's environmental transformations, emphasizing the dual challenges of forest loss and coastal erosion. The findings are intended not only to document the extent of these changes but also to contribute to discussions on sustainable environmental management and policy-making in Albania.

2. LITERATURE REVIEW

Deforestation and forest degradation have long been recognized as pressing environmental issues globally (Achard et al. 2014), with profound ecological, social, and climatic implications. Remote sensing has become the primary tool for detecting and monitoring these changes, offering objective, repeatable, and large-scale observations of forest cover dynamics. Seminal works such as Hansen et al. (2013) provided the first high-resolution global forest cover and change maps based on Landsat imagery, setting a benchmark for subsequent national and regional studies (Curtis et al. 2018). Building on these global datasets, Potapov et al. (2015) demonstrated the effectiveness of Landsat time-series analysis in Eastern Europe, showing that satellite-derived forest change products could be adapted for regional assessments. Similar region-specific applications, such as in the Czech Republic, have shown how environmental factors strongly influence land cover changes (Brovkina et al. 2017). Comparable analyses in other regions revealed the rise of small-scale deforestation processes detectable through dense Landsat time series (Kalamandeen et al. 2018).

Recent studies have continued to refine these approaches; for example, Hirschmugl et al. (2017) and Mitchell et al. (2017) reviewed optical remote sensing methods for forest disturbance detection and highlighted challenges in separating forest degradation from complete deforestation, especially in MRV systems designed for REDD+. Gao et al. (2020) expanded on this by stressing that while outright tree cover loss is relatively straightforward to detect, measuring forest degradation and biomass reduction requires more advanced techniques and dense temporal datasets. Fassnacht et al. (2024) further noted that even with improved satellite systems such as Sentinel-2 and Landsat 8/9, challenges remain in translating spectral indices into meaningful forest health indicators, underscoring the importance of long-term monitoring with consistent data. At the global scale, human activities such as grazing and intensive forest management have been shown to exert unexpectedly large impacts on vegetation biomass, altering carbon dynamics and regional ecological balance (Erb et al. 2018). Recent reviews emphasize that the usability of global land cover products depends strongly on their scale and resolution (Linyucheva and Kindlmann 2021).

Beyond global methodological advances, case studies in Europe and the Western Balkans provide more context for Albania's forest dynamics. Senf et al. (2018), for instance, documented widespread canopy mortality across European temperate forests using multi-decadal satellite records, drawing attention to structural forest change in addition to land-cover transitions. Senf et al. (2018) applied MODIS time series to Southeastern Europe and found that annual vegetation dynamics were strongly linked with socio-ecological pressures and climate variability. At the national scale, Albania's forests have attracted growing but still limited attention. Müller et al. (2008) explored how institutional collapse and policy shifts in the 2000s accelerated deforestation in Albania, highlighting the role of governance in driving land-cover change. Laze (2014) combined remote sensing with geographically weighted regression to investigate patterns of forest cover change between Albania and Kosovo from 1988 to 2007, showing that socio-economic pressures and accessibility strongly influenced forest loss. Later reviews by Laze (2014, 2022) emphasized that while remote sensing has become widely adopted across Southeastern Europe, most applications have focused narrowly on mapping forest extent, with

limited efforts directed toward forest health, degradation, or integration with socio-environmental drivers. This pattern was confirmed in broader reviews such as Hirschmugl et al. (2017) and Gao et al. (2020), who observed that while deforestation mapping has matured, degradation monitoring lags behind.

Other regional applications provide comparative insights. Garbarino et al. (2012) used remote sensing to examine structural forest change in Bosnia and Herzegovina, illustrating that combining spectral indices with field validation yields more accurate assessments of forest disturbance. Similarly, Cvitanović et al. (2016, 2017) examined forest change in Croatia, finding that deforestation patterns were often linked to socio-economic transformations such as urbanization, infrastructure expansion, and energy demands. Potić et al. (2022) extended this type of analysis by linking deforestation to hydrological consequences, showing how forest loss can increase surface runoff and exacerbate environmental risks. While not strictly focused on Albania, these studies illustrate the methodological potential of combining Earth observation with ecological modeling. Emerging methods such as deep learning are also entering the domain: Fodor and Conde (2023) developed multimodal learning systems for deforestation and burned area detection, demonstrating how machine learning may soon enhance early warning systems in temperate as well as tropical zones. Likewise, Manasat-Zadeh et al. (2022) showed that remote sensing combined with machine learning can detect bark beetle infestations, highlighting the broader applicability of satellite imagery for forest health monitoring.

In Albania specifically, a number of applied studies underscore both the promise and the limitations of current approaches. Begu and Bygjymi (2025) analyzed deforestation in protected areas of the Albanian Alps, illustrating how remote sensing and GIS can document spatial patterns of loss even within legally protected zones. Hysa and Teqja (2020) applied remote sensing to assess forest health and disturbances in selected Albanian forests, though the lack of consistent long-term imagery limited their conclusions. These findings echo broader assessments that satellite-based monitoring in Albania remains fragmented and often project-specific rather than systematic. Compared with global frameworks like Hansen et al. (2013), national-scale monitoring remains underdeveloped. Yet the technical opportunities are significant: with freely available Landsat and Sentinel imagery, combined with Google Earth Engine's cloud-computing capacity, national and sub-national deforestation mapping can now be conducted with relative efficiency and reproducibility.

Taken together, the literature reveals several key gaps. First, although deforestation mapping in Albania and the Balkans is feasible and increasingly practiced, degradation monitoring (e.g., selective logging, forest thinning, biomass decline) is far less common. Second, few studies explicitly connect forest loss with downstream ecological impacts such as erosion, runoff, or biodiversity decline, despite evidence from neighboring countries. Third, the integration of advanced methods time-series analysis, spectral unmixing, and machine learning remains underexplored in Albania compared with global best practices. Finally, while many global products exist, their validation at national and local scales is often lacking, which can lead to misinterpretation of forest trends. This gap may explain why national discourse sometimes underestimates the extent of deforestation, even when satellite evidence indicates significant forest cover loss. By situating Albania within both regional and global research, this study contributes to bridging these gaps by using Landsat time series (2000-2025), NDVI differencing, and Hansen v1.8 datasets to produce updated and transparent insights into forest loss, with an emphasis on linking remote sensing evidence to environmental realities.

3. DATA AND METHODS

This study used multi-temporal Landsat imagery processed on the Google Earth Engine (GEE) platform to assess both forest cover change and shoreline retreat across Albania. The datasets included Landsat 5 TM, Landsat 7 ETM+, and Landsat 8/9 OLI surface reflectance composites from 2000 to 2025. Cloud masking was performed using the *pixel_qa* band and a seasonal filter (April - October) was applied to maintain phenological consistency. For deforestation analysis, the Normalized Difference Vegetation Index (NDVI) was calculated using the formula:

$$NDVI = \frac{(NIR-RED)}{(NIR+RED)} \quad (1)$$

where:

NIR represents the near-infrared band (Band 4 for Landsat 5, Band 5 for Landsat 8) and
RED corresponds to the red band (Band 3 for Landsat 5, Band 4 for Landsat 8).

NDVI values range from –1 to +1, with higher values indicating denser vegetation. NDVI composites were generated for 2000 and 2025, and a difference layer ($\Delta NDVI = NDVI_{(2025)} - NDVI_{(2000)}$) was produced to visualize zones of vegetation decline. Pixels showing $\Delta NDVI < 0$ were interpreted as potential deforestation areas. To complement this, the Hansen Global Forest Change v1.8 dataset (Hansen et al., 2013) was used to quantify cumulative forest loss between 2000 and 2025 at 30 m resolution.

The Hansen dataset was processed within the Google Earth Engine environment through a reproducible JavaScript workflow (Appendix A). Forest areas were defined as pixels with ≥ 30 % canopy cover in 2000 using the treecover2000 band, while annual tree cover loss for 2001–2020 was derived from the lossyear band. A mask operation limited the analysis to areas classified as forest in 2000, and cumulative loss between 2001 and 2020 was then calculated as the sum of all loss years within this baseline mask.

The dataset defines forest as areas with >30% canopy cover in 2000, with annual loss layers identifying tree cover removal events. Forest loss percentage was computed using:

$$Forest\ Loss\ (\%) = \frac{A_{loss}}{A_{forest_{2000}}}\ x\ 100 \quad (2)$$

where:

A_{loss} is the number of pixels classified as forest loss and
$A_{forest_{2000}}$ the number of forest pixels in the base year.

For coastal erosion, the Modified Normalized Difference Water Index (MNDWI) was applied to delineate shoreline positions:

$$MNDWI = \frac{(GREEN-SWIR)}{(GREEN+SWIR)} \quad (3)$$

where:

GREEN is the green band (Band 2 for Landsat 5, Band 3 for Landsat 8) and
SWIR the short-wave infrared band (Band 5 for Landsat 5, Band 6 for Landsat 8).

Binary water masks were generated by applying a threshold of MNDWI > 0, where pixels classified as “water” in 2025 but not in 2000 represented erosion zones, and the inverse (water in 2000 but not in 2025) indicated land gain. An XOR operator was further applied to highlight any type of shoreline change.

The entire coastal change analysis was performed through a reproducible GEE JavaScript workflow, automating the steps of image pre-processing, cloud masking, compositing, index calculation, thresholding, and shoreline change detection. The code uses Landsat 5 TM Level-2 data for the year 2000 and Landsat 8/9 OLI Level-2 imagery for the 2024–2025 period, ensuring radiometric consistency by applying standard scaling coefficients (0.0000275 × SR + –0.2).

Values greater than 0 were classified as water pixels, allowing a binary mask of land/water to be created for both 2000 and 2025. The difference between these masks revealed areas where water replaced land, identifying shoreline retreat. Spatial overlay and pixel differencing in GEE quantified these transitions, while visual inspection validated erosion zones in Golem beach and Viluni Lagoon. Final maps were exported at 30 m resolution and reprojected to WGS 84 / UTM Zone 34N.

This approach ensures reproducibility and enables future extension to precise quantification (e.g., shoreline shift in meters or forest loss in hectares). All indices and calculations were implemented in the Google Earth Engine environment using the JavaScript API, ensuring full reproducibility and transparency of the spatial analysis workflow. Visualization layers were overlaid on false-color composites, using red to represent water advancement (erosion) and blue for water retreat (land gain). Additional edges were extracted using the Canny edge detector to delineate the 2025 shoreline. The results were visually cross-checked with Sentinel-2 imagery and OpenStreetMap shoreline references for consistency. The results are shown in **figure 1** for Golem beach and in **figure 2** for Viluni Lagoon, with red-marked areas identifying zones of erosion where water advanced inland.

Pixel-based differencing of the 2000 and 2025 MNDWI masks within GEE indicates inland shoreline displacement typically spanning one Landsat pixel (≈ 30 m) at Golem and about half a pixel (≈ 15 m) at Viluni Lagoon, with localized maxima reaching 40–50 m.

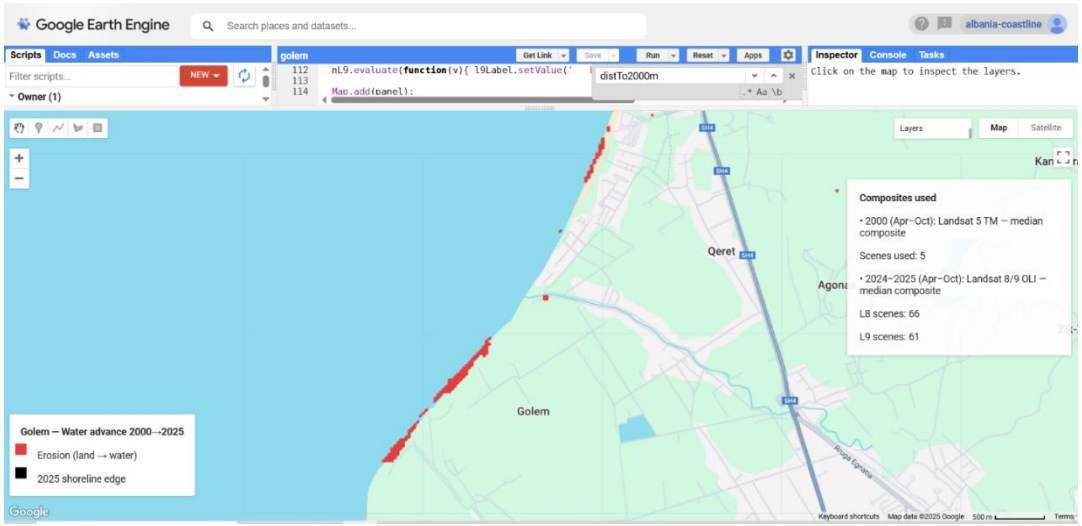


Fig. 1. Coastal erosion between 2000 and 2025 at Golem. Red indicates shoreline retreat where water advanced inland.

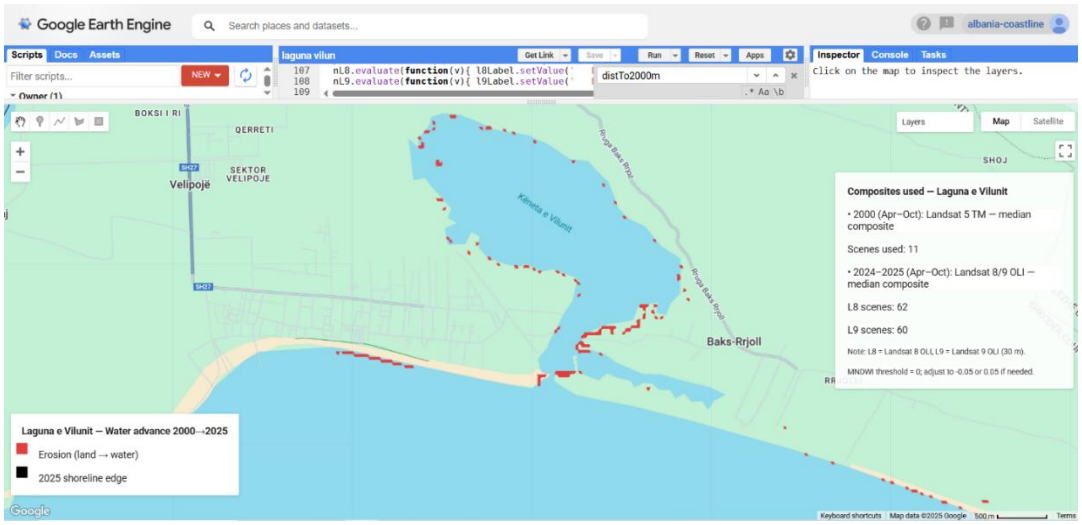


Fig. 2. Coastal erosion between 2000 and 2025 at Viluni Lagoon. Red indicates shoreline retreat where water advanced inland.

These magnitudes correspond to an average retreat rate of roughly 1 m yr^{-1}, consistent with regional Mediterranean erosion assessments (Vousdoukas et al., 2020).

For deforestation, two complementary approaches were applied. First, the Hansen Global Forest Change dataset (v1.8) was used to map tree cover in 2000 and cumulative forest loss between 2001 and 2020 at 30 m resolution. This classification, using a 30% canopy cover threshold, is shown in **figure 3**, where green pixels represent remaining forest and red pixels indicate tree cover loss. Second, a focused analysis of northern Albania was conducted to illustrate spatial deforestation hotspots more clearly. These results are presented in **figure 4**, highlighting concentrated areas of forest removal in mountainous zones. Cloud masking and seasonal filtering (April-October) were applied to ensure comparability, and median composites minimized noise from outlier images. The combined outputs provide both national-scale insights and local detail on Albania's forest and coastal change dynamics.

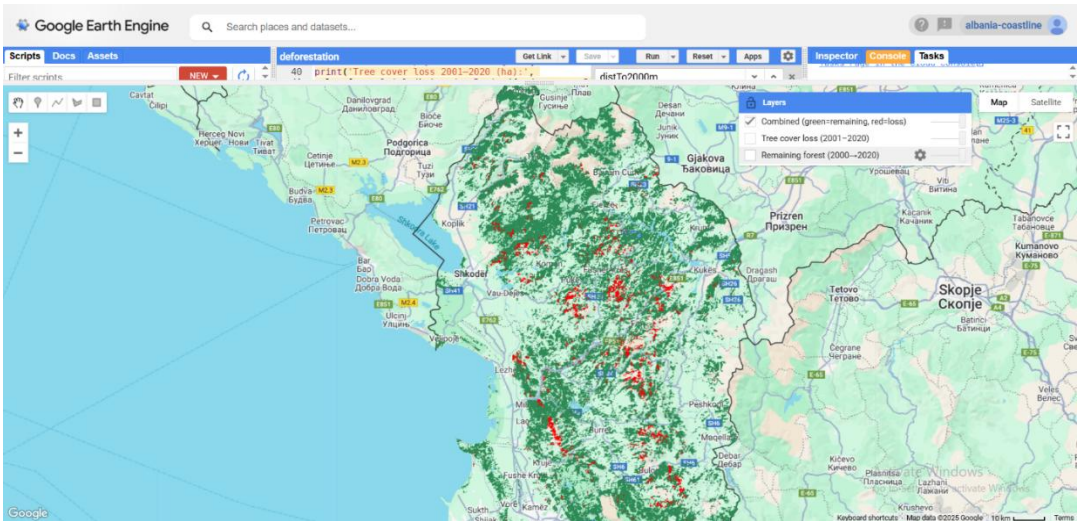


Fig. 3. Forest cover loss and remaining forest in Albania (2000-2020) based on Hansen Global Forest Change dataset. Green = remaining forest; red = deforestation.

Quantitative estimation of deforestation was derived directly within the Google Earth Engine (GEE) workflow developed for this study, covering the full 2000-2025 period through Landsat-based NDVI differencing. To validate and complement these results, the Hansen Global Forest Change v1.8 dataset (Hansen et al., 2013) was integrated as a reference layer within the same GEE environment, enabling cross-checking of spatial patterns and magnitude. Within GEE, all forest pixels with ≥30 % canopy cover in 2000 were extracted using the treecover2000 band, while cumulative annual losses (2000-2025) were aggregated through pixel-based masking and area computation. The analysis revealed approximately 47,300 ha of gross tree-cover loss, equivalent to around 7.3 % of the 2000 baseline forest cover and an average annual loss rate of about 0.21 % yr^{-1}. These values align closely with FAO FRA 2025 and World Bank estimates, confirming that while the total national forest extent remains broadly stable, recurring canopy disturbances persist in localized areas. Spatially, the GEE-based outputs identify pronounced deforestation hotspots in northern Albania (Shkodër, Kukës, Dibër), where disturbance intensity exceeds 7-9 % of local forest area, whereas central and southern regions exhibit lower relative losses (≈ 3-4 %).

The integration of multi-temporal Landsat composites with globally validated datasets within GEE thus provided both an internally consistent and externally verifiable quantification of forest loss, effectively linking the visual and numerical dimensions of environmental change across the 2000-2025 period.

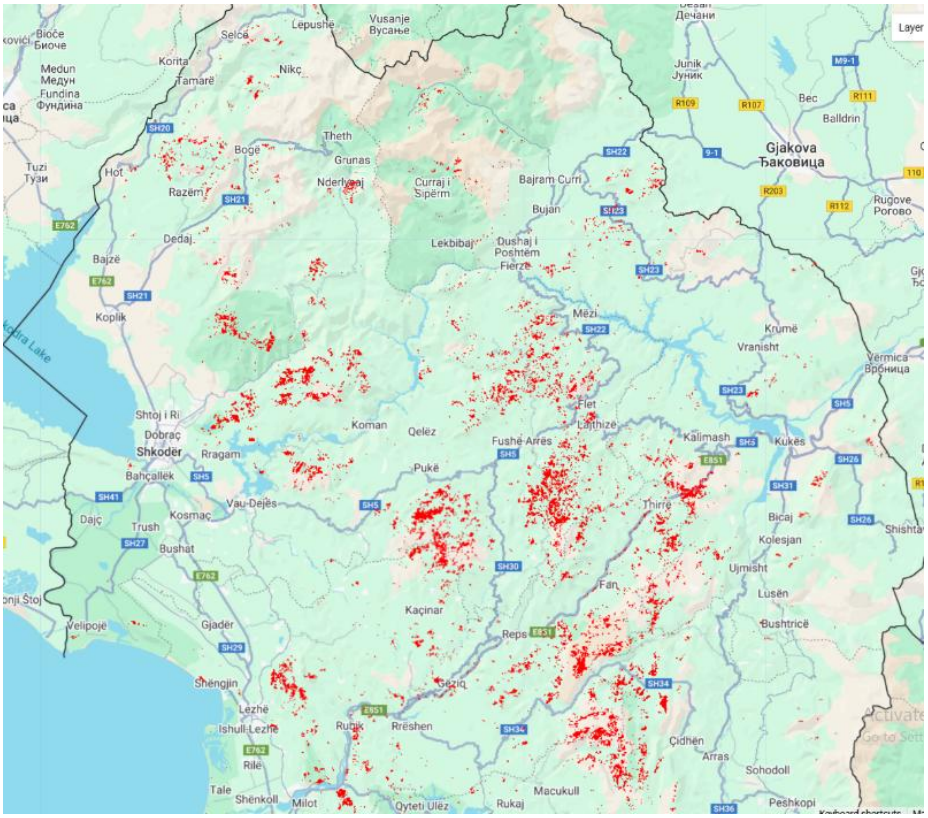


Fig. 4. Deforestation hotspots (detailed map of northern Albania).

3. RESULTS

The analysis revealed significant evidence of both coastal erosion and forest loss in Albania over the study period. The coastal assessment using MNDWI showed that large parts of the shoreline have retreated, particularly in zones subject to human pressure and natural dynamics. At Golem beach, the comparison between 2000 and 2025 composites highlights a clear inland shift of the shoreline (Figure 1). Red-marked erosion areas indicate that water has advanced into previously terrestrial zones, reflecting both wave-driven processes and intensified land use in a highly urbanized coastal stretch. A similar pattern was observed at Viluni Lagoon, where erosion is particularly visible around the lagoon outlet and adjacent beach (Figure 2). Here, water encroachment suggests a combination of sea-level rise and sediment imbalance that has reduced the protective beach zone, leaving coastal habitats increasingly vulnerable.

The deforestation analysis confirmed widespread tree cover loss across Albania. According to the Hansen Global Forest Change dataset, substantial forest loss occurred between 2001 and 2020, with forest remaining in 2020 primarily located in more remote mountainous areas. The classification results (Figure 3) demonstrate the spatial distribution of these changes: green areas indicate stable forest, while red patches mark tree cover loss. The visual evidence suggests that deforestation has been more pronounced in northern and central Albania, where accessibility and logging activities are greater. To illustrate this in more detail, a hotspot analysis was performed, focusing on northern Albania. The results (Figure 4) show concentrated clusters of deforestation in mountainous counties such as Shkodër, Kukës, and Dibër. These localized maps confirm that forest loss has not been uniform but rather spatially concentrated, reflecting a combination of economic pressures and limited enforcement of forest protection policies.

Overall, the results underline the dual challenge faced by Albania: on one hand, forest ecosystems are shrinking and fragmenting due to deforestation and degradation; on the other, coastal systems are increasingly exposed to shoreline retreat. Together, these processes highlight a critical need for integrated strategies that address both terrestrial and coastal vulnerabilities.

4. DISCUSSION

The combined results of this study provide clear evidence that Albania is facing two major and interconnected environmental challenges: the ongoing retreat of its Adriatic shoreline and the steady decline of forest resources. Both processes are visible when comparing multi-decadal satellite imagery, demonstrating the usefulness of Earth observation for identifying large-scale environmental transformations.

The coastal results, particularly from Golem and Viluni Lagoon, confirm the findings of earlier reports that highlight Albania's vulnerability to erosion due to sea-level rise, sediment imbalance, and human modification of the coast. This pattern reflects global trends, as sandy coastlines worldwide are under increasing threat of erosion (Vousdoukas et al. 2020). Similar challenges have been observed across Europe, where coastal protection strategies are being redesigned to respond to accelerated shoreline retreat (Pranzini and Williams 2021). Comparable applications of Sentinel-2 imagery for burned and eroded landscapes confirm the effectiveness of such satellite-based methods in Mediterranean contexts (Kovács 2019). Regional studies of the Bulgarian Black Sea coast also confirm the risk of flooding and erosion in densely inhabited coastal zones (Palazov and Stanchev 2009). Erosion in these areas not only reduces beach width but also threatens habitats, infrastructure, and tourism-based economies. Similarly, the deforestation maps corroborate reports of intensified forest exploitation, illegal logging, and land-use conversion in northern and central Albania. The spatial clustering of forest loss in mountainous regions suggests that economic activity and accessibility play a significant role in driving deforestation patterns.

Importantly, this study demonstrates that even with freely available satellite data, it is possible to generate compelling visual evidence of environmental change. NDVI- and MNDWI-based indices, applied through Google Earth Engine, provide fast and reproducible methods for monitoring land cover and shoreline dynamics. However, the current approach is largely qualitative and descriptive, focusing on the visual identification of erosion and deforestation hotspots.

The next step of this research will therefore be to move beyond qualitative mapping and concentrate on mathematical calculations to quantify the extent of change. This includes measuring the number of meters of shoreline retreat in specific coastal stretches, calculating the hectares of forest lost across different time periods, and estimating the percentage of remaining forest cover at national and regional scales. Such quantitative outputs will not only strengthen the scientific rigor of future analyses but also provide policymakers with concrete numbers that can guide adaptation strategies, conservation efforts, and land-use planning. Machine learning approaches, such as those applied for peatland carbon mapping in Indonesia, show the potential for future integration into deforestation monitoring (Musthofa et al. 2022). In this way, remote sensing will not only visualize environmental change but also provide the statistical basis for evidence-driven environmental governance in Albania.

The results highlight an urgent need for coordinated policies linking forest management, coastal protection, and land-use planning in Albania. Integrating satellite monitoring into national strategies could improve early detection of illegal logging and coastal retreat. Sustainable measures such as reforestation incentives, dune and wetland restoration, and stricter environmental enforcement should be prioritized. Future research should focus on integrating higher-resolution data (Sentinel-2, LiDAR) and machine-learning models for precise quantification of shoreline retreat and forest degradation, providing stronger evidence for policy and climate adaptation planning.

5. CONCLUSION

This study demonstrates the effectiveness of satellite remote sensing in documenting long-term environmental change in Albania, with a focus on deforestation and coastal erosion. By comparing Landsat imagery from 2000 with 2025, two critical trends were identified: the retreat of the shoreline

in vulnerable coastal zones such as Golem and Viluni Lagoon, and the loss of forest cover, particularly concentrated in northern Albania. These findings align with previous reports of environmental degradation in the country and highlight the dual pressures facing both terrestrial and coastal ecosystems.

The use of indices such as NDVI and MNDWI within the Google Earth Engine platform proved to be an efficient and accessible method for monitoring change across multi-decadal timescales. The results presented here are primarily descriptive, offering clear visualizations of change hotspots. However, they establish a foundation for the next stage of research, which will involve quantitative calculations of shoreline retreat (in meters) and forest loss (in hectares) to provide precise measurements of environmental change.

In conclusion, the integration of remote sensing with environmental monitoring offers a powerful approach for assessing Albania's ecological challenges. By combining visual evidence with future quantitative analyses, such studies can directly support evidence-based decision-making, inform conservation strategies, and contribute to the sustainable management of Albania's forests and coastlines.

REFERENCES

Achard, F., Beuchle, R., Mayaux, P., et al. (2014). Determination of tropical deforestation rates and related carbon losses from 1990 to 2010. *Global Change Biology*, 20(8), 2540–2554. https://doi.org/10.1111/gcb.12605.

Begu, E., & Bygjymi, X. (2025). Deforestation in protected areas: A GIS/RS based study of National Park of Albanian Alps. *Proceedings of The International Conference on Research in Humanities and Social Sciences*, 2(1), 78–85. https://doi.org/10.33422/icrhs.v2i1.1307.

Brovkina, O., Zemek, F., Novotný, J., Heřman, M., & Štěpánek, P. (2017). Analysing changes in land cover in relation to environmental factors in the districts of Znojmo and Třebíč (Czech Republic). *European Journal of Environmental Sciences*, 7(2), 82–94. https://doi.org/10.14712/23361964.2017.9.

Curtis, P. G., Slay, C. M., Harris, N. L., Tyukavina, A., & Hansen, M. C. (2018). Classifying drivers of global forest loss. *Science*, 361(6407), 1108–1111. https://doi.org/10.1126/science.aau3445.

Cvitanovic, M., Blackburn, G. A., & Jepsen, M. R. (2016). Characteristics and drivers of forest cover change in the post-socialist era in Croatia: Evidence from a mixed-methods approach. *Regional Environmental Change*, 16(6), 1751–1763. https://doi.org/10.1007/s10113-016-0928-0.

Erb, K.-H., Kastner, T., Plutzar, C., et al. (2018). Unexpectedly large impact of forest management and grazing on global vegetation biomass. *Nature*, 553, 73–76. https://doi.org/10.1038/nature25138.

Fassnacht, F. E., White, J. C., Wulder, M. A., & Næsset, E. (2024). Remote sensing in forestry: Current challenges, considerations and directions. Forestry: *An International Journal of Forest Research*, 97(1), 11–37. https://doi.org/10.1093/forestry/cpad024.

Fodor, G., & Conde, M. V. (2023). Rapid Deforestation and Burned Area Detection using Deep Multimodal Learning on Satellite Imagery. *arXiv*:2307.04916. https://doi.org/10.48550/arXiv.2307.04916.

Forzieri, G., Pecchi, M., Girardello, M., Mauri, A., Klaus, M., Nikolov, C., Rüetschi, M., Gardiner, B., Tomaštík, J., Small, D., Nistor, C., Jonikavicius, D., Spinoni, J., Feyen, L., Giannetti, F., Comino, R., Wolynski, A., Pirotti, F., Maistrelli, F., Savulescu, I., Wurpillot-Lucas, S., Karlsson, S., Zieba-Kulawik, K., Strejczek-Jazwinska, P., Mokroš, M., Franz, S., Krejci, L., Haidu, I., Nilsson, M., Wezyk, P., Catani, F., Chen, Y.-Y., Luyssaert, S., Chirici, G., Cescatti, A., and Beck, P.S.A. (2020). A spatially explicit database of wind disturbances in European forests over the period 2000–2018. *Earth System Science Data*, 12(1): 257–276. https://doi.org/10.5194/essd-12-257-2020.

Furtuna P., Haidu I., Maier N. (2018). Synoptic processes generating windthrows. A case study in the Apuseni mountains (Romania). *Geographia Technica*, 13(2), 52-61. https://doi.org/10.21163/GT_2018.132.04

Gao, Y., Skutsch, M., Paneque-Gálvez, J., & Ghilardi, A. (2020). Remote sensing of forest degradation: A review. *Environmental Research Letters*, 15(10), 103001. https://doi.org/10.1088/1748-9326/abaad7.

Garbarino, M., Borgogno Mondino, E., Lingua, E., Nagel, T. A., Dukić, V., Govedar, Z., & Motta, R. (2012). Gap disturbances and regeneration patterns in a Bosnian old-growth forest: A multispectral remote sensing and ground-based approach. *Annals of Forest Science*, 69(5), 617–625. https://doi.org/10.1007/s13595-011-0177-9

Haidu I., Furtuna P.R., Lebaut S. (2019). Detection of old scattered windthrow using low-cost resources. The case of Storm Xynthia in the Vosges Mountains, 28 February 2010. *Open Geosciences*, 11(1), 492-504. https://doi.org/10.1515/geo-2019-0040.

Hansen, M. C., Potapov, P. V., Moore, R., Hancher, M., Turubanova, S. A., Tyukavina, A., Thau, D., Stehman, S. V., Goetz, S. J., Loveland, T. R., Kommareddy, A., Egorov, A., Chini, L., Justice, C. O., & Townshend, J. R. G. (2013). High-resolution global maps of 21st-century forest cover change. *Science*, 342(6160), 850–853. https://doi.org/10.1126/science.1244693.

Hirschmugl, M., Gallaun, H., Dees, M., Datta, P., Deutscher, J., Koutsias, N., & Schardt, M. (2017). Methods for mapping forest disturbance and degradation from optical Earth observation data: A review. *Current Forestry Reports*, 3(1), 32–45. https://doi.org/10.1007/s40725-017-0047-2.

Kalamandeen, M., Gloor, E., Mitchard, E., et al. (2018). Pervasive rise of small-scale deforestation in Amazonia. *Scientific Reports*, 8, 1600. https://doi.org/10.1038/s41598-018-19358-2.

Kovács, K. D. (2019). Evaluation of burned areas with Sentinel-2 using SNAP: The case of Kineta and Mati, Greece, July 2018. *Geographia Technica*, 14(2), 20–38. https://doi.org/10.21163/GT_2019.142.03

Laze, K. (2014). Identifying and understanding the patterns and processes of forest cover change in Albania and Kosovo. *European Scientific Journal*, Special Edition 2014, vol. 2, 198–207. ISSN: 1857-7431. https://www.econstor.eu/bitstream/10419/103750/1/796910839.pdf

Laze, K. (2022). Preliminary findings on remote sensing of forest cover change, forest and tree health in Southeastern Europe. *The International Archives of the Photogrammetry, Remote Sensing and Spatial Information Sciences*, XLIII-B4-2022, 133–140. https://doi.org/10.5194/isprs-archives-XLIII-B4-2022-133-2022.

Linyucheva, A., & Kindlmann, P. (2021). A review of global land cover maps in terms of their potential use for habitat suitability modelling. *European Journal of Environmental Sciences*, 11(1), 46–54. https://doi.org/10.14712/23361964.2021.6.

Manasat-Zadeh, S. M., Goodsman, D., Ray, N., & Eftelioglu, N. (2023). Early detection of bark beetle attack using remote sensing and machine learning: A review. *ACM Computing Surveys*, 56(4), Article 97, 1–40. https://doi.org/10.1145/3625387.

Mitchell, A. L., Rosenqvist, Å., & Mora, B. (2017). Current remote sensing approaches to monitoring forest degradation in support of countries measurement, reporting and verification (MRV) systems for REDD+. *Carbon Balance and Management*, 12(9), 1–22. https://doi.org/10.1186/s13021-017-0078-9.

Müller, D., & Munroe, D. K. (2008). Changing rural landscapes in Albania: Cropland abandonment and forest clearing in the postsocialist transition. *Annals of the Association of American Geographers*, 98(4), 855–876. https://doi.org/10.1080/00045600802262323

Musthofa, F., Widyatmanti, W., Ariasakusuma, S., Umariadi, D. A., Puteri, D., Raharjo, F. F., & Arasyd, M. K. (2022). Machine learning for mapping spatial distribution of thickness and carbon stock of tropical peatland based on remote sensing data: A case study in Lake Sentarum National Park, Indonesia. *Geographia Technica*, 17(1), 46–57. https://doi.org/10.21163/GT_2022.171.04.

Palazov, A., & Stanchev, H. (2009). Risks for the population along the Bulgarian Black Sea coast from flooding caused by extreme rise of sea level. *Information & Security: An International Journal*, 24(2), 65–75. https://doi.org/10.11610/isij.2407

Potapov, P. V., Turubanova, S. A., Tyukavina, A., Krylov, A. M., McCarty, J. L., Radeloff, V. C., & Hansen, M. C. (2015). Eastern Europe's Forest cover dynamics from 1985 to 2012 quantified from the full Landsat archive. *Remote Sensing of Environment*, 159, 28–43. https://doi.org/10.1016/j.rse.2014.11.027.

Potić, I., Mihajlović, Lj. M., Šimunić, V., Ćurčić, N. R., & Milinković, M. (2022). Deforestation as a cause of increased surface runoff in the catchment: Remote sensing and SWAT approach—A case study of Southern Serbia. *Frontiers in Environmental Science*, 10, 896404. https://doi.org/10.3389/fenvs.2022.896404.

Pranzini, E., & Williams, A. T. (2021). Coastal Erosion and Protection in Europe: Challenges Ahead. Elsevier. ISBN 9780128218190.

Senf, C., Pflugmacher, D., Zhiqiang, Y., & Seidl, R., et al. (2018). Canopy mortality has doubled in Europe's temperate forests over the last three decades. *Nature Communications*, 9(1). https://doi.org/10.1038/s41467-018-07539-6.

Vousdoukas, M. I., Ranasinghe, R., Mentaschi, L., et al. (2020). Sandy coastlines under threat of erosion. *Nature Climate Change*, 10(3), 260–263. https://doi.org/10.1038/s41558-020-0697-0.

GEOSPATIAL IDENTIFICATION OF SOIL EROSION HOTSPOTS EXACERBATING THE CATASTROPHIC FLASH FLOOD IN BALI, INDONESIA

Ni Made TRIGUNASIH [1], ***Moh SAIFULLOH*** [2,3*], ***I Nyoman SUNARTA*** [4], ***Ida Bagus Putu BHAYUNAGIRI*** [1] ***& Zulkarnain ZULKARNAIN*** [5]

DOI: 10.21163/GT_2026.211.09

ABSTRACT

The catastrophic flash flood that struck the Biluk Poh Watershed in Bali on October 16, 2022, was a complex disaster. While triggered by extreme rainfall, its catastrophic scale was critically exacerbated by landscape-level factors, particularly massive sediment mobilization. This study investigates the spatial contribution of soil erosion to the flood's severity by quantifying its extent and intensity using the Universal Soil Loss Equation (USLE). The analysis integrates CHIRPS rainfall data, ALOS PALSAR DEM, vegetation indices from Sentinel-2, and field-based measurements of soil structure, texture, and organic matter. High-resolution erosion modelling (10 m) revealed soil loss ranging from 0 to 4664.78 t ha^{-1} yr^{-1}, with a watershed average of 168.03 t ha^{-1} yr^{-1}. The results show a landscape of stark contrasts: while 39.30% of the area experiences only Slight erosion (0–15 t ha^{-1} yr^{-1}), a combined 55.97% suffers from Moderate (18.56%), Heavy (29.42%), and Very Heavy (7.99%) erosion. Erosion was most severe in the Penyaringan and Yeh Embang Kauh villages. These findings demonstrate that uncontrolled erosion from these specific hotspots, which are concentrated upstream and along steep river corridors, functioned as the key exacerbating factor. They supplied the massive sediment loads that blocked the main river channel, catastrophically worsening the flood event triggered by high rainfall. This study provides the first high-resolution erosion assessment for the Biluk Poh Watershed, offering critical evidence for targeted mitigation. The urgency of these findings is underscored by the catastrophic September 2025 Bali floods, which demonstrated that the sediment-driven mechanisms modeled in this study are a primary, escalating, and regional-scale threat.

Keywords: *Erosion modeling; Bali flooding; Flash flood; Disaster risk reduction; Watershed management.*

1. INTRODUCTION

Soil erosion is one of the most widespread and critical forms of land degradation, particularly in tropical regions where high rainfall intensity and complex topography prevail (Ao et al., 2025; Kardhana et al., 2024; Mahmood et al., 2024). The detachment and transport of topsoil by surface runoff not only reduce land productivity but also contribute to sedimentation in rivers, reservoirs, and irrigation systems, impairing hydrological function and increasing the risk of downstream flooding (Rashmi et al., 2022). These impacts are frequently intensified by unsustainable land management practices, including deforestation and insufficient conservation infrastructure (Hirabayashi et al., 2021). While flash floods are typically associated with short-duration, high-intensity rainfall, their severity is often exacerbated by pre-existing landscape vulnerabilities such as soil erosion, sediment accumulation, and reduced river channel capacity (Chen et al., 2024; Singh & Kansal, 2024).

---

[1]*Soil Sciences and Environment Laboratory, Faculty of Agriculture, Udayana University, Denpasar, Indonesia. trigunasih@unud.ac.id (NMT), bhayunagiri@unud.ac.id (IBPB).*

[2]*Spatial Data Infrastructure Development Centre (PPIDS) Udayana University, Denpasar, Indonesia.*

[3*]*Marine Sciences Study Program, Faculty of Marine Sciences and Fisheries, Udayana University-Badung, Indonesia. Corresponding author: m.saifulloh@unud.ac.id (MS).*

[4]*Doctoral Program of Tourism, Faculty of Tourism, Udayana University, Denpasar, Indonesia. nyoman_sunarta@unud.ac.id (INS).*

[5]*Agroecotechnology Study Program, Faculty of Agriculture, Mulawarman University, Samarinda, East Kalimantan, Indonesia. zulkarnain@faperta.unmul.ac.id (ZZ).*

Erosion accelerates surface runoff, mobilizes sediment, and contributes to channel clogging, creating hazardous conditions during storm events (Wink Junior et al., 2024). This sediment influx promotes channel aggradation, which reduces the hydraulic conveyance capacity of the river. Consequently, channel overbank flow can occur at lower discharge volumes, amplifying the flood's magnitude and spatial extent (Addy & Wilkinson, 2021; Ahrendt et al., 2022). Despite this direct link, soil erosion is rarely included as a central parameter in flood risk studies, which often emphasize rainfall variability or land-use change (Wu et al., 2023; Zhang et al., 2024). This oversight can limit the understanding of flood generation processes, particularly in watersheds susceptible to high sediment yields.

Flash flood risk is primarily driven by the temporal variability of high-intensity precipitation. However, the impacts of these rainfall events are spatially heterogeneous at the watershed scale. This variability is shaped by landscape-level exacerbating factors, including land-use change and the inherent susceptibility of the landscape to soil erosion, which influences runoff generation, sediment transport, and other key physical processes (Abu El-Magd et al., 2021; Bauer et al., 2019). This landscape vulnerability to erosion is captured by the components of the Universal Soil Loss Equation (USLE) model: soil vulnerability (K factor), topographic vulnerability (LS factor), the impact of land use practices (P factor), and the protective role of vegetation cover (C factor). Global research has increasingly demonstrated how soil erosion acts as this critical exacerbating factor, rather than a direct driver, in flash flood risk. For example, in Makkah City, high erosion was concentrated in 11% of the watershed, determining where flood risk was highest (Othman et al., 2023). In China's Wuding River Basin, erosion hotspots at river confluences were identified as the source of sedimentation that triggered severe flash floods (Lai et al., 2024). Similarly, long-term analysis in North Africa linked climate extremes and urban development to a 24.14% increase in erosion-driven exposure of human populations (Salhi et al., 2024).

The USLE and its revised form (RUSLE) are two examples of empirical approaches that have become more popular for modeling soil erosion around the world (Lamane et al., 2025; Prasad et al., 2024; Taloor et al., 2025), especially when combined with Geographic Information Systems (GIS) and satellite-based remote sensing. Many studies in Asia, Africa, and Europe have used these models successfully to measure yearly soil loss at the watershed and regional levels using open-access geospatial datasets, especially from sensors like Landsat and Sentinel-2 (Dou et al., 2022; Dzwairo et al., 2025; Milazzo et al., 2023; Panagos et al., 2024). But a lot of these apps tend to make assumptions about important factors like the soil erodibility factor (K) based on old databases or broad soil classification maps, which might not show how complicated the land is in previous case studies (Soniari et al., 2024). Also, the Normalized Difference Vegetation Index (NDVI) is often the only source of vegetation cover, even though it does not work well in areas with mixed or sparse vegetation (Gwapedza et al., 2021; Okacha & Salhi, 2024). This leads to assessments that are too simple and may miss important micro-scale erosion processes, especially in tropical landscapes that change quickly.

This study makes a new contribution by combining high-resolution remote sensing with detailed field-based soil observations to make erosion models more accurate. The K factor is based on ground-measured soil texture, organic matter, and structural conditions. This makes it possible to get realistic estimates of how easily the soil can be eroded that are specific to the geomorphological and geological diversity of the Biluk Poh Watershed. We also use the Perpendicular Vegetation Index (PVI) and the Normalized Difference Soil Vegetation Index (NDSVI) in addition to NDVI. These are better at picking up on changes in vegetation and canopy density (Adnyana et al., 2024; Adnyana et al., 2025). These changes make it much easier to guess the C factor. Our dataset is cheaper and more scalable than previous studies in Bali Province, which mostly used traditional field-based erosion assessments with limited spatial coverage (Soniari et al., 2024; Trigunasih et al., 2018; Trigunasih & Saifulloh, 2023). It also helps with early-warning and risk reduction strategies in tropical watersheds that are prone to erosion. In Indonesia, many watershed studies focus on land-use dynamics, with limited exploration of soil erosion as a key hydrological variable. For instance, research in Aceh Jaya's Teunom Watershed identified that 68% of the area was exposed to moderate to high flood risk due to

declining forest and agricultural cover (Sugianto et al., 2022). Similarly, the Garang Watershed in Semarang experienced spatial degradation driven by overlapping management and weak planning enforcement (Sejati et al., 2024). Although these studies reveal the importance of land use, few have incorporated detailed erosion assessments or quantified sedimentation hazards directly (Merten et al., 2020; Wardhani et al., 2022). This oversight is especially problematic in regions like Bali, where steep volcanic slopes, intense rainfall, and degraded soils contribute to heightened erosion susceptibility.

On 16 October 2022, the Biluk Poh Watershed in Jembrana Regency, Bali, experienced a flash flood that inflicted widespread damage to settlement, roads, and bridges. While the intense rainfall is documented as the temporal trigger, the role of geomorphic and soil-related factors as key exacerbating factors remains unexplored. This study addresses that critical knowledge gap. The primary objective is to provide a rapid geospatial identification of soil erosion hotspots, framing them as the principal landscape-level factors that amplified the flood's catastrophic severity by contributing massive volumes of sediment to the river system. To achieve this, the novelty of our research lies in its high-resolution (10 m), field-calibrated methodology. This approach is specifically designed to overcome the limitations of broader regional studies that rely on generalized soil databases. Our methodology integrates ground-measured soil parameters (texture, organic matter, and structure) to derive a locally-specific K factor and utilizes advanced vegetation indices (PVI and NDSVI) from Sentinel-2 for a more accurate C factor. This field calibration is essential for accurately capturing the high spatial variability of tropical volcanic landscapes like the Biluk Poh Watershed. This robust USLE model allows us to quantify erosion rates by integrating the rainfall driver (R factor) with the spatial landscape variables that control susceptibility (K, LS, C, and P). This study then conceptually links the resulting erosion hotspot map to the observed flood impacts through a visual analysis of high-resolution Unmanned Aerial Vehicle (UAV) imagery captured post-event. This combined analysis provides a critical, spatially-explicit evidence base for strategic soil conservation planning aimed at reducing future sedimentation-driven flood risks in this vulnerable tropical watershed.

2. STUDY AREA

This study was conducted in the Biluk Poh Watershed, located in Jembrana Regency, Bali Province, Indonesia. The watershed spans an area of 9,109.67 ha and is geographically situated between latitudes 8°12′30″S and 8°22′30″S and longitudes 114°00′00″E and 114°47′30″E (**Fig. 1**).

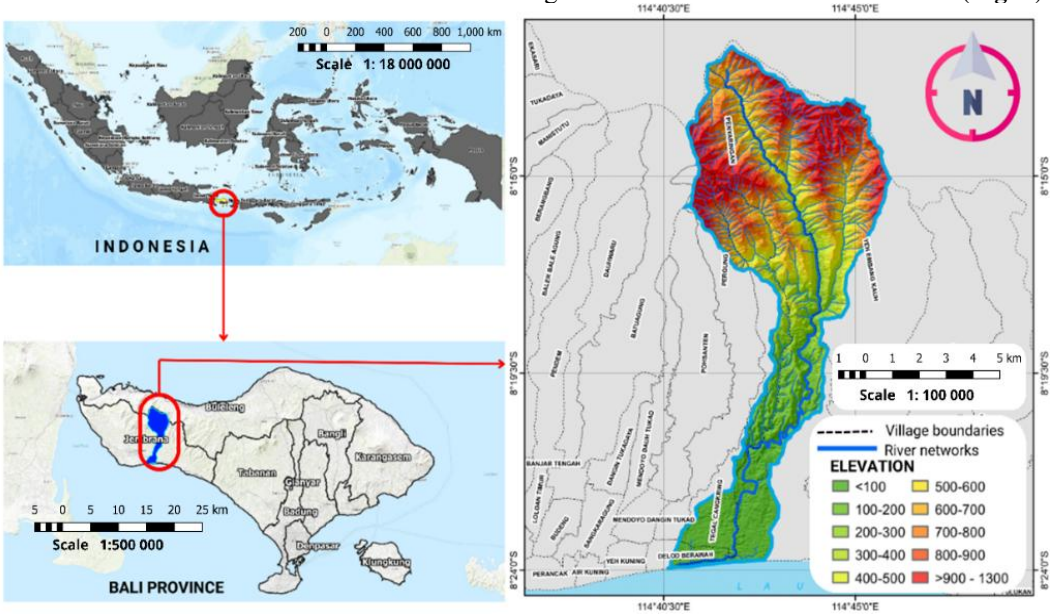


Fig. 1. Geographical location of the catastrophic flash flood event in Bali, Indonesia.

Based on the geomorphological map produced by Suyarto and Wiyanti (2023), the landscape is predominantly volcanic. Mid-slope volcanic terrain accounts for 69.06% of the total area, while additional volcanic landforms include upper volcanic slopes (8.98%), lower volcanic slopes (8.91%), and volcanic footslopes (2.18%). In the downstream section of the watershed, coastal landforms are present, consisting of fluviomarine plains (9.83%) and alluvial plains (2.03%).

Elevation across the watershed ranges from 0 to 1,318 meters above sea level (masl). The majority of the area (67.15%) lies above 500 masl, followed by 16.31% within the 0–100 masl range, and 12.54% between 100–500 masl. This geomorphological heterogeneity, encompassing both volcanic and coastal landforms, contributes significantly to variations in surface runoff, sediment transport, and erosion potential. These conditions establish the Biluk Poh Watershed as a highly suitable site for detailed spatial erosion analysis and for understanding upstream-to-downstream sediment dynamics.

3. METHOD

3.1. Data Sources

This study employed an integrated approach combining remote sensing datasets and field-based soil data to quantify erosion hazards in the watershed. All datasets represent conditions for the year 2022, corresponding to the period in which the major flash flood occurred on 16 October 2022.

Data preprocessing and spatial analysis were performed using Google Earth Engine (GEE), a cloud-based platform for geospatial computation widely adopted for environmental monitoring (Gorelick et al., 2017). Rainfall data were sourced from the Climate Hazards Center InfraRed Precipitation with Station data (CHIRPS), while vegetation indices, land use classification, and topographic data were extracted from Sentinel-2 MSI Level-2A imagery and ALOS PALSAR digital elevation models (DEM). Soil texture, structure, permeability, and organic matter were determined through field sampling and laboratory analysis carried out in 2022. This multi-source data integration enabled robust spatial modeling of soil erosion factors with high accuracy. **Table 1** provides a summary of each dataset and its application in USLE parameter estimation.

Table 1.

Summary of data sources and their uses in soil erosion calculations.

No.	Data	Data Sources	Data Use
1	Daily rainfall during 2022	Climate Hazards Center InfraRed Precipitation with Station data (CHIRPS) analyse by Google Earth Engine (GEE), https://developers.google.com/earth-engine/datasets/catalog/UCSB-CHG_CHIRPS_DAILY	To analyse the rainfall erosivity (*R*) factor
2	Soil properties i.e., (structure, texture, permeability and organic matter)	Field observation and soil laboratory analyst in 2022	To analyse the soil erodibility (*K*) factor
3	Perpendicular Vegetation Index (PVI) and Normalized Difference Senescent Vegetation Index (NDSVI)	Sentinel-2 MSI Level-2A analyse by GEE https://developers.google.com/earth-engine/datasets/catalog/COPERNICUS_S2_SR_HARMONIZED , acquired in 2022	To analyse the vegetation cover (*C*) factor
4	Land use map		To analyse the support practices (*P*) factor
5	Topography	ALOS PALSAR – Radiometric Terrain Correction DEM (12.5 m) free access https://asf.alaska.edu/	To analyse Slope length and steepness factor (*LS*)

3.2. Soil Sampling and Laboratory Analysis

To analyse the soil erodibility (K) factor, soil properties were determined through a combination of field sampling and laboratory analysis. The watershed was stratified into representative land units, and a composite sampling strategy was employed. Within each land unit, five sub-samples were collected from a depth of 0-60 cm. This depth was selected because the areas represent dry land dominated by annual plants, and this layer encompasses the primary rooting zone relevant to soil stability and nutrient cycling. These sub-samples were then thoroughly homogenized to create a single composite sample, ensuring it was representative of the unit.

This process yielded a total of 18 composite samples, each weighing approximately 1 kg. These samples were placed in sealed bags for transport and analysis. Several parameters were measured. Soil structure was determined by visual observation in the field at each sampling site. Soil permeability was measured using undisturbed soil cores collected with a sample ring. In the laboratory, the composite samples were first air-dried. The soil organic matter content was then quantified using the (Walkley & Black, 1934) method. Finally, soil texture was analysed to determine the percentage of sand, silt, and clay, as well as the specific very fine sand (0.1–0.05 mm) and finer silt fractions (0.05–0.02 mm) required by the erodibility equation.

3.3. Soil Erosion Calculations

The Universal Soil Loss Equation (USLE), developed by (W. H. Wischmeier & Smith, 1965) and refined in 1978 (Wischmeier & Smith, 1978), is widely recognized for estimating long-term average annual soil erosion. It enables assessment of erosion risk across landscapes by integrating climatic, topographic, vegetative, and management factors. The general form of the equation is expressed as:

$$\boldsymbol{A = R \times K \times LS \times C \times P} \quad (1)$$

where: A is the estimated soil loss (t ha^{-1} yr^{-1}), R represents the rainfall erosivity factor (MJ mm ha^{-1} h^{-1} yr^{-1}), K is the soil erodibility factor (t ha^{-1} MJ^{-1} mm^{-1}), LS denotes the slope length and steepness factor (dimensionless), C is the cover-management factor (dimensionless), and P is the erosion control practice factor (dimensionless).

a. Rainfall erosivity factor (R)

Rainfall erosivity (R) quantifies the potential of rainfall to detach and transport soil particles. Because continuous, high-resolution precipitation data required for direct EI_{30} calculation are often unavailable in many regions, an empirical model must be used. We calculated the monthly rainfall erosivity using the equation proposed by (Bols, 1978), which is specifically adapted for tropical climates using more readily available meteorological station data (Eq. 2):

$$EI_{30} = 6.119(\mathrm{RAIN})^{1.21} \times (\mathrm{DAYS})^{-0.47} \times (\mathrm{MAXP})^{0.53} \quad (2)$$

EI_{30} represents the monthly rainfall erosivity, $RAIN$ is the average monthly rainfall (cm), $DAYS$ refers to the average number of rainy days in a month, and $MAXP$ denotes the maximum rainfall on a single day within the month (cm). The spatial output was interpolated via kriging to produce a 10 m resolution raster of R values.

b. Soil erodibility factor (K)

The soil erodibility factor (K) measures the inherent susceptibility of a soil to erosion caused by rainfall and surface runoff. It is an integrated measure of how soil properties, such as texture, structure, and composition, collectively resist detachment and transport. The K value was calculated using the following (Eq. 3), which empirically links these key soil properties:

$$100K = 1.292\ [2.1M^{1.14}(10^{-4})(12 - a) + 3.25(b - 2) + 2.5(c - 3)] \quad (3)$$

where: K is the soil erodibility value (t ha^{-1} MJ^{-1} mm^{-1}), M is the percentage of very fine sand (0.1–0.05 mm) and finer fractions (0.05–0.02 mm) multiplied by (100 – the percentage of clay), a is the percentage of organic matter, b is the soil structure code, and c is the soil profile permeability class. Soil data were derived from laboratory tests of samples collected in representative land units.

c. Slope length and steepness factor (LS)

The topographic factor (LS) is calculated as the ratio of soil erosion from a given slope length and steepness to erosion from a standard reference slope. This factor combines two crucial topographic influences: slope length (L), which determines the cumulative volume and velocity of runoff, and slope steepness (S), which primarily controls runoff velocity and the gravitational force acting on soil particles. We calculated the LS factor using the (Eq. 4) proposed by (Moore & Burch, 1986), an approach based on unit stream power theory that is well-suited for distributed modeling with Digital Elevation Models (DEMs).

$$LS = \left(\frac{\text{Flow accumulation} \times \text{Cell size}}{22.13} \right)^{0.4} \times \left(\frac{\sin(\text{Slope})}{0.0896} \right)^{1.3} \quad (4)$$

Topographic inputs (specifically flow accumulation and slope gradient, which are required for Eq. 4) were derived from ALOS PALSAR DEM at 12.5 m resolution, resampled to match the final 10 m analysis grid.

d. Vegetation cover and crop management factor (C)

The C factor represents the ratio of soil erosion from a specific vegetation cover and land management practice to erosion from a continuous bare soil condition. It quantifies the protective effects of vegetation, which include intercepting rainfall, reducing runoff velocity, and binding soil with roots. Because direct field measurements of C are impractical over large areas, we used a remote sensing-based approach to capture the spatial and temporal dynamics of vegetation cover. The C factor was calculated using the algorithm (Eq. 5) developed by (Feng et al., 2018):

$$C = \big(0.681 - (0.523 \times PVI)\big) - (1.255 \times NDSVI) \quad (5)$$

where: PVI is perpendicular vegetation index (Feng et al., 2018; Richardson & Wiegand, 1977). This index is sensitive to the amount of green (photosynthetically active) vegetation, which provides the primary canopy cover against raindrop impact. NDSVI is normalized difference senescent vegetation index (Qi et al., 2002). This index was included to account for the protective cover provided by non-photosynthetic vegetation, such as dry grass or crop residues, which also contribute to soil protection. The formulas for calculating PVI (Eq. 6) and NDSVI (Eq. 7) using Sentinel-2A bands are:

$$PVI = \frac{NIR - (1.088 \times Red) - 0.056}{\sqrt{1.088^2 + 1}} \quad (6)$$

$$NDSVI = \frac{SWIR\ 1 - Red}{SWIR\ 1 + Red} \quad (7)$$

e. Erosion control practice factor (P)

The P factor accounts for the effectiveness of specific conservation practices (such as terracing or contour farming) in reducing runoff and soil loss compared to cultivation without such practices. It is a critical factor that represents the direct human intervention on the landscape to mitigate erosion.

It modifies the erosion potential by altering runoff pathways, slowing water velocity, and trapping sediment. The P factor ranges between 0 (indicating excellent, highly effective erosion control) and 1 (indicating no conservation practice). To account for the combination of different practices found in tropical agricultural landscapes, the P factor was estimated based on the approach proposed by As-syakur et al. (2022), (Eq. 8)

$$P = P_C \times P_T \times P_{CT} \quad (8)$$

where: P_C is the contour farming factor, P_T and P_{CT} are sub-factors for terracing and strip cropping, respectively. The values for these sub-factors depend on land use and slope class. Detailed values can be found in the study by (Adnyana et al., 2024).

To spatially assign the P factor values, we first developed a classification of land management techniques. This classification was based on integrating the land use/land cover map (also used for the C factor) with the slope steepness map (derived from the DEM). A specific value for each sub-factor (P_C, P_T, and P_{CT}) was then assigned to every pixel in the study area using a lookup table. This table links specific land use types (e.g., 'rice paddy', 'mixed agriculture', 'forest') and slope gradient classes (e.g., '0-3%', '3-8%') to a corresponding conservation practice value. For instance, agricultural areas on steep slopes known to be terraced were assigned a low P_T value, while agricultural areas on gentle slopes were evaluated for contour farming (P_C). Following this classification, any land use class identified as having no conservation practices (such as bare land or unmanaged shrubland) was assigned a P value of 1, representing the absence of erosion control.The specific values for each sub-factor (P_C, P_T, and P_{CT}) based on this land use and slope classification were adopted from the detailed tables established for tropical regions in the study by (Adnyana et al., 2024). Finally, the sub-factor rasters were multiplied together (as per Eq. 8) to generate the final P factor map.

3.4. Soil erosion classification

The final step in the analysis was to translate the quantitative soil erosion rates (measured in t/ha/year) into a qualitative hazard assessment. This was achieved by categorizing the final computed soil loss values, which represent the spatial output of the combined R, K, LS, C, and P factors, into five distinct classes. These classification thresholds are not universal; they were specifically based on benchmarks established in prior research conducted in tropical regions (Adnyana et al., 2024; Almagro et al., 2019), making them relevant to the study area's environmental conditions.

The classification is as follows: very light erosion (<1 t/ha/year), light erosion (1–5 t/ha/year), moderate erosion (>5–10 t/ha/year), heavy erosion (>10–50 t/ha/year), and very heavy erosion (>50 t/ha/year). This reclassification process transforms the continuous numerical data into a discrete hazard map. These categories provide a clear and actionable framework for identifying erosion hotspots and prioritizing conservation efforts. The final computed erosion rates and the resulting classified map were standardized to the Universal Transverse Mercator (UTM) Zone 50S projection and represented in a raster format with a spatial resolution of 10 meters. This high-resolution format was maintained throughout the analysis to allow for detailed spatial analysis, enhancing the precision of the final erosion hazard assessment.

3.5. Approach for Mitigation Strategy Identification

It is important to clarify that this study's primary methodological objective was the high-resolution spatial identification of erosion hotspots. This focus was chosen because these are the principal sources of sediment that cause blockage of the main river channel and subsequently drive flash flood events in the Biluk Poh Watershed. By identifying the source of the sediment (the erosion hotspots), our mitigation recommendations are inherently designed to address the root cause of the

river channel blockage and, consequently, the flash flood risk. The research did not involve the field implementation or testing of new conservation structures.

Therefore, the mitigation strategies presented in the discussion section of this paper were identified through a descriptive approach. Following the classification of erosion hazards (as described in section f), we conducted a targeted literature review. This review focused on identifying established soil and water conservation techniques (both vegetative and mechanical) that are effective in not only reducing on-site soil loss but also in trapping sediment and reducing peak runoff, which are the two key processes linking upstream erosion to downstream flooding. Our recommendations are thus based on this synthesis of previous research, specifically targeting interventions suitable for areas classified with moderate to very heavy erosion levels, which correspond to the hotspots identified as the primary contributors to the watershed's sediment load and flood vulnerability.

4. RESULTS

4.1. Rainfall erosivity factor (R)

The rainfall erosivity factor (R) was calculated using CHIRPS satellite precipitation data, extracted from 16 pixels distributed across the watershed (**Fig. 2**). To generate a continuous 10 m resolution raster, the data were interpolated using the kriging method in ArcGIS. The resulting R values ranged from 1,296 to 1,776 MJ mm ha^{-1} h^{-1} yr^{-1} (**Fig. 3**). Spatially, higher erosivity values were concentrated in the upstream region, while the downstream area exhibited lower values. This gradient reflects differences in total annual precipitation, the number of rainy days, and maximum daily rainfall intensity.

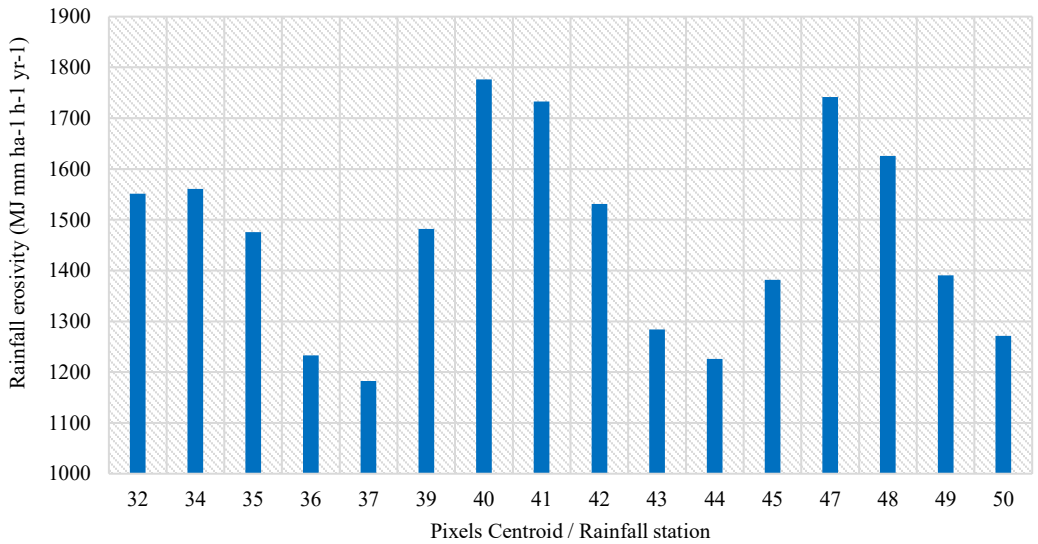


Fig. 2. CHIRPS-derived R factor values from sampled pixels in the study area.

These findings are consistent with (Nikolova et al., 2024), who reported that watersheds with high rainfall erosivity, coupled with poor land management, face elevated erosion risks. Similarly, previous researchers state that linked extreme erosivity patterns in Southeast Asia to climate anomalies such as ENSO, which influence rainfall regimes and storm intensity in tropical regions (Adnyana et al., 2024; Adnyana et al., 2025). The upper portions of the Biluk Poh Watershed thus represent critical erosion-prone zones due to their combined climatic and topographic conditions.

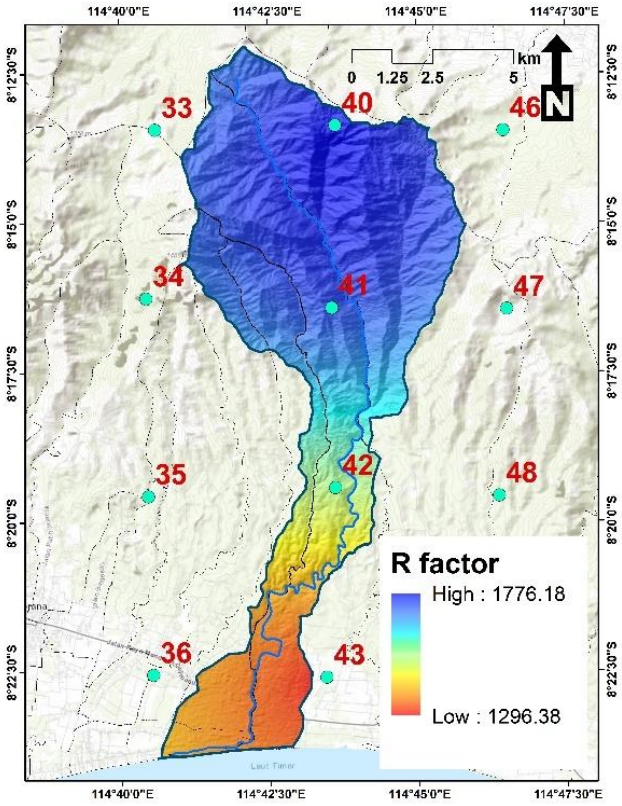


Fig. 3. Interpolated spatial distribution of the R factor across the watershed.

4.2 Soil erodibility factor (K)

The soil erodibility factor (K) quantifies the intrinsic vulnerability of soil to erosion, based on physical and chemical characteristics such as texture, structure, organic matter, and permeability (Renard et al., 2023). K values in the Biluk Poh Watershed ranged from 0.14 to 0.48 t ha h MJ^{-1} mm^{-1}. The most dominant category was moderately high erodibility, covering 70.01% of the area (**Fig. 4**). Spatial analysis indicated that higher K values occurred in the midstream to upstream regions, whereas lower values were found in the flatter, downstream zones (**Fig. 5a**).

These elevated K values were primarily associated with dryland farming and mixed forest systems underlain by Latosol and Litosol soil types. These soils often exhibit poor aggregation, low organic matter, and fine textures that are highly susceptible to detachment. Lal (2001) emphasized that soils with weak structure and poor infiltration capacity are especially prone to erosion under intense rainfall. Previous researchers demonstrated the protective role of vegetation in reducing erodibility by improving soil porosity and root cohesion (J. Liu et al., 2019).

4.3. Slope length and steepness factor (LS)

The LS factor is a dimensionless index that quantifies the combined effect of slope length and slope gradient on erosion potential, relative to a standard reference plot. The resulting LS index values for the Biluk Poh Watershed, which ranged from 0 to 45, were grouped into five classes to map the spatial distribution of topographic vulnerability (**Fig. 5b**).

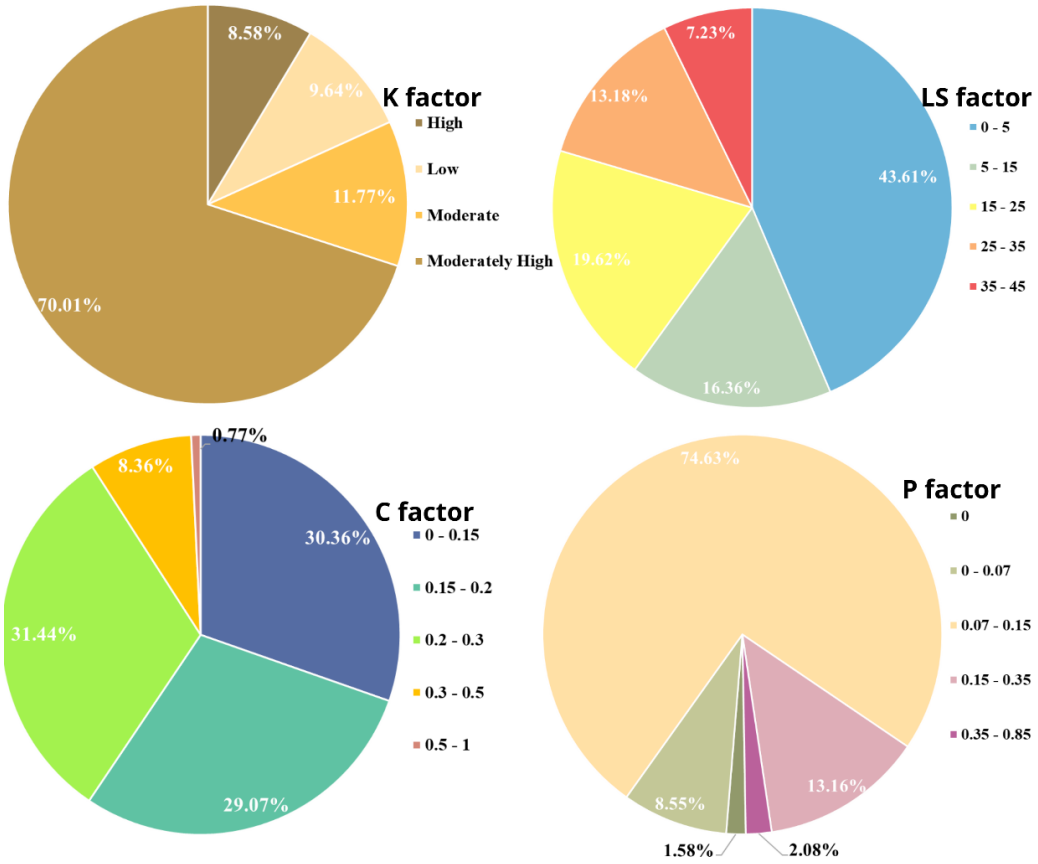


Fig. 4. Percentage Diagram of area coverage for each erosion factor (K, LS, C, and P).

The 0–5 class, representing the lowest topographic vulnerability, dominates 43.61% of the area (**Fig. 4**), corresponding to the flat, downstream alluvial plains. Conversely, the higher-value classes (e.g., 25-35 and 35-45) are concentrated in the upstream regions. In these areas, the high LS values indicate that the combination of steep slopes and long flow paths significantly increases runoff energy and reduces infiltration time, thereby enhancing soil detachment rates. This is in line with findings by (Chaplot & Le Bissonnais, 2003), who showed that slope-induced kinetic energy is a major driver of surface erosion. As stressed by Hou et al. (2021), these upstream regions with the highest LS values are particularly vulnerable and require slope-based conservation interventions such as contour terracing, vegetation reinforcement, and slope stabilization.

4.4. Vegetation Cover and Management Factor (C)

The C factor reflects the effectiveness of vegetation in protecting soil from raindrop impact and surface runoff (Ayalew et al., 2020; Karaburun, 2010). It was calculated using Sentinel-2 imagery, specifically the Perpendicular Vegetation Index (PVI) and Normalized Difference Senescent Vegetation Index (NDSVI), which distinguish between healthy and degraded vegetation. C values ranged from 0 to 1. The watershed was classified into five categories based on C values (**Fig. 5c**). The largest portion of the watershed (31.44%) fell within the 0.2–0.3 class, followed closely by the 0–0.15 class (30.36%) and the 0.15–0.2 class (29.07%). These areas represent moderate to dense vegetation cover with relatively low erosion potential. Conversely, higher C values in the 0.3–0.5 range covered 8.36% of the area, while the highest values (0.5–1) comprised 0.77% (**Fig. 4**).

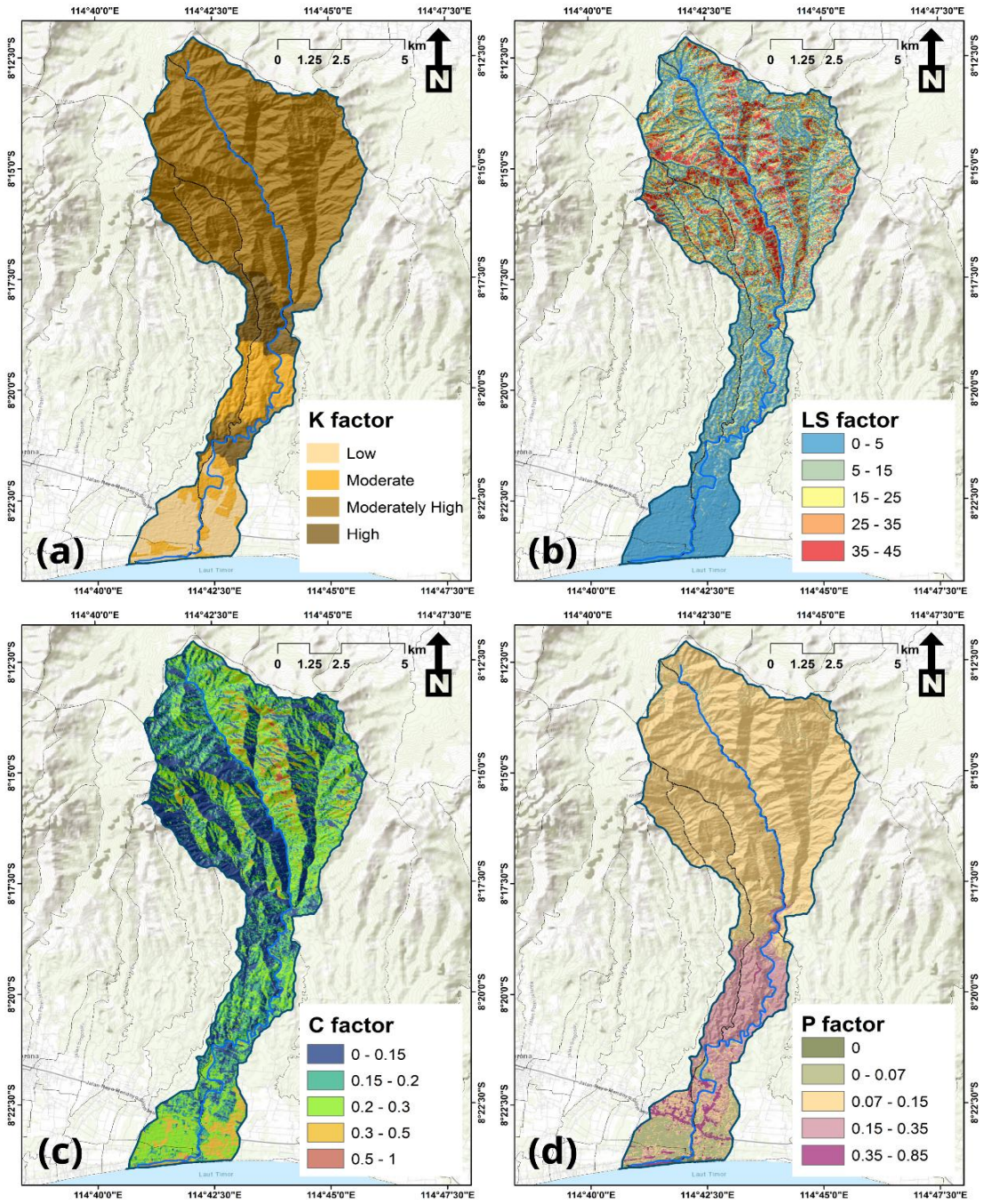


Fig. 5. Spatial distribution of K factor (a), LS factor (b), C factor (c), and P factor (d).

Spatially, a critical finding is the concentration of higher C values (0.3–1) in the upper part of the watershed. These zones, which collectively cover just over 9% of the area, spatially correlate with areas where both dense forest vegetation and annual agriculture are relatively sparse (**Fig. 5c**). This lack of protective cover in the upstream regions is a significant finding, as it leaves soil exposed to raindrop impact and facilitates higher runoff velocities, directly influencing the erosion hotspots

identified in the watershed. These results reinforce previous findings by (Alexakis et al., 2021; Biddoccu et al., 2020), who noted that strong vegetative cover enhances infiltration, binds soil aggregates, and reduces runoff. Targeted reforestation, agroforestry integration, and riparian vegetation rehabilitation in high-C value zones would significantly mitigate erosion vulnerability.

4.5. Conservation practices factor (P)

The conservation practices factor (*P*) represents the extent to which conservation measures reduce soil erosion risk, including techniques such as terracing, conservation tillage, and vegetative cover (Ebabu et al., 2022). Based on the analysis, the P factor values in the Biluk Poh Watershed ranged from 0 to 0.85, with high values spatially dominant in the midstream area of the watershed (**Fig. 5d**). The land area proportions revealed that the most prevalent *P* factor category was 0.07–0.15, covering 74.63% of the total study area, followed by the 0.15–0.35 category, which accounted for 13.16% (**Fig. 4**). High P factor values indicate areas with minimal adoption of conservation practices, particularly on steep slopes. Conversely, areas with low P factor values reflect effective conservation measures, such as the implementation of terracing and vegetative cover. Negese et al. (2021) emphasized the importance of soil conservation practices in reducing erosion, especially on land with steep slopes. Similarly, Panagos et al. (2015) demonstrated that the application of appropriate conservation techniques can reduce erosion risks by up to 70%. The implementing strategies such as terracing and vegetative rehabilitation significantly decreases erosion rates in vulnerable areas (Dharmawan et al., 2023; Nugroho et al., 2022).

4.6. Soil erosion hotspot

Soil erosion remains one of the most critical land degradation processes threatening agricultural productivity, ecological stability, and the long-term sustainability of tropical watersheds. In the Biluk Poh Watershed, high-resolution spatial modeling using remote sensing data, field observations, and laboratory analyses revealed significant variation in annual erosion rates, ranging from 0 to 4664.78 t ha^{-1} yr^{-1}, with an average rate of 168.03 t ha^{-1} yr^{-1}. This heterogeneity reflects the combined influence of rainfall erosivity, topographic steepness, land cover dynamics, and land management practices, as also noted in Mediterranean and tropical landscapes (Panagos et al., 2015). Erosion classification revealed that Slight erosion (0–15 t ha^{-1} yr^{-1}) dominated the watershed, covering 39.30% of the area. This was followed by the Heavy class (180–480 t ha^{-1} yr^{-1}) at 29.42%, the Moderate class (60–180 t ha^{-1} yr^{-1}) at 18.56%, the Very Heavy class (>480 t ha^{-1} yr^{-1}) at 7.99%, and the Light class (15–60 t ha^{-1} yr^{-1}) covering 0.73% (**Fig. 6**), underscoring the spatial complexity of erosion processes.

While the Very Heavy erosion category constitutes a relatively small portion of the total area at 7.99%, it represents a critical baseline finding due to its spatial distribution. The highest erosion intensities were concentrated in the midstream to upstream regions, particularly along steep slopes and fluvial corridors that exhibited both high LS values and low vegetation cover. These zones, depicted in orange to red on the erosion map (**Fig. 7**), are characterized by accelerated overland flow and sediment detachment during periods of intense rainfall. The strategic location of these hotspots means that eroded material can be delivered directly into the main river, posing a significant risk of blockage. The October 2022 flash flood event exemplified how this upstream erosion hotspots can rapidly deliver sediment into the main river channel, resulting in reduced discharge capacity and triggering downstream inundation. At the village scale, the erosion hazard was most acute in Penyaringan and Yeh Embang Kauh, with 11.95% and 13.39% of their land areas, respectively, falling within the heavy erosion class (**Fig. 6**). These areas share common characteristics, including steep terrain, weakly aggregated soils, and minimal conservation infrastructure, making them high-priority zones for erosion mitigation. The erosion hazard maps highlight these critical microzones, emphasizing the need for site-specific interventions such as slope stabilization, vegetative ground cover, and improved runoff diversion and drainage systems.

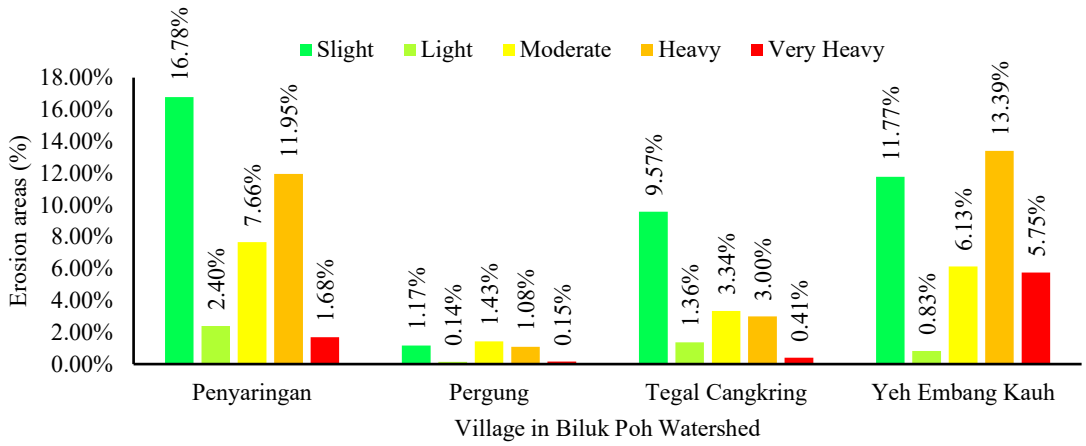


Fig. 6. Village areas surrounding the watershed based on the extent of erosion hazard levels.

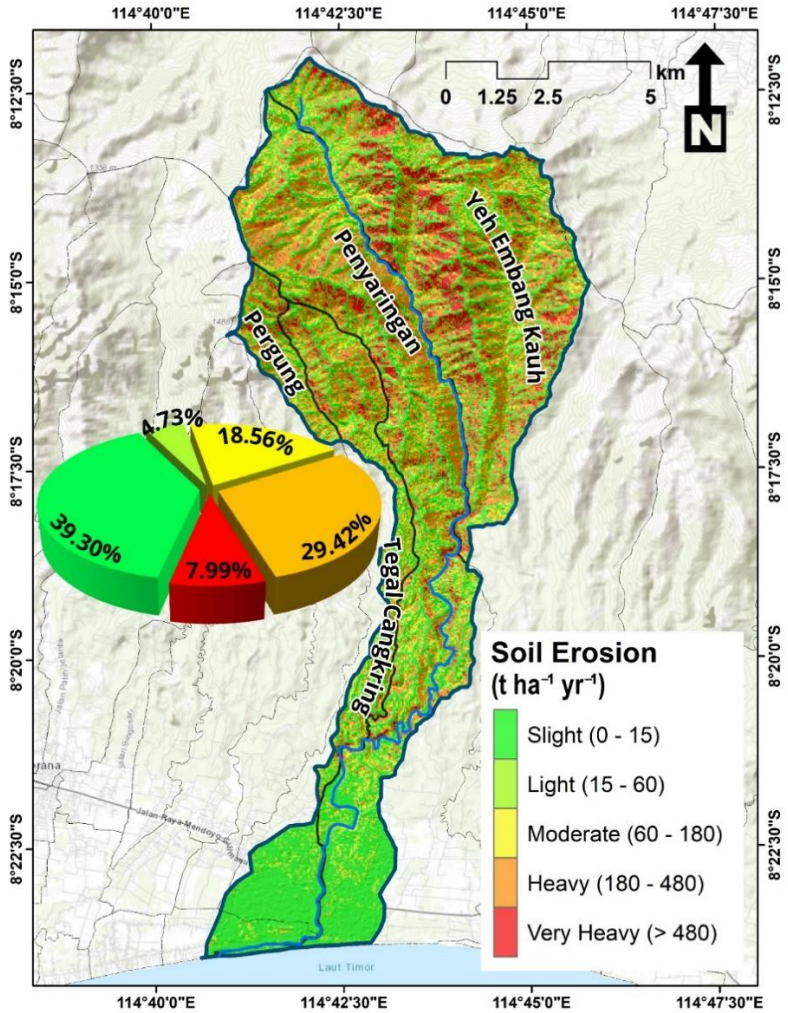


Fig. 7. Spatial distribution of soil erosion hazard along with area percentages.

5. DISCUSSION

Evidence from surrounding regions in Bali corroborates the patterns observed in Biluk Poh. Trigunasih & Saifulloh (2023) documented erosion rates ranging from 20.17 to 995.48 t ha^{-1} yr^{-1} in nearby watersheds, while (Trigunasih et al., 2018; Trigunasih & Saifulloh, 2022) reported rates between 0.32 and 1,535.34 t ha^{-1} yr^{-1} in the Penet Watershed. These findings underscore the influence of terrain morphology and anthropogenic land use on spatial erosion risk. Additionally, (Diara et al., 2022, 2023; Suyarto et al., 2023) emphasized that the Baturiti Highlands and adjacent uplands face dual threats from erosion and shallow landslides due to deforestation on steep volcanic slopes.

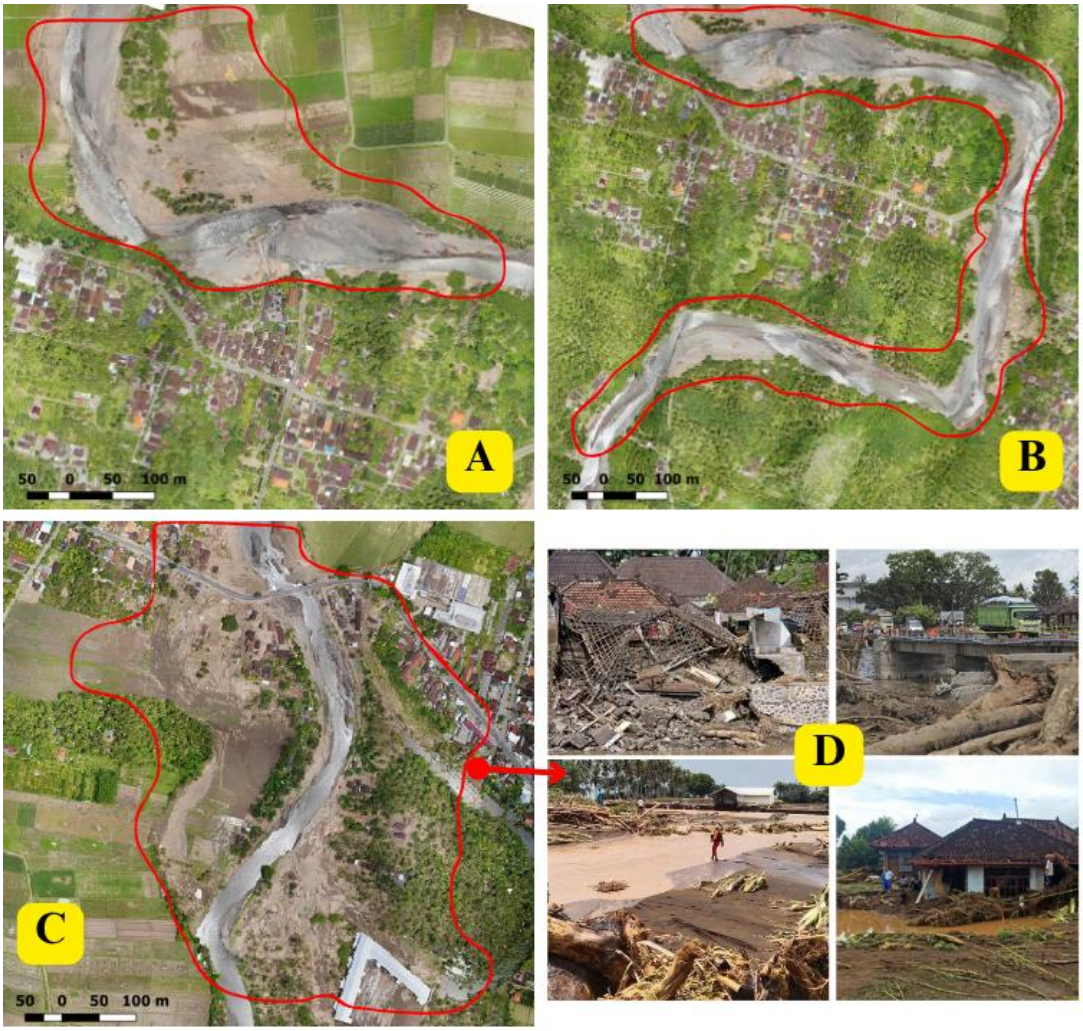


Fig. 8. Aerial and ground views of erosion-affected areas and flash flood damage in the Biluk Poh Watershed. (A-C) Sediment accumulation and slope failure in downstream and midstream zones. (D) Infrastructure damage and debris after the 16 October 2022 flood.

From a soil perspective, Bali's dominant Entisols are particularly vulnerable to erosion due to their sandy texture and low aggregate stability (Araújo Filho et al., 2021; G. Liu et al., 2009). This vulnerability is supported by findings in the Telagawaja Sub-Watershed, where (Soniari et al., 2024) reported moderate to high erodibility (K) values. The consequences of this susceptibility extend

beyond physical degradation; studies have confirmed that erosion results in significant nutrient depletion especially nitrogen, phosphorus, and soil organic carbon thereby undermining long-term soil fertility (Kartini et al., 2023, 2024; Trigunasih et al., 2023).

This study contributes to the field by applying a 10-meter resolution raster-based erosion model, enabling fine-scale detection of erosion-prone microzones. In contrast to conventional methods that rely on homogeneous land units, this pixel-based approach captures detailed spatial variability, which is essential for managing complex landscapes like Biluk Poh, where topographic and land-use changes occur over short distances.

The watershed's geomorphological characteristics further intensify its susceptibility to hydrological extremes (Soniari et al., 2024). Its radial drainage pattern, consisting of multiple upstream tributaries converging into a single outlet, creates a discharge bottleneck during high rainfall events. In October 2022, rainfall increased by 79.78% from the previous month, with several days exceeding critical thresholds. This surge led to rapid runoff and widespread soil detachment in slope-dominant regions. The C factor analysis confirmed substantial degradation of vegetative cover in these zones, weakening the land's capacity to intercept rainfall and retain soil particles (J. Liu et al., 2019). UAV imagery from post-flood assessments (**Fig. 8A-C)** revealed bare hillslopes, riverbank collapse, and sediment deposition in key river sections (**Fig. 8D**), corroborating the spatial accuracy of the modeled erosion data. These observations affirm that soil erosion not only degrades land productivity but also acts as a precursor to flash flood disasters. Sediments mobilized from unstable upstream areas accumulated in constricted river segments, obstructing flow and intensifying flooding impacts. Field documentation revealed widespread damage to farmland, transportation infrastructure, and riverbanks, validating the sedimentation pathways identified in the erosion model.

A closer analysis of the spatial erosion map (**Fig. 7**) provides the quantitative basis for this sediment mobilization. The model revealed extreme erosion values reaching up to 4664.78 t ha^{-1} yr^{-1} in localized hotspots. More critically, the combined area of the Heavy (29.42%) and Very Heavy (7.99%) erosion classes covers 37.41% of the watershed. These high-risk zones are not randomly distributed; they form a contiguous network concentrated along the steep fluvial corridors and denuded slopes identified in the upstream and midstream regions. This specific geographic arrangement creates a highly efficient delivery system, funneling detached soil directly into the main river. This process of rapid, large-scale sediment loading is the primary driver of the channel blockages and reduced discharge capacity that were directly responsible for the 2022 flash flood event.

The broader relevance of these findings is underscored by the recent large-scale flooding in Bali during September 2025. This catastrophic event, which caused widespread damage to key tourism, industrial, and capital areas, was extensively documented by international media and humanitarian organizations (e.g., BBC Weather, 2025; ClimaMeter, 2025; DW News, 2025; IFRC, 2025; The Guardian, 2025). Preliminary reports indicate a familiar pattern: intense, sustained rainfall acting upon watersheds compromised by degraded upstream vegetation, leading to critical blockages in main river channels. While the 2025 disaster was compounded by urban drainage inadequacies, it demonstrates that the core mechanism of sediment-driven channel blockage, as modeled in Biluk Poh, is not an isolated issue but a primary, recurrent, and escalating threat to the entire region. This context lends a new and critical urgency to implementing the mitigation strategies proposed in this paper.

Conservation strategies in the Biluk Poh watershed must therefore address both physical land degradation and the associated loss of soil fertility to support a sustainable agroecosystem (Bhayunagiri & Saifulloh, 2022; Kartini et al., 2023, 2024; Susila et al., 2024). This is critical, as soil erosion leads to the significant depletion of key agricultural nutrients, including nitrogen, phosphorus, and soil organic carbon (Trigunasih et al., 2023). This nutrient depletion directly threatens crop yields, necessitating interventions that protect both the environment and agricultural livelihoods. In this context, the study's application of multi-temporal Sentinel-2 imagery proved highly effective. By enabling a detailed calculation of the C factor, the Sentinel-2 data was instrumental in identifying the specific erosion hotspots where poor or degraded vegetation cover corresponds with high soil loss risk. This methodological approach, which connects the dynamic state of vegetation directly to soil

protection, provides the precise spatial information needed for implementing targeted, climate-smart land management (Plybour et al., 2025; Laosuwan et al., 2025) in the vulnerable microzones of Biluk Poh.

Mitigation of these hazards requires a holistic watershed management approach. Based on the erosion hazard map developed in this study, a clear prioritization of these efforts is possible. Interventions must be focused on the most impacted zones. These were identified as the moderate erosion class (covering 18.56% of the area), the heavy erosion class (affecting 29.42%), and the very heavy erosion class (covering 7.99%). Cumulatively, the moderate and heavy classes represent the most widespread threat, covering a combined 47.98% of the watershed. These areas, combined with the substantial and highly intense very heavy hotspots (7.99%), function as the primary sediment sources for the entire watershed. Treating them is the most direct way to prevent the river channel blockage that causes flash floods.

For the most severe hotspots, particularly the very heavy class and the steepest slopes within the heavy erosion class, reforestation using native deep-rooted species such as *Samanea saman* and *Cassia siamea* is recommended. This provides slope stability at the source, preventing the initial soil detachment (Escalante & Messa, 2023; Maridi et al., 2015). Simultaneously, riparian zones bordering all critical sediment-source areas should be reinforced with *Bambusa* spp. and *Chrysopogon zizanioides* (vetiver grass). This acts as a 'last line of defense' to trap sediment that does mobilize and keep it from reaching the main river channel, thereby reducing bank erosion and sediment accumulation downstream.

For the widespread moderate and heavy erosion areas, which often overlap with agricultural land, a combination of agroforestry and structural measures is essential. Agroforestry systems (60-70% native trees, 30-40% crops) are recommended for 25-45% slopes to balance ecological function and economic productivity (Budiastuti et al., 2020; Kaur et al., 2023). Additionally, contour terracing and vegetative ground cover are crucial. These practices work by slowing runoff velocity, which dramatically reduces the water's power to carry sediment, and by enhancing infiltration, which reduces the total volume of surface runoff that causes the river to swell (Fajeriana et al., 2024).

The integration of high-resolution remote sensing, erosion modeling, and field validation has revealed the spatial extent and severity of erosion across the Biluk Poh Watershed. These findings offer a critical evidence base for implementing these spatially targeted, ecologically sound conservation strategies. By prioritizing interventions in the identified moderate, heavy, and very heavy erosion hotspots, stakeholders can systematically reduce sediment loads at their source and, in turn, enhance watershed resilience and mitigate the long-term risks associated with sediment-driven flash flood events.

6. CONCLUSIONS

The catastrophic flash flood of October 16, 2022, was triggered by intense rainfall, but its severity was critically exacerbated by widespread soil erosion within the Biluk Poh Watershed. This study provides the first rapid geospatial identification of the erosion hotspots that functioned as the principal spatial factors amplifying the disaster.

Our high-resolution analysis revealed that 55.97% of the watershed is susceptible to moderate (18.56%), heavy (29.42%), or very heavy (7.99%) erosion. These hotspots are concentrated in steep upstream and riparian landscapes characterized by high slope gradients, highly erodible soils, inadequate vegetative cover, and limited conservation practices. During the rainfall event, these vulnerable areas mobilized massive sediment loads, leading to the channel aggradation and blockage that worsened downstream flooding. The strong spatial correlation between our modeled hotspots and the flood-damaged areas, confirmed by post-flood UAV imagery, demonstrates that this uncontrolled erosion was a major contributor to the disaster's scale.

The findings from this study provide actionable insights for targeted mitigation. The identification of these erosion-prone microzones confirms the need for an integrated watershed-scale conservation strategy, prioritizing reforestation, agroforestry, and riparian buffers in the identified

risk zones. This research highlights the critical importance of incorporating soil erosion as an exacerbating factor in tropical flood risk management to build resilience against future sediment-driven disasters.

ACKNOWLEDGEMENTS

We sincerely thank the Fly for Humanity Movement for their generous support. Special appreciation is extended to Septian Firmansyah (Sky Volunteer/Synersia) for his key role in aerial data acquisition and to Dewa Putu A. M. from the SIAP SIAGA program (Australia–Indonesia Partnership for Disaster Risk Management) for his valuable assistance. We also gratefully acknowledge the Aviation Technology Research Center of the National Research and Innovation Agency (BRIN) for providing technical expertise and high-resolution aerial imagery, and the Bali Provincial Disaster Management Agency (BPBD Bali) for facilitating field operations and logistics.

FUNDING

This research was financially supported by Universitas Udayana through the DIPA PNBP Fiscal Year 2024 (Research Assignment Agreement No. B/255.614/UN14.4.A/PT.01.03/2024, dated 17 April 2024) and the DIPA PNBP Fiscal Year 2025 (Research Assignment Agreement No. B/229.51/UN14.4.A/PT.01.03/2025, dated 28 April 2025).

REFERENCES

Abu El-Magd, S. A., Orabi, H. O., Ali, S. A., Parvin, F., & Pham, Q. B. (2021). An integrated approach for evaluating the flash flood risk and potential erosion using the hydrologic indices and morpho-tectonic parameters. *Environmental Earth Sciences*, *80*(20). https://doi.org/10.1007/s12665-021-10013-0

Addy, S., & Wilkinson, M. E. (2021). Embankment lowering and natural self-recovery improves river-floodplain hydro-geomorphic connectivity of a gravel bed river. *Science of the Total Environment*, *770*. https://doi.org/10.1016/j.scitotenv.2020.144626

Adnyana, I. W. S., As-syakur, A. R., Suyarto, R., Sunarta, I. N., Nuarsa, I. W., Diara, I. W., Saifulloh, M., & Wiyanti. (2024). Geospatial Technology for Climate Change: Influence of ENSO and IOD on Soil Erosion. In *Technological Approaches for Climate Smart Agriculture* (pp. 249–275). Springer.

Ahrendt, S., Horner-Devine, A. R., Collins, B. D., Morgan, J. A., & Istanbulluoglu, E. (2022). Channel Conveyance Variability can Influence Flood Risk as Much as Streamflow Variability in Western Washington State. *Water Resources Research*, *58*(6). https://doi.org/10.1029/2021WR031890

Alexakis, D. D., Manoudakis, S., Agapiou, A., & Polykretis, C. (2021). Towards the assessment of soil-erosion-related c-factor on european scale using google earth engine and sentinel-2 images. *Remote Sensing*, *13*(24). https://doi.org/10.3390/rs13245019

Almagro, A., Thomé, T. C., Colman, C. B., Pereira, R. B., Marcato Junior, J., Rodrigues, D. B. B., & Oliveira, P. T. S. (2019). Improving cover and management factor (C-factor) estimation using remote sensing approaches for tropical regions. *International Soil and Water Conservation Research*, *7*(4). https://doi.org/10.1016/j.iswcr.2019.08.005

Ao, L., Wu, Y., Xu, Q., Zhou, Y., Chen, X., Liang, P., Fu, Z., & Chen, H. (2025). The Role of Bedrock Topography in the Runoff Process and Soil Erosion on Karst Steep Slopes. *Land Degradation & Development*, *36*(2), 533–544.

Araújo Filho, R. N., Holanda, F. S. R., Cunha Filho, M., Piscoya, V. C., MELO, J. D. E. O., & Guimarães, D. V. (2021). Relationship between physical and chemical properties of entisols-fluvents and erosion in the sao francisco river. *Revista Caatinga*, *34*(2), 422–431.

As-syakur, A. R., Adnyana, I. W. S., & Osawa, T. (2022). (2022). *Erosion prediction based on USLE*

method using remote sensing data and GIS in small scale watershed.

Ayalew, D. A., Deumlich, D., Šarapatka, B., & Doktor, D. (2020). Quantifying the sensitivity of NDVI-based C Factor Estimation and Potential Soil Erosion Prediction using Spaceborne Earth Observation Data. *Remote Sensing*, *12*(7). https://doi.org/10.3390/rs12071136

BBC Weather. (2025). Bali flash floods report. BBC News. https://www.bbc.com/weather/articles/cevzegvjw7jo

Bauer, M., Dostal, T., Krasa, J., Jachymova, B., David, V., Devaty, J., Strouhal, L., & Rosendorf, P. (2019). Risk to residents, infrastructure, and water bodies from flash floods and sediment transport. *Environmental Monitoring and Assessment*, *191*(2). https://doi.org/10.1007/s10661-019-7216-7

Bhayunagiri, I. B. P., & Saifulloh, M. (2022). Mapping of subak area boundaries and soil fertility for agricultural land conservation. *Geographia Technica*, *17*(2). https://doi.org/10.21163/GT_2022.172.17

Biddoccu, M., Guzmán, G., Capello, G., Thielke, T., Strauss, P., Winter, S., Zaller, J. G., Nicolai, A., Cluzeau, D., Popescu, D., Bunea, C., Hoble, A., Cavallo, E., & Gómez, J. A. (2020). Evaluation of soil erosion risk and identification of soil cover and management factor (C) for RUSLE in European vineyards with different soil management. *International Soil and Water Conservation Research*, *8*(4). https://doi.org/10.1016/j.iswcr.2020.07.003

Bols, P. L. (1978). The iso-erodent map of Java and Madura. *Soil Res. Inst. Bogor*.

Budiastuti, M. T. S., Purnomo, D., Hendro, H., Sudjianto, U., & Gunawan, B. (2020). Rehabilitation of critical land by Implementing complex agroforestry at the prioritized subwatersheds in the Muria Region. *Sains Tanah*, *17*(1). https://doi.org/10.20961/stjssa.v17i1.37704

Chaplot, V. A. M., & Le Bissonnais, Y. (2003). Runoff Features for Interrill Erosion at Different Rainfall Intensities, Slope Lengths, and Gradients in an Agricultural Loessial Hillslope. *Soil Science Society of America Journal*, *67*(3). https://doi.org/10.2136/sssaj2003.8440

Chen, X., Tian, S., Chen, N., Hu, G., Hou, R., & Peng, T. (2024). Why did localized extreme rainfall trigger a rare mega flash flood in the mountains of western China? *International Journal of Disaster Risk Reduction*, 105090.

ClimaMeter. (2025). Bali floods September 9-10, 2025. ClimaMeter. https://www.climameter.org/20250909-10-bali-floods

Dharmawan, I. W. S., Pratiwi, Siregar, C. A., Narendra, B. H., Undaharta, N. K. E., Sitepu, B. S., Sukmana, A., Wiratmoko, M. D. E., Abywijaya, I. K., & Sari, N. (2023). Implementation of Soil and Water Conservation in Indonesia and Its Impacts on Biodiversity, Hydrology, Soil Erosion and Microclimate. In *Applied Sciences (Switzerland)* (Vol. 13, Issue 13). https://doi.org/10.3390/app13137648

Diara, I. W., Suyarto, R., & Saifulloh, M. (2022). Spatial distribution of landslide susceptibility in new road construction Mengwitani-Singaraja, Bali-Indonesia: based on geospatial data. *International Journal of GEOMATE*, *23*(96). https://doi.org/10.21660/2022.96.3320

Diara, I. W., Wahyu Wiradharma, I. K. A., Suyarto, R., Wiyanti, W., & Saifulloh, M. (2023). Spatio-temporal of landslide potential in upstream areas, Bali tourism destinations: remote sensing and geographic information approach. *Journal of Degraded and Mining Lands Management*, *10*(4). https://doi.org/10.15243/jdmlm.2023.104.4769

Dou, X., Ma, X., Zhao, C., Li, J., Yan, Y., & Zhu, J. (2022). Risk assessment of soil erosion in Central Asia under global warming. *Catena*, *212*, 106056.

DW News. (2025). Indonesia: 19 dead after flash floods. Deutsche Welle. https://www.dw.com/en/indonesia-19-dead-after-flash-floods/a-73959609

Dzwairo, R., Singh, S. K., & Patel, A. (2025). Soil erosion susceptibility assessment through morphometric analysis and morphotectonic implications in Rietspruit sub-basin, South Africa. *Environment, Development and Sustainability*, *27*(7), 16503–16524.

Ebabu, K., Tsunekawa, A., Haregeweyn, N., Tsubo, M., Adgo, E., Fenta, A. A., Meshesha, D. T., Berihun, M. L., Sultan, D., Vanmaercke, M., Panagos, P., Borrelli, P., Langendoen, E. J., & Poesen, J. (2022). Global analysis of cover management and support practice factors that control soil erosion and conservation. In *International Soil and Water Conservation Research* (Vol. 10, Issue 2). https://doi.org/10.1016/j.iswcr.2021.12.002

Escalante, E. E., & Messa, H. F. (2023). Silvopastoral Systems with Native Tree Species in Venezuela. In *Silvopastoral systems of Meso America and Northern South America*. https://doi.org/10.1007/978-3-031-43063-3_12

Fajeriana, N., Ali, A., & Rini, R. P. (2024). Soil Tillage and Planting Along the Contour on Sloping Land to Minimize the Potential for Erosion and Surface Runoff. *Sarhad Journal of Agriculture*, *40*(1). https://doi.org/10.17582/journal.sja/2024/40.1.82.93

Feng, Q., Zhao, W., Ding, J., Fang, X., & Zhang, X. (2018). Estimation of the cover and management factor based on stratified coverage and remote sensing indices: a case study in the Loess Plateau of China. *Journal of Soils and Sediments*, *18*(3). https://doi.org/10.1007/s11368-017-1783-4

Gorelick, N., Hancher, M., Dixon, M., Ilyushchenko, S., Thau, D., & Moore, R. (2017). Google Earth Engine: Planetary-scale geospatial analysis for everyone. *Remote Sensing of Environment*, *202*. https://doi.org/10.1016/j.rse.2017.06.031

Gwapedza, D., Hughes, D. A., Slaughter, A. R., & Mantel, S. K. (2021). Temporal influences of vegetation cover (C) dynamism on MUSLE sediment yield estimates: NDVI evaluation. *Water*, *13*(19), 2707.

Hirabayashi, Y., Alifu, H., Yamazaki, D., Imada, Y., Shiogama, H., & Kimura, Y. (2021). Anthropogenic climate change has changed frequency of past flood during 2010-2013. *Progress in Earth and Planetary Science*, *8*(1). https://doi.org/10.1186/s40645-021-00431-w

Hou, T., Filley, T. R., Tong, Y., Abban, B., Singh, S., Papanicolaou, A. N. T., Wacha, K. M., Wilson, C. G., & Chaubey, I. (2021). Tillage-induced surface soil roughness controls the chemistry and physics of eroded particles at early erosion stage. *Soil and Tillage Research*, *207*. https://doi.org/10.1016/j.still.2020.104807

International Federation of Red Cross and Red Crescent Societies (IFRC). (2025). Field Report: Indonesia: Floods (17886). https://go.ifrc.org/field-reports/17886

Karaburun, A. (2010). Estimation of C factor for soil erosion modeling using NDVI in Buyukcekmece watershed. *Ozean Journal of Applied Sciences*, *3*(1).

Kardhana, H., Wijayasari, W., & Rohmat, F. I. W. (2024). Assessing basin-wide soil erosion in the Citarum watershed using USLE method. *Results in Engineering*, *22*, 102130.

Kartini, N. L., Saifulloh, M., Trigunasih, N. M., & Narka, I. W. (2023). Assessment of Soil Degradation Based on Soil Properties and Spatial Analysis in Dryland Farming. *Journal of Ecological Engineering*, *24*(4). https://doi.org/10.12911/22998993/161080

Kartini, N. L., Saifulloh, M., Trigunasih, N. M., Sukmawati, N. M. S., & Mega, I. (2024). Impact of Long-Term Continuous Cropping on Soil Nutrient Depletion. *Ecological Engineering & Environmental Technology (EEET)*, *25*(11).

Kaur, A., Paruchuri, R. G., Nayak, P., Devi, K. B., Upadhyay, L., Kumar, A., Pancholi, R., & Yousuf, M. (2023). The Role of Agroforestry in Soil Conservation and Sustainable Crop Production: A Comprehensive Review. *International Journal of Environment and Climate Change*, *13*(11). https://doi.org/10.9734/ijecc/2023/v13i113478

Lai, R., Li, J., Wang, P., Guo, Y., Xu, L., Zhang, X., Wang, M., & Zhang, X. (2024). Cumulative sedimentation hazard map of urban areas subject to hyperconcentrated flash flood: A case study of Suide County in the Wuding River basin, China. *Journal of Flood Risk Management*, e12996.

Lal, R. (2001). Soil degradation by erosion. *Land Degradation and Development*, *12*(6). https://doi.org/10.1002/ldr.472

Lamane, H., Mouhir, L., Zouahri, A., Baghdad, B., El Bilali, A., & Moussadek, R. (2025). Modeling soil erosion and sediment yield under climate change: a comparison of RUSLE and MUSLE integrated with SDR using variable soil data resolutions. *Modeling Earth Systems and Environment*, *11*(5), 1–29.

Liu, G., Li, L., Wu, L., Wang, G., Zhou, Z., & Du, S. (2009). Determination of soil loss tolerance of an entisol in Southwest China. *Soil Science Society of America Journal*, *73*(2), 412–417.

Liu, J., Zhang, X., & Zhou, Z. (2019). Quantifying effects of root systems of planted and natural vegetation on rill detachment and erodibility of a loessial soil. *Soil and Tillage Research*, *195*. https://doi.org/10.1016/j.still.2019.104420

Mahmood, S., Naeem, N., Ahamad, M. I., Tariq, Z., & Song, J. (2024). Spatial modeling of soil erosion potential

in the Panjkora Basin, Eastern Hindu Kush: integrated RUSLE and geospatial approaches. *Environment, Development and Sustainability*, 1–22.

Maridi, Agustina, P., & Saputra, A. (2015). Potential Vegetation for Soil and Water Conservation : Case Study in Samin Watershed , Central Java. *International Conference on Science, Technology and Humanit*, *December*.

Merten, J., Stiegler, C., Hennings, N., Purnama, E. S., Röll, A., Agusta, H., Dippold, M. A., Fehrmann, L., Gunawan, D., Hölscher, D., Knohl, A., Kückes, J., Otten, F., Zemp, D. C., & Faust, H. (2020). Flooding and land use change in Jambi Province, Sumatra: Integrating local knowledge and scientific inquiry. *Ecology and Society*, *25*(3). https://doi.org/10.5751/ES-11678-250314

Milazzo, F., Francksen, R. M., Zavattaro, L., Abdalla, M., Hejduk, S., Enri, S. R., Pittarello, M., Price, P. N., Schils, R. L. M., & Smith, P. (2023). The role of grassland for erosion and flood mitigation in Europe: A meta-analysis. *Agriculture, Ecosystems & Environment*, *348*, 108443.

Moore, I. D., & Burch, G. J. (1986). Physical Basis of the Length-slope Factor in the Universal Soil Loss Equation. *Soil Science Society of America Journal*, *50*(5). https://doi.org/10.2136/sssaj1986.03615995005000050042x

Negese, A., Fekadu, E., & Getnet, H. (2021). Potential Soil Loss Estimation and Erosion-Prone Area Prioritization Using RUSLE, GIS, and Remote Sensing in Chereti Watershed, Northeastern Ethiopia. *Air, Soil and Water Research*, *14*. https://doi.org/10.1177/1178622120985814

Nikolova, V., Nikolova, N., Stefanova, M., & Matev, S. (2024). Annual and Seasonal Characteristics of Rainfall Erosivity in the Eastern Rhodopes (Bulgaria). *Atmosphere*, *15*(3). https://doi.org/10.3390/atmos15030338

Nugroho, H. Y. S. H., Basuki, T. M., Pramono, I. B., Savitri, E., Purwanto, Indrawati, D. R., Wahyuningrum, N., Adi, R. N., Indrajaya, Y., Supangat, A. B., Putra, P. B., Auliyani, D., Priyanto, E., Yuwati, T. W., Pratiwi, Narendra, B. H., Sukmana, A., Handayani, W., Setiawan, O., & Nandini, R. (2022). Forty Years of Soil and Water Conservation Policy, Implementation, Research and Development in Indonesia: A Review. In *Sustainability (Switzerland)* (Vol. 14, Issue 5). https://doi.org/10.3390/su14052972

Okacha, A., & Salhi, A. (2024). Refining erosion assessment with NDVI-based modeling: a case study in diverse climatic zones. *Mediterranean Geoscience Reviews*, *6*(3), 219–232.

Othman, A., El-Saoud, W. A., Habeebullah, T., Shaaban, F., & Abotalib, A. Z. (2023). Risk assessment of flash flood and soil erosion impacts on electrical infrastructures in overcrowded mountainous urban areas under climate change. *Reliability Engineering and System Safety*, *236*. https://doi.org/10.1016/j.ress.2023.109302

Panagos, P., Borrelli, P., Meusburger, K., Alewell, C., Lugato, E., & Montanarella, L. (2015). Estimating the soil erosion cover-management factor at the European scale. *Land Use Policy*, *48*. https://doi.org/10.1016/j.landusepol.2015.05.021

Panagos, P., Matthews, F., Patault, E., De Michele, C., Quaranta, E., Bezak, N., Kaffas, K., Patro, E. R., Auel, C., & Schleiss, A. J. (2024). Understanding the cost of soil erosion: An assessment of the sediment removal costs from the reservoirs of the European Union. *Journal of Cleaner Production*, *434*, 140183.

Plybour, C., Uttaruk, Y., Jeefoo, P., Laosuwan, N., & Laosuwan, T. (2025). Spatial drought occurrence and distribution using data from Sentinel-2 satellite and vegetation indices. *Geographia Technica*, *20*(1).

Prasad, B., Tiwari, H. L., Garia, S., Dwivedi, V., & Mishra, K. (2024). A comparative study on the modeling of soil erosion by USLE, RUSLE, and USPED. *ISH Journal of Hydraulic Engineering*, *30*(4), 501–510.

Qi, J., Marsett, R., Heilman, P., Biedenbender, S., Moran, S., Goodrich, D., & Weltz, M. (2002). RANGES improves satellite-based information and land cover assessments in Southwest United States. *Eos*, *83*(51). https://doi.org/10.1029/2002EO000411

Rashmi, I., Karthika, K. S., Roy, T., Shinoji, K. C., Kumawat, A., Kala, S., & Pal, R. (2022). Soil Erosion and Sediments: A Source of Contamination and Impact on Agriculture Productivity. In *Agrochemicals in Soil and Environment: Impacts and Remediation*. https://doi.org/10.1007/978-981-16-9310-6_14

Renard, K. G., Lane, L. J., Foster, G. R., & Laflen, J. M. (2023). Soil Loss Estimation. In *Soil Erosion, Conservation, and Rehabilitation*. https://doi.org/10.1201/9781003418177-9

Richardson, A. J., & Wiegand, C. L. (1977). Distinguishing vegetation from soil background information.

Photogrammetric Engineering and Remote Sensing, *43*(12).

Salhi, A., Benabdelouahab, S., & Heggy, E. (2024). Growing soil erosion risks and their role in modulating catastrophic floods in North Africa. *International Journal of Applied Earth Observation and Geoinformation*, *133*, 104132.

Sejati, A. W., Waskitaningsih, N., Sukmawati, D. P., Buchori, I., Putri, S. N. A. K., Muzaki, A. J., & Sugiyantoro, Y. (2024). More developed means dangerous: spatial evidence of multi-decadal urbanising watershed and its impact to flash flood in metropolitan Semarang-Indonesia. *Environmental Hazards*, 1–22.

Singh, S., & Kansal, M. L. (2024). A comparative study of morphometric, hydrologic, and semi-empirical methods for the prioritization of sub-watersheds against flash flood-induced landslides in a part of the Indian Himalayan Region. *Environmental Science and Pollution Research*, *31*(41). https://doi.org/10.1007/s11356-023-30613-6

Soniari, N. N., Trigunasih, N. M., Sumarniasih, M. S., & Saifulloh, M. (2024). Exploring soil erodibility: integrating field surveys, laboratory analysis, and geospatial techniques in sloping agricultural terrains. *Journal of Degraded & Mining Lands Management*, *12*(1).

Sugianto, S., Deli, A., Miswar, E., Rusdi, M., & Irham, M. (2022). The Effect of Land Use and Land Cover Changes on Flood Occurrence in Teunom Watershed, Aceh Jaya. *Land*, *11*(8). https://doi.org/10.3390/land11081271

Susila, K. D., Trigunasih, N. M., & Saifulloh, M. (2024). Monitoring Agricultural Drought in Savanna Ecosystems Using the Vegetation Health Index--Implications of Climate Change. *Ecological Engineering & Environmental Technology (EEET)*, *25*(9).

Suyarto, R., Diara, I. W., Susila, K. D., Saifulloh, M., Wiyanti, W., Kusmiyarti, T. B., & Sunarta, I. N. (2023). Landslide inventory mapping derived from multispectral imagery by Support Vector Machine (SVM) algorithm. *IOP Conference Series: Earth and Environmental Science*, *1190*(1). https://doi.org/10.1088/1755-1315/1190/1/012012

Suyarto, R., & Wiyanti. (2023). Studi geomorfologi bentuklahan (landform) skala regional Provinsi Bali. Lembaga Penelitian dan Pengabdian kepada Masyarakat, Universitas Udayana. https://research.unud.ac.id/uploads/penelitian/laporan_akhir/laporan_akhir_penelitian_10865.pdf?655c9490bad81

Taloor, A. K., Khajuria, V., Parsad, G., Bandral, S., Mahajan, S., Singh, S., Sharma, M., & Kothyari, G. C. (2025). Geospatial assessment of soil erosion in the Basantar and Devak watersheds of the NW Himalaya: A study utilizing USLE and RUSLE models. *Geosystems and Geoenvironment*, *4*(2), 100355.

The Guardian. (2025, September 11). Flash floods in Indonesia: Bali deaths. https://www.theguardian.com/world/2025/sep/11/flash-floods-indonesia-bali-deaths

Trigunasih, N. M., Kusmawati, T., & Yuli Lestari, N. W. (2018). Erosion Prediction Analysis and Landuse Planning in Gunggung Watershed, Bali, Indonesia. *IOP Conference Series: Earth and Environmental Science*, *123*(1). https://doi.org/10.1088/1755-1315/123/1/012025

Trigunasih, N. M., Narka, I. W., & Saifulloh, M. (2023). Measurement of Soil Chemical Properties for Mapping Soil Fertility Status. *International Journal of Design and Nature and Ecodynamics*, *18*(6). https://doi.org/10.18280/ijdne.180611

Trigunasih, N. M., & Saifulloh, M. (2022). The Investigating Water Infiltration Conditions Caused by Annual Urban Flooding Using Integrated Remote Sensing and Geographic Information Systems. *Journal of Environmental Management & Tourism*, *13*(5), 1467–1480.

Trigunasih, N. M., & Saifulloh, M. (2023). Investigation of soil erosion in agro-tourism area: guideline for environmental conservation planning. *Geographia Technica*, *18*(1). https://doi.org/10.21163/GT_2023.181.02

Walkley, A., & Black, I. A. (1934). An examination of the degtjareff method for determining soil organic matter, and a proposed modification of the chromic acid titration method. *Soil Science*, *37*(1). https://doi.org/10.1097/00010694-193401000-00003

Wardhani, F. A., Pravitasari, A. E., & Ridwansyah, I. (2022). Flash flood assessment at Upper Cisadane Watershed using land use/land cover and morphometric factors. *IOP Conference Series: Earth and*

Environmental Science, *1109*(1). https://doi.org/10.1088/1755-1315/1109/1/012002

Wayan Sandi Adnyana, I., Rahman As-syakur, A., Wayan Nuarsa, I., Saifulloh, M., & Setiawati, M. D. (2025). Comparing Soil Erosion Rate Predictions Using USLE Method Based on Conventional and Remote Sensing Data Calculations. In *Remotely Sensed Rivers in the Age of Anthropocene* (pp. 357–392). Springer.

Wink Junior, M. V., dos Santos, L. G., Ribeiro, F. G., & da Trindade, C. S. (2024). Natural disasters and poverty: evidence from a flash flood in Brazil. *Environment, Development and Sustainability*, *26*(9). https://doi.org/10.1007/s10668-023-03623-0

Wischmeier, W. H., & Smith, D. D. (1965). Predicting Rainfall-Erosion Losses From Cropland east of the Rocky Mountains: Guide for Selection of Practices for Soil and Water Conservation. *U.S. Department of Agriculture Handbook No.282*, *28*.

Wischmeier, W., & Smith, D. (1978). Predicting rainfall erosion losses: a guide to conservation planning. In *U.S. Department of Agriculture Handbook No. 537*. https://doi.org/10.1029/TR039i002p00285

Wu, Z., Bhattacharya, B., Xie, P., & Zevenbergen, C. (2023). Improving flash flood forecasting using a frequentist approach to identify rainfall thresholds for flash flood occurrence. *Stochastic Environmental Research and Risk Assessment*, *37*(1). https://doi.org/10.1007/s00477-022-02303-1

Zhang, B., Zhang, G., Fang, H., Wu, S., & Li, C. (2024). Risk assessment of flash flood under climate and land use and land cover change in Tianshan Mountains, China. *International Journal of Disaster Risk Reduction*, *115*, 105019.

SUB-HOURLY PRECIPITATION EXTREMES IN ROMANIA AND THEIR LONG-TERM TEMPORAL TREND

***Adrian IRAȘOC*[1,2]*, *Nicoleta IONAC*[1], *Andreea BETERINGHE*[1], *Alexandru DUMITRESCU*[2]**

DOI: 10.21163/GT_2026.211.10

ABSTRACT

Sub-hourly precipitation extremes represent a critical aspect of climate variability, particularly in regions prone to convective storms. This study analyzes the climatology and trends of extreme short-duration rainfalls in Romania, by using high-resolution precipitation data from 107 weather stations. We computed five sub-hourly precipitation indices (Rx5min, Rx10min, Rx20min, Rx30min, and Rx1hr) and assessed their temporal trends by using the Mann-Kendall test and Theil-Sen's slope estimator. Our results reveal substantial spatial variability in extreme sub-hourly precipitation amounts, with values mounting up to 29.3 mm in 5 minutes and 106.3 mm in one hour. Significant increasing trends are observed in several regions, particularly in areas influenced by Mediterranean cyclones and cut-off low-pressure systems. However, decreasing trends are also present, notably in the Curvature Subcarpathian Hills, where foehn effects may suppress convective activity. These findings highlight the importance of high-resolution precipitation data for understanding extreme rainfall trends, as sub-hourly indices exhibit distinct patterns as compared to daily-scale analyses. Given Romania's vulnerability to flash floods, the observed intensification of short-duration precipitation requires enhanced flood risk management and adaptation strategies.

Keywords: *Sub-hourly precipitation; Heavy rainfall; Pluviograph, Trend analysis.*

1. INTRODUCTION

Heavy precipitation is nowadays the subject of plenty of research papers on climatic changes. Heavy rainfalls and storms frequently cause significant damage and casualties across many regions. Therefore, gaining a deeper understanding of precipitation extremes and their variability is essential for helping communities to better adapt to the challenges posed by a warming climate (Handmer et al., 2012). Recognizing how and why extreme precipitation patterns fluctuate is crucial for disaster preparedness and effective water resource management. This requires both an analysis of historical variations in extreme precipitations and the ability to assess their observed trends and future changes within scenario-based climate projections.

A key statement from the IPCC (Intergovernmental Panel on Climate Change) Sixth Assessment Report highlights the changing nature of extreme precipitations, saying that "*the frequency and intensity of heavy precipitation events have increased since the 1950s over most land area for which observational data are sufficient for trend analysis*" and also that "*it is very likely that heavy precipitation events will intensify and become more frequent in most regions*" (IPCC, 2021). Observations from global datasets based on station data reveal increasing trends in annual sums of daily maximum precipitations (Westra et al., 2013).

---

[1]*University of Bucharest, Faculty of Geography, Department of Geography, Bucharest, Romania.*
**Corresponding author: (AI) adrian.irasoc@s.unibuc.ro; (IN) ionac.nicoleta@geo.unibuc.ro; (AB) andreea.beteringhe@s.unibuc.ro*
[2]*National Meteorological Administration, Department of Climatology, Bucharest, Romania, dumitrescu@meteoromania.ro*

In recent decades, a growing body of research has identified significant positive trends in extreme precipitation events across Europe, at both continental and regional scale studies (Casanueva et al., 2014; Erić et al., 2021; Lakatos et al., 2021; Berényi et al., 2023; Beranová et al, 2025), mostly by analyzing the core indices recommended by the Expert Team on Climate Change Detection and Indices (ETCCDI) (http://etccdi.pacificclimate.org/list_27_indices.shtml).

In Romania, researchers have been studying extreme precipitation since the 20th century. Numerous studies have examined intense rainfall events and their underlying causes across the country (Topor, 1964, 1970; Ion-Bordei, 1988). Several authors have highlighted the significant role of the Mediterranean and retrograde cyclones in driving these extreme weather phenomena (Șorodoc, 1962; Topor & Stoica, 1965; Ion-Bordei, 1983; Apostol, 2008; Garabă & Sfică, 2015; Dobri et al., 2017).

Other studies shaped the climatology of (heavy) precipitation in Romania, by analyzing their (long-term) variability and, in some cases, their specific return periods (Ciulache & Ionac, 1993, 2000, 2004; Haidu, 2002; Sorocovschi & Haidu, 2003; Dragotă, 2006; Sandu et al., 2008; Tudose et al., 2013). The maximum (daily) rainfall intensity and several dynamic parameters of convective cells and atmospheric stability indices (for storms that generated torrential rain showers) were also subjects of the climatological research in Romania (Tudose & Haidu, 2012; Haidu & Tudose, 2014).

In the last two decades, Romanian researchers focused on analyzing the precipitation extremes and their trends by using the ETCCDI indices, both at regional and national scales (Croitoru et al., 2013, 2015, 2018; Micu et al., 2016, 2021; Horvath & Croitoru, 2023). We noticed that some previously analyzed indices have a similar trend pattern with the ones we found for the sub-hourly indices. However, a high temporal resolution dataset was used only in a few studies before (Busuioc et al., 2015, 2017; Lakatos et al., 2021) and the sub-hourly indices being presented in this study were only tested and investigated, by Irașoc et al. (2024), at regional scale (the Dobrudjan Tableland area) in Romania, based on maximum sub-hourly, sub-daily and daily precipitation amounts.

The main objectives of this study were to highlight the climatology of sub-hourly rainfall extremes in Romania and to quantify the changes in sub-hourly precipitation indices over the last half of a century, by using statistical trend tests. This paper is structured as follows: Introduction (including the Characteristics of the Study Area), Data and Methods (with the following sub-chapters: Data Collection; Data Processing and Analysis; Long-term trend estimation), Results (including two sub-chapters: Climatology of the sub-hourly maximum precipitation amounts in Romania; Observed trends in sub-hourly maximum precipitation amounts in Romania), Discussion and Conclusions.

The ensuing findings could provide valuable support for enhancing rainwater management plans and improving the population's response and resilience to (flash) floods. Given Romania's high vulnerability to flooding, as identified both by a government project through national hazard and risk maps (https://inundatii.ro/portal-harti/) and by researchers in academia (Zaharia et al., 2015; Romanescu et al., 2018; Török, 2018; Albano et al., 2020; Arseni et al., 2020; Albulescu et al., 2022), these insights become particularly relevant for mitigating flood-related risks.

2. STUDY AREA

The study area is represented by the entire Romanian territory, located in the South-East of Europe (**Fig. 1**). Romania is bounded to the North by Ukraine and to the East by Republic of Moldova and Ukraine, through the natural borders created by the Prut and Danube rivers. It is bounded to the South-East by the Black Sea and to the South by Bulgaria, mostly through the natural border created by the Danube River. To the South-West, Romania is separated from the Republic of Serbia by both natural (the Danube) and conventional borders. To the West and North-West, it is bounded by Hungary.

Romania's territory extends between the 43°37' to 48°15' North latitude and the 20°15' to 29°41' East longitude. The distance between its northernmost and southernmost points is 525 km, and between its westernmost and easternmost points is 740 km (Badea et al., 1983). Thus, Romania is located halfway between the Equator and the Poles, in the mid-latitude zone.



Fig. 1. Study area (Romania) - location, topography and meteorological network.

The relief elevation in Romania varies between 0 and 2,544 m and its main landforms include: the Alpine mountains (the Carpathians) mostly in the center, the Hercynian mountains (Măcin) in the South-East, plateaus and hilly landforms across all the territory, but mostly inside and on the outer borders of the Carpathians respectively, plains in the South and West, delta landforms (Danube Delta) as well as shoreline landforms, including beaches, cliffs, sandbars and a lagoon system along the shoreline of the Black Sea.

The resident population in Romania is 19,053,815 inhabitants, 52.2% of them living in urban areas (National Institute of Statistics, 2023). During the 2000‑2025 period, an average of approximately 17,569 inhabitants were affected by flood events in years with reported impacts (Delforge et al., 2025). Most flood occurrences in Romania are associated with extreme or persistent heavy precipitation, reflecting the dominant hydro-meteorological trigger in the region. Notably, when individual high-impact years are considered, the number of affected persons increases sharply; for example, the 2005 flood events affected more than 120,000 people, illustrating the substantial societal consequences of severe precipitation extremes. In the same year, 78 deaths were reported, representing 32.8% of the flood-related deaths during the 2000-2025 period (Delforge et al., 2025).

According to the Köppen-Geiger classification, as carried out in a recent Romanian study (Cheval et al., 2023), Romania is characterized by six types of climate: **BSk** (cold semi-arid) in the Danube Delta; **Cfa** (warm temperate humid with hot summer) in the Romanian Plain, Western Plain, Dobrogea Plateau and Prut River meadow; **Cfb** (warm temperate humid with warm summer) in most of the hilly and plateau regions and on the peaks of Măcin mountains; **Dfb** (cold humid with warm summer) in some mountainous and sub-mountainous areas; **Dfc** (cold humid with cool summer) in most of the Carpathians and **ET** (alpine tundra) on the peaks of the Carpathians, at elevations above 2,500 m.a.s.l.

3. DATA AND METHODS

3.1. Data collection

For this research we used sub-hourly precipitation data from 107 weather stations (WSs) of Romania's national network. These data were provided by the National Meteorological Administration of Romania (NMAR). The dataset has a temporal resolution up to 1 minute and was recorded by two automatic instruments: the pluviographs, which were in use until 2007-2008 (at most of the stations) and the automatic rain gauges (with tipping bucket and weighing system) from this time period onward. The recordings from pluviographs were only available for the convective season (April to October), due to technical requirements (as this instrument can only measure liquid water). Thus, the current study is representative only for the rainfall events related to the convective season, the cold interval from November to March not being included in the present analysis due to missing data. The time range of the dataset varies at each weather station (WS), with the first recordings starting in 1898 at București-Filaret WS. The WSs are located at elevations between 1.4 and 1,897.0 m.a.s.l.

3.2. Data Processing and Analysis

The statistical processing of the rainfall data and the precipitation maps were based on several scripts we developed in the R programming language (R Core Team, 2024).

The maximum precipitation amounts at different time spans were calculated by means of the running sums (moving sums) method rather than by using a fixed time interval, simply because the results of some previous studies demonstrated that the first method can yield better estimates of the intensity and duration of extreme rainfall events, even if spanning over two or more days on end (Boughton & Jakob, 2017; Morbidelli et al., 2017, 2018; Weder et al., 2017; Irașoc et al., 2024).

Next, the quantitative analysis on sub-hourly maximum precipitation in Romania was based on the annual values of five ETCCDI indices (as shown in **Table 1**), which were adapted to a finer temporal resolution (e.g., Rx1day), similar to other scientists' approach (Barbero et al., 2019; Lakatos et al., 2021; Buda et al., 2024).

Table 1.

List of indices used in this study.

No	Short name	Definition	Unit
1	Rx5min	Maximum value of total precipitation that falls in 5 consecutive minutes	mm
2	Rx10min	Maximum value of total precipitation that falls in 10 consecutive minutes	mm
3	Rx20min	Maximum value of total precipitation that falls in 20 consecutive minutes	mm
4	Rx30min	Maximum value of total precipitation that falls in 30 consecutive minutes	mm
5	Rx1hr	Maximum value of total precipitation that falls in one hour	mm

3.3. Long-term trend estimation

For the trend analysis, we used two statistical tests, the Mann-Kendall trend test and the Theil-Sen's slope estimator, respectively.

The Mann-Kendall (MK) test is a robust non-parametric method widely used to assess long-term trends in climatological and hydrological studies. The first version of the MK test was used by Mann (1945) to investigate trends in rainfall and temperature time series and it was further studied by Kendall (1975).

The MK test provides the following statistical outputs: the Kendall (Tau) value, the p-value (at 95% confidence) and z-statistics. The z-score, a positive or negative value, suggests an increasing or decreasing trend, respectively, in the time series. The MK test can be expressed as:

$$S = \sum_{i=1}^{n-1} \sum_{j=i+1}^{n} sign(x_j - x_i) \quad (1)$$

where n represents the number of data points, xi and xj are the data values in the time series i and j, respectively, and sign(x_j-x_i) is the sign function:

$$sign(x_j - x_i) = \begin{cases} +1 & x_j - x_i > 0 \\ 0 & x_j - x_i = 0 \\ -1 & x_j - x_i < 0 \end{cases} \quad (2)$$

The variance can be expressed as:

$$Var(S) = \frac{n(n-1)(2n+5) - \sum_{i=1}^{p} t_i(t_i-1)(2t_i+5)}{18} \quad (3)$$

where p represents the number of tied groups and t_i is the number of values in the p^{th} tied group.

The Sen's slope (SS) is a non-parametric test used to estimate the linear trend slopes, expressing the magnitude (rate) of observed changes in the time series. For each set of data values (k = 1, 2, ..., n), the slope is calculated as follows:

$$SS_k = \frac{x_j - x_i}{j - i} \quad (4)$$

where x_j and x_i are the data values of rank j and i (j > i), respectively.

Further, SS is calculated as the median from all SS_k slopes, involving different formulas based on whether n is odd or even:

$$SS_{med} = \begin{cases} SS_{\left[\frac{n+1}{2}\right]} & \dots (if\ n\ is\ odd) \\ \frac{SS_{\left[\frac{n}{2}\right]} + SS_{\left[\frac{n+2}{2}\right]}}{2} & \dots (if\ n\ is\ even) \end{cases} \quad (5)$$

In this study, the trend analysis was performed by using the *trend* R package (Pohlert, 2015), on a common time range for all WSs (1970-2021). Thus, we computed the trends for 88 WSs which have less than 33% missing data during this time window and we used a statistical significance threshold of 95% (p-level < 0.05).

4. RESULTS

In order to assess the maximum values of the aforementioned indices and to provide a more accurate representation of (short-duration) extreme rainfall events occurring in Romania, we used all the data that were available at the start of this research work, despite their variations in the time range across the WSs. Notably, the national records for these indices were set up during periods when comprehensive data were available for most stations, especially that, for the trend analysis, we had to use a consistent time span across all WSs.

4.1. Climatology of the sub-hourly maximum precipitation amounts in Romania

The values of the maximum **Rx5min** index in Romania (**Fig. 2**) vary between 10 mm (at Voineasa and Gura Portiței WSs, located in the Southern Carpathians and Danube Delta, respectively) and 29.3 mm (Făgăraș WS, in the Transylvanian Depression). The highest amount (29.3 mm), with a rainfall intensity of 5.86 mm/min, occurred at Făgăraș on July 16th, 1991. This precipitation event was associated to the advection of a humid air mass from the North-West of Europe which, most likely, upon contact with the northern slopes of the Făgăraș Mountains, was subject to orographic convection. Over 25 mm were also recorded at Caracal (2005) and Sibiu (1970).

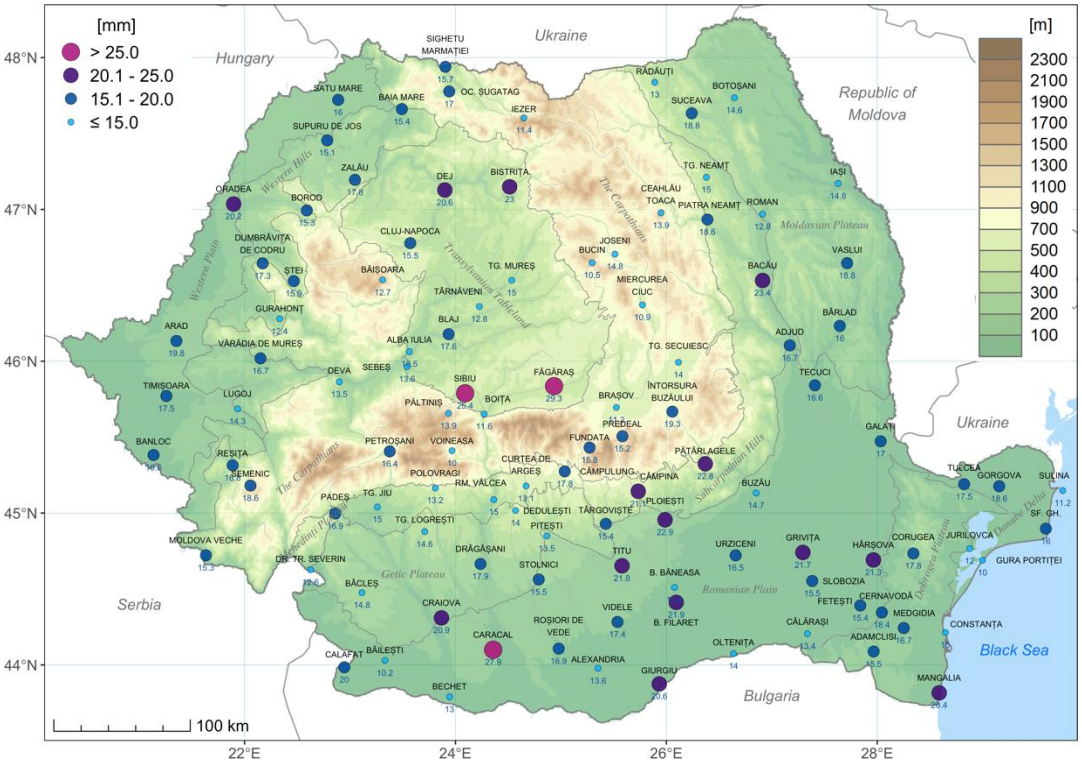


Fig. 2. Spatial distribution of the maximum precipitation amount during 5 minutes (*Rx5min)* in Romania.

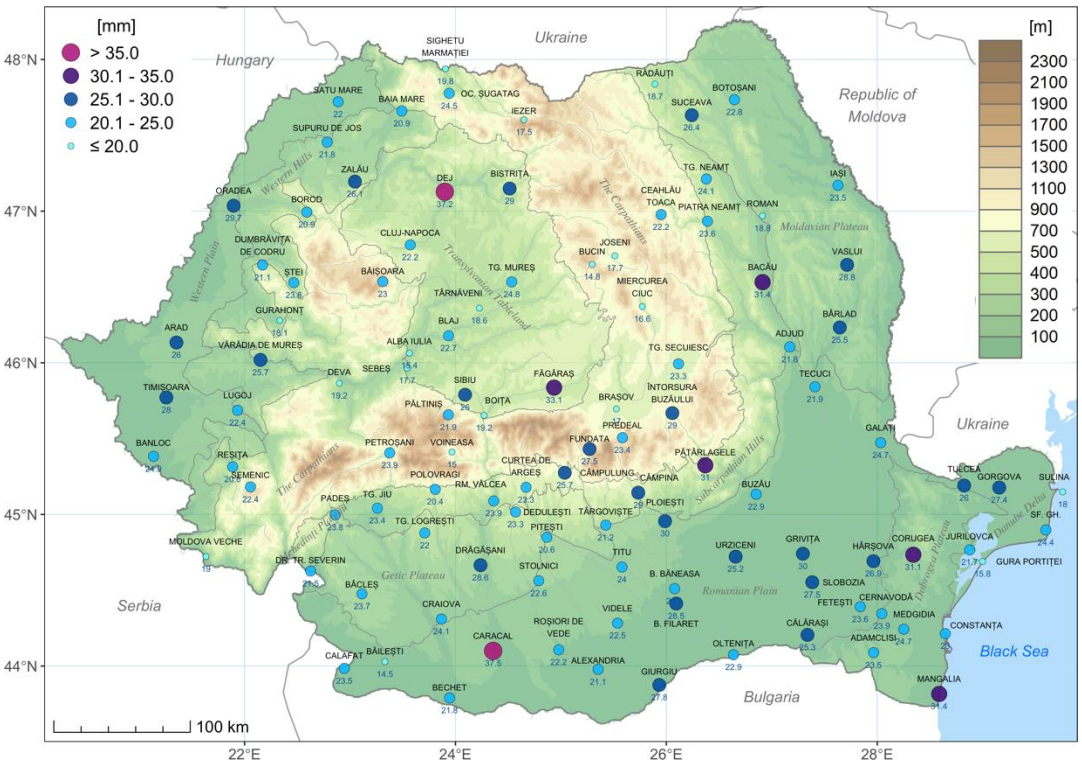


Fig. 3. Spatial distribution of the maximum precipitation amount during 10 minutes (*Rx10min)* in Romania.

The maximum values of the **Rx10min** index in Romania (**Fig. 3**) ranged from 14.5 mm (Băilești, in the Great Romanian Plain) to 37.5 (Caracal, in the Romanian Plain as well). A maximum amount, exceeding 37 mm, occurred at Dej WS, in the Transylvanian Depression, on July 16th, 1975. The maximum value recorded at Dej WS resulted from the interaction between the western atmospheric circulation and the Carpathian Mts., as the largely-opened topography of north-western Romania facilitated the rapid advection of humid air into the Transylvanian Tableland. Furthermore, on July 16th, 1975, the northern parts of the Transylvanian Tableland were quite under the contact line between a low-pressure system located in northern Europe and an anticyclone to the South.

Actually, the values of these two indices exhibit an extremely uneven spatial distribution, so, in order to identify any distinct clusters, the highest values had to be excluded as statistically non-relevant singularities. Consequently, in both cases, significant precipitation amounts were recorded outside the mountain area, primarily in the southern and south-eastern regions of the country, including the Subcarpathian Hills, the Romanian Plain and the Dobrudjan Plateau. However, significant precipitation amounts were also recorded locally in the Transylvanian Depression, the Western (Pannonian) Plain and the Moldavian Subcarpathian Hills, showing that both dynamic factors and local topography may greatly influence pluviogenetic processes.

The maximum values of **Rx20min** index in Romania (**Fig. 4**) vary between 19.4 mm (at Joseni, in the Eastern Carpathians) and 60 mm (at Bacău, in the Moldavian Subcarpathian Hills). The highest Rx20min value at Bacău was recorded on July 20th, 2002 and during the exact same rainfall event, the country's maximum records of Rx30min (74.8 mm) and Rx1hr (106.3 mm) have also occured at the Bacău WS (**Fig. 5** and **Fig. 6**).

These extreme values resulted from an intense atmospheric instability associated with a long-wave trough extending from north-western to south-eastern Europe, thus facilitating the advection of moisture from the western basin of the Black Sea and contributing to the development of Cumulonimbus clouds. This synoptic pattern is characteristic of summer convective storms and has been previously studied by Dobri et al., 2017, but a more detailed analysis of this synoptic event, including several reanalysis maps could be accessed from www.wetter3.de and www.metoffice.com.

However, if excluding the Bacău WS case, a clearer spatial pattern emerges in the distribution of the Rx20min, **Rx30min and Rx1hr indices**, with the highest precipitation amounts being recorded in Romania's southern and south-eastern areas, where rainfall exceeded 50-60 mm in 30 minutes and 80 mm in one hour. These regions are particularly prone to extreme rainfall events due to the higher atmospheric instability triggered by the Mediterranean cyclones (Ion-Bordei, 1983; Garabă & Sfîcă, 2015), as well as to the long-wave troughs and cut-off low systems, specific of the mid-latitude North-Atlantic air-circulation (Dobri et al., 2017). In some coastal areas, however, the proximity of the Black Sea seems to have a rather inhibiting effect on convection, leading to much lower sub-hourly precipitation extremes as compared to the inland areas.

Thus, significant Rx30min values occurred in Eastern Romanian Plain, at Grivița (65.1 mm/September 5th, 1992) and Slobozia (62.8 mm/June 13th, 2020) WSs. In the case of Grivița WS, the value was recorded due to the atmospheric instability triggered by an Atlantic cyclone's long-wave trough, which finally turned into a cut-off low system. In the case of Slobozia WS, from 2020, the Black Sea played a significant role by supplying water vapors to a low-pressure system located over its western basin.

The regions with the lowest precipitation amounts include the Transylvanian Tableland area, the Western Hills, most of the intra-Carpathian depressions (as result of a shelter effect), and certain areas along the Black Sea coast. Regarding the areas on the Black Sea coast, though the sea-water bodies are generally known as inhibitors of convective processes, in this case, depending on the atmospheric circulation patterns, the Black Sea can play a crucial role in generating heavy rainfalls by supplying significant amounts of water vapor to the surrounding regions, especially when retrograde cyclones get powerful enough. This was the case on July 15-16, 1994, when 97.2 mm of rainfall was recorded in just one hour at Fetești WS (**Fig. 6**).

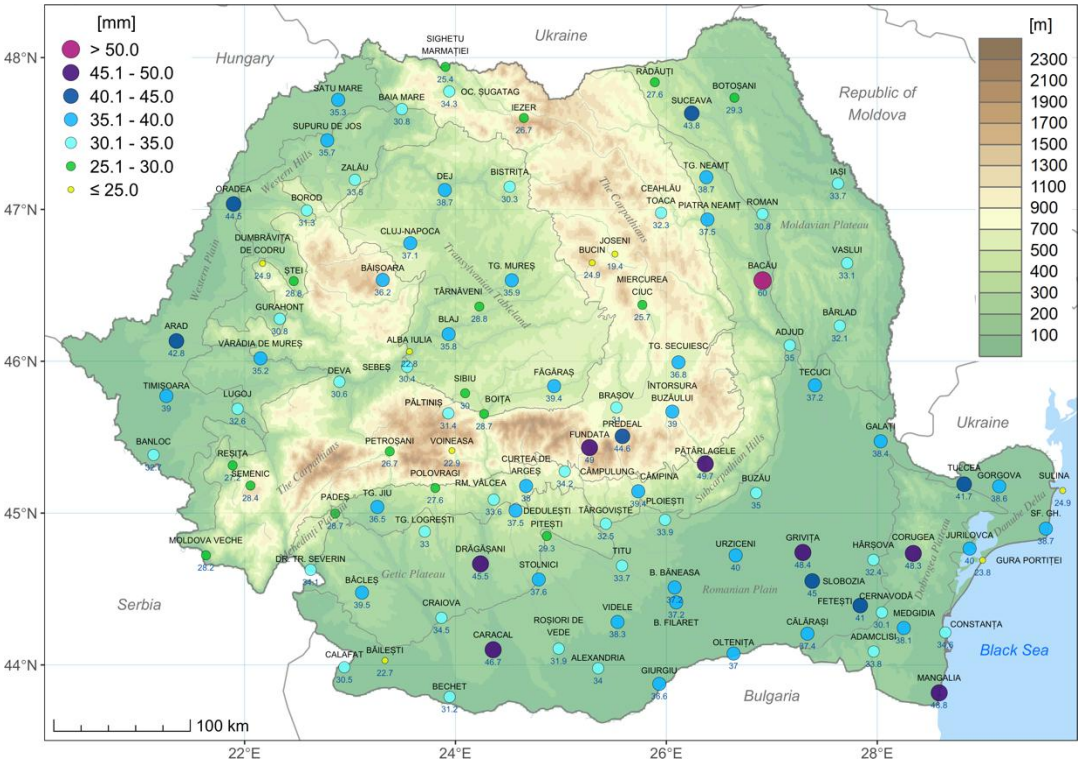


Fig. 4. Spatial distribution of the maximum precipitation amount during 20 minutes *(Rx20min)* in Romania.

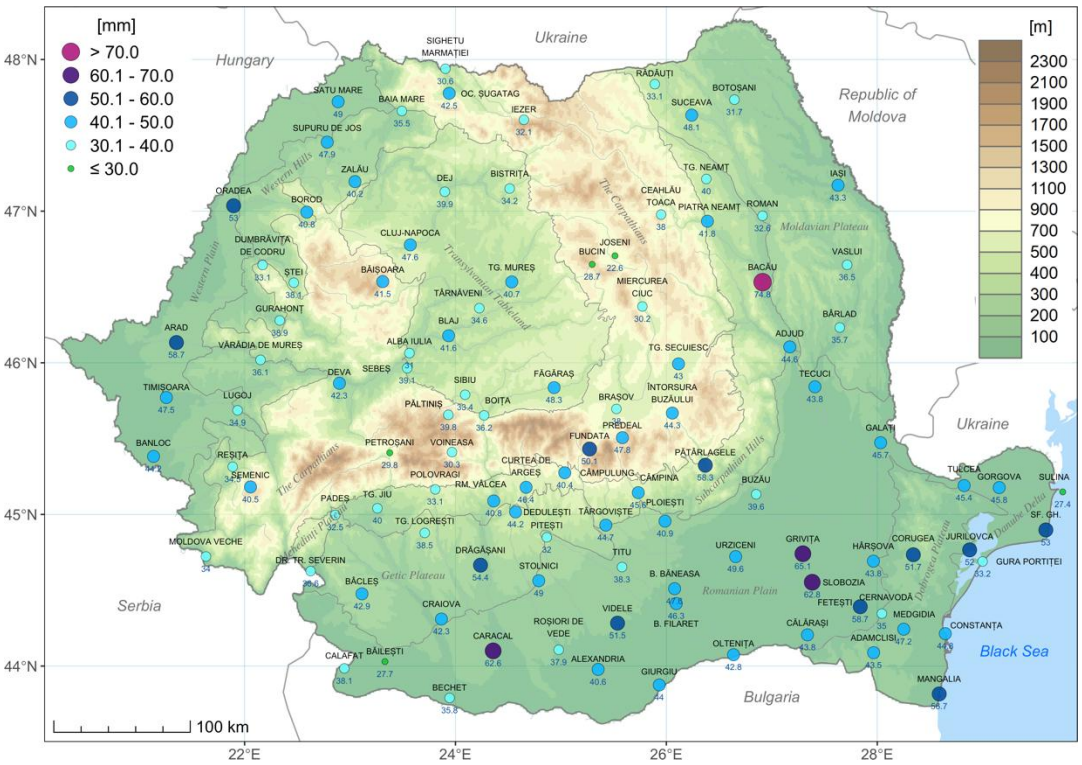


Fig. 5. Spatial distribution of the maximum precipitation amount during 30 minutes (*Rx30min)* in Romania.

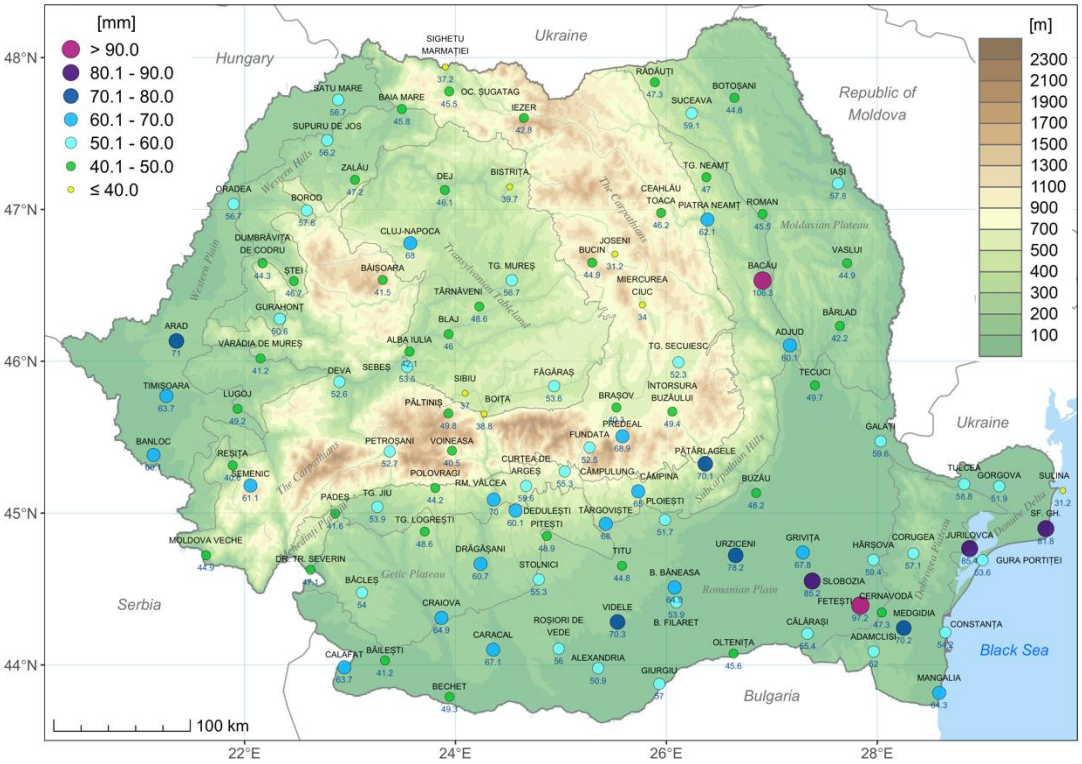


Fig. 6. Spatial distribution of the maximum precipitation amount during one hour (*Rx1hr)* in Romania.

4.2. Observed trends in sub-hourly maximum precipitation amounts in Romania

The spatial distribution of extreme rainfall amounts in Romania, for any sub-hourly duration considered in this study (**Fig. 7-11**), reveals complex patterns with both increasing and decreasing trends scattered across the country.

Overall, 52.3% of the analyzed weather stations recorded decreasing trends, 41.5% recorded increasing trends and for 6.2% of the WSs no trend was identified (as an average value for all durations).

The differences are, nevertheless, particularly interesting in some regions like the South-East one, where stations in close proximity one to another show opposing trends, some even with statistically significant changes and high magnitudes. This situation could be due to the fact that short-lived extreme precipitation events are often driven by convective storms, which are highly limited to a rather small area and cause nearby stations to record opposite trends, especially in flat terrain areas.

The spatial distribution of maximum precipitation trends in south-eastern Romania, particularly in the Dobrudjan Tableland area, exhibits a significant variability, with adjacent weather stations recording (statistically significant) contrasting trends. This complex pattern could be attributed to several interrelated factors: the local climatic conditions, the land-sea interactions and the topographical effects. The region's topography, with varying elevations along the shoreline of the Black Sea, plays a crucial role in modulating precipitation amounts. That's why coastal areas may experience different rainfall amounts and intensities as compared to inland locations, due to sea breezes and moisture availability. Additionally, subtle elevation changes can influence the development and movement of convective cells, contributing to the observed spatial variability.

Moreover, for the Black Sea shore, the trends in sub-hourly precipitation extremes are similar to the trends of several daily indices analyzed by Croitoru et al. (2013).

On the contrary, Romania's Western Plain has a notable cluster of decreasing trends around Arad WS, with significant changes (Rx10min), while the nearby areas like Reșița and Semenic show increasing trends, obviously due to their location at higher altitudes.

In the North-West of the Transylvanian Depression, Zalău WS records a statistically significant decreasing trend in Rx20min, Rx30min and Rx1hr.

In the Curvature Subcarpathian Hills, particularly around Buzău WS, the trends are exclusively negative, with high magnitudes exceeding 1.5 mm/decade for Rx1hr (**Fig. 11**). This pattern may be attributed to foehn winds in the region, which suppress convective activity and largely limit precipitations.

The mountainous areas (The Carpathians) exhibit mixed trends, likely due to orographic effects, which can enhance or suppress convective activity based on local wind patterns, moisture availability and elevation gradients (Ion-Bordei, 1988). The presence of opposing trends over relatively short distances suggests that local topography plays a critical role in determining precipitation patterns at sub-hourly scales.

The **Rx5min index** has decreasing trends at most of the WSs located in the Romanian Plain, Dobrudja and Moldova Plateaus, but also on large areas in the Transylvanian Tableland (**Fig. 7**). The highest negative magnitudes, exceeding 0.6 mm/decade, occur at Corugea, Hârșova, Botoșani and Arad WSs. The trends of Rx5min are statistically significant only in the Dobrudjan Plateau. Increasing trends of this index mostly occur in the western regions of the country, but also in the Central Moldavian Plateau and on the Black Sea coast. However, the positive magnitudes hardly exceed 0.3 mm/decade.

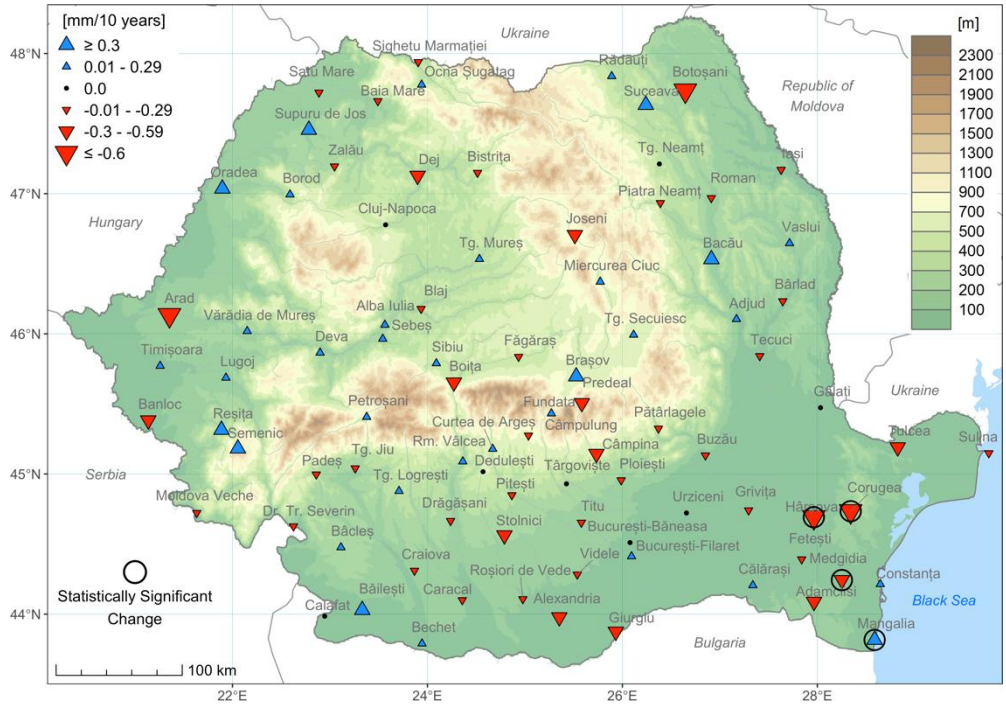


Fig. 7. Long-term trends in the maximum precipitation amount during 5 minutes (*Rx5min*) in Romania for the period 1970-2021.

Regarding the trends of the **Rx10min index** (**Fig. 8**), it should be noted that the positive trends have higher magnitudes in the extra-Carpathian regions and are statistically significant at three WSs. Statistically significant positive trends also occurred for Rx5min and Rx20min indices, but only for one WS.

During the trend analysis, we observed that the sign of the trend does not usually vary at the same WS significantly. This pattern becomes more reliable when increasing the duration of the analysed indices (e.g. Rx20min, Rx30min, Rx1hr, in this study).

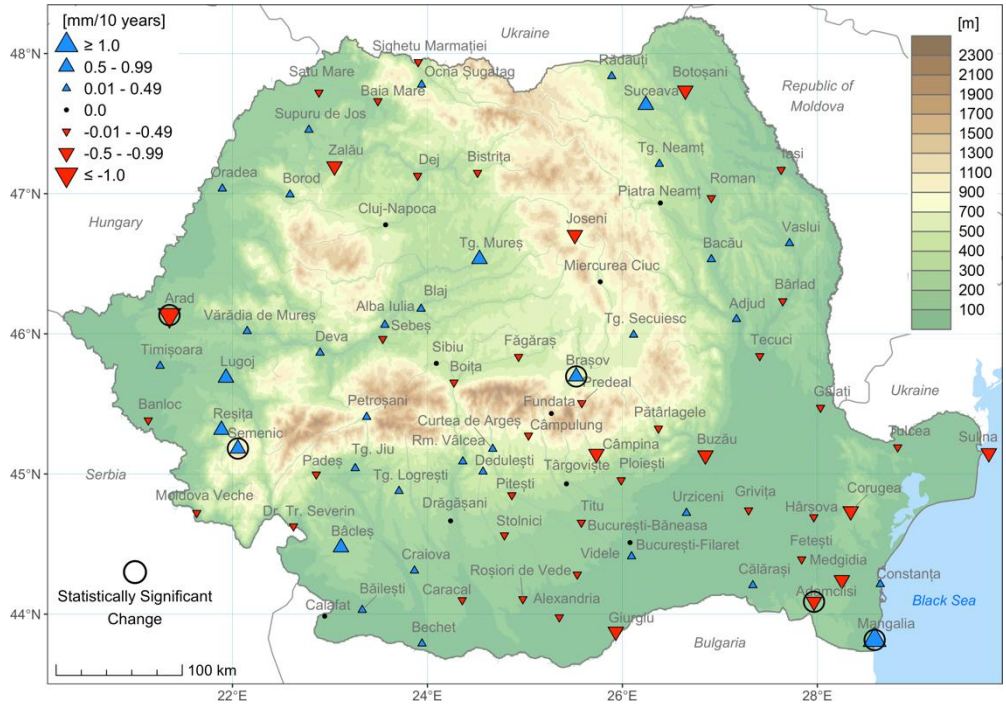


Fig. 8. Long-term trends in the maximum precipitation amount during 10 minutes (*Rx10min*) in Romania for the period 1970-2021.

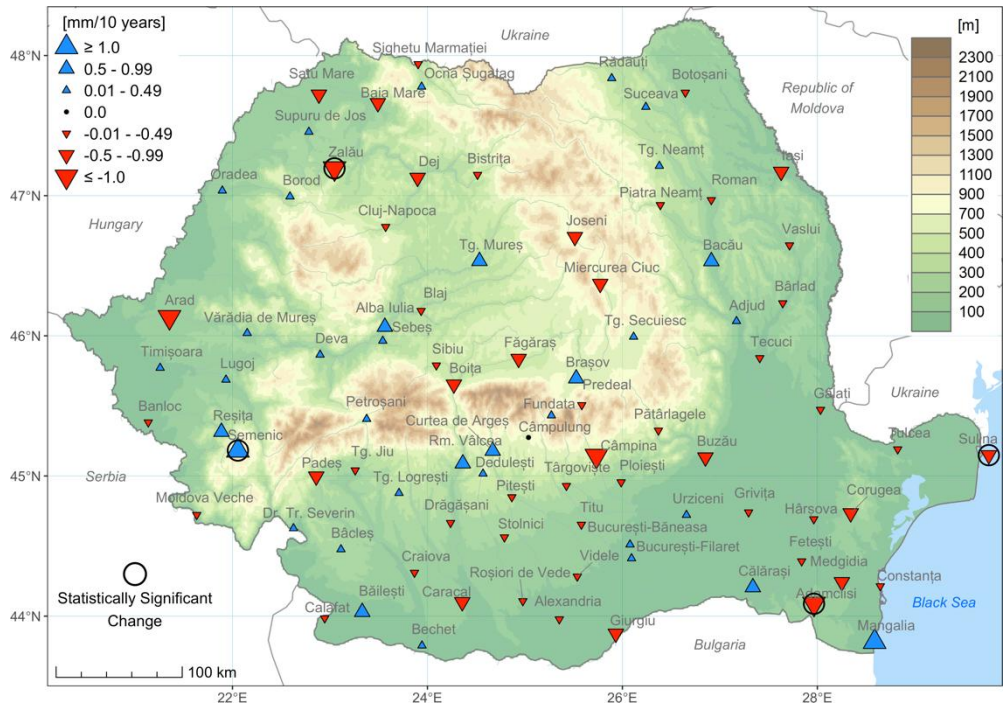


Fig. 9. Long-term trends in the maximum precipitation amount during 20 minutes (*Rx20min*) in Romania for the period 1970-2021.

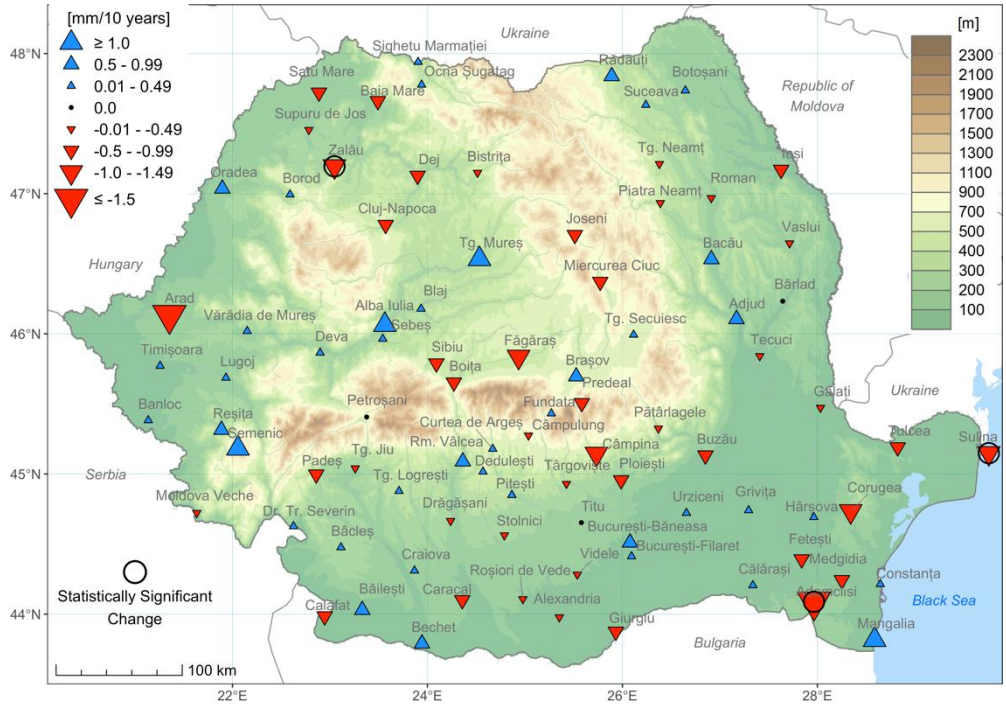


Fig. 10. Long-term trends in the maximum precipitation amount during 30 minutes (*Rx30min*) in Romania for the period 1970-2021.

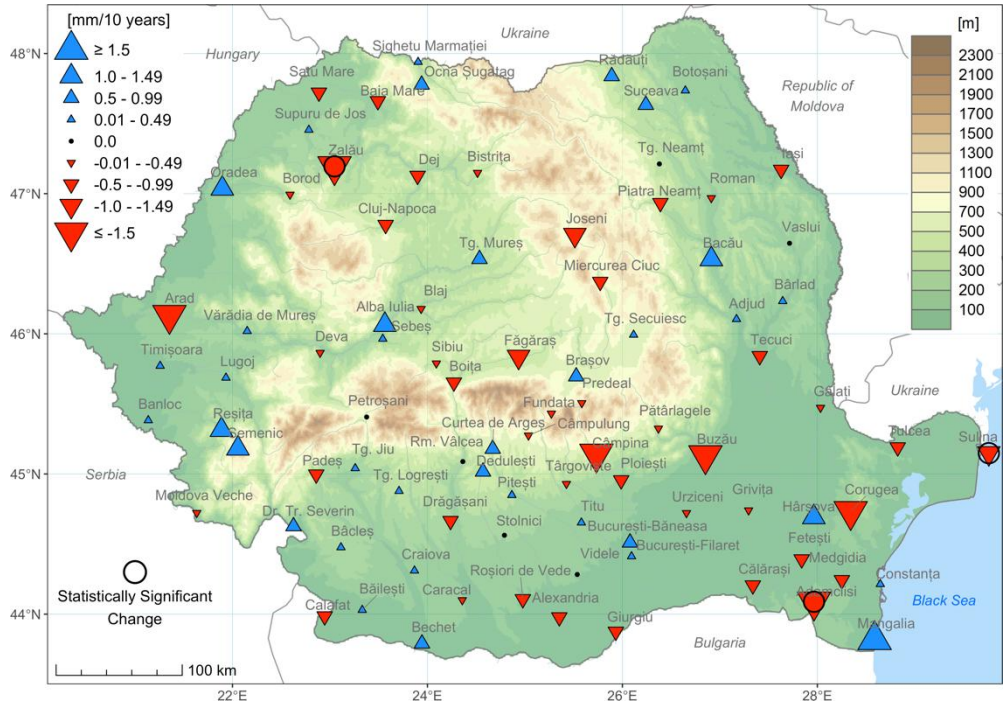


Fig. 11. Long-term trends in the maximum precipitation amount during one hour (*Rx1hr*) in Romania for the period 1970-2021.

Furthermore, we can notice that the greater the duration of the index gets, the higher the magnitude of the negative trends becomes. Thus, the negative trend clusters occurring in the North-West of the country, in the Curvature Subcarpathian Hills and the Dobrudjan Plateau are better highlighted by the **Rx30min and Rx1hr indices** (**Fig. 10** and **Fig. 11**). For these two indices, the negative rate of change exceeds 1.5 mm/decade at several WSs.

4.2.1. Observed trends in sub-hourly maximum precipitation amounts in Bucharest

București-Filaret is one of the three weather stations that provide meteorological observations for Romania's capital, Bucharest. It holds the longest sub-hourly precipitation record in the country, with measurements dating back to 1898. However, 23.2% of the data is missing over the entire 125-year period analysed in this paper. Even so, the remaining 96 years of observations offer a valuable basis for examining long-term patterns in sub-hourly precipitation.

To explore these patterns, five plots were produced to visualize the interannual variability of the maximum precipitation amounts corresponding to the five indices used in the national-scale analysis (**Fig. 12**). Each plot includes a simple linear regression trend line as well as the breakpoints identified using the *strucchange* R package (Zeileis et al., 2002). This method allowed us to analyse all available data while excluding missing values, and to detect structural changes in precipitation trends.

For most indices (Rx10min, Rx20min, Rx30min, and Rx1hr), the breakpoint analysis identified two periods characterized by increasing trends. The earliest segment, covering years prior to 1920, exhibits a particularly steep increase for these four indices. After 1920, the upward trend becomes more moderate. Although the overall trend is positive for all indices, the Rx5min series shows a decreasing trend between 1898 and 1951. Given the substantial gaps in the record, especially consecutive missing years, it is difficult to provide a robust explanation for this behaviour.

Nevertheless, one conclusion is clear: extreme short-duration rainfall events have occurred both in the early historical period and in recent decades, as illustrated by the maximum 20- and 60-minutes precipitation amounts (**Fig. 12**).

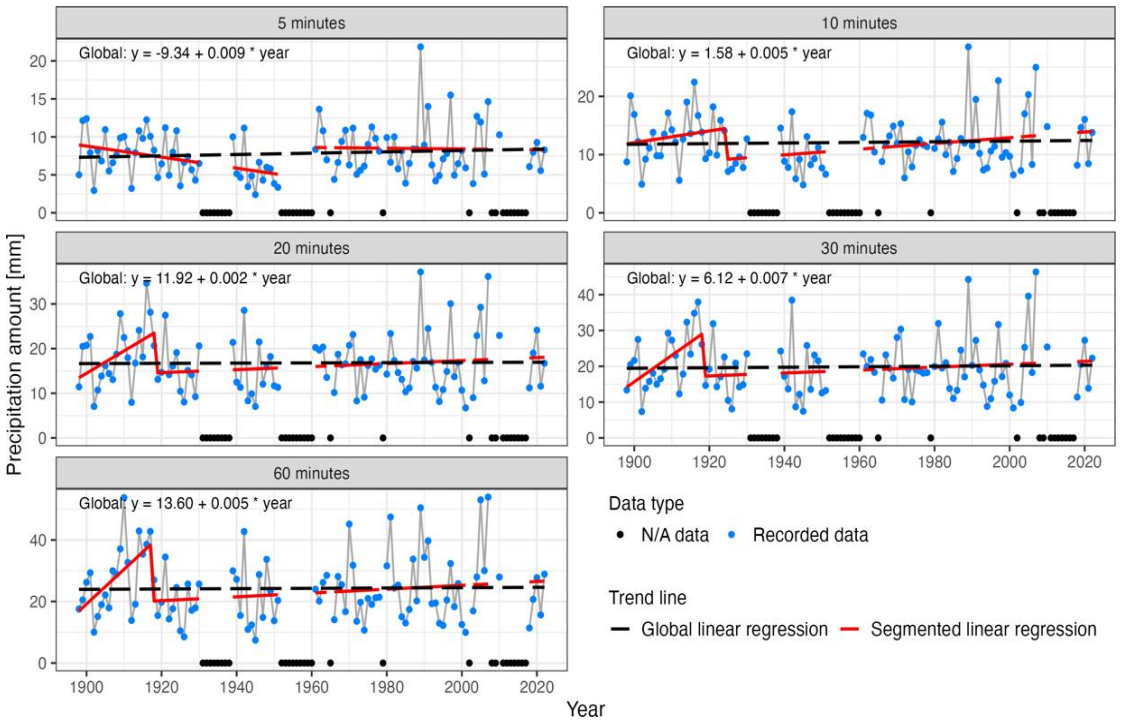


Fig. 12. Long-term trends in the sub-hourly maximum precipitation amounts at București-Filaret weather station for the period 1898-2022.

5. DISCUSSION

This study provides a comprehensive assessment of sub-hourly precipitation extremes in Romania, offering new insights into their climatology and temporal trends. Our findings highlight the spatio-temporal variability of short-duration extreme rainfall events, thus confirming their increasing intensity in several regions. These results align with previous studies that documented rising trends in extreme precipitation on a daily basis (Croitoru et al., 2013, 2015; Micu et al., 2016, 2021), reinforcing concerns over the intensification of short-term convective storms.

The observed trends in sub-hourly precipitation extremes demonstrate considerable heterogeneity across Romania. This variability is consistent with findings from other European studies (Casanueva et al., 2014; Erić et al., 2021; Berényi et al., 2023), which emphasize the influence of local geographic and climatic factors on precipitation dynamics.

Several synoptical processes may explain the observed trends. The increase in extreme rainfall amounts in southern and south-eastern Romania can be attributed to the combined effects of Mediterranean cyclones, long-wave troughs and cut-off low-pressure systems (Ion-Bordei, 1983; Dobri et al., 2017), which may enhance atmospheric instability, fostering convective developments that lead to extreme short-duration precipitation events. Additionally, the Black Sea's influence on moisture advection may amplify rainfall intensity along coastal regions, particularly under specific circulation patterns.

The complex orographic influences within the Carpathian Mts. introduce additional spatial variability, as upslope and downslope airflows affect precipitation distribution (Ion-Bordei, 1988).

The comparison between sub-hourly and daily extreme precipitation indices suggests that high-resolution data provide a more detailed understanding of rainfall dynamics. Previous studies (Busuioc et al., 2015, 2017; Lakatos et al., 2021) emphasized the importance of high temporal resolution datasets for detecting subtle changes in extreme rainfall. Our study dwells on this perspective, showing that sub-hourly trends may differ from those observed at daily scales due to the nature of convective precipitation processes.

6. CONCLUSIONS

This study provides a detailed assessment of sub-hourly precipitation extremes in Romania, highlighting both their climatological characteristics and temporal trends. The highest recorded values reached 29.3 mm in 5 minutes at Făgăraș (1991) and 106.3 mm in one hour at Bacău (2002), demonstrating the intensity of short-duration rainfall events.

The trend analysis over the 1970-2021 period reveals a complex spatial distribution, with both increasing and decreasing trends scattered across the country. The south-eastern region, particularly the Dobrudjan Tableland area, exhibits notable variability, with adjacent weather stations showing very contrasting trends, influenced by local climatic conditions, land-sea interactions, and topography. While some areas in southern and western Romania display significant decreasing trends, such as around Arad, Zalău and in the Curvature Subcarpathian Hills, other locations, including Reșița and Semenic, show significant increasing trends. In mountainous areas, the trends are mixed, likely due to orographic effects modulating convective activity.

Our findings emphasize the importance of high-resolution precipitation data for detecting local changes in extreme rainfall patterns and for understanding their hydrological implications. The documented regional variability and the increasing frequency of short-duration extreme rainfall events, combined with Romania's high exposure to flash floods, underscore the need for more localized flood risk management strategies and adaptive urban planning measures to enhance climate resilience.

Additionally, future research should focus on refining climate projections at high temporal resolutions to enhance predictive capabilities for extreme precipitation events.

REFERENCES

Albano, R., Samela, C., Crăciun, I., Manfreda, S., Adamowski, J., Sole, A., Sivertun, Å., & Ozunu, A. (2020) Large Scale Flood Risk Mapping in Data Scarce Environments: An Application for Romania. *Water*, *12*(6), 1834. https://doi.org/10.3390/w12061834.

Albulescu, A. C., Minea, I., Boicu, D., & Larion, D. (2022) Comparative multi-criteria assessment of hydrological vulnerability – case study: drainage basins in the Northeast Region of Romania. *Water*, *14*(8), 1302. https://doi.org/10.3390/w14081302.

Arseni, M., Rosu, A., Calmuc, M., Calmuc, V. A., Iticescu, C., & Georgescu, L. P. (2020) Development of Flood Risk and Hazard Maps for the Lower Course of the Siret River, Romania. *Sustainability*, *12*(16), 6588. https://doi.org/10.3390/su12166588.

Apostol, L. (2008) The Mediterranean cyclones – the role in ensuring water resources and their potential of climatic risk, in the east of Romania. *Present environment and sustainable development*, *2*, 143-163. http://pesd.ro/articole/nr.2/14.%20Apostol_PESD_2008.pdf.

Badea, L., Bugă, D., Cioflica, G., Cucu, V., Donisă, I., Gâștescu, P., Iordan, I., Morariu, T., Niculescu, G., Oancea, D., Pișota, I., Posea, G., Savu, A., Sencu, V., Șandru, I., & Velcea, V. (1983) *Geografia României – vol. 1: Geografia Fizică [Geography of Romania – vol. 1: The Physical Geography].* Editura Academiei Republicii Socialiste România.

Barbero, R., Fowler, H. J., Blenkinsop, S., Westra, S., Moron, V., Lewis, E., Chan, S., Lenderink, G., Kendon, E., Guerreiro, S., Li, X.-F., Villalobos, R., Ali, H., & Mishra, V. (2019) A synthesis of hourly and daily precipitation extremes in different climatic regions. *Weather and Climate Extremes*, *26*, 100219. https://doi.org/10.1016/j.wace.2019.100219.

Beranová, R., Huth, R., & Vít, V. (2025) A Multidataset Analysis of Precipitation Trends in Europe. *Journal of Hydrometeorology*, 26(7), pp.1003–1015. https://doi.org/10.1175/jhm-d-24-0114.1.

Berényi, A., Bartholy, J., & Pongrácz, R. (2023) Analysis of precipitation-related climatic conditions in European plain regions. *Weather and Climate Extremes*, *42*, 100610. https://doi.org/10.1016/j.wace.2023.100610.

Boughton, W., & Jakob, D. (2008) Adjustment factors for restricted rainfall. *Australasian Journal of Water Resources*, *12*(1), 37-47. https://doi.org/10.1080/13241583.2008.11465332.

Buda, A. R., Millar, D. J., Kennedy, C. D., Welsh, M. K., & Wiegman, A. R. (2024) Trends in extreme rainfall over the past 55 years suggest springtime subhourly rainfall extremes have intensified in Mahantango Creek, Pennsylvania. *Scientific Reports*, *14*(1), 27837. https://doi.org/10.1038/s41598-024-79196-3.

Busuioc, A., Baciu, M., Breza, T., Dumitrescu, A., Stoica, C., & Băghină, N. (2017) Changes in intensity of high temporal resolution precipitation extremes in Romania: Implications for Clausius-Clapeyron scaling. *Climate Research*, *72*(3), 239–249. https://doi.org/10.3354/cr01469.

Busuioc, A., Baciu, M., & Stoica, C. (2015) A new index quantifying the precipitation extremes. *EGU General Assembly Conference Abstracts*, 12039. https://meetingorganizer.copernicus.org/EGU2015/EGU2015-12039.pdf.

Casanueva, A., Rodríguez-Puebla, C., Frías, M. D., & González-Reviriego, N. (2014) Variability of extreme precipitation over Europe and its relationships with teleconnection patterns. *Hydrology and Earth System Sciences*, *18*(2), 709-725. https://doi.org/10.5194/hess-18-709-2014.

Cheval, S., Dumitrescu, A., Amihăesei, V., Irașoc, A., Paraschiv, M.-G., & Ghent, D. (2023) A country scale assessment of the heat hazard-risk in urban areas. *Building and Environment*, *229*, 109892. https://doi.org/10.1016/j.buildenv.2022.109892.

Ciulache, S., Ionac, N. (1993) Long-Term Rainfall Variations in Romania. *Analele Universităţii din Bucureşti,* seria Geografie, XLII, 61-68.

Ciulache, S., Ionac, N. (2000) Mean Annual Rainfall in Romania. *Analele Universităţii din Bucureşti*, seria Geografie, XLIX, 77-85.

Ciulache, S., Ionac, N. (2004) Rainfall Amounts in Romania. *Buletinul Societăţii de Geografie din România*, CD Press, 47-57.

Croitoru, A.E., Chiotoroiu, B.C., Todorova, V.I., & Torică, V. (2013) Changes in precipitation extremes on the Black Western Coast. *Global and Planetary Change*, 102, 10–19, https://doi.org/10.1016/j.gloplacha.2013.01.004.

Croitoru, A.E., Piticar, A., & Burada, D.C. (2015) Changes in precipitation extremes in Romania. *Quaternary International*, 415, 1–11, https://doi.org/10.1016/j.quaint.2015.07.028.

Croitoru, A.E., Piticar, A., Sfîcă, L., Roşca, C.F., Tudose, T., Horvath, C., Ionuţ, M., Ciupertea, A.F., Scripcă, S., & Harpa, G. (2018) *Extreme temperature and precipitation events in Romania*. Editura Academiei Române.

Delforge, D., Wathelet, V., Below, R., Sofia, C.L., Tonnelier, M., van Loenhout, J.A.F., & Speybroeck, N. (2025) EM-DAT: The emergency events database. *International Journal of Disaster Risk Reduction*, [online] 124, p.105509. https://doi.org/10.1016/j.ijdrr.2025.105509.

Dobri, R. V., Sfîcă, L., Ichim, P., & Harpa, G. V. (2017) The distribution of the monthly 24-hour maximum amount of precipitation in Romania according to their synoptic causes. *Geographia Technica*, 12, 62-72. http://dx.doi.org/10.21163/GT_2017.122.06.

Dragotă, C.-S. (2006) *Precipitaţiile excedentare în România [Excessive Precipitation in Romania]*. Editura Academiei Române.

Erić, R., Kadović, R., Đurđević, V., & Đukić, V. (2021) Future changes in extreme precipitation in central Serbia. *Journal of Hydrology and Hydromechanics*, *69*(2), 196-208. https://doi.org/10.2478/johh-2021-0006.

ETCCDI Climate Change Indices. http://etccdi.pacificclimate.org/list_27_indices.shtml. (Accessed 15th February 2025).

Garabă, L., & Sfîcă, L. (2015) Climatic features of the romanian territory generated by the action of mediterranean cyclones. *Lucrările Seminarului Geografic "Dimitrie Cantemir"*, *39*, 11-24. http://dx.doi.org/10.15551/lsgdc.v39i0.02.

Haidu, I. (2002) Analiza de frecvenţă şi evaluarea cantitativă a riscurilor [Frequency analysis and quantitative risk assessment]. *Riscuri şi Catastrofe*, 1, 180-207. https://riscurisicatastrofe.reviste.ubbcluj.ro/Volume/I_2002/PDF/Haidu.pdf.

Haidu, I., & Tudose, T. (2014) Validation of several atmospheric stability indices for the storms generating torrential rain showers in the North-West of Romania. *Studia Universitatis Babes-Bolyai, Geographia*, *59*(1). http://studiageographia.geografie.ubbcluj.ro/12014-2/haidu_tudose/.

Handmer, J., Honda, Y., Kundzewicz, Z. W., Arnell, N., Benito, G., Hatfield, J., Mohamed, I. F., Peduzzi, P., Wu, S., Sherstyukov, B., Takahashi, K., Yan, Z., … & Yamano, H. (2012) Changes in impacts of climate extremes: Human systems and ecosystems. In C. B. Field, V. Barros, T. F. Stocker, D. Qin, D. J. Dokken, K. L. Ebi, M. D. Mastrandrea, K. J. Mach, G.-K. Plattner, S. K. Allen, M. Tignor, & P. M. Midgley (Eds.), *Managing the risks of extreme events and disasters to advance climate change adaptation: Special Report of the Intergovernmental Panel on Climate Change* (pp. 231–290). Cambridge University Press. https://doi.org/10.1017/CBO9781139177245.007.

Horvath, C., & Croitoru, A. E. (2023) Analysis of precipitation extremes related to agriculture and water resources sectors based on gridded daily data in Romania. *Theoretical and Applied Climatology*, *151*(1), 355-373. https://doi.org/10.1007/s00704-022-04271-6.

Intergovernmental Panel on Climate Change (IPCC). (2021) *Summary for policymakers.* In V. Masson-Delmotte, P. Zhai, A. Pirani, S. L. Connors, C. Péan, S. Berger, N. Caud, Y. Chen, L. Goldfarb, M. I. Gomis, M. Huang, K. Leitzell, E. Lonnoy, J. B. R. Matthews, T. K. Maycock, T. Waterfield, O. Yelekçi, R. Yu, & B. Zhou (Eds.), *Climate change 2021: The physical science basis. Contribution of Working Group I to the Sixth Assessment Report of the Intergovernmental Panel on Climate Change* (pp. 3–32). Cambridge University Press. https://doi.org/10.1017/9781009157896.001.

Inundatii.ro – Flood Risk Management. https://inundatii.ro/portal-harti/ (Accessed 17th February 2025).

Ion-Bordei, E. (1983) *Rolul lanţului alpino-carpatic în evoluţia ciclonilor mediteraneeni [The role of the alpine-carpathian mountain chain for the evolution of the mediterranean cyclones]*, Editura Academiei RSR.

Ion-Bordei, N. (1988) *Fenomene meteoclimatice induse de configuraţia Carpaţilor în Câmpia Română [Meteoclimatic phenomena induced by the configuration of the Carpathians in the Romanian Plain]*. Editura Academiei RSR.

Irașoc, A., Ionac, N., Dumitrescu, A., & Beteringhe, A. (2024) Extreme Rainfall Intensities at Sub-Hourly Temporal Scale in Dobrudja (Romania). *Geographia Technica*, *19*(1). http://dx.doi.org/10.21163/GT_2024.191.08.

Kendall, M.G. (1975) *Rank Correlation Methods. 4th Edition*, Charles Griffin, London.

Lakatos, M., Szentes, O., Cindrić Kalin, K., Nimac, I., Kozjek, K., Cheval, S., Dumitrescu, A., Irașoc, A., Stepanek, P., Farda, A., Kajaba, P., Mikulová, K., Mihic, D., Petrovic, P., Chimani, B., & Pritchard, D. (2021) Analysis of Sub-Daily Precipitation for the PannEx Region. *Atmosphere*, *12*(7), 838. https://doi.org/10.3390/atmos12070838.

Mann, H. B. (1945) Nonparametric tests against trend. *Econometrica: Journal of the econometric society*, 245-259.

Met Office Archive. www.metoffice.com (Accessed 18th February 2025).

Micu, D. M., Dragotă, C.-S., & Havriş, L. E. (2016) Temporal Variations of Multi-Day Precipitation Extremes in Southern Romania: 1961-2014. *Air & Water Components of the Environment/Aerul şi Apa Componente ale Mediului*. http://dx.doi.org/10.17378/AWC2016_38.

Micu, D. M., Amihăesei, V. A., Milian, N., & Cheval, S. (2021) Recent changes in temperature and precipitation indices in the Southern Carpathians, Romania (1961–2018). *Theoretical and Applied Climatology*, *144*(1), 691-710. https://doi.org/10.1007/s00704-021-03560-w.

Morbidelli, R., Saltalippi, C., Flammini, A., Cifrodelli, M., Picciafuoco, T., Corradini, C., Casas-Castillo, M. C., Fowler H. J., & Wilkinson, S. M. (2017) Effect of temporal aggregation on the estimate of annual maximum rainfall depths for the design of hydraulic infrastructure systems. *Journal of Hydrology*, *554*, 710-720. https://doi.org/10.1016/j.jhydrol.2017.09.050.

Morbidelli, R., Saltalippi, C., Flammini, A., Corradini, C., Wilkinson, S. M., & Fowler, H. J. (2018) Influence of temporal data aggregation on trend estimation for intense rainfall. *Advances in Water Resources*, *122*, 304-316. https://doi.org/10.1016/j.advwatres.2018.10.027.

National Institute of Statistics. (2023) https://www.recensamantromania.ro/rezultate-rpl-2021/rezultate-definitive/ (Accessed 6th February 2025).

Pohlert, T. (2015) *trend: Non-Parametric Trend Tests and Change-Point Detection, R package version 0.0.1*. https://doi.org/10.13140/RG.2.1.2633.4243.

R Core Team. (2024) *R: A Language and Environment for Statistical Computing*. R Foundation for Statistical Computing. https://www.R-project.org/.

Romanescu, G., Hapciuc, O. E., Minea, I., & Iosub, M. (2018) Flood vulnerability assessment in the mountain–plateau transition zone: a case study of Marginea village (Romania). *Journal of Flood Risk Management*, *11*, S502-S513. https://doi.org/10.1111/jfr3.12249.

Sandu I., Pescaru V.I., Poiană I., Geicu A., Cândea I., & Ţâştea D. (2008) *Clima României [Climate of Romania]*. Editura Academiei Române.

Sorocovschi, V., & Haidu, I. (2003) Quelques aspects spatiaux des pluies extremes. *Dokumentacja Geograficzna*, 16(29), 313-316.

Şorodoc C. (1962) *Formarea şi evoluţia ciclonilor mediteraneeni şi influenţa lor asupra timpului în R.P.R. [Development and evolution of the mediterranean cyclones and their influence upon the weather conditions in Romania]*. In *Culegerea de lucrări a Institutului Meteorologic pe anul 1960*. C.S.A. Institutul Meteorologic.

Topor, N. (1964) Ani ploioşi şi secetoşi în R.P.R. [Rainy and dry years in Romania]. *C.S.A. Institutul Meteorologic,* p. 304.

Topor, N. (1970) Cauzele unor ploi cu efect catastrofal în România [The causes of some exceptional rainfalls in Romania], *Hidrotehnica*, XV, 11, p. 584-592.

Topor, N., Stoica, C. (1965) Tipuri de circulaţie şi centri de acţiune atmosferică deasupra Europei [Circulation types and barometric action centers in Europe], *C.S.A. Institutul Meteorologic*.

Török, I. (2018) Qualitative Assessment of Social Vulnerability to Flood Hazards in Romania. *Sustainability*, 10(10), 3780. https://doi.org/10.3390/su10103780.

Tudose, T., Croitoru, A. E., & Haidu, I. (2013) Some aspects on rainfall maximum intensity in Northwestern Romania. *Proceedings of the 13th International Multidisciplinary Scientific GeoConference: SGEM2013*, 1, 771-778.

Tudose, T., & Haidu, I. (2012) Some aspects of the relationship between synoptic-scale wind and convective cells' motion generating heavy rains in the North-Western Romania. *Proceedings of Air and Water. Components of the Environment International Conference*, 273-280. https://aerapa.conference.ubbcluj.ro/2012/Tudose_Haidu.htm.

Weder, C., Müller, G., & Brümmer, B. (2017) Precipitation extremes on time scales from minute to month measured at the Hamburg Weather Mast 1997-2014 and their relation to synoptic weather types. *Meteorologische Zeitschrift*, *26*, 507-524. https://doi.org/10.1127/metz/2017/0812.

Westra, S., Alexander, L. V., & Zwiers, F. W. (2013) Global increasing trends in annual maximum daily precipitation. *Journal of climate*, *26*(11), 3904-3918. https://doi.org/10.1175/JCLI-D-12-00502.1.

Wetter3.de Archive. www.wetter3.de (Accessed 18th February 2025).

Zaharia, L., Costache, R., Prăvălie, R., & Minea, G. (2015) Assessment and mapping of flood potential in the Slănic catchment in Romania. *Journal of Earth System Science*, *124*, 1311-1324. https://doi.org/10.1007/s12040-015-0608-3.

Zeileis, A., Leisch, F., Hornik, K., & Kleiber, C. (2002) strucchange: An R Package for Testing for Structural Change in Linear Regression Models. *Journal of Statistical Software*, [online] 7(2). https://doi.org/10.18637/jss.v007.i02.

SPEI-BASED DROUGHT PROJECTIONS FOR UGANDA UNDER CLIMATE CHANGE SCENARIOS USING THE CANESM5 CMIP6 MODEL

***Obed BYAMUKAMA*[1], *Ronald SSEMBAJWE*[2,3], *Mihai VODA*[4*] & *Brian Odhiambo AYUGI*[5]**

DOI: 10.21163/GT_2026.211.11

ABSTRACT

Drought is one of the most recurrent and damaging climate extremes in Uganda, affecting agriculture, water resources, and livelihoods. However, its future trends under changing climate conditions remain poorly understood. This study analyzed historical and projected drought characteristics across Uganda. We used the Standardized Precipitation–Evapotranspiration Index (SPEI) derived from the bias-corrected CanESM5 model within the NASA Earth Exchange Global Daily Downscaled Projections (NEX-GDDP-CMIP6) framework. Three Shared Socioeconomic Pathways (SSP1-2.6, SSP2-4.5, and SSP5-8.5) representing low, medium, and high emissions scenarios were considered. Terra-Climate data for 1985–2014 were used for bias correction and validation. Drought duration, frequency, severity, and intensity were calculated from 3-month SPEI, and spatial clustering was assessed using the Getis-Ord Gi* statistic. Historical analysis shows drying trends in northern and central Uganda. Future projections reveal spatially heterogeneous drought responses. During the mid-century (2041–2070), drought occurrence increases under SSP1-2.6 in central and northern regions but decreases under SSP2-4.5 in the central-west and under SSP5-8.5 in Karamoja. Toward the late century (2071–2100), SSP1-2.6 indicates a general decline in drought occurrence, SSP2-4.5 shows increasing droughts in the east and reductions in the northwest, and SSP5-8.5 projects widespread intensification across southern, western, and northern Uganda. Hotspot analysis identifies persistent drought clusters along the cattle corridor, extending from the Ankole–Kigezi regions and Karamoja. These findings provide a detailed understanding of Uganda's evolving drought risks and support targeted adaptation planning, water resource management, and climate-resilient livelihood strategies.

Keywords: *Climate models; Drought projection; SPEI; NEX-GDDP-CMIP6; Uganda.*

1. INTRODUCTION

Droughts are among the most complex and devastating environmental hazards worldwide, evolving slowly yet with long-lasting ecological and socioeconomic consequences. Unlike sudden extreme events such as floods or hurricanes, droughts evolve slowly, persisting for months or years and affecting vast areas (Krishna Prabhakar, 2022; Orimoloye et al., 2022). Their gradual onset makes detection, monitoring, and management particularly challenging. Intensifying climate change is projected to exacerbate both the frequency and severity of droughts, heightening risks for vulnerable regions (IPCC, 2022).

[1]*Department of Natural Resources and Environmental Management, IPB University, Bogor 16680, Indonesia, byamukamaobed@apps.ipb.id*
[2]*College of Agricultural and Environmental Sciences, Makerere University, P.O. Box 7062 University Rd, Kampala, Uganda, nazirte.sronald@yahoo.ca*
[3]*National Coffee Research Institute, National Agricultural Research Organization, P.O. Box 185, Mukono, Uganda*
[4]*Faculty of Geography, Dimitrie Cantemir University, Bodoni Sándor Street 3–5, Târgu Mureș, Romania.*
** Corresponding author: mihaivoda@cantemir.ro*
[5]*East African Hub, Wyss Academy for Nature at the University of Bern, Nanyuki 10400, Kenya, ayugi.o@gmail.com*

Sub-Saharan Africa faces a disproportionate drought burden due to structural vulnerabilities such as poverty, dependence on rainfed agriculture, and limited adaptive capacity (Lombe et al., 2024; Voda et al., 2019). Recurrent droughts have reduced agricultural productivity, disrupted livelihoods, and deepened food insecurity (Onyeaka et al., 2024). These events also drive water scarcity and rural-urban migration. This intensifies competition for limited resources and puts pressure on urban infrastructure (Calverley and Walther, 2022; Ceola et al., 2023; Li et al., 2023). Recent studies indicate an upward trend in drought frequency and intensity across Africa, driven by reduced precipitation and rising evapotranspiration (Elkouk et al., 2021; Han et al., 2022; Mathivha et al., 2024; Orke and Li, 2022; Satoh et al., 2022; R Ssembajwe, Nguefack, et al., 2025; Uwimbabazi et al., 2022).

Uganda exemplifies this regional vulnerability. Nearly 80 percent of households in Uganda rely on agriculture as their main economic activity (UBOS, 2024), and most of this agriculture is rainfed. As a result, the country's economy and food systems are highly sensitive to rainfall variability. Despite the increasing frequency and impacts of drought, most research efforts in Uganda have remained localized, focusing on specific districts or regions and relying largely on a single meteorological variable such as precipitation (Byakatonda et al., 2021; Kyatengerwa et al., 2020; Mulinde et al., 2016; Najjuma et al., 2021; Nakalembe, 2018; Nalwanga et al., 2024; Onyutha and Kerudong, 2022). While such studies provide valuable local insights, they lack the spatial continuity, resolution, and bias correction consistency required for robust national-scale projections (Voda AI et al., 2018). Furthermore, it is not clear how the projected warming will affect regional and local water balances especially in countries like Uganda where the vulnerability is high.

The availability of advanced downscaled climate model datasets now provides new opportunities to address these limitations. The NASA Earth Exchange Global Daily Downscaled Projections based on CMIP6 (NEX-GDDP-CMIP6) is one such datasets. This dataset offers bias-corrected and statistically downscaled data for up to 16 climate variables at approximately 25 km spatial resolution for the period 1950–2100 (Thrasher et al., 2022). It has been successfully applied in several regions to assess hydrological and climatic extremes. For example, it has been used to project rainfall variability in the Brazilian Amazon and Cerrado (de Mendonça et al., 2024), temperature and precipitation changes in China (Wu et al., 2023), and extreme weather indices across the Arabian Peninsula and the UAE (Baogang et al., 2024; Rao et al., 2024; Vinodhkumar et al., 2024). In Africa, it has demonstrated skill in reproducing observed precipitation patterns, though regional performance varies with the reference dataset used (Samuel et al., 2025). In Uganda, (Ronald Ssembajwe et al., 2025) used it to track future atmospheric circulations such as wind and humidity. However, its potential in simulating droughts especially based on the water balance remains largely unexplored in Uganda.

This study employs the bias-adjusted and statistically downscaled NEX-GDDP-CMIP6 CanESM5 model to project future drought dynamics in Uganda based on scale 3 SPEI. Specifically, it aims to (1) simulate and validate historical droughts using TerraClimate-based SPEI droughts as a reference, (2) analyse historical and future drought characteristics and long-term trends based on SSP1-2.6, SSP2-4.5 and SSP5-8.5, and (3) identify historical and future spatial drought hotspots. By integrating advanced CMIP6 projections with observational datasets, this study provides new insights to inform climate-resilient development, drought preparedness, and formulation of effective national adaptation strategies.

2. STUDY AREA

This study was conducted in Uganda, an inland country located in East Africa along the equator (Byamukama et al., 2025). It lies between longitudes 29°E and 35.2°E and latitudes 4.5°N and 1.5°S (**Fig. 1**). Uganda covers 241,551 km² (UBOS, 2025) and is bordered by Kenya, South Sudan, the Democratic Republic of Congo, Tanzania, and Rwanda.

The country's terrain is diverse, consisting of elevated plateaus, highlands, and extensive wetlands. Prominent features include the Rwenzori Mountains in the west, Mount Elgon in the east, and the Albertine Rift Valley. Major lakes such as Victoria, Kyoga, and Albert, together with the

River Nile, play a key role in influencing local convection and humidity, resulting in spatial variability in rainfall patterns.

Uganda's climate is shaped by the seasonal migration of the Intertropical Convergence Zone (ITCZ), monsoon systems, and large-scale circulation patterns (Jury, 2018). The country experiences a bimodal rainfall regime, with the long rains from March to May (MAM) and short rains from September to November (SON) (Ngoma et al., 2021). Annual rainfall ranges from about 500 mm in the semi-arid northeast to more than 2,000 mm in the southern and western highlands (Nuwagira and Yasin, 2022). The mean near-surface annual temperature is approximately 21°C, with monthly values ranging from 15°C in July to 30°C in February (Nsubuga and Rautenbach, 2018).

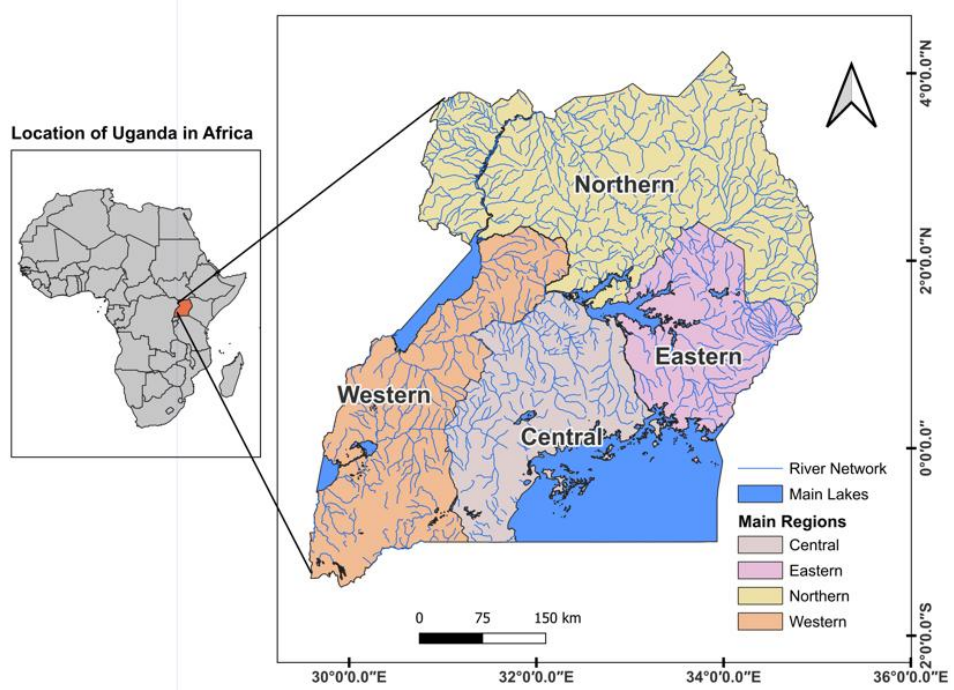


Fig. 1. Map showing location of Uganda in Africa, the four major regions, major lakes, and river networks that influence regional climatic and hydrological patterns.

3. DATA AND METHODS

3.1. Data acquisition

3.1.1. CanESM5 projected data

We used NEX-GDDP-CMIP6, the latest version of NASA's global downscaled climate projection product. NEX-GDDP-CMIP6 provides bias-corrected and statistically downscaled daily climate projections from CMIP6 models at a 0.25° × 0.25° (~25 km) spatial resolution (Thrasher et al., 2022). The NEX-GDDP scheme uses the bias correction and statistical downscaling (BCSD) method to downscale global climate models (GCMs) from parent coarse resolutions ranging from 1◦ × 1◦ to 2.5◦ × 2.5◦ to a finer 0.25◦ × 0.25◦ (Ronald Ssembajwe et al., 2025). The dataset covers a reference period (1950–2014) and future projections (2015–2100) under Shared Socioeconomic Pathways (SSP1-2.6, SSP2-4.5, SSP3-7.0, and SSP5-8.5). For consistency with TerraClimate, the 1985–2014 period was used as the reference period. The dataset is publicly available through NASA's Earth Exchange platform at https://ds.nccs.nasa.gov/thredds/catalog/AMES/NEX/GDDP-CMIP6/catalog.html.

For this study, we selected CanESM5 model based on its demonstrated skill in reproducing East African climate regimes and their associated drivers such as El Nino Southern Oscillations, Dipole modes and orientation and strength of high-pressure cells (Ayugi et al., 2022; Dufatanye Umwali et al., 2024). Thus, we obtained CanESM5 daily downscaled and bias-corrected climate variables from the NEX-GDDP-CMIP6 archive for SPEI computation. This included precipitation (P) and mean air temperature, relative humidity (RH), 2-m wind speed, and downwelling shortwave radiation. All data were accessed in NetCDF format for both the historical (1985–2014) and future (2041–2070 and 2071–2100) periods. Although multi-model ensembles provide a wider uncertainty range (Akinsanola et al., 2021), we used a single, well-performing earth systems model. This allowed a detailed bias-adjusted analysis while ensuring computational efficiency in dataset handling.

3.1.2. CanESM5 projected data

Monthly precipitation and potential evapotranspiration (PET) from TerraClimate were used as reference data for model validation and bias correction. TerraClimate provides globally consistent 4 km gridded climate data. It integrates the University of East Anglia CRU TS dataset, JRA-55 reanalysis, and WorldClim datasets, effectively capturing both long-term climatological means and monthly anomalies (Abatzoglou et al., 2018). Its integration of ground, satellite, and reanalysis data ensures high consistency and spatial detail, making it well-suited for regional drought analysis, particularly in data-sparse regions such as Uganda. TerraClimate has been widely validated and shown to perform well against station-based and reanalysis datasets, making it suitable for near-surface climate variability and water balance studies (Kolling Neto et al., 2024). For East Africa, studies like Kobusinge et al., (2024) and Ronald Ssembajwe et al., (2025) have relied on it for hydrological and agroclimatic assessments. A recent validation study against station observations by R Ssembajwe, Ngatia, et al., (2025) has shown Terra-Climate's reliability in reproducing the climatology of hydrothermal variables such as temperature, humidity and vapor pressure deficit over East Africa thus, justifying its adoption.

The dataset was accessed at http://www.climatologylab.org/terraclimate.html. Additionally, the ASTER Global Digital Elevation Model (DEM) at 30 m spatial resolution was used to derive surface atmospheric pressure for the FAO-56 Penman–Monteith PET computation.

3.2. Preprocessing

3.2.1. Data curation and quality control

All climate datasets were processed within the MATLAB R2025b environment. The NEX-GDDP-CMIP6 data were obtained as single year NetCDF files and concatenated into continuous 30-year time series for each climate variable per period: 1985-2014, 2041-2070 and 2071-2100. The datasets were then spatially subset and masked to Uganda's administrative boundaries using MATLAB's spatial masking tools. Because the NEX-GDDP-CMIP6 grid (~25 km) differed from the Terra-Climate grid (~4 km), a second-order conservative regridding technique was applied to align the CanESM5 data with the reference Terra-Climate resolution. We then explored the datasets for completeness and validity using isnan function and logical operators, respectively. The completeness test indicated no missing values.

3.2.2. Computation of PET and SPEI

3.2.2.1. Potential Evapotranspiration

The modified FAO56 (Penman-Monteith) method (equation 1) was applied to compute historical simulated and future PET using daily air mean temperature, RH, downwelling shortwave radiation, windspeed, and surface pressure derived from the DEM. We chose FAO56 because of its robustness over humid equatorial regions like Uganda (Ssembajwe et al., 2024), and its global recommendation as the empirical standard for PET computation (Allen et al., 1998). The FAO56 Penman-Monteith equation is expressed as:

$$PET = \frac{0.408\Delta(R_n - G) + \gamma \frac{900}{T + 273} U_2(e_s - e_a)}{\Delta + \gamma(1 + 0.34u_2)} \quad (1)$$

where PET is the potential evapotranspiration (mm day^{-1}), Rn is the net radiation at the crop surface (MJ m^{-2} day^{-1}), G is soil heat flux density (MJ m^{-2} day^{-1}), T is mean daily air temperature at 2 m height (°C), u_2 is wind speed at 2 m height (m s^{-1}), e_s is saturation vapor pressure (kPa), e_a is actual vapor pressure (kPa), ($e_s - e_a$) is vapor pressure deficit (kPa), Δ is slope of the saturation vapor pressure–temperature curve (kPa °C^{-1}) and γ is psychrometric constant (kPa °C^{-1}). All intermediate parameters were computed following the FAO-56 guidelines (Allen et al., 1998).

Daily PET and precipitation from CanESM5 were aggregated to monthly means to maintain temporal consistency with TerraClimate. The process involves binning daily precipitation and PET datasets into annual and monthly cycles based on the time/datetime vector corresponding to each dataset using the unique function in MATLAB (R Ssembajwe, Twah, et al., 2025). The outputs are then reshaped to the original dimensions and aggregated according to each month's length using a for loop. The resulting monthly PET and precipitation series were subsequently used in the computation of SPEI.

3.2.2.2. Standardized Precipitation-Evapotranspiration Index (SPEI)

SPEI, developed by Vicente-Serrano et al., (2010), is a widely applied multiscalar drought index that integrates both precipitation and PET to provide a more comprehensive measure of drought conditions. Unlike the Standardized Precipitation Index (SPI), which relies solely on precipitation, SPEI incorporates temperature-driven evapotranspiration, making it particularly relevant for assessing droughts under a changing climate (Vicente-Serrano et al., 2010; Wang et al., 2021). Its sensitivity to both moisture deficits and warming trends allows it to detect drought onset, persistence, and intensity across multiple timescales, from short-term agricultural droughts to long-term hydrological droughts (Wang et al., 2021).

In this study, we applied SPEI at a 3-month timescale (SPEI-03) to account for vegetation's delayed response to shocks and seasonal variability. This choice reflects Uganda's bimodal rainfall regime, where the March–May and September–November rainy seasons are critical for agriculture and water availability. Shorter timescales (1–3 months) have been shown to effectively characterize meteorological and agricultural droughts, which directly impact soil moisture and crop production (Vicente-Serrano et al., 2010). Previous East African drought studies have also adopted 3-month drought indices to assess seasonal drought dynamics in regions with strong rainfall seasonality (Ayugi et al., 2022).

The SPEI was computed by first estimating the monthly climate water balance, D, as the difference between precipitation (P) and PET (equation 2).

$$D = P - PET \quad (2)$$

where D is the monthly water balance (deficit or surplus in mm), P is the total monthly precipitation (mm), and PET is the potential evapotranspiration for the same month (mm). Positive values of D indicate moisture surplus (conditions are wetter than normal), while negative values reflect deficits, signifying drought conditions.

The accumulated water balance series (D) were fitted to a log-logistic probability distribution, following Vicente-Serrano et al., (2010). The probability density function is expressed as in equation (3).

$$f(x) = \frac{\beta}{\alpha}\left(\frac{x - \gamma}{\alpha}\right)\left[1 + \left(\frac{x - \gamma}{\alpha}\right)\right]^{-2} \quad (3)$$

where f(x) is the cumulative probability function of x (the water balance deficit D), α, β, and γ are the scale, shape, and location parameters of the distribution, respectively for D values in the range ($\gamma < x < \infty$).

Parameters of the log-logistic distribution can be estimated following the L-moment procedure (Ahmad et al., 1988). Hence, the probability distribution function of the D series, according to the log-logistic distribution, is given by equation (4).

$$F(x) = \left[1 + \left(\frac{\alpha}{x - \gamma}\right)^{\beta}\right]^{-1} \quad (4)$$

After fitting the distribution, the water balance values are transformed into standardized SPEI values. These standardized values enable comparisons across different time periods and regions. As described by Vicente-Serrano et al., (2010), the SPEI is obtained by standardizing values of $F(x)$ as in equation (5)

$$SPEI = w - \frac{c_0 + Cw + C_2 w^2}{1 + d_1 w + d_2 w^2 + d_3 w^3} \quad (5)$$

when P≤0.5, $w = \sqrt{-2\,ln(P)}$ and when P>0.5, $w = \sqrt{-2\,ln(1-P)}$

where C0 = 2.5155, C1 = 0.802853, C2 = 0.010328, d1 = 1.432788, d2 = 0.189269, and d3 = 0.001308. All these parameters are defined in the study by Vicente-Serrano et al., (2010).

The negative and positive SPEI values indicate dry and wet conditions, respectively. **Table 1** summarizes the category of dry and wet conditions based on SPEI values following the description by Mckee et al., (1993).

Table 1

Categories of dry and wet conditions indicated by SPEI values.

SPEI value	Category
2 and above	Extremely wet
1.5 to 1.99	Very wet
1.0 to 1.49	Moderately wet
-0.99 to 0.99	Near normal
−1.0 to −1.49	Moderately dry
-1.5 to -1.99	Severely dry
-2 and less	Extremely dry

3.3. Data analysis

3.3.1. Empirical Quantile Mapping (EQM) for SPEI bias correction

Although the NEX-GDDP-CMIP6 data used for SPEI computation were already downscaled and bias-corrected, we applied an additional correction to further align CanESM5-simulated SPEI values with the TerraClimate-based SPEI. This was achieved using the EQM technique.

EQM corrects systematic deviations by mapping the cumulative distribution function (CDF) of the model outputs to that of the reference dataset (Li et al., 2023; Niranjan Kumar et al., 2022; Ernawati et al., 2018). Unlike parametric approaches, EQM does not assume a specific theoretical distribution for the data (Niranjan Kumar et al., 2022). This makes it suitable for climate variables such as precipitation and SPEI that often exhibit skewed or multimodal behavior. Mathematically, the bias-adjusted value x_a can be expressed by equation (6).

$$x_a = F_o^{-1}\left(F_m(x_m)\right) \quad (6)$$

where F_m and F_o^{-1} and represent the empirical cumulative distribution and its inverse for the model and observed datasets, respectively.

The corrected SPEI outputs were validated against TerraClimate-based SPEI for the historical period using histogram and kernel density estimation (KDE) plots. This helped to assess distributional consistency. It was also validated through grid-level time series comparisons to evaluate temporal coherence.

3.3.2. Drought characteristics

Drought events were identified using the run theory approach as proposed by Li et al. (Yevjevich, 1967). A run is the portion of all values in a time series that is below or above a cutoff threshold. Here, sequences of consecutive periods during which the drought index remained below -1 (SPEI ≤ –1) were isolated. Each continuous sequence below this threshold was defined as a single drought event, beginning at the onset (first month below –1) and ending when SPEI exceeded –1. This approach allowed for the systematic identification and quantification of individual drought events from a continuous SPEI time series. After identifying drought events, key drought characteristics including duration, severity, intensity, and frequency were computed using equations (7–10).

i. Drought Duration (DD) refers to the number of consecutive months from onset (SPEI≤-1) until cessation (SPEI > -1). Average drought duration across the study period was calculated using equation (7).

$$\overline{DD} = \frac{\sum_{i=1}^{N} DDi}{N} \tag{7}$$

where i is the event and *N* is the total number of drought events

ii. Drought Severity (DS) refers to the cumulative magnitude of drought over its duration, defined as the absolute sum of SPEI values below the threshold as in equation (8).

$$\mathrm{DS} = \sum_{t=t_{stat}}^{t_{end}} |SPEI_t| \tag{8}$$

where $\boldsymbol{S}PEI_t$ is the SPEI value at time t and *N* is the duration of the drought in months

iii. Drought Intensity (DI) refers to the average severity per month during a drought event and is given by equation (9).

$$DI = \frac{DS}{DD} \tag{9}$$

iv. Drought Frequency (DF) refers to the number of drought events relative to the length of the study period, given by equation (10).

$$DF = \frac{Number\ of\ drought\ events}{Total\ number\ of\ months} \tag{10}$$

3.3.3. Hotspot analysis

Spatial hotspots of drought intensity and frequency were identified using the Getis-Ord Gi* statistic (Getis and Ord, 1992) implemented, in MATLAB R2025b. The method detects statistically significant clusters by comparing the local sum of each grid cell and its neighbors to the global mean of the study area (Nejadrekabi et al., 2021; Rousta et al., 2017). The Gi* statistic measures whether high or low values occur together in space more often than would be expected by random chance, thereby highlighting hotspots (clusters of high drought values) and coldspots (clusters of low drought values). The Getis-Ord Gi* statistic is given by Equation (11) with its terms defined by equations (12) and (13).

$$G_i^* = \frac{\sum_{j=1}^{n} w_{ij}x_j - \bar{x}\sum_{j=1}^{n} w_{ij}}{S\sqrt{\frac{n\sum_{j=1}^{n} w_{ij} - \left(\sum_{j=1}^{n} w_{ij}\right)^2}{n-1}}} \quad (11)$$

$$\bar{X} = \frac{1}{n}\sum_{j=1}^{n} x_j \quad (12)$$

$$S = \sqrt{\frac{1}{n}\sum_{j=1}^{n} x_j^2 - (\bar{x})^2} \quad (13)$$

where G_i^* is the Getis-Ord local statistic for location i, x_j is the drought variable value at location j. w_{ij} is the spatial weight between locations i and j, n is the total number of locations (grid cells), $\bar{X}$ is the mean of all x_j and S is the standard deviation of x_j. The weights w_{ij} define spatial proximity based on a fixed-distance band, such that nearby grid cells exert stronger influence on Gi* values.

Each grid cell receives a Z-score indicating the degree of spatial clustering. High positive Z-scores denote hotspots (areas with significantly high drought values), whereas negative Z-scores indicate coldspots (areas with low drought values). Z-scores close to zero reflect random spatial patterns. Statistical significance was evaluated at $p < 0.05$, with larger absolute Z-scores corresponding to stronger spatial clustering.

The Getis-Ord Gi* method was selected because it effectively captures localized spatial dependence, accounting for both the magnitude and spatial context of drought indicators. Compared with global statistics such as Moran's I, Gi* detects fine-scale clustering of extremes (Akhter and Afroz, 2024; Nejadrekabi et al., 2021), making it particularly suitable for identifying regions with persistently high drought stress. This approach has been widely used in environmental and climate risk analyses for detecting areas of recurrent hazard concentration (Azeez et al., 2025; Nejadrekabi et al., 2021; Rousta et al., 2017).

3.3.4. Trend analysis

Temporal trends in SPEI and derived drought characteristics were analyzed using the Mann–Kendall test (Kendall, 1975; Mann, 1945; Haidu, 1997; Haidu & Magyari-Sáska, 2009) and Sen's slope estimator (Sen, 1968). The Mann–Kendall test is a non-parametric approach that determines the direction and significance of trends without requiring data normality. It is robust to missing values and outliers, making it suitable for climatological time series. Sen's slope estimator provides the rate of change by computing the median of all pairwise slopes between observations, thereby reducing the influence of extreme values and non-uniform sampling. All results were visualized in MATLAB's geospatial mapping toolbox using interpolation and k-means clustering to enhance spatial representation.

4. RESULTS

4.1. Model bias correction and validation

Fig. 2 illustrates the distributional comparison between observed, modelled, and bias-adjusted SPEI-03 values. The upper panel shows histograms, while the lower panel presents the corresponding KDE. Before bias correction, both historical and future modelled SPEI values exhibited systematic deviations from the observed distribution, with noticeable shifts around the mean and differences in tail behaviour. After applying EQM, the bias-adjusted SPEI distributions closely matched the observed pattern across the entire range of values. The KDE curves demonstrate a strong overlap between the observed (black line) and the historical bias-adjusted (purple) and future (blue) series.

This indicates a substantial correction of mean and variance biases. This alignment suggests that the EQM approach effectively removed systematic errors associated with the CanESM5 model, ensuring consistent representation of both dry (negative SPEI) and wet (positive SPEI) extremes. The strong correspondence between observed and adjusted datasets indicates that the CanESM5 outputs, after correction, are reliable for subsequent drought characterization and projection analysis.

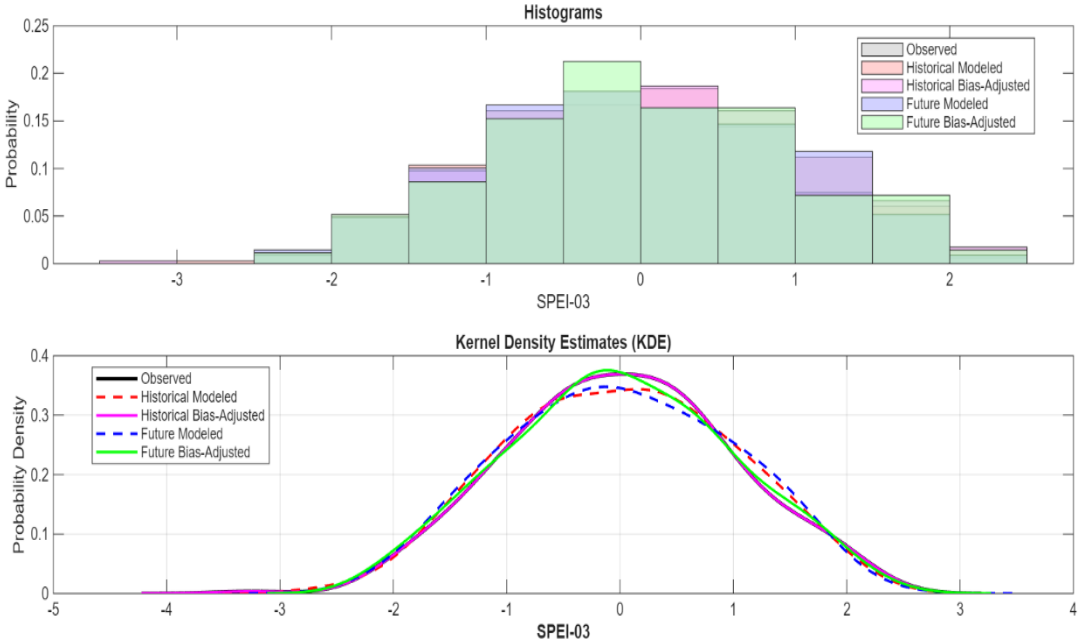


Fig. 2. Comparisons of observed, modeled, and bias-adjusted SPEI-03 distributions using histograms (top) and kernel density estimates (bottom).

4.2. Observed drought characteristics (1985-2014)

Fig. 3 illustrates the spatial distribution of historical drought duration, severity, intensity, and frequency across Uganda from 1985 to 2014, derived from SPEI-03. Observed drought duration (**Fig. 3a**) generally ranged between 2–4 months per event, with the longest durations (3–4 months) concentrated in the Southern Uganda and parts of Lake Victoria basin. The north, eastern and central regions exhibit relatively shorter events lasting 2–4 months. The spatial pattern of drought severity (**Fig. 3b**) indicates that the northwestern and central parts of Uganda experienced the most severe droughts, with mean severity values exceeding 1.5. In contrast, eastern and some parts of western Uganda show lower severity, suggesting that droughts there tend to be milder and shorter-lived.

Drought intensity (**Fig. 3c**), representing the average magnitude of water deficit per month, is highest across northwestern and some localized western parts of the country, with mean values approaching 0.7. Moderate intensity (0.4–0.6) occurs in the central, western, and parts of the Lake Victoria basin, whereas the northeastern, western highlands, and localized areas around Lake Victoria record the lowest intensities (≈0.3). This spatial pattern indicates that drought events exert stronger stress in the semi-arid north and southwestern subregions, consistent with their lower rainfall and higher evapotranspiration regimes.

Drought frequency (**Fig. 3d**) ranges between 10% and 25%, with the highest recurrence (>20%) observed across the northeastern, southern, southwestern, and Lake Victoria basin regions. The central parts of Uganda exhibit moderate frequencies (10–15%). This spatial pattern corresponds with historical records of recurrent droughts in the semi-arid north and the cattle corridor, highlighting these areas as long-standing zones of climatic stress.

Overall, the observed drought characteristics highlight a north–south gradient, with droughts becoming more frequent, severe, and intense toward the semi-arid north while the central remain relatively resilient. To further identify areas with spatial clustering of drought extremes, a hotspot analysis was conducted using the Getis-Ord Gi statistic based on drought frequency.

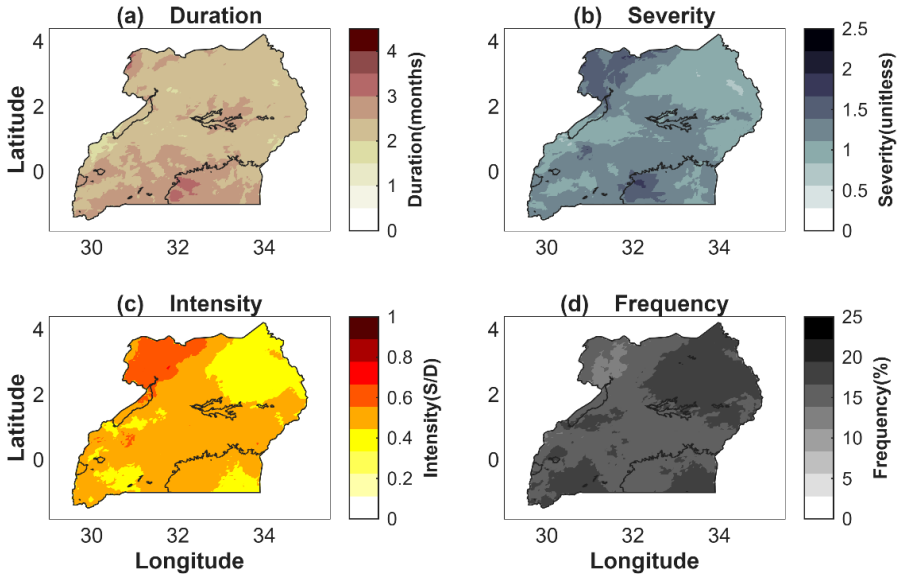


Fig. 3. Spatial distribution of observed drought characteristics across Uganda for 1985–2014 derived from SPEI-03: (a) drought duration (months), (b) drought severity (unitless), (c) drought intensity (average severity per drought month, S/D), and (d) drought frequency (%).

4.3. Observed drought hotspots

The observed drought hotspot analysis (**Fig. 4**) reveals distinct spatial clustering of historically drought-prone areas across Uganda. Significant hotspots are concentrated in the northeastern and eastern regions, covering parts of Teso, Lango, Acholi and much of Karamoja subregions. Additional clusters appear around the southwestern areas, particularly the Ankole subregion. All these areas fall within the famous Uganda's cattle corridor which has been severally reported as a drought hotspot. Another significant hotspot patch was revealed in the Lake Victoria basin. These areas represent zones with higher drought intensity and frequency, indicating persistent exposure to recurrent dry conditions. In contrast, most of central and northwestern Uganda show statistically insignificant patterns, suggesting relatively lower drought clustering during the observation period.

4.4. Observed SPEI-03 drought trends

The spatial pattern of the observed SPEI-03 (**Fig. 5**) shows that most parts of Uganda experienced increasing drought trends between 1985 and 2014. Results from the Mann–Kendall test indicate that the northern and western regions had statistically significant positive trends (stippling in **Fig 5**). This indicates that droughts have become more frequent and severe in these areas. The strongest drying is observed in northern Uganda, particularly in the Lango and Acholi subregions, where Sen's slope values exceed 8×10^{-5} units month^{-1}. In contrast, some parts of the southwestern highlands and the far northeast show decreasing drought tendencies, although these changes are not statistically significant and do not suggest a reversal of the overall trend. Overall, the findings suggest that Uganda has been getting progressively drier over the past four decades. The northern and western regions stand out as the most drought-prone zones. These are key agricultural and pastoral areas, implying growing vulnerability of rain-fed farming and livestock production to declining water availability.

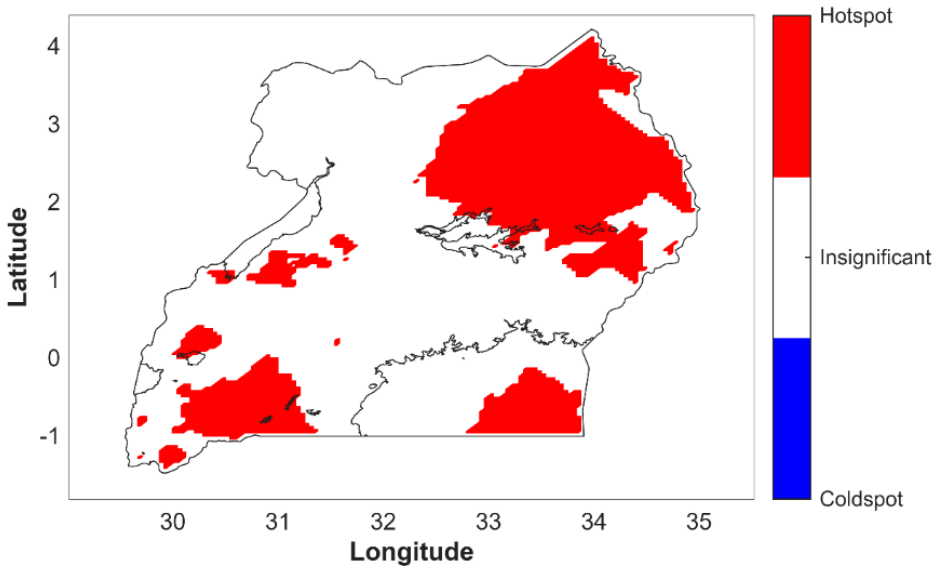


Fig. 4. Spatial distribution of drought hotspots across Uganda based on the Getis-Ord Gi* statistic derived from TerraClimate-based SPEI-03 data. Red areas indicate statistically significant drought hotspots ($p < 0.05$), blue areas represent cold spots, and white areas are insignificant regions.

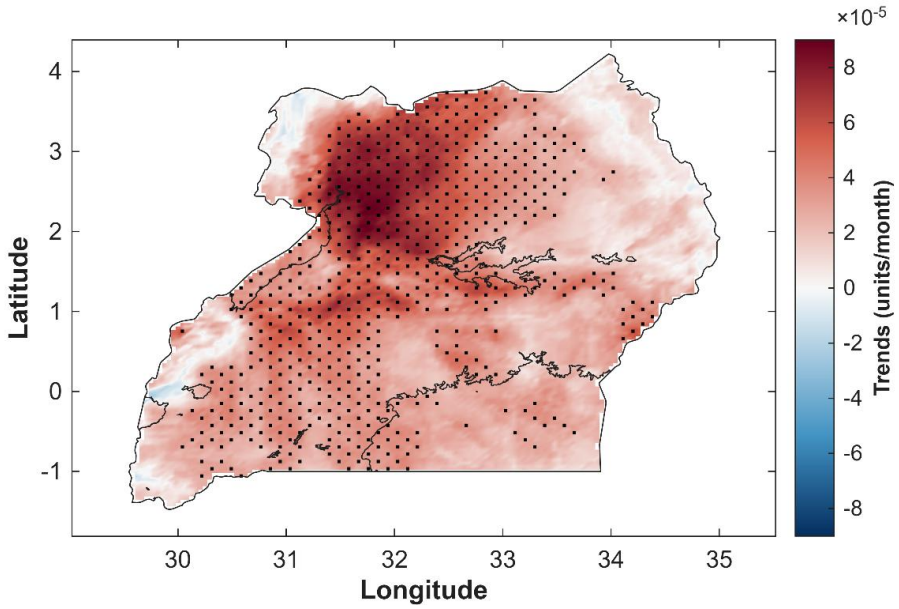


Fig. 5. Historical trends in SPEI-03 droughts (1985–2014) across Uganda derived from TerraClimate data. Stippling indicates areas where trends are statistically significant at $p < 0.05$ based on the Mann–Kendall test.

4.5. Projected drought characteristics

Projected drought characteristics exhibit substantial spatial and temporal variability across Uganda under the three emission scenarios (SSP1-2.6, SSP2-4.5, and SSP5-8.5) and two future periods (2041–2070 and 2071–2100). Generally, droughts are projected to become more frequent, longer, and more severe under higher-emission scenarios, especially toward the late century.

4.5.1. Duration

Projected drought duration shows distinct spatial and temporal variability across Uganda (**Fig. 6**). Under SSP1-2.6, droughts remain relatively short, averaging 1.5–2.5 months, with minimal spatial change throughout the century. In contrast, SSP2-4.5 projects longer droughts, particularly in northern Uganda, where the mean duration reaches 3–4 months during both mid- and late-century. Under SSP5-8.5, prolonged drought episodes expand toward central and western Uganda by the late century, with durations exceeding 3 months in several grid cells. Overall, longer drought events are projected under higher-emission scenarios, emphasizing increased persistence of dry spells with rising radiative forcing.

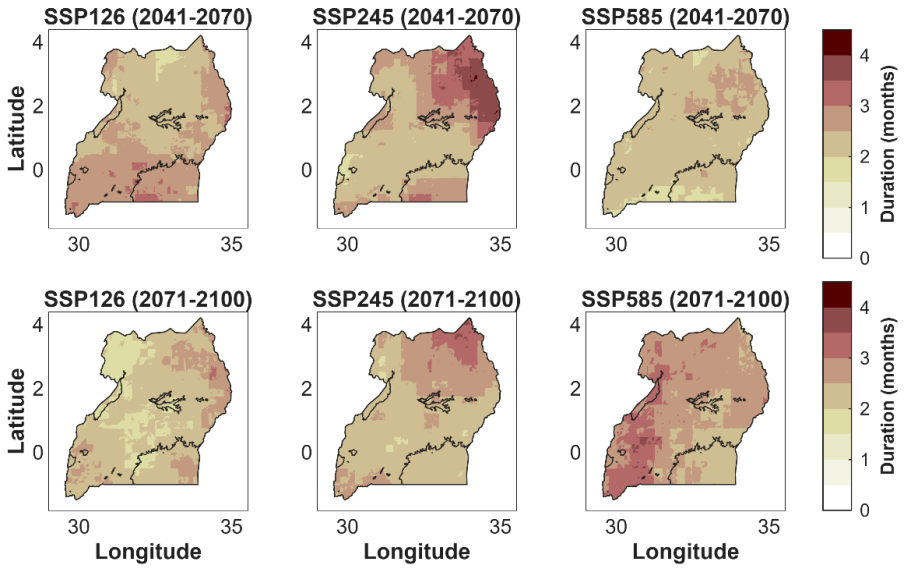


Fig. 6. Projected spatial distribution of mean drought duration (months) for SPEI-03 drought events in Uganda under three SSPs and two future periods. Top: mid-century (2041–2070); bottom: late-century (2071–2100).

4.5.2. Drought frequency

Projected drought frequency displays almost similar patterns in specific regions of the country (**Fig. 7**). Generally, drought occurrence remains moderate (10–15%) in the central and northwestern parts of the country throughout century. Higher recurrence is confined to the northeastern, southern and southwestern parts (up to 25%).

4.5.3. Drought severity

Projected drought severity exhibits clear spatial heterogeneity across Uganda, with the northern regions emerging as the most drought-prone areas (**Fig. 8**). During the mid-century period (2041–2070), drought severity across Uganda remains moderate under SSP1-2.6, with most areas exhibiting values below 1.5, except for localized areas of higher severity in the northwestern region. Under SSP2-4.5, severity increases markedly in the north, exceeding 1.5, suggesting longer and more intense dry episodes. Conversely, severity reduces under SSP5-8.5 for mid-century, showing values generally below 1.5 across the country. By the late century (2071–2100), drought severity slightly weakens nationwide under SSP1-2.6 and SSP2-4.5, indicating possible recovery under low-emission stabilization. However, there is intensification of severity under SSP5-8.5 across most parts of the country. The northwestern region experiences a clear intensification, with severity values surpassing 2.0, implying the occurrence of more extreme and prolonged droughts. Meanwhile, the southern and parts of the central regions maintain lower severity levels. These findings reveal a northward shift and amplification of drought severity under intermediate to high emission scenarios.

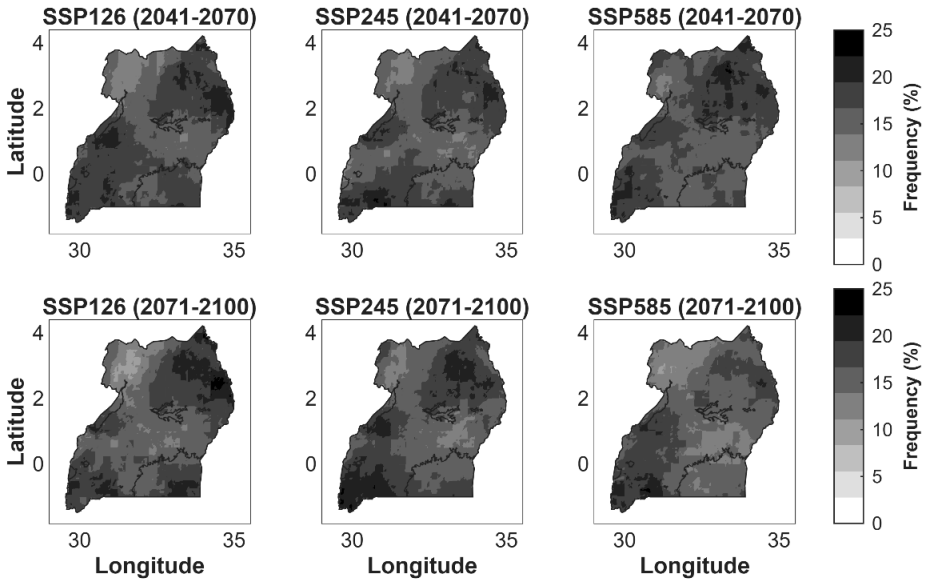


Fig. 7. Projected spatial distribution of drought frequency (%) across Uganda under three SSP scenarios for mid-century (2041-2070, top) and late century (2071-2100, bottom). Darker shades indicate higher drought recurrence based on SPEI ≤ –1

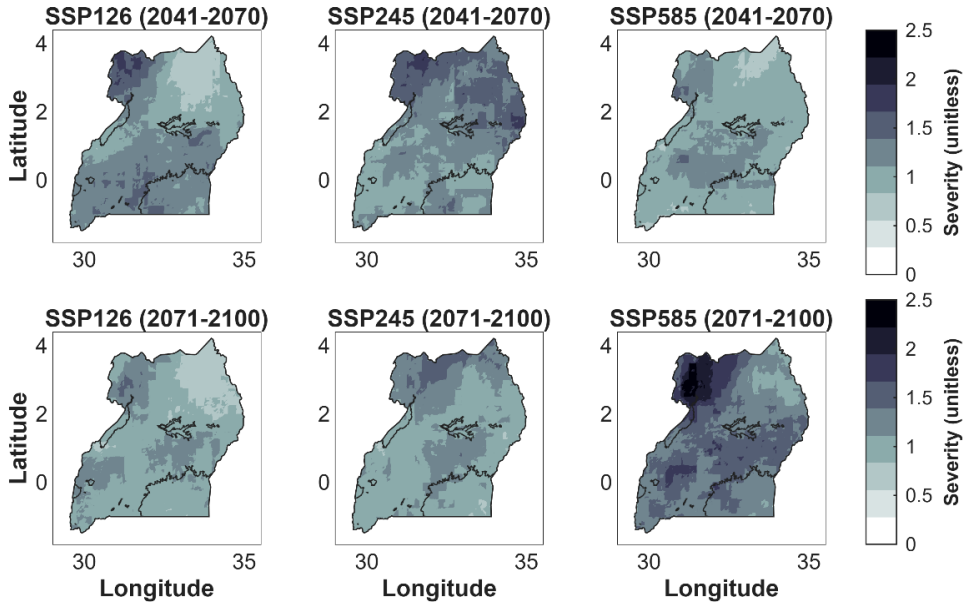


Fig. 8. Projected spatial distribution of drought severity across Uganda under SSP1-2.6, SSP2-4.5, and SSP5-8.5 for mid-century (2041–2070, top) and late-century (2071–2100, bottom). Darker shades indicate higher drought severity.

4.5.4. Drought intensity

During the mid-century (2041–2070), drought intensity is highest in the northwestern parts, with S/D values commonly between 0.5 and 0.8 under all the SSPs (**Fig. 9**). The central, western, and

southern Uganda remains moderate (≈0.3–0.5). By the late century (2071–2100), intensity increases and broadens under SSP5-8.5, exhibiting the strongest amplification, with extensive areas in the north, central, and eastern regions reaching S/D ≈0.7–1.0. These patterns indicate that, under higher emissions, drought months are projected to become substantially more severe on average, posing greater stress to agriculture and water resources.

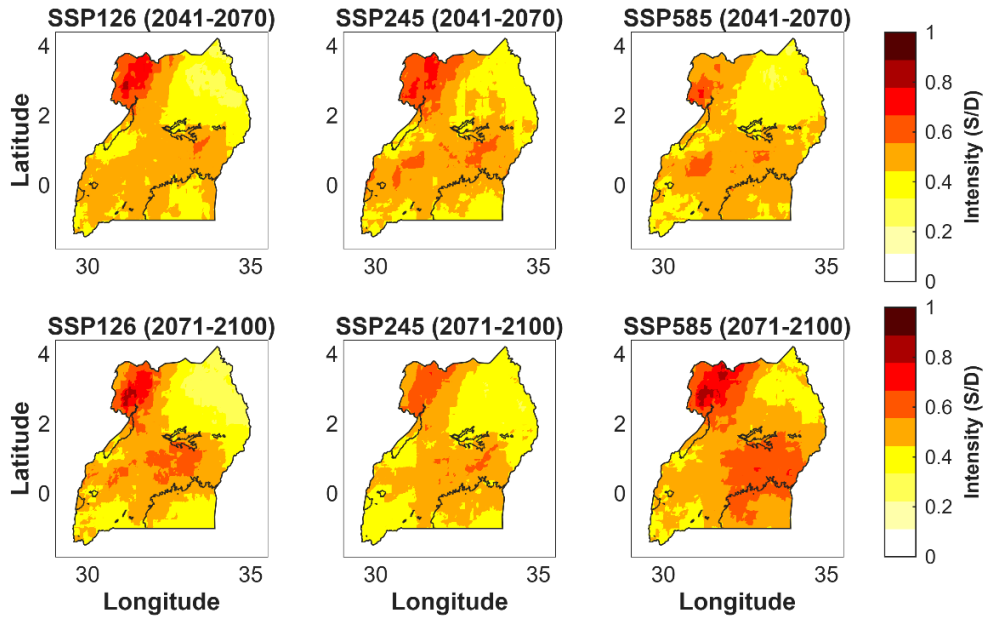


Fig. 9. Projected spatial distribution of drought intensity (average severity per drought month, S/D) for mid-century (2041–2070, top row) and late-century (2071–2100, bottom row) under SSP1-2.6, SSP2-4.5 and SSP5-8.5. Higher S/D values (darker red) indicate stronger average monthly drought deficits.

4.6. Projected hotspots

The Getis-Ord Gi* spatial statistic identified statistically significant and persistent drought hotspots primarily concentrated in northeastern, western and southwestern Uganda for the entire century (**Fig. 10**). This is particularly across the Karamoja, Kigezi and Ankole sub regions. These regions, which form the core of Uganda's cattle corridor, exhibited recurrent spatial clustering of high drought intensity and frequency ($p < 0.05$). Additional hotspot clusters were observed around the Lake Victoria basin, particularly under low emission scenarios for both mid and late centuries, reflecting localized drought susceptibility in this humid zone. They become less extensive under high emission scenarios.

The spatial persistence of these hotspots from the mid-century (2041–2070) to the late-century (2071–2100) periods suggests a sustained spatial anomaly in drought occurrence relative to surrounding areas. In certain areas, such as the northeastern and western zones, hotspots expand and intensify. In others, particularly parts of the Lake Victoria basin and eastern Uganda, they shrink or shift, suggesting evolving drought regimes.

The alignment of these statistically significant clusters with key agricultural and pastoral landscapes indicates that drought risks in these regions are likely to remain recurrent under future climatic conditions. This necessitates targeted adaptation strategies focused on water resource management, livestock systems, and agricultural resilience.

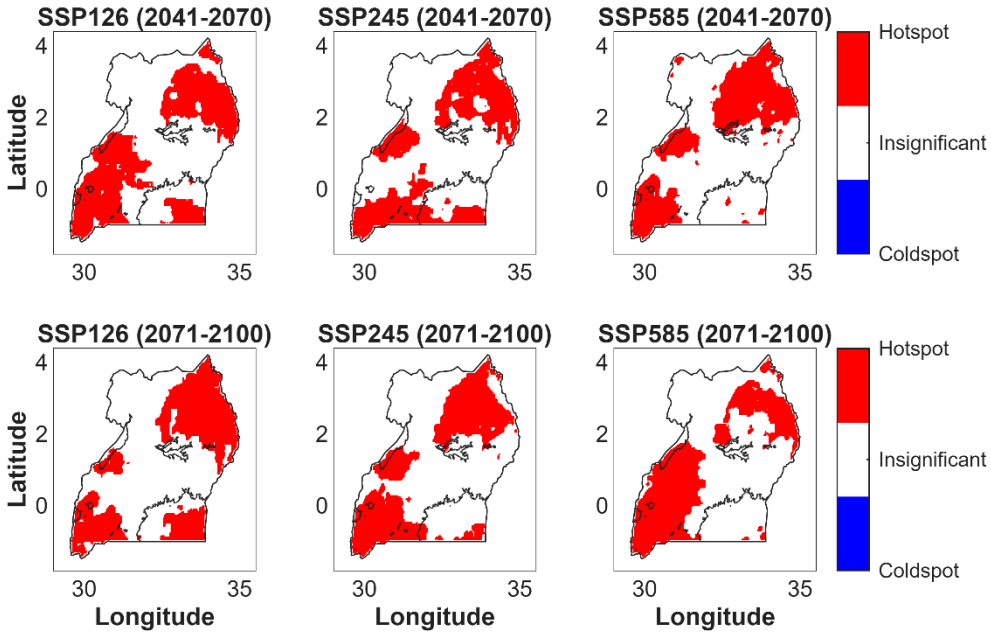


Fig. 10. Projected drought hotspot clusters (Getis-Ord Gi*, $p < 0.05$) for mid-century (2041–2070, top row) and late-century (2071–2100, bottom row) under SSP1-2.6, SSP2-4.5 and SSP5-8.5. Red indicates statistically significant drought hotspots; blue indicate cold spots and white indicates areas with insignificant hotspots.

4.7. Projected drought trends under different SSP scenarios

Projected SPEI-03 drought trends show marked spatial variability across Uganda, with the direction and magnitude of change differing between the mid-century (2041–2070) and late-century (2071–2100) periods across all emission scenarios (**Fig. 11**).

During the mid-century, drought occurrence significantly increases under SSP1-2.6, especially across central and northern Uganda, including areas around Lake Kyoga and the upper northern districts. Under SSP2-4.5, significant decreases in drought occurrence are projected across the central–western stretch of the country, while isolated increases persist over the Kyoga–Teso subregion. The high-emission SSP5-8.5 scenario, meanwhile, projects significantly decreasing drought trends over the Karamoja region in northeastern Uganda, suggesting localized improvement in short-term moisture conditions.

By the late century, the spatial configuration of droughts changes considerably. Under SSP1-2.6, most of the country experiences decreasing drought trends, especially across the western highlands, Lake Victoria basin, and northern zones. SSP2-4.5 exhibits a contrasting spatial pattern, with increasing drought trends concentrated in eastern Uganda, while decreasing trends dominate the West Nile. In contrast, the high-emission SSP5-8.5 scenario is dominated by significant increases in drought occurrence across southern, western, southwestern, and northern Uganda. These widespread positive trends indicate that droughts are projected to intensify and occur more frequently by the end of the century. Overall, the strongest increasing trends are projected under SSP5-8.5 during the late-century period, underscoring heightened drought risks under high-emission pathways.

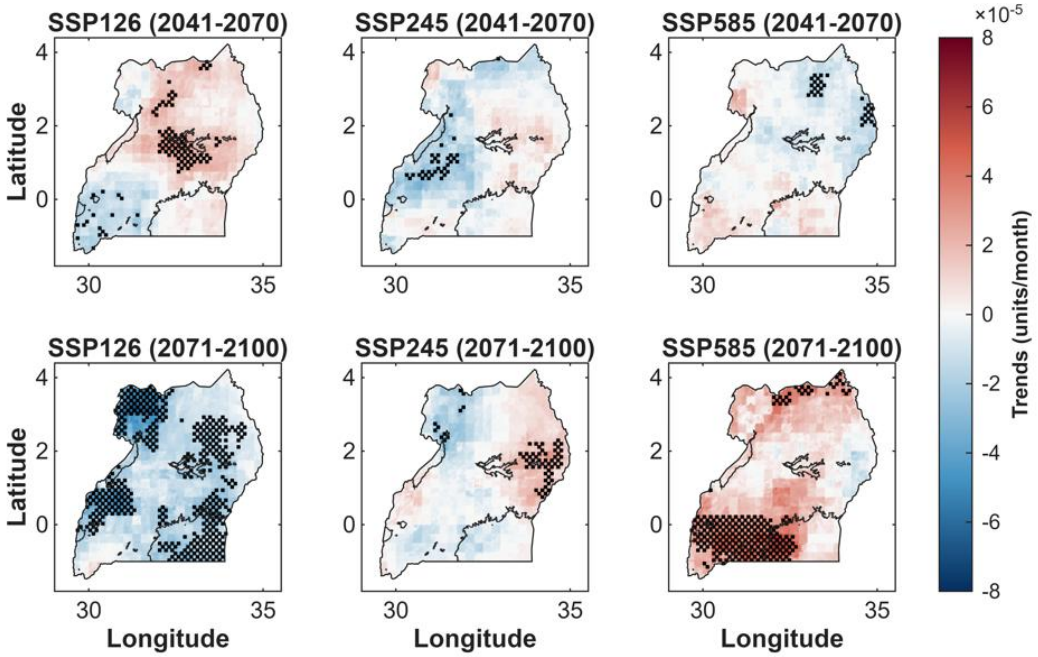


Fig. 11. Projected SPEI-03 trends across Uganda under SSP1-2.6, SSP2-4.5, and SSP5-8.5 for mid-century (2041–2070) and late-century (2071–2100) periods. Stippled areas denote statistically significant changes ($p < 0.05$).

5. DISCUSSION

5.1. Spatial and temporal dynamics of drought in Uganda

This study reveals that drought patterns in Uganda exhibit regional, scenario, and temporal variations. Under SSP1-2.6, drought occurrence increases during the mid-century in central and northern Uganda but decreases toward the late century. Under SSP2-4.5, droughts decrease in the central and western regions during the mid-century, then increase in eastern Uganda by the late century. Under SSP5-8.5, droughts decrease in Karamoja during the mid-century but become widespread and intense across the north, west, and south toward the late century. These shifts reflect the strong influence of rising temperatures and higher evapotranspiration (Ojara et al., 2024), which can offset rainfall gains and produce uneven drought outcomes.

The semi-arid north remains the most sensitive region. Droughts there often last two to four months and occur more frequently than in other parts of the country. This supports earlier evidence that Karamoja and the surrounding districts face persistent agricultural and hydrological droughts linked to short wet seasons and delayed rainfall onset (Byakatonda et al., 2021). Central and northwestern Uganda also shows signs of increasing drought risk, in line with past assessments by Kyatengerwa et al., (2020).

Hotspot analysis confirms that drought clusters remain strongest in the cattle corridor and extend from southwestern Uganda through the west and into the northeast. These are critical regions that support mixed farming and livestock. Mulinde et al., (2016) similarly identified the cattle corridor as a major climate risk zone due to its frequent dry spells and limited water storage capacity. Nalwanga et al., (2024) also reported that droughts in this region often persisted for several months, occasionally extending over multiple years under high-emission conditions. The persistence of these hotspots across scenarios and time periods suggests that drought risk is entrenched and unlikely to diminish. The Lake Victoria basin also exhibits localised hotspots in several scenarios, highlighting the sensitivity of this humid zone to short dry spells.

Across the country, drought patterns do not follow a single direction. Some regions experience temporary reductions in drought severity, particularly under SSP1-2.6 and mid-century SSP5-8.5, while others show apparent intensification. This mixed response aligns with the East African climate paradox, where rainfall may increase in parts of the region, but water stress still rises due to warming. Uganda's future drought landscape will therefore be shaped by localised hotspots rather than uniform drying. These areas, particularly the cattle corridor, Lake Victoria basin, and Karamoja, already experience livelihood stress (Nalwanga et al., 2025). Therefore, they should remain priority zones for targeted adaptation, improved water management, and climate-resilient livelihood strategies.

5.2. Contributions

High-resolution drought modelling using NEX GDDP CMIP6 downscaled to about 4 km for detailed national analysis. Integration of multiple drought metrics and hotspot detection to identify not only where droughts intensify but also where they cluster persistently in the whole country.

Scenario-based insights that show how drought patterns may diverge under low and high emissions, providing valuable input for policy and planning. Clear linkage between mapped hotspots and key livelihood zones that need targeted adaptation.

5.3. Limitations and future work

The analysis used a single GCM (CanESM5) from NEX-GDDP-CMIP6, which does not capture inter-model variability and uncertainty. Although the spatial resolution was improved through downscaling, localised microclimatic variations, especially in complex terrains such as highlands, may not be fully resolved. Future work should utilise multi-model ensembles and incorporate soil moisture, runoff, and vegetation indices to deepen the understanding. Linking drought metrics to crop yield, livestock loss, and water supply impacts would strengthen the practical value of the results. Including socioeconomic exposure and vulnerability data would also improve national drought risk assessments.

6. CONCLUSIONS

This study provides a national-scale assessment of historical and future droughts in Uganda using bias-adjusted CanESM5 data and SPEI. The combination of TerraClimate observations and downscaled projections produced a consistent picture of drought behavior across the country. Historical analysis shows strong drying in the north and parts of central Uganda. Future patterns differ across scenarios and time periods. Under SSP1-2.6, drought conditions remain mild except for a mid-century increase in central and northern Uganda. Under SSP2-4.5, droughts decrease in the central west during the mid-century but increase in eastern Uganda toward the late century. Under SSP5-8.5, droughts weaken in Karamoja during the mid-century but intensify across the north, west, and south by the end of the century.

Hotspot analysis reveals persistent clusters along the cattle corridor, extending from the Ankole and Kigezi regions to the west, through to Karamoja. These clusters indicate long-term drought stress in areas that depend on rainfed farming and pastoralism. The duration and frequency of droughts in these zones point to limited recovery capacity under future warming. Uganda's drought future is therefore uneven, with risks concentrated in specific agroecological regions. These findings support the need for locally tailored adaptation strategies and improved water management. They also emphasize the importance of integrating fine-scale climate information with agricultural systems, livestock, and livelihood resilience planning.

ACKNOWLEDGEMENTS

The corresponding author wishes to thank for the support from the European Commission through the Erasmus+ KA171 program which enabled the contribution to the development of education and research in the partner country Uganda. Dimitrie Cantemir University IR-BE-200465 project provided funding for the open access publication of this paper.

REFERENCES

Abatzoglou JT, Dobrowski SZ, Parks SA, et al. (2018) TerraClimate, a high-resolution global dataset of monthly climate and climatic water balance from 1958–2015. *Scientific Data* 5(1): 170191.

Ahmad MI, Sinclair CD and Werritty A (1988) Log-logistic flood frequency analysis. *Journal of Hydrology* 98(3–4): 205–224.

Akhter J and Afroz R (2024) Influence of climate variability and land cover dynamics on the spatio-temporal NDVI patterns in western hydrological regions of Bangladesh. *Heliyon* 10(12): e32625.

Akinsanola AA, Ongoma V and Kooperman GJ (2021) Evaluation of CMIP6 models in simulating the statistics of extreme precipitation over Eastern Africa. *Atmospheric Research* 254: 105509.

Allen RG, Raes D, Smith M, et al. (1998) *Crop Evapotranspiration : Guidelines for Computing Crop Water Requirements*. F.A.O.

Ayugi B, Shilenje ZW, Babaousmail H, et al. (2022) Projected changes in meteorological drought over East Africa inferred from bias-adjusted CMIP6 models. *Natural Hazards* 113(2). Springer Science and Business Media B.V.: 1151–1176.

Azeez M, Al Sharaa H and Ziboon AR (2025) Mapping agricultural lands at risk of meteorological drought in iraq using geostatistics. *Engineering and Technology Journal* 0(0): 1–14.

Baogang Y, Linxiao W, Hongyu T, et al. (2024) Future changes in extremes across China based on NEX-GDDP-CMIP6 models. *Climate Dynamics*. Springer Science and Business Media Deutschland GmbH. Epub ahead of print 1 October 2024. DOI: 10.1007/s00382-024-07408-7.

Byakatonda J, Openy G, Sempewo JI, et al. (2021) Over a century evidence of historical and recent dryness/wetness in sub-humid areas: A Uganda, East African case. *Meteorological Applications* 28(5).

Byamukama O, Ridwan WA and Biney MA (2025) Sustainability assessment of Uganda's Mabira, Budongo, and Kibale forest reserves. *Discover Environment* 3(1): 131.

Calverley CM and Walther SC (2022) Drought, water management, and social equity: Analyzing Cape Town, South Africa's water crisis. *Frontiers in Water* 4.

Ceola S, Mård J and Di Baldassarre G (2023) Drought and Human Mobility in Africa. *Earth's Future* 11(12). de Mendonça LM, Blanco CJC and da Silva Cruz J (2024) Performance and projections of the NEX-GDDP-CMIP6 in simulating precipitation in the Brazilian Amazon and Cerrado biomes. *International Journal of Climatology* 44(11): 3726–3741.

Dufatanye Umwali E, Chen X, Odhiambo Ayugi B, et al. (2024) Estimating the Effects of Climate Fluctuations on Precipitation and Temperature in East Africa. *Atmosphere* 15(12): 1455.

Elkouk A, El Morjani ZEA, Pokhrel Y, et al. (2021) Multi-model ensemble projections of soil moisture drought over North Africa and the Sahel region under 1.5, 2, and 3 °C global warming. *Climatic Change* 167(3–4): 52.

Ernawati NM, Torpan A, Voda M (2018) Geomedia role for Mountain Routes Development. Mesehe and Pisoiu Waterfall comparative study. *Geographia Technica* 13(1), 41-51.

Getis A and Ord JK (1992) The Analysis of Spatial Association by Use of Distance Statistics. *Geographical Analysis* 24(3): 189–206.

Haidu, I., (1997) Analiza seriilor de timp. Aplicatii în hidrologie. (*Time series analysis. Applications in hydrology* In romanian). Editura *H*G*A*, Bucuresti. ISBN: 973-98077-39. https://www.researchgate.net/publication/297032182_Analiza_seriilor_de_timp_Aplicatii_in_hidrologie

Haidu I. & Magyari-Sáska Z. (2009) *Animated sequential trend signal detection in finite samples*, Proceedings of the ITI 2009, 31st *International Conference on Information Technology Interfaces*, Cavtat, Croatia, Publisher: IEEE, pp. 249-254, DOI: 10.1109/ITI.2009.5196088.

Han X, Li Y, Yu W, et al. (2022) Attribution of the Extreme Drought in the Horn of Africa during Short-Rains of 2016 and Long-Rains of 2017. *Water* 14(3): 409.

IPCC (2022) *Technical Summary Frequently Asked Questions Part of the Working Group II Contribution to the Sixth Assessment Report of the Intergovernmental Panel on Climate Change*. Available at: www.environmentalgraphiti.org.

Jury MR (2018) Uganda rainfall variability and prediction. *Theoretical and Applied Climatology* 132(3–4): 905–919.

Kendall (1975) *Rank Correlation Methods*. 4th ed. London: Charles Griffin.

Kobusinge J, Twesigye CK, Kagezi GH, et al. (2024) Soil Moisture Content Suitability for Coffee Growing under Climate Change East African Scholars Journal of Agriculture and Life Sciences Soil Moisture Content Suitability for Coffee Growing under Climate Change Scenarios in Uganda. *East African Scholars Journal of Agriculture and Life Sciences* 7(11).

Kolling Neto A, Ribeiro RB, Fraga M de S, et al. (2024) Estimating water balance in a Brazilian semiarid watershed using different spatial data. *Journal of South American Earth Sciences* 140: 104930.

Krishna Prabhakar SVR (2022) Implications of Regional Droughts and Transboundary Drought Risks on Drought Monitoring and Early Warning: A Review. *Climate* 10(9): 124.

Kyatengerwa C, Kim D and Choi M (2020) A national-scale drought assessment in Uganda based on evapotranspiration deficits from the Bouchet hypothesis. *Journal of Hydrology* 580. Elsevier B.V.

Li X, Wu H, Nanding N, et al. (2023) Statistical Bias Correction of Precipitation Forecasts Based on Quantile Mapping on the Sub-Seasonal to Seasonal Scale. *Remote Sensing* 15(7). MDPI.

Li L, Du Q, Ren F, Huang L, Voda M, Ning P (2023) Geolocated social media data for measuring park visitation in Shenzhen, China, Urban Forestry & Urban Greening, Volume 88,128069, https://doi.org/10.1016/j.ufug.2023.128069

Lombe P, Carvalho E and Rosa-Santos P (2024) Drought Dynamics in Sub-Saharan Africa: Impacts and Adaptation Strategies. *Sustainability* 16(22): 9902.

Mann HB (1945) Nonparametric Tests Against Trend. *Econometrica* 13(3): 245.

Mathivha FI, Mabala L, Matimolane S, et al. (2024) El Niño-Induced Drought Impacts on Reservoir Water Resources in South Africa. *Atmosphere* 15(3): 249.

Mckee TB, Doesken NJ and Kleist J (1993) *The Relationship of Drought Frequency and Duration to Time Scales*. *Eighth Conference on Applied Climatology*.

Mulinde C, Mwanjalolo M and Egeru A (2016) *Meteorological Drought Occurrence and Severity in Uganda*. Available at: https://www.researchgate.net/publication/316701990.

Najjuma M, Nimusiima A, Sabiiti G, et al. (2021) Characterization of Historical and Future Drought in Central Uganda Using CHIRPS Rainfall and RACMO22T Model Data. *International Journal of Agriculture and Forestry* 2021(1): 9–15.

Nakalembe C (2018) Characterizing agricultural drought in the Karamoja subregion of Uganda with meteorological and satellite-based indices. *Natural Hazards* 91(3). Springer Netherlands: 837–862.

Nalwanga FS, Nanteza J, Obua J, et al. (2024) Insights into meteorological drought: navigating Uganda's cattle corridor through past trends and future projections. *Natural Hazards* 120(9). Springer Science and Business Media B.V.: 8695–8721.

Nalwanga FS, Kisira Y and Mukwaya PI (2025) Resilience to drought in Uganda's cattle corridor: gendered assets, expenditure, and decision-making. *BMC Environmental Science* 2(1). Springer Science and Business Media LLC.

Nejadrekabi M, Eslamian S and Zareian MJ (2021) Using spatial statistics to identify drought-prone regions (A case study of Khuzestan Province, Iran). *Advances in Environmental Technology* 7(4). Iranian Research Organization for Science and Technology: 231–262.

Ngoma H, Wen W, Ojara M, et al. (2021) Assessing current and future spatiotemporal precipitation variability and trends over Uganda, East Africa, based on CHIRPS and regional climate model datasets. *Meteorology and Atmospheric Physics* 133(3). Springer: 823–843.

Niranjan Kumar K, Thota MS, Ashrit R, et al. (2022) Quantile mapping bias correction methods to IMDAA reanalysis for calibrating NCMRWF unified model operational forecasts. *Hydrological Sciences Journal* 67(6): 870–885.

Nsubuga FW and Rautenbach H (2018) Climate change and variability: a review of what is known and ought to be known for Uganda. *International Journal of Climate Change Strategies and Management* 10(5): 752–771.

Nuwagira U and Yasin I (2022) Review of the Past, Current, and the Future Trend of the Climate Change and its Impact in Uganda. *East African Journal of Environment and Natural Resources* 5(1): 115–126.

Ojara MA, Babaousmail H, Aribo L, et al. (2024) Patterns of rainfall and temperature and their relationships with potential evapotranspiration rates over the period 1981–2022 in parts of central, western, southern, and southwestern Uganda. *Environmental Monitoring and Assessment* 196(10): 898.

Onyeaka H, Nwauzoma UM, Akinsemolu AA, et al. (2024) The ripple effects of climate change on agricultural sustainability and food security in Africa. *Food and Energy Security* 13(5).

Onyutha C and Kerudong PA (2022) Changes in Meteorological Dry Conditions across Water Management Zones in Uganda. *KSCE Journal of Civil Engineering* 26(12). Korean Society of Civil Engineers: 5384–5403.

Orimoloye IR, Belle JA, Orimoloye YM, et al. (2022) Drought: A Common Environmental Disaster. *Atmosphere* 13(1): 111.

Orke YA and Li M-H (2022) Impact of Climate Change on Hydrometeorology and Droughts in the Bilate Watershed, Ethiopia. *Water* 14(5): 729.

Rao KK, Al Mandous A, Al Ebri M, et al. (2024) Future changes in the precipitation regime over the Arabian Peninsula with special emphasis on UAE: insights from NEX-GDDP CMIP6 model simulations. *Scientific Reports* 14(1): 151.

Rousta I, Doostkamian Mehdi, Haghighi Esmaeil, et al. (2017) Analysis of Spatial Autocorrelation Patterns of Heavy and Super-Heavy Rainfall in Iran. *ADVANCES IN ATMOSPHERIC SCIENCES* 34(9): 1069–1081.

Samuel S, Mengistu Tsidu G, Dosio A, et al. (2025) Assessment of Historical and Future Mean and Extreme Precipitation Over Sub-Saharan Africa Using NEX-GDDP-CMIP6: Part I—Evaluation of Historical Simulation. *International Journal of Climatology* 45(2).

Satoh Y, Yoshimura K, Pokhrel Y, et al. (2022) The timing of unprecedented hydrological drought under climate change. *Nature Communications* 13(1): 3287.

Sen PK (1968) Estimates of the Regression Coefficient Based on Kendall's Tau. *Journal of the American Statistical Association* 63(324): 1379–1389.

Ssembajwe R, Mulinde C, Ddumba SD, et al. (2024) Dynamics and associations of selected agrometeorological variables in Robusta growing regions of Uganda. *Agricultural Water Management* 307: 109257.

Ssembajwe R, Twah A, Kagezi GH, et al. (2025) Assessment and Validation of FAPAR, a Satellite-Based Plant Health and Water Stress Indicator, over Uganda. *Remote Sensing* 17(20): 3501.

Ssembajwe R, Ngatia M, Kagezi GH, et al. (2025) Evaluation of gridded and reanalysis vapour pressure deficit datasets over East Africa. *Journal of Southern Hemisphere Earth Systems Science* Drumond A (ed.) 75(3).

Ssembajwe R, Nguefack J, Mezafack KL, et al. (2025) Spatiotemporal dynamics and drivers of agricultural droughts in the agroecological zones of Cameroon. *International Journal of Applied Earth Observation and Geoinformation* 140: 104581.

Ssembajwe Ronald, Twah A, Nakabugo R, et al. (2025) Wind and Humidity Nexus over Uganda in the Context of Past and Future Climate Volatility. *Climate* 13(5): 86.

Thrasher B, Wang W, Michaelis A, et al. (2022) NASA Global Daily Downscaled Projections, CMIP6. *Scientific Data* 9(1): 262.

UBOS (2024) *Uganda Annual Agricultural Survey 2021/22*. Kampala. Available at: https://www.ubos.org/wp-content/uploads/publications/UHIS_2021_22-Report-Final.pdf (accessed 14 November 2025).

UBOS (2025) Uganda Profile. Available at: https://www.ubos.org/uganda-profile/ (accessed 14 November 2025).

Uwimbabazi J, Jing Y, Iyakaremye V, et al. (2022) Observed Changes in Meteorological Drought Events during 1981–2020 over Rwanda, East Africa. *Sustainability* 14(3): 1519. 17.

Voda M, Kithiia S, Jackiewicz E, Du Q, Sarpe CA (2019) Geosystems 'pathways to the future of Sustainability, *Scientific reports*, 9(1), 1-11. https://www.nature.com/articles/s41598-019-50937-z

Voda AI, Sarpe CA, and Voda M (2018). Methods of maximum discharge computation in ungauged river basins. Review of procedures in Romania. *Geographia Technica*, 13(1), 130-137.

Vicente-Serrano SM, Beguería S and López-Moreno JI (2010) A multiscalar drought index sensitive to global warming: The standardized precipitation evapotranspiration index. *Journal of Climate* 23(7): 1696–1718.

Vinodhkumar B, Ullah S, Kumar TVL, et al. (2024) Amplification of temperature extremes in Arabian Peninsula under warmer worlds. *Scientific Reports* 14(1): 16604.

Wang Q, Zeng J, Qi J, et al. (2021) A multi-scale daily SPEI dataset for drought characterization at observation stations over mainland China from 1961 to 2018. *Earth System Science Data* 13(2). Copernicus Publications: 331–341.

Wu F, Jiao D, Yang X, et al. (2023) Evaluation of NEX-GDDP-CMIP6 in simulation performance and drought capture utility over China – based on DISO. *Hydrology Research* 24(5). IWA Publishing: 703–721.

Yevjevich (1967) *An Objective Approach to Definitions and Investigations of Continental Hydrologic Droughts*.

SOME CHARACTERISTICS OF CONVECTIVE PHENOMENA IN THE AREA OF "MIHAIL KOGĂLNICEANU" INTERNATIONAL AIRPORT CONSTANȚA, IN THE PERIOD 2003 – 2022

Andreea BETERINGHE [1*], ***Adrian IRAȘOC*** [1,2] ***& Nicoleta IONAC*** [3]

DOI: 10.21163/GT_2026.211.12

ABSTRACT

This study investigates the thermodynamic and environmental conditions associated with convective activity in the vicinity of "Mihail Kogălniceanu" International Airport in Constanța, Romania, using a combination of ERA5 reanalysis data, radiosonde-derived instability indices, radar observations and multiannual severe-weather reports. Frequency-based analyses of CAPE, CIN, KI and TT for the April-September period (2003-2022) reveal a warm-season environment characterized by moderate to high convective potential, with a maximum CAPE and a minimum CIN occurring predominantly in June-August and during the early afternoon hours. Despite this thermodynamic predisposition, the observed number of cases of thunderstorms, rain showers, hail and squalls remains comparatively low, reflecting the strong moderating influence of the Black Sea, which reduces lapse rates and limits deep convection. The climatological analysis of local phenomena confirms the coastal suppression: thunderstorms, hail and squalls occur infrequently, with marked inter-annual variability but low multiannual averages. A detailed case study on 31 July 2022 illustrates that intense convective systems can still develop when synoptic forcing and thermodynamic profiles align. Radar data documented a multicellular storm producing high reflectivity, elevated VIL values and significant hail signatures, consistent with ESWD ground reports. Overall, the combined results highlight the contrast between the region's thermodynamic potential for convection and the relatively low occurrence of severe weather, emphasizing the decisive role of coastal boundary-layer processes in shaping convective outcomes.

Keywords: *Convective phenomena; Air-instability indices; Airport operation area; Radar, Upper air soundings.*

1. INTRODUCTION

Convective weather phenomena, such as heavy precipitation, hail, thunderstorms and strong winds are of particular importance in researching their influence and impact on airport operations and air-flights. Understanding the environmental factors that lead to convective development is therefore essential for maintaining safe and efficient airport activity. Accurate assessments of atmospheric instability, particularly through indices such as CAPE, LI or KI, allow forecasters and operational teams to anticipate hazardous conditions before they directly impact flight operations.

For airports located in regions prone to rapid convection evolution, continuous monitoring and analysis become even more critical. By correlating instability parameters with observations of storm occurrence and intensity, airport authorities can better evaluate operational risks and optimize delay management. Atmospheric instability refers to the tendency of air parcels in the atmosphere to continue rising when they are lifted. It is a key ingredient for cloud development, thunderstorms and severe weather. Convection occurs due to the uneven heating of the underlying surface, leading to strong upward motions. To better understand these processes, meteorologists use various instability indices, such as CAPE (Convective Available Potential Energy), the SWEAT index (Severe Weather Threat Index), LI (Lifted Index), K-index (KI), TT (Total Totals Index), SI (Showalter Index) and CIN (Convective Inhibition).

---

[1] *University of Bucharest, Faculty of Geography, Doctoral School "Simion Mehedinți", Bucharest, Romania.*
[*] *Corresponding author: andreea.beteringhe@s.unibuc.ro; adrian.irasoc@s.unibuc.ro*
[2] *National Meteorological Administration, Department of Climatology, Bucharest, Romania.*
[3] *University of Bucharest, Faculty of Geography, Bucharest, Romania, ionac.nicoleta@geo.unibuc.ro*

Such quantitative indices allow the estimation of the risk and intensity of storm formation. Their effectiveness in forecasting convective phenomena has been demonstrated by numerous researchers, including Haklander and Delden (2003), Manzato (2005), Maier (2011), Haidu and Tudose (2014) Istrate et al. (2015, 2021), Sfîcă et al. (2015), Beteringhe et. al. (2025). These indices typically combine measurements of thermal and moisture characteristics of air parcels in the lower and mid-troposphere, providing estimates on the atmosphere's potential to generate convective phenomena. Many of these indices were specifically developed to improve the forecasting of thunderstorms and severe weather events.

The meteorological and climatic risks for aircraft operations and flights on the Mihail Kogălniceanu Airport in Constanța have been studied by Florea Dan (2004). In this respect, he studied the heavy atmospheric precipitation, which causes difficulties in aircraft navigation by reducing visibility, and then he further analysed the types of precipitation and their effects on the runway.

Some research works focusing on atmospheric risk phenomena in relation to aviation at European level, include specific topics highlighting the most effective methods for forecasting atmospheric phenomena, climate modelling concerning the development of convective storms, mesoscale convective systems and their impact on airports, early warning systems for meteorological events, and the use of radar and satellite data for climate predictability (Schultz et al., 2018; Guijo-Rubio et al., 2019; Kirschenstein et al., 2019; Taszarek et al., 2020; Jardines et al., 2021; Zatula et al., 2021).

At international level, several studies have highlighted the impact of atmospheric risk phenomena on airports in the United States (Liu et al., 2019; Niță et al., 2024), China (Chen și Wan, 2019; Wan et al. 2021), Brazil (Franca et al., 2018) and Australia (Roux et al., 2021).

2. DATA AND METHODS

2.1. Study area

The study area refers to the ”Mihail Kogălniceanu” International Airport, lying at a 26 km’ distance to the North-Northwest off Constanța’s city centre, within the commune of Mihail Kogălniceanu, in Constanța county (**Fig. 1 C**). It has initially been built in 1955 as an air force base but in 1960, it was opened to civil air traffic. In 2023, the number of passengers has drastically increased as compared to previous years and, therefore, a series of infrastructure modernization works were being initiated on the airport.

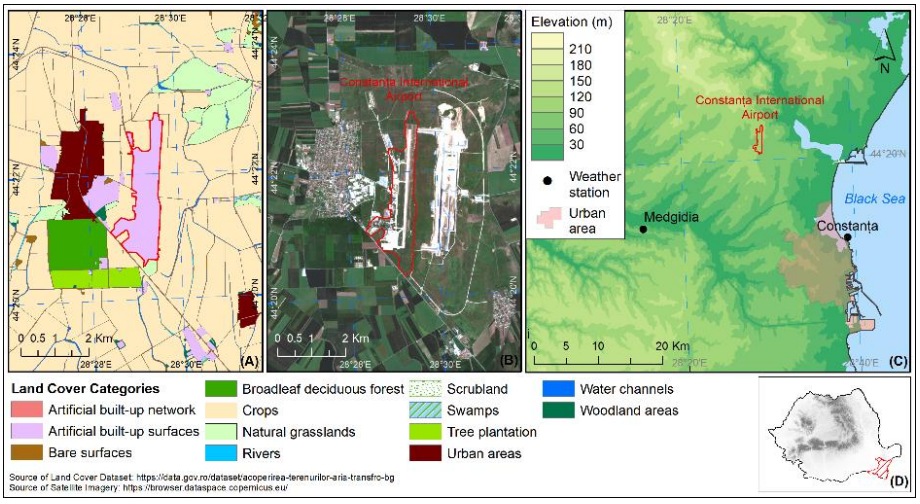


Fig. 1. The location of the ”Mihail Kogălniceanu” International Airport in the proximity of Constanța city, alongside the land-use map of the area

The map of the ”Mihail Kogălniceanu” International Airport and its surroundings illustrate a combination of hypsometric features and land-use patterns that play an important role in shaping the

local meteorological conditions. Hypsometrically, the airport is located on a relatively elevated plateau, with altitudes generally ranging from 50 to 120 meters **(Fig. 1 B)**. The mildly undulating topography facilitates air drainage and local circulations, while the absence of steep relief ensures that orographic lifting keeps minimal. Toward the Black Sea coastline, the terrain gradually descends, contributing to the development of sea-land breeze systems that strongly influence the thermal and moisture structure of the boundary-layer in the region.

Land use in the vicinity of the airport is dominated by agricultural areas which generally support strong daytime heating and can enhance low-level turbulent mixing. These open surfaces favour the development of convective thermals under sufficient insolation, although the proximity of the Black Sea frequently moderates overall instability. Patches of urbanized land and artificial built-up surfaces, seen to the west and southwest of the airport area, can introduce localized heat island effects, potentially reinforce vertical mixing and enhance small-scale convergence boundaries, which may serve as triggering mechanism for shallow convection **(Fig. 1 A)**.

2.2. Materials and Methods

In this study we used daily meteorological records from the Constanța weather station (Latitude: 44.21°N, Longitude: 28.29°E, Elevation: 10 m) over the 2003 – 2022 period, because it is the closest station to the study area – ”Mihail Kogălniceanu” International Airport. The meteorological data from the station included: the number of days with rain showers and the number of days with some convection-associated meteorological phenomena (hail, thunderstorms, squalls).

To properly understand the source of the data and the way it was collected, it is essential to define each meteorological element considered in the study. According to the National Meteorological Administration, a **squall** is characterized by a sudden and sharp increase in wind speed lasting for a short period, often accompanied by an equally rapid change in wind direction. More than that, a squall is also associated with the sudden increase in air pressure and relative humidity and the decrease in air temperature (Institutul de Meteorologie și Hidrologie, 1974). A **thunderstorm** is identified by one or more atmospheric electrical discharges, manifested as a brief and intense flash light (lightning) or a low rumbling sound (thunder). The phenomenon is classified as a thunderstorm even if only thunder is heard and the lightning is not visible. **Hail** refers to precipitation composed of ice particles, either transparent or partially to fully opaque, generally spherical or irregular in shape, with diameters typically ranging from 5 to 50 mm. **Rain showers** are defined by sudden onset and rapid cessation, as well as quick and sometimes intense fluctuations in precipitation rate. They are generally short in duration and can produce either substantial amounts of rainfall or very small quantities (Institutul de Meteorologie și Hidrologie, 1974). In addition, rain showers occur when Cumulonimbus clouds are involved. Then, we compared the data on convective phenomena with the analysis of instability indices in the airport area, in order to understand the way in which the atmospheric instability identified in the study area correlates with the occurrence and intensity of convective phenomena observed at the Constanța weather station. Thus, this comparison allows for the validation of instability analyses using direct observation of the convective phenomena; the assessment of the extent to which high instability values actually translate into convective development within the study area and the improvement of meteorological interpretation by correlating the atmospheric predisposition to convection with the phenomena observed in reality.

The occurrence of convective phenomena was examined through the frequency distribution of several key instability indices - CAPE (Convective Available Potential Energy), K-index, TT (Total Totals), and CIN (Convective Inhibition). The frequency of these indices within predefined classes provides valuable information on the likelihood and the intensity of convective processes that may affect the operational area of the ”Mihail Kogălniceanu” International Airport in Constanța (**Table 1**). For this purpose, ERA5 reanalysis data provided by the European Centre for Medium-Range Weather Forecast (ECMWF) were used. These data provide physically consistent climate fields at hourly resolution and a horizontal spatial resolution of 0.25° × 0.25°, allowing a detailed representation of atmospheric conditions over south-eastern Romania. The datasets were retrieved from Copernicus Climate Data Store (www.cds.climate.copernicus.eu). Because convection varies on a daily basis, as

a function of surface heating and moisture availability, hourly data at 00, 06, 12 and 18 UTC were extracted for the months of April to September over the 2003-2022 period. These summer months were specifically selected to capture the warm-season conditions under which convective activity is most likely to occur in this region.

Table 1

The instability indices based on ERA5 reanalysis data.

Parameters	Formulas	Values
CAPE – Convective available potential energy (Moncrieff and Miller, 1967; Doswell and Rassmussen, 1994	$CAPE = \int_{z_f}^{z_n} g(\frac{T_{vp} - T_{venv}}{T_{venv}})dz$	0 = Stable 0 – 1000 = Marginally unstable 1000 – 2500 = Moderately unstable 2500 – 3500 = Very unstable > 3500 = Extremely unstable
KI – K-index (George, 1960) (SUA)	$K = (T_{850} - T_{500}) + T_{d850} - (T_{700} - T_{d700})$	< 20 = No thunderstorms 20 – 25 = Isolated thunderstorms 25 – 30 = Widely scattered thunderstorms 30 – 35 = Scattered thunderstorms. > 35 = Numerous thunderstorms
TT – Total totals index (Miller, 1967; Darkow, 1968)	TT = VT + CT VT = T_{850}- T_{500} CT = T_{d850} – T_{500}	< 45 = Thunderstorms not likely 45 – 50 = Thunderstorms likely 50 – 55 = Widely scattered severe thunderstorms > 55 = Scattered severe thunderstorms more likely
CIN – Convective inhibition (Colby, 1984; Glickman, 2000)	$CIN = -\int_{z_{bottom}}^{z_{top}} g\,(\frac{T_{vp} - T_{venv}}{T_{venv}})dz$	0 – 50 = Weak inhibition 50 – 200 = Moderate inhibition > 200 = Strong inhibition

To extract the above-mentioned data from the ERA5 netCDF files, we firstly vectorized the airport boundary within Google Earth. Then, we projected the resulted kml file to fit the same coordinate system as the netCDF files. We further used the *terra* r-package within the R programming language (R Core Team, 2025) and the RStudio Integrated Development Environment (IDE) to extract the values of the raster layers contained by the netCDF files. The data extraction we made represents the mean of the pixels intersecting the airport area (the reprojected kml polygon). Further, the post-processing of the index's values, including frequency analysis, was made also by means of R programming language. To build the frequency graphs we used the Python programming language.

Table 2

Instability indices based on data from upper-air soundings from Bucharest-Băneasa and from the www.rawinsonde.com/ERA5_Europe website, with ERA5 data.

Parameters	Formulas	Values
SWEAT index – Severe Weather Threat Index (Binder, 1970; Miller, 1972)	$SWEAT = 12T_{d850} + 20(TTI - 49) + 2f_{850} + f_{500} + 125(s + 0.2)$	150 – 300 = Potential for moderate thunderstorms > 300 = Potential for severe thunderstorms > 400 = Potential for tornadoes
LI - Lifted index (Galway, 1956)	$LI = T_{500} - T_{p500}$	> 2 = Stable 2 to 0 = Weak unstable 0 to -3 = Marginally unstable -3 to-6 = Moderately unstable -6 to -9 = Very unstable < -9 = Extremely unstable
SI – Showalter index (Showalter, 1953)	$SI = T_{500}$- T_{p850}	> 0 = Stable 0 to -3 = Moderately unstable -4 to -6 = Very unstable < -6 = Extremely unstable
KO index (Europe) (Deutsches Wetterdienst)	$KO = (\theta_ä500 + \theta_ä700) - (\theta_ä850 + \theta_ä1000)/2$	> 6 = No thunderstorms 2 – 6 = Thunderstorms possible < 2 = Thunderstorms likely

In addition, the conditions of atmospheric instability that could influence the occurrence and development of convective phenomena at "Mihail Kogălniceanu" International Airport in Constanța,

were also inferred from the synoptic maps (showing the configuration of the surface air pressure field and the geopotential map at 500 hPa) provided by the Global Forecast System archive (www.wetter3.de), as well as by the maps of air instability indices such as CAPE, Lifted Index, and KO-index (www.wetter3.de). Upper-air soundings (thermodynamic skew-T log P diagrams) from Bucharest-Băneasa station (www.weather.uwyo.edu) were also used, alongside with extra data from www.rawinsonde.com/ERA5_Europe/, where the forecasted values of instability indices are also available – CAPE, SWEAT index, LI, K-index, TT, SI and CIN (**Table 2**).

Moreover, the characteristics of the convective phenomena on July 31, 2022, were highlighted by using the radar images of the convective cells as viewed by the WSR Doppler radar in Medgidia, part of the National Meteorological Administration (NMA) network.

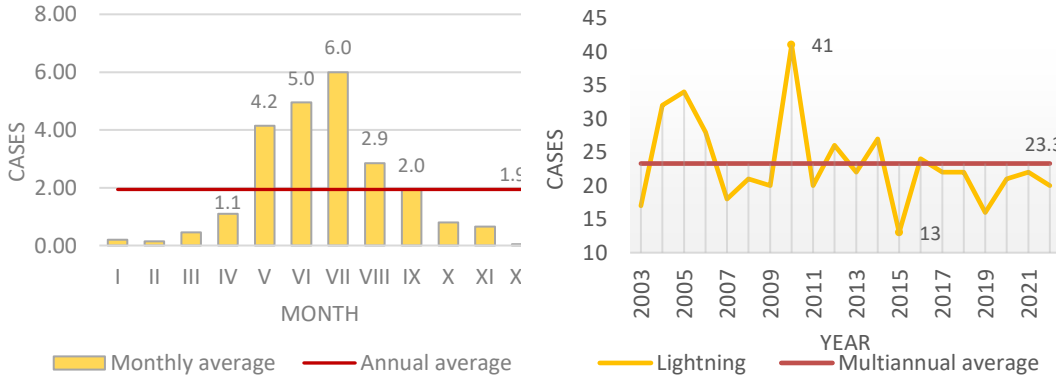
3. RESULTS

The atmospheric instability conditions influencing the formation and development of convective storms within the operational area of the ”Mihail Kogălniceanu” International Airport in Constanța were assessed by correlating meteorological observations from the Constanța weather station with instability index data calculated for the airport area. This approach provides a more accurate representation of local convective potential, as it captures both the regional weather patterns and the specific characteristics of the airport environment.

3.1. Analysis of significant meteorological phenomena

3.1.1. Lightning

From 2003 to 2022, the highest mean monthly number of thunderstorms cases at the Constanța meteorological station usually occurs in July (6 cases) and the lowest in April (1.1 cases) (**Fig. 2 A**), with an annual average value of 1.9 lightning cases. Additionally, the multiannual analysis revealed a peak in thunderstorm activity in 2010 (with 41 lightning cases) and a minimum in 2015 (13 cases) (**Fig. 2 B**), provided that the multi-annual mean value keeps around 23.3 lightning cases. The lower number of lightning cases at the Constanța meteorological station is mainly due to the climatically moderating influence of the Black Sea on the nearby shores as it lowers air-temperatures through increased humidity levels, thereby reducing atmospheric instability. Additionally, the sea breezes have a significant impact on air circulation patterns as they alter the distribution of updrafts and downdrafts, thus decreasing the frequency of severe convective phenomena such as storms.



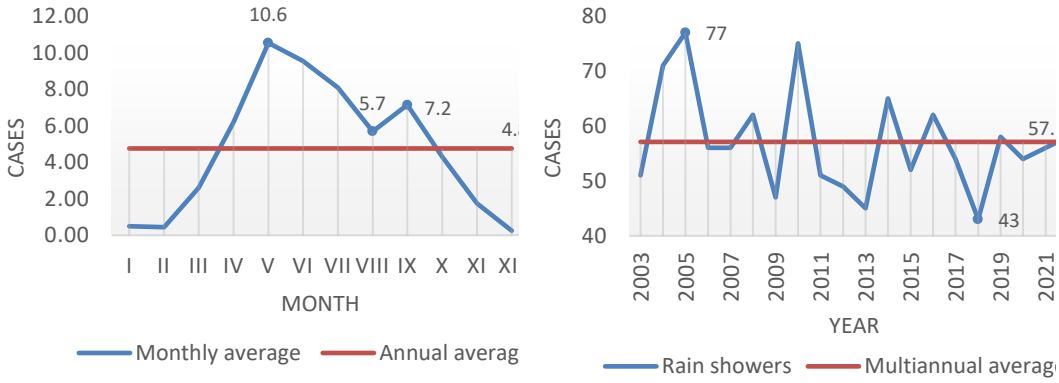
(A) **(B)**

Fig. 2. The monthly mean number of lightning cases (**A**) and the multiannual number of lightning cases (**B**) at the Constanța meteorological station from 2003 to 2022, data source: NMA.

3.1.2. Rain showers

At the Constanța meteorological station (**Fig. 3 A**), the monthly mean number of rain shower cases display two peaks: a first one from April to May, reaching a maximum of 10.6 cases, and a

second period of increase from August to September, with 7.2 cases. Interestingly, the lowest value was recorded in August (5.7 cases), due to the higher air-temperatures in August, favourable to a more stable atmosphere, as warm, dry air reduces the instability needed for convective storm development. In contrast, the increased number of showers in September may be due to the seasonal changes that favour atmospheric instability. The annual mean number of rain showers from 2003 to 2022 was 4.8 cases. As for the multiannual number of rain shower cases, a maximum number of 77 cases has been recorded in 2005 and a minimum number of 43 cases in 2018 (**Fig. 3 B**).

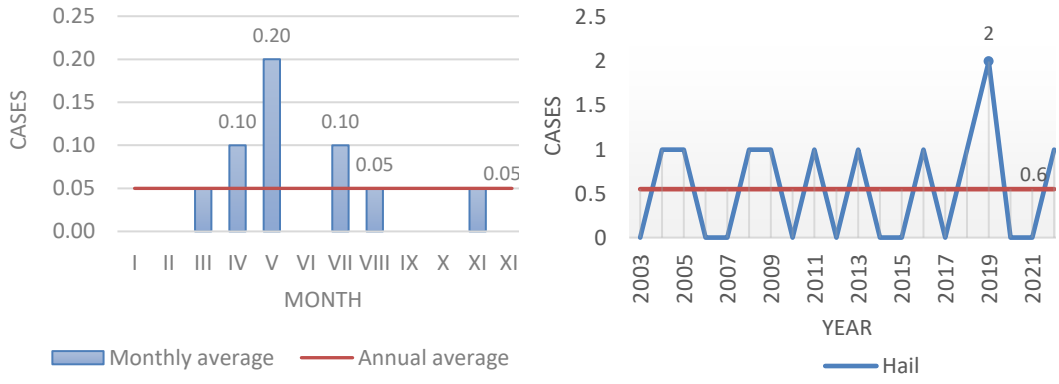


(A) **(B)**

Fig. 3. The monthly mean number of rain showers cases (A) and the multiannual number of rain showers cases (B) at the Constanța meteorological station from 2003 to 2022, data source: NMA.

3.1.3. Hail

The monthly mean number of hail cases at the Constanța meteorological station is generally low but nevertheless two significant increases and two notable decreases are evident. The first spike occurs in May (with a maximum of 0.2 cases), and the second one in April and July (with 0.1 cases) (**Fig. 4 A**). The two decreases occurred in June and September, both with 0 cases. The annual mean number of hail cases for the entire 2003-2022 period was 0.05 cases, while the multiannual number of hail cases shows a maximum of 2 cases in 2019 and a minimum of 0 cases in 2003, 2006, 2010, 2012, 2014, 2015, 2017, 2020 and 2021. In the remaining years, there has been recorded only one hail case for each year (**Fig. 4 B**). As hailstorms are more likely to occur in areas with high atmospheric instability and as in coastal regions the 0°C isotherm usually rises up to higher altitudes than in other parts of the country, hail gets less frequent onto the ground in the coastal region.

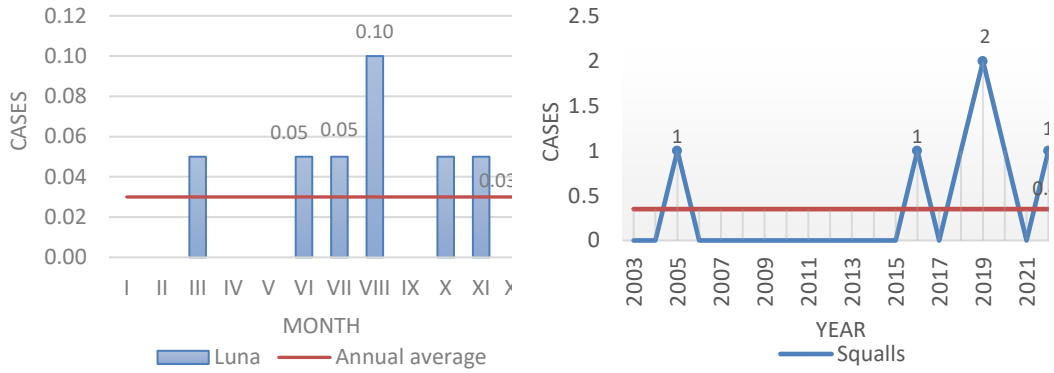


(A) **(B)**

Fig. 4. The monthly mean number of hail cases (A) and the multiannual number of hail cases (B) at the Constanța meteorological station from 2003 to 2022, data source: NMA.

3.1.4. Squalls

At the Constanța meteorological station, the monthly mean number of squall cases increases in August (0.1 cases) and decreases in September, with 0 cases recorded (**Fig. 5 A**). The annual mean value for the entire 2003–2022 period was 0.03 cases. As for the multiannual number of squall cases from 2003 to 2022, one can notice that a peak of 2 cases occurred in 2019, with other years recording one case each (2005, 2016, 2022). No squall was recorded in the remaining years (**Fig. 5 B**). As we have previously stated, Constanța's location near the Black Sea greatly inhibits the occurrence and development of convective processes, leading to more stable atmosphere conditions and a very low number of squalls in the study area.



(A) **(B)**

Fig. 5. The monthly mean number of squalls cases (A) and the multiannual number of squalls cases (B) at the Constanța meteorological station from 2003 to 2022, data source: NMA.

3.2. Analysis of instability indices

In order to assess the thermodynamic state of the atmosphere in the area of interest, we illustrated the frequency distribution of CAPE, CIN, KI and TT values, grouped by classes and analysed at different hours (00, 06, 12, 18 UTC), for the April-September period at "Mihail Kogălniceanu" International Airport (Constanța), during 2003-2022. The results reveal a pronounced seasonal cycle, accompanied by well-defined diurnal variability.

During April and early May, **CAPE** values remain predominantly low, with the 0 and 0-1000 J kg^{-1} classes being dominant **(Fig. 6 A)**. These conditions reflect a generally stable atmosphere, with limited convective potential. Beginning in June, the frequency of CAPE increases significantly, and the 0-1000 J kg^{-1} interval becomes predominant, although moderate CAPE values (1000-2500 J kg^{-1}) are also recorded **(Fig. 6 A)**. In July and August, the convective potential reaches its maximum, with the 1000-2500 J kg^{-1} category being more common. Occasional episodes of high CAPE (2500-3000 J kg^{-1}) are observed, and values above 3500 J kg^{-1} occur rarely. By September, the atmosphere becomes progressively more stable, which is reflected in the increasing frequency of low CAPE values. Diurnally, CAPE peaks consistently around 12 UTC and 18 UTC, underscoring the influence of daytime heating and the accumulation of buoyant energy.

In terms of **CIN**, April is characterized by relatively high frequencies in the 0-50 J kg^{-1} class and moderate values in the 50-200 J kg^{-1} class, indicating a slightly stable environment at the beginning of the season. Values exceeding 200 J kg^{-1} occur frequently, suggesting strong convective inhibition associated with cooler and more stable spring air masses. In May, CIN decreases visibly, and the 0-50 J kg^{-1} category becomes dominant as lower-tropospheric temperatures increase. Convective inhibition continues to weaken in June and July, and values above 200 J kg^{-1} become significantly less common, corresponding to an environment more favourable for convective development **(Fig. 6 B)**. In August, a slight increase in the 50-200 J kg^{-1} interval suggests a balance between enhanced warm-season instability and the intermittent episodes of subsident or dry air reinforcing the CIN layer.

By September, values above 200 J kg^{-1} reappear more often due to the progressive cooling of the lower troposphere.

At 00 UTC and 06 UTC, CIN is generally higher compared to daytime hours, with a greater presence of the 50-200 J kg^{-1} and >200 J kg^{-1} classes **(Fig. 6 B)**. This reflects nocturnal stabilization of the boundary layer through radiative cooling.

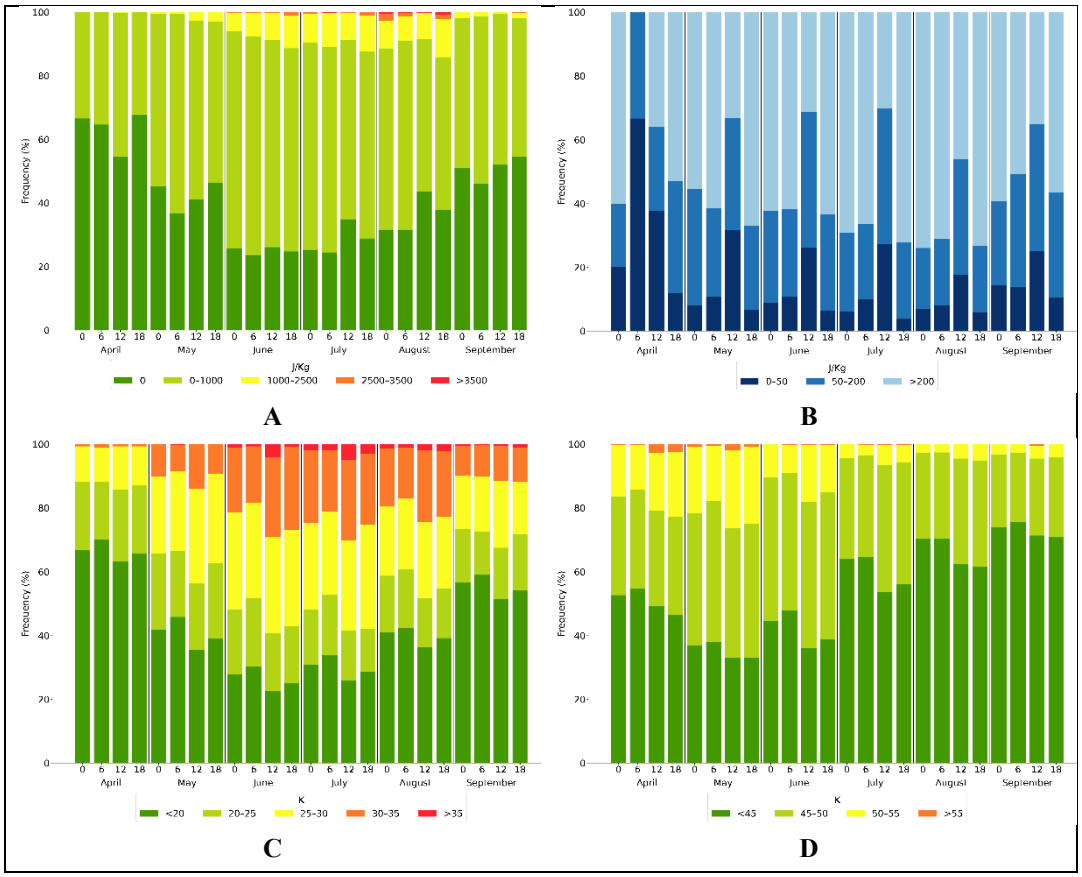


Fig. 6. The frequency distribution of CAPE **(A)**, CIN **(B)**, KI **(C)** and TT **(D)** values, grouped by classes at 00:00, 06:00, 12:00, and 18:00 UTC, for the "Mihail Kogălniceanu" International Airport (Constanța), during 2003-2022, data source: ERA5 data, www.cds.climate.copernicus.eu

The **K-index** is an indicator of atmospheric instability and the likelihood of convective precipitation. Higher values are associated with an increased risk of organized convection. In April, low values (<20 K) dominate across all hours **(Fig. 6 C)**, indicative of a stable atmosphere and a low probability of organized convection. Moderate values (20-25 K and 25-30 K) increase significantly in May, especially at 12 UTC and 18 UTC, marking the transition to the warm season, when moisture advection in the lower troposphere becomes more pronounced. In June, the seasonal maximum becomes evident, characterized by dominant frequencies in the 25-30 K interval and increasingly frequent occurrences of 30-35 K values. This indicates a high probability of convective development, including showers and summertime thunderstorms. July exhibits a shift toward higher classes, with the 30-35 K values widespread at all hours and occasional values exceeding 35 K, signalling pronounced instability. August continues to show a strongly convective profile, similar to July but slightly more balanced, while in September, the frequencies of moderate and high KI values decrease progressively, and the <20 K class becomes dominant again during morning and nighttime hours, reflecting the establishment of a more stable thermal regime.

Total Totals is a classical indicator of thunderstorm potential and reflects a clear warm-season evolution. Low values (<45 K) dominate in April, especially at 00 UTC and 06 UTC, reflecting a stable atmosphere typical of early warm-season conditions **(Fig. 6 D)**. By contrast, moderate values (45-50 K) appear regularly during the midday and afternoon hours (12-18 UTC), indicating a slight increase in diurnal instability. In May, the distribution becomes more balanced as 45-50 K and 50-55 K values increase at 12 UTC and 18 UTC, signalling a heightened likelihood of convective showers and lightning activity. TT reaches a pronounced convective level in June, with 45-50 K values frequent at all hours and 50-55 K values dominant at 12 UTC and 18 UTC. July exhibits one of the strongest convective signatures, with 50-55 K values particularly common during the daytime hours and occasional occurrences of TT >55 K, indicative of severe instability. August maintains a similar profile, with high frequencies of 45-50 K and 50-55 K, though slightly reduces compared to July due to moderate increase in atmospheric stability. In September, TT values decrease once again, with the <45 K interval dominating at 00 UTC and 06 UTC, consistent with the seasonal transition toward a more stable thermodynamic environment.

3.3. Case study: Weather conditions in the area of the ”Mihail Kogălniceanu” International Airport on the 31st July 2022

3.3.1. Synoptic conditions

At continental scale, an active low-pressure area was present over Iceland (**Fig. 7**), with a short-wave trough extending eastwards, over much of the Scandinavian Peninsula. Concurrently, the expansion of the Azores ridge over the western regions of Europe was notable and its eastwards extent, in conjunction with the Iceland's cyclone, facilitated the transport of polar maritime air over the central and south-eastern regions of the continent. Thus, the synoptic context was ideal for a massive zonal circulation over much of the European continent, particularly in the upper layers of the troposphere (**Fig. 7**).

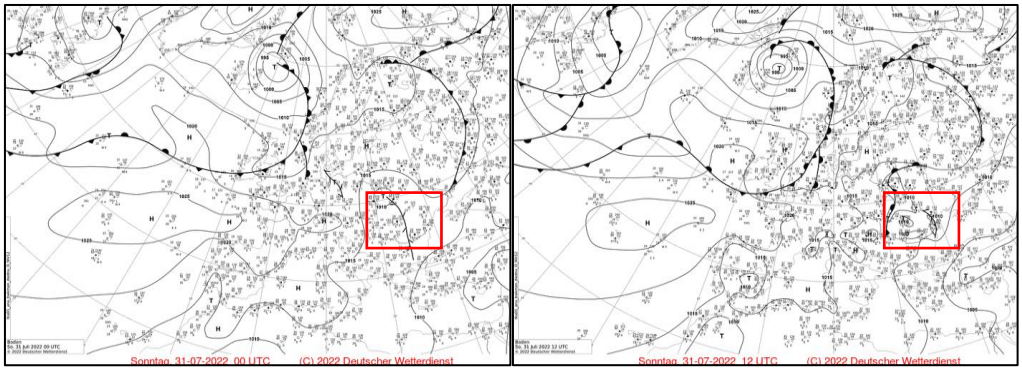
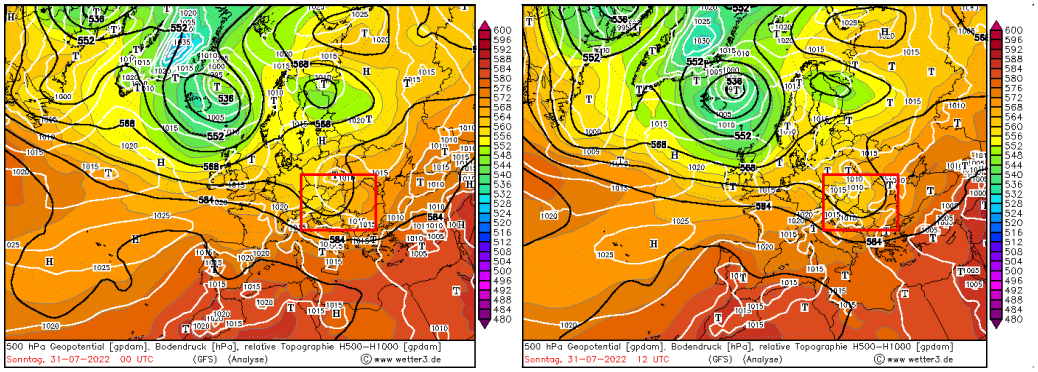


Fig. 7. The configuration of the surface air-pressure field on 31.07.2022, at 00 UTC (A) and 12 UTC (B), data source: www1.wetter3.de.

The surface pressure centers could largely be associated with those at the 500 hPa geopotential level, so not only the presence of the low-pressure area located over Iceland but also the eastward extension of the Azores high and the presence of the short-wave trough over Central Europe and the Scandinavian region could easily be identified (**Fig. 8**). Additionally, the expansion of this low-pressure area towards the central and south-eastern regions of Europe acted as a source of cold air aloft, creating ideal conditions for the initiation of convective processes, especially with warm, moisture-rich air in the lower troposphere. For the territory of Romania, the periphery of the mentioned depressionary area was of particular importance, as it resulted in the formation of a low-pressure area.



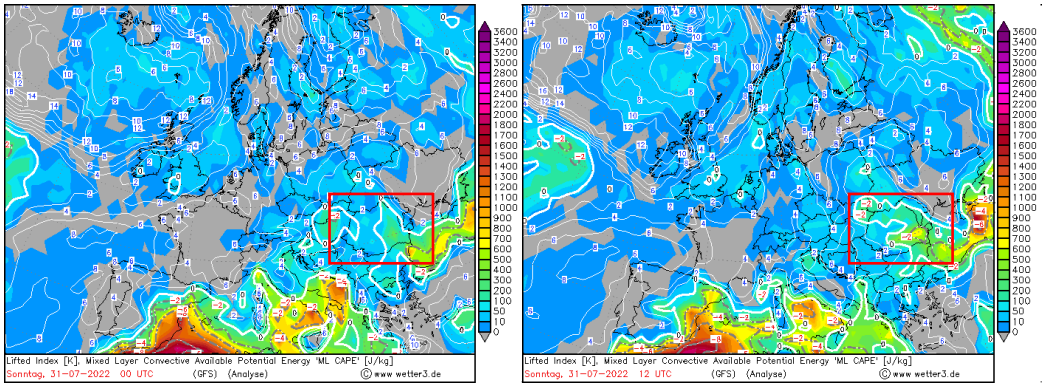
(A) **(B)**

Fig. 8. The geopotential map at 500 hPa on 31.07.2022, at 00 UTC (A) and 12 UTC (B), data source: www1.wetter3.de.

The presence of the upper-lever trough induces positive vorticity advection and large-scale ascent **(Fig. 8).** The synoptic configuration typically enhances convective potential, facilitates the decrease of inhibition during daytime and contributes to development of deep convection. As a result, such trough passages over or near Romania are commonly associated with episodes of heavy rainfall, thunderstorms and locally severe convective weather during the warm season (Dobri et al., 2017).

3.3.2. Air-instability indices

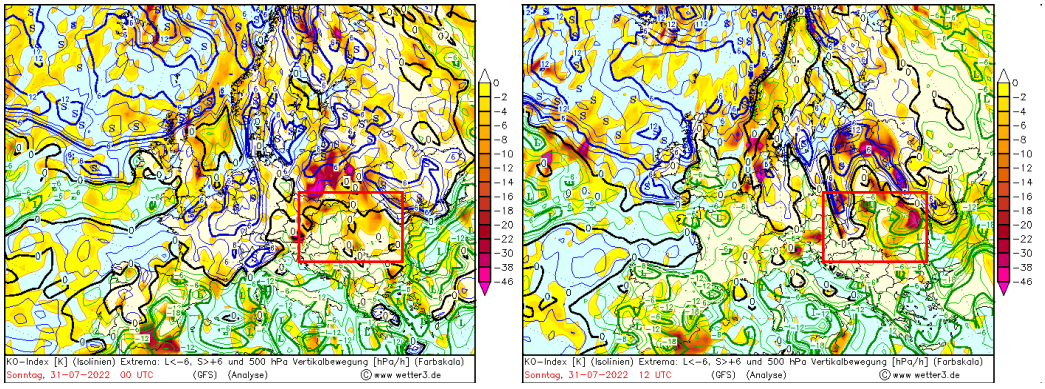
The **Lifted Index and CAPE** values for the south-eastern regions of Romania, including the area of interest, showed a gradual increase from 00 UTC to 12 UTC on July 31, 2022 (**Fig. 9 A and B**). At 00 UTC, the Lifted Index was 0 K but it decreased to -2 K by 12 UTC, thus indicating a marginally unstable atmosphere. A similar trend was observed for CAPE values which increased from 300 J/kg at 00 UTC to 800–900 J/kg by 12 UTC, also indicating a marginally unstable atmosphere, concordant with the Lifted Index values.



(A) **(B)**

Fig. 9. The spatial distribution of Lifted Index and CAPE on 31.07.2022, at 00 UTC (A) and 12 UTC (B), data source: www1.wetter3.de.

The values of the KO index (**Fig. 10 A and B**) show an increase from 0 K at 00 UTC to -6 K at 12 UTC, indicating a strong convective potential. In addition, the vertical ascent values at the 500 hPa level decrease to -20 hPa/h, pointing to high-intensity upward air-currents, which could lead to the development of severe convective storms.



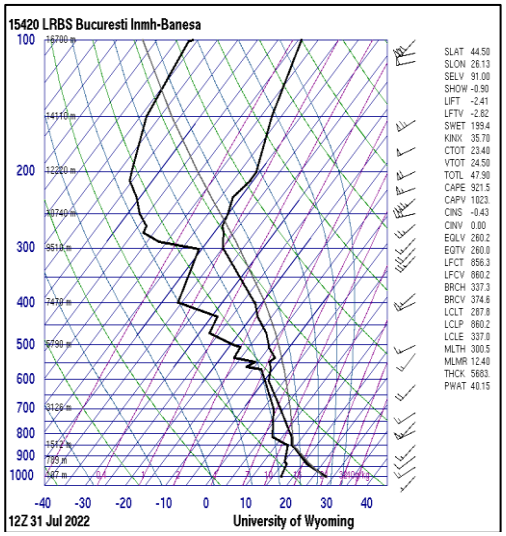
(A) **(B)**

Fig. 10. The spatial distribution of KO-index and the vertical ascent to the level of 500hPa on 31.07.2022, at 00 UTC (A) and 12 UTC (B), data source: www1.wetter3.de.

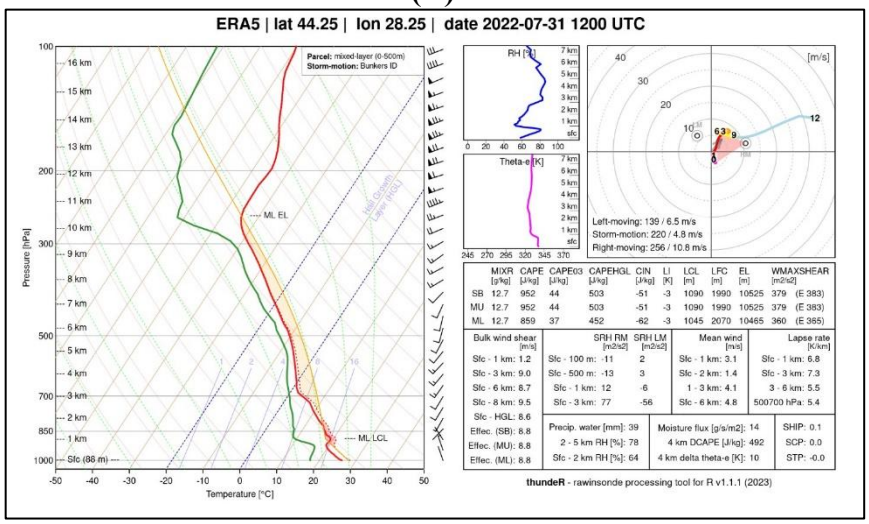
However, in order to analyse and compare the radiosonde data generated by ERA5 with the real ones, we had to refer to the Bucharest-Băneasa meteorological station, as it is the only one in Romania running real-time aerological observations. So, we compared the upper-air sounding at 12 UTC from the Bucharest-Băneasa weather station with the 12 UTC sounding generated by the ERA5 reanalysis data for the Constanța area (**Fig. 11 A and B**). Consequently, the analysis of the skew-T-log P diagram from the Bucharest-Băneasa meteorological station indicates a CAPE value of 921.5 J/kg, while the CAPEV value (based on the virtual temperature) is 1023 J/kg (**Fig. 11 A and Table 3**), thus suggesting a marginally unstable atmosphere. In parallel, the ERA5 radiosonde data indicate similar CAPE values to those from Bucharest-Băneasa: both SB-CAPE (surface-based parcel) and MU-CAPE (most-unstable parcel) maintaining at 952 J/kg, and the ML-CAPE (mixed-layer parcel) at 859 J/kg (**Fig. 11 B and Table 3**). These values actually correlate with those obtained from the analysis of the Lifted Index and CAPE maps, which are based on GFS data (**Fig. 9**).

Provided that these convective phenomena manifested mainly in the afternoon, the MU-CAPE value is no more as significant as the SB-CAPE and ML-CAPE values, which seem more appropriate for daytime convection. Under specific conditions, an intense convection cannot be supported by a surface air-layer but rather from a higher-altitude air-layer, which often occurs at night, when a thermal inversion is present just above the ground surface or on the cold side of a warm surface front, where MU-CAPE is more applicable (Craven et al., 2002). Since the mean-layer parcel provides a more accurate estimate of the height up to which the base of a convective cloud might develop, it is reasonable to conclude that the ML-CAPE value is a far better indicator of potential buoyancy as compared to the SB-CAPE value, especially in a well-mixed boundary layer. Furthermore, the moisture content in the lower troposphere was very high (**Fig. 11**) and, therefore, a significant difference between the air parcel temperature and the dew point can be observed in the mid-troposphere (500 hPa), thus creating ideal conditions for winds to reach squall speeds.

Regarding the Lifted Index, it recorded values of -2.41 K (LIFT) and -2.82 K for LFTV (based on virtual temperature) at the Bucharest-Băneasa radio-sounding, while the thermodynamic diagram based on ERA5 reanalysis data displayed a value of -3 K for all the three air parcels of reference: SB-LI, MU-LI, and ML-LI (**Fig. 11 A and B and Table 3**). The values obtained from the two radio-soundings are close, suggesting a marginally unstable convective potential, as also shown by the spatial distribution of Lifted Index values (**Fig. 9**). Initially, the Lifted Index was developed as a predictor for local severe storm forecasting in the United States, where Dennis et al. (1967) and Lyons (1964) suggested that low Lifted Index values are associated with hail occurrences in western South Dakota. Then, in 1968, Musil and Dennis used the Lifted Index alongside with other parameters to forecast hailstorms in western Nebraska. Also, in 2014 Haidu and Tudose showed that the LI is a good indicator for identifying convective storms that produce torrential rainfall, triggered either by convective or frontal lifting. Moreover, the correlation between the CAPE and the Lifted Index values point to favourable conditions for hail events in the area.



(A)



(B)

Fig. 11. The thermodynamic skew-T – log P diagram, alongside the meteorological parameters and the instability indices for the București-Băneasa meteorological station **(A)** (12 UTC) and based on ERA 5 data for the Constanța Airport **(B)** (12 UTC), on 31 July 2023, data source: www.weather.uwyo.edu; www.rawinsonde.com.

The Showalter Index values indicate a moderately unstable atmosphere, according to the radiosounding data from Bucharest-Băneasa (-0.90 K – SHOW), but a stable atmosphere according to the aerological diagram based on ERA5 data (1.67 K) (**Fig. 11 A and Table 3**). The Showalter Index is a static thermodynamic measure allowing a rapid assessment of the likelihood of thunderstorms, as inferred in the concept of potential (convective) instability (Showalter, 1953). However, its applicability is limited to mountainous regions and becomes ineffective in extremely dry air conditions, as it relies solely on the value at 850 mb to represent low-level moisture and temperature. However, although Carson (1954) demonstrated a good correlation between radiosonde data and precipitation amounts during the summer showers in Miami, Showalter (1953) suggested that values of +3 or lower can typically be linked to the occurrence of showers and possibly thunderstorms. The likelihood of thunderstorms increases as the values of the corresponding index decrease from +1 to -2, with severe thunderstorms possibly developing at values of -3 and below.

The SWEAT index recorded values of 199.4 units (SWET) for the Bucharest-Băneasa radio-sounding and of 112.95 units for the ERA5 sounding data, thus indicating a potential for moderate convective storms. Miller et al. (1972) emphasize that the index could best serve as an indicator of the potential for severe storms to develop, provided that a triggering mechanism lifts the air and utilizes this potential. However, one limitation of this index is that it uses data only from the 850 hPa and 500 hPa levels.

Table 3

The values of air-instability indices based on the sounding data at the București- Băneasa meteorological station and from ERA5 dataset, on 31 July 2022, for the "Mihail Kogălniceanu" International Airport Constanța

Indices	Radio sounding București-Băneasa	ERA5 data
CAPE	921.5 J/kg 1023 J/kg -CAPV	1436 J/kg – SB-CAPE, MU-CAPE 1286 J/kg – ML-CAPE
Lifted index	-2.41 K -2.82 K - LFTV	-3 K – SB-LI, MU-LI, ML-LI
SI	-0.90 K - SHOW	1.67 K
SWEAT index	199.4 - SWET	112.95
KI	35.70 K - KINX	30.98 K
TT	47.90 K (TOTL)	44.81 K
CIN	-0.42 J/kg 0 J/kg - CINV	-52 J/kg – SB-CIN, MU-CIN -62 J/kg – ML-CIN

Data source: www.weather.uwyo.edu.

The K-index recorded a value of 35.70 K (KINX) for the Bucharest-Băneasa radio-sounding data (**Fig. 11 A and Table 3**) and a value of 30.98 K (**Table 3**) for the ERA5 radio-sounding data, pointing to some probable scattered thunderstorms. The results from both radio-soundings seem quite similar, highlighting highly-probable storm conditions in both cases. Thus, the K-index has proven to be the most effective indicator in forecasting rain showers and less severe storms, but poorly indicative of severe storm conditions (Peppler, 1988). However, although the KI values may be indicative of storm occurrence, they greatly vary depending on the season and geographic location, proving to be much more relevant in the United States, during the summer months. In Europe, the KO index is used by The German Weather Bureau because it better integrated the effect of humidity as compared to other existing instability indices.

The Total Totals index recorded a value of 47.90 K (TOTL) in the Bucharest-Băneasa radiosonde (**Fig. 11 A and Table 3**) and a value of 44.81 K for the ERA5 reanalysis data, implying that thunderstorms are likely to occur within the operational area of ”Mihail Kogălniceanu” International Airport in Constanța (**Table 3**).

The Convective Inhibition index reached a value of -0.46 J/kg (CINS), while the CINV (based on virtual temperature) was 0 J/kg (**Fig. 11 A and Table 3**) at the Bucharest-Băneasa meteorological station. In comparison, the ERA5 radio-sounding data indicated a higher convective inhibition than at the Bucharest-Băneasa station, with SB-CIN and MU-CIN both at -52 J/kg, and ML-CIN at -62 J/kg (**Fig. 11 B and Table 3**). The lower CIN values suggest a moderately stable atmosphere; though both the radiative and dynamic factors on July 31, 2022 allowed convective processes to develop in the study area. When used alongside with CAPE, CIN provides useful insight on the potential of convective storms to develop, as shown by Beteringhe et al. (2025) in their study.

3.3.3. Radar images

To further investigate on the convective processes at ”Mihail Kogălniceanu” International Airport in Constanța, we correlated the data on the instability indices obtained from the two radio-sounding sources (Bucharest-Băneasa and ERA5 reanalysis data) with the radar images of the convective cells that developed in the area of Mihail Kogălniceanu (marked with a black border on the images below) on July 31, 2022. The convective cells started to become evident on the south-eastern areas of the

Mihail Kogălniceanu International Airport in Constanța at 2:53 p.m. (**Fig. 12**). They moved from the SE to the NW, and after surpassing the airport's perimeter, they headed northwards.

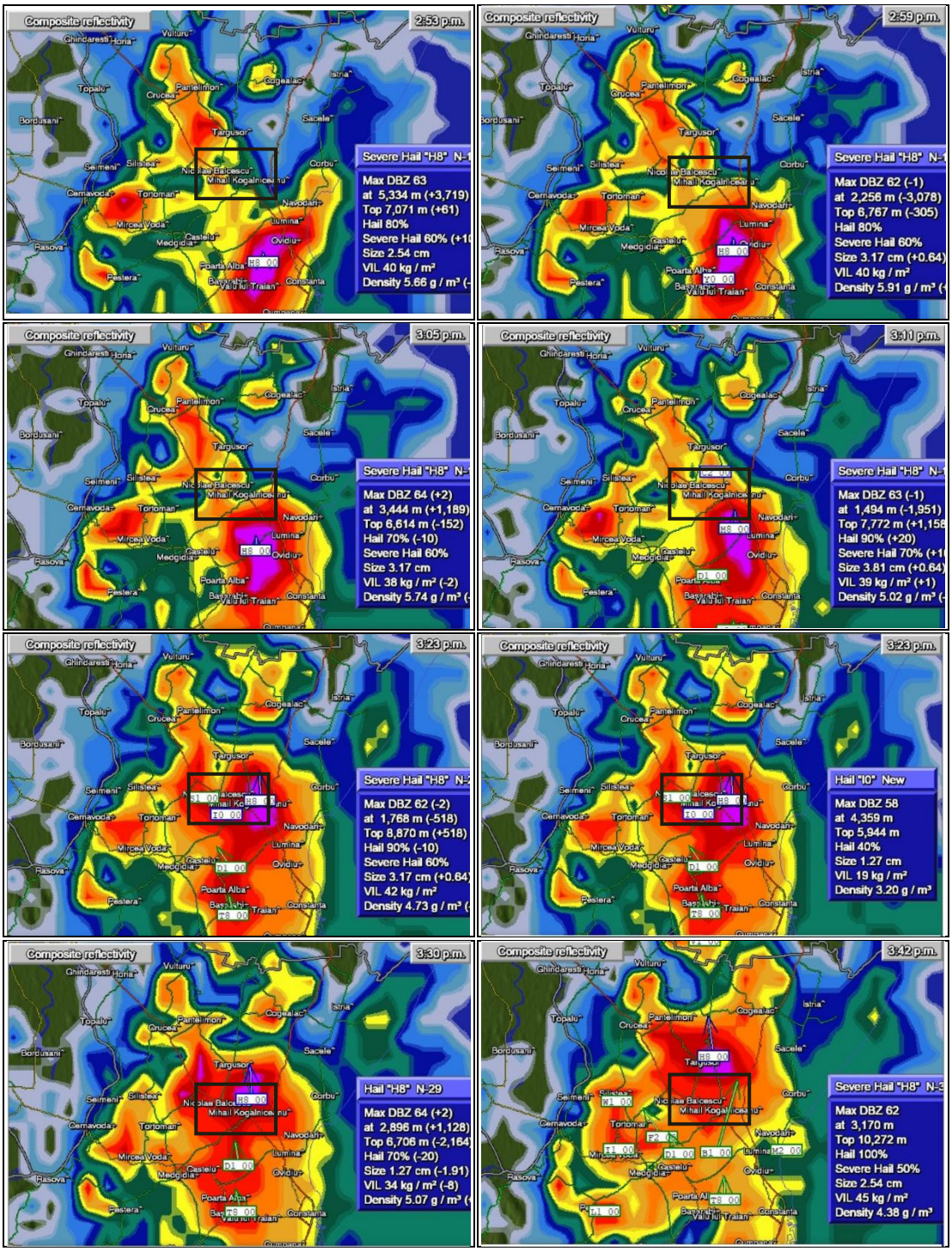


Fig. 12. Radar images of convective cells by the OmiWxTrac application in the operational area of the "Mihail Kogălniceanu" International Airport Constanța, on 31 July 2022, data source: NMA.

At 2:53 p.m., **cell H8** could be observed with several significant characteristics: an 80% probability for hail to occur and a 50% probability for severe hail to occur, with hail sizes up to 2.54 cm in diameter, provided that the radar reflectivity reached 63 dbZ and the cloud height rose to 7,010 m (**Fig. 12**). The cell was well-developed, as indicated by the high reflectivity, knowing that values above 55 dbZ are typically associated with hail in the cloud (Schuster et al., 2006; Kunz and Puskeiler, 2010). At 2:59 p.m., another cell (**Y8**) appeared (**Fig 12**), pointing to the multicellular nature of the system moving towards the "Mihail Kogălniceanu" International Airport in Constanța. Additionally, cell **H8** showed an increase in its convective parameters: hail sizes of 3.17 cm and a 60% probability for severe hail to occur. By 3:11 p.m., cell **H8** continued to grow and give birth to new accompanying convective cells, nearer to the airport. Thus, although reflectivity kept at 63 dbZ, hail increased to 3.81 cm inside the cloud, the probability of hail occurrence rose to 90%, the probability of severe hail increased to 70%, and the cloud top reached 7,772 m. Additionally, VIL (Vertical Integrated Liquid) recorded a value of 39 kg/m² (**Fig. 12**). This parameter is used in weather forecasting to estimate the water content inside the cloud, particularly in storm clouds. High VIL values are generally associated with severe storms and hail (Amburn and Wolf, 1997; Witt et al., 1998). Elevated VIL values, combined with high CAPE, indicate a very unstable atmosphere, favourable for severe storms to develop, especially inside highly-convective Cumulonimbus clouds.

At 3:23 p.m., cell **H8** was right over the perimeter of "Mihail Kogălniceanu" International Airport in Constanța, directly affecting the area (**Fig. 12**). Although its convective parameters have slightly diminished, the cell still remained vigorous enough. Additionally, the newly formed cell I0 was already exhibiting high values for most convective parameters: reflectivity of 53 dbZ, hail size of 1.27 cm, with a 40% probability of storm occurrence, and a VIL of 19 kg/m² (moderate VIL – moderate storms).

Starting at 3:30 p.m., cell **H8** continued its movement northwards, past the area of "Mihail Kogălniceanu" International Airport in Constanța, while displaying a decrease in all convective characteristics. However, at 3:42 p.m., there appeared a significant convective increase, with reflectivity rising back to 62 dbZ, hail size growing to 2.54 cm, the probability of hail occurrence increasing to 100% and the probability of severe hail to 50%, the cloud height mounting up to 10,272 m, and a VIL reaching as high as 45 kg/m² (high VIL – severe storms) (**Fig. 12**). Additionally, new green cells formed to the southern periphery of the main cell (H8), indicating a multicellular system.

The onset of convective activity in the area of Mihail Kogălniceanu International Airport in Constanța as reflected by the radar images perfectly coincides with the information derived from the analysis of instability indices from the two sounding diagrams (București-Băneasa radio-sounding and ERA5 reanalysis data). Their corresponding values suggested favourable conditions for the development of convective storms, with heavy rainfall, strong gusts and hail, in the area, as also shown by the radar images (**Fig. 12**).

The intensity of the convective phenomena was further supported by reports published in the European Severe Weather Database (ESWD), all classified with QC1 confidence level. The convective cell responsible for the severe wind and heavy rainfall observed near Valu lui Traian is the same system that subsequently propagated toward the study airport area, while the hail event reported at Topraisar is likewise attributable to this convective structure.

4. DISCUSSION

The analysis of convective weather reports at the Constanța meteorological station reveals a clear attenuation of severe convective activity along the Black Sea coast, consistent across all investigating phenomena. Thunderstorm frequency shows a pronounced seasonal cycle, with a peak in July and a minimum in April, while multiannual variability indicates years with markedly enhanced (2010) or suppressed (2015) lightning activity. This pattern reflects the moderating influence of the Black Sea, which lowers near-surface air temperatures and increases humidity, thereby reducing lapse rates and inhibiting deep convection. A similar coastal imprint is visible in the distribution of rain showers, which exhibit seasonal maxima – one in late spring and another in early autumn – suggesting that transitional seasons provide more favourable instability compared to midsummer, when warm and

relatively dry air masses promote atmospheric stability. Hail and squalls occur only rarely, with most years recording zero or one event. This scarcity is consistent with the elevated 0°C isotherm height in coastal environments and overall reduction of strong updrafts needed for hail formation and severe wind gust. Altogether, these findings underscore that the proximity to the Black Sea exerts a persistent stabilizing effect on the boundary layer, substantially limiting the development of intense convective phenomena in Constanța region.

The observed seasonal and diurnal patterns in CAPE, CIN, KI and TT are consistent with thermodynamic evolution of the lower troposphere in coastal south-eastern Romania. The pronounced increase in CAPE during June-August, combined with sustained weakening of CIN during the same interval, highlights the role of strong surface heating and enhanced low-level moisture supply in promoting convective development. The systematic diurnal peaks in CAPE at 12 and 18 UTC further support this interpretation and align with previous studies documenting the timing of convective initiation over the western Black Sea coastal region.

The behaviour of CIN provides additional insight into boundary-layer processes influencing convection. Elevated CIN during night-time and early-morning hours, particularly during spring and late summer, correspond to stronger nocturnal radiative cooling and reduced turbulent mixing. Conversely, the marked decline in CIN during midday in summer underscores the effectiveness of surface heating in eroding inhibition and facilitating convective initiation when sufficient moisture is present.

The seasonal evolution of KI and TT corroborates these findings: both indices exhibit their strongest convective signatures in June and July, with frequent occurrences of values associated with significant thunderstorm potential. Occasional KI >35 K and TT >55 K highlight the presence of days with pronounced instability capable of supporting organized convective systems, even in a coastal environment typically characterized by mesoscale circulations that modulate convective development. Overall, the combined thermodynamic indicators portray a consistent picture of a warm season characterized by moderate to high convective potential, particularly in midsummer, modulated by strong diurnal forcing and seasonal changes in low-level moisture availability. When interpreted alongside the low observed frequency of thunderstorms, hail and squalls, these results highlight the decisive role of coastal boundary-layer processes in constraining convective outcomes and provide a comprehensive framework for forecasting local convective behaviour in the airport area.

The convective episode of 31 July 2022 provides an illustrative example of how high instability conditions, as indicated by both radiosonde-derived and ERA5-based instability indices, can translate into the rapid development of severe convective cells near the ”Mihail Kogălniceanu” International Airport. Despite the general climatological tendency for the Black Sea to suppress the occurrence of intense convection in the Constanța region, this case demonstrates that under sufficiently favourable thermodynamic conditions, vigorous multicellular systems can still develop and impact the coastal area. Radar observations clearly captured the lifecycle of a well-organized convective system, with cell **H8** exhibiting substantial reflectivity values (>60 dBZ), large VIL signatures and hail-size estimates exceeding 3 cm. The system’s multicellular structure – visible through the emergence of successive cells such as **Y8** and **I0** – highlights a sustained inflow environment capable of supporting repeated updraft regeneration. The temporal evolution of the radar convective metrics underscores the dynamic behaviour of the storm as it crossed the airport area. Notably, the intensification observed after 3:42 p., following an initial weakening phase, is characteristic of multicellular convective system, which often undergo cycles of decay and regeneration. This behaviour is consistent with instability conditions indicated by high CAPE and reduces CIN during the afternoon hours, conditions that are frequently conducive to convective redevelopment.

The research conducted allowed the deduction of time series for atmospheric instability indices, providing a solid basis for analysing convective variability in the vicinity of the investigated airport. We suggest that future studies should include a frequency analysis of these indices, using the probabilistic methodology proposed by I. Haidu (2002). Such an approach would aim to quantify the risk associated with the occurrence of exceptional convection and its potential impact on air navigation.

5. CONCLUSIONS

This study highlights the importance of air-instability indices in evaluating the formation and development of convective storms in the area of the ”Mihail Kogălniceanu” International Airport in Constanța. The analysis of daily meteorological parameters from 2003 to 2022 (number of days with rain showers, hail, lightning and squalls) emphasized the general characteristics of convective phenomena in the study area, where the thermoregulatory role of the Black Sea is evident, as it moderates air-temperatures in the region during summer and contributes to atmospheric stability, thereby reducing the intensity of convective events. The average number of cases with severe weather phenomena indicate a predominance of thunderstorms in July (6 cases), rain showers in May (10.6 cases), hail in May (0.2 cases) and squalls in August (0.1 cases).

The frequency-based assessment of the instability indices (CAPE, CIN, KI and TT) over the ”Mihail Kogălniceanu” International Airport area provides a coherent picture of the thermodynamic environment that characterizes the western Black Sea region. The results indicate that, although moderate to high convective potential frequently develops during warm season – particularly in June, July and August - the actual occurrence of severe convective phenomena remains comparatively low. The contrast reflects the persistent moderating influence of the Black Sea, which reduces lapse rates, enhances boundary-layer stability.

The observed diurnal cycle, with CAPE maxima and CIN minima at midday and the early afternoon, confirms that daytime heating is the primary driver of convective potential in this area. KI and TT frequencies further highlight the presence of environments occasionally supportive of organized convection.

Regarding the case study from July 31, 2022, at ”Mihail Kogălniceanu” International Airport in Constanța, the overall synoptic context showed favourable conditions for convective processes to develop in the area. Thus, the Lifted Index and CAPE values for Romania’s south-eastern parts were indicating a "marginally unstable" atmosphere, based on both data from the Bucharest-Băneasa radio-soundings and the ERA5 reanalysis data, as well as from the maps showing the distribution of the index values by means of GFS data (www.wetter3.de). The Showalter, SWEAT, and Total Totals indices derived from both radiosonde sources indicated a favourable atmosphere for the formation and development of convective storms. Additionally, the K-index suggested scattered thunderstorms, while the KO index indicated strong convective potential.

Regarding CIN, the values derived from the Bucharest-Băneasa soundings showed a low inhibition, while the ERA5 data indicated a moderate inhibition. Elevated CIN values would normally indicate a moderately stable atmosphere but the specific radiative and dynamic factors contributed to the development of a strong convective activity at Mihail Kogălniceanu International Airport in Constanța, on July 31, 2022, as was confirmed by the radar images displaying the convective cells from that day.

The analysis of the radar images from July 31, 2022 confirms that the initial values calculated for various instability indices were indicating optimal conditions for convective phenomena to occur that day. Consequently, a series of convective cells developed over the operational area of ”Mihail Kogălniceanu” International Airport in Constanța, displaying high convective parameter values: reflectivity of 63 dbZ, hail up to 3.81 cm in diameter, a 90% probability of hail and a 70% probability of severe hail, with cloud tops reaching as high as 7,772 m. Although the main convective cell showed a decrease in its convective characteristics, after moving past the airport perimeter, it continued to be fuelled by a warm air inflow and kept on growing, by forming additional cells to its southern ends. The onset of convective activity in the area of ”Mihail Kogălniceanu” International Airport in Constanța fully corresponds with the values of the instability indices derived from the data provided by the two upper air-soundings (Bucharest-Băneasa and ERA5 reanalysis data) that were taken into consideration.

The radar-derived convective signatures were validated by ESWD reports, as observed hail and severe weather occurrences matched the storm characteristics indicated by radar data.

ACKNOWLEDGEMENTS

The completion of this research paper would not have been possible without the support of Romania's National Meteorological Administration, which provided the dataset used for our analysis. In addition, we would like to thank to all the colleagues from Active Interventions in Atmosphere Iași for the advice and support throughout the research process.

REFERENCES

Amburn, S., A., Wolf, P., L. (1997) VIL density as a hail indicator. *Wea. Forecasting*., 12, 473–478, https://doi.org/10.1175/1520-0434(1997)012%3C0473:VDAAHI%3E2.0.CO;2.

Beteringhe, A., Irașoc, A., Ionac, N., Ilie, N., Sîrbu, D., A., Popescu, E. (2025) The relevance of air-instability indices in assessing the thermoconvective phenomena within the operation area of the "Traian Vuia" airport in Timișoara, on 10 July 2021, *Present Environment and Sustainable Development*, Volume 19, Issue no.1/2025, https://doi.org/10.47743/pesd2025191012

Carson, R., B. (1954) Some objective quantitative criteria for summer showers at Miami, Florida. Mon. *Wea. Rev*., 82, 9-28, https://doi.org/10.1175/1520-0493(1954)082<0009:SOQCFS>2.0.CO;2.

Chen, Z., & Wang, Y. (2019) Impacts of severe weather events on high-speed rail and aviation delays. *Transportation Research Part D*, 69, 168-183.

Craven, J., P., Jewell, R., E., Brooks, H., E. (2002) Comparison between observed convective cloud-base heights and lifting condensation level for two different lifted parcels. *Wea. Forecasting*, 17, pp. 885–890, https://doi.org/10.1175/1520-0434(2002)0172.0.CO;2.

Dennis, A. S., Schock, M. R. Koscielski, A. & Mielke, P. M. (1967) *Evaluation of cloud seeding experiments in South Dakota during 1965 and 1966*. Institute of Atmospheric Sciences Report No. 67-1, South Dakota School of Mines and Technology, Rapid City, 71 pp.

Dobri, R.,-V., Sfică, L., Ichim, P., Harpa, G.,-V. (2017) The Distribution of the Monthly 24-Hour Maximum Amount of Precipitation in Romania According to their Synoptic Causes, *Geographia Technica*, Vol. 12, Issue 2, pp 62 to 72, http://dx.doi.org/10.21163/GT_2017.122.06

Doswell, C., A., III, & Rasmussen., E., N. (1994). The effect of neglecting the virtual temperature correction on CAPE calculations. *Wea. Forecasting*, 9, 625–629, https://doi.org/10.1175/1520-0434(1994)009%3C0625:TEONTV%3E2.0.CO;2.

Florea, D. (2004) *Riscurile meteorologice şi climatice pentru navigaţia aeriană în spaţiul de zbor al aerodromului Mihail Kogălniceanu – Constanţa [Meteorological and climatic risks for air navigation in the flight space of the Mihail Kogălniceanu - Constanta airport]*, Teză de doctorat, Universitatea din București.

Franca, G. B., Almeida, M. V., Bonnet, S. M., & Albuquerque Neto, F. L. (2018). Nowcasting model of low wind profile based on neural network using SODAR data at Guarulhos Airport, Brazil. *International Journal of Remote Sensing*, 39(8), 2506–2517. https://doi.org/10.1080/01431161.2018.1425562.

Galway, J., G. (1956) The lifted index as a predictor of latent instability. *Bull. Amer. Meteor. Soc*., 37, 528–529, https://doi.org/10.1175/1520-0477-37.10.528

George, J., J. (1960) *Weather Forecasting for Aeronautics*. Academic Press, Waltham, MA, 673

Glickman, T., S. (2000) *Glossary of Meteorology*. Amer. Meteor. Soc., 855 pp.

Guijo-Rubio, D., Casanova-Mateo, C., Sanz-Justo, J., Gutiérrez, P. A., Cornejo-Bueno, S., Hervás, C. & Salcedo-Sanz, S. (2020) Ordinal regression algorithms for the analysis of convective situations over Madrid-Barajas airport. *Atmospheric Research*, 236 (November 2019), 104798. https://doi.org/10.1016/j.atmosres.2019.104798

Haidu, I. (2002) Analiza de frecvență și evaluarea cantitativă a riscurilor [Frequency analysis and quantitative risk assessment]. *Riscuri și Catastrofe*, 1, 180-207.
https://riscurisicatastrofe.reviste.ubbcluj.ro/Volume/I_2002/PDF/Haidu.pdf.

Haidu, I., Tudose, T. (2014) Validation of several atmospheric stability indices for the storms generating torrential rain showers in the north-west of Romania, *STUDIA UBB GEOGRAPHIA*, LIX, 1, pp. 37-46

Haklander, A., J.& Delden, A., V. (2003). Thunderstorm predictors and their forecast skill for the Netherlands. *Atmospheric Research*, 67–68, 273–299. https://doi.org/10.1016/S0169-8095(03)00056-5

Institutul de Meteorologie și Hidrologie (1974) *Instrucțiuni pentru stațiile meteorologice. Efectuarea observațiilor meteorologice și prelucrarea lor în scopuri climatologice [Instructions for meteorological stations. Conducting meteorological observations and their processing for climatological purposes]*, București

Istrate, V., Apostol, L., Sfîcă, L., Iordache, I., Bărcăcianu, F. (2015). The status of atmospheric instability indices associated with hail events throughout Moldova. *Air and Water Components of the Environment*, August, 323–331. https://doi.org/10.17378/AWC2015_43.

Istrate, V., Dobri, R., V., Bărcăcianu, F., Cobanu, R., A., Apostol, L. (2021) Sounding-derived parameters associated with severe hail events in Romania, *Idojaras - Quarterly journal of the Hungarian Meteorological Service*, Vol. 125, No. 1, Pages 1–166, https://doi.org/10.28974/idojaras.2021.1.2

Sfîcă, L., Apostol, L., Istrate, V., Lesenciuc, D., & Necula, M. F. (2015). Instability indices as predictors of atmospheric lightning - Moldova region study case. *International Multidisciplinary Scientific GeoConference* Surveying Geology and Mining Ecology Management, SGEM, 1(3), 387–394. https://doi.org/10.5593/sgem2015/b31/s12.050

Jardines, A., Soler, M., Cervantes, A., García-Heras, J. & Simarro, J. (2021) Convection indicator for pre-tactical air traffic flow management using neural networks. *Machine Learning with Applications*, 5(June), 100053. https://doi.org/10.1016/j.mlwa.2021.100053

Kirschenstein, M., Krasuski, K., Kozuba, J. & Kelemen, M. (2019) Assessment of the variability of many years of thunderstorm activity in the aspect of potential threats to aircraft at selected airports in Poland. *International Journal of Environmental Research and Public Health*, 17(1). https://doi.org/10.3390/ijerph17010144

Kunz, M., Puskeiler, M. (2010) High-resolution Assessment of the Hail Hazard over Complex Terrain from Radar and Insurance Data. *Met. Z.* 19: 427–439, http://dx.doi.org/10.1127/0941-2948/2010/0452

Liu, Y., Liu, Y., Hansen, M., Pozdnukhov, A., Zhang, D. (2019) Using machine learning to analyze air traffic management actions: Ground delay program case study, *Transportation Research, Part E 131*, 80-95, https://doi.org/10.1016/j.tre.2019.09.012

Lyons, R., D. (1964) A randomized cloud seeding experiment in western South Dakota. *Institute of Atmospheric Sciences Progress Report I*, South Dakota School of Mines and Technology, Rapid City, 46 pp.

Maier, N. (2011) *Studiul instabilității atmosferice și a ecourilor radar în scopul realizării prognozei de tip "Now Casting" a precipitațiilor din Munții Apuseni [The study of atmospheric instability and radar echoes for the purpose of nowcasting precipitation in the Apuseni Mountains],* Rezumat Teză de Doctorat, Universitatea „Babeș-Bolyai", Cluj-Napoca

Manzato, A. (2005) The use of sounding-derived indices for a neural network short-term thunderstorm forecast. *Weather and Forecasting*, 20, 896–917, https://doi.org/10.1175/WAF898.1

Miller, R., C. (1967) *Notes on analysis and severe storm forecasting procedures of the Military Weather Warning Center*. AWS Tech. Rep. 200 (revised), 170 pp. [Available from Headquarters, Air Force Weather Agency, Scott AFB, IL 62225.].

Miller, R., C. (1972). *Notes on analysis and severe storm forecasting procedures of the Air Force Global Weather Central*. Tech. Report 200 (Revised), AWS, USAF. [Headquarters, AWS, Scott AFB, IL 62225]

Moncrieff, M., W. & Miller, M., J. (1976) The dynamics and simulation of tropical cumulonimbus and squall lines. *Quarterly Journal of the Royal Meteorological Society*, 102(432), 373–394. https://doi.org/10.1002/qj.49710243208

Musil, D., J. & Dennis, A., S. (1968) *Convective storms of 1966 and 1967 in western Nebraska*. Institute of Atmospheric Sciences Report No. 6 8-7, South Dakota School of Mines and Technology, Rapid City, 27 pp.

Niță, I.,-A., Radu, C., Cheval, S., Bîrsan, M.,-V. (2024) Aviation accidents related to atmospheric instability in the United States (2000–2020), *Theoretical and Applied Climatology*; Wien Vol. 155, Iss. 6, https://doi.org/10.1007/s00704-024-04968-w

Peppler, R., A. (1988). *A review of static stability indices and related thermodynamic parameters*. Illinois State Water Survey. Retrieved from https://www.ideals.illinois.edu/handle/2142/48974

R Core Team (2025). R: A Language and Environment for Statistical Computing. R Foundation for Statistical Computing, Vienna, Austria. https://www.R-project.org/

Roux, B., Potts, R., Siems, S., Manton, M. (2021) Towards a better understanding of fog at Perth Airport, *Journal of Hydrology* 600(3–4):126516, https://doi.org/10.1016/j.jhydrol.2021.126516

Schultz, M., Lorenz, S., Schmitz, R. & Delgado, L. (2018). Weather Impact on Airport Performance. *Aerospace*, 5(4), 109. https://doi.org/10.3390/aerospace5040109

Schuster S., Blong, R., McAneey, K., J. (2006) Relationship between radar-derived hail kinetic energy and damage to insured buildings for severe hailstorms in Eastern Australia. *Atmos. Res*., 81, 215-235, https://doi.org/10.1016/j.atmosres.2005.12.003

Showalter, A., K. (1953). A stability index for thunderstorm forecasting. *Bull. Amer. Meteor. Soc*.,34, 250–252, https://doi.org/10.1175/1520-0477-34.6.250

Taszarek, M., Kendzierski, S. & Pilguj, N. (2020) Hazardous weather affecting European airports: Climatological estimates of situations with limited visibility, thunderstorm, low-level wind shear and snowfall from ERA5. *Weather and Climate Extremes*, 28(January), 100243. https://doi.org/10.1016/j.wace.2020.100243

Wan, Z., Liu, X., Xu, C. (2021). Multi-source observations and high-resolution numerical model applied on the analysis of a severe convective weather affecting the airport. *Meteorological Applications*, 28(4), 1–14. https://doi.org/10.1002/met.2012

Witt, A., Eilts, M., D., Stumpf, G., J., Johnson, J., T., Mitchell, E., D., Thomas, K., W. (1998) An enhanced hail detection algorithm for the WSR-88D. *Wea. Forecasting*, 13, 286-303, https://doi.org/10.1175/1520-0434(1998)013%3C0286:AEHDAF%3E2.0.CO;2

Zatula, V., I., Zatula, N., I. & Symonets, T., S. (2021) Observation and forecasting of thunderstorms in the modern practice of advisory of Kyiv International Airport (Zhuliany). *European Association of Geoscientists & Engineer,* Geoinformatics, May 2021, Volume 2021, p.1 – 6 https://doi.org/10.3997/2214-4609.20215521076

Web resources:

ECMWF - The European Centre for Medium-Range Weather Forecasts: www.cds.climate.copernicus.eu. (20.10.2024)

European Severe Weather Database (ESWD): https://www.essl.org/cms/european-severe-weather-database/ (18.11.2025)

Global Forecast System archive: www.wetter3.de (20.10.2024)

National Meteorological Administration: www.meteoromania.ro (10.10.2024)

University of Wyoming. College of Engineering: www.weather.uwyo.edu/upperair/sounding.html (20.10.2024)

ThundeR rawinsonde package: www.rawinsonde.com/ERA5_Europe/ (27.10.2024)

GIS-BASED SPATIAL BIAS ADJUSTMENT OF RADAR-DERIVED RAINFALL ESTIMATES DURING STORM DISSIPATION IN CENTRAL THAILAND

Apichaya KANGERD [1] ***& Nattapon MAHAVIK*** [1,2*]

DOI: 10.21163/GT_2026.211.13

ABSTRACT

Thailand lies in a tropical monsoon region and is frequently affected by the decay of tropical storms during the rainy season, with 2–5 storms typically occurring each year. Accurate quantitative precipitation estimates (QPE) are therefore essential for assessing storm-related rainfall and associated flood risks. Radar-based rainfall estimation is particularly suitable but is prone to systematic bias arising from the radar reflectivity–rainfall (Z–R) relationship. This study develops a Geographic Information System (GIS)-based analytical approach to evaluate and compare Z–R relationships and to reduce bias between radar-estimated and gauge-observed rainfall. The analysis was conducted across lowland and mountainous areas in northern and central Thailand using data from the Phitsanulok C-band weather radar and 89 rain gauge stations during Tropical Storm Son-Tinh (2018). This study integrates radar data with Geographic Information Systems (GIS) to systematically compare multiple Z–R relationships alongside spatial bias correction, and to evaluate differences in rainfall estimation accuracy between lowland and mountainous areas. Three Z–R relationships Marshall–Palmer (MP), Rosenfeld Tropical (RF), and Summer Deep Convection (SD) were employed to generate event-based radar rainfall estimates. Spatial bias correction was conducted using the Inverse Distance Weighting (IDW) method, and accuracy was assessed through five-fold cross-validation. The results indicate that uncorrected radar rainfall estimates generally underestimate actual precipitation, whereas the IDW-based correction significantly reduces the Mean Field Bias (MFB) and improves estimation accuracy across diverse terrains. Among the three Z–R relationships, the Marshall–Palmer equation yielded the lowest errors, with a root mean square error (RMSE) of 17.517 mm and a mean absolute error (MAE) of 13.405 mm. The event-based spatial adjustment demonstrates that integrating an appropriate Z–R relationship with GIS-based bias correction substantially enhances radar QPE reliability, particularly in regions with complex topography. This framework offers practical value for hydrological applications and flood risk management in tropical monsoon regions.

Keywords: *Quantitative Precipitation Estimation (QPE); Bias correction; GIS-based analysis; Tropical Storm Son-Tinh.*

1. INTRODUCTION

Thailand was among the countries in Southeast Asia that were impacted by Tropical Storm Son-Tinh in July 2018. The storm resulted in substantial damage to infrastructure and agriculture, notably in the northeastern and northern regions of Thailand, as well as flash floods, widespread inundation, and heavy rainfall (Thai Meteorological Department, 2018; National Water Resources Agency, 2018). The predominance of convective clouds over stratiform clouds was observed in radar-based analyses of storm decomposition in central Thailand, as evidenced by multi-station radar mosaics (Mahavik & Tantanee, 2020a). This incident underscores the significance of accurate rainfall estimation in the context of disaster management and early warning systems. However, because spatial bias varies across different radar rainfall relationships, applying spatial bias correction may improve radar rainfall estimates within the water basin. Accordingly, this study investigates whether such correction can enhance the accuracy of radar-derived rainfall.

[1]*Department of Natural Resources and Environment, Faculty of Agriculture Natural Resources and Environment, Naresuan University, Phitsanulok 65000, Thailand, apichayakan66@nu.ac.th*
[2]*Water Resources Research Center, Faculty of Engineering, Naresuan University, Phitsanulok 65000, Thailand,*
**Corresponding author: nattaponm@nu.ac.th*

The spatial resolution and reliability of precipitation data are critical factors in the study of floods and rainfall. The upper Chao Phraya basin and its tributaries Ping, Wang, Yom, and Nan are distinguished by their complex topography, which encompasses narrow valleys, foothills, and ridges. Abro et al. (2019) have demonstrated that highland regions typically receive a greater amount of annual rainfall than lowlands. However, satellite-based precipitation products frequently underestimate rainfall in these regions, particularly during severe storms with highly heterogeneous precipitation rates. The sparse and uneven distribution of ground-based rain gauges results in high uncertainty in rainfall datasets, despite the fact that they provide precise point-scale measurements (Brauer et al., 2016). This is due to the fact that mountainous and remote areas are underrepresented.

Weather radar provides spatially and temporally detailed rainfall observations that are appropriate for medium to small basins (Harrison et al., 2009). Nevertheless, radar measurements are susceptible to a variety of sources of uncertainty, such as attenuation, anomalous propagation, ground clutter, calibration errors, partial beam blockage, and bright band contamination (Gourley & Calvert, 2003; Krajewski et al., 2010; Krajewski et al.,2011; Sharif et al., 2020; Mahavik et al., 2025). The quality of radar echoes is further compromised by clutter from communication towers, towering buildings, or mountains, resulting in the misclassification of non-precipitation signals as rainfall (Mahavik et al., 2025). Nevertheless, the integration and processing of multi-station radar data have been demonstrated to improve rainfall monitoring in storm decay events across vast basins, despite these challenges (Mahavik & Tantanee, 2020; Mahavik et al., 2025).

The relationship between radar reflectivity and rainfall rate (Z–R relationship) is a fundamental component of radar-based quantitative precipitation estimation (QPE), as it provides the empirical link between radar reflectivity (Z) and the surface rainfall rate (R). The Z–R relationship is not universal; rather, it varies depending on factors such as drop size distribution (DSD), storm type, and topographic conditions (Morin et al., 2003; Wu et al., 2018). Accurate QPE therefore requires selecting an appropriate Z–R relationship that best represents the rainfall characteristics of each region. The Marshall–Palmer (MP) (Marshall & Palmer, 1948), Rosenfeld Tropical (RF) (Rosenfeld et al., 1993), and Summer Deep Convection (SD) (Battan, 1973) equations are widely used examples that represent distinct environmental and microphysical rainfall characteristics. Specifically, the MP relationship is most suitable for stratiform rainfall characterized by small raindrop sizes, the RF for tropical convective rainfall typical of humid climates, and the SD for deep convective rainfall associated with intense summer thunderstorms.

Radar-based rainfall estimates are frequently combined with rain gauge data to rectify systematic biases, thereby further reducing uncertainties. Spatial interpolation and other bias correction techniques are employed to mitigate the discrepancy between radar areal estimates and point-scale gauge observations (Ahrens, 2006; Mahavik, 2017; Mapium et al., 2022). Geographic Information Systems (GIS) offer robust instruments for the integration of spatial data, the management of rainfall fields, and the application of bias correction techniques, thereby increasing the value of radar datasets for hydrological and meteorological applications (Xie et al., 2005; Cho, 2020; Mahavik et al., 2021).

Therefore, the integration of radar-based rainfall estimates with ground-based rain gauge measurements, which can be effectively implemented through Geographic Information Systems (GIS), is crucial for enhancing rainfall estimation accuracy, particularly in regions with complex terrain. This study systematically applies atmospheric radar data in conjunction with GIS in the central region of Thailand to analyze rainfall associated with Tropical Storm Son-Tinh (2018). Radar data were obtained from the Phitsanulok C-band radar station, while rainfall measurements were collected from 89 ground-based rain gauge stations. The primary objective was to evaluate the suitability of three Z–R relationships: Summer Deep Convection (SD), Rosenfeld Tropical (RF), and Marshall–Palmer (MP). To address spatial bias, the Inverse Distance Weighting (IDW) method was applied, and the estimation accuracy was assessed using five-fold cross-validation to examine the consistency between radar-derived rainfall and gauge observations. Accuracy was further evaluated using two categories of statistical metrics: (1) error-based measures, including Root Mean Square Error (RMSE) and Mean Absolute Error (MAE), and (2) bias-based measures, such as Mean Field Bias (MFB).

2. STUDY AREA

The ground-based weather radar at the Phitsanulok Weather Radar Station, operated by the Thai Meteorological Department, is located at an elevation of 47 meters above mean sea level (MSL) at geographic coordinates 16.775531°N, 100.217901°E, as shown in **Fig. 1** The radar operates in the C-band frequency with an observation radius of 240 km and performs four scans per hour at elevation angles of 0.5°, 1.5°, 2.4°, and 3.4° (Kangerd et al., 2024; Mahavik et al., 2025). The area covered by the weather radar encompasses diverse topography, ranging from flood-prone lowland plains in the central and southern regions to mountainous terrain distributed along the western, northern, and eastern edges of the radar detection range. This region also includes key river basins within the Chao Phraya watershed, such as the Ping, Wang, Yom, and Nan rivers. In mid-July, the study area experienced intense rainfall and flooding associated with Tropical Storm Son-Tinh, which moved from Vietnam into the upper northeastern region of Thailand, coinciding with a strong southwest monsoon. The combination of the storm and monsoon resulted in prolonged heavy rainfall, particularly over the upper northern and northeastern regions. Consequently, this event was selected as a case study within a 120-kilometer radar observation radius.

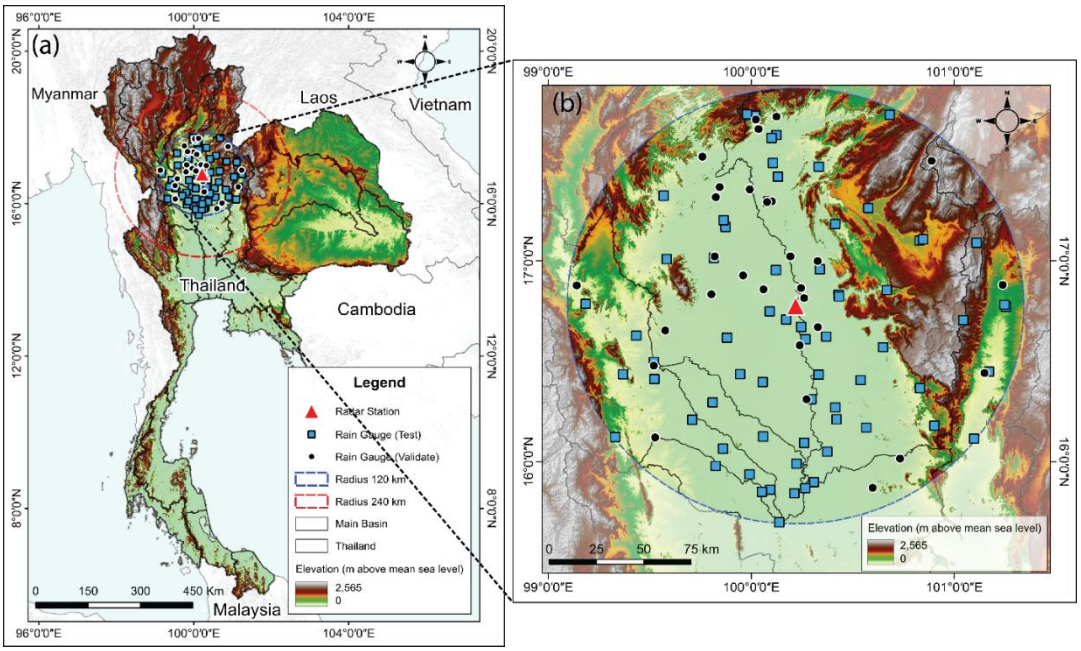


Fig. 1. Study area: (a) the national boundary of Thailand; (b) the observational domain of the Phitsanulok weather radar within the Chao Phraya Basin. The red triangle denotes the location of the radar station. The blue dashed circle represents the radar's observation coverage with a radius of 120 kilometers. Blue squares with black outlines indicate the locations of ground-based rain gauge stations used as the testing dataset, while black circles with white outlines represent the validation dataset. In total, 89 rain gauge stations were employed in this study.

3. DATA AND METHODS

3.1. Radar Data Observed by Ground-Based Radar Station

In order to minimize uncertainty and more accurately represent near-surface rainfall, radar data at the lowest available elevation angles were chosen for this investigation, as per the methodology of Kangerd et al. (2024). To analyze the rainfall associated with Tropical Storm Son-Tinh over a nine-day period (15–23 July 2018), a Constant Altitude Plan Position Indicator (CAPPI) was generated at 2 km above mean sea level. The Thai Meteorological Department (TMD) operates the Phitsanulok Weather Radar Station in Thailand (16.775531°N, 100.217901°E; 47 m a.s.l.), from which the data

were obtained. This C-band dual-polarization radar has a 240 km observation radius, which allows it to cover lower northern and central Thailand. It conducts scans every 15 minutes (four times per hour) at elevation angles of 0.5°, 1.5°, 2.4°, and 3.4° (Mahavik et al., 2025). Only daily accumulated rainfall files with a scan availability of at least 80% (≥19 hours of data per day) were retained for quality control. All 825 radar files that met these criteria have been used in the analysis.

3.2. Rain gauge rainfall data

Within a 120 km radar observation radius, rainfall data and station locations were obtained from the Automatic Telemetry Stations of the Water Resources Information Institute (Public Organization; WRI). It is imperative to resolve radar limitations, including signal attenuation with distance and beam broadening, which can result in a discrepancy between radar reflectivity and actual ground rainfall (Mahavik et al., 2024). These stations are thus crucial. The WRI API was used to access the data in CSV format (https://tiservice.hii.or.th/opendata/data_catalog/hourly_rain/0all_stn_meta data. csv) for the duration of Tropical Storm Son-Tinh, local Thailand time. After quality control and the removal of anomalous or lacking data, 89 stations were chosen for the study in accordance with the gauge-density standards of the World Meteorological Organization (2008), as shown in **Fig. 1b** Initially, 96 stations were considered. We employed these hourly rainfall data as ground truth for the bias correction procedure, comparing them to radar-derived rainfall.

3.3. Digital elevation model (DEM)

A 30-meter spatial resolution Digital Elevation Model (DEM) from the United States Geological Survey (USGS) was used. The researchers developed code to classify areas based on slope values derived from the DEM. The slope classification was adapted from Mokarram & Hojati (2016), where areas with slopes $\leq 5^{\circ}$ were defined as flat or lowland (Class 1), and those $>5^{\circ}$ as hilly or mountainous (Class 2), with no-data areas assigned as Class 0. The resulting raster-based classification (lowland vs. mountainous) was then converted into vector format for GIS-based spatial analysis.

3.4. Software and Libraries

Data analysis was conducted using Python. The open-source Py-ART library (Helmus & Collis, 2016) was employed for processing and analyzing ground-based radar data and is fully compatible with other Python libraries, including NumPy, Scikit-learn, Matplotlib, CartoPy, and Xarray (Bowden et al., 2025; Mahavik et al., 2024, 2025). Py-ART was specifically used for filtering and removing signal noise (Signal-to-Noise Ratio: SNR) and for attenuation correction using dual-polarimetric variables, which compensates for signal weakening with distance and improves radar observations of convective cloud systems in the C-band radar (Gu et al., 2011), providing accurate input for rainfall estimation. Open-source GIS software QGIS (QGIS Development Team, 2024) was used for geospatial visualization of radar data, both in preliminary data preparation and spatial analysis. In this study, a workflow was developed in QGIS to process accumulated rainfall, facilitating efficient handling of both spatial and temporal data for subsequent analyses.

3.5. Z-R relationships

The Z–R relationship, which describes the correlation between radar reflectivity and rainfall rate, is used to estimate rainfall from radar reflectivity measurements. Radar reflectivity, representing the scattering of radar waves by raindrops in the atmosphere, cannot directly indicate the amount of rainfall reaching the ground, unlike ground-based rain gauge measurements. Therefore, radar reflectivity (Z), measured in dBZ, must be converted into rainfall rate (R) (Mahavik et al., 2021; Mapiam & Sriwongsitanon, 2008) using a power-law relationship, as expressed in Eq. (1)

$$Z = aR^b \tag{1}$$

where, Z denotes the radar reflectivity factor, expressed in units of (mm6 /m^{-3}) while R represents the rainfall rate, expressed in (mm/h). Constants a and b (**Table 1**.) are empirical coefficients that depend on the raindrop size distribution and may vary according to rainfall characteristics, precipitation type, and seasonal conditions. In Thailand, commonly adopted coefficient values have been defined for operational use.

Table 1.

Z–R relationships used for converting radar reflectivity to rainfall rate.

Z-R relationship	Equation	Description
Marshall/Palmer (MP)	$Z = 200R^{1.6}$	Represents stratiform rainfall events or small raindrop sizes in mid-latitudes (Marshall & Palmer, 1948).
Rosenfeld Tropical (RF)	$Z = 250R^{1.2}$	Represents rainfall events in tropical regions (Rosenfeld et al., 1993).
Summer Deep Convection (SD)	$Z = 300R^{1.4}$	Represents convective rainfall events associated with vertically developed clouds or intense convective storms during summer (Battan, 1973).

3.6. Evaluation metrics

In order to assess the performance of radar-estimated rainfall in comparison to ground-based measurements, three statistical metrics were used: Root Mean Square Error (RMSE) and Mean Absolute Error (MAE), which quantify the magnitude of differences between radar and observed rainfall, and Mean Field Bias (MFB), which evaluates whether radar rainfall tends to systematically overestimate or underestimate rainfall relative to gauge observations. Based on Mahavik et al. (2024), these statistics are frequently employed to assess the discrepancies between observed and model-derived data. MFB is a method that is frequently employed in meteorological research to evaluate the accuracy and bias of radar precipitation estimates. It is specifically used to evaluate the difference between radar-estimated rainfall (RR) and gauged rainfall (GR).

3.6.1. Root mean squared error: RMSE

RMSE is a statistical measure used to quantify the magnitude of errors in estimated rainfall compared with ground observations. It is computed by squaring the differences between radar and gauge rainfall, averaging these squared differences, and then taking the square root of the mean. RMSE therefore reflects the average magnitude of error in quantitative terms. Because squaring emphasizes larger deviations, substantial errors exert greater influence on the RMSE than smaller ones. The RMSE is expressed as Eq. (2)

$$\mathrm{RMSE} = \sqrt{\frac{1}{n}\sum_{i=1}^{n}(\mathrm{GR_i} - \mathrm{RR_i})^2} \tag{2}$$

3.6.2. Mean absolute error: MAE

MAE is a statistical index used to assess the accuracy of radar-estimated rainfall by comparing it against ground-based observations. It is calculated as the mean of the absolute differences between radar estimates and gauge measurements. Unlike RMSE, MAE does not disproportionately weight larger errors, thereby providing a balanced representation of the average magnitude of discrepancies, regardless of whether they result from overestimation or underestimation. This property makes MAE a neutral and intuitive measure of the average difference between radar and ground rainfall. The MAE is expressed as Eq. (3)

$$\mathrm{MAE} = \frac{1}{n}\sum_{i=1}^{n}|\mathrm{GR_i} - \mathrm{RR_i}| \tag{3}$$

3.6.3. Mean field bias: MFB

MFB is a fundamental technique used to adjust systematic multiplicative biases in radar-derived rainfall estimates. This metric is critical for improving the accuracy of rainfall estimation derived from radar reflectivity (Hanchoowong et al., 2012). Following Krajewski & Smith (2002), MFB is calculated by dividing the accumulated radar-estimated rainfall over a given period by the accumulated gauge-measured rainfall for the same period. An MFB value greater than 1 indicates that radar estimates tend to underestimate actual rainfall, while an MFB value less than 1 indicates that radar estimates tend to overestimate rainfall relative to ground observations. The formulation is given in Eq. (4)

$$\mathrm{MFB} = \frac{\sum_{i=1}^{n} \mathrm{GR_i}}{\sum_{i=1}^{n} \mathrm{RR_i}} \tag{4}$$

where GR_i represents the accumulated rainfall from a ground-based gauge at observation point i, and RR_i denotes the corresponding radar-estimated rainfall covering that point.

3.7. Spatial Interpolation

Spatial interpolation is commonly applied in meteorology to reduce biases in radar-estimated rainfall by integrating point-scale gauge measurements with spatially continuous radar data. In general, interpolation estimates rainfall values at unsampled locations using information from surrounding stations, thereby addressing the sparse or uneven distribution of rain gauges. Among deterministic approaches, which are widely used for bias correction, Inverse Distance Weighting (IDW) is particularly well established. IDW assumes that observations closer to the target location exert greater influence than those farther away, making it suitable for local rainfall adjustment (Chang & Kang-tsung, 2002). Previous studies have demonstrated its effectiveness: Ahrens (2006) highlighted its utility in producing daily rainfall maps and filling missing values in time series, while Chen & Liu (2012) successfully applied IDW for spatial rainfall interpolation in complex environments. More recently, Sokol et al. (2021) emphasized the relevance of deterministic methods such as IDW for radar–gauge integration. In this study, IDW was employed as a deterministic bias-correction technique to adjust radar-estimated rainfall against gauge observations. The formulation used is presented in Eq. (5) and Eq. (6)

$$\hat{R}_p = \sum_{i=1}^{N} w_i R_i \tag{5}$$

$$w_i = \frac{d_i^{-\alpha}}{\sum_{i=1}^{N} d_i^{-\alpha}} \tag{6}$$

where $\hat{R}_p$ is the unknown rainfall at location p (mm), R_i is the observed rainfall at the i ground station (mm), N is the number of stations used for interpolation, w_i is the weight assigned to station i, d_i is the distance from station i to the radar pixel, and α is the power parameter controlling the influence of distance, typically set to 2 (Kangerd et al., 2024; Lin & Yu, 2008).

3.8. K-Fold Cross-Validation

To assess the robustness of radar rainfall adjustment against ground-based observations, a K-fold cross-validation framework was implemented. Cross-validation is widely used to evaluate model performance by partitioning the dataset into multiple folds, thereby reducing dependence on a single train–test split and minimizing bias. In this study, the rain gauge dataset comprising 89 stations was randomly divided into five folds (K = 5) using QGIS tools. For each iteration, approximately 70% of the stations were assigned to the calibration subset and 30% to the validation subset. This procedure ensured that all stations were used for both calibration and validation across different folds, providing a reliable measure of model stability and accuracy.

3.9. Radar data correction

Removal of Clutter and Noise (Signal-to-Noise Ratio: SNR). Raw radar reflectivity data were preprocessed to remove contamination from non-meteorological sources, such as ground clutter, using the open-source Py-ART library (Helmus & Collis, 2016). SNR was calculated for each radar gate, and a gate filter was applied to exclude values below 1 dBZ or above 70 dBZ. These thresholds were selected to eliminate anomalous signals typically associated with clutter or spurious atmospheric variability. The Top of Atmosphere (TOA) parameter was set to 15,000 m to further suppress non-meteorological echoes.

Because C-band radar is highly sensitive to signal attenuation, which increases with both propagation distance and rainfall intensity, and because the study area contains mountain ranges that cause partial and complete beam blockage, resulting in reduced returned reflectivity (Mahavik & Tantanee, 2020b), an attenuation correction was also applied to the reflectivity field (Gu et al., 2011). After correction, the data were considered most reliable within a 120 km range, where radar estimates exhibited the highest consistency with ground-based rainfall observations (Mahavik et al., 2025). The establishment of the 120 km radar coverage boundary is based on the technical limitations of the C-band radar system and the degradation of reflectivity signal quality with increasing distance, primarily due to noise contamination and attenuation effects. As the radar beam propagates farther from the radar site, beam broadening and loss of spatial resolution become significant, leading to reduced radar performance and decreased accuracy in quantitative precipitation estimation (QPE), consistent with the findings of Mahavik et al. (2025). together, these preprocessing steps clutter, and noise filtering, TOA adjustment, and attenuation correction were essential to ensure that the reflectivity inputs used in Z–R rainfall estimation were physically consistent and of high quality.

3.10. Workflow of data analysis

The data analysis framework of this study comprised four main steps: (1) data collection, (2) data processing, (3) development of analytical methods in GIS, and (4) data analysis (**Fig. 2**).

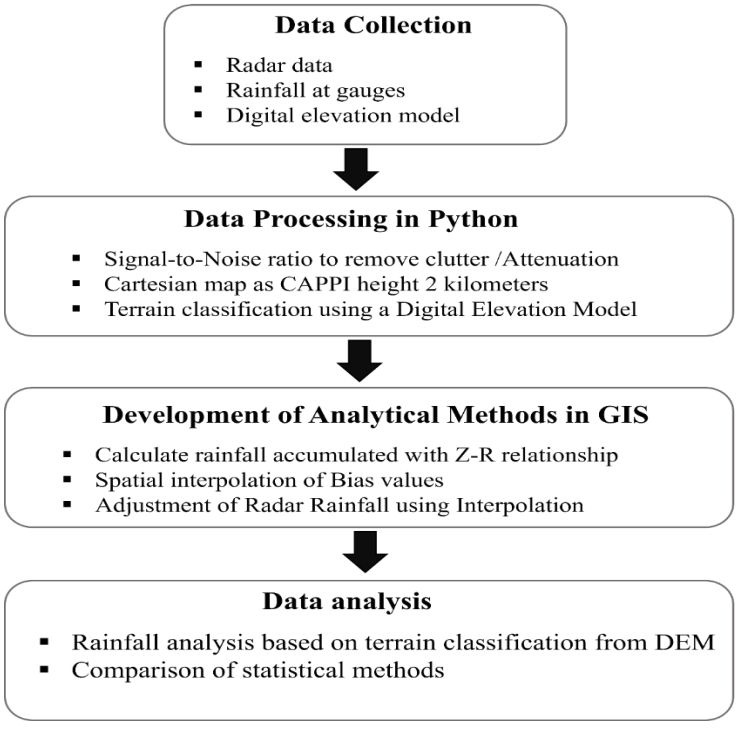


Fig. 2. Conceptual framework of the research workflow.

Data Collection. Three types of data were used: radar observations, ground-based rainfall measurements, and topographic information. Radar data were obtained from the Phitsanulok C-band ground-based weather radar operated by the Thai Meteorological Department. Four elevation angles (0.5°, 1.5°, 2.3°, and 3.4°) were selected for the period 15–23 July 2018, covering the passage of Tropical Storm Son-Tinh. To ensure temporal completeness, only days with at least 80% scan availability (≥19 hours) (Mahavik et al., 2025) were retained, resulting in 825 UF-format files recorded in UTC. Rainfall data were collected from 96 automatic telemetry stations within a 120 km radius of the radar. After quality control and removal of abnormal stations, 89 stations were retained. Data were retrieved via a Python API and synchronized to local Thai time, following the approach of Kangerd et al. (2024) to ensure temporal consistency with radar scans. Topographic information was derived from a USGS Digital Elevation Model (DEM) with 30 m resolution. The DEM was used to classify terrain into three categories: flat (slope ≤ 5°), mountainous (slope > 5°), and no-data areas.

Data Processing. Radar data were preprocessed using Python and the open-source Py-ART library (Helmus & Collis, 2016). The procedure included ground clutter filtering, attenuation correction, and transformation from polar to Cartesian coordinates. Reflectivity fields were converted into rainfall products in Constant Altitude Plan Position Indicator (CAPPI) format at 2 km altitude, generated for four scans per hour (00, 15, 30, and 45 minutes). The outputs were exported as GeoTIFF files for further spatial analysis in QGIS.

Development of Analytical Methods in GIS. A rainfall estimation and bias-correction model was implemented in GIS using the Processing Modeler. This design improved efficiency and minimized redundancy in data handling. Radar reflectivity (Z) was converted into rainfall rate (R) using three Z–R relationships: Marshall–Palmer (Marshall & Palmer, 1955), Rosenfeld Tropical (Rosenfeld et al., 1993), and Summer Deep Convection (Battan, 1973). Radar rainfall was aggregated into hourly, daily, and event-based totals, with values extracted at gauge locations (30% validation stations) for evaluation prior to bias correction. Model performance was assessed using five-fold cross-validation (K = 5), implemented in QGIS with a 70:30 calibration–validation split. Spatial bias correction was conducted by interpolating gauge‑radar differences using Inverse Distance Weighting (IDW) with the search radius and the number of interpolation points set according to the software defaults. The Distance coefficient (P) was tested from 1 to 6 using K-fold cross-validation, and model accuracy was evaluated based on RMSE, MAE, and correlation. It was found that P = 2 produced the optimal results after bias correction. (Kangerd et al., 2024) Corrected rainfall fields were subsequently re-extracted at validation stations for post-correction analysis.

Data Analysis. Spatial error patterns were analyzed in QGIS by comparing radar–gauge discrepancies across DEM-derived terrain classes. Accuracy was assessed using error metrics RMSE and MAE as well as bias metrics including MFB. These analyses provided a systematic evaluation of radar rainfall estimates before and after bias correction. Kangerd et al. (2024).

4. RESULTS AND DISCUSSIONS

4.1. Radar data correction process

The preprocessing workflow that was performed to the radar reflectivity data is shown in **Fig. 3** In **Fig. 3a**, we can see that the raw reflectivity field is heavily contaminated with ground clutter and non-precipitation echoes, especially in the vicinity of the radar station. To eliminate out-of-the-ordinary signals from surface objects and atmospheric variability, a gate filter based on signal-to-noise ratio (SNR) thresholds (1-70 dB) was implemented using the free and open-source Py-ART package. With non-meteorological echoes properly suppressed, the precipitation structure is more clearly highlighted by the resultant filtered reflectivity (**Fig. 3c**). The next step was to implement attenuation correction in order to overcome the limitations of C-band radar. In places with heavy precipitation and at larger distances from the radar, the uncorrected reflectivity underestimates the rainfall intensity, as demonstrated in **Fig. 3d** Better detection of faraway and severe rainstorms is made possible by the restored signals brought about by the corrected field (**Fig. 3e**).

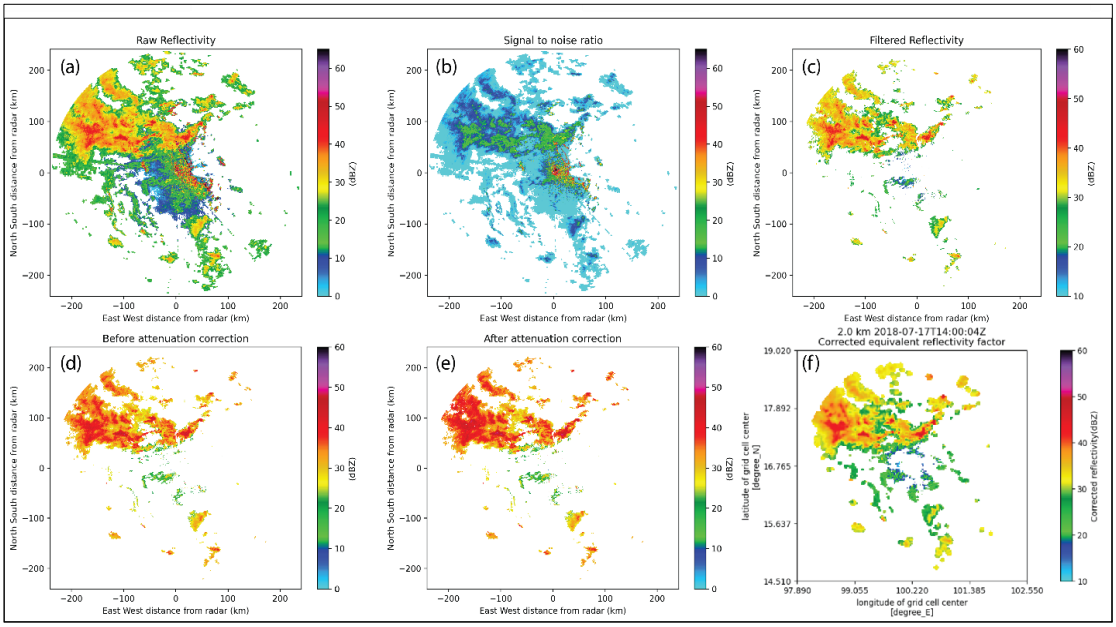


Fig. 3. Radar clutter and attenuation correction process during Tropical Storm Son-Tinh on 17 July 2018 at 21:00 local time (14:00 UTC). (a) Raw reflectivity, (b) Signal-to-Noise Ratio (SNR), (c) Filtered reflectivity using SNR-based gate filter, (d) Before attenuation correction, (e) After attenuation correction, (f) Conversion from polar coordinates to Cartesian grid. Reflectivity values are shown in the range of 0–60 dBZ.

Lastly, **Fig. 3f** shows the results of transforming the reflectivity data from polar to Cartesian coordinates. This created a gridded dataset that is spatially consistent and may be used for future rainfall estimation and analysis using GIS.

4.2. Development of the Radar Analysis Process in a GIS System

Using the open-source GIS program QGIS, which offers efficient capabilities for processing huge spatial datasets, the researchers in this work computed the accumulated rainfall on an hourly basis using radar measurements (Kangerd et al., 2024). Due to the complexity and lack of compatibility with spatial analysis in raw radar data, the reflectivity fields were converted into GIS-ready forms that could be used to integrate analytical models. For the purpose of reproducibility and adaptability in dealing with the massive amounts of data and high temporal resolution of radar scans, open-source software was chosen. The approach was optimized by using a QGIS automated processing model (**Fig. 4**).

Fig. 5 shows how this approach uses the three Z-R relationships to systematically transform raw reflectivity into hourly rainfall fields, which are then aggregated to create event-based rainfall datasets. The regional diversity induced by distinct Z-R relationships is illustrated in **Fig. 5**, which depicts the event-based accumulated rainfall during Tropical Storm Son-Tinh (15-23 July 2018). A no-data zone above the radar site was created by the cone of silence, and rainfall was scattered throughout most of the 120 km radar sweep.

The storm's most affected regions in the eastern and northeastern sectors also had the densest concentrations of heavy rainfall. The Z-R connections diverged significantly. The most intense rainfall was produced by the ZR-RF connection (**Fig. 5b**), which highlighted the presence of isolated convective cores. Strong rainfall was also recorded by the ZR-SD relationship (**Fig. 5c**), although it was less concentrated than ZR-RF. In comparison to the other two formulations, the ZR-MP relationship (**Fig. 5a**) produced a less concentrated and more evenly distributed rainfall field, which understated the severity of isolated extremes.

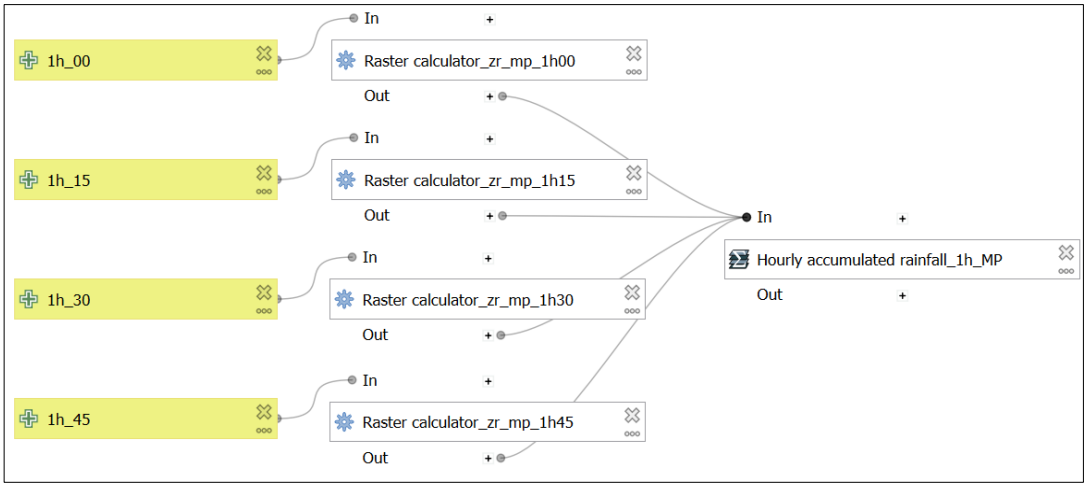


Fig. 4. Automated model for calculating hourly accumulated rainfall using the Marshall–Palmer Z–R relationship.

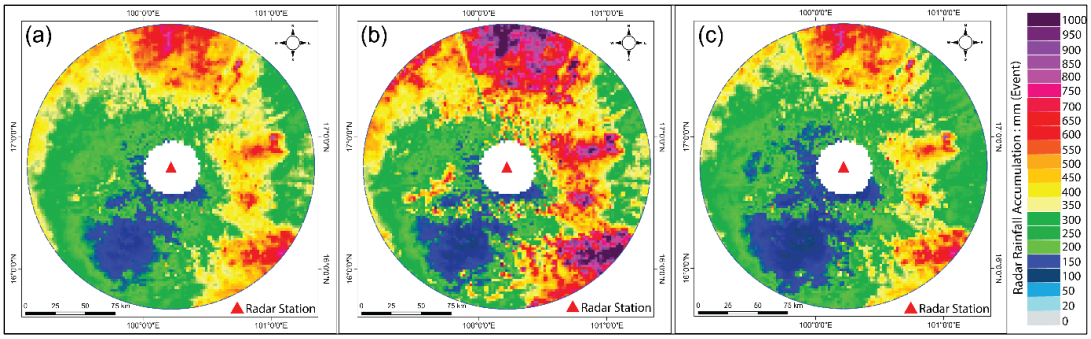


Fig. 5. Illustrates the event-based accumulated rainfall maps of Tropical Storm Son-Tinh from 15–23 July 2018 derived using different Z-R relationships: (a) ZR-MP, (b) ZR-RF, and (c) ZR-SD.

Rainfall measurements at test rain gauge locations (**Fig. 1b**) were obtained using radar-derived rainfall maps, retaining only nonzero pairs for analysis. This combination facilitated the computation of bias between radar and gauge data, subsequently spatially interpolated by the IDW method. **Fig. 6** provides an example of the interpolation findings for the ZR-MP connection. The bias distribution displays distinct spatial patterns: radar consistently overestimates rainfall in the eastern region of the coverage area (red shading) while underestimating rainfall in the mountainous west (blue shading), where topographic blockage diminishes radar signal reliability. While **Fig. 6** shows the ZR-MP scenario, same spatial bias tendencies were noted for the ZR-RF and ZR-SD correlations.

Following bias correction with the adjustment factors generated from the IDW, **Fig. 7** shows the rainfall fields locations where the radar had previously overestimated rainfall now have lower values, and locations where it had underestimated rainfall have had their value adjusted upwards to match gauge observations. This is clearly visible in the revised maps. By validating the results against separate stations, we can see that the correction process successfully reduced systematic deviations and confirmed a significant decrease in MBE. Because the bias's spatial distribution doesn't change over time, we can infer that the inaccuracies are systematic and caused mostly by differences in station placement and topography. One way to improve radar rainfall estimates is to use the spatially averaged bias as a correction factor. However, the distribution and density of rain gauges limit the precision of the corrections; in areas where there are few gauges, residual errors could be left over since the bias estimation isn't as accurate.

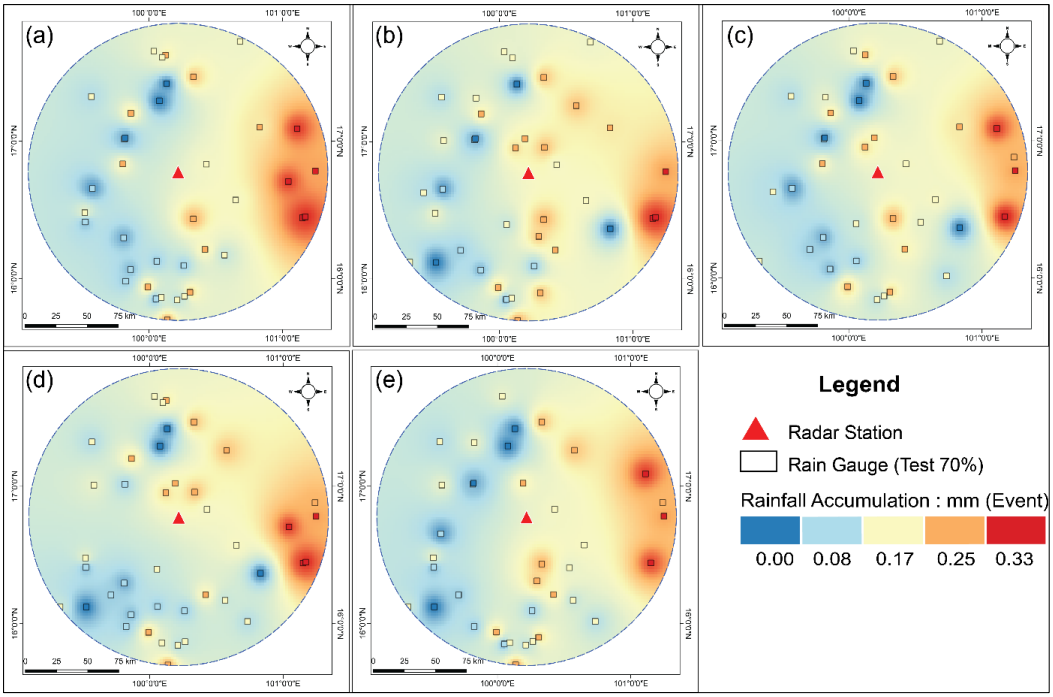


Fig. 6. Event-based spatial interpolation of bias using the IDW method derived from the Marshall–Palmer (ZR-MP) relationship, based on 70% of ground rain gauge stations used as the test set through K-fold cross-validation, with panels representing (a) K-fold = 1, (b) K-fold = 2, (c) K-fold = 3, (d) K-fold = 4, and (e) K-fold = 5.

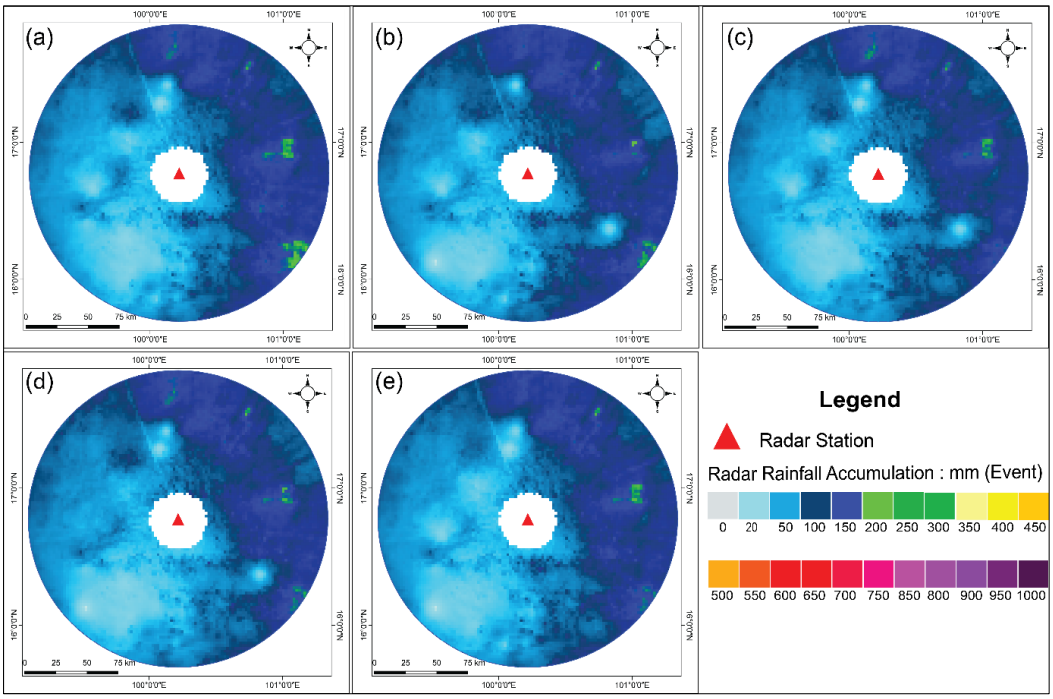


Fig. 7. Event-based radar rainfall maps after spatial bias correction using the IDW method, derived from the Marshall–Palmer (ZR-MP) relationship, with K-fold cross-validation applied, where (a) K-fold = 1, (b) K-fold = 2, (c) K-fold = 3, (d) K-fold = 4, and (e) K-fold = 5.

4.3. Spatial Bias Correction

Five-fold cross-validation (K = 5) was used to adjust MFB using rainfall values from test rain gauge locations. **Table 2.** shows that this procedure's estimations of Mean Rain Gauge, Mean Rain Radar, Bias, and MFB contain both geographical and temporal variability, and that it minimized dependent on a single train-test split by averaging findings across five rounds. Different behaviors were displayed by the three Z-R connections. The ZR-RF equation yielded the lowest Bias (0.115 mm), but it provided extremely high radar totals (331.333 mm compared to 37.047 mm from gauges), suggesting a significant overestimation that would skew estimations of cumulative rainfall. The ZR-SD relationship, on the other hand, reflected systematic underestimation by producing lower radar totals but the largest Bias (0.168 mm). The most balanced findings were produced by the ZR-MP relationship, which avoided significant overestimation while still providing accurate radar rainfall of 247.100 mm with a mild Bias of 0.150 mm. When it came to this event, ZR-MP consistently performed the best.

Table 2.

Adjustment of Mean Field Bias using k-fold cross validation.

k-fold cross validation	Mean Rain gauge (mm)	Mean Rain radar (mm)	Bias (mm)	MFB (mm)
Marshall/Palmer	37.047	247.100	0.150	37.047
Rosenfeld Tropical	37.047	321.334	0.115	37.047
Summer Deep Convection	37.047	220.003	0.168	37.047

The initial evaluation of the bias between radar-derived rainfall and gauge observations was conducted using the 30% validation set prior to correction. Substantial biases were observed in the northern and eastern sectors of the study area, particularly over mountainous terrain, as illustrated in **Fig. 8(a–e)** for the ZR-MP relationship. The largest deviations between radar and gauge values were observed in these regions, which were influenced by topographic factors such as anomalous propagation, beam obstruction, and signal attenuation. In contrast, the central lowlands exhibited relatively lesser biases, which is consistent with the more stable radar performance in flat terrain.

Discrepancies were substantially reduced throughout the study area following bias correction (**Fig. 8(f–j)**). The bias magnitudes in mountainous regions experienced a significant decrease, whereas the lowland areas exhibited only minor alterations as a result of their preexisting lower bias levels. The correction enhanced agreement with gauge data in all three Z–R relationships, although the degree of improvement differed. The residual biases of the ZR-RF and ZR-SD equations were higher than those of the ZR-MP equation, suggesting that the ZR-MP equation was more effective in reducing systematic errors. This result is in accordance with the results summarized in **Table 3.**, which indicate that ZR-MP exhibited the lowest average bias across K-folds and terrain categories.

The performance of the three Z–R equations—ZR-MP, ZR-RF, and ZR-SD—before and after bias correction is summarized in **Table 3.** The correlation and determination coefficients (R^2) for all three relationships were enhanced by the correction, which was implemented through IDW spatial interpolation with five-fold cross-validation. The most consistent results were obtained by ZR-MP, which also had the highest post-correction correlation (0.761) and R^2 (0.850) and an MBE of 0.999 mm, indicating excellent agreement with gauge observations.

ZR-SD, which initially exhibited the highest bias prior to correction, significantly improved following correction and nearly matched the performance of ZR-MP (Correlation = 0.757; R^2 = 0.848; MBE = 0.990 mm). Conversely, ZR-RF demonstrated inferior post-correction performance, as evidenced by its reduced correlation (0.729) and R^2 (0.829), despite its negligible pre-correction bias. In conclusion, these findings verify that bias correction employing IDW with cross-validation effectively mitigates systematic errors and enhances radar rainfall accuracy. The most balanced and reliable estimates were provided by ZR-MP, while ZR-SD exhibited significant post-correction potential. ZR-RF was less effective for this event.

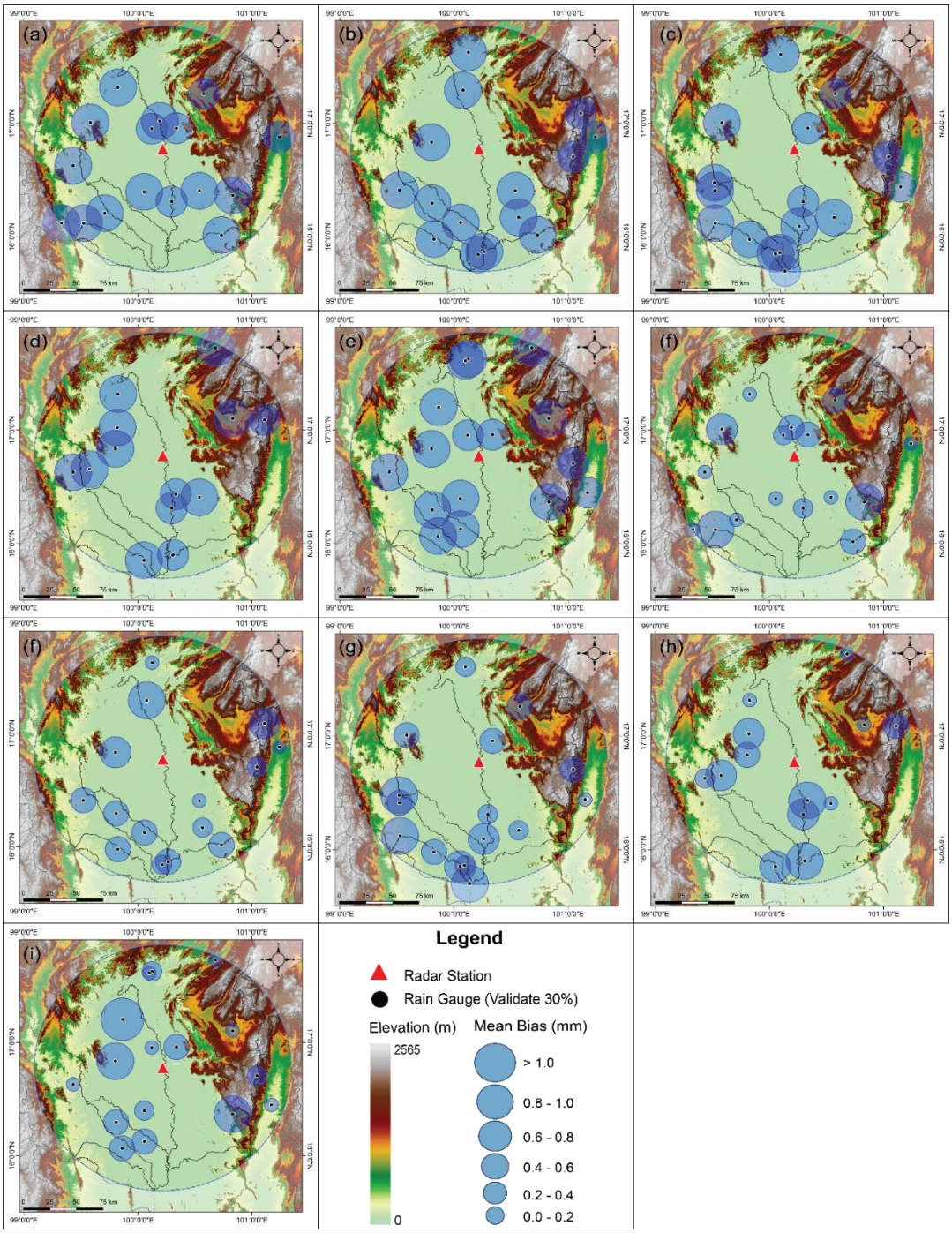


Fig. 8. Maps illustrating the bias between radar-derived rainfall and ground-based rain gauge measurements before (a–e) and after correction (f–j) using the bias values from the ZR-MP relationship, with K-folds as follows: K-fold=1 (a, f), K-fold=2 (b, g), K-fold=3 (c, h), K-fold=4 (d, i), and K-fold=5 (e, j).

Table 3.

Results Before and After Bias Correction of Validation Stations using k-fold cross validation.

Z-R Relationship	Correlation (mm)		R^2 (mm)		Mean Bias (mm)	
	Before	After	Before	After	Before	After
Marshall/Palmer	0.678	0.761	0.808	0.850	0.154	0.999
Rosenfeld Tropical	0.618	0.729	0.775	0.829	0.120	0.948
Summer Deep Convection	0.670	0.757	0.805	0.848	0.176	0.990

The error metrics (RMSE and MAE) for radar-derived rainfall that were compared to gauge observations before and after the application of IDW spatial bias correction are presented in **Table 4.** Confirming the efficacy of IDW interpolation in enhancing rainfall estimation accuracy, the correction significantly reduced errors across all Z–R relationships. ZR-MP demonstrated the most significant improvement among the three equations, with a reduction in RMSE from 218.186 mm to 17.517 mm and MAE from 199.004 mm to 13.405 mm. This represents the most significant error reduction overall. At first, ZR-RF exhibited the lowest pre-correction errors; however, its post-correction performance was marginally inferior to that of ZR-MP. This suggests that despite a robust baseline, ZR-RF has limited responsiveness to spatial bias adjustment. ZR-SD exhibited the highest pre-correction errors (RMSE = 309.163 mm; MAE = 265.412 mm). However, these values were reduced to 19.263 mm and 14.483 mm, respectively, by bias correction. Consequently, they remained higher than those of ZR-MP and ZR-RF. Overall, these results indicate that IDW spatial interpolation effectively mitigates systematic errors in radar rainfall estimates. Particularly, the ZR-MP equation demonstrated the most balanced enhancement, as it combined substantial error reductions with consistent agreement across terrain types.

Table 4.

Statistical Values Before and After Adjustment Using the IDW Spatial Interpolation Method.

Z-R Relationship	Before Correction		After correction	
	RMSE (mm)	MAE (mm)	RMSE (mm)	MAE (mm)
Marshall/Palmer	218.186	199.004	17.517	13.405
Rosenfeld Tropical	309.163	265.412	19.263	14.483
Summer Deep Convection	191.622	170.765	17.719	13.571

4.4. Analysis of Flat and Mountainous Rainfall Considering Topography

Utilizing a DEM-based classification, the bias correction performance was evaluated separately for flat and mountainous regions in order to evaluate terrain-related effects (**Fig. 9**). Slopes that were less than 5° were classified as level, while those that exceeded 5° were classified as mountainous. Then, statistical indicators of radar‑gauge agreement were computed for each terrain zone, allowing for the comparison of the efficacy of corrections in contrasting topographic conditions.

The mean radar-estimated rainfall for flat and mountainous areas is compared in **Fig. 10** before and **Fig. 11** after bias correction. The ZR-RF relationship produced the highest totals, followed by ZR-MP and ZR-SD, and all three Z–R relationships substantially overestimated rainfall prior to correction. The uncorrected radar estimates exhibit a significant degree of variability, as evidenced by the large error bars in both terrain types. The mean rainfall estimates decreased consistently across all relationships after the IDW bias correction was implemented, with reductions of approximately 60 mm in both flat and mountainous zones. Reduced variability and enhanced reliability of the corrected radar data were also indicated by the narrowing of the error bars. ZR-MP demonstrated the most statistically robust performance of the three equations, resulting in rainfall estimates that were most closely aligned with gauge observations and the lowest post-correction variability.

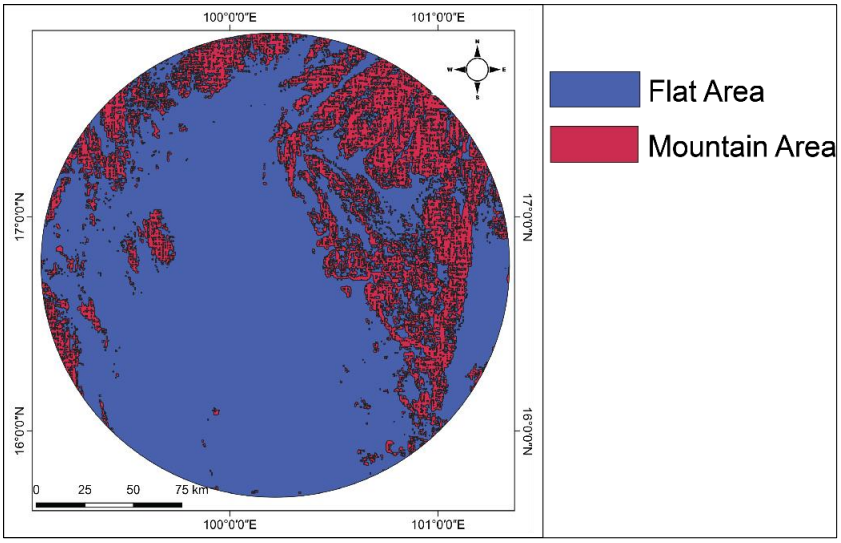


Fig. 9. Topographic map showing flat areas (slope ≤ 5°) and mountainous areas (slope > 5°).

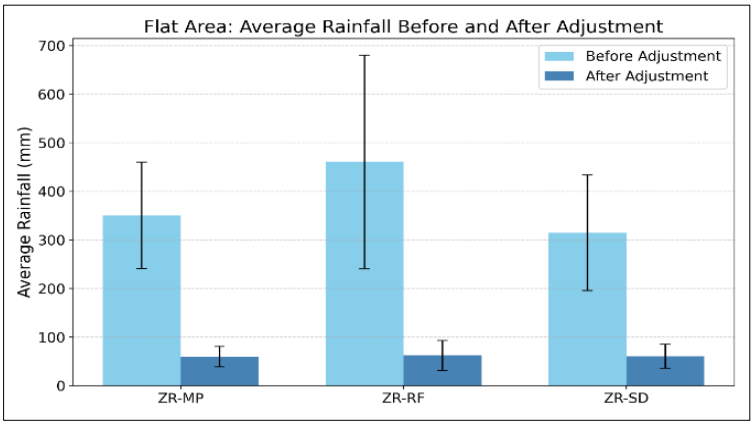


Fig. 10. Mean radar-estimated rainfall before spatial bias correction in flat areas and mountainous areas for the three Z-R relationships.

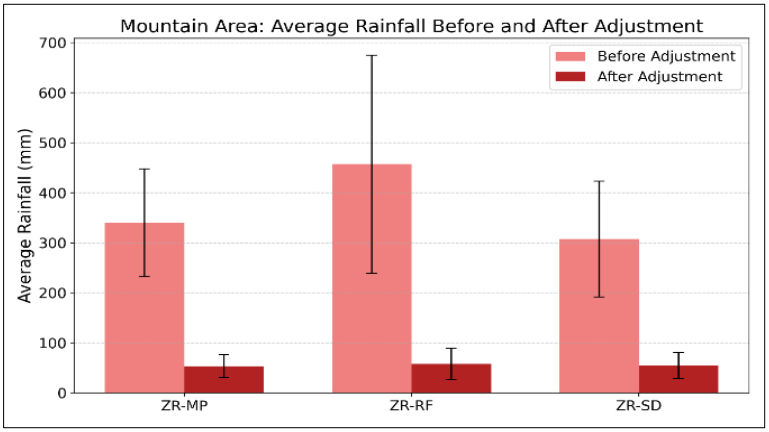


Fig. 11. Mean radar-estimated rainfall after spatial bias correction in flat areas and mountainous areas for the three Z-R relationships.

5. DISCUSSION

The suitability of various Z–R relationships for radar rainfall estimation and bias adjustment during Tropical Storm Son-Tinh (15–23 July 2018) over the central river basin of Thailand was assessed in this study. Radar data from the Phitsanulok C-band station were combined with gauge observations from 89 rain stations. Spatial bias correction was implemented using IDW, and accuracy was evaluated through five-fold cross-validation. The results emphasize the necessity of bias correction before the operational use of radar rainfall products, particularly in regions with complex terrain that encompasses both lowlands and mountainous areas. The analysis indicates that the selection of the Z–R relationship significantly impacts the accuracy of radar rainfall, which is in accordance with previous findings (Mahavik et al., 2021; 2025). ZR-MP relationship was the most dependable of the three equations that were tested, as evidenced by the firm agreement between post-correction performance and gauges ($r = 0.761$, $R^2 = 0.850$, and MBE ≈ 0.999 mm). The RMSE and MAE experienced considerable reductions in error, with the former decreasing to 17.517 mm and the latter to 13.405 mm. These results verify that the combination of ZR-MP and IDW bias correction produces highly dependable rainfall fields, which is in accordance with prior research (Goudenhoofdt & Delobbe, 2009; Mahavik, 2017; Mahavik et al., 2024; 2025).

In contrast, ZR-RF and ZR-SD initially appeared to perform better in terms of numerical bias; however, they both significantly overestimated rainfall. This may be indicative of the spatial and temporal variability of Z–R performance, which is indicative of variations in storm structure in relation to the conditions under which these relationships were established (Mapiam & Sriwongsitanon, 2008; Mahavik et al., 2011). The results also suggest that spatial bias correction has a more significant impact on the ultimate accuracy than Z–R selection. This study confirms that the accuracy of radar rainfall across diverse terrain is considerably enhanced by the application of spatial bias correction with IDW, which is supported by cross-validation. In addition to deterministic correction methods, the integration of machine learning with ground-based rainfall data presents a promising opportunity to further mitigate spatial bias and improve quantitative precipitation estimates (Hassan et al., 2022; Mihulet et al., 2023; Mahavik et al., 2024; 2025).

6. CONCLUSIONS

Using reflectivity data from the Phitsanulok C-band radar in Thailand and rain gauge observations, this investigation assessed the bias correction of event-based radar rainfall during Tropical Storm Son-Tinh (15–23 July 2018). Clutter and attenuation effects were effectively eliminated through data preprocessing with Py-ART, and rainfall was estimated using three Z–R relationships. Initially, all equations overestimated rainfall, with Rosenfeld Tropical leading to the largest deviations. Conversely, the Marshall–Palmer (ZR-MP) relationship provided the most balanced estimates. Spatial bias correction, as well as five-fold cross-validation and IDW, significantly enhanced radar–gauge agreement in both flat and mountainous regions. The most dependable performance was obtained by ZR-MP among the tested relationships, as evidenced by its significantly reduced errors and closer adherence to gauge measurements. These findings verify that it is imperative to incorporate a spatial bias correction and an appropriate Z–R relationship in order to enhance radar quantitative precipitation estimates in complex terrain. In order to improve radar rainfall estimation during tropical storm events in Thailand and similar monsoon-dominated regions, However, this study still has limitations regarding the number of rainfall observation stations, which may not be sufficient, and radar data that are affected by blockage due to terrain characteristics, remaining a constraint within the study area. For future research, the investigators suggest expanding the analysis to include more advanced techniques, such as comparing the IDW method with other bias correction and estimation approaches, including Kriging, co-Kriging, Bayesian adjustment, or machine learning-based methods. These approaches could potentially improve quantitative rainfall estimation in both mountainous and lowland areas, thereby supporting more effective flood prevention planning and rainfall management.

ACKNOWLEDGEMENTS

This work was supported by Naresuan University (NU) and the National Science, Research, and Innovation Fund (NSRF) under Grant No. N25A660467. Additional support was provided by the Fundamental Fund (FF), Naresuan University, under Grant No. R2569B057, and by the Appropriate Technologies for Waste Reuse and Management Research Unit.

REFERENCES

Abro, M. I., Zhu, D., Wei, M., Majidano, A. A., Khaskheli, M. A., Ul Abideen, Z., & Memon, M. S. (2019). Hydrological appraisal of rainfall estimates from radar, satellite, rain gauge and satellite–gauge combination on the Qinhuai River Basin, *China. Hydrological Sciences Journal*, 64(16), 1957–1971. https://doi.org/10.1080 /02626667 .2018.1557335

Ahrens, B. (2006). Distance in spatial interpolation of daily rain gauge data. *Hydrology and Earth System Sciences*, 10, 197–208. https://doi.org/10.5194/hess-10-197-2006

Battan, L. J. (1973). Radar observation of the atmosphere. University of Chicago: University of Chicago Press.

Bowden, J. H., et al. (2025). Stormy Subtropics and Stratiform South: Radar-Based Classification and Analysis of Australian Rainfall Events. *Journal of Geophysical Research*: Atmospheres. https://doi.org/10.1029/2024JD041790

Brauer, C.C., Overeem, A., Leijnse, H., and Uijlenhoet, R. (2016). The effect of differences between rainfall measurement techniques on groundwater and discharge simulations in a lowland catchment. *Hydrological Process*, 30(21), 3885-39000.

Chang and Kang-tsung. (2002). Introduction to Geographic Information Systems. New York: *McGraw Hill Higher Education*.

Chen, F. W., & Liu, C. W. (2012). Estimation of the spatial rainfall distribution using inverse distance weighting (IDW) in the middle of Taiwan. *Paddy and Water Environment*, 10(3), 209–222.

Cho, Y. (2020). Application of NEXRAD radar-based quantitative precipitation estimations for hydrologic simulation using ArcPy and HEC software. *Water*, 12(1), 273. https://doi.org/10.3390/w12010273

Goudenhoofdt, E., & Delobbe, L. (2009). Evaluation of radar-gauge merging methods for quantitative precipitation estimates. Hydrology and Earth System Sciences, 13(2), 195–203. https://doi.org/10.5194/hess-13-195-2009

Gourley, J. J., & Calvert, C. M. (2003). Automated Detection of the Bright Band Using WSR-88D Data. *Weather and Forecasting*, 18(4), 585-599. https://doi.org/10.1175/1520-0434(2003)018<0585:ADOTBB>2.0.CO;2

Gu, J., Ryzhkov, A., Zhang, P., Neilley, P., Knight, M., Wolf, B., & Lee, D. (2011). Polarimetric Attenuation Correction in Heavy Rain at C Band. *Journal of Applied Meteorology and Climatology*, 50(1), 39-58. https://doi.org/10.1175/2010JAMC2258.1

Hanchoowong, R., Weesakul, U., and Chumchean, S. (2012). Bias correction of radar rainfall estimates based on a geostatistical technique. *Science Asia*, 38(4), 373–385.

Harrison, D., Smith, J., and Brown, P. (2009). Exploring the Transient Behavior of Z–R Relationships: Implications for Radar Rainfall Estimation. *Journal of Applied Meteorology and Climatology*, 48(10), 2055–2067. https://doi.org/10.1175 /2009JAMC2165.1

Hassan, D., Isaac, G. A., Taylor, P. A., & Michelson, D. (2022). Optimizing Radar-Based Rainfall Estimation Using Machine Learning Models. *Remote Sensing*, 14(20), 5188. https://doi.org/10.3390/rs14205188

Helmus, J. J., and Collis, S. M. (2016). The Python ARM Radar Toolkit (Py-ART), a library for working with weather radar data in the Python programming language. *Journal of Open Research Software*, 4(1), Article e25. https://doi.org/10.5334/jors.119

Kangerd, A., Mahavik, N., Masthawee, F., Arthayakun, S., Ket-Ord, R., Samaksaman, U., Umponstira, C., Kunwilai, J., Promta, W., Kongmuang, C., and Tantanee, S. (2024, November 17–21). Analysis of spatial bias of precipitation estimated from weather radar data during storm dissipation with geographic information system in Central Thailand. *Paper presented at the 45th Asian Conference on Remote Sensing (ACRS 2024)*, Colombo, Sri Lanka.

Krajewski, W. F., & Smith, J. A. (2002). Radar hydrology: Rainfall estimation. *Advances in Water Resources*, 25(8–12), 1387–1394. https://doi.org/10.1016/S0309-1708(02)00062-3

Krajewski, W. F., Vignal, B., Seo, B.-C., & Villarini, G. (2011). Statistical model of the range-dependent error in radar–rainfall estimates due to the vertical profile of reflectivity. *Journal of Hydrology*, 402(3–4), 306–316. https://doi.org/10.1016/j.jhydrol.2011.03.024

Krajewski, W. F., Villarini, G., & Smith, J. A. (2010). Radar–rainfall uncertainties: Where are we after thirty years of effort?. *Bulletin of the American Meteorological Society*, 91(1), 87–94.

Lin XS, Yu Q (2008) Study on the spatial interpolation of agroclimatic resources in Chongqing. *J Anhui Agric* 36(30): 13431–13463, 13470

Mahavik, N. (2017). Bias adjustments of radar rainfall during seasonal march of the summer monsoon in the middle of Thailand. *International Journal of Applied Environmental Sciences*, 12(4), 577-594.

Mahavik, N., & Tantanee, S. (2020a). Radar Quality Index for a mosaic of radar reflectivity over Chao Phraya River Basin, Thailand. *Applied Environmental Research*, 42(3), 92‑104.

Mahavik, N., Kangerd, A., Masthawee, F., Arthayakun, S., and Tantanee, S. (2025). Optimizing rainfall prediction in central Thailand with weather radar and machine learning during the monsoon. *Environmental Earth Sciences*, 84(137). https://doi.org/10. 1007/s12665-025-12149-9

Mahavik, N., Kangerd, A., Masthawee, F., Arthayakun, S., and Tantanee, S. (2024). Investigate ensemble machine learning models to reduce the daily mean field bias of radar rainfall estimates derived from ZR relationships in the sub-river basins in the middle of Thailand. *Environment, Development and Sustainability*. https://doi.org/10.1007/s10668-024-05778-w

Mahavik, N., Masthawee, F., Tantanee, S., (2021). Investigation Z-R relationships during tropical storm in GIS using implemented mosaicking algorithms of radar rainfall estimates from weather radars in the Yom river basin, *Thailand. Applied Geomatics*. 13, 645-657.

Mahavik, N., Satomura, T., and Baimuang, S. (2011). Investigation Z–R relationships of precipitation characteristic by weather radar in Thailand. *In Proceedings of the IMPAC-T Joint with SEA Water 9th Conference* (pp. 212–217). Bangkok, Thailand.

Mahavik, N., Tantanee, S., (2020b). Precipitating clouds analysis based on the developed radar mosaic products over the Chao Phraya River basin. *International Journal of Geoinformatics*, 16(3), 21-35.

Mapiam, P. P., and Sriwongsitanon, N. (2008). Climatological Z-R relationship for radar rainfall estimation. *ScienceAsia*, 34, 215-222. https://doi:10.2306/scienceasia1513-1874.2008.34.215

Mapiam, P. P., Methaprayun, M., Bogaard, T., Schoups, G., & Ten Veldhuis, M.-C. (2022). Citizen rain gauges improve hourly radar rainfall bias correction using a two-step Kalman filter. *Hydrology and Earth System Sciences*, 26(3), 775–794.

Marshall, J.S. and Palmer, W.M. (1948). The distribution of raindrops with size. *Journal of Atmospheric Sciences*, 5(6), 165–166

Marshall, J.S., Walter, H., and Gunn, K.L. (1955). Advances in radar weather. *Advances in Geophysics*, 2, 1-56.

Mihulet, E., Burcea, S., Mihai, A., & Czibula, G. (2023). Enhancing the Performance of Quantitative Precipitation Estimation Using Ensemble of Machine Learning Models Applied on *Weather Radar Data. Atmosphere*, 14(1), 182. https://doi.org/10.3390/atmos14010182

Mokarram, M., & Hojati, M. (2016). Comparison of landform classifications of elevation, slope, relief and curvature with topographic position index in south of Bojnoord. *Ecopersia, 4*(2), 1343–1357. https://doi.org/10.18869/modares.Ecopersia.4.2.1343

Morin, E., Krajewski, W. F., Goodrich, D. C., Gao, X., & Sorooshian, S. (2003). Estimating rainfall intensities from weather radar data: The scale-dependency problem. *Journal of Hydrometeorology*, 4(5), 782–797. https://doi.org/10.1175/1525-7541(2003)004<0782:ERIFWR>2.0.CO;2

National Water Resources Office. (2018). 20-year master plan for water resource management (2018-2037).

QGIS Development Team. (2024). QGIS Geographic Information System (Version 3.34). QGIS Association. https://qgis.org

Rosenfeld, D., Wolff, D. B., and Atlas, D. (1993). General probability-matched relations between radar reflectivity and rain Rate. *Journal of Applied Meteorology Climatology*, 32(1), 50–72.

Sharif, R. B., Habib, E. H., & ElSaadani, M. (2020). Evaluation of radar-rainfall products over coastal Louisiana. *Remote Sensing*, 12(9), 1477. https://doi.org/10.3390/rs12091477

Sokol, Z., Szturc, J., Orellana-Alvear, J., Popová, J., Jurczyk, A., & Célleri, R. (2021). The role of weather radar in rainfall estimation and its application in meteorological and hydrological modelling A review. *Atmosphere*, 13(3), 351.

Thai Meteorological Department. (2018). Member report: Thailand. ESCAP/WMO Typhoon Committee, 13th Integrated Workshop, Chiang Mai, Thailand. https://www.jma.go.jp/jma/en/Activities/qmws_2010/docs/Workshop_ver0.98_ins.pdf

World Meteorological Organization. (2008). Guide to hydrological practices: Volume I. Hydrology ‐ From measurement to hydrological information (6th ed.) (WMO-No. 168). World Meteorological Organization. https://unstats.un.org/unsd/envaccounting/waterGuidelines/Material/WMO_Guide_168_Vol_I_en_hydrological_practices.pdf

Wu, W., Zou, H., Shan, J., & Wu, S. (2018). A dynamical Z–R relationship for precipitation estimation based on radar echo-top height classification. *Advances in Meteorology*, 2018, Article 8202031. https://doi.org/10.1155/2018/8202031

Xie, H., Zhou, X., Vivoni, E. R., Hendrickx, J. M. H., & Small, E. E. (2005). GIS-based NEXRAD Stage III precipitation database: Automated approaches for data processing and visualization. *Computers & Geosciences*, 31(1), 65–76.

DRIVERS OF ELEVATED CHLOROPHYLL-A IN LUMAJANG WATERS: A COMPARATIVE ANALYSIS OF UPWELLING AND TERRESTRIAL RUNOFF MECHANISMS

***Bayu MUNANDAR*[1,3*], *Adzkia Noerma ARIFA*[1,2], *Annisa Aulia LUKMAN*[1], *Anindya WIRASATRIYA*[1] & *Yusuf Jati WIJAYA*[1]**

DOI: 10.21163/GT_2026.211.14

ABSTRACT

The Lumajang Waters (LW) is located in South Java and is one of the waters with outstanding primary productivity. The variation in primary productivity in a water body serves as an indicator of its aquatic fertility. Many seasonal parameters and physical oceanographic phenomena (currents, upwelling, nutrients, wind and waves) can influence the variability of chl-a in the ocean. In the current study, we conducted a comprehensive analysis of chl-a variability using both horizontal and vertical data. We found the highest chl-a in Lumajang waters occurred from July to October, and the El Niño Southern Oscillation (ENSO) and the Indian Ocean Dipole (IOD) events make higher chl-a. The peak chl-a concentration in 2019 was 2.03 mg/m³ in July, whereas in 2023 it reached 3.01 mg/m³ in October. However, we found the value of correlation between wind (Ekman Mass Transport (EMT)) and Chl-a was stronger in 2019 than in 2023. The coastal upwelling that increases in chl-a concentration in 2019 and 2023 is observable as a lifted water mass with a density of 23 kg/m³ from 100 meters depth to the surface. Despite lower intensity of coastal upwelling, chl-a concentration in 2023 was higher than in 2019. On the other hand, Rrs 555 in 2023 which represents Total Suspended Solids (TSS) exhibited a 2-times higher than the other years, particularly from August to October. The high Rrs 555 may be associated with the increase of TSS brought by river runoff, considering that many rivers flow from the upper land and fertilize the waters of Lumajang. These characteristics make Lumajang waters very unique, as two mechanisms run together influencing the chl-a variation.

Keywords: *Rrs 555; Upwelling; Chlorophyll-a; Density; Lumajang Waters.*

1. INTRODUCTION

The Lumajang Waters (LW) is located in South Java and is one of the waters that has outstanding primary productivity. This primary productivity is influenced by the location of the LW, which has a compact bathymetry and is passed by the South Java Current and the exit of the Indonesian Throughflow (Krabbenhoeft *et al*., 2010; Wijaya *et al.,* 2023; Guo *et al*., 2023; Sartimbul et al., 2023). This complexity creates the phenomena of oceanographic physics and the interaction of the atmosphere and the ocean. Rachman *et al.* (2024) stated that in the waters off southern Java, a coastal upwelling phenomenon occurs, which contributes to the variability of primary productivity in this region. The variation in primary productivity in a water body serves as an indicator of its aquatic fertility. The clean primary productivity in the form of plankton is an important element in the food chain of a body of water (Sarker *et al.,* 2023).

[1]*Oceanography, Faculty of Fisheries and Marine Sciences, Diponegoro University.* [*]*Corresponding author: (BM) bymunandar@gmail.com; (ANA) adzkia@lecturer.undip.ac.id; (AAL) aulialukman@lecturer.undip.ac.id; (AW) anindyawirasatriya@lecturer.undip.ac.id; (YJW) yusuf.jatiwijaya@live.undip.ac.id.*

[2] *Marine Science, Faculty of Fisheries and Marine Sciences, Diponegoro University.*

[3]*Technology and Business of Fisheries and Marine, Faculty of Fisheries and Marine Sciences, Diponegoro University.*

The abundance of phytoplankton can be monitored using chlorophyll-a (chl-a) concentration (Garini *et al*., 2021). Chl-a is the dominant color pigment in phytoplankton (Yun *et al.,* 2019). Furthermore, the variability of chl-a in the ocean can be influenced by many seasonal parameters and phenomena, including currents (An et al., 2025), upwelling (Munandar et al., 2023; Wirasatriya et al., 2023), nutrients (Maslukah et al., 2023), wind (Zampollo et al., 2025), and waves (Liu et al., 2025).

According to earlier research, variability of chl-a in the southern Indonesian seas is influenced by local and global scales of oceanographic phenomena. The local scale, such as monsoon (Haryanto et al., 2021), and the global scale, such as the IOD (Kunarso et al., 2023; Rachman et al., 2024), ENSO (Wijaya et al., 2020; Hidayat et al., 2025), Kelvin waves (Xu et al., 2018; Wijaya et al., 2024), precipitation (Kim et al., 2014; Wirasatriya et al., 2021). The high variability of chl-a concentration is a central indicator of marine productivity and a basis for predicting potential fishing ground area. Furthermore, many studies have indicated that plentiful fishery production in the southern Indonesian seas occurs during the upwelling season (Pet-Soede et al., 1999; Syamsuddin et al., 2013; Nugroho et al., 2022).

Previously, numerous researchers have conducted studies on the influence of IOD and ENSO on the variability of chl-a concentration in Indonesian seas. Susanto et al. (2001) was one of the early studies to identify the impact of ENSO on chl-a in this region. Additionally, Iskandar et al. (2022) investigated the extreme positive Indian Ocean dipole in 2019 and its impact on Indonesia. Rachman et al. (2024) examined the influence of ENSO and IOD on upwelling variability in the southern Indonesian region. The results indicated that IOD and ENSO can cause South Java Island's sea surface temperature to drop and its chlorophyll-a to rise. However, these studies often lack comprehensive information (Rachman et al., 2024; Iskandar et al., 2022; Susanto et al., 2001), which only analyzed the impact of IOD and ENSO on chl-a concentration in surface water and did not provide comprehensive vertical profile information to influence chl-a in surface water. Therefore, it is essential to conduct a more comprehensive analysis of the relationship between surface and vertical profile phenomena and the variation of chl-a. Further, we need to investigate the impact of EMT, TSS, IOD, and ENSO on these phenomena. Therefore, this study can provide more comprehensive insights into surface and vertical phenomena of chl-a and its connection to global phenomena. This research will establish a crucial scientific foundation for ocean management, with immediate implications for the prediction of fishery yields, the issuance of early warnings for harmful algal blooms, and the evaluation of the effects of climate change on marine ecosystems.

2. STUDY AREA

This research was carried out in the LW with coordinates of 7º S to 10º S and 111.5º E to 114.5º E (**Fig. 1**). This area is known to have a high upwelling due to strong wind, complex bathymetry and topography. We analyze the coastal and marine areas represented by the box in **Fig. 1**.

3. DATA AND METHODS

3.1. Data

To identify the variability of chl-a, we used data derived from the Ocean Colour Climate Change Initiative (OC-CCI), which is a program from the European Space Agency (ESA). OC-CCI are compelling from more than one satellite image with the high atmospheric correction and chl-a algorithm (Sathyendranath et al., 2019; Munandar et al., 2023) with the Root-Mean-Square Deviation (RMSD) reaches 0.34 (Garnesson et al., 2022) (OCEANCOLOUR_GLO_BGC_L4_MY_009_104). We used daily level 4 data with 0.04º spatial resolution interpolated to fill in missing data values. To examine the possible corruptions of satellite chl-a observation by the muddy water, we used reflectance remote sensing at 555 (Rrs 555) (https://oceancolor.gsfc.nasa.gov/l3/).

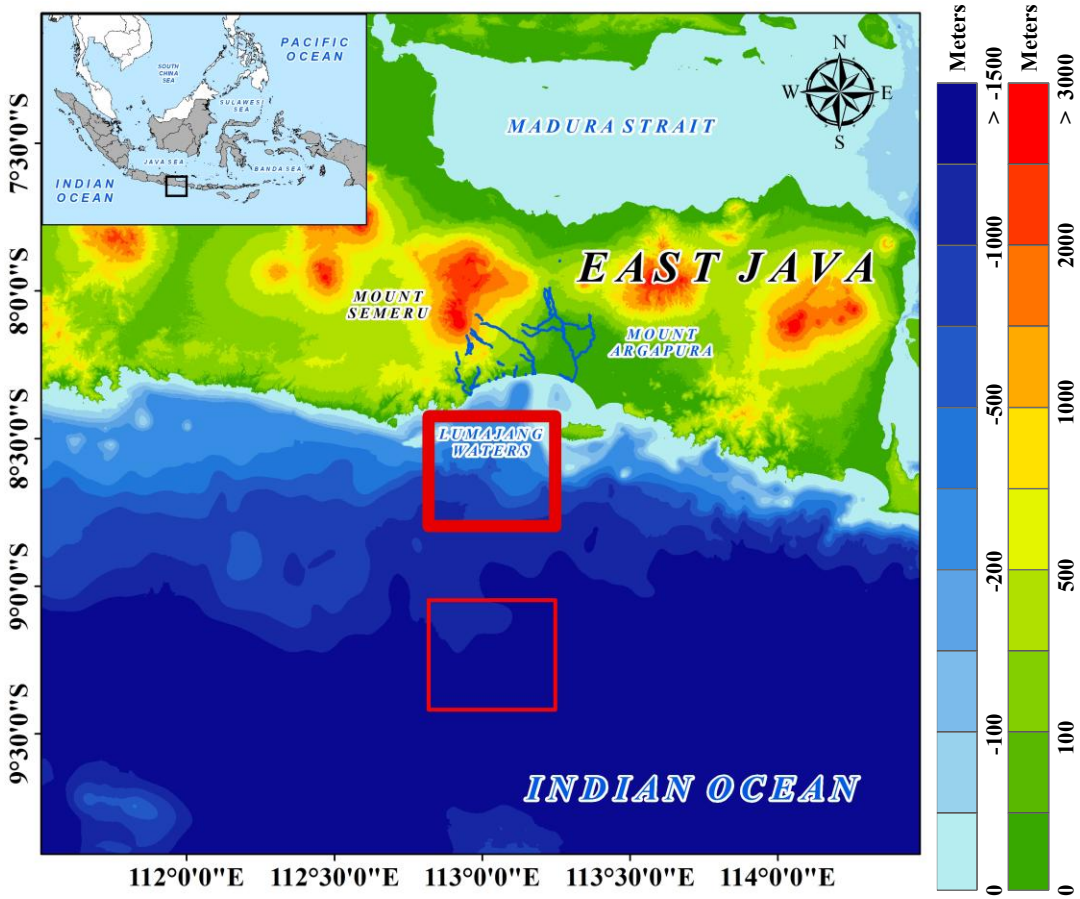


Fig. 1. Bathymetry and topography of the research area and names of the major seas. The thick and thin boxes depict the two area. The blue line is a river in Lumajang Regency.

To investigate the relationship between interannual phenomena and chl-a variability, we used IOD and ENSO. IOD and ENSO are calculated from the difference in anomaly of sea surface temperature in the Indian Ocean (IOD) and Pacific Ocean (ENSO). We obtained IOD data from https://stateoftheocean.osmc.noaa.gov/sur/ind/dmi.php#:~:text=The%20DMI%20index%20is%20an,Ocean%20Dipole%20or%20Zonal%20Mode. Next, ENSO data was obtained from https://origin.cpc.ncep.noaa.gov/products/analysis_monitoring/ensostuff/detrend.nino34.ascii.txt. The ONI data describes the value of the sea surface temperature anomaly (SSTA) found in the Niño 3.4 region. The frequencies of IOD and ENSO months during 2015–2024 are presented in **Fig. 2**.

To understand the vertical profile, we analyzed potential seawater density, which is calculated from seawater potential temperature and seawater salinity. The Copernicus Marine Environment Monitoring Service (CMEMS) (GLOBAL_MULTIYEAR_PHY_001_030) provides the temperature and salinity data. Both data have a spatial resolution of 0.083º × 0.083º, and the value of RMSD reaches 0.4ºC (temperature) and 0.2 psu (salinity). We obtained the precipitation data from ERA5 monthly averaged data on single levels (https://cds.climate.copernicus.eu) and this data has good accuracy (Jiao et al., 2021).

For wind and EMT analysis, the wind data can be accessed at https://www.remss.com/measurements/ccmp/. The data is combined with satellite data, mooring buoys, and model wind data (Mears et al., 2019). CCMP provides a spatial resolution of 0.25º×0.25º and an observation interval of 6 hours and the value of RMSE reaches 0.5 m/s (Atlas et al., 2011).

Next, the wind data is then further analyzed to obtain the EMT value. Bathymetry and topography were obtained from the Geospatial Information Agency of the Republic of Indonesia (https://tanahair.indonesia.go.id/). The observation period in this research is from January 2015 to December 2024. All the data will be calculated in each extreme phenomenon condition. Moreover, the satellite and reanalysis data have passed many quality checks and preprocessing procedures by the data source.

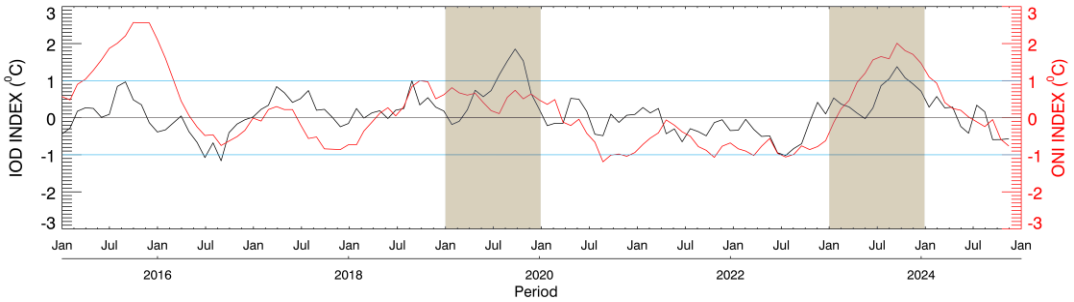


Fig. 2. Time series of the IOD and ENSO years from 2015–2024 based on the ONI 3.4 and DMI.

3.2. Method

Some of the data are daily time series data, so they need to be combined into monthly climatological data. The calculation of the monthly climatology follows the following equation:

$$\bar{X}(x,y) = \frac{1}{n}\sum_{i=1}^{n} x_i(x,y,t) \quad (1)$$

where $\bar{X}(x,y)$ is an average of the pixels data, $x_i(x,y,t)$ is the ith value of the data at position (x, y) and time (t). Further, n is a number of data (i.e., from 2015-2024). x_i is excluded from the calculation if that pixel has a missing data value. To investigate the EMT, first, we converted surface wind data into wind stress (τ) by using the following equation:

$$\tau = \rho_a C_d U_{10}^2 \quad (2)$$

where ρ_a is the density of air (1.25 kg m^3), Cd is the drag coefficient (WAMDI group, 1988) and U_{10} is the wind speed 10 m above sea level. The value of Cd follows WAMDI (1988). Next, we calculated classical EMT by following equations (i.e. Wang and Tang, 2014):

$$1000C_d = 1.29 \quad \text{for } 0 \text{ m/s} < U_{10} < 7.5 \text{ m/s}$$
$$1000C_d = 0.8 + 0.0065U_{10} \quad \text{for } 7.5 \text{ m/s} < U_{10} < 50 \text{ m/s}$$

$$EMT = -\frac{\tau}{\rho_w f} \quad (3)$$

where ρ_w is the density of seawater (1.025 kg m^3) and f is the Coriolis parameter ($f = 2\Omega \sin\theta$) (Stewart, 2008; Antonini & Caldeira, 2021). We also calculated potential seawater density at the normal atmospheric pressure from the profiles of temperature and salinity by using the UNESCO's (2015) formula. We also calculate *Pearson correlation* (bivariate correlaation) to determine the dominant role to chl-a variability.

4. RESULTS AND DISCUSSIONS

4.1. Monthly Variation of Surface Layer

We analyzed the monthly chl-a, IOD, ENSO, surface wind, wind stress, precipitation, Rrs 555, and EMT along the LW region from January to December over the periods of each dataset. **Figure 2** displays the IOD and ENSO conditions from 2015 to 2024. The peak condition of IOD occurred in 2019 and 2023, shown by the positive extreme values of 1.85269 and 1.37728, which occurred in October. Further, the peak of ENSO conditions arose in August 2019 and August 2023, showing ENSO positive reaches of 0.74 and 2.01, respectively (**Fig. 2**). Therefore, the present study focuses on 2019 and 2023, as the impact of EMT, upwelling, Rrs 555, IOD positive extremes and ENSO on chl-a concentrations is robust in both years.

The mean of monthly and climatological chl-a concentrations provides an overview of the time series evolution and spatial distribution of chl-a concentration in LW (**Fig. 3**). As shown in **Fig. 3B**, the highest chl-a concentration in 2019 reached 2.03 mg/m³ (July) and in 2023 reached 3.01 mg/m³ (October). This shows IOD+ and the El Niño event in 2023 had a stonger influence on increasing chl-a compared to the extreme IOD+ and the ENSO normal event in 2019 (**Fig. 2**). The patterns of monthly chl-a variation in 2019 and 2023 differed from the climatological pattern which has the highest chlorophyll-a in September (2.4 mg/m³) (**Fig. 3B**). The results prove that climate variation (IOD and ENSO) affects the variability of chlorophyll-a in LW.

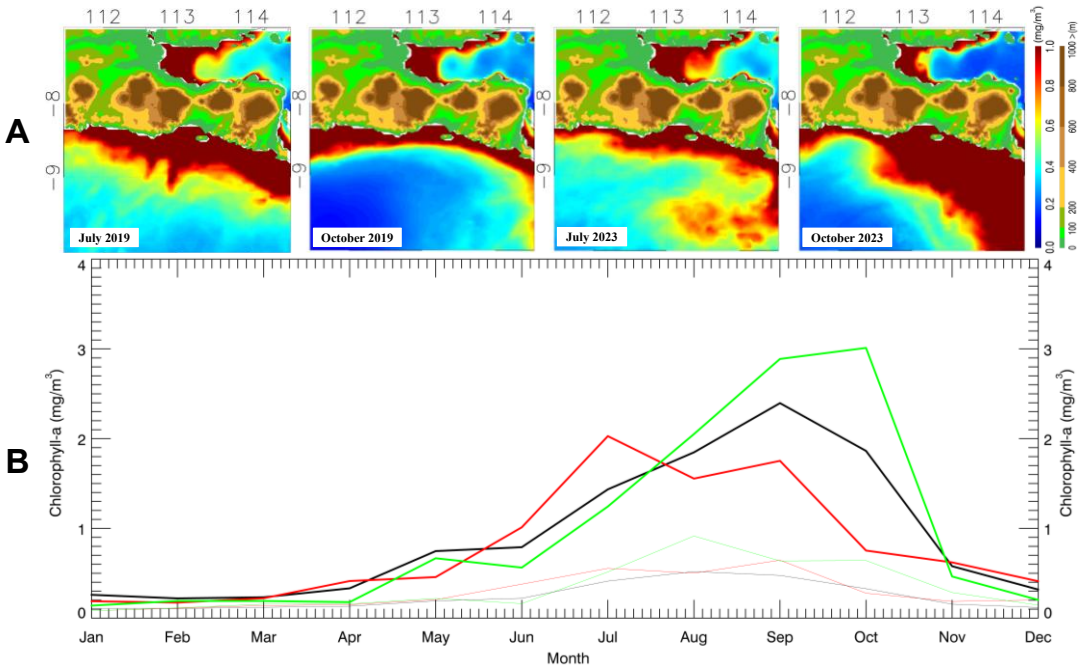


Fig. 3. The spatial distribution (A) and time series (B) variation of chl-a in LW and over the area 8.42º - 8.8º S, 112.82º - 113.24º E (thick box) and 9º - 9.42º S, 112.82º - 113.24º E (thin box). The thick box is represented onshore, and the thin box is shown offshore. The red line represents 2019, the green line shows 2023, and the black line shows climatology data. The peak of chl-a concentration in both areas is different from the peak of the same IOD and ENSO.

To investigate the variation of upwelling in 2019 and 2023, we calculated wind speed and EMT in this region. First, we generated the spatial distribution of wind speed and EMT (**Fig. 4**) and examined the relation with chl-a.

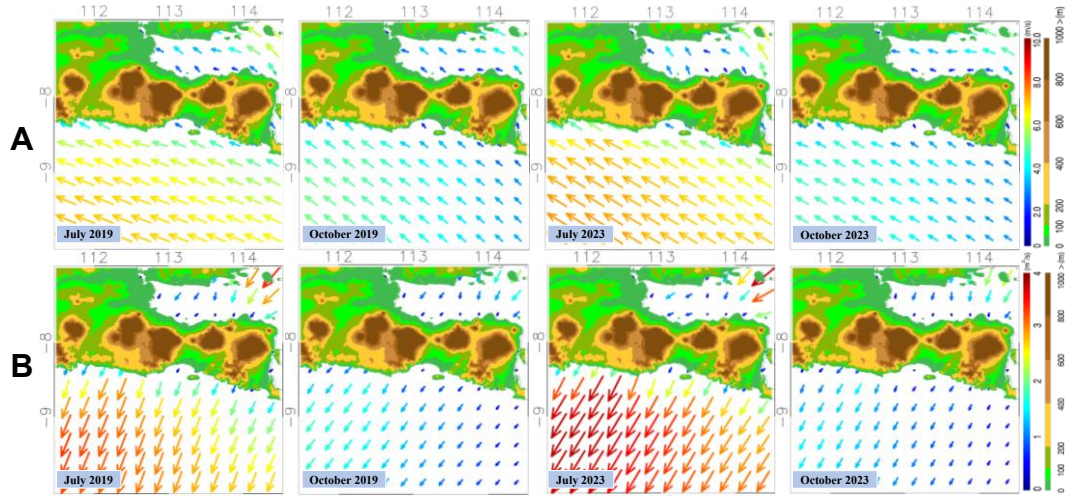


Fig. 4. Illustrates the spatial distribution of wind speed (A) and EMT (B) in LW. July and October represent peaks of IOD and ENSO events in 2019 and 2023.

Previous studies have confirmed that wind speed is a major physical factor that generatese the coastal upwelling process and then influences chl-a variability (Setiawan & Habibi, 2011; Wirasatriya et al., 2017; 2020; Kunarso et al., 2023; Munandar et al., 2023). **Figure 4** shows the distribution of wind speed and EMT in LW. In July and October, wind speed had the same direction to the northwest, with the highest speed occurring in February (8 m/s) and May (6.8 m/s) (**Fig. 5A**).

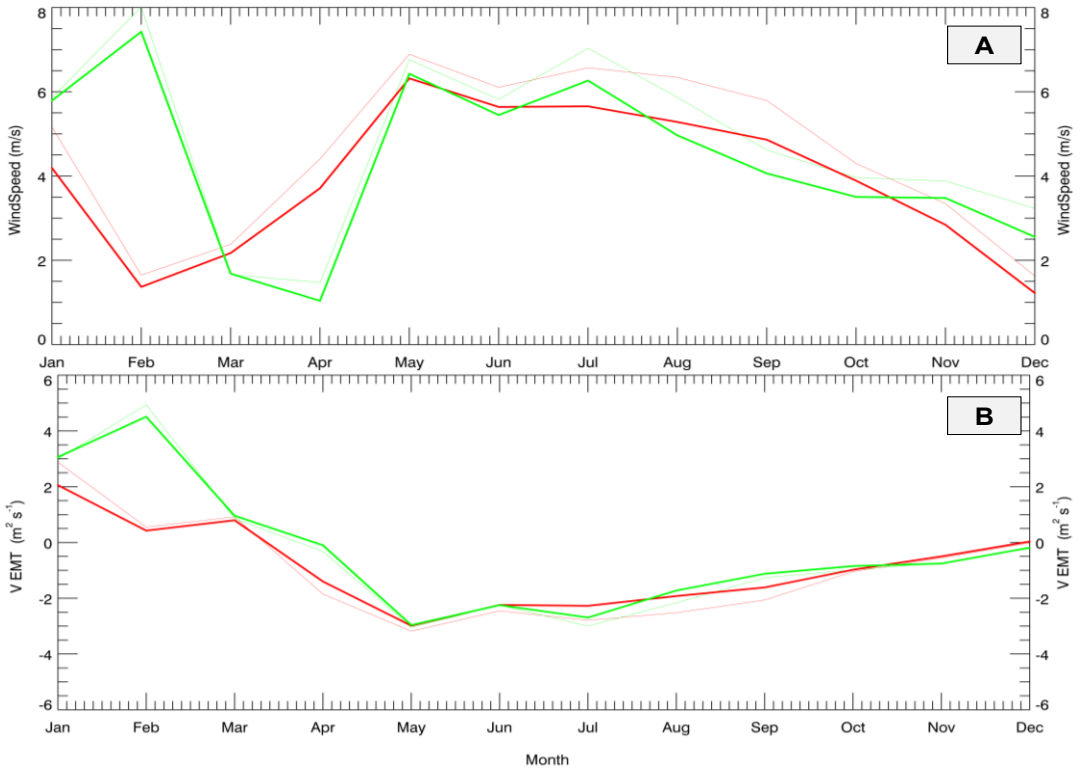


Fig. 5. Time series monthly of wind speed (A) and meridional EMT (B) in 2019 (red line) and 2023 (green line) (averaged from the thick box and thin box in Fig. 1). Negative (positive) meridional EMT means offshore (onshore) EMT.

The spatial and temporal data of wind speed revealed that the thick box (onshore) has lower wind speed compared with the thin box (offshore). Wirasatriya et al. (2019) demonstrated that the Coriolis effect may influence the impact of wind direction on EMT. The direction of the EMT is deflected clockwise in the northern hemisphere and counterclockwise in the southern hemisphere (Nouri et al., 2020). This is consistent with the EMT results obtained, where the wind direction in July and October is northwest, so that the direction of EMT is deflected counterclockwise to the southwest. The result of the EMT revealed that increased (decreased) offshore EMT occurred from May to December (from January to April) and the chl-a concentration was also higher from May to December than from January to April in both 2019 and 2020 (**Figs. 4B and 5B**). Wirasatriya et al. (2020) and Rachman et al. (2024) identified the steady southeast-to-northwest winds generate offshore EMT, which induces coastal upwelling and enhances chl-a concentrations.

4.2. Monthly Variation of Vertical Layer

The previous studies and analysis indicated coastal upwelling occurred, which explains the increased chl-a concentration in the surface layer (Rachman et al., 2024). The offshore EMT exhibited nearly the same value in 2019 and 2023. On the other hand, chl-a concentration in 2023 was higher than in 2019, with differences reaching up to 1 mg/m³ (**Fig. 3**). To prove that the increasing chl-a in 2019 and 2023 resulted from coastal upwelling, we calculated the vertical profile of potential seawater density from temperature and salinity data. We focused on the thick box (**Fig. 1**) due to its highest concentration of chl-a.

The lifting of higher-density water masses signified the occurrence of coastal upwelling in both years. The lifting isopycnal of 23 kg/m³ reached a surface of 10 m from June to November, indicating the coastal upwelling process in 2019 (**Fig. 6a**). In contrast, the lifting isopycnal of 23 kg/m³ reached a surface of 10 m from August to October indicates the coastal upwelling process in 2023. This observation is consistent with the findings of Wirasatriya et al. (2020) and Rachman et al. (2024), who reported that coastal upwelling in the south of Java occurs in the eastern season, marked by the occurrence of shoaling of pycnocline depth. Nevertheless, the result indicates that coastal upwelling in 2019 was stronger than in 2023, as denoted by the higher surface density (i.e., more than 22.5 kg/m³) from June to November.

In accordance with the previous studies (Wang & Tang, 2014; Wirasatriya et al., 2020; Munandar et al., 2023; Rachman et al., 2024; Xu et al., 2025), upwelling clearly had an impact on the higher chl-a concentration in 2019 in LW. On the opposite side, the highest chl-a in 2023 did not seem to have a clear effect of upwelling on the increasing chl-a concentrations in LW.

Furthermore, we conducted a statistical analysis to determine the association between chl-a, EMT, and wind speed for both years, as shown in **Table 1**. In 2019, the correlation between chl-a and meridional EMT was very significant (-0.62*), and the correlation between chl-a and wind speed was also very significant (0.6*). In contrast, the correlation between chl-a and meridional EMT in 2023 was lower (0.41), while no significant correlation was found between chl-a and wind speed in 2023 (0.03). These result suggest that meridional EMT (upwelling event) had a greater impact on chl-a variation in 2019 compared to 2023. Thereby, other phenomena likely contributed to the increase in chl-a concentration in LW in addition to upwelling in 2023. In the next section, we examine the possible mechanisms that explain why chl-a levels in 2023 was higher than those in 2019 in LW.

Table 1.
Highly significant correlation analysis ($p < 0.05$) among monthly chl-a, meridional EMT, and wind speed in Jan – Dec 2019 and Jan – Dec 2023 inside the thick boxes as shown in Fig. 1.

	Variable	Meridional EMT	Wind Speed
Chl-a	2019	-0.62*	0.6*
	2023	-0.41	0.03

** Correlation is significant at the 0.05 level (1-tailed).*

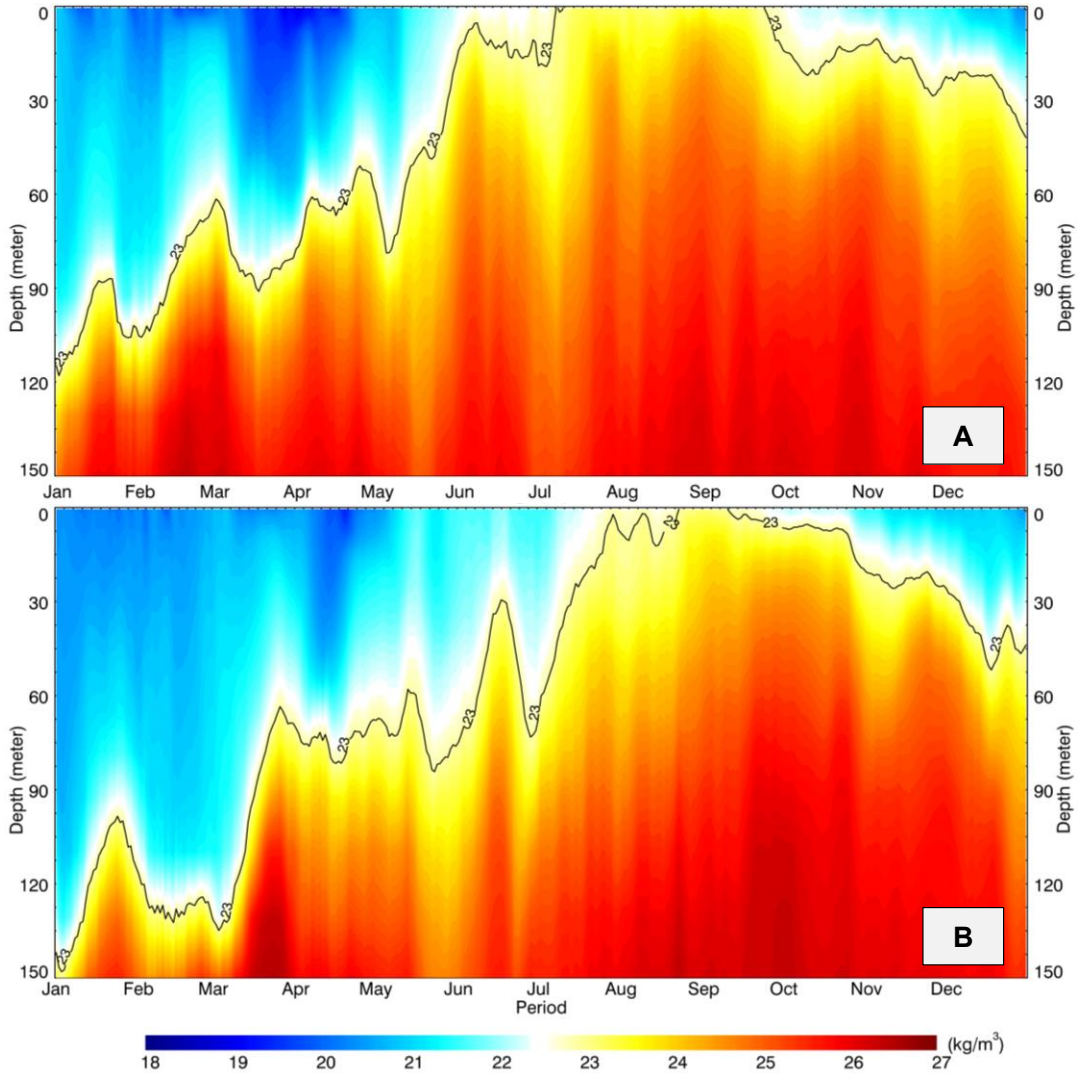


Fig. 6. Vertical profile of daily potential seawater density in Lumajang Waters in 2019 (A) and 2023 (B) (average from the thick box) using reanalysis data. The black contours in A) and B) are isopycnals of 23 kg/m³.

4.3. Possibility of Total Suspended Solids impact on chlorophyll-a

To investigate other possibilities for the mechanism to influence the highest chl-a, we analyzed time series precipitation and Rrs 555. To address the incongruity of the relationship between meridional EMT and Chl-a, we plot the temporal variability of precipitation and Chl-a in both years in **Fig. 7**. We expand the average precipitation area to the upland area to account for the potential impact of the river runoff during the rainy season. Wirasatriya et al. (2021) demonstrated the river runoff may increase the chl-a concentration; this rise is due to the existence of anthropogenic compounds.

September and October did not clearly show a significant increase in precipitation in the Lumajang area. Nevertheless, the topography of Lumajang Regency can affect river runoff. Lumajang Regency is surrounded by volcanoes (Mount Semeru and Mount Argopuro) and the ocean (Indian Ocean). Mount Semeru last erupted in 2023, while no eruptions occurred in 2019 (Handoko et al., 2025). The eruption of Mount Semeru was expected to increase the sediment influx into the LW rather than the precipitation.

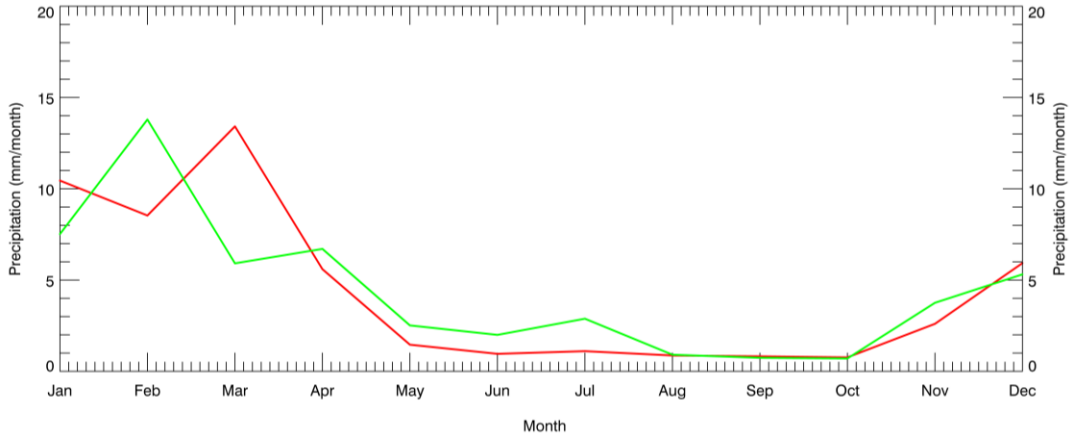


Fig. 7. Time series of monthly precipitation in 2019 (red line) and 2023 (green line) (averaged from the thick box in **Fig. 1**).

Furthermore, many rivers discharge into the Lumajang Waters (i.e., Bondoyudo River, Mujur River, Rakinten River and others). Volcanic material was probably transported from upper land to the sea through these rivers. The TSS from river runoff can influence the results of imagery from satellite observations (Maslukah et al., 2024). Volcanic ash or volcanic material (sediment) can also affect the variability of chl-a concentration in seawater (Katada et al., 2025). The apparent rise in chl-a concentrations may result from erroneous satellite image observations attributed to TSS.

To investigate the possibility of TSS influencing the error of the observations of chl-a concentration, we used Rrs 555 to identify TSS in the ocean. Many previous studies have used Rrs 555 for the identification of TSS, including Mobley et al. (2004); Siswanto et al. (2011); Matsushita et al. (2012); Wang & Tang (2014); Wirasatriya et al. (2021); Munandar et al. (2023); and Wijaya et al. (2024). According to Matsushita et al. (2012), the ocean is categorized into case-1 and case-2 waters. Case-1 waters are clean waters and have less contamination, while case-2 waters are more complex and contain more contaminat. The increase in Rrs 555 suggests that the chlorophyll-a measurements obtained from satellite images is inaccurate, as they represent a lot more than just phytoplankton. From 2015 to 2022 and in 2024, Rrs 555 was at most 0.0025 sr^{-1} throughout the year. In contrast, Rrs 555 in 2023 exhibited a 2-times higher than the other years, particulary from August to October (**Fig. 8**). To convince the influence of Rrs 555 to chl-a, we calculated the correlation between Rrs 555 and chl-a. In 2019 and 2023, the value of correlation between Rrs 555 and chl-a was categorized as high, However, it was higher in 2023 (0.83**), than in 2019 (0.53) (**Table 2**).

As discussed earlier, the TSS in 2019 is lower than that in 2023, but overall, the Lumajang Waters can be categorized as case-2 water. This condition may be attributed to the increase in river runoff, considering that many rivers flow into the waters of Lumajang and originate from the surrounding volcanoes. The precipitation data is not clearly seen to capture the increasing river runoff in Lumajang Waters, besides upwelling. Therefore, further in-situ observations of river runoff and TSS are needed to understand the TSS source in Lumajang waters. Consequently, the findings suggest that the anthropogenic activities in the upland area may contributed to the variability of chl-a concentration in Lumajang Waters.

Table 2.

Highly significant correlation analysis ($p < 0.01$) between monthly chl-a and Rrs 555 in Jan – Dec 2019 and Jan – Dec 2023 inside the thick boxes as shown in **Fig. 1.**

	Variable	Rrs 555
Chl-a	2019	0.53
	2023	0.83**

**. *Correlation is significant at the 0.01 level (1-tailed).*

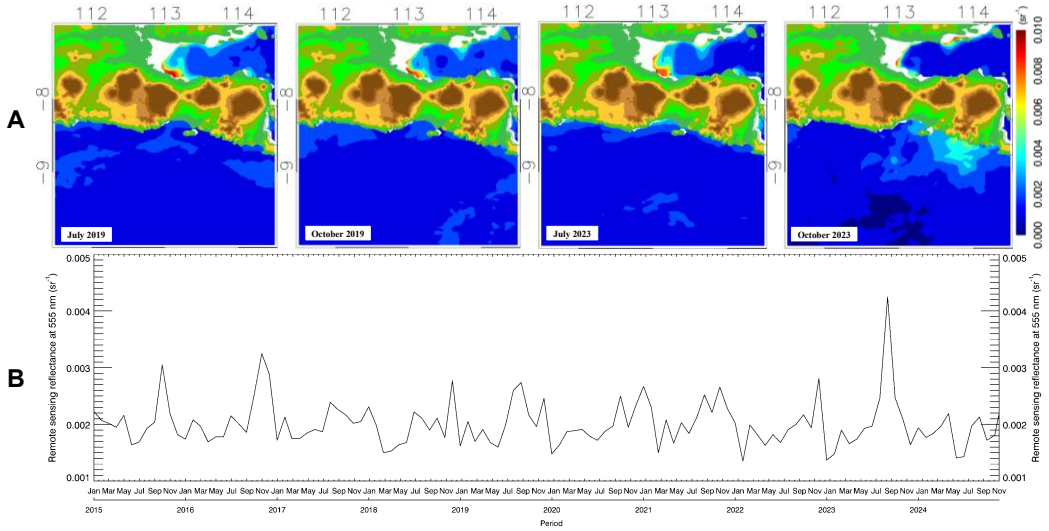


Fig. 8. The spatial distribution (A) and time series (B) variation of Rrs 555 in LW from 2015 to 2024 (averaged from the thick box in **Fig. 1**).

6. CONCLUSIONS

Blended satellite-based data provide effective means to investigate water parameters in Lumajang waters. Lumajang Waters have been identified as having the highest chl-a concentration, which occurred during the east monsoon and transition II seasons due to the coastal upwelling. The monthly chl-a variations in 2019 and 2023 ranges from 0.1 mg/m³ to 2 mg/m³ and 0.1 mg/m³ to 3 mg/m³, respectively. The coastal upwelling that increases in chl-a concentration in 2019 and 2023 is observable as a lifted water mass with a density of 23 kg/m³ from 100 meters depth to the surface. Despite lower intensity of coastal upwelling, chl-a concentration in 2023 was higher than in 2019. On the other hand, Rrs 555 in 2023 which represents TSS exhibited a 2-times higher than the other years, particularly from August to October. The high Rrs 555 may be associated with the increase of TSS brought by river runoff, considering that many rivers flow from the upper land and fertilize the waters of Lumajang. These characteristics make Lumajang waters very unique, as two mechanisms run together influencing the chl-a variation.

ACKNOWLEDGEMENT

This research was funded by the non-APBN DPA LPPM 2025, Universitas Diponegoro, under Contract No: 222-150/UN7.D2/PP/IV/2025, with Addendum No: 745/UN7.D2/PP/X/2025. The authors also extend their gratitude to the National Aeronautics and Space Administration (NASA) and the Copernicus Marine Environment Monitoring Service (CMEMS) and all related agencies for providing the satellite data that was essential for this study. Additionally, we appreciate the expertise of the anonymous reviewers who greatly enhanced the paper.

REFERENCES

An, L., Huang, Y., Xu, C., Xu, F., Chen, J., Liu, X. & Huang, B. 2025. Biogeochemical characteristics and phytoplankton community diversity of the Western North Equatorial current. *Global and Planetary Change,* 252, 104895. https://doi.org/10.1016/j.gloplacha.2025.104895.

Antonini, E.G.A. & Caldeira, K. 2021. Atmospheric pressure gradients and coriolis forces provide geophysical limits to power density of large wind farms. *Appl. Energy*, 281, 116048. https://doi.org/10.1016/j.apenergy.2020.116048.

Atlas, R., Hoffman, R. N., Ardizzone, J., Leidner, S. M., Jusem, J. C., Smith, D. K. & Gombos, D. 2011. A Cross-calibrated, Multiplatform Ocean Surface Wind Velocity Product for Meteorological and Oceanographic Applications. *Bulletin of the American Meteorological Society,* 92(2): 157–174. https://doi.org/10.1175/2010BAMS2946.1.

Garini, B. N., Suprijanto, J. & Pratikto, I. 2021. Chlorophyll-a Content and Abundance in The Waters of Kendal, Central Java. *Journal of Marine Research*, 10(1): 102-108. https://doi.org/10.14710/jmr.v10i1.28655.

Guo, Y., Li1, Y., Cheng, L., Chen, G., Liu, Q., Tian, Hu, S., Wang, J. & Wang, F. 2023. An Updated Estimate of the Indonesian Throughflow Geostrophic Transport: Interannual Variability and Salinity Effect. *Geophysical Research Letters*, 50, e2023GL103748. https://doi.org/10.1029/2023GL103748.

Garnesson, P., Mangin, A. & Bretagnon, M. 2022. OCEAN COLOUR PRODUCTION CENTRE Satellite Observation Copernicus-GlobColour Products. ⟨https://catalogue. marine.copernicus.eu/documents/QUID/CMEMS-OC-QUID-009–101to104–116-118.pdf.

Handoko, E. Y., Maulida, P. & Syaifullah, S. A. 2025. TheEffect of Semeru VolcanicEruption on Variatioin in Precipitation Water Vapor Using the GPS measurementin Period 2020–2023. *Jurnal Geosains dan Remote Sensing,* 6(1): 65-80. https://doi.org/10.23960/jgrs.ft.unila.356.

Haryanto, Y. D., Riama, N. F., Purnama, D. R., Pradit, N., Ismah, S. F., Suryo, A. W., Fadli, M., Hananto, N. D., Li, S. & Susanto, R. D. 2021. Effect of Monsoon Phenomenon on Sea Surface Temperatures in Indonesian Throughflow Region and Southeast Indian Ocean. *Journal of Southwest Jiaotong University*, 56(6): 914-923. https://doi.org/10.35741/issn.0258-2724.56.6.80.

Hidayat, M. N., Wafdan, R., Iskandar, T., Dewi, C. D., Nurhayati, N., Ramli, M., Muchlisin, Z. A. & Rizal, S. 2025. The influence of El Niño-Southern Oscillation and the Indian Ocean Dipole on chlorophyll-a in the Aceh waters during 1999–2023. *International Journal of Remote Sensing*, *46*(7): 2888–2908. https://doi.org/10.1080/01431161.2025.2460244.

Iskandar, I., Lestari, D. O., Saputra, A. D., Setiawan, R. Y., Wirasatriya, A., Susanto, R. D., Mardiansyah, W., Irfan, M., Rozirwan, Setiawan, J. D. & Kunarso. 2022. Extreme Positive Indian Ocean Dipole in 2019 and Its Impact on Indonesia. *Sustainability*, 14(22): 15155. https://doi.org/10.3390/su142215155.

Jiao, D., Xu, N., Yang, F. & Xu, K. 2021. Evaluation of spatial-temporal variation performance of ERA5 precipitation data in China. *Scientific Reports,* 11, 17956. https://doi.org/10.1038/s41598-021-97432-y.

Katada, R., Ariyoshi, S., Ayuzawa, H., Saito, K., Ishizaka, J. & Iwabuchi, H. 2025. Relation between eruption at Nishinoshima and chlorophyll-a concentration at Ogasawara Islands in 2020. *Progress in Earth and Planetary Science,* 12, 85. https://doi.org/10.1186/s40645-025-00761-z.

Kim, T., Najjar, R.G. & Lee, K. 2014. Influence of precipitation events on phytoplankton biomass in Coastal Waters of the Eastern United States. *Glob. Biogeochem. Cycles*, 28(1): 1–13. https://doi.org/10.1002/2013GB004712.

Krabbenhoeft, A., Weinrebe, R. W., Kopp, H., Flueh, E. R., Ladage, S., Papenberg, C., Planert, L. & Djajadihardja, Y. 2010. Bathymetry of the Indonesian Sunda margin-relating morphological features of the upper plate slopes to the location and extent of the seismogenic zone. *Natural Hazards and Earth System Sciences,* 10(9): 1899–1911. https://doi.org/10.5194/nhess-10-1899-2010.

Kunarso, Ismunarti, D. H., Rifai, A., Munandar, B., Wirasatriya, A. & Susanto, R. D. 2023. Effect of Extreme ENSO and IOD on the Variability of Chlorophyll-a and Sea Surface Temperature in the North and South of Central Java Province. *ILMU KELAUTAN: Indonesian Journal of Marine Sciences*, 28(1): 1-11. https://doi.org/10.14710/ik.ijms.28.1.1-11.

Liu, X., Pu, X., Qu, D. & Xu, Z. 2025. The role of wave-induced mixing in spring phytoplankton bloom in the South Yellow Sea. *Marine Pollution Bulletin,* 211, 117374. https://doi.org/10.1016/j.marpolbul.2024.117374.

Maslukah, L., Handoyo, G., Wulandari, S. Y., Sihite, C. B. & Sarjito. 2023. The Chlorophyll-a Response of Phytoplankton to Ratio N/P in Different Coastal Waters. *Ecological Engineering & Environmental Technology*, 24(9): 121–129. http://dx.doi.org/10.12912/27197050/172292.

Maslukah, L., Wirasatriya, A., Wijaya, Y. J., Ismunarti, D. H., Widiaratih, R. & Krisna, H. N. 2024. The assessment of chlorophyll-a retrieval algorithm and its spatial-temporal distribution using sentinel-2 MSI off the Banjir Kanal Timur River, Semarang, Indonesia. *Regional Studies in Marine Science*, 75. 103556. https://doi.org/10.1016/j.rsma.2024.103556.

Matsushita, B., Yang, W., Chang, P., Yang, F. & Fukushima, T. 2012. A simple method for distinguishing global case-1 and case-2 waters using SeaWiFS measurements. *ISPRS J. Photogramm. Remote Sens*. 69, 74–87. https://doi.org/10.1016/j.isprsjprs.2012.02.008.

Mears, C. A., Scott, J., Wentz, F. J., Ricciardulli, L., Leidner, S. M., Hoffman, R. & Atlas, R. 2019. A Near-Real-Time Version of the Cross-Calibrated Multiplatform (CCMP) Ocean Surface Wind Velocity Data Set. *Journal of Geophysical Research: Ocean,* 124(10): 6997-7010. https://doi.org/10.1029/2019JC015367.

Mobley, C.D., Stramski, D., Bissett, W. P. & Boss, E. 2004. Optical modeling of ocean waters: is the case 1 - case 2 classification still useful. *Oceanography*, 17 (2): 60–67. https://doi.org/10.5670/oceanog.2004.48.

Munandar, B., Wirasatriya, A., Sugianto, D. N., Susanto, R. D., Purwandana, A. & Kunarso. 2023. Distinct mechanisms of chlorophyll-a blooms occur in the Northern Maluku Sea and Sulu Sill revealed by satellite data. *Dynamics of Atmospheres and Oceans,* 102, 101360. https://doi.org/10.1016/j.dynatmoce.2023.101360.

Nouri, R., Vasel-Be-Hagh, A. & Archer, C. L. 2020. The Coriolis force and the direction of rotation of the blades significantly affect the wake of wind turbines. *Applied Energy,* 277. 115511. https://doi.org/10.1016/j.apenergy.2020.115511.

Nugroho, S. C., Setiawan, R. Y., Setiawati, M. D., Djumanto, Priyono, S. B., Susanto, R. D., Wirasatriya, A. & Larasati, R. F. 2022. Estimation of Albacore Tuna Potential Fishing Grounds in the Southeastern Indian Ocean. *IEEE Access,* 11: 1141 – 1147. https://doi.org/10.1109/ACCESS.2022.3233353.

Pet-Soede, C., Cesar, H. S. J. & Pet, J. S. 1999. An Economic Isuues Related to Blast Fishing on Indonesia Coral Reefs. *Enviromental Conservation*, 26(2): 83-93. https://doi.org/10.1017/S0376892999000132.

Rachman, H. A., Setiawati, M. D., Hidayah, Z., Syah, A. F., Nandika, M. R., Lumban-Gaol, J., As-syakur, A. R. & Syamsudin, F. 2024. Dynamic of upwelling variability in southern Indonesia region revealed from satellite data: Role of ENSO and IOD. *Journal of Sea Research,* 202: 102543. https://doi.org/10.1016/j.seares.2024.102543.

Sarker, S., Hossain, M. S., Sonia, M. I., Huda, A. N. M. S., Riya, S. C., Das, N., Liyana, E., Basak, S. C. & Kabir, M. A. 2023. Predicting the impacts of environmental variability on phytoplankton communities of a sub-tropical estuary. *Journal of Sea Research*, 194. 102404. https://doi.org/10.1016/j.seares.2023.102404.

Sartimbul, A., Winata, V.A. Kasitowati, R.D., Iranawati, F., Rohadi, E., Yona, D., Anjeli, U.G., Pranowo, W.S. & Lauro, F. M. 2023. Seasonal Indonesian Throughflow (ITF) across southern Java determines genetic connectivity of Sardinella lemuru (Bleeker, 1835). *Deep-Sea Research Part II,* 209, 105295. https://doi.org/10.1016/j.dsr2.2023.105295.

Sathyendranath, S., Brewin, R. J. W., Brockmann, C., Brotas, V., Calton, B., Chuprin, A., Cipollini, P., Couto, A.B., Dingle, J., Doerffer, R., Donlon, C., Dowell, M., Farman, A., Grant, M., Groom, S., Horseman, A., Jackson, T., Krasemann, H., Lavender, S., Martinez-Vicente, V., Mazeran, C., M´elin, F., Moore, T.S., Müller, D., Regner, P., Roy, S., Steele, C.J., Steinmetz, F., Swinton, J., Taberner, M., Thompson, A., Valente, A., Zühlke, M., Brando, V.E., Feng, H., Feldman, G., Franz, B.A., Frouin, R., Gould Jr, R.W., Hooker, S.B., Kahru, M., Kratzer, S., Mitchell, B.G., Muller-Karger, F.E., Sosik, H.M., Voss, K.J., Werdell, J. & Platt, T. 2019. An oceancolour time series for use in climate studies: the experience of the ocean-colour climate change initiative (OC-CCI). *Sensors*, 19(19), 4285. https://doi.org/10.3390/s19194285.

Setiawan, R.Y. & Habibi, A. 2011. Satellite detection of summer chlorophyll-a bloom in the Gulf of Tomini. IEEE J. Sel. Top. Appl. Earth Obs. *Remote Sens*., 4(4): 944–948. https://doi.org/10.1109/JSTARS.2011.2163926.

Siswanto, E., Tang, J., Yamaguchi, H., Ahn, Y., Ishizaka, J., Yoo, S., Kim, S., Kiyomoto, Y., Yamada, K., Chiang, C. & Kawamura, H. 2011. Empirical ocean-color algorithms to retrieve chlorophyll-a, total suspended matter, and colored dissolved organic matter absorption coefficient in the Yellow and East China Seas. *J. Oceanogr.* 67, 627–650. https://doi.org/10.1007/s10872-011-0062-z.

Susanto, R. D., Gordon, A. L. & Zheng, Q. 2001. Upwelling along the coasts of Java and Sumatra and its relation to ENSO. *Geophysical Research Letters,* 28(8): 1599-1602. https://doi.org/10.1029/2000GL011844.

Syamsuddin, M. L., Saitoh, S., Hirawake, T., Bachri, S. & Harto, A. B. 2013. Effects of El Niño–Southern Oscillation eventson catches of Bigeye Tuna (Thunnus obesus) inthe eastern Indian Ocean off Java. *Fishery Bulletin,* 111(2): 175-188. https://doi.org/10.7755/FB.111.2.5.

UNESCO, 2015. Tenth Report of the Joint Panel on Oceanographic Tables and Standards. UNESCO Technical Papers in Marine Science. Paris. 25p.

Wang, J.J. & Tang, D.L. 2014. Phytoplankton patchiness during spring intermonsoon in Western Coast of South China Sea. *Deep-Sea Res. II,* 101: 120–128. https://doi.org/10.1016/j.dsr2.2013.09.020.

WAMDI group. 1988. The WAM model: a third-generation ocean wave prediction model. *J. Phys. Oceanogr*., 18 (12): 1775–1810. https://doi.org/10.1175/1520-0485(1988)018<1775:TWMTGO>2.0.CO;2.

Wijaya, A., Zakiyah, U., Sambah, A. B. & Setyohadi, D. 2020. Spatio-temporal variability of temperature and chlorophyll-a concentration of sea surface in Bali Strait, Indonesia. *Biodiversitas,* 21(11): 5283-5290. https://doi.org/10.13057/biodiv/d211132.

Wijaya, Y. J., Wisha, U. J., Rejeki, H. A. & Ismunarti, D. H. 2023. Variability of the South Java Current from 1993 to 2021, and its relationship to ENSO and IOD events. *Asia-Pacific Journal of the Atmospheric Sciences,* 60(17): 15. http://dx.doi.org/10.1007/s13143-023-00336-2.

Wijaya, Y. J., Wisha, U. J., Maslukah, L. Windarto, S., Wirasatriya, A. & Zainuri, M. 2024. Seasonal variation of chlorophyll-a in South Java over the past quarter-century. *Ocean Dynamics,* 74: 703–724. https://doi.org/10.1007/s10236-024-01629-4.

Wirasatriya, A., Setiawan, R.Y. & Subardjo, P. 2017. The effect of ENSO on the variability of chlorophyll-a and sea surface temperature in the Maluku Sea. *IEEE J. Sel. Top. Appl. Earth Obs. Remote Sens*., 10(12): 5513–5518. https://doi.org/10.1109/JSTARS.2017.2745207.

Wirasatriya, A., Sugianto, D.N., Helmi, M., Setiawan, R.Y. & Koch, M. 2019. Distinct characteristics of SST variabilities in the Sulawesi Sea and the Northern Part of the Maluku Sea during the southeast monsoon. *IEEE J. Sel. Top. Appl. Earth Obs. Remote Sens*., 12 (6): 1763–1770. https://doi.org/10.1109/JSTARS.2019.2913739.

Wirasatriya, A., Susanto, R.D., Setiawan, J. D., Ramdani, F., Iskandar, I., Jalil, A. R., Puryajati, A. D., Kunarso & Maslukah, L. 2021. High Chlorophyll-a Areas along the Western Coast of South Sulawesi-Indonesia during the Rainy Season Revealed by Satellite Data. *Remote Sens.,* 13, 4833. https://doi.org/10.3390/rs13234833.

Wirasatriya, A., Susanto, R. D., Setiawan, J. D., Agustiadi, T., Iskandar, I., Ismanto, A., Nugraha, A. L., Puryajati, A. D., Kunarso, Purwandana, A., Ramdani, F., Lestari, T. A., Maro, J. F., Kitarake, Y. N. S., Sailana, Y. L., Goro, M. S., Hidayah, B. K., Widiaratih, R., Fitria, S. & Dollu, E. A. 2023. Extreme Upwelling Events in the Seas of the Alor Kecil, Alor Island, Indonesia. *Oceanography,* 36(1): 28 – 37. https://doi.org/10.5670/oceanog.2023.107.

Xu, Y., Li, S., Hamzah, F., Setiawan, A., Susanto, R. D., Cao, G. & Wei, Z. 2018. Intraseasonal flow and its impact on the chlorophyll-a concentration in the Sunda Strait and its vicinity. *Deep-Sea Research Part I*, 136: 84-90. https://doi.org/10.1016/j.dsr.2018.04.003.

Xu, Wang, D., Wei, Q., Li, S., Susanto, R. D., Wang, G., Teng, F., Agustiadi, T., Trenggono, M., Santoso, P. D. & Wei, Z. 2025. Satellite-detected Sea surface chlorophyll-a penetrating fronts off the south coast of Java Island. *Deep Sea Research Part I: Oceanographic Research Papers,* 225. 104593. https://doi.org/10.1016/j.dsr.2025.104593.

Yun, C., Hwang, K., Han, S. & Ri, H. 2019. The effect of salinity stress on the biofuel production potential of freshwater microalgae chlorella vulgaris YH703. *Biomass and Bioenergy*, 127, 105277. https://doi.org/10.1016/j.biombioe.2019.105277.

Zampollo, A., Murray, R. O., Gallego, A. & Scott, B. 2025. Does the oceanographic response to wind farm wind-wakes affect the spring phytoplankton bloom?. *Progress in Oceanography,* 237, 103512. https://doi.org/10.1016/j.pocean.2025.103512.

CLIMATIC TRENDS AND CLASSIFICATION SHIFTS IN THE MAT RIVER BASIN IN ALBANIA, BASED ON THE KÖPPEN- GEIGER AND KÖPPEN-TREWARTHA CLIMATE CLASSIFICATION

Albana HASIMI [1*], Elvin ÇOMO [1], Gazmir ÇELA [1], Entela VAKO [2], Amarildo SHALLAS [1], Mirela DVORANI [2], Anira GJONI [2] & Blerina PAPAJANI [3]

DOI: 10.21163/GT_2026.211.15

ABSTRACT

The Mati River flows in the centre of the northern geographical region of the Republic of Albania. From a climatic perspective, this region exhibits significant variability in temperature and precipitation, influenced by its diverse topography, with altitudes ranging from 1,800 meters above sea level to sea level at the estuary. The operation of multiple hydroelectric power plants along the Mati River underscores the significance of this study, as precipitation variability directly influences hydropower generation and, consequently, Albania's energy sector. On the other hand, the occurrence of extreme temperatures in this region directly impacts the quality of life, agricultural productivity, and the agro-industrial sector. Also, the presence of old mining dumps, along with the region's geological formation, which is known to be mineral-rich, explains the occurrence of heavy metals in the river's water. Climatic conditions directly influence the concentration of these pollutants, making this a key reason for undertaking this study. The comparative analysis of climatic data across seven meteorological stations within the Mat River Basin indicates a consistent and measurable warming trend, accompanied by spatially variable precipitation changes over the past three decades. The evolution of the Köppen Climate Classification (KCC) and Köppen -Trewartha Climate Classification (KTC) further supports an ongoing transition toward warmer and, in some cases, drier climatic regimes across the basin.

Keywords: *Climate data; Köppen climate classification; Köppen – Trewartha; Climatic shifts classification; Mati River basin.*

1. INTRODUCTION

Climate monitoring is mostly based either directly on station measurements of climate characteristics (surface air temperature, precipitation, cloud cover, etc.), or on some post-processed form of those measurements, such as gridded datasets. The analysis of climate patterns can be performed for each individual climate variable separately, or the data can be aggregated, for example, by using some kind of climate classification that integrates several climate characteristics (Belda et al., 2014). Climate, defined as a comprehensive statistical description of climatic conditions over a sufficiently long period at a wide range of temporal scales (D. Chen & Chen, 2013), is one of the most critical determinants of Earth's ecosystems (H. Chen et al., 2013; Schröter et al., 2005). Controlled by the dominant climatic conditions and prevailing vegetation formations, major ecosystems are distributed on land in a predictable pattern. Major ecosystem regions are largely defined based on the climate zones following the Köppen climate classification system (Köppen, 1931). This land climate classification can incorporate the amplitude and seasonal phase of temperature and precipitation

[1] *Department of Meteorology, Institute of Geosciences, Polytechnic University of Tirana, Albania.*
[*] *Corresponding author (AH) a.hasimi@geo.edu.al; (EC) e.como@geo.edu.al; (GC) g.cela@geo.edu.al; (AS) a.shallas@geo.edu.al, (AG) a.gjoni@geo.edu.al.*
[2] *Department of Hydrology, Institute of Geosciences, Polytechnic University of Tirana, Albania. (EV) e.vako@geo.edu.al; (MD) m.dvorani@geo.edu.al.*
[3] *Department of Physics, Faculty of Natural Science, University "Aleksander Xhuvani" of Elbasan, Albania. (BP) b.papajani@uniel.edu.al.*

annual cycles. It is a highly effective means to simplify spatial variability and aggregate climate gradients into simple but ecologically meaningful classes(C. Beck et al., 2005; H. E. Beck et al., 2018; Haidu, 2006).

Climatic classifications also represent a convenient tool for the validation of climate models and for the analysis of simulated future climate changes(Wang et al., 2023). Basic concepts are presented by applying climate classification to the global Climate Research Unit (CRU) TS 3.1 global dataset. We focus on definitions of climate types according to the Köppen-Trewartha climate classification (KTC) with special attention given to the distinction between wet and dry climates (Xin, 2023). The distribution of KTC types is compared with the original Köppen classification (KCC) for the period 1961−1990. In addition, we provide an analysis of the time development of the distribution of KTC types throughout the 20th century. There are observable changes identified in some subtypes, especially semi-arid, savanna and tundra (Belda et al., 2014). Global climate classifications were originally constructed in order to designate the manifold existing local climates to an adequate number of climate types and to determine the spatial distribution of these types on the basis of climatic data for a reference period. Thus, climate classifications are introduced in order to reflect the mean spatial climate characteristics. However, the underlying climate variables are subject to temporal variations and so are the results of climate classifications(C. Beck et al., 2005; Haidu et al., 2024).

Hydrographically, the Mati River Basin features a highly integrated network of watercourses, with increased density in its middle and lower sections, where ultrabasic lithological formations predominate. The presence of diverse lentic and lotic water bodies further enhances the basin's hydrological complexity, making it a significant subject for scientific investigation (Group of authors, 1984; Pano, 2008), (Grontmij et al., 2010; Magyari-Sáska & Magyari-Sáska, 2023).

1.1. Albania's Climate

According to the Albanian clime classification such as the Köppen Classification Albania's Climate primarily falls under the Csa – Hot-Summer Mediterranean Climate and, in some higher-altitude areas, the Csb – Warm-Summer Mediterranean Climate (H. E. Beck et al., 2018; Group of authors, 1985).

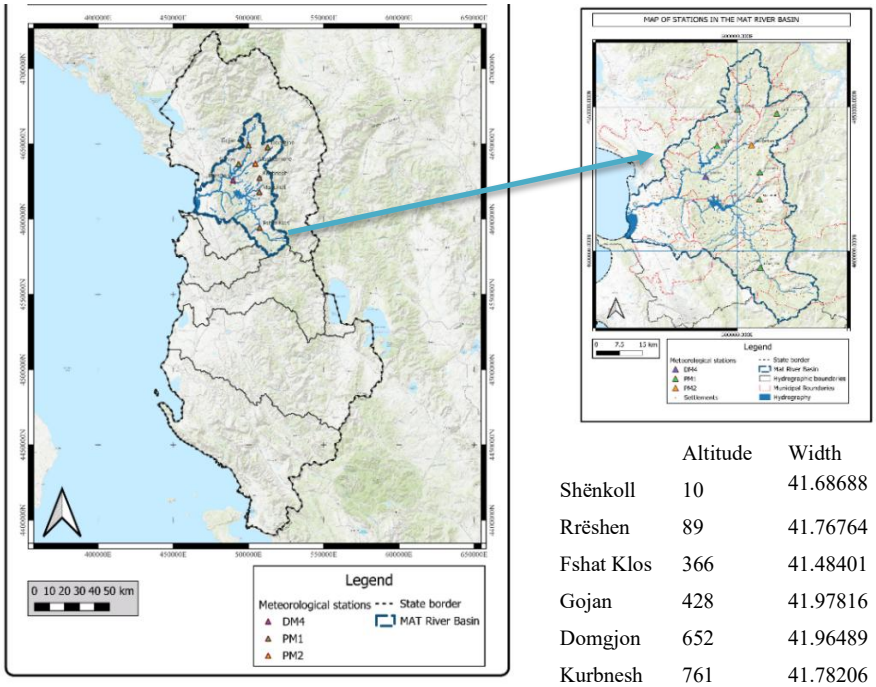
Csa – Hot-Summer Mediterranean Climate found in most coastal and lowland areas, including Tirana, Durrës, Vlorë, and Saranda. Summers are hot and dry, with temperatures often exceeding 30.0°C (86°F). Winters are mild and wet, with temperatures usually staying above 0.0°C (32°F). Annual precipitation is moderate, mostly occurring in the cooler months.

Csb – Warm-Summer Mediterranean Climate found in hilly and mountainous regions, such as Pogradec, parts of Korçë, and the Northern Highlands. Summers are cooler than in the lowlands, with temperatures usually staying below 30.0°C (86°F). Winters are wetter and mild, but snowfall is more common in elevated areas.

In the Albanian Alps and other high-altitude regions, there are some influences of the Dfb – Humid Continental Climate, characterized by cold, snowy winters and cool summers.

2. STUDY AREA

Based on the geographical classification of Albania, the Mat River basin belongs to the North Central Highlands (**Fig. 1**). This basin is characterized by a geographical diversity both in terms of relief and because it includes a range of altitudes, starting from 1800 m above sea level to 0 m at the mouth. From a climatic point of view, these areas are characterized by a variety of temperatures and precipitation. According the Albanian Climate classification the Mat River basin belongs to Mediterranean climate with continental tendencies and other high-altitude regions, there are some influences of the Dfb – Humid Continental Climate, characterized by cold, snowy winters (H. E. Beck et al., 2018; Group, 1985). From the entire database, the most representative and complete stations were selected, ensuring that the entire basin was covered with information regarding the typology of observations and the relief, so that all microclimates of the study area were represented. The selected meteorological stations are marked on the map shown in **Fig. 1** where the coordinates are also presented.



	Altitude	Width	Length
Shënkoll	10	41.68688	19.65046
Rrëshen	89	41.76764	19.87675
Fshat Klos	366	41.48401	20.08921
Gojan	428	41.97816	20.0003
Domgjon	652	41.96489	20.15431
Kurbnesh	761	41.78206	20.08814
Macukull	1007	41.69741	20.08666

Fig. 1. Map of Albania and Study Area. The watershed of the Mati River (left) and the meteorological stations with geographic coordinates (right).

3. DATA AND METHODS

3.1. Data Source and Description

Meteorological data from a decade (2014-2024) were previously filtered to perform some in-depth calculations and analyses to calculate monthly and annual average values, both in terms of temperatures and precipitation. All data sourced from Albania's National Meteorological Monitoring System which belong to the Department of Meteorology, Institute of Geoscience. In this analysis, daily data from several meteorological stations (**Fig. 1**) were used, which contained gaps distributed unevenly throughout the observation period. Since the gaps were not distributed at all stations simultaneously, an approach based on the inter-station daily average was applied, which is considered one of the most reliable methods in situations with sporadic gaps. The missing values for each station were replaced by the average calculated on this day. This step was performed carefully to maintain climate extremes. To fill data gaps, the reanalysed dataset from Copernicus ERA5 has been utilized (Copernicus Climate Change Service (C3S), 2025).

For the climate classification analysis, the historical average values from the reference period 1960–1990 were used as climatological norms, while the computed values for the last decade were applied for comparative evaluation (Cui et al., 2021). The database was processed using standard statistical procedures, and a custom algorithm developed in the Python programming language was employed to calculate and classify the climatic parameters. The algorithm was based on the modified Köppen–Geiger and Köppen–Trewartha climate classification criteria, following the methodological framework outlined by Belda et al (Belda et al., 2014). For data visualization and statistical interpretation, OriginLab Pro software was used to generate the graphical representations and comparative analyses.

4. RESULTS AND DISCUSSION

As preparatory work for the assessment we present in this paper, and within the broader project for the MAT River Basin, a series of works on extreme weather events, drought events and climate change have been carried out (Hasimi, Papajani, et al., 2025). **Table 1** shows the changes in temperatures and precipitation over the last decade compared to the norms, expressed as a percentage, for each meteorological station of Mati basin river, Albania.

The climatic data from meteorological stations within the Mat River Basin reveal a clear pattern of warming accompanied by a concurrent decline in annual precipitation during the period 1990–2025. These changes are consistently reflected in the observed shifts in both the Köppen Climate Classification (KCC) and the Köppen–Trewartha Climate Classification (KTC), indicating a progressive transformation of the basin's climatic regime.

Table 1.

The changes in temperatures and precipitation for meteorological station of Mati basin river, Albania and Climate type according to the Köppen-Geiger and the Köppen-Trewartha classification.

Meteo Station	Altitude m a.s.l	ΔT_{mes} annual	ΔP_{mes} annual	KCC		KTC	
		%	%	norms 1990	Last decade results	norms 1990	Last decade results
Shënkoll	10	*no last decade data*		Cfa		Cf	
Rrëshen	89	+ 8.15	**+12.96**	Cfa	Csa	Da	Da
F Klos	366	+ 19.60	-5.90	Cfa	Cfa	Da	Cf
Gojan	428	+ 11.77	-3.78	Cfb	Cfa	Da	Cf
Domgjon	652	+ 24.66	-21.63	Cfb	Bkf	Da	Da
Kurbnesh	761	+ 21.64	- 2.57	Cfb	Cfa	Da	Da
Macukull	1007	*no historical data*			Cfb		Da

4.1. Meteorological Data Analysis

The climate classification applied in this study relies exclusively on-air temperature and precipitation. Accordingly, the multiyear variability and long-term evolution of these two parameters across the Mati River Basin are analyzed below using stations with complete and reliable records.

4.1.1. Temperature Trends

Long-term temperature records reveal a coherent and statistically significant warming signal across all meteorological stations in the basin. Mean annual air temperature has increased by approximately **1.5–2.7 °C** relative to the 1961–1990 climatic norms, indicating a persistent basin-wide thermal shift over recent decades. This warming is evident from the coastal lowlands to the highest mountain stations, highlighting the pervasive influence of regional climate change

At the lowest elevation, Shën Koll (10 m a.s.l.) exhibits a humid subtropical climate with a long-term mean annual temperature of 15.47 °C. Although complete data for the most recent decade are unavailable, the station is retained as a climatological reference. Rrëshen (89 m a.s.l.; **Fig. 2**) shows a clear warming signal, with mean annual temperature increasing by **+1.09 °C**, indicating progressive inland warming even at low elevations. October–November temperatures display relative stability with a slight decreasing tendency, potentially linked to localized microclimatic effects associated with river regulation and the construction of small and medium hydropower reservoirs, during the past decade which may influence heat exchange and moisture conditions. Alterations to the riverbed and the creation of artificial reservoirs have modified the local microclimate, influencing both temperature and precipitation patterns and, consequently, the overall water balance of the basin.

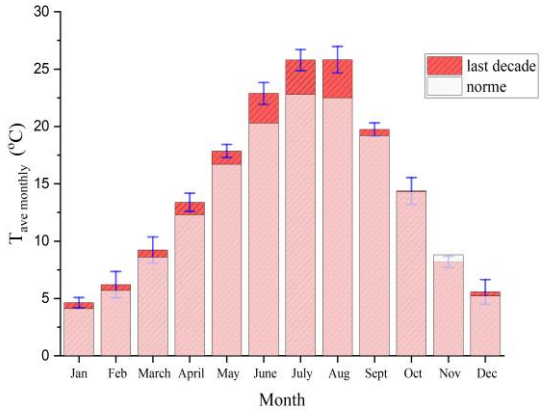


Fig. 2. Monthly average temperature (T_{ave}) at Rrëshen station. The last decade is presented with standard deviation (blue line).

Mid-altitude stations demonstrate more pronounced warming. F. Klos (366 m a.s.l.) records the strongest increase (+2.6 °C), suggesting thermal amplification at intermediate elevations where topography and atmospheric circulation may enhance heat retention. Gojan (428 m a.s.l.) exhibits a comparable rise of +1.5 °C, reinforcing the elevation-dependent nature of the warming trend.

High-elevation stations show similarly strong responses (**Fig. 3**). Domgjon (652 m a.s.l.) experiences an increase of +2.7 °C, with mean annual temperature rising from 10.9 °C to 13.6 °C. Kurbnesh (761 m a.s.l.) records a +2.2 °C increase, while Macukull (1007 m a.s.l.), the highest station in the basin, now exhibits a mean annual temperature of 11.6 °C. These results confirm that even traditionally cooler upland environments are undergoing substantial thermal shifts

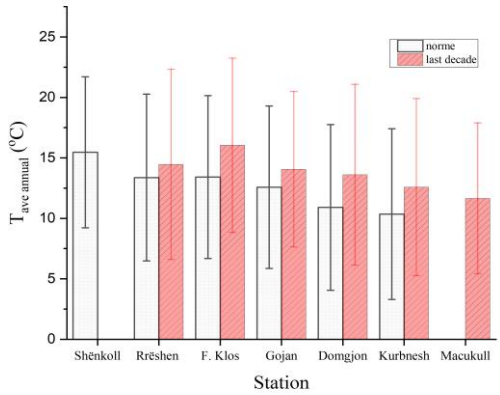
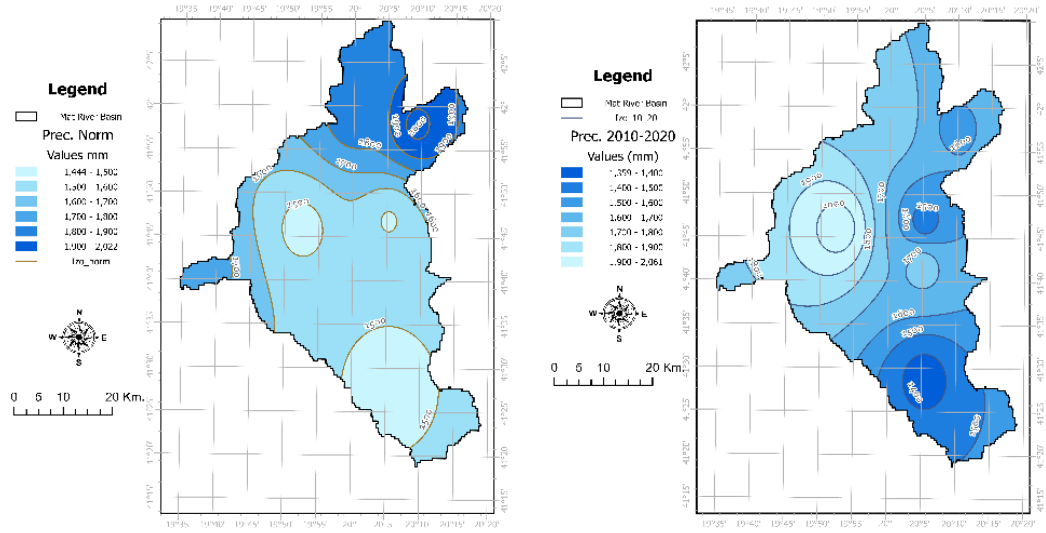


Fig. 3. Annual average temperature ($T_{ave\ annual}$) of all station with standard deviations, presented from low to higher-altitude.

Overall, the results indicate a consistent, elevation-dependent warming pattern across the basin, with stronger increases from coastal areas toward mountainous zones, suggesting that higher-altitude ecosystems may be experiencing accelerated climate impacts. Such spatial differentiation has important implications for hydrological processes, vegetation dynamics, and ecosystem resilience. The observed warming rates are consistent with regional trends reported for the Western Balkans, where mean temperature has increased by more than 0.4 °C per decade since the 1990s (European Commission. Joint Research Centre., 2024; Haidu et al., 2024)

4.1.2. Precipitation Trends

The spatial distribution of long-term precipitation norms (1961–1990) across the Mati River Basin shows a clear south–north and lowland–mountain gradient (**Fig. 4a**). Northern and northeast high-altitude zones receive the highest annual totals (>1900–2000 mm), driven by orographic uplift and moist Adriatic air masses. In contrast, southern and central low-elevation areas receive lower amounts, typically **1400 – 1600 mm yr^{-1}** consistent with the basin's topographic configuration and the prevailing circulation patterns.



a *b*

Fig. 4. The distribution of precipitation of the Mat River basin for the time period 1961-1990 (*a*) and anomalies in mm of precipitation for the last decade (*b*).

Precipitation anomalies for the most recent decade (Fig. 4b) reveal substantial departures from these historical norms. Central-western and southwestern sectors exhibit negative anomalies exceeding **–300 mm**, indicating a marked decline in annual rainfall. These areas coincide with stations showing the strongest warming (e.g., F. Klos and Domgjon), suggesting enhanced evapotranspiration and reduced effective moisture availability, with potential implications for hydrological balance and water resource sustainability.

Conversely, positive anomalies of **+200 to +400 mm** are observed in the northeast mountainous sector. This localized increase may reflect intensified orographic effects, microclimatic feedbacks, and possible land-surface modifications associated with hydropower infrastructure, including reservoir development, which can influence local humidity and convection. Overall, the precipitation regime appears increasingly irregular, characterized by declining totals in interior mountainous areas and relatively stable conditions in coastal and lowland zones(Nistor et al., 2020).

4.2. Climate Analysis

According The Köppen Climate Classification (KCC) reveals a gradual **transition from temperate oceanic (Cfb)** to **humid subtropical (Cfa)** or **Mediterranean (Csa)** types in several stations (**Table 1**).

On the other hand, the Köppen–Trewartha Climate Classification (KTC) shows consistent evolution, with most stations shifting from *Da* to *Cf*, reflecting warmer conditions and reduced thermal seasonality. **Figure 5** synthesizes the spatial distribution of observed climatic changes and classification shifts. The detected trends are consistent with previous regional studies of our group's studies for other regions of Albania.(Hasimi, Çomo, et al., 2025), (Çela et al., 2024), (Papajani et al., 2025).

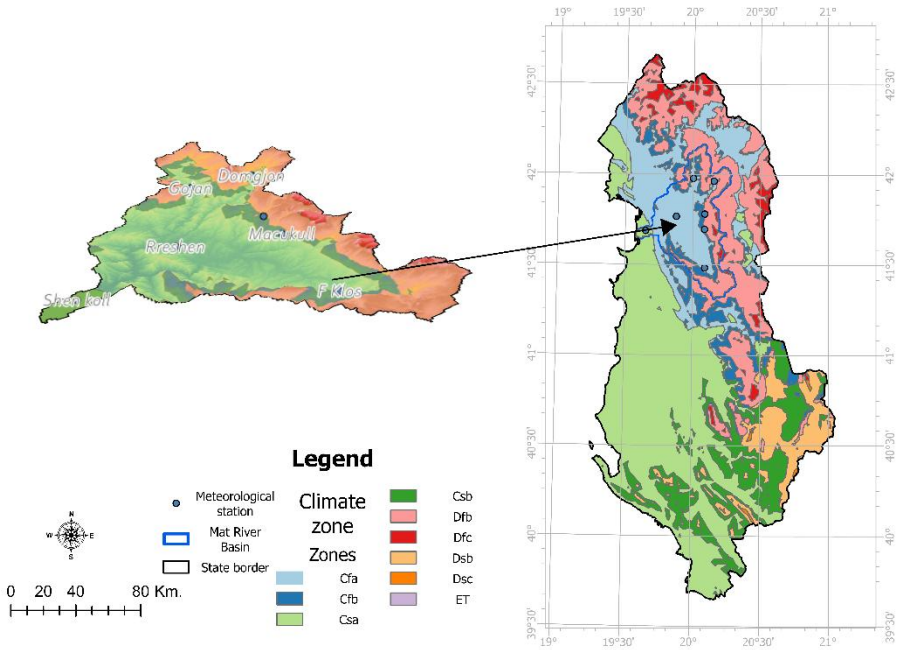


Fig. 5. Albania maps of Köppen climate classification KCC, data for the period of 1980−2016 (H. E. Beck et al., 2018) and the same maps generation from our results for Mati basin river for the period 2014-2024

At F. Klos station (366 m a.s.l.), Despite the reduced rainfall, the Köppen classification remains within the Cfa category (humid subtropical climate), while the KTC changes from Da to Cf, indicating a subtle thermal shift toward a warmer and slightly more humid microclimate. At Domgjon station (652 m a.s.l.), the transition from a Cfb to Bkf Köppen type, with the KTC remaining Da, suggests that Domgjon is undergoing a significant climatic transition from a temperate oceanic toward a drier, more continental climate regime. Similarly, Kurbnesh station (761 m a.s.l.) The shift from Cfb to Cfa in the Köppen classification further supports the warming tendency observed throughout the basin, indicating a gradual replacement of temperate oceanic features with those characteristics of a warmer and less humid climate. For Gojan station (428 m a.s.l.), the 1990 climatic data indicate a Cfb classification with Da thermal characteristics, spatial continuity and elevation similarity with the neighboring stations imply a parallel trend of warming and decreasing precipitation. Data for Macukull station (1007 m a.s.l.) based on altitudinal gradients and regional coherence, it can be inferred that this higher-elevation site experiences a smaller thermal increase compared to lower altitudes, but may still exhibit a decline in annual precipitation consistent with the overall basin trend.

The dataset provides robust evidence of climatic transformation within the Mat River Basin, characterized by: Systematic warming across all elevation zones (1.5–2.7°C increase); Moderate to significant precipitation decline in mid- and high-altitude stations; and Progressive reclassification of climates toward warmer and more arid types (Cfb → Cfa/Csa).

These changes align with broader Mediterranean and Balkan climate trends, marked by increased summer aridity and altered regional circulation patterns. (Knez et al., 2022) (Kostopoulou et al., 2009). Overall, when precipitation anomalies are interpreted together with temperature trends, they reveal a clear **spatial polarization of climate change** within the Mati River Basin. Low- and mid-altitude areas are experiencing progressive warming accompanied by drying, whereas upper catchment zones show signs of localized moistening, likely driven by topographic effects and anthropogenic influences. This divergence highlights the complex interactions among topography, land-use change, and regional climate forcing, all of which are reshaping the basin's the temperatures and hydrological regimes (Nigrelli & Chiarle, 2023; Nistor et al., 2022).

6. CONCULSIONS

The documented climatic shifts are expected to exert substantial impacts on the basin's hydrology and ecosystem dynamics (Palmer & Ruhi, 2019). The observed increase in mean annual temperature (**1.5–2.7 °C**) combined with reduced precipitation at several stations suggests intensified evapotranspiration, leading to declining surface runoff and groundwater recharge. As a result, river discharge is likely to decrease progressively, particularly during summer and early autumn, when precipitation deficits coincide with peak thermal stress(Hasimi, Çomo, et al., 2025) (De Castro et al., 2007).

The transition from temperate oceanic (*Cfb*) to warmer subtropical and Mediterranean climate types (*Cfa–Csa*) further indicates a shift in the basin's hydrological seasonality. Elevated temperatures enhance soil-moisture depletion and alter snow accumulation and melt processes in upland areas such as Domgjon, Kurbnesh, and Macukull. Consequently, streamflow peaks are expected to occur earlier in the hydrological year, while low-flow periods may become longer and more severe. These changes increase vulnerability to hydrological droughts, soil erosion, and fluctuations in sediment transport (Anghileri et al., 2014; Hasimi, Çomo, et al., 2025).

From an ecological perspective, rising temperatures and reduced moisture availability are likely to drive shifts in vegetation composition and distribution. Thermophilus and drought-tolerant species may expand to higher elevations, while mesophilic species adapted to cooler and wetter conditions may retreat or decline, with direct implications for biodiversity, forest productivity, and landscape stability (Kong et al., 2017; Sparey et al., 2023).

Socio-environmentally, these climatic changes pose growing challenges for water-resource management, agricultural planning, and ecosystem conservation within the Mati River Basin (D. Chen & Chen, 2013). Reduced dry-season water availability may limit irrigation potential and hydropower efficiency, while increased precipitation variability could heighten flood risk in downstream areas and drought frequency in upper sub-catchments (Forzieri et al., 2014).

Overall, the integration of climatic and hydrological evidence indicates a trajectory toward **warmer, drier, and more hydrologically unstable conditions** in the Mati River Basin. Continued long-term monitoring and high-resolution climate modelling are therefore essential to evaluate future water-balance scenarios and to support adaptive management strategies aimed at mitigating environmental and socio-economic impacts.

In summary, observed temperature increases of **2.0–2.5 °C** across all meteorological stations, together with a mean precipitation decline of **5–20 %**, demonstrate a systematic regional trend toward warming and drying. The spatial pattern of change suggests an elevation-dependent response, with stronger thermal increases and climate-classification shifts at low- and mid-elevations. These transformations imply a reorganization of hydrological processes, including evapotranspiration, runoff generation, and vegetation dynamics, with long-term consequences for water availability and ecosystem stability (Lenton et al., 2008).

The pronounced interannual variability detected in the dataset further reflects the influence of large-scale atmospheric and oceanic circulation patterns affecting the Balkan Peninsula. To enhance understanding of ongoing dynamics and improve anticipation of future environmental change, several key research priorities emerge. These include the establishment of long-term monitoring programs for climatic, hydrological, cryospheric, and ecological indicators in mountain regions, alongside integrated, model-based approaches that couple climate, hydrology, ecosystems, and land-use processes. Such approaches should explicitly account for land–atmosphere feedbacks and support policy-relevant impact assessments. In addition, process-oriented investigations across altitudinal gradients and headwater basins are needed to evaluate environmental sensitivity at critical climatic and ecological thresholds. Finally, the development of sustainable land- and water-management strategies is essential, particularly those addressing changes in forest cover, mountain agriculture, food security, and associated socio-economic pressures. Collectively, these research directions are fundamental to the design of adaptive management frameworks capable of responding to the accelerating impacts of climate change on mountain environments, including the Mati River Basin.

ACKNOWLEDGMENT

This study is conducted as part of the project titled "Impacts of Heavy Metals from the Mining Industry and Assessment of Pollution Distribution in the Mati River Basin." The project is funded by the National Agency for Scientific Research and Innovation (NASRI) of Albania under the National Research and Development Projects (NRDP) program for the period 2024–2026.

REFERENCES

Anghileri, D., Pianosi, F., & Soncini-Sessa, R. (2014). Trend detection in seasonal data: From hydrology to water resources. *Journal of Hydrology*, *511*, 171–179. https://doi.org/10.1016/j.jhydrol.2014.01.022

Beck, C., Grieser, J., & Kottek, M. (2005). *Characterizing Global Climate Change by means of Köppen Climate Classification.* Deutscher Wetterdienst. vol. In *Klimastatusbericht 2005,* 139–149.

Beck, H. E., Zimmermann, N. E., McVicar, T. R., Vergopolan, N., Berg, A., & Wood, E. F. (2018). Present and future Köppen-Geiger climate classification maps at 1-km resolution. *Scientific Data*, *5*(1), 180214. https://doi.org/10.1038/sdata.2018.214

Belda, M., Holtanová, E., Halenka, T., & Kalvová, J. (2014). Climate classification revisited: From Köppen to Trewartha. *Climate Research*, *59*(1), 1–13. https://doi.org/10.3354/cr01204

Çela, G., Gjoni, A., Zorba, P., Hasimi, A., Çomo, E., & Rexhepi, I. (2024). *Long-term trends in average air temperature in the Central Lowland Mediterranean Climate Zone of Albania*. 4th International Conference on Contemporary Academic Research, Turkey, ISBN 978-625-5954-79-4, 384–390.

Chen, D., & Chen, H. W. (2013). Using the Köppen classification to quantify climate variation and change: An example for 1901–2010. *Environmental Development*, *6*, 69–79. https://doi.org/10.1016/j.envdev.2013.03.007

Chen, H., Zhu, Q., Peng, C., Wu, N., Wang, Y., Fang, X., Gao, Y., Zhu, D., Yang, G., Tian, J., Kang, X., Piao, S., Ouyang, H., Xiang, W., Luo, Z., Jiang, H., Song, X., Zhang, Y., Yu, G., … Wu, J. (2013). The impacts of climate change and human activities on biogeochemical cycles on the Qinghai- Tibetan Plateau. *Global Change Biology*, *19*(10), 2940–2955. https://doi.org/10.1111/gcb.12277

Copernicus Climate Change Service (C3S). (2025). *European State of the Climate 2024*. Copernicus Climate Change Service (C3S). https://doi.org/10.24381/14J9-S541

Cui, D., Liang, S., & Wang, D. (2021). Observed and projected changes in global climate zones based on Köppen climate classification. *WIREs Climate Change*, *12*(3), e701. https://doi.org/10.1002/wcc.701

De Castro, M., Gallardo, C., Jylha, K., & Tuomenvirta, H. (2007). The use of a climate-type classification for assessing climate change effects in Europe from an ensemble of nine regional climate models. *Climatic Change*, *81*(S1), 329–341. https://doi.org/10.1007/s10584-006-9224-1

European Commission. Joint Research Centre. (2024). *Status of environment and climate in the Western Balkans.* Publications Office. https://data.europa.eu/doi/10.2760/1865356

Forzieri, G., Feyen, L., Rojas, R., Flörke, M., Wimmer, F., & Bianchi, A. (2014). Ensemble projections of future streamflow droughts in Europe. *Hydrology and Earth System Sciences*, *18*(1), 85–108. https://doi.org/10.5194/hess-18-85-2014

Grontmij, Carl Bro, & CEC. (2010, September). *Implementation of the National Plan for Approximation of Environmental Legislation in Albania Mati River Basin Management Plan*. Commission of European Communities, for and on behalf of the Government of Albania; Ref.: EuropeAid/124909/C/SER/AL.

Group of authors. (1984). *Hydrology of Albania*, Institute of HydroMeterological. Academy of Sciences, Albania.

Group of authors. (1985). *Clime of Albania*, Academy of Sciences, Albania.

Haidu, I. (2006). *Comparaison entre tests statistiques concernant le changement climatique global*. In vol. Les risques liés au temps et au climat, 282–287. https://www.researchgate.net/publication/236897294_Comparaison_entre_tests_statistiques_concernant_le_changement_climatique_global

Haidu, I., Ionac, N., & Irașoc, A. (2024). The new climatic normals and their impact on bioclimatic indices. Case study: Oradea (Romania). *Present Environment and Sustainable Development*, *18*(2), 5–19. https://doi.org/10.47743/pesd2024182001

Hasimi, A., Çomo, E., Ormeni, R., Vako, E., Dvorani, M., & Çela, G. (2025). *Comparison of Various Drought Indices for Assessing Drought Status of the Mati River Basin, Albania*. 77–86. https://doi.org/10.5593/sgem2025/3.1/s11.10

Hasimi, A., Papajani, B., & Çomo, E. (2025). Mati basin study. "Climate change and water: Together to close the early warning gap" Academy of Sciences, Albania, *Proceedings Book*, ISBN 978-625-5900-30-2978-625-5900-30-2, 31–44, 55-61,162-170.

Knez, S., Štrbac, S., & Podbregar, I. (2022). Climate change in the Western Balkans and EU Green Deal: Status, mitigation and challenges. *Energy, Sustainability and Society*, *12*(1), 1. https://doi.org/10.1186/s13705-021-00328-y

Kong, D., Zhang, Q., Singh, V. P., & Shi, P. (2017). Seasonal vegetation response to climate change in the Northern Hemisphere (1982–2013). *Global and Planetary Change*, *148*, 1–8. https://doi.org/10.1016/j.gloplacha.2016.10.020

Köppen, W. (1931). *Grundriß der Klimakunde*. De Gruyter. ISBN 103-11-128304-6

Kostopoulou, E., Tolika, K., Tegoulias, I., Giannakopoulos, C., Somot, S., Anagnostopoulou, C., & Maheras, P. (2009). Evaluation of a regional climate model using in situ temperature observations over the Balkan Peninsula. *Tellus A*, *61*(3), 357–370. https://doi.org/10.1111/j.1600-0870.2009.00389.x

Lenton, T. M., Held, H., Kriegler, E., Hall, J. W., Lucht, W., Rahmstorf, S., & Schellnhuber, H. J. (2008). Tipping elements in the Earth's climate system. *Proceedings of the National Academy of Sciences*, *105*(6), 1786–1793. https://doi.org/10.1073/pnas.0705414105

Magyari-Sáska, Z., & Magyari-Sáska, A. (2023). Changes and Trends in Ideal Holiday Period Based on Holiday Climate Index Applied to the Carpathian Basin. *Geographia Technica*, *18*(2/2023), 225–237. https://doi.org/10.21163/GT_2023.182.17

Nigrelli, G., & Chiarle, M. (2023). 1991–2020 climate normal in the European Alps: Focus on high-elevation environments. *Journal of Mountain Science*, *20*(8), 2149–2163. https://doi.org/10.1007/s11629-023-7951-7

Nistor, M.-M., Haidu, I., Dezsi, Ş., & Ştefan, C. (2020). A Comprehensive Gridded Dataset Associated to the Climate Change Effect on the Water Resources in the Grand Est Region, France. *Atmosphere*, *11*(10), 1026. https://doi.org/10.3390/atmos11101026

Nistor, M.-M., Satyanaga, A., Dezsi, Ş., & Haidu, I. (2022). European Grid Dataset of Actual Evapotranspiration, Water Availability and Effective Precipitation. *Atmosphere*, *13*(5), 772. https://doi.org/10.3390/atmos13050772

Palmer, M., & Ruhi, A. (2019). Linkages between flow regime, biota, and ecosystem processes: Implications for river restoration. *Science*, *365*(6459), eaaw2087. https://doi.org/10.1126/science.aaw2087

Pano, N. (2008). *Water Resources of Albania* (*Pasuritë Ujore të Shqipërisë)*. Academy of Sciences, Albania ISBN: 978-99956-10-87-6.

Papajani, B., Hasimi, A., Çomo, E., Çela, G., & Dvorani, M. (2025). *Temporal and spatial variability of the beginning and end of daily freeze/thaw cycles for Mati Basin River area, Albania*. 4th International Conference on Scientific and Innovative Studies, Turtye, ISBN 978-625-5900-30-2, 2015–2221.

Schröter, D., Cramer, W., Leemans, R., Prentice, I. C., Araújo, M. B., Arnell, N. W., Bondeau, A., Bugmann, H., Carter, T. R., Gracia, C. A., De La Vega-Leinert, A. C., Erhard, M., Ewert, F., Glendining, M., House, J. I., Kankaanpää, S., Klein, R. J. T., Lavorel, S., Lindner, M., … Zierl, B. (2005). Ecosystem Service Supply and Vulnerability to Global Change in Europe. *Science*, *310*(5752), 1333–1337. https://doi.org/10.1126/science.1115233

Sparey, M., Cox, P., & Williamson, M. S. (2023). Bioclimatic change as a function of global warming from CMIP6 climate projections. *Biogeosciences*, *20*(2), 451–488. https://doi.org/10.5194/bg-20-451-2023

Wang, X.-J., Tuo, Y., Li, X.-F., & Feng, G.-L. (2023). Features of the new climate normal 1991–2020 and possible influences on climate monitoring and prediction in China. *Advances in Climate Change Research*, *14*(6), 930–940. https://doi.org/10.1016/j.accre.2023.11.007

Xin, L. (2023). *Proposal of a new climate classification based on Köppen and Trewartha*. Physical Sciences and Mathematics. https://doi.org/10.31223/X5CM1D

URBAN WATER SUPPLY AND DEMAND ASSESSMENT UNDER SOCIOECONOMIC SITUATION OF CHANCHO TOWN, CENTRAL ETHIOPIA, USING WEAP MODEL

Merry Amensisa TOLA [1], Tamru Tesseme ARAGAW [2] & Mihai VODA [3]*

DOI : 10.21163/GT_2026.211.16

ABSTRACT

Urban water supply and requirements evaluation is crucial for long-term management, particularly in quickly rising regions of developing countries such as Ethiopia. This article addresses the issue of urban water supply and demand under socioeconomic stress in Chancho town, Ethiopia, while highlighting potential solutions. The WEAP (Water Evaluation and Planning) model was used in the study to investigate the town's demand and supply of water trends and provide solutions for this issue in relevant regions around the world. The rainfall discharge and climate data were collected on a monthly basis for model calibration and scenario development in WEAP. The findings show that the current annual water supply of 1.53 million cubic meters meets only 51% of the total demand. Over the next 15 years, rising population and urbanization will push total annual demand from 65 to 78 million cubic meters. Additionally, the climate change scenario is expected to reduce groundwater availability by 1.68 million cubic meters annually. Supply-side management scenarios suggest that integrating surface and groundwater sources for industrial and livestock use improves water supply reliability and reduces pressure on individual sources. This strategy ensures sustainable water use, supporting both the growing population and key economic sectors. The study concluded that increased water demand under socioeconomic stress requires strategic planning and resource allocation in developing countries with limited water resources.

Keywords: *Water supply; Socioeconomic factors; Water demand; WEAP model; Urbanization; Ethiopia.*

1. INTRODUCTION

As the universal population grows and urbanization increases globally, the demand for urban water is rising (Rathnayaka et al., 2016). Currently, almost 50% of people on the globe have moved to cities (Bach *et al.*, 2014). This urban growth puts strain on urban infrastructure and service delivery and has forced governments and other organizations to come up with novel adaptation strategies. Urbanization growth contributes to climate change, which has an impact on municipal water supply systems (Herslund and Mguni, 2019). Developing countries are experiencing significant and fast urbanization, which is increasing demand for urban services, particularly those related to water supply (Panwar and Antil, 2015). Many studies show that there is limited access to water supply in numerous urban areas as a result of the significant population growth. Researchers projected that the rapid urbanization scenario will continuously threaten resource sustainability due to the exploitation of natural resources (Rufino et al., 2018; Voda et al., 2019). Water scarcity is defined as the inability to provide adequate resources of clean water to satisfy needs (Tzanakakis, Paranychianakis and Angelakis, 2020). Urban growth also reshapes the hydrologic response at city scale, with altered runoff pathways and increased surface-runoff volumes documented in long-term urban case studies (Haidu & Ivan, 2016).

[1]*Department of Water Management, University of Addis Ababa, Ethiopia; merryamen84@gmail.com.*
[2]*Faculty of Water Supply and Environmental Engineering, Arba Minch Water Technology Institute, Arba Minch University, Arba Minch, Ethiopia; tamruiit@gmail.com.*
[3]*Geography Department, Dimitrie Cantemir University, Targu Mures, Romania; mmvoda@yahoo.com.*
**Corresponding author: mihaivoda@cantemir.ro*

Socioeconomic shifts, such as population growth and rising living standards, are expected to cause inadequate water supply and raise water demand (Rathnayaka et al., 2016, Berredjem, et al., 2023, Tufa et al., 2024). Improper geographical population distribution and poor river basins management are also additional main drivers of the urban water supply issue (Madani, 2014, Voda et al., 2018; He et al., 2021). The demand for water resources is rising due to a multitude of factors, including population growth, urbanization, industry, climate change, tourism, and navigation(Mensah et al., 2022; Wang et al., 2021; Haque et al., 2015).

Ethiopia, a country situated in the Horn of Africa, has been grappling with significant urban water challenges that have profound implications for the well-being and development of its rapidly growing cities (Assefa *et al.*, 2018). Despite the abundance of water resources, with 12 river basins and an estimated 2.6-6.5 billion m^3 of groundwater, the distribution and availability of water are not satisfactory within time and space, leading to the country being considered highly water-scarce(Ali, M., and Terfa, 2012, Kedir, 2023). Several studies on urban areas in Ethiopia indicate significant water shortages across these regions. According to Beker B.K. and Kansal M.L.'s study, one of the primary challenges facing Ethiopia's urban centers is the inadequate provision of water supply infra-structure and services (Assefa et al., 2018, Beker and Kansal, 2024). Poor water quality and low coverage levels are Ethiopia's two main water issues (Arsiso et al., 2017). Population density, accessibility, topography, precipitation, and socioeconomic factors can all lead to an unequal distribution of water in Ethiopia's urban area (Ali, M., and Terfa, 2012). Several studies on urban areas in Ethiopia indicate significant water shortages across these regions.

Chancho is a rapidly expanding town with high population growth and urbanization. Like other urban areas in Ethiopia facing water shortages, Chancho town encounters significant challenges in meeting the water supply needs of its expanding population. Therefore, in-depth assessment of the town's water supply and consumption circumstances, examining the factors contributing to shortages and identifying potential strategies to address the growing demand was performed. Various socioeconomic aspects, including expansion of the population, water consumption rates, urbanization, livestock reproduction water use, and climate variation are taken consideration in the study.

There are several tools for modelling water, including SWAT and MODFLOW. MODFLOW is perfect for analyzing aquifer dynamics and simulating recharge, extraction, and surface water interactions because it specializes in groundwater flow modelling. But its main focus is groundwater, and it doesn't integrate socioeconomic aspects or urban water demand very well. It also requires a lot of setup and calibration skill (Harbaugh and McDonald, 1996). SWAT is an excellent tool for long-term hydrological modelling, especially when evaluating the effects of agricultural activities, land use, and climate change. It can be data-intensive to set up, and while it is reliable for assessing water quality and sediment transport at the watershed scale, it is less successful when addressing urban water supply and demand (Douglas-Mankin et al., 2014). However, researchers have used the Water Evaluation and Planning (WEAP) model to assess the dynamics of water supply and demand in the study area in order to address the water demand challenges. The WEAP model is the most popular of the software that has been utilized significantly in various parts of the world. WEAP is a more recent and advanced approach, particularly well-suited for integrated modeling, scenario analysis, and addressing urban water demand (Purkey et al., 2018). The model was used by means of the decision support system (DSS) tool for water supply resource management in different regions (Saketa, 2022). WEAP allows different stakeholders to input their data, assumptions, and preferences, facilitating collaboration and consensus-building in water management (Al-Mukhtar and Mutar, 2021). However, the main drawback of WEAP is its dependence on reliable data sources, which can be challenging to obtain in areas with limited data availability (Al-Shutayri and Al-Juaidi, 2019). Despite this, researchers in Ethiopia rarely utilize the WEAP model to estimate urban

water supply and demand. This study assesses the water supply and demand in Chancho town central Ethiopia. Previously, no studies have been conducted in the area relevant to this study issue.

In view of this, this study's primary objective is to use the WEAP model in a specific area, Chancho Town, Ethiopia to evaluate and simulate urban water availability and demand in order to accurately and effectively allocate the town's water resources. The research will highlight the main issues with this specific area's freshwater availability and demand and provide evidence-based suggestions for efficient management. Furthermore, the findings will serve as a valuable reference for other regions worldwide facing similar water-related challenges.

2. STUDY AREA

The Chancho town is located in Ethiopia's North Shewa Zone of the Oromia Regional State, in the country's center region and close to the capital, Addis Ababa (**Fig. 1**). It is found 40 kilometers north of Addis Ababa on the Gojam road. In Ethiopian history, Chancho town was established in the nineteenth century. There are currently about 98900 people living in the town, which has a total land area of 4,277 hectares, of which 88.37% is flat, 10.29% is mountainous, and 1.34% is valley. The region is situated at the crossroads of rural and urban development, and its strategic location drives rapid population growth and accelerated urbanization. Town's geographical coordinates are 38°42'55" - 39° 5' 39" East longitude and 9°15'45" - 9° 24' 4" North latitude. The elevation spans from 2,503 to 2,711 meters above sea level. The climate in the area is characterized by the short-wet season (March-May) and the lengthy rainy season (June-September), which is locally known as the Belg rains and Kiremt rains respectively. The average annual lowest record temperature for Chancho in August is 7.22°C and the highest in March 29°C degrees in a year. On aver-age, the region receives 995.63 mm of rainfall annually (**Fig 2).**

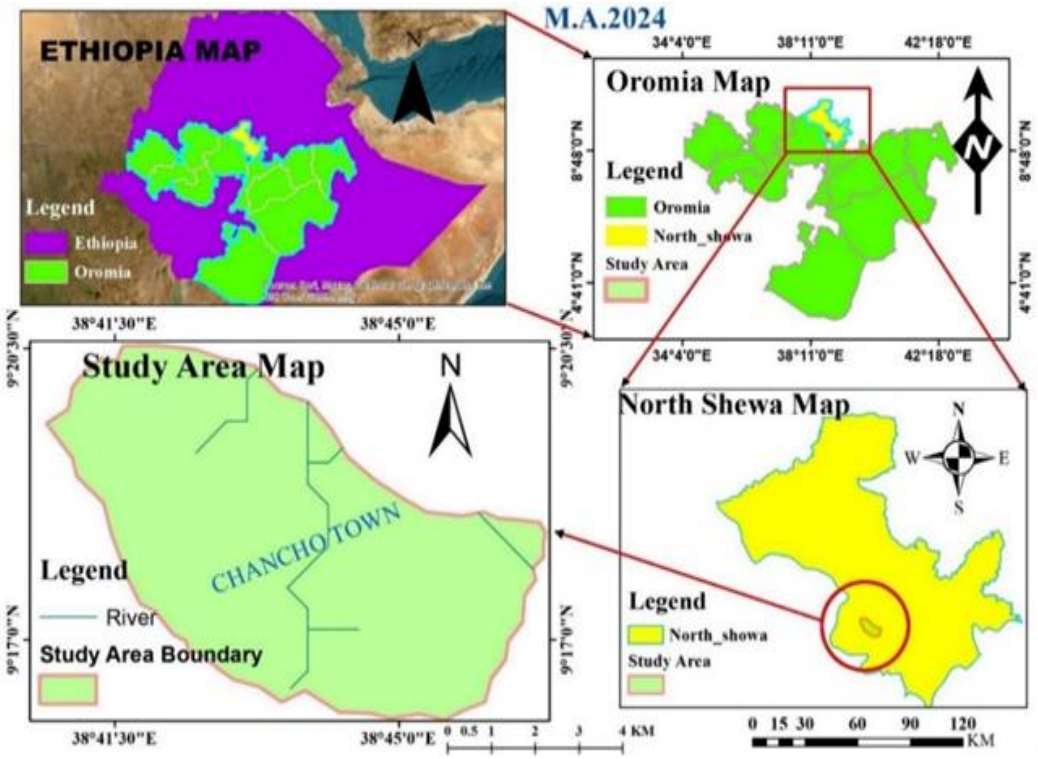


Fig. 1. Map of study area.

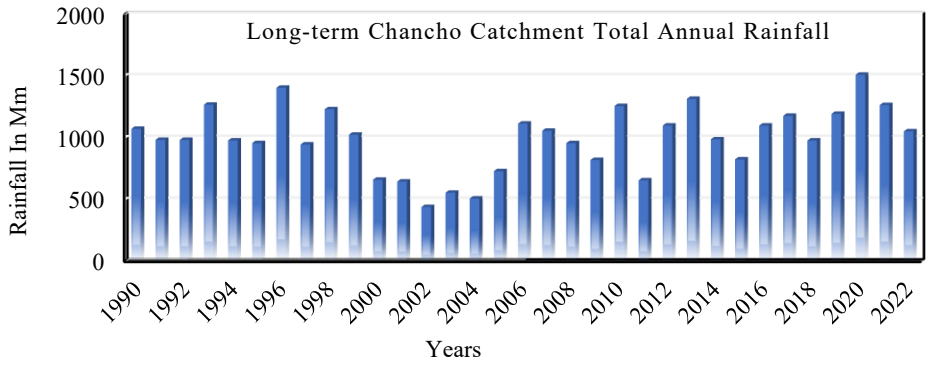


Fig. 2. Study area annual rainfall data.

2.1. Organizational Structure of the Town's Water Supply System.

The Chancho town water service office is administered under the North Shewa zone water board. The main participants in the water delivery system of Chancho town are depicted in the attached diagram. A local board was appointed by the regional water bureau to manage the utility office located in Chancho Town. As illustrated in **Fig. 3**, this utility office was founded in accordance with regional proclamation number 97/1997. The local board is responsible for managing, distributing, and supplying water for the community. It ensures the com-munity receives water services in an effective manner and manages the water infrastructure.

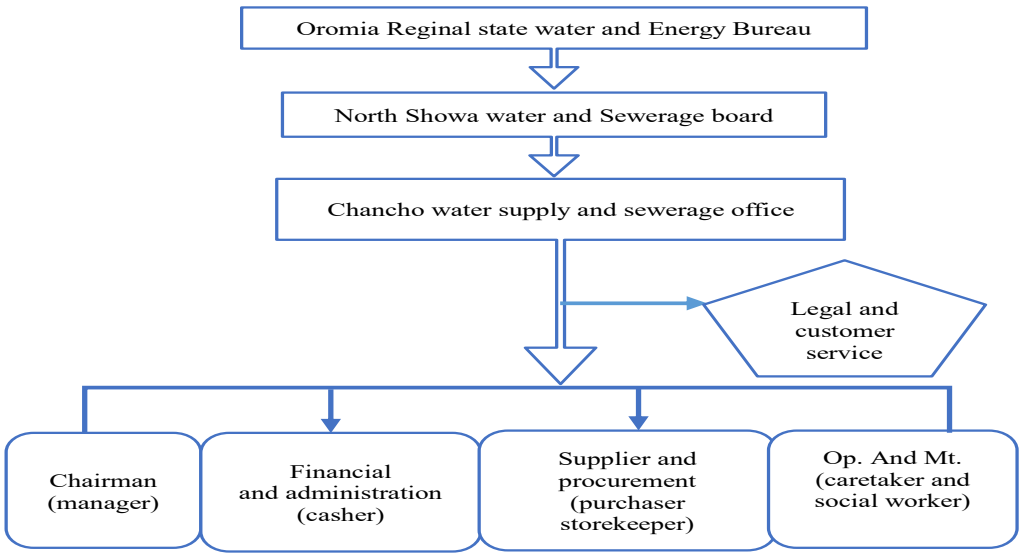


Fig. 3. The town's water utility service organizational structure.
Note: Op. is operation; Mt. is maintenance.

2.2. The Town's Current Water Supply Situation and Available Water Sources

Groundwater is the main source of water supply for the Chancho town. In 1986, the town's water supply system was first established when a borehole named Oche was drilled and connected to an elevated concrete tank (source: CHTWSS). The town's water supply currently depends on eight public boreholes, excluding those allocated for industrial use (**Table 1**). The municipality has a total of twelve boreholes, which include both publicly operated and privately-owned ones.

Table 1.

The town's public service boreholes description.

S/N	BH Name	Location			Depth (m)	working hour per day	current yield average (l/s)	daily production (Liter)
		X	Y	Z				
1	Arbi akako	38.461	9.1801	2621	88	16	1	57600
2	Oche	38.442	9.175	2552	90	16	3	172800
3	Gulele	38.445	9.182	2618	155	16	5	288000
4	Kore roba	38.46	9.1617	2585	220	16	2.5	144000
5	Lega sibilu	38.436	9.1731	2546	271	16	5	288000
6	Lega lencha	38.434	9.1721	2545	331	16	5	288000
7	Gaba robi	38.406	9.2111	2461	180	8	5	144000
8	Lega germama	38.455	9.1824	2621	500	16	12	691200
Total							38.5	2,073,600

Source: Chancho town water supply utility (CHTWSU).

These boreholes provide a mix of municipal and private water supply sources, contributing to the area's overall groundwater usage for residential, commercial, or industrial purposes. The data on borehole production was provided by the local water supply utility service, and measurements were made of the actual discharges. Knowing the borehole discharges in detail is essential to determining the monthly and annual water production of the town. Underground sources pump water out of boreholes, store it in a service reservoir, and then gravity-feed it to the customer's location. A specific formula was applied to calculate (Howard et al., 2020) the total working hours and actual discharges for each borehole in order to compute the daily, monthly, and annual water product:

$$\text{V. prod (in liters)} = \text{BH disc}\left(\frac{\text{L}}{\text{s}}\right) * \text{BH working time(s)} \quad (1)$$

where: Vprod is volume of production; BH is borehole; L is litter; S = second. Vprod was divided to 1,000 in order to determine the volume in cubic meters (because 1000 liters equal one cubic meter).

All government boreholes have a combined water production of 2,073.6 m3/day. To find out how much water is produced daily by all of the boreholes, the total volume produced (Vprod) can be calculated from liters into cubic meters. Key observation from the above table is that the most productive borehole is Lega Germama, which produces 691,200 liters per day at a rate of 12 liters per second for 16 hours per day. With a yield of 1 l/s, Arbi Akako produces the least amount of water each day, only 57.6 cubic meters. This is calculated by multiplying the yield by the total number of seconds in a day (86,400 seconds), resulting in 86,400 liters, which converts to 57.6 cubic meters. As a result, Arbi Akako contributes the smallest volume of water to the total supply in the study area. The limited production capacity of this borehole may result from its depth, constraints in the pumping or extraction equipment, or a combination of these factors.

Private boreholes collectively produce 2,937.6 cubic meters per day, which is significantly more than the 864 cubic meters produced by government-owned boreholes (**Table 2**). This higher yield from private boreholes is often due to factors such as advanced drilling techniques, better maintenance practices, and access to deeper or more productive aquifers. In contrast, government boreholes may face challenges such as limited funding, less frequent maintenance, or less optimal sitting, which can result in lower yields. The analysis revealed that the town's capacity to extract groundwater is reflected in the total borehole production, including both public and private boreholes, which amounts to 5,011.2 m^3 per day, or approximately 1.83 million cubic meters annually.

Table 2.

Description of private boreholes in the town.

S/N	Private borehole	Location			Current yield average (l/s)	Daily production (Liter)
		longitude	latitude	elevation(m)		
1	Maya pp bag factory (BH-1)	38.45	9.17	2570	15	1296000
2	Abyssinia cement factory (BH-2)	38.43	9.18	2567	5	432000
3	Ethio cement (BH-3)	38.44	9.18	2552	4	345600
4	ELPA station (BH-4)	38.46	9.18	2637	10	864000
Total					**34**	**2,937,600**

Source: Chancho town business sector.

2.2.1. The Town's Existing Water Service Reservoir

This section provides an overview of the current water service reservoir in the town, detailing its capacity to meet the town's water supply needs. A reservoir's capacity is the greatest amount of water it can contain, typically measured in cubic meters (m^3), liters, or gallons. Larger reservoirs with higher capacities are better at satisfying long-term water demands, particularly during dry periods. In addition to their storage role, reservoirs can help manage the flow of water, guaranteeing a consistent and reliable supply throughout the year. To ensure an adequate supply of water and account for balancing purposes, it is recommended to have a minimum total reservoir storage capacity ranging from 30% to 50% of the average daily demand for small towns with stable water sources and minimal risk of disruption as stated in M0WR 2012 guidelines (Howard et al., 2020). In the study area, there are seven reservoirs with capacities of 500 m3, 300 m3, 200 m3, 100 m3, 50 m3, 50 m3, and 25 m3, resulting in a total reservoir capacity of 1225 m3.

Table 3 indicates that the R1 Gera Michael reservoir has the largest capacity, with a volume of 500 m^3. This means that R1 Gera Michael has the highest water storage capacity, allowing it to store more water than the other reservoirs. Such a large capacity is crucial for meeting water demand, particularly during dry periods or peak usage times, ensuring a consistent and reliable water supply to the surrounding area. Conversely, with a capacity of 25 m^3, R7 Geba Robi is the smallest reservoir. The calculated average daily demand, which is 8192 m3/day, need to be compared to the total reservoir storage capacity in order to determine whether it is adequate. In this case, this corresponds to a range of 2,457.6 m3 to 4,096 m3.

Table 3.

Existing reservoir in the town with their yield.

Reservoirs Name	Reservoir existing area	Distance from Center of town(km)	Location			Working hour (24)	Capacity (m^3)
			X	Y	Z		
R1	Gera Michael	2	38.46	9.17	2643	Daily	500
R2	Gera Michael	2	38.46	9.17	2644	>>	100
R3	Gera Buba	1.5	38.44	9.18	2692	>>	300
R4	Gera Michire	0.8	38.44	9.18	2618	>>	200
R5	Egzarab Church	0.3	38.45	9.18	2649	>>	50
R6	Kore Roba	3.5	38.45	9.16	2607	>>	50
R7	Geba Robi	7	38.41	9.20	2613	>>	25
Total							**1,225**

Source: *Chancho town water supply utility (CHTWSU).*

Based on the analysis, the current reservoirs in the study area clearly do not meet the specified minimum storage capacity requirements, highlighting a significant shortfall in the system's ability to ensure adequate water storage for safety and reliability. This shortcoming makes it difficult to maintain a regular water supply, especially during peak demand or unexpected events. To address this issue, constructing new reservoirs with sufficient storage capacity is essential. Expanding the storage infrastructure will not only enhance the system's resilience but also ensure that future water demands can be met effectively while safeguarding against potential shortages.

2.3. Population Projection

To estimate population growth, the geometrical increase approach, an exponential growth model, was applied. This method is particularly suitable for estimating population increases in rapidly expanding urban areas. Based on the base year population, the annual growth rate is projected at 3.4% growth rate **(Table 4)**. This approach aims to reduce the uncertainty that often arises from inaccurate estimations.

$$Pt = P0 \times e^{r \times t} \quad (2)$$

where, pt = projected population at future time, po = base population, r = growth rate in percentage, t = number of years.

Table 4.

Population projection and growth rate.

Year	Initial population	Estimated population	Growth rate (%)
2019	57387	-	-
2023	-	98900	3.4

In 2002, Ethiopia's Statistical Service (CSS) collaborated with zonal and municipal governments to establish development offices aimed at improving local population assessments. For this study, population data from the Ethiopian Statistical Service and the Chancho town administration office were considered to project the population of Chancho town, given that its data was initially grouped with Sululta Woreda. This method allowed for a more accurate population estimate by referencing unique survey data specific to Chancho town.

2.4. Water Demand Projection

Water demand is the overall amount of water needed to satisfy the demands of different sectors, such as residential, commercial, institutional, and environmental usage. The formula for calculating a town's water demand depends on various factors such as population, per capita water consumption, and specific demand categories:

$$Total\ Water\ Demand = (Population \times Per\ Capita\ Demand) + Industrial\ Demand + Institutional\ Demand + Commercial\ Demand \quad (3)$$

The population in the area is 98,900 people, with a per capita water demand of 60 liters per day. Industrial water demand accounts for 15% of the household demand, while commercial and institutional water demand represents 25% of the domestic demand. According to the investigation, the total quantity of water that is provided is around 1.83 million cubic meters per year, which is less than the present water demand of around 3.03 million cubic meters annually (as of 2023). This indicates a shortfall in water supply, suggesting that the existing water sources may not be sufficient to meet the demand, especially during peak usage periods or in the case of population growth.

Based on the analysis, demand coverage measures the percentage of water demand that is met by the available water supply. The formula to calculate water coverage for a study area is typically expressed as:

$$Demand\ Coverage = volume\ of\ water \frac{supply}{Total\ Water\ Demand} \times 100 \quad (4)$$

This formula expresses the proportion of the total water demand that is met by the available water supply, presented as a percentage. The calculation results show that the water demand coverage in the study area is approximately 51%. This means that only about half of the total water demand is being met by the available water supply showing a significant gap between the water supply and the actual demand, meaning that nearly half (49%) of the water requirements are unmet. To ensure water security, it is crucial to explore strategies for increasing supply, improving water efficiency, and expanding infrastructure to meet the growing demand.

3. MATERIALS AND METHODS

3.1. Data Collection and Design Period

Discharge and climate data were collected on a monthly basis for model calibration and scenario development in WEAP. The Ethiopian Statistical Service (ESS) and the Chancho Town Administration Office (CHTAO) provided population size from 2007 to 2019 in order to compare the present population number, establish baseline trends, and guarantee data reliability in the study area. However, the data used for the analysis were obtained from the Chancho town administration office because the surrounding villages have merged into the town and the ESS does not have an accurate current population of the study area due to population in Ethiopia did not count after 2007. Climate data obtained from Ethiopian meteorological agencies were used to establish baseline trends for the study period. The climate data derived from historical records spanning 2003 to 2022. **Fig. 4** illustrates the average monthly climate parameters, such as temperature and precipitation, providing valuable insights for analyzing long-term climate patterns.

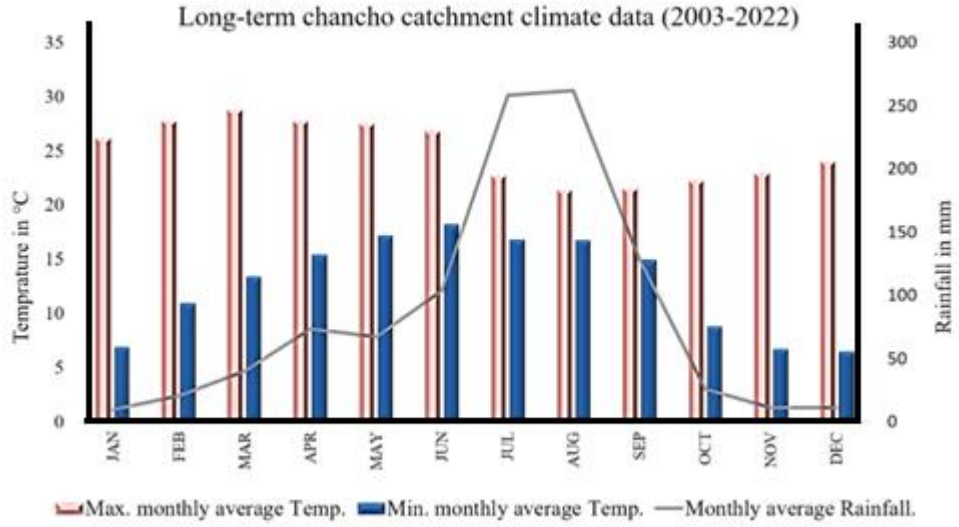


Fig. 4. Long-term Chancho catchment climate data (2003-2022).

In line with recent gridded climate-water products that emphasize actual evapotranspiration and effective precipitation for availability assessments, we use monthly climate forcings to frame supply scenarios (Nistor et al., 2022). According to the analysis, maximum temperatures reach their highest point in March (29°C) and stay high throughout February and April. This occurs at the same time that the demand for water increases due to higher evaporation rates. During the rainy season (June to August), August receives the most rainfall (262 mm), which helps restore water supplies. With little rainfall (as little as 11 mm in December) during the dry season (November to February), there may be a pressure on water supplies.

The design period for this study spans from 2023 to 2038. This 15-year timeframe was selected to analyze projected changes in urban water demand and supply under various scenarios, allowing for the assessment of long-term trends and potential water management challenges. Both primary and secondary data sources were utilized for the investigation. Using a mixed-methods approach, the study integrated quantitative and qualitative da-ta. Primary data included information on water consumption, socioeconomics, water supply, and demand. These data were gathered through observations, interviews, and field surveys. They were obtained from the Ethiopian statistical service, the Chancho town administration office, relevant water authorities, and utility companies, and through conducting interviews, surveys, and observations. Socioeconomic data, which was crucial for comprehending the elements influencing water demand, contains details on the town's population, growth rate, and eco-nomic activity. Those data helped in projecting present and future water supply and demand by taking into consideration the effects of population growth, urbanization, and changes in living standards. Information about the accessible water sources, such as groundwater, surface water, and existing infrastructure, was included in the water supply data. Those data revealed the town's ability to supply water to meet present and future demands. Demand data focused on water consumption patterns in a range of sectors, including institutional, livestock, industrial, and residential.

This study used various types of tools and approaches for modeling and data analysis. The techniques used in this study to investigate water supply and demand are made possible by the combination of many software pro-grams, including GIS (version: 10.7.11595), GPS, and Google Earth Pro (version: 7.3.6.9796) with WEAP (version: 24.0.0.0). GIS was utilized to map and analyze the study area, providing a detailed spatial representation of key features relevant to urban water demand and supply. This included defining the boundaries of the study area, which covers residential and industrial zones in Chancho town. Google Earth provided satellite imagery to verify land use classifications and validate the locations of industrial and residential areas within the study area. GPS was used to gather coordinates for groundwater and surface water sources in Chancho town, ensuring precise mapping and modeling of these resources within the WEAP model.

The WEAP model was created in 1988 by the Stockholm Environment Institute (SEI) for integrated planning and management of water resources (Purkey et al., 2018). WEAP uses a combination of algorithms and linear programming to address the issue of the water delivery challenge (Saketa, 2022). The water demand algorithm calculation used in the WEAP model is indicated as follows:

$$Total\ Demand = Total\ activity\ level * annual\ water\ use\ rate \tag{5}$$

$$Annual\ Demand = sum(Total\ activity\ levelBr * water\ use\ rateBr'x \ldots \tag{6}$$

Total activity level for a bottom-level branch is the product of the activity levels in all branches from bottom branches back up to the demand site branch (where Br = bottom-level branch, Br' = parent of Br, Br'' = grandparent of Br, etc.).

$$Total\ Activity\ level\ Br\ x\ Activity\ level\ Br\ x\ Activity\ level\ Br'' \tag{7}$$

Andersson, E. (2019) study highlights that the WEAP model allows users to simulate and analyze water supply and demand patterns, assess various water management scenarios, and evaluate the impacts of different interventions and policies on water resources (Andersson, 2019). WEAP is made up of the following five program structures:

Schematic - A graphical user interface for building the water system graphically
Data - A repository for entering and organizing all the data needed for the model
Results - Shows the model runs' outputs and visuals.
Scenario Explore-This tool enables the construction and contrast of various policy and management scenarios.
Notes: This area allows you to record assumptions, sources of data, and other details.

The study used a variety of methodologies and procedures to examine and model the town's water supply and demand. These techniques analyze data, anticipate future demand, and assess resource availability by using modeling tools, data collection, and analysis.

3.2. Methodology

This study follows a multi-step methodological approach that includes data collecting, processing, model creation, scenario development, and model output analysis. **Fig. 5** illustrates the methodological framework used in this investigation.

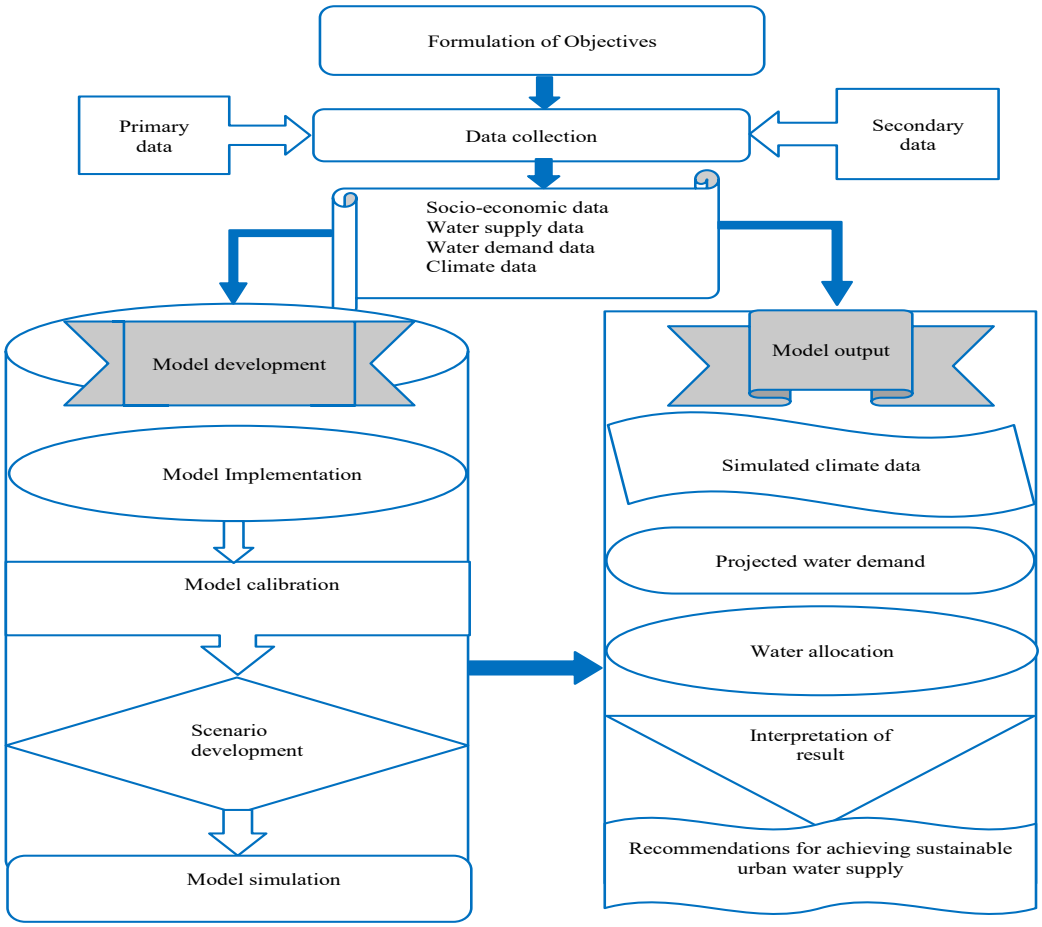


Fig. 5. Workflow of research methodology.

3.3. Future Water Supply and Demand Analysis Scenario Developed

Scenario 1: Baseline scenario or reference scenario

The existing or anticipated future state of the water supply, demand, and management practices is represented by this scenario, which is a baseline or starting point scenario (Andersson, 2019, Rathnayaka et al, 2016). All other factors and assumptions in this scenario remain consistent with the base year; however, socioeconomic demographic indicators, specifically population size, increase at the previously projected rate.

Scenario 2: External factor driven scenarios

It refers to a scenario where the drivers and assumptions are based on factors that are largely outside the control of the water management system being modeled. The key purpose is to inform strategic planning, risk assessment, and the development of adaptive water

management strategies that can be managed with a wide range of potential future challenges and uncertainties. To determine the impact of external-driven scenarios (population growth (HPG), expansion of urbanization (UE), change in live standard, combination of HPG and UE, livestock reproduction enhancement, and climate variation), assumption cases were developed.

I. High population growth (HPG): In this case the population growth rate was increased from 3.4% to 5% to simulate a scenario reflecting potential future challenges, such as increased migration, urbanization, or economic developments, which could accelerate demographic growth. This adjustment helps to evaluate the potential impacts of higher population pressure on water demand, resource allocation, and infrastructure needs, enabling the development of proactive strategies for sustainable water management under such conditions.

II. Expansion of urbanization (UE): this scenario aims to assess the impacts of urbanization on water demand and supply systems. The water use rate for industry increased from 15% to 25% of domestic demand, while the rate for commercial and institutional use rose from 25% to 30%. These adjustments reflect the anticipated rise in water consumption due to urban growth. The scenario emphasizes the need for efficient resource management and infrastructure development to meet the growing water requirements of urban areas.

III. Climate change: this scenario considers an increase in temperature by 0.5°C accompanied by a decrease in rainfall. This reflects the potential impacts of global warming, where higher temperatures intensify evaporation and reduce water availability, while decreased rainfall further strains water resources. The scenario aims to evaluate the implications of these climatic changes on water demand, supply reliability, and resource sustainability, emphasizing the importance of adaptive measures such as efficient water use, enhanced storage systems, and ecosystem-based approaches to mitigate the effects of climate variability.

IV. Change of living standard (CLS): In this case water use rate was increased from 60LCPD to 80 LCPD. This indicates the effect of rising living standards, which often result in higher water usage per person because of changes in lifestyle, including greater use of goods, improved sanitation, and increased household demands. The scenario evaluates the effects of this shift on overall water demand and highlights the need for efficient water management strategies to balance rising consumption with sustainable resource availability.

V. Livestock reproduction enhancement (LRE): Each Tropical Livestock Unit (TLU) in developing nations is projected to require about 25 liters of water per day, according to research from the Food and Agriculture Organization and the Global Livestock Studies Institute (Schlink et al., 2010). The scenario includes an average increase in the daily water consumption rate for livestock from 25 liters per head (l/h/d) to 30 l/h/d. This increase to 30 l/h/d reflects an adjustment to account for higher water demands during reproductive processes, increased activity, or changing environmental conditions. The scenario assesses the impact of these changes on total water demand and resource allocation, emphasizing the importance of efficient water use practices and planning to support sustainable livestock production.

VI. High population growth and expansion of urbanization: The scenario assumed a 5% population growth rate and an increased water use rate due to urbanization. The water use rate for industries has been increased to 15% of domestic water use, while the water use rate for commercial and institutional sectors has been increased to 25% of domestic water demand. This combination reflects the significant increase in water demand driven by both a growing population and higher water consumption resulting from urbanization, including increased industrial, commercial, and institutional water use.

Scenario 3. Water management scenarios

The Demand-Side Management (DSM) Scenario focuses on strategies to regulate and reduce water usage by enhancing efficiency, minimizing waste, and encouraging

conservation practices among users. This scenario assumed a 20% reduction in water usage, achieved through a combination of measures. These measures include improving water efficiency by adopting advanced technologies, reducing water losses in the distribution network through infrastructure upgrades, and promoting behavioral changes among consumers via awareness campaigns.

Supply-side management (SSM) involves implementing an integrated water source system to optimize the use of available resources. This approach combines surface water and groundwater sources to ensure a reliable and sustainable supply. By minimizing reliance on a single source and considering seasonal variations, it enhances resilience to shortages and improves the efficiency of water resource allocation.

4. RESULTS

A yearly population growth rate of 3.4% was adapted in this study to reflect the unique characteristics of the research area, where the town has rapidly grown in population by absorbing neighboring villages. The population projection was first calculated using an annual growth rate of 3.4%, resulting in an estimated population of 98,900 people in 2023. This projection served as the basis for estimating population levels during the scenario analysis period from 2024 to 2038. Following this, the water consumption in the base year 2023 was calculated to establish a reference point for analyzing future water requirements. The water demand in the current account year (2023) indicates that domestic demand is the largest, totaling 2.1659 million cubic meters (MCM), which accounts for 72.57% of the annual consumption. Institutional and commercial demand contribute 0.22 MCM, while industrial demand is 0.32 MCM (10.7%) and livestock demand is 0.28 MCM (9.36%). These components bring the total yearly water consumption to 2.99 MCM. These demand site, combined with seasonal variations and limited water sources, presented the causes of water demand within the current account framework. As result, there is a significant unmet demand of 49%, indicating water supply stress in the system, with total unmet demand projected to reach 1.46 million cubic meters over time (**Fig. 6**).

However, current water supply stands at 1.53 million cubic meters, covering only 51% of overall demand. This underscores the critical need for improved water management strategies, including the expansion of water sources, enhancement of distribution infrastructure, and the adoption of more efficient water use practices. Comparing our results with other studies is challenging due to the socioeconomic differences, which make the findings specific to our study area.

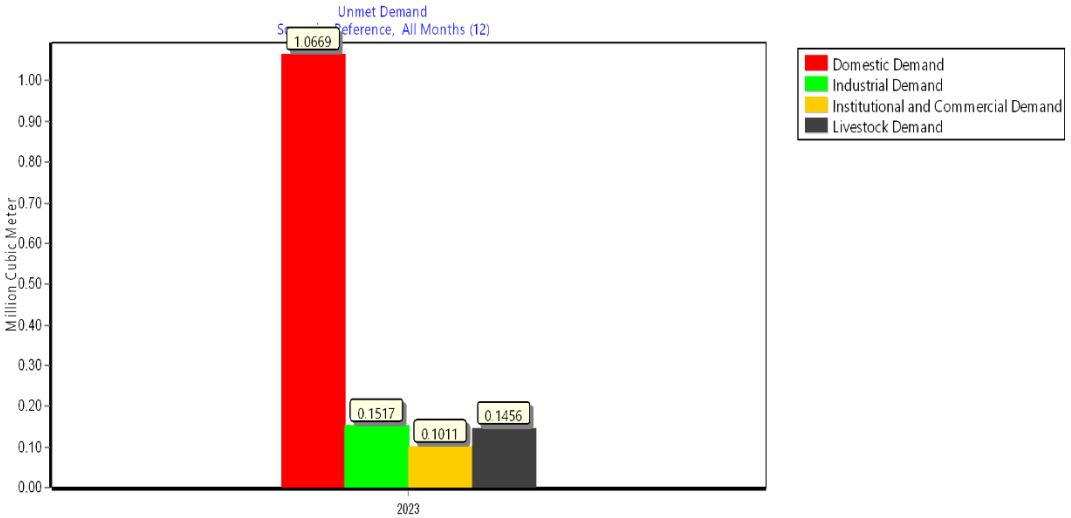


Fig. 6. Annual unmet water demand per all demand site in current account year.

Even so, our examination of the model's output reveals that our study and Alemu and Dioha's (2022) work, which employed the WEAP model to evaluate Addis Ababa's water supply and demand prospects, have comparable unmet water demand. While our analysis similarly demonstrates notable increases in unmet demand, driven by factors such as population growth and urbanization, their study anticipates a 48% increase in unmet demand in Addis Ababa by 2030, highlighting the necessity of proactive water management (Alemu & Dioha, 2020). A similar study conducted in Pakistan identified a predicted unmet water demand of 134 million cubic meters (Amin et al., 2018).

In the current account year (2023), there were also noticeable seasonal fluctuations in the demand for water, with residential, livestock and industrial activity being the main drivers of peak usage from February to May. Monthly total water demand was increased from 305.5 thousand cubic meter (in august) to 417.0 thousand cubic meters (in march). During the dry season, warmer temperatures accelerate the pace at which water evaporates from soil, rivers, and reservoirs. A greater reliance on stored water, which can need extra extraction efforts, results from the dry season's decreased rainfall, which restricts the natural replenishment of water sources like rivers and underground aquifers. Municipal and industrial water requirements rise to address the resulting shortage. In order to stay hydrated and maintain cooling systems, people and animals frequently use more water in hotter climates.

4.1. Reference scenario

In the reference scenario, the total requirement for water is expected to rise from 3.42 million cubic meters in 2024 to 5.37 million cubic meters in 2038, totaling 65.04 million cubic meters over 15 years.

Table 5.

Scenario: Reference, All Branch, Annual Total.

Year	2024	2025	2026	2027	2028	2029	2030	2031	2032	2033	2034	2035	2036	2037	2038
Domestic Demand	2.24	2.32	2.39	2.48	2.56	2.65	2.74	2.83	2.93	3.03	3.13	3.24	3.35	3.46	3.58
Industrial Demand	0.56	0.57	0.59	0.61	0.63	0.65	0.67	0.69	0.71	0.73	0.75	0.77	0.80	0.82	0.84
Institutional and Commercial Demand	0.33	0.34	0.36	0.37	0.38	0.39	0.40	0.41	0.42	0.44	0.45	0.46	0.48	0.49	0.51
Livestock Demand	0.29	0.30	0.31	0.32	0.33	0.35	0.36	0.37	0.38	0.40	0.41	0.42	0.43	0.44	0.44
Sum	**3.42**	**3.54**	**3.65**	**3.77**	**3.90**	**4.03**	**4.16**	**4.30**	**4.44**	**4.59**	**4.74**	**4.89**	**5.04**	**5.21**	**5.37**

Note: Water Demand (not including loss, reuse and DSM) (in million Cubic Meter).

As shown in **Table 5**, this scenario was created using the current account year 2023 as a basis and extended future estimates up to 2038 without any interventions. Assuming no changes with all other factors, including urbanization expansion (UE), changes in living standards, livestock reproduction, and climate variation, remaining constant, the population is expected to grow from 98,900 in 2023 to 198,830 by 2038, reflecting an annual growth rate of 5%. The outcome shows that demand has been steadily rising as a result of population growth. The total water demand increases significantly from 3.42 million cubic meters (MCM) in 2024 to 5.37 MCM in 2038, representing a 57% growth over 15 years. Domestic demand remains the largest contributor, rising MCM (15.6%), reflecting steady industrial expansion. Institutional and commercial demand also shows consistent demand grows

moderately from 0.56 MCM (16.4%) to 0.84 from 2.24 MCM (65.5%) in 2024 to 3.58 MCM (67%) in 2038, driven by population growth and lifestyle changes. Industrial growth, increasing from 0.33 MCM (9.6%) to 0.51 MCM (9.5%), while livestock demand rises gradually from 0.29 MCM (8.5%) to 0.44 MCM (8.2%). Domestic water use contributes the largest share of the overall growth, accounting for 67% of the total increase, followed by industrial, institutional/commercial, and livestock demands. The consistent increase in water demand across all sectors underscores the critical need for proactive water resource planning. In comparison to the reference scenario results, Shahraki et al. (2016) found that unmet demand in the Hirmand catchment in Iran increased from 193 to 200 million cubic meters, highlighting a similar upward trend in water demand, which aligns with the growth observed in our study (Shahraki et al., 2016).

4.2. High population growth model scenario

In this scenario, the population is expected to grow from 98,900 in 2023 to almost 198,830 by 2038, reflecting an increase in the population growth rate from 3.4% to 5%. The projected population growth rate of 3.4% to 5% is a hypothetical scenario designed to evaluate the potential impacts of rapid demographic changes. The scenario assumes accelerated growth driven by increased migration from rural areas to the town and significant changes in socioeconomic conditions (Tegegne, 2019). Given a 5% annual population growth rate, the high population growth scenario forecasts significant increases in water usage. The results show that rapid population growth will lead to a projected water demand of 6.68 million cubic meters, an increase of 1.31 million cubic meters (20.53%) compared to the reference scenario. **Fig. 7** illustrates the water demand trend corresponding to a 5% annual population growth rate from 2024 to 2038. As the population increases consistently each year, the water demand rises significantly over the design period. Specifically, the demand grows from 3.42 million cubic meters (MCM) in 2024 to 6.7 MCM in 2038, reflecting the direct correlation between population growth and water consumption. Dividing the annual water demand reveals that the average monthly water demand increases from 4.3 thousand cubic meters to 4.9 thousand cubic meters, representing a 12.5% increase over the period. This trend highlights the potential for significant water supply shortages due to the rapid population growth. A similar study by Unto, P. B. (2024) utilized the WEAP model to project water demand in Addis Ababa, assuming an annual population growth rate of 4.46%.

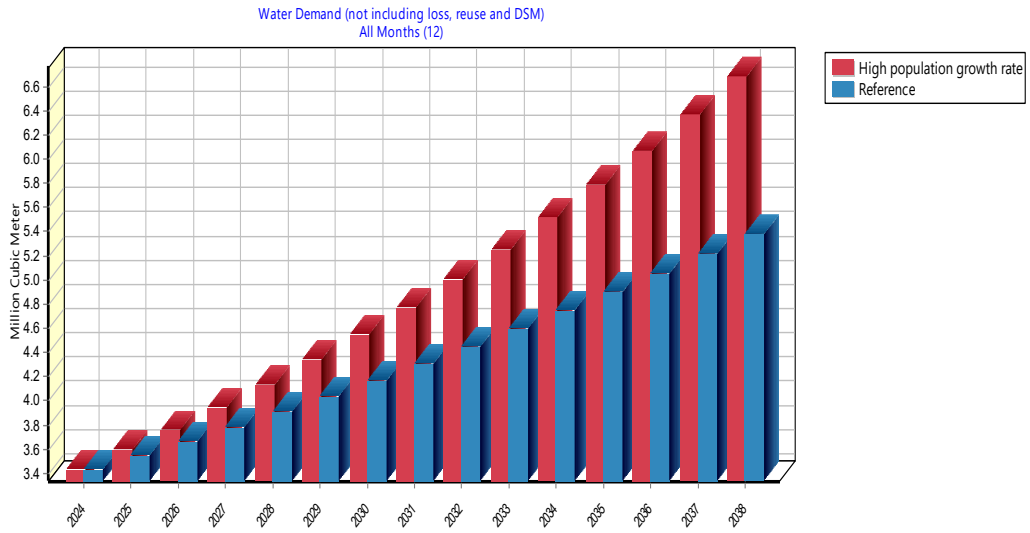


Fig. 7. Annual water demand of high population growth rate scenario.

The projections revealed a substantial increase in water demand, rising from 382 million cubic meters (Mm^3) in 2023 to approximately 915 Mm^3 by 2043. This trend underscores the significant challenges that rapid population growth presents to water supply systems, necessitating effective water resource management and planning to meet future demands (Unto, 2024). Another related study utilized the WEAP model to analyze various water supply and demand scenarios in the Yala Catchment, Kenya. The analysis revealed substantial increases in water demand under different scenarios, underscoring the urgent need for effective water resource management to address the challenges posed by population growth (Okungu, Adeyemo and Otieno, 2017).

4.3. Change in living standards model scenario

In accordance with the recommendations from the relevant study by Crouch, M. L., et al. (2021), the domestic water use rate in this scenario was increased from 60 liters to 80 liters per person per day (Crouch et al., 2021). By applying a domestic water use rate of 80 liters per person per day, the WEAP results demonstrate the impact of rising per capita water demand due to lifestyle changes. Table 6 compares water demand trends under two scenarios change in living standards and reference over a 15-year period from 2024 to 2038. Both scenarios show a gradual increase in water demand, with the Change in living standards scenario rising from 3.42 million cubic meters (MCM) in 2024 to 6.56 MCM in 2038, while the reference scenario increases from 3.42 MCM to 5.37 MCM over the same period. The cumulative water demand for the change in living standards scenario is 73.63 MCM, which is 8.58 MCM higher than the 65.05 MCM recorded for the reference scenario. This difference highlights the significant impact of improved socioeconomic conditions, such as increased per capita water usage, on water demand. Yearly increments are slightly higher in the change in living standards scenario. For instance, between 2024 and 2025, the demand increases by 0.19 MCM, compared to 0.12 MCM in the reference scenario. By 2038, water demand under the change in living standards scenario is 22.15% higher than in the reference scenario. These findings emphasize the need for proactive water resource management to accommodate the rising demand associated with socioeconomic development (Ernawati et al., 2018). A relevant study by Soula et al. (2020) in Tunisia's Nabhana watershed, study analysis stressed the importance of integrated strategies for managing rising water demand owing to socioeconomic growth (Soula et al., 2020). Similarly, Alemu and Dioha (2020) conducted a study in Addis Ababa, Ethiopia, examining the ways in which socioeconomic advancements influence water availability and demand, considering factors such as improved living standards. The analysis underscores the importance of integrating socioeconomic factors into future water planning to mitigate potential shortages. In order to meet rising demand and prevent shortages, it underlined the necessity of sustainable water management techniques (Alemu and Dioha, 2020).

Table 6.

All Scenario Branch: Demand site and Catchment, Annual Total.

Year	2024	2025	2026	2027	2028	2029	2030	2031	2032	2033	2034	2035	2036	2037	2038	Sum
Change in Live Standard	3.42	3.61	3.81	4.02	4.24	4.47	4.66	4.87	5.08	5.29	5.52	5.77	6.02	6.29	6.56	73.63
Reference	3.42	3.54	3.65	3.77	3.90	4.03	4.16	4.30	4.44	4.59	4.74	4.89	5.04	5.21	5.37	65.05

Note: Water Demand (not including loss, reuse and DSM) (Cubic Meter).

4.4. Expansion of urbanization model scenario

In this scenario, the water use rate for industries is increased to 25% of domestic water use, while the rate for commercial and institutional sectors rises to 30% of domestic water demand over the 15-year period from 2024 to 2038. This increase in the water use rate was

made to better reflect the growing water requirements driven by urbanization and the expansion of infrastructure (Paul and Elango, 2018). This adjustment led to an increase in water demand, as shown in **Fig. 8**, which compares two scenarios: the expansion of urbanization and the reference for the years 2024 to 2038. In the expansion of urbanization scenario, water demand increases steadily from 3.4 in 2024 to 6.6 in 2038, resulting in a total cumulative demand of 74.9 cubic meters over 15 years.

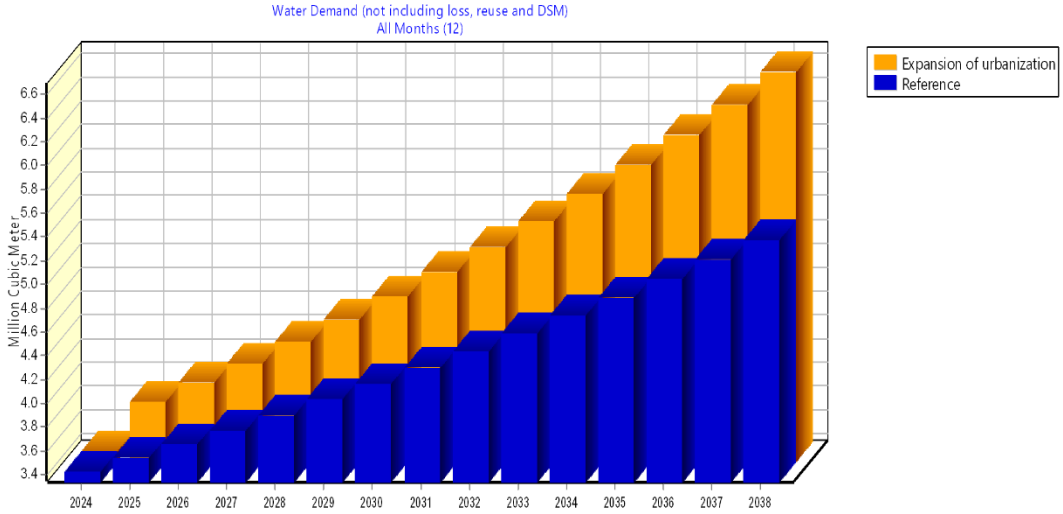


Fig. 8:Annual water demand for expansion of urbanization scenario

This growth reflects the increasing water usage driven by urbanization, which includes the expansion of residential, commercial, and industrial infrastructure. In contrast, the reference scenario exhibits a more moderate rise in water demand, starting at 3.4 in 2024 and reaching 5.4 by 2038, with a cumulative total of 65.0 cubic meters. The demand in this scenario is primarily influenced by factors such as population growth and general economic development, without the additional pressure of urban expansion. The difference in total demand between the two scenarios (9.9 cubic meters) highlights the significant impact of urbanization on water requirements. The unmet demand increased by 1.25 million cubic meters, reflecting the additional water demand from urbanization and limitations in water supply to meet this growth. Relative to comparable research conducted in South Chennai City, India by Arunprakash, M., and Giridharan, the high-growth scenario in this study aligns with their findings, demonstrating a typical pattern where rapid urban growth significantly increases water demand (Arunprakash et al., 2015). Another study conducted in Xiamen City, China, by Tang et al. (2013), examined urban development and planning strategies under rapid urbanization. The research analyzed the relationship between urbanization and water resource management, highlighting the need for adaptive measures to support sustainable growth (Tang *et al.*, 2013; Li *et al.*, 2023).

4.5. Livestock reproduction model scenario

The scenario created for domestic animal reproduction assesses the impact of improved livestock reproductive methods on water use. Improved breeding practices result in higher reproduction rates, enhancing livestock production efficiency and significantly increasing the water demand needed to support the expanding animal population. Using an average water consumption rate of 30 liters per animal per day in the livestock reproduction enhancement scenario throughout the design period, there is a corresponding increase in water demand (Mekonnen et al., 2011). As shown in **Table 7**, the comparison between the livestock reproduction enhancement and reference scenarios from 2024 to 2038 reveals

notable differences in water demand trends. In the livestock reproduction improvement scenario, water demand starts at 3.4 million cubic meters in 2024 and increases steadily to 5.8 million cubic meters in 2038, with a total increase of 2.4 thousand cubic meters over the 15- year period. In comparison, the reference scenario shows a slightly lower increase, starting at 3.4 million cubic meters in 2024 and reaching 5.3 million cubic meters in 2038, with a total increase of 1.9 million cubic meters.

Table 7.

All Scenario, Branch: Demand site Catchment, Monthly Average.

Year	2024	2025	2026	2027	2028	2029	2030	2031	2032	2033	2034	2035	2036	2037	2038	Sum
Livestock reproduction improvement	3.4	3.6	3.7	3.8	4.0	4.1	4.3	4.4	4.6	4.8	5.0	5.1	5.3	5.5	5.8	67.3
Reference	3.4	3.5	3.6	3.8	3.9	4.0	4.1	4.3	4.4	4.6	4.7	4.8	5.0	5.1	5.3	64.6

Note: Water Demand (not including loss, reuse and DSM) (Cubic Meter).

The livestock reproduction enhancement scenario projects a total water demand of 67.3 million cubic meters, which is 2.7 million cubic meters higher than the reference scenario. This notable increase in yearly water demand is primarily attributed to improved breeding practices and a broader diversity of livestock species, highlighting the impact of enhanced reproduction on water resource requirements. A study conducted by Wisser et al. (2024) globally investigates water use in livestock-based agri-food systems, employing regionally distributed models to determine the extent to which livestock production contributes to local water scarcity. The research identifies hotspots where water consumption exacerbates scarcity and underscores the importance of sustainable livestock water management to alleviate pressure on water resources and adapt to the growing food demand in water-limited regions (Wisser *et al.*, 2024). Similarly, Potopová et al. (2023) analyzed historical water use in livestock systems and projected future trends under varying climate change scenarios. The study highlights challenges in meeting livestock water demands within changing climatic conditions and proposes adaptive strategies to mitigate future water stress. By emphasizing long-term trends and climatic impacts, it offers valuable insights for sustainable livestock management in water-scarce areas (Potopová et al., 2023).

4.6. High population growth and expansion of urbanization model scenario

The high population growth + urban expansion (HPG + UE) scenario presents significant challenges to the sustainability of water supply and demand in the towns. **Fig. 9** compares the water demand trends between the HPG + UE and Reference scenarios from 2024 to 2038. In the HPG + UE scenario, water demand begins at 3.4 million cubic meter in 2024 and steadily increases, reaching 7.8 million cubic meters by 2038, with a total cumulative demand of 82.0 million cubic meters over the 15 years. This notable rise reflects the combined effects of high population growth and urban expansion, resulting in increased water needs across both residential and commercial sectors. The water demand in this scenario grows at a faster rate compared to the reference scenario, which aligns with the assumption that urbanization and rapid population growth drive higher water consumption. In contrast, the reference scenario exhibits a more moderate increase in water demand, starting at 3.4 million cubic meter in 2024 and reaching 5.4 million cubic meters by 2038, with a total cumulative demand of 65.0 million cubic meters.

The cumulative demand difference of 17.0 million cubic meters between the two scenarios underscores the significant impact of high population growth and urban expansion on water demand. This highlights the need for strategic planning and resource management to address the growing water requirements in areas undergoing rapid urbanization and population growth. Saketa, Y. (2022) conducted a relevant study in Assossa, Ethiopia, examining the effects of socioeconomic shifts on water supply and demand.

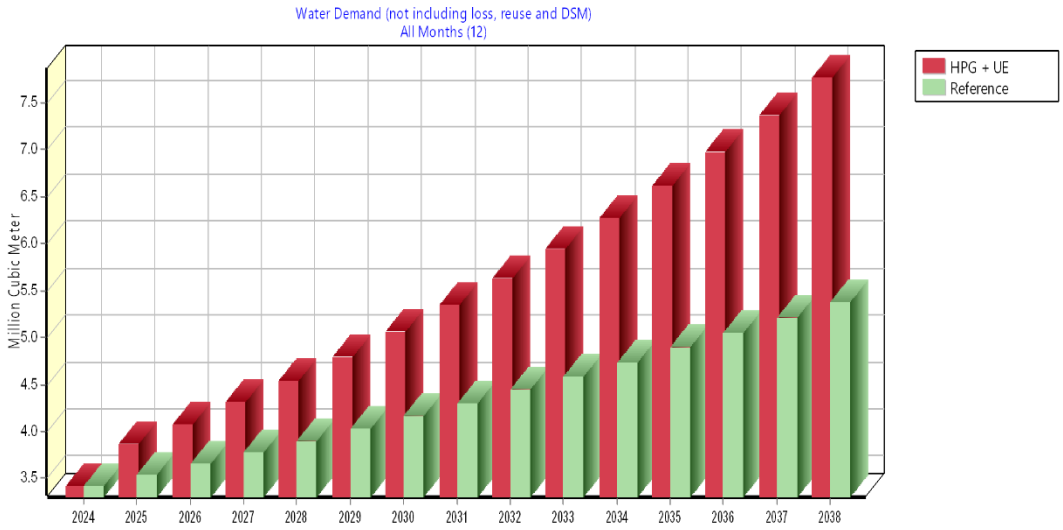


Fig. 9. High population growth and urban expansion water demand scenario.

The study emphasized the importance of proactive policy measures to balance water demand and supply in the face of rapid urbanization and changing socioeconomic conditions (Saketa, 2022). Similarly, a study conducted in Kampala, Uganda, by Vermeiren et al. (2012) explored urban water challenges arising from population growth and increased urbanization. The findings highlighted that enhanced water storage and distribution systems could significantly reduce unmet water demand (Vermeiren et al., 2012). This comparison underscores the need for integrated urban planning and strategic water resource management to address the challenges posed by urban growth in different regions.

4.7. Climate change model scenario

The climate change scenario predicts a temperature increase of 0.5 degrees Celsius and a reduction in rainfall. Under this scenario, total groundwater storage is projected to decrease to 42.95 million cubic meters, compared to 44.63 million cubic meters in the reference scenario. This results in an annual decrease of 1.68 million cubic meters throughout the 15-year study period. This significant reduction may lead to more severe water supply shortages during high-demand periods and the dry season, impacting local ecosystems and straining community water supply (**Fig.10**).

The climate change scenario investigated how water availability and demand would be affected by anticipated temperature rises and less rainfall (Ayt Ougougdal et al., 2020; Alamanos *et al.*, 2020). All demand sectors see an increase in water demand when temperatures rise, whereas home demand is particularly high, resulting in higher household water use for personal use and cooling. At the same time, less rainfall lowers the amount of surface water available and lowers the rate at which groundwater recharge occurs, which lowers the availability of water resources overall. These changes put additional strain on an existing stressed water delivery system and increase the likelihood of water shortages, especially during the dry season and during periods of high demand from February to May. This hypothetical situation highlights how urgent it is to include climate change adaptation strategies in the town's water management plans in order to prevent future water shortages and preserve a steady supply in the face of shifting climate conditions. According to a related study conducted by Cosgrove and Loucks (2015) and Paul and Elango (2018), the analysis emphasized the growing gap between water supply and demand, especially under deficit and normal conditions (Cosgrove and Loucks, 2015, Paul and Elango, 2018).

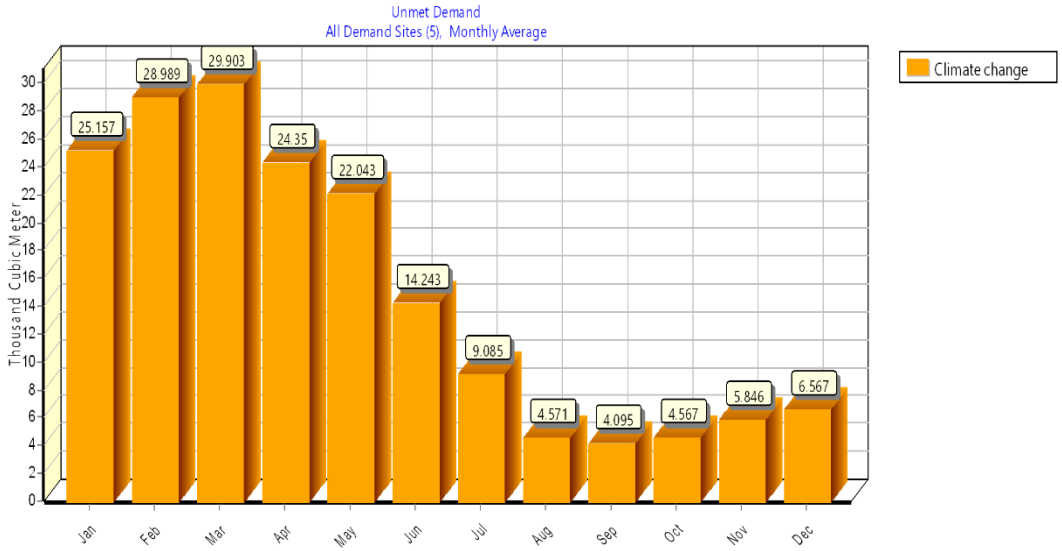


Fig. 10. Monthly unmet water demand under climate variation scenario.

To address these challenges, the studies suggested the adoption of sustainable water management practices.

4.8. Demand side management model scenario

Demand-Side Management (DSM) aims to regulate water usage by enhancing water efficiency, reducing wasteful spending, and modifying user behavior to guarantee that the available water supply adequately satisfies demand. A 20% reduction in water usage was assumed in this scenario, achieved through a combination of strategies. Based on this assumption, **Fig.11** compares the water demand trends for the DSM and reference scenarios from 2024 to 2038. In the DSM scenario, water demand starts at 3.4 million cubic meters in 2024, decreases to 2.9 million cubic meter in 2025, and then gradually increases, reaching 4.3 cubic meters by 2038.

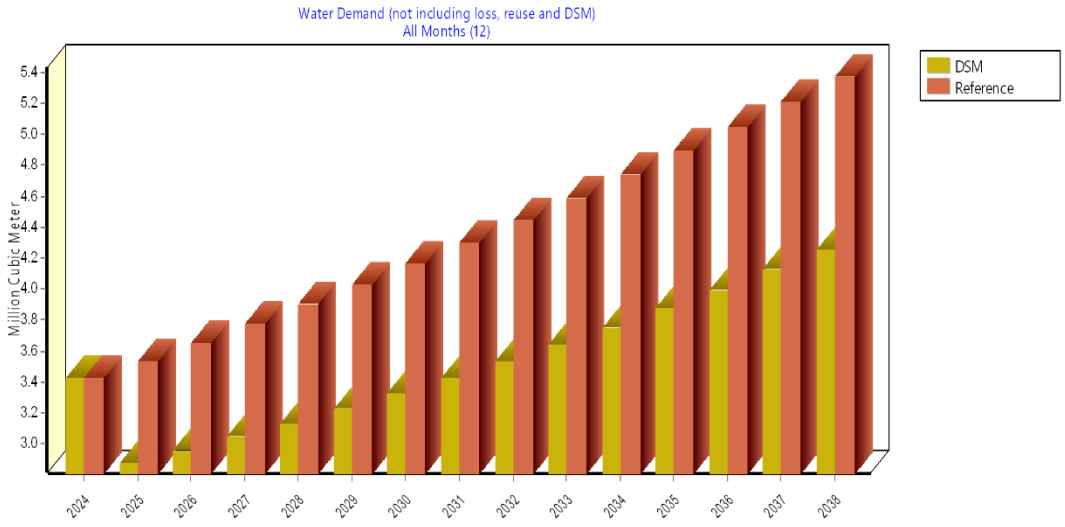


Fig. 11. Annual water demand under demand side management scenario.

The total cumulative demand for this scenario is 52.6 million cubic meters over 15 years, reflecting a 19.08% reduction in water usage compared to the reference scenario. This reduction is attributed to the implementation of water conservation strategies, including reducing losses in the distribution network and promoting efficient water use through behavioral changes among consumers.

In contrast, the reference scenario shows a steady increase in water demand, starting at 3.4 million cubic meters in 2024 and reaching 5.4 million cubic meters by 2038, with a total cumulative demand of 65.0 million cubic meters. Consequently, the total annual unmet demand is reduced by 11.41%, with the difference in cumulative water demand between the two scenarios amounting to 12.4 million cubic meters, highlighting the significant impact of DSM measures in reducing water demand. This analysis emphasizes the effectiveness of demand-side management strategies in minimizing water consumption, which can help address growing water demands while optimizing the available water supply. A similar study conducted in South Africa's water-stressed basins found that DSM strategies included scenarios with 10%, 20%, and 30% reductions in water demand to address future water scarcity (Lévite et al., 2003). Another Research conducted by Assefa et al. (2018) on Ethiopian household and industrial water use utilized the Water Evaluation and Planning (WEAP) model to assess DSM scenarios, focusing on enhancing domestic water efficiency and reducing industrial water consumption. Their findings demonstrate that water conservation strategies significantly mitigate water scarcity issues while ensuring a consistent water supply. It emphasized integrating water management with urban planning to address the challenges posed by increased demand, urban expansion, and limited (Assefa *et al.*, 2018).

4.9. Supply side management model scenario

The results reveal significant differences between the reference and supply-side management (SSM) scenarios from 2024 to 2038, highlighting variations in cumulative totals and annual trends in water supply delivery. The total cumulative water supply delivery for the reference scenario is 63.6 million cubic meters, whereas the SSM scenario achieves a lower total of 53.5 million cubic meter, representing a reduction of 10.1 million cubic meter or 15.9% (**Fig. 12**).

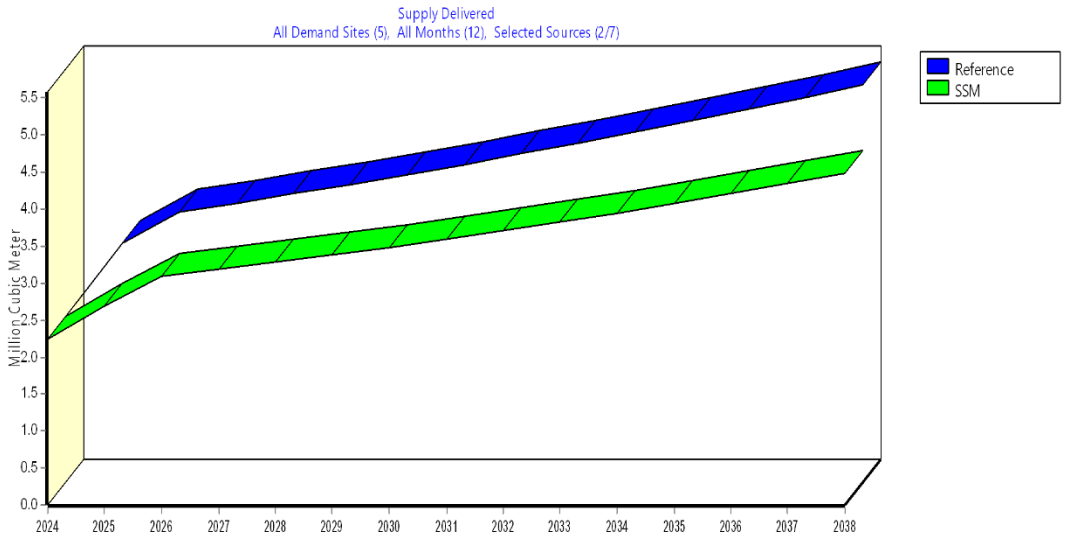


Fig. 12. Annual water supply under supply side management scenario.

This reduction reflects implementing measures in the SSM scenario aimed at managing and optimizing water supply delivery. Both scenarios start with the same value of 2.3 million cubic meter in 2024. However, from 2025 onward, the SSM scenario consistently delivers less water than the reference scenario. For instance, in 2025, the SSM scenario delivers 2.7 million cubic meter, 0.5 million cubic meters less than the reference scenario's 3.2 million cubic meter. By 2038, this gap will widen to 0.9 million cubic meters, with the reference scenario delivering 5.4 million cubic meter and the SSM scenario delivering 4.5 million cubic meters. The average annual growth rate of water supply delivery is approximately 0.22 million cubic meter per year for the reference scenario and 0.15 million cubic meter per year for the SSM scenario. Over the entire period, the SSM scenario achieves 84.1% coverage of the reference scenario's total water supply delivery. This indicates that the SSM scenario fulfills most of the projected demand while achieving a 15.9% reduction in total delivery through the implementation of efficiency measures.

The findings emphasize the effectiveness of the SSM scenario in sustainably managing water supply by integrating surface and groundwater sources. This approach enhances water availability for livestock and industrial use, ensuring that demand is met more efficiently while reducing pressure on individual sources. By integrating multiple water sources, the SSM scenario supports balanced resource utilization, minimizes the risk of shortages, and promotes long-term water sustainability in the face of growing demand. The relevant study by RaziSadath et al. (2023) examines several future scenarios, assessing their potential impacts on water resources and proposing strategies to ensure sustainable water management in the region. The study underscores the importance of integrating water demand management, conservation strategies, and alternative water supplies to mitigate water scarcity challenges arising from urbanization, climate change, and increasing demand (RaziSadath et al., 2023). Additionally, the study by Koop et al. (2022) explores the integration of technological advancements and policy changes in supply-side water management approaches, with an emphasis on sustainable urban water management techniques (Omar and Nangia, 2023).

5. DISCUSSION

The demand and supply dynamics for urban water in Chancho town underscore the critical need for sustainable and adaptable water management strategies to address increasing socioeconomic pressures. The primary aim of the study is to provide insights into the town's water supply and demand status using the WEAP model. The analysis revealed a significant water deficit across all demand locations, with unmet demand accounting for 49% of total water needs. As the town's population grows from 98,900 in 2023 to 198,830 in 2038, water demand increases substantially, indicating that existing infrastructure and water resources are insufficient to meet future needs (He et al., 2021, Hassan et al., 2019). Water demand rises by 70.63% during the dry season, which runs from March to May, when temperatures reach their highest point in March at 29°C. The reference scenario, developed using the current account year 2023 as a baseline, extends forecasts to 2038 without any interventions. The results demonstrate that population growth drives a continual rise in water demand. Annual water demand under external factor-driven scenarios considers the influence of factors such as rapid population growth and urban expansion. Population growth increases water requirements for households, public services, and infrastructure(Rachidi, 2014).

Similarly, urbanization increases demand by introducing new public spaces, transit systems, and industries. Beyond volumetric demand growth, urban expansion typically modifies runoff pathways and peak volumes, which complicates storage and reliability planning (Haidu & Ivan, 2016). Water consumption for businesses, organizations, and industries has increased from 3.42 million cubic meters to 6.62 million cubic meters as a result of the area's urban expansion scenario. Lifestyle changes associated with rising living

standards also contribute to increased water demand. Higher living standards have resulted in increased consumption of water-intensive products and services, such as landscaped areas and improved residential water use. Sensitivity analysis identified population growth and urban expansion as the most critical drivers of water demand, followed by urbanization and lifestyle changes. To address these challenges, effective water resource management must prioritize strategies to mitigate the impacts of rapid urban growth and increasing water demand (Nivesh et al., 2022).

The climate change scenario further revealed that rising temperatures and reduced rainfall exacerbate water shortages, leading to a projected annual reduction of 1.7 million cubic meters in groundwater storage compared to the reference scenario. Incorporating adaptive measures into water management plans is essential to mitigate the potential impacts of climate variability These measures include building climate-resilient infrastructure, implementing flexible resource allocation plans, and anticipating future changes in temperature and precipitation patterns (Gedefaw and Denghua, 2023). The primary source of groundwater recharge is runoff and infiltration from the catchment, contributing 67.57 million cubic meters in total. On the outflow side, domestic water demand is the largest consumer, withdrawing 41.11 million cubic meters, followed by industrial demand (9.95 million cubic meters), institutional and commercial demand (5.97 million cubic meters), and livestock demand (5.32 million cubic meters). These withdrawals exceed the groundwater replenishment rate, leading to a continuous decline in storage.

The balance of inflows and outflows fluctuates slightly, but overall, the system is experiencing depletion, with groundwater loss increasing over time. This trend indicates a long-term risk of groundwater depletion, which could lead to water shortages in the future. With growing water demand across all sectors, sustainable management strategies such as efficient water use, recharge enhancement, and alternative water sources will be essential to prevent severe water stress. Tracking availability through effective precipitation and AET-based indicators provides a scalable lens for anticipating storage deficits under warming (Nistor et al., 2022).

Integrating groundwater and surface water sources for industrial and livestock use increased overall water supply availability in the supply-side scenario. Diversifying water sources for non-potable uses can help reduce reliance on groundwater and storage tanks(Bahri, Brikké and Vairavamoorthy, 2016). This approach balances demand across resources, alleviating pressure on individual sources and promoting sustainable water management.

Demand-side management strategies focus on improving water-use efficiency, reducing waste, and encouraging behavioral changes to ensure that available supplies meet demand. Expanding the storage capacity of existing reservoirs or constructing new ones would allow for better management of excess water during peak demand periods. Promoting water-saving technologies and reducing waste in the commercial, industrial, and residential sectors can significantly lower overall water demand(Dos Santos *et al.*, 2017). Active stakeholder engagement spanning local governments, industries, and communities is crucial for enhancing coordination, accountability, and the success of water management programs.

6. CONCLUSION

The study's findings emphasize the significance of appropriate water management techniques for the town, especially in terms of growing urbanization, population increase, and climate change. Based on the WEAP findings, there was an observable water shortage in demand during the analyzed time span, particularly during the dry season. It shows a current annual unmet of 1.16 million cubic meters (MCM) between the supply of 1.83 MCM and the demand of 2.99 MCM. This confirmed that the water resources and infrastructure were inadequate to meet the increasing demand.

A significant rise in water demand over the baseline levels set in the reference scenario was predicted by future scenarios, which include rapid population growth, changes in living standards,

and urbanization. These forecasts indicate that water consumption will climb sharply as the population grows and urban areas spread and the changes in lifestyle that frequently accompany urban expansion. Such scenarios highlight the necessity of capacity expansion and strategic planning to meet the expected increase in demand, guaranteeing that the water supply will be robust and able to sustain important economic sectors as well as the expanding population in the face of future demands.

On the other hand, supply-side management scenarios predicted that integrating surface water and groundwater sources for industrial and livestock use proved to be an effective solution for balancing demand and improving water supply reliability. This approach reduced strain on individual sources and promoted sustainable water usage, ensuring that both the growing population and key sectors, like industry, were supported. The increasing demand emphasizes the need for proactive planning, infrastructure development, and efficient water management practices. Overall, ongoing monitoring and management will be crucial for addressing future challenges and ensuring water availability for all sectors.

The study recommends that further research is required to examine how climate change affects the region's water supply and demand. Furthermore, by integrating data from supply sources, future research should also use the model to assess water quality across the system.

The study considered climate change by analyzing its potential impact on water demand and availability in the town. It particularly investigated the consequences of rising temperatures and shifting precipitation patterns, predicting an increase in water demand during times of higher temperatures and lower rainfall. The study also looked at how these climate changes may increase water scarcity, especially during peak demand months. The study highlighted the need for adaptive water management measures to ensure a reliable and sustainable water supply under future climate conditions.

ACKNOWLEDGMENTS

The authors would like to acknowledge the WEAP Institute for granting access to the WEAP software used in this research. The corresponding author wishes to thank for the support from the European Commission through the Erasmus+ KA171 program which enabled the contribution to the development of education and research in the partner country Ethiopia. Dimitrie Cantemir University IR-BE-200465 project provided funding for the open access publication of this paper.

REFERENCES

Al-Mukhtar, M.M. and Mutar, G.S., 2021. Modelling of future water use scenarios using WEAP model: a case study in Baghdad City, Iraq. *Eng. Technol. J*, *39*, pp.488-503.

Al-Shutayri, A.S. and Al-Juaidi, A.E., 2019. Assessment of future urban water resources supply and demand for Jeddah City based on the WEAP model. *Arabian Journal of Geosciences*, *12*(14), p.431.

Alamanos, A., Sfyris, S., Fafoutis, C. and Mylopoulos, N., 2020. Urban water demand assessment for sustainable water resources management, under climate change and socioeconomic changes. *Water Supply*, *20*(2), pp.679-687.

Alemu, Z.A. and Dioha, M.O., 2020. Modelling scenarios for sustainable water supply and demand in Addis Ababa city, Ethiopia. *Environmental Systems Research*, *9*(1), p.7.

Ali, M. and Terfa, A.B., 2012. State of water supply and consumption in urban areas at household level: a case study of East Wollega Zone, Ethiopia. *British journal of humanities and social sciences*, *5*(2), pp.1-15.

Andersson, E., 2019. Water demand and supply in Dar es Salaam: A WEAP-model to estimate future scenarios.

Arsiso, B.K., Tsidu, G.M., Stoffberg, G.H. and Tadesse, T., 2017. Climate change and population growth impacts on surface water supply and demand of Addis Ababa, Ethiopia. *Climate Risk Management*, *18*, pp.21-33.

Arunprakash, M., Giridharan, L., Krishnamurthy, R.R. and Jayaprakash, M., 2014. Impact of urbanization in groundwater of south Chennai City, Tamil Nadu, India. *Environmental Earth Sciences*, *71*(2), pp.947-957.

Assefa, Y.T., Babel, M.S., Sušnik, J. and Shinde, V.R., 2018. Development of a generic domestic water security index, and its application in Addis Ababa, Ethiopia. *Water*, *11*(1), p.37.

Ayt Ougougdal, H., Yacoubi Khebiza, M., Messouli, M. and Lachir, A., 2020. Assessment of future water demand and supply under IPCC climate change and socio-economic scenarios, using a combination of models in Ourika Watershed, High Atlas, Morocco. *Water*, *12*(6), p.1751.

Bach, P.M., Rauch, W., Mikkelsen, P.S., McCarthy, D.T. and Deletic, A., 2014. A critical review of integrated urban water modelling–Urban drainage and beyond. *Environmental modelling & software*, *54*, pp.88-107.

Beker, B.A. and Kansal, M.L., 2024. Complexities of the urban drinking water systems in Ethiopia and possible interventions for sustainability. *Environment, Development and Sustainability*, *26*(2), pp.4629-4659.

Berredjem, A.F., Boumaiza, A. and Hani, A., 2023. Simulation of current and future water demands using the WEAP model in the Annaba province, Northeastern Algeria: a case study. *AQUA—Water Infrastructure, Ecosystems and Society*, *72*(9), pp.1815-1824.

Brikké, F. and Vairavamoorthy, K., 2016. Managing change to implement integrated urban water management in African cities. *Aquatic Procedia*, *6*, pp.3-14.

Cosgrove, W.J. and Loucks, D.P., 2015. Water management: Current and future challenges and research directions. *Water resources research*, *51*(6), pp.4823-4839.

Crouch, M.L., Jacobs, H.E. and Speight, V.L., 2021. Defining domestic water consumption based on personal water use activities. *AQUA—Water Infrastructure, Ecosystems and Society*, *70*(7), pp.1002-1011.

Dos Santos, S., Adams, E.A., Neville, G., Wada, Y., De Sherbinin, A., Bernhardt, E.M. and Adamo, S.B., 2017. Urban growth and water access in sub-Saharan Africa: Progress, challenges, and emerging research directions. *Science of the Total Environment*, *607*, pp.497-508.

Douglas-Mankin, K.R., Srinivasan, R. and Arnold, J.G., 2010. Soil and Water Assessment Tool (SWAT) model: Current developments and applications. *Transactions of the ASABE*, *53*(5), pp.1423-1431.

Ernawati, N.M., Torpan, A., Voda, M. (2018) Geomedia role for Mountain Routes Development. Mesehe and Pisoiu Waterfall comparative study. *Geographia Technica* 13(1), 41-51.

Gedefaw, M. and Denghua, Y., 2023. Simulation of stream flows and climate trend detections using WEAP model in awash river basin. *Cogent Engineering*, *10*(1), p.2211365.

Haidu, I. & Ivan, K. (2016). Urban runoff pathways and surface water volumes evolution. Case study : Bordeaux 1984-2014, France. (Évolution du ruissellement et du volume d'eau ruisselé en surface urbaine. Étude de cas: Bordeaux 1984-2014, France). *La Houille Blanche, 5*, 51–56. https://doi.org/10.1051/lhb/2016050.

Haque, M.M., Egodawatta, P., Rahman, A. and Goonetilleke, A., 2015. Assessing the significance of climate and community factors on urban water demand. *International Journal of Sustainable Built Environment*, *4*(2), pp.222-230.

Harbaugh, A.W. and McDonald, M.G., 1996. *Programmer's documentation for MODFLOW-96, an update to the US Geological Survey modular finite-difference ground-water flow model* (No. 96-486). US Geological Survey; Branch of Information Services [distributor],.

Hassan, D., Rais, M.N., Ahmed, W., Bano, R., Burian, S.J., Ijaz, M.W. and Bhatti, F.A., 2019. Future water demand modeling using water evaluation and planning: A case study of the Indus Basin in Pakistan. *Sustainable Water Resources Management*, *5*(4), pp.1903-1915.

He, C., Liu, Z., Wu, J., Pan, X., Fang, Z., Li, J. and Bryan, B.A., 2021. Future global urban water scarcity and potential solutions. *Nature communications*, *12*(1), p.4667.

Herslund, L. and Mguni, P., 2019. Examining urban water management practices–Challenges and possibilities for transitions to sustainable urban water management in Sub-Saharan cities. *Sustainable Cities and Society*, *48*, p.101573.

Kedir, E.G., 2023. Assessing Challenges of Potable Water Supply, Demand and Enhancing Sustainability. *American Journal of Water Science and Engineering*, *9*(2), pp.36-40.

Lévite, H., Sally, H. and Cour, J., 2003. Testing water demand management scenarios in a water-stressed basin in South Africa: application of the WEAP model. *Physics and Chemistry of the Earth, Parts a/b/c*, *28*(20-27), pp.779-786.

Li, L., Du, Q., Ren, F., Huang, L., Voda, M., Ning, P. (2023) Geolocated social media data for measuring park visitation in Shenzhen, China, *Urban Forestry & Urban Greening*, Volume 88,128069, https://doi.org/10.1016/j.ufug.2023.128069

Madani, K., 2014. Water management in Iran: what is causing the looming crisis?. *Journal of environmental studies and sciences*, *4*(4), pp.315-328.

Mekonnen, S., Descheemaeker, K., Tolera, A. and Amede, T., 2011. Livestock water productivity in a water stressed environment in northern Ethiopia. *Experimental Agriculture*, *47*(S1), pp.85-98.

Mensah, J.K., Ofosu, E.A., Akpoti, K., Kabo-Bah, A.T., Okyereh, S.A. and Yidana, S.M., 2022. Modeling current and future groundwater demands in the White Volta River Basin of Ghana under climate change and socio-economic scenarios. *Journal of Hydrology: Regional Studies*, *41*, p.101117.

Nistor, M.-M., Satyanaga, A., Dezsi, Ş., & Haidu, I. (2022). European Grid Dataset of Actual Evapotranspiration, Water Availability and Effective Precipitation. *Atmosphere*, *13*(5), 772. https://doi.org/10.3390/atmos13050772

Nivesh, S., Patil, J.P., Goyal, V.C., Saran, B., Singh, A.K., Raizada, A., Malik, A. and Kuriqi, A., 2023. Assessment of future water demand and supply using WEAP model in Dhasan River Basin, Madhya Pradesh, India. *Environmental Science and Pollution Research*, *30*(10), pp.27289-27302.

Okungu, J., Adeyemo, J. and Otieno, F., 2017. Scenario analysis of water supply and demand using WEAP model: a case of Yala Catchment, Kenya. *American Journal of Water Resources*, *5*(4), pp.125-131.

Omar, M.E.D. and Nangia, V., 2023. On-farm water energy food carbon-footprint nexus index for quantitative assessment of integrated resources management for wheat farming in Egypt. *Water-Energy Nexus*, *6*, pp.122-130.

Panwar, A.M. and Antil, M.S., 2015. Issues, challenges and prospects of water supply in urban India. *Google Scholar*.

Paul, N. and Elango, L., 2018. Predicting future water supply-demand gap with a new reservoir, desalination plant and waste water reuse by water evaluation and planning model for Chennai megacity, India. *Groundwater for Sustainable Development*, *7*, pp.8-19.

Potopová, V., Musiolková, M., Gaviria, J.A., Trnka, M., Havlík, P., Boere, E., Trifan, T., Muntean, N. and Chawdhery, M.R.A., 2023. Water Consumption by Livestock Systems from 2002–2020 and Predictions for 2030–2050 under Climate Changes in the Czech Republic. *Agriculture*, *13*(7), p.1291.

Purkey, D.R., Escobar Arias, M.I., Mehta, V.K., Forni, L., Depsky, N.J., Yates, D.N. and Stevenson, W.N., 2018. A philosophical justification for a novel analysis-supported, stakeholder-driven participatory process for water resources planning and decision making. *Water*, *10*(8), p.1009.

Rachidi, M.F., 2014. Challenges of water management towards socio-economic development in sub-Saharan Africa. *Mediterranean Journal of Social Sciences*, *5*(27), pp.1391-1396.

Rathnayaka, K., Malano, H. and Arora, M., 2016. Assessment of sustainability of urban water supply and demand management options: a comprehensive approach. *Water*, *8*(12), p.595.

RaziSadath, P.V., RinishaKartheeshwari, M. and Elango, L., 2023. WEAP model-based evaluation of future scenarios and strategies for sustainable water management in the Chennai Basin, India. *AQUA—Water Infrastructure, Ecosystems and Society*, *72*(11), pp.2062-2080.

Rufino, I.A., Alves, P., Grangeiro, E.L. and Santos, K.A., 2018. Dynamic scenarios and water management simulations: towards to an integrated spatial analysis in water urban planning. In *13th International Conference on Hydroinformatics, EPiC Series in Engineering*.

Saketa, Y., 2022. Assessment of future urban water demand and supply under socioeconomic scenarios: a case of Assosa town. *Water Supply*, *22*(10), pp.7405-7415.

Schlink, A.C., Nguyen, M.L. and Viljoen, G.J., 2010. Water requirements for livestock production: a global perspective. *Soil and Water Management & Crop Nutrition Subprogramme*, *6*, pp.603-619.

Shahraki, A.S., Shahraki, J. and Monfared, S.H., 2016. An application of WEAP model in water resources management considering the environmental scenarios and economic assessment case study: Hirmand catchment. *Modern Applied Science*, *10*(5), pp.49-56.

Soula, R., Chebil, A., McCann, L. and Majdoub, R., 2021. Water scarcity in the Mahdia region of Tunisia: Are improved water policies needed?. *Groundwater for Sustainable Development*, *12*, p.100510.

Tang, L., Zhao, Y., Yin, K. and Zhao, J., 2013. Xiamen. *Cities*, *31*, pp.615-624.

Tegegne, T.K., 2019. Socioeconomic determinants of youth unemployment in Ethiopia, the case of Wolaita Sodo Town, Southern Ethiopia. *Journal of Economics and Sustainable Development*, *10*(23), pp.46-53.

Tufa, F.G., Feyissa, F.F., Kebede, A.B., Gudeta, B.G., Kitessa, W.M., Debela, S.K., Tumsa, B.C., Yenehun, A., Van Camp, M. and Walraevens, K., 2024. Estimation of groundwater recharge in a volcanic aquifer system using soil moisture balance and baseflow separation methods: The case of gilgel gibe catchment, Ethiopia. *Hydrology*, *11*(7), p.109.

Tzanakakis, V.A., Paranychianakis, N.V. and Angelakis, A.N., 2020. Water supply and water scarcity. *Water*, *12*(9), p.2347.

Vermeiren, K., Van Rompaey, A., Loopmans, M., Serwajja, E. and Mukwaya, P., 2012. Urban growth of Kampala, Uganda: Pattern analysis and scenario development. *Landscape and urban planning*, *106*(2), pp.199-206.

Voda, M., Kithiia, S., Jackiewicz, E., Du, Q., Sarpe, C.A. (2019) Geosystems 'pathways to the future of Sustainability, Scientific reports, 9(1), 1-11. https://www.nature.com/articles/s41598-019-50937-z

Voda, A.I., Sarpe, C.A., and Voda, M. (2018). Methods of maximum discharge computation in ungauged river basins. Review of procedures in Romania. Geographia Technica, 13(1), 130-137.

Wang, K., Wang, M., Gan, C., Chen, Q. and Voda, M., 2021. Tourism economic network structural characteristics of national parks in the central region of China. *Sustainability*, 13(9), p.4805.

Wisser, D., Grogan, D.S., Lanzoni, L., Tempio, G., Cinardi, G., Prusevich, A. and Glidden, S., 2024. Water use in livestock agri-food systems and its contribution to local water scarcity: A spatially distributed global analysis. *Water*, *16*(12), p.1681.

EXTRACTING THE SPACE-BORNE RADAR BACKSCATTERING RESPONSES OF DIFFERENT ROCK UNITS FOR GEOLOGICALLY MAPPING TAFILALET REGION IN MOROCCO

Naoual El HAMMOUCH[1,*], Fatima El HAMMICHI[1], Hassan TABYAOUI[1], Ahmed GABER[2], Magaly KOCH[3] & Mohammed MOURJANE[1]

DOI: 10.21163/GT_2026.211.17

ABSTRACT

Rock surfaces affected by weathering usually exhibit distinctive spectral characteristics compared to their unaffected counterparts. Furthermore, certain rock units, particularly those with white color, such as carbonate rocks, evaporites, and white sandstone, have very similar spectral responses. This makes it extremely difficult to classify data using only optical remote sensing. On the other hand, by capturing these rock units' radar backscattering responses, completely polarimetric Synthetic Aperture Radar (PolSAR) data offer important insights about their external geometry and surface roughness. Their external geometries differ according to the different lithologies and geological formations since every rock unit has specific physical and chemical weathering characteristics. Consequently, such information facilitates improved classification and mapping. To achieve more accurate classification and geological mapping, this research uses fully polarimetric ALOS/PALSAR-2 data to extract the unique radar scattering responses of rock units along the Tafilalet region. The utilized imagery is decomposed into entropy, alpha, and anisotropy (H- α -A) distribution, Pauli decomposition, Wishart supervised classification with eight classes, and their polarization signatures (PS). Additionally, field validation is conducted to verify the classification outcomes. The Wishart supervised classification based on Synthetic Aperture Radar (SAR data), exhibits alignment with the geological map, surpassing the accuracy achieved using ASTER optical data. These findings indicate that the rocks within the Tafilalet study area have undergone varying degrees of weathering, resulting in distinct the surface roughness and corresponding scattering mechanisms of Synthetic Aperture Radar (SAR) data, which facilitate improved classification and mapping efforts.

Keywords: *Radar images, Space-based; Supervised classification; Geologic mapping; Morocco.*

1. INTRODUCTION

Synthetic Aperture Radar (SAR) is essentially a useful imaging radar method for achieving high spatial resolution from space-based platforms. Imaging radar has developed as a useful and indispensable earth remote sensing technique since the successful 1978 launch of the SEASAT satellite, which was equipped with a Synthetic Aperture Radar (SAR). Several space-borne polarimetric SAR (PolSAR) systems, notably the Advanced Land Observing Satellite (ALOS), TerraSAR-X, and RADARSAT-2, have since been launched with success. These three satellites, each equipped with Polarimetric SAR (PolSAR) systems operating at a different frequency, provide a

[1] *Geo-Resources and Environment Laboratory, Sidi Mohammed Ben Abdellah University, Fez, Morocco;*
[*] *Corresponding author naoual.elhammouch@usmba.ac.ma (N.H), fatima.elhammichi@usmba.ac.ma (F.E.H), has-san.tabyaoui@usmba.ac.ma (H.T), mourjanemohammed@gmail.com (M.M)*
[2] *Faculty of Science, Port Said University, Egypt; ahmedgaber_881@hotmail.com (A.G)*
[3] *Dept. Earth & Environment, Boston University, USA; mkoch@bu.edu (M.K).*

comprehensive data source for Earth environmental monitoring, including applications such as hazard monitoring, soil moisture estimation, snow cover and snow content assessment, water and forest detection, urban planning, ocean current and wave dynamics detection, and evaluation of geophysical constraints and changes.

Radar polarimetry, derived from polarimetry and remote sensing principles, analyzes the vector character of electromagnetic waves (Deschamps, 1951; Boerner et al., 1985; Boerner, 2004). The goal is to characterize targets based on their responses to different transmission and reception polarizations. The following references provide a detailed history of radar polarimetry, Cloude and Pottier (1996), Boerner and Cloude (2002), Oliver and Quegan (2004), Lee and Pottier (2009), López-Martínez and Pottier (2021).

In land cover classification, selecting an effective classification algorithm is an essential area for research (Lu and Weng, 2007). The Wishart classification system is the most frequently employed polarimetric synthetic aperture radar (SAR) classification technique (Lee et al., 1994). Furthermore, the polarization signature, which is provided as a 3D graphic, is extremely useful for classification. This visualization technique thoroughly elucidates the polarization powers of an object by displaying variations in the orientation and ellipticity angles of the polarization ellipse (Vanzyl et al., 1987).
In the context of geological mapping, optical satellite sensors have some limitations. Optical sensors usually provide surface-level data on geological formations and structures, making them inefficient for detailed geological mapping in vegetated areas. However, radar sensors provide considerable advances in geological mapping. Polarimetric data make it possible to characterize the physical properties of geological materials in detail, including internal structure, composition, and roughness. Polarimetric data can be combined with additional geological information to overcome the limitations of optical data, resulting in a more exact and comprehensive classification of geological formations.

The external geometry of different rock units reveals information about their spatial distribution, structural properties, and morphological features. Researchers use remote sensing techniques, such as satellite imagery and aerial photography, to delineate boundaries between disparate rock units, identify structural features, folds and faults, characterize landforms influenced by the underlying geology, and quantify morphological parameters that indicate distinct rock types. Integrating information from exterior geometry with complementing geology data sets enables radar remote sensing to permit more precise and complete classifications, improving our understanding of the earth's dynamic geologic processes and spatial diversity across varied terrains.

In this study, polarimetric information from various surface features and rock units was extracted and correlated with geological classifications. Subsequently, supervised classification was performed using the statistical properties of polarimetric SAR. Notably, the polarization signatures of these distinct geological units were first defined within the study area, facilitating enhanced discrimination.

2. STUDY AREA

The study area is situated in southeastern Morocco, limited by the coordinates 4° 30' W & 31° 15' N and 3° 45' W & 30° 45' N (**Fig. 1**). It located in the southern Tafilalet valley, surrounded by the Kem Kem plateau to the south and the Hamada du Guir to the east. The valley is underlain by a Paleozoic basement and covered by Cretaceous and Tertiary sedimentary rocks from the Kem Kem plateau. A continental Miocene complex capped by a Pliocene limestone cover characterizes the Hamada du Guir. The drainage system is influenced by the Oued Ziz corridor and its tributaries, which are affected by winds transporting Saharan sand and dust towards the northeast, contributing to the Erg Chebbi dune system. Altitudes range from around 730 m a.s.l. on the plain to more than 880 m of the dune crests and 950 m in the Paleozoic reliefs west of Oued Ziz. The Kem Kem plateaus and Hamada du Guir feature sub-tabular topography with a moderate northward slope. Altitudes reach about 1000 m in the Hamada de Guir and 860 m in the Kem Kem, with a semi-desert environment and a large river network (Joly, 1962). The study area comprises an arid climate with infrequent precipitation. Vegetation is sparse, except for the Marzouga palm grove.

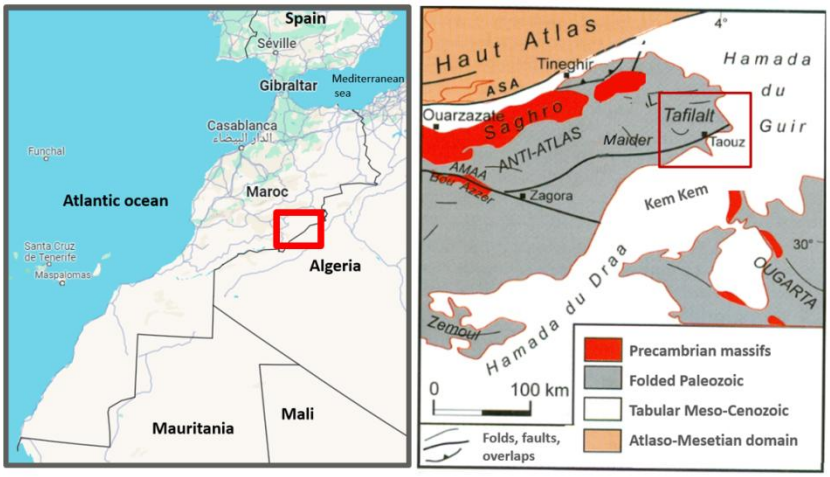


Fig. 1. Location of the study area on the structural map of Morocco at scale 1:2,000,000 [20]. Geological map of SE Morocco at scale 1:1,000,000.

3. DATA AND METHODS

To facilitate the comparison of spectral responses between radar polarimetry data and optical sensors, a preliminary analysis was conducted using the Advanced Spaceborne Thermal Emission and Reflection Radiometer (ASTER) sensor to identify distinct unit classes within the study area. Five ASTER Level 1B "radiance-at-sensor" data sets covering the region of interest were acquired from the Earth Resources Observation and Science (EROS) Center of the National Aeronautics and Space Administration (NASA) (https://LPDAAC.usgs.gov). These data sets underwent preprocessing steps that included resampling, stacking, mosaicking, clipping, radiometric calibration, and atmospheric correction. Subsequently, radiometric calibration was performed to convert the digital numbers (DNs) in the original image pixels (16-bit integers) into physical radiance values. Atmospheric correction was applied to the VNIR and SWIR bands using the Fast Line-of-sight Atmospheric Analysis of Spectral Hypercubes (FLAASH) algorithm (Cooley et al., 2002). An unsupervised classification was carried out using the K-means clustering algorithm with an initial 12 classes and 7 iterations. Field investigations in conjunction with a supervised classification using the maximum likelihood classifier (MLC) for parametric input data revealed that the initial 12 unsupervised classes could be refined into only 8 supervised classes (**Fig. 2**). Due to the limited availability of ground reference samples in several inaccessible areas of the Tafilalet region, a comprehensive quantitative accuracy assessment could not be performed. The reliability of the eight supervised classes was therefore confirmed by field observations, lithological consistency, and analysis of polarimetric scatter mechanisms.

The Radar data used in this study were collected via the phased array L-band Synthetic Aperture Radar (PALSAR-2) onboard the Advanced Earth Observation Satellite (ALOS) in ascending orbit mode with full polarization (HH, HV, VV, VH). Acquired on November 29, 2009, the data exhibited a 2.79 m azimuthal resolution and a 4.81 m look direction resolution. JAXA, Japan supplied the data in L-band, product level 1.1, Single Look Complex (SLC) format, which were accessible through the ALOS-2 6th RA PI-3131 agreement. Preprocessing of SAR data entailed geocoding, speckle filtering using the adaptive Lee filter with a 7 × 7 window size (Lee et al., 2008), and conversion to a coherency matrix (T matrix).

Furthermore, to aid in the comprehension of terrain feature scattering behavior, the fully polarized data acquired from ALOS PALSAR-2 was decomposed into entropy (H), alpha (α), and anisotropy (A) values. Depolarizing elements are demarcated using entropy, whereas alpha angle differentiates surface elements with volume diffusion from those with single or double-bounce

diffusion. Entropy and alpha values can be used to characterize weathering zones based on physical surface attributes. Anisotropy, a quantity that complements entropy, becomes relevant when entropy is considerably elevated (Woodhouse, 2006).

Furthermore, the Pauli decomposition, widely used and based on the coherence matrix. Each parameter has a distinct physical meaning. In specifically, the diagonal elements |HH + VV|, |HH-VV|, and |HV| harbor the most valuable polarimetric data. The Pauli RGB composite image, constructed from the intensities |HH - VV| (red), |HV + VH| (green), and |HH + VV| (blue), provides visual discernment of the three primary diffusion mechanisms in the region under investigation (Qi et al., 2012).

Consequently, the Wishart supervised classification was performed using the training domains specified in the consistency matrix, as explained by (Varghese and Joshi, 2014). Furthermore, the polarization signature (PS) was extracted to identify between the different land cover classes, providing a three-dimensional visual depiction of each target's backscatter properties. While polarimetric signatures have been reported in other arid regions of North Africa (e.g., Saharan and Atlas studies), this study is the first to systematically define them in the Tafilalet region, demonstrating the added value of full-polarimetric SAR for lithological mapping in structurally complex areas.

Field validation was conducted to verify the classification results, which involved collecting rock samples from several locations within the study area. Field validation consisted of qualitative observations carried out at accessible places, supported by the official 1:100,000 geological map and high-resolution Google Earth images. Although no GPS devices were utilized, the geolocation accuracy supplied by Google Earth (usually a few meters) was adequate to verify lithological limits and support the interpretation of polarimetric diffusion behavior.

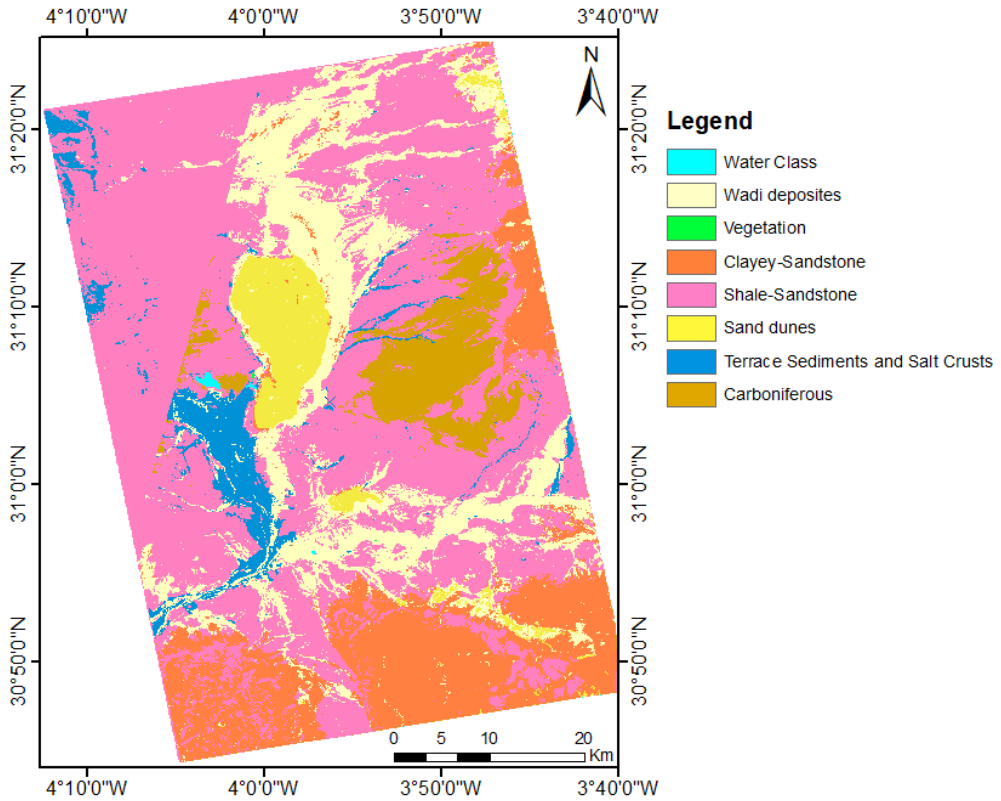


Fig. 2. Supervised classification map obtained from the ASTER optical data.

4. RESULTS

4.1. Entropie (H)

Entropy values range from 0 to 1 (Cloude and Pottier, 1997). **Fig. 3** shows the entropy (H) image, dividing the study area into three main regions: light blue representing low entropy, yellow representing medium entropy, and red representing high entropy. Regions with H = 0 (dark blue) correspond to flat, bare soils with low surface roughness, mainly found in the Oued Ziz valley. Areas with medium entropy (yellow) exhibit rougher surfaces with weathered rocks that enhance depolarized wave scattering. High entropy zones (red) coincide with argillic alteration areas containing clay minerals, particularly on the crests of the Erg Chebi sand dunes. The constant wind in the study area produces slightly rough water surfaces, resulting in a single-bounce scattering mechanism and low entropy values.

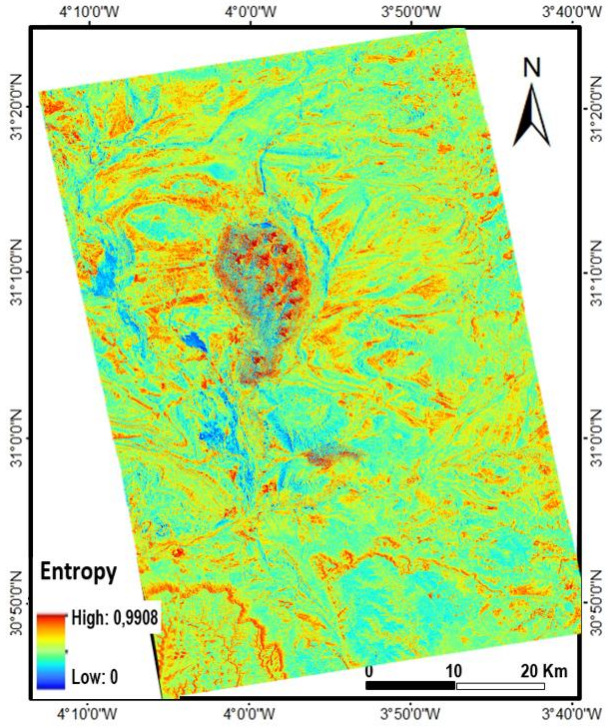


Fig. 3. Spatial variation of Entropy decomposition (H) along the study area.

4.2. Angle alpha (α)

The alpha angle (α) ranges from 0° to 90°, reflecting the nature of the scattering mechanism. **Fig. 4** distinguishes three main classes. Regions shown in dark blue have a very low alpha angle, below 10°, corresponding to surfaces with negligible specular backscatter. These surfaces, mainly weathering deposits, are located in the Oued Ziz valley and its tributaries. Surfaces with moderate backscatter appear light blue and correspond to alteration zones of the Kem Kem plateau's tabular reliefs, where ground observations indicate dominant advanced argillaceous weathering. Yellowish areas exhibit alpha angles between 30° and 50°, reflecting high soil and surface exposure and associated with volume scattering. The highest alpha angle class, exceeding 60°, represents dominant dihedral scattering and is observed as yellowish points on clay-based sand dune ridges. L-band Polarimetric SAR (PolSAR) data, oriented along the radar line of sight, allow accurate characterization of terrain features using the alpha angle.

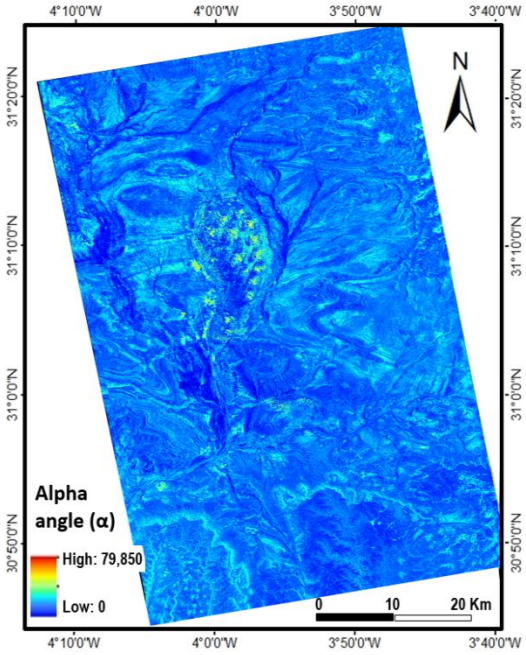


Fig. 4. Spatial variation of Alpha angle

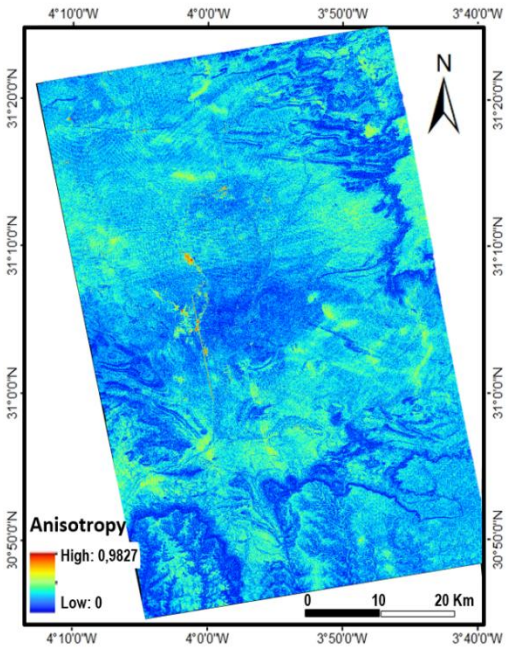


Fig. 5. Spatial variation of anisotropy (A).

4.3. Anisotropie (A)

Anisotropy (A) varies across the study area, reflecting the relative contribution of different scattering mechanisms. Areas of low anisotropy (dark blue) correspond to surfaces where two scattering mechanisms contribute equally. Medium anisotropy (light blue to yellowish) indicates surfaces where dominant scattering mechanisms occur with roughly equal probability, independent of entropy values, surface dielectric properties, or incidence angle variations (Cloude, 1999; Mattia and Le Toan, 1999). This shows that anisotropy is a useful indicator of surface roughness variations. High anisotropy values ($A \approx 0.6$), typically shown in orange to red, represent surfaces dominated by a single scattering mechanism, such as water surfaces with significant Bragg scattering. Wet surfaces with near-unity anisotropy were not observed in the study area (**Fig. 5**).

4.4. Alpha-Entropy decomposition

The Alpha-Entropy (H–α) decomposition, derived from an eigenvalue-based target decomposition, reveals overlapping classes that predominantly exhibit surface scattering with intermediate alpha values and comparatively high entropy values under full-polarization mode (**Fig. 6a**). Minimal alpha values correspond to surface scattering typical of flat surfaces, while volume scattering indicates surfaces composed of anisotropic particles.

In the study area, Zones 9 and 6 display surface diffusion processes at low and moderate entropy (H), respectively, within a spatial range of alpha angle values below 42.5°. Zone 9 delineates the drainage system of the Ziz plain, including temporary lakes (Dayat Tamazguidat) and saline crusts of the sebkhas, which occur west of the Erg Chebi in depressions filled with fine, highly saline sediments, reflecting low precipitation and high evaporation. Zone 6 exhibits increased entropy due to variations in surface roughness and reduced alpha angles. This zone comprises diverse continental land surfaces from the Quaternary, flat limestone-to-flint surfaces of the Kem Kem plateau from the Upper Cretaceous, and Pliocene calcareous-sandstone slabs covering the Hamada de Guir.

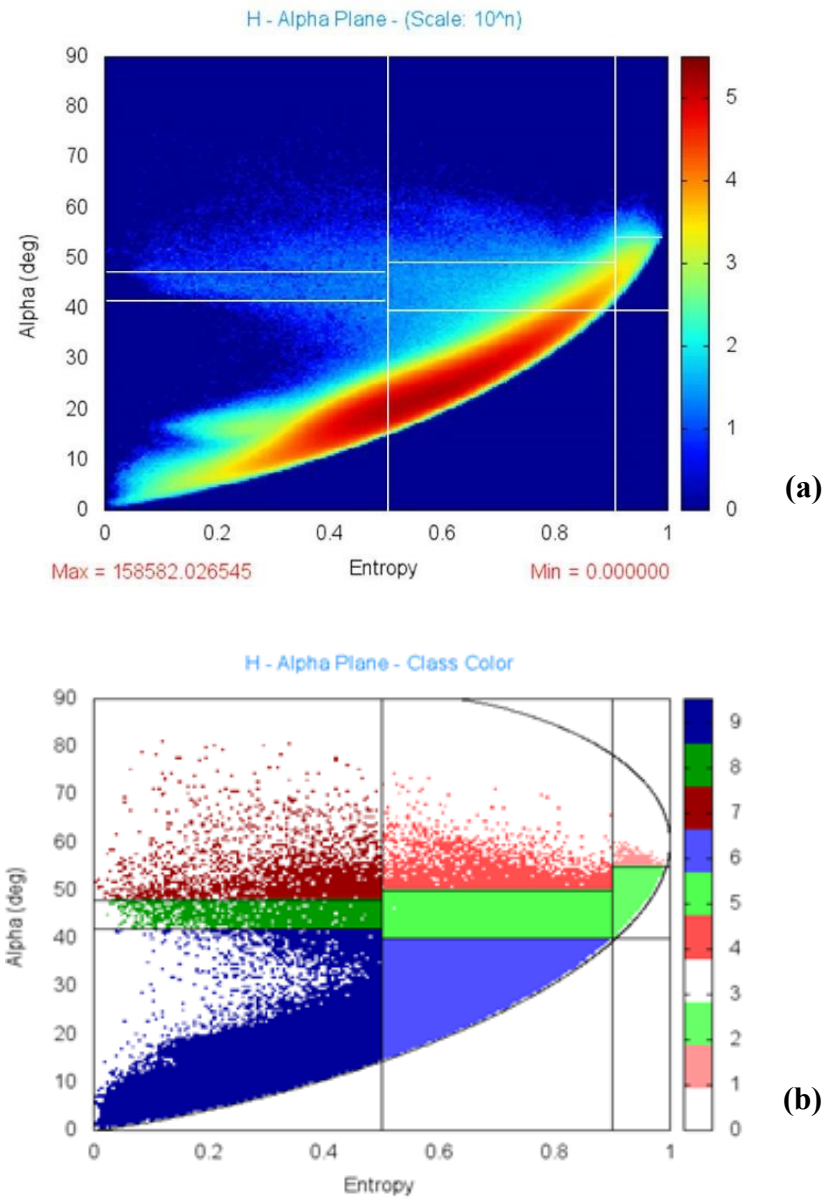


Fig. 6. (a) α-H distribution for scattering mechanism. (b) α-H scattering mechanism identification plane of the study area.

Zones 8 and 5 show predominantly dipolar scattering patterns corresponding to low and moderate entropy values, originating from anisotropic scatterers within the Paleozoic basement clay-sandstone interfaces, exhibiting moderate correlation in their orientations. Zones 7 and 4 correspond to multiple scattering events at low and moderate entropy, respectively, with PolSAR pixels ranging from 47.5° to less than 62°. Zone 7 includes Cretaceous gypsum marls forming cliffs at the Kem Kem plateau edges and Paleozoic relief crests, while sand dunes on Erg Chebi show multiple scattering under low entropy conditions. Zone 4 represents the escarpments of the Hamada de Guir, including Mio-Pliocene conglomerates and sandstones. As entropy increases from 0.6 to 0.9 in this area, alpha values decrease correspondingly to around 55°.

High entropy diffusion processes dominate Zones 2 and 1, resulting from single scattering events by anisotropic particle clouds. Scant vegetation and specific geological formations, particularly clay alteration zones and sand dune crests, further influence these scattering patterns.

The strength of this approach lies in estimating the observed environment type based on a physical interpretation of canonical scattering mechanisms. This is evident in **Fig 6b**, where variations in polarimetric characteristics enable meaningful classification of natural environments. Additionally, the H–α color composite provides detailed information on the polarimetric properties of the scene (**Fig. 7**), with the false-color image highlighting additional rock units and lineaments not visible on the geological map.

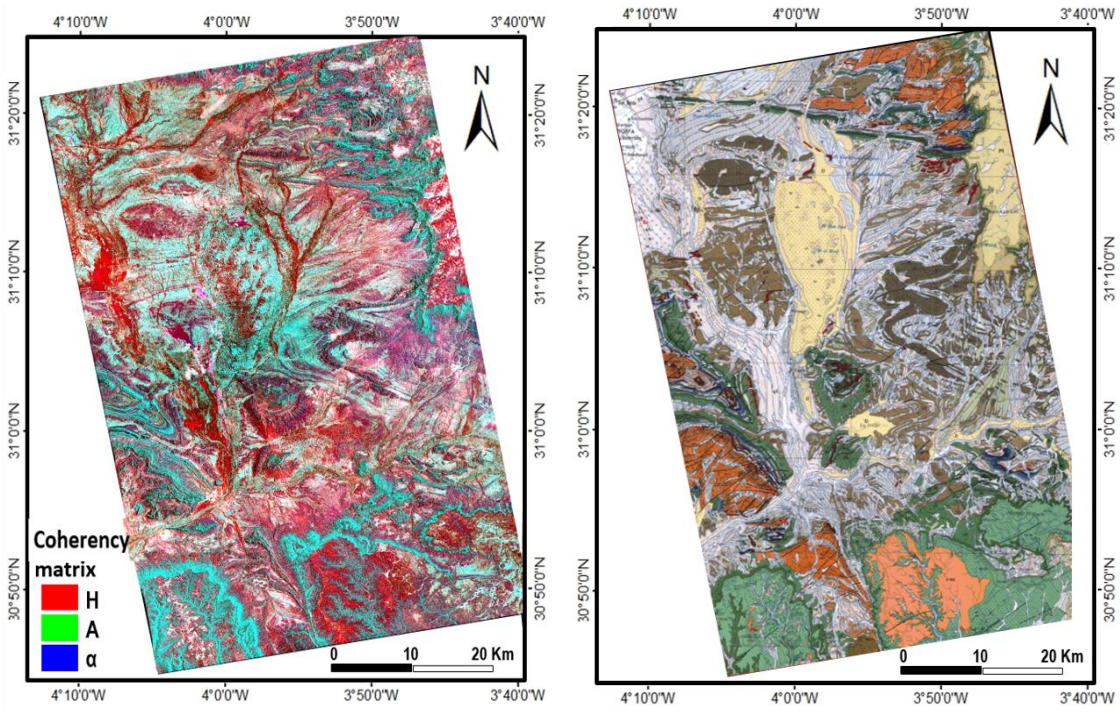


Fig. 7. The Cloude–Pottier decomposition (Red is entropy (H), green is anisotropy (A), blue is alpha angle (α)) and corresponding detailed geological map of Tafilalet-Taouz at 1/200000 (Destombes and Hollard, 1975).

4.5. Pauli RGB

The Pauli RGB image of the study area is presented as a class map, revealing several distinct main units (**Fig. 8**). The central part of the image, corresponding to the Tafilalet plain intersected by the Oued Ziz, displays these units. Blue areas indicate surface scattering, exemplified by the dry valley of Oued Ziz. In this region, the polarimetric channel |HH+VV| shows a high amplitude relative to others, reflecting a weak |HV| amplitude and a phase difference between |HH| and |VV| close to zero. Olive-green dots with elevated green and red components correspond to high |HV| values, indicating volume scattering associated with the crests of sand dunes in Erg Chebi.

In the southern and eastern regions, including the Kem Kem plateau and the Hamada of Guir, the Pauli decomposition shows pronounced multiple scattering, indicative of highly rugged surfaces. Areas appearing black in the Pauli RGB image represent Bragg scattering, where radar signals undergo complete dispersal or attenuation

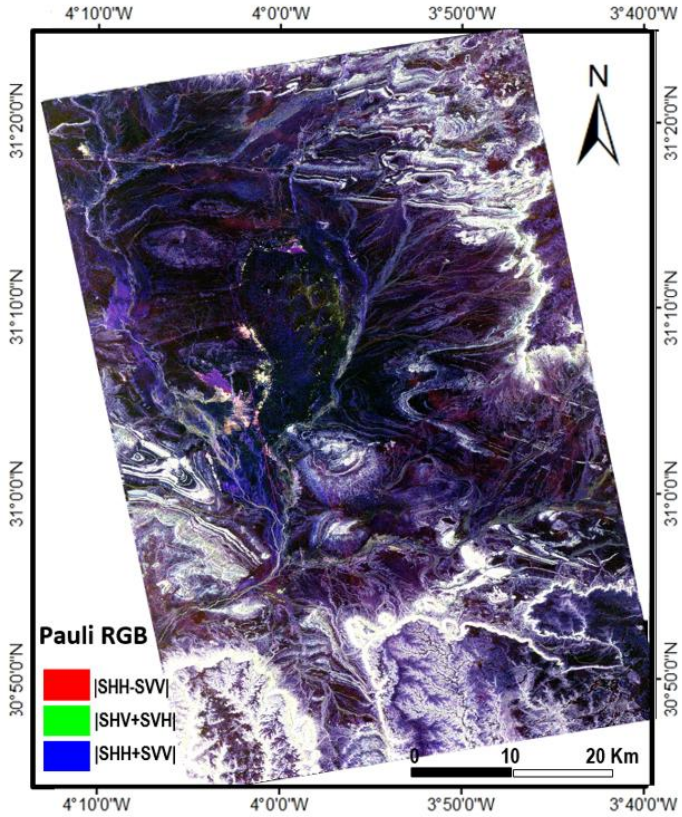


Fig. 8. Pauli-decomposition of the study area.

4.6. The supervised classification of Wishart

The Supervised Wishart Classification identifies eight distinct classes across the study area (**Fig. 9**). This algorithm was applied within each scattering category, producing classes that group pixels exhibiting the same diffusion mechanism (Lee et al., 1999; Lee et al., 2004). The resulting classification effectively distinguishes surface types and scattering behaviors, providing a detailed characterization of the geological and geomorphological units in the Tafilalet plain and surrounding regions.

4.7. Polarization Signatures

The co-polarization and cross-polarized signatures derived from ALOS/PALSAR-2 of distinct geological units within the Tafilalet plain, which include dune-associated coarse sands, clayey sandstone, sandstone and conglomerates, shale-sandstone, exposed limestone surfaces, fine-grained erosion sediments (aeolian sands), terrace sediments and salt crusts, water bodies, and vegetation (**Fig. 10**).

Sand dunes. The pedestal height range of this class extends from a maximum of -26.54 dB to a minimum of -31.21 dB for the co-polarized channel and from a maximum of -27.88 dB to a minimum of -35.68 dB for the cross-polarized channel. The mean values of its alpha (a°), entropy (H), and anisotropy (A) are 26.302, 0.623, and 0.368, respectively, with standard deviations of 6.286, 0.110, and 0.114 (**Table 1**). Its polarization response exhibits angles near ($\psi = 0°$), indicating a dominance of vertically aligned scatterers. The maximum response is higher at HH than at VV, with the maximum of this signature shifted from the horizontal to the vertical position. The ellipticity angle is 0°, denoting linear polarization.

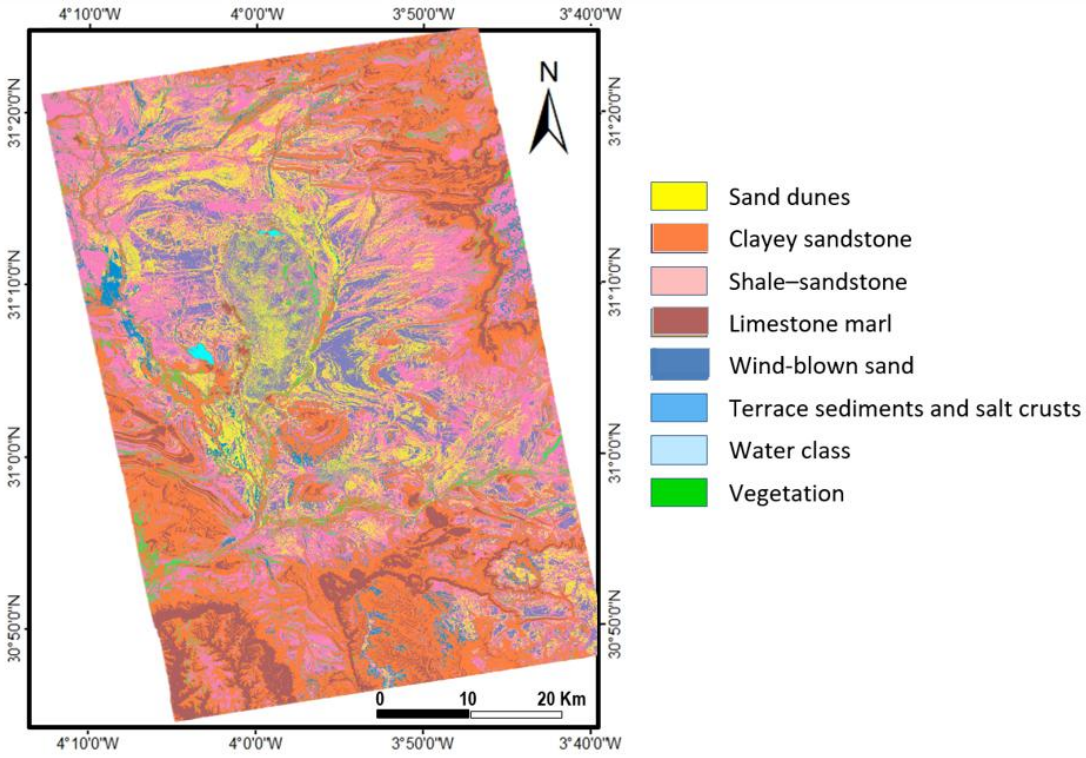


Fig. 9. The supervised Wishart classification of the study area.

Clayey sandstone. The pedestal height of this class exhibits a maximum of -6.68 dB and a minimum of -37.11 dB for the co-polarized channel and a maximum of -6.77 dB and a minimum of -42.59 dB for the cross-polarized channel, values which closely approach the noise floor system of the PALSAR sensor. The mean values of its alpha (a°), entropy (H), and anisotropy (A) are 21.482, 0.511, and 0.325, respectively, with standard deviations of 6.212, 0.123, and 0.120 (**Table 1**). The polarization response reveals angles near ($\psi = 90^{o}$), signifying a preponderance of vertically oriented scatterers, and exhibits a maximum response higher at VV than at HH, with the maximum of this signature shifted from the vertical to the horizontal position. The ellipticity angle of 0° indicates linear polarization.

Shale–sandstone. The pedestal height of this category exhibits a maximum of -17.30 dB and a minimum of -25.32 dB for the co-polarized channel and a maximum of -18.54 dB and a minimum of -30.33 dB for the cross-polarized channel. Analysis of the polarization response reveals that angles approximating ($\psi = 0^{o}$) denote a preponderance of scatterers oriented vertically. Furthermore, the maximum response is greater for HH than for VV, exhibiting a shift from the horizontal to the vertical position for the maximum of this signature. The ellipticity angle of 0° indicates linear polarization.

Limestone marl. The baseline height for this class exhibits a maximum value of -5.26 dB and a minimum value of -21.66 dB for the co-polarized channel, while the cross-polarized channel presents a maximum value of -7.06 dB and a minimum value of -29.52 dB. The mean values of its alpha (a°), entropy (H), and anisotropy (A) are 23.177, 0.559, and 0.278, respectively, with corresponding standard deviations of 6.726, 0.127, and 0.120 (as detailed in **Table 1**). The polarization response reveals that angles approaching ($\psi = 90°$) signify a preponderance of vertically oriented scatterers. The maximum response is more pronounced at VV than at HH, exhibiting a shift from vertical to horizontal alignment. The ellipticity angle of 0° indicates linear polarization characteristics.

Wind-blown sand. The pedestal height for this class exhibits a maximum value of -21.61 dB and a minimum value of -30.07 dB for the co-polarized channel. The cross-polarized channel exhibits a

maximum value of -23.12 dB and a minimum value of -33.83 dB. Statistical analysis reveals mean values of 18.343, 0.473, and 0.342 for alpha (a°), entropy (H), and anisotropy (A), respectively. Standard deviations for these parameters are 3.563, 0.075, and 0.106, respectively (**Table 1**). The polarization response indicates a predominance of vertically oriented scatterers ($\psi = 0^{o}$), with a maximum response observed at HH polarization. This maximum response is shifted towards the vertical position compared to VV polarization. The ellipticity angle of 0° implies linear polarization.

Terrace sediments and salt crusts. The pedestal height for this class spans from a maximum of -21.19 dB to a minimum of -43.33 dB for the co-polarized channel, while ranging from -14.28 dB to -32.34 dB for the cross-polarized channel. The polarization response indicates that angles approaching 90 degrees, signifying a preponderance of vertically oriented scatterers, yield the highest maximum response for the VV polarization relative to the HH polarization. Notably, the maximum of this signature exhibits a shift from the vertical to the horizontal plane for the HH polarization.

Water class. The pedestal height of this class exhibits a maximum of -11.76 dB and a minimum of -27.34 dB for the co-polarized channel, while the cross-polarized channel exhibits a maximum of -14.28 dB and a minimum of -32.34 dB. The mean values of its alpha (α°), entropy (H), and anisotropy (A) are 16.6, 0.296, and 0.350, respectively, with standard deviations of 2.772, 0.089, and 0.114 (**Table 1**). The polarization response indicates a predominance of vertically oriented scatterers, with a stronger response at VV than at HH. This suggests a deviation of the maximum response from the vertical to the horizontal position. The ellipticity angle is 0°, indicating linear polarization, which is consistent with the conventional Bragg scattering mechanism for water.

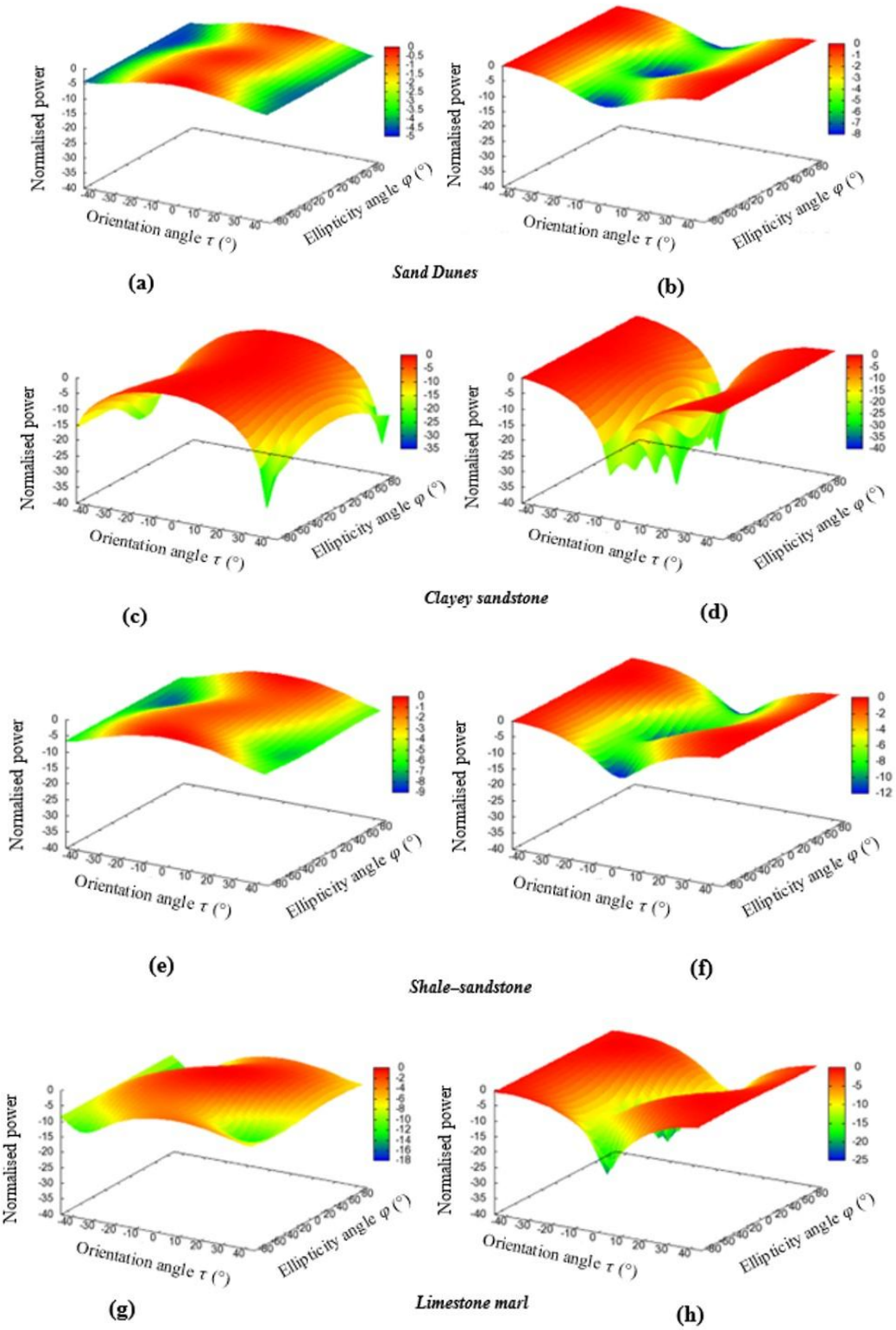
Vegetation. The pedestal height for this class exhibits a maximum of -16.63 dB and a minimum of -25.89 dB for the co-polarized channel, and a maximum of -17.91 dB and a minimum of -30.06 dB for the cross-polarized channel. The mean values of its alpha (a°), entropy (H), and anisotropy (A) are determined as 18.343, 0.603, and 0.363, respectively, with corresponding standard deviations of 6.944, 0.118, and 0.117 (refer to **Table 1** for detailed values).

Table 1.

The SAR scattering responses of all classes covering the study area.

Classes	**Area Km²**	**SAR Scattering Mechanism**					
		Alpha(a)		**Entropy (H)**		**Anisotropy (A)**	
		Mean	**STD**	**Mean**	**STD**	**Mean**	**STD**
Sand Dunes	609,1	36,302	6,286	0,623	0,110	0,368	0,114
Clayey sandstone	506,2	21,482	6,212	0,511	0,118	0,325	0,120
Shale–sandstone	811,3	19,738	4,022	0,474	0,080	0,367	0,112
Limestone marl	359,9	23,177	6,726	0,559	0,127	0,278	0,119
Wind-blown Sand	203,4	18,343	3,563	0,473	0,075	0,342	0,106
Terrace sediments and salt crusts	119,4	12,203	3,350	0,332	0,078	0,353	0,111
Water	7,3	16,623	2,772	0,296	0,0819	0,350	0,114
Vegetation	144,7	25,269	6,944	0,603	0,123	0,363	0,117

***Note**: Values are expressed in decibels (dB). STD = standard deviation.*


Normalised power
Orientation angle τ (°)
Ellipticity angle φ (°)
(a)
(b)
Sand Dunes
(c)
(d)
Clayey sandstone
(e)
(f)
Shale–sandstone
(g)
(h)
Limestone marl

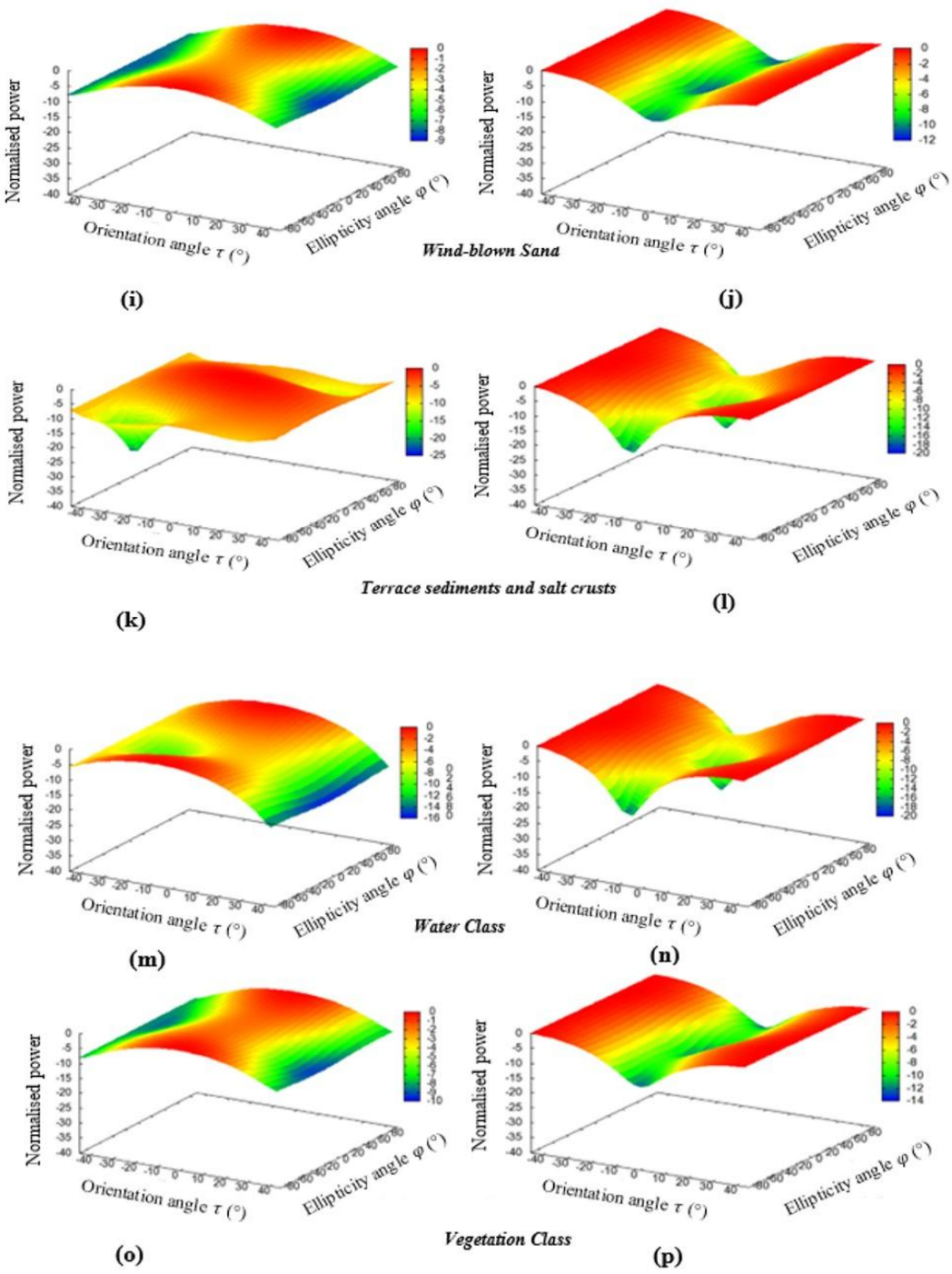


Fig. 10. Polarization signatures of different geological units of the Tafilalet : (a,c,e,g,i,k,m,p) Co-polarization signature and (b,d,f,h,j,l,n,o) Cross-polarization signature.

5. DISCUSSION

The investigated region, a desert characterized by prominent outcrops devoid of vegetation cover, exhibits four contrasting geomorphic domains. To the west and north, regions with substantial relief, akin to the Appalachian Mountains, correspond to the Paleozoic sequence dating from the Ordovician to Devonian periods. The central area encompasses the alluvial plain of Oued Ziz, overlying bedrock belonging to the later Paleozoic folded series of Lower Carboniferous to Visean age, which is further concealed by a notable dune system, namely the Erg Chebbi and Erg Znaigui. Extending southward and eastward are the Kem Kem Plateau and the Hamada de Guir. The exposed terrains comprise Ordovician sandstones (First Bani, Ktaoua Formation, and Second Bani), Silurian clay-limestone sequences, limestones and marly limestones (Erfoud Group, Tafilalet Group), and Devonian sandstones (Taouz Group), along with detrital deposits (claystones, siltstones, and sandstones) from the Lower Carboniferous to Visean periods. The overlying strata include undeformed sedimentary rocks from the Cretaceous and Tertiary periods on the Kem Kem Plateau, capped by a continental Miocene complex and, further eastward, a Pliocene limestone cover on the Hamada du Guir (Benharref et al., 2014). The Quaternary epoch is marked by a diverse array of continental surface formations, including interlocked glacis-terrace systems, loamy, halomorphic, and sebkha soils, and a well-developed dune system. These formations, whether associated with elevated regions (glacis) or valleys (terraces, halomorphic soils, dunes), reflect the distinct climatic conditions characteristic of this sub-Saharan environment.

These varying surface roughness characteristics lead to distinct scattering mechanisms of synthetic aperture radar (SAR), enabling more precise delineation of geological units by incorporating lithological information obtained from multispectral sensors. Eight distinct class categories are clearly identified for the first time based on their polarization indices, Pauli decomposition, and polarization signatures:

Sand dunes. Aeolian sands correspond to mobile sandy accumulations and outcrop in the dunes of Erg Znaigui and Erg Chebi (**Fig. 11a**). The highest dunes attain an elevation of approximately 150 m above the surrounding plain. Locally, the dune crests exhibit random to volume diffusion, characterized by elevated HV values relative to other channels.

Clayey sandstone. They correspond in the field to the coarse-grained sandstones and conglomerates of the Upper Cretaceous period, the micaceous sandstones and pelites of the Upper Devonian period, and the sandstones and argillite-sandstones of the Tachilla formations, Bani Group, and upper Ktaoua formation of the Ordovician period (**Fig. 11b**). These deposits exhibit primarily dipolar diffusion at moderate entropy, characterized by a moderate correlation in the orientations of the scatterers. Additionally, the response shows a stronger maximum at VV polarization than at HH polarization, indicative of linear polarization.

Shale–sandstone. These formations, belonging to the Visean age, constitute the base of the Tafilalet plain. They comprise the Oued Znaïgui formation, characterized by 300-500 m of gray-green micaceous pelites and sandstones (**Fig. 11c**), the Mardani formation, consisting of 400-700 m of dark gray clayey shales intercalated with sandstone; and the Mougui-Ayoun formation, featuring sandstones intercalated with shales. The maximum response occurs at HH polarization, exceeding that at VV polarization. Notably, the maximum response shifts from the horizontal to vertical direction. Furthermore, the ellipticity angle of 0° signifies linear polarization.

Limestone and marl-limestone. They correspond to the limestone to marl-limestone sequence of the Upper Devonian of Tafilalet (Achguig Formation approximately 350 m thick in the reliefs west of Oued Ziz), the flint limestones, bedded limestones, and marls of the Upper Cretaceous of Kem Kem plateau (**Fig. 11b**), south of the study area, and the Pliocene limestone covering slab of the Hamada du Guir. The Pauli decomposition results reveal very strong multiple scattering and double rebound scattering, suggesting the presence of very rough and blocky surfaces.

Wind-blown Sand. These deposits are present in both the beds of wadis and secondary ravines, composed of pebbles and gravel with an unconsolidated silty-clay fraction to which a sandy fraction is added due to wind transport. This sandy contribution can evolve into small dunes depending on the

strength of the wind and the presence of local obstacles (**Fig. 11d**). These deposits exhibit moderate entropy and a rougher surface consisting of more rugged and weathered rocks. In certain areas, these sands occupy relatively smooth open water surfaces, producing single-bounce scattering with more variation between all polarization responses.

Terrace sediments and salt crusts. These saline crusts, which are found in depressions filled by fine, highly saline sediments, are located within the Oued Ziz valley). Their accumulation is attributed to the combination of low precipitation and high evaporation rates. These facies exhibit low entropy and correspond to pure targets characterized by exposed soil and minimal surface roughness.

Water class. The water surfaces of the temporary lakes located west and north of Erg Chebbi display Bragg-type scattering, which indicates a Bragg scattering of signals.

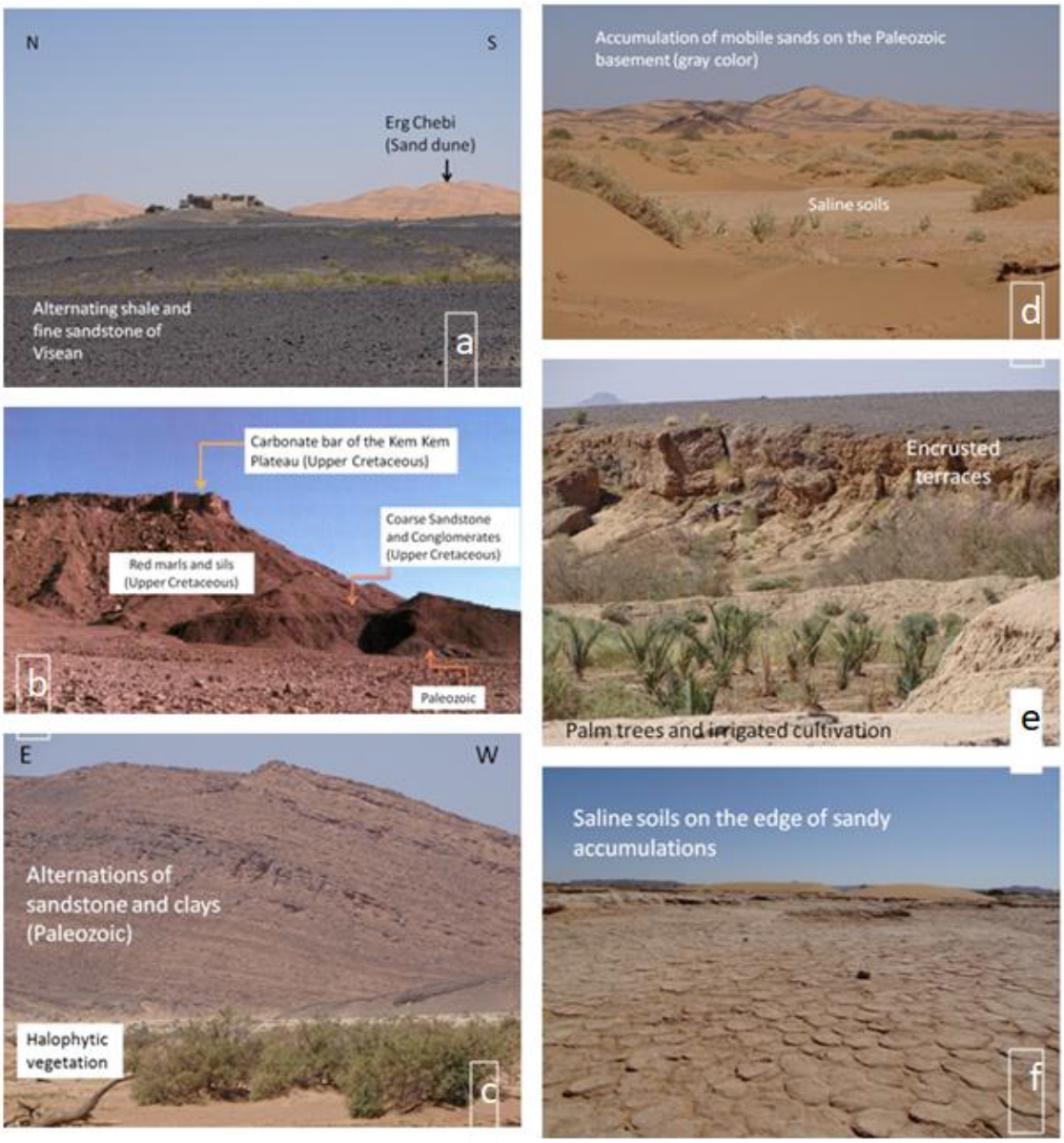


Fig. 11. Field photos of the different geological units along the study area.

Vegetation. This halophytic vegetation, encompassing samphire, tamarisk, palm trees, and irrigated cultivation, represents the natural flora that flourished in these narrow valleys. Essential to its development were the small water bodies and alluvial soil, which became enriched with organic matter over time.

It is noteworthy that the investigated terrains are situated within regions of moderate anisotropy (ranging from 0.32 to 0.36). Consequently, the surfaces under examination exhibit a propensity towards diffusion-dominated mechanisms, with an equivalent likelihood of manifestation on surfaces characterized by varying degrees of entropy.

6. CONCLUSION

In this study, surface land cover in the Tafilalet plain and surrounding areas was classified using ASTER and full-polarimetric SAR images. The integration of various polarimetric decomposition techniques significantly improved the classification results. Full-polarimetric data acquired by ALOS/PALSAR-2 demonstrated superior detection capabilities compared to optical imagery, providing clearer discrimination of lithological units, while ASTER images showed lower contrast and ambiguities due to spectral limitations and shadowing. Quantitative accuracy assessment was limited by the availability of ground-reference data.

The classification process employed L-band polarimetric signatures from ALOS/PALSAR-2, including decomposition into entropy, alpha, and anisotropy values, Alpha-Entropy analysis to identify dominant scattering mechanisms, Entropy-Anisotropy-Alpha color composites to examine the geometry of rock units, and Pauli decomposition to separate the three main scattering mechanisms. The supervised Wishart algorithm was applied as an object-based classifier.

For the first time in this arid desert region, polarimetric signatures were established for eight land cover classes, grouped into three roughness categories. Low-roughness surfaces include dry valleys and aeolian sand deposits, moderate-roughness surfaces correspond to sandstone–clay, shale, and limestone terrains, and very rough surfaces with multiple scattering are associated with sand dune ridges. These results highlight the strong potential of SAR polarization signatures for characterizing surface roughness and the morphological properties of geological units. The classification based on full-polarimetric SAR data showed a high consistency with official geological maps, demonstrating superior accuracy compared to optical image-based classification.

REFERENCES

Benharref, M., Alvaro, J.J., Hibt, M., Pouclet, A., El Hadi, H. & Boudad, L. (2014) Carte géologique du Maroc au 1/50 000, feuille Marzouga. *Notes et Mémoires du Service Géologique du Maroc*, No. 553, 119 p.

Boerner, W.M. (2004) Recent advances in radar polarimetry and polarimetric SAR interferometry. Paper presented at the *RTO SET Lecture Series on Radar Polarimetry and Interferometry*. http://dx.doi.org/10.1016/j.asr.2017.04.018

Boerner, W.M., Cloude, S.R., (2002) Radar polarimetry and interferometry: Past, present and future trends. *Proceedings of the XXVIIth General Assembly of the International Union of Radio Science (URSI)*, Maastricht Exhibition and Congress Centre, The Netherlands, 17–24 August 2002.

Boerner, W.M., et al. (1985) *Inverse Methods in Electromagnetic Imaging.* Proceedings of the NATO Advanced Research Workshop, Bad Windsheim, FR Germany, 18–24 September 1983, Parts 1 & 2, NATO-ASI C-143, D. Reidel Publishing Co. https://doi.org/10.1007/978-94-009-5271-3

Cloude, S.R. & Pottier, E. (1996) A review of target decomposition theorems in radar polarimetry. *IEEE Transactions on Geoscience and Remote Sensing*, 34(2), 498–518. https://doi.org/10.1109/36.485127

Cloude, S.R. & Pottier, E. (1997) An entropy-based classification scheme for land applications of polarimetric SAR. *IEEE Transactions on Geoscience and Remote Sensing*, 35, 68–78. https://doi.org/10.1109/36.551935

Cloude, S.R. (1999) Eigenvalue parameters for surface roughness studies. *Proceedings of SPIE – International Society for Optics and Photonics*, 3754, 2–13.

Cooley, T., Anderson, G.P., Felde, G.W., Hoke, M.L., Ratkowski, A.J., Chetwynd, J.H., Gardner, J.A., Adler-Golden, S.M., Matthew, M.W., Berk, A., Bernstein, L.S., Acharya, P.K., Miller, D. & Lewis, P. (2002) FLAASH, a MODTRAN4-based atmospheric correction algorithm, its application and validation. *Proceedings of the IEEE International Geoscience and Remote Sensing Symposium (IGARSS '02)*, 1413–1418. https://doi.org/10.1109/IGARSS.2002.1026134

Deschamps, G.A. (1951) Geometrical representation of the polarization of a plane electromagnetic wave. *Proceedings of the IRE*, 39, 540–544.

Destombes, J. & Hollard, H.C. (1975) Carte géologique du Maroc, Tafilalt–Taouz au 1/200 000. *Notes et Mémoires du Service Géologique du Maroc*, No. 244.

Joly, F. (1962) *Étude sur le relief du Sud-Est marocain.* Travaux de l'Institut Scientifique Chérifien, Série Géographie Physique, 10, Rabat, 578 p.

Lee, J.S. & Pottier, E. (2009) *Polarimetric radar imaging: From basics to applications.* CRC Press, New York. https://doi.org/10.1201/9781420054989

Lee, J.S., Grunes, M.R., Pottier, E. & Ferro-Famil, L. (2004) Unsupervised terrain classification preserving polarimetric scattering characteristics. *IEEE Transactions on Geoscience and Remote Sensing*, 42, 722–731. https://doi.org/10.1109/TGRS.2004.836769

Lee, J.S., Grunes, M.R. & Kwok, R. (1994) Classification of multi-look polarimetric SAR imagery based on complex Wishart distribution. *International Journal of Remote Sensing*, 15(1), 2299–2311. https://doi.org/10.1080/01431169408954244

Lee, J.S., Grunes, M.R., Ainsworth, T.L., Du, L.J., Schuler, D.L. & Cloude, S.R. (1999) Unsupervised classification using polarimetric decomposition and the complex Wishart classifier. *IEEE Transactions on Geoscience and Remote Sensing*, 37(5), 2249–2258. https://doi.org/10.1109/36.789621

Lee, J.S., Wen, J.H., Ainsworth, T., Chen, K.S. & Chen, A.J. (2008) Improved sigma filter for speckle filtering of SAR imagery. *IEEE Transactions on Geoscience and Remote Sensing*, 47, 202–213. https://doi.org/10.1109/TGRS.2008.2002881

López-Martínez, C. & Pottier, E. (2021) Basic principles of SAR polarimetry. In: Hajnsek, I. & Desnos, Y.-L. (eds.) *Remote Sensing and Digital Image Processing*, Vol. 25, 1–58. Springer, Cham. https://doi.org/10.1007/978-3-030-56504-6

Lu, D. & Weng, Q. (2007) A survey of image classification methods and techniques for improving classification performance. *International Journal of Remote Sensing*, 28, 823–870. https://doi.org/10.1080/01431160600746456

Mattia, F. & Le Toan, T. (1999) Backscattering properties of multi-scale roughness surfaces. *Journal of Electromagnetic Waves and Applications*, 13, 491–526. https://doi.org/10.1163/156939399X00240

Michard, A., Frizon de Lamotte, D., Liégeois, J.P., Saddiqi, O. & Chalouan, A. (2008) Conclusion: Continental evolution in western Maghreb. In: Michard, A., Saddiqi, O., Chalouan, A. & Frizon de Lamotte, D. (eds.) *Continental Evolution: The Geology of Morocco. Lecture Notes in Earth Sciences*, 119, 395–404. Springer, Berlin.

Oliver, C. & Quegan, S. (2004) *Understanding synthetic aperture radar images.* SciTech Publishing, Raleigh.

Qi, Z., Yeh, A.G.O., Li, X. & Lin, Z. (2012) A novel algorithm for land use and land cover classification using RADARSAT-2 polarimetric SAR data. *Remote Sensing of Environment*, 118, 21–39. https://doi.org/10.1016/j.rse.2011.11.001

Vanzyl, J.J., Zebker, H.A. & Elachi, C. (1987) Imaging radar polarization signatures: theory and observation. *Radio Science*, 22(4), 529–543. https://doi.org/10.1029/RS022i004p00529

Varghese, A.O. & Joshi, A.K. (2014) Polarimetric classification of C-band SAR data for forest density characterization. *Current Science*, 108(1), 100–106.

Woodhouse, I.H. (2006) *Introduction to microwave remote sensing.* Taylor & Francis, Boca Raton. https://doi.org/10.1201/9781315272573

ADVANCING LOW-COST MANGROVE ECOSYSTEM MAPPING: PRECISION VALIDATION OF IPHONE 12 PRO LIDAR FOR DTM GENERATION ACROSS CANOPY DENSITY GRADIENT

Sigit Bayhu IRYANTHONY [1], *Anindya WIRASATRIYA* [2*], *Rudhi PRIBADI* [3] & *Pujiono Wahyu PURNOMO* [4]

DOI: 10.21163/GT_2026.211.18

ABSTRACT

Precise Digital Terrain Models (DTMs) are essential for mangrove carbon accounting and Measurement, Reporting, and Verification (MRV) frameworks that facilitate climate change mitigation. Although airborne photogrammetry and LiDAR are frequently employed for terrain extraction, their utilization in dense mangrove wetlands is limited by elevated expenses and operational intricacies. This work offers a novel assessment of the iPhone 12 Pro LiDAR sensor as an economical and portable option for Digital Terrain Model (DTM) development in mangrove ecosystems, filling a significant void in accessible carbon monitoring technology. Utilizing the 3D Scanner App for iOS, the study gathered data from 12 locations (55 points per location) encompassing open regions, sparse canopies, and dense canopies, corroborated by 660 NRTK positioning points. The precision of the LiDAR-derived Digital Terrain Model (DTM) was assessed by extensive statistical criteria, such as Root Mean Square Error (RMSE), Mean Absolute Error (MAE), Bias, Pearson correlation coefficient, and 95% confidence intervals, thereby ensuring rigorous validation of consumer-grade mobile LiDAR for high-resolution topographic mapping. The results indicated exceptional accuracy in open environments (MAE < 0.1 m, negligible RMSE and bias), moderate precision in sparse canopies (MAE 0.086-0.381 m), and diminished performance in dense vegetation (MAE up to 1.064 m, positive bias of 0.928 m). Statistical analysis indicated negligible elevation fluctuation in open areas, however substantial outliers were seen in dense canopies. Regression analysis indicated a robust association in open areas (R^2 = 0.956), a moderate correlation in sparse vegetation (R^2 = 0.799), and a lesser correlation in dense canopies (R^2 = 0.663), implying possibility for enhancement by allometric modifications. Although professional LiDAR systems exhibit superior accuracy, the iPhone LiDAR is a pragmatic and cost-effective option for Digital Terrain Model production in open to moderately vegetated regions. The system's portability and affordability render it especially advantageous for ecological monitoring and geoscientific applications in resource-constrained environments, however dense vegetation poses significant challenges. These findings underscore the capability of consumer-grade LiDAR technology to facilitate precise environmental monitoring while markedly decreasing expenses relative to professional systems.

Keywords: *LiDAR; IPhone; DTM; Mangrove; Allometric.*

1. INTRODUCTION

Mangroves are salt-tolerant vegetation, comprising trees and shrubs, that flourish in coastal salty or brackish aquatic ecosystems (Shapiro, 2024). Mangrove has essential role for coastal region as the protector from great waves energy (Arnaud et al., 2023). Mangroves also offer the feeding and nursery

[1]*Doctoral Program of Aquatic Resources Management, Faculty of Fisheries and Marine Sciences, Universitas Diponegoro. Semarang, Indonesia; sigitbayhuiryanthony@gmail.com*
[2*]*Department of Oceanography, Faculty of Fisheries and Marine Science, Universitas Diponegoro, Semarang, Indonesia. Corresponding author: anindyawirasatriya@lecturer.undip.ac.id*
[3]*Department of Marine Science, Faculty of Fisheries and Marine Science, Universitas Diponegoro, Semarang, Indonesia; rudhipribadi@gmail.com*
[4]*Department of Aquatic Resource Management, Universitas Diponegoro, Semarang, Indonesia; purnomopoed@gmail.com*

ground for marine live cycle through its large and branched roots (Sasmito et al., 2023; Suwa et al., 2021). Its density coverage contributes to enhance carbon accumulation in coastal areas due to their advantageous intertidal location (Alongi, 2022; S. Song et al., 2023; Basyuni et al., 2023; Wirasatriya et al., 2022). Kauffman et al. (2018) discovered that mangroves possess a significantly greater carbon stock compared to terrestrial forests. This is attributed to their capacity to store more carbon both in their above-ground biomass and below the surface in their roots and sediment (e.g., Mcleod et al. 2011; Donato et al. 2011, 2012). The measurement of carbon biomass offers critical insights into facilitating biodiversity conservation and climate change mitigation initiatives (Amelia et al., 2023; Paul et al., 2023; Wainwright et al., 2023). Unfortunately, mangrove forests have historically experienced substantial reductions, decreasing from 225,000 km^2 in the 1970s to 137,000 km^2 by 2014, mostly owing to deforestation and deterioration (Friess et al., 2019; Lovelock et al., 2022). This loss has resulted in negative consequences (Arifanti et al., 2022), including weakened coastal protection, lower fisheries, heightened greenhouse gas emissions, and decreased ecosystem services such as nutrient cycling, which also impacts neighboring ecosystems like coral reefs and seagrass meadows (Bimrah et al., 2022; Friess et al., 2019).

The integration of satellite imagery with UAV-based photogrammetry is growing as an efficient technique for evaluating biomass in mangrove forests (Gao et al., 2022; Hu et al., 2020; Tian et al., 2023). Photogrammetry generates aerial photos, Digital Surface Models (DSM), and Digital Terrain Models (DTM) (Amuyou et al., 2022; Chan et al., 2021). Unfortunately, Digital Terrain Models generated by drones is limited in precision for wetland (tidal) regions. Basyuni et al., (2023) and Wirasatriya et al., (2022) utilize a Global Navigation Satellite Survey (GNSS) to develop a digital terrain model that facilitates the generation of canopy height models. Nevertheless, GNSS accuracy will decrease within the dense mangrove, resulting in a range of 0.6 to 10 meters. (Feng et al., 2021; Tomaštík & Everett, 2023). The other method options at the millimeter scale, void of canopy and signal constraints, may employ a water pass measurement or electronic total station; however, it necessitates more surveyors and a substantial expenditure (Jurado et al., 2020; Krause et al., 2019; Lynch et al., 2024). Thus, the DTM measurement causes the AGB investigation more costly and challenging for novice researchers with constrained financial resources.

Commencing in the 2020’s iPhone integrated the Light Detection and Ranging (LiDAR) sensor in both the iPhone and iPad Pro (Corradetti et al., 2022), utilized for measurement and 3D object scanning (Luetzenburg et al., 2021; B. Song et al., 2023; Teppati Losè et al., 2022). This concept has attracted significant attention in both consumer and professional domains, especially for uses in geosciences, historical documentation, and digital mapping (Kottner et al., 2023; Mêda et al., 2023). Initial assessments, like those by (Vogt et al., 2021a) and (Murtiyoso et al., 2021), have contrasted precision with the conventional techniques such as terrestrial laser scanning (TLS) and close-range photogrammetry. These studies illustrate that the iPhone 12 Pro LiDAR's is potential for particular applications, including industrial 3D scanning and heritage preservation (Teppati Losè et al., 2022), however it exhibits limitations in accuracy and elevated point cloud noise (Gollob et al., 2021a; Teo & Yang, 2023). Implementing LiDAR into mobile devices represents a significant advancement in the accessibility of advanced geospatial data collection for all individuals. This is particularly crucial in extreme situations (Teo & Yang, 2023), such as the identification of forests and wetland regions, where further research is evidently required (Gollob et al., 2021a).

The estimation of above-ground biomass (AGB) in mangrove ecosystems presents significant challenges, particularly in topographic mapping due to the dense canopy coverage (Basyuni et al., 2023; Wirasatriya et al., 2022). Traditional methods rely heavily on GNSS and interpolation data to construct Digital Terrain Models (DTMs) (Li et al., 2023; Raza et al., 2023), yet these techniques often suffer from high bias and poor signal reception due to canopy obstruction (Tong et al., 2023). In this context, the integration of the iPhone 12 Pro LiDAR offers a promising alternative for efficient, compact, and instant topographic scanning (Corradetti et al., 2022; Di Stefano et al., 2021). Capable of capturing point clouds at approximately 9,745 points per square meter, the iPhone 12 Pro LiDAR provides a convenient solution for dense canopy environments, though its point density is considerably lower than that of traditional terrestrial laser scanning (TLS) systems, which can achieve

around 469,856 points per square meter (Razali et al., 2022; Teppati Losè et al., 2022). Despite its potential, the application of iPhone 12 Pro LiDAR for AGB estimation, particularly in DTM development, remains underexplored. Nonetheless, with the growing adoption of LiDAR-equipped smartphones in multidisciplinary science, there is significant promise for advancing the accuracy and accessibility of mangrove ecosystem assessments.

Referring (Giri et al., 2011), Indonesia encompasses more than 3.39 million hectares of mangrove forests, representing roughly 22% of the global mangrove area. Estimating biomass in these environments is difficult (Basyuni et al., 2023; Wirasatriya et al., 2022), mostly due to GNSS field surveying limitations in marshes and forests, such as signal obstruction, multipath errors, and atmospheric influences (Tomaštík & Everett, 2023; Yang et al., 2020). This research seeks to address these issues by developing and validating novel allometric models that calibrate iPhone LiDAR-derived Digital Terrain Models (DTMs) for mangrove ecosystems and forests. This project aims to enhance the accuracy of allometric correction and the utilization of cost-effective LiDAR data for generating Digital Terrain Models (DTM) for biomass evaluation and various topographic applications. This is achieved by combining high-precision GNSS-RTK data with the characterization of mangrove canopy density. This will enhance environmental monitoring in complex coastal and forest ecosystems, making it more efficient and economical.

2. STUDY AREA

The study was conducted in Rembang Regency, focusing on the villages of Pasar Banggi, Tireman, and Kabongan Lor (6° 42'7.01"S - 111° 22'51.76"E, **Fig. 1**). This region encompasses approximately 36 to 45 hectares over a 3.8 km coastal line.

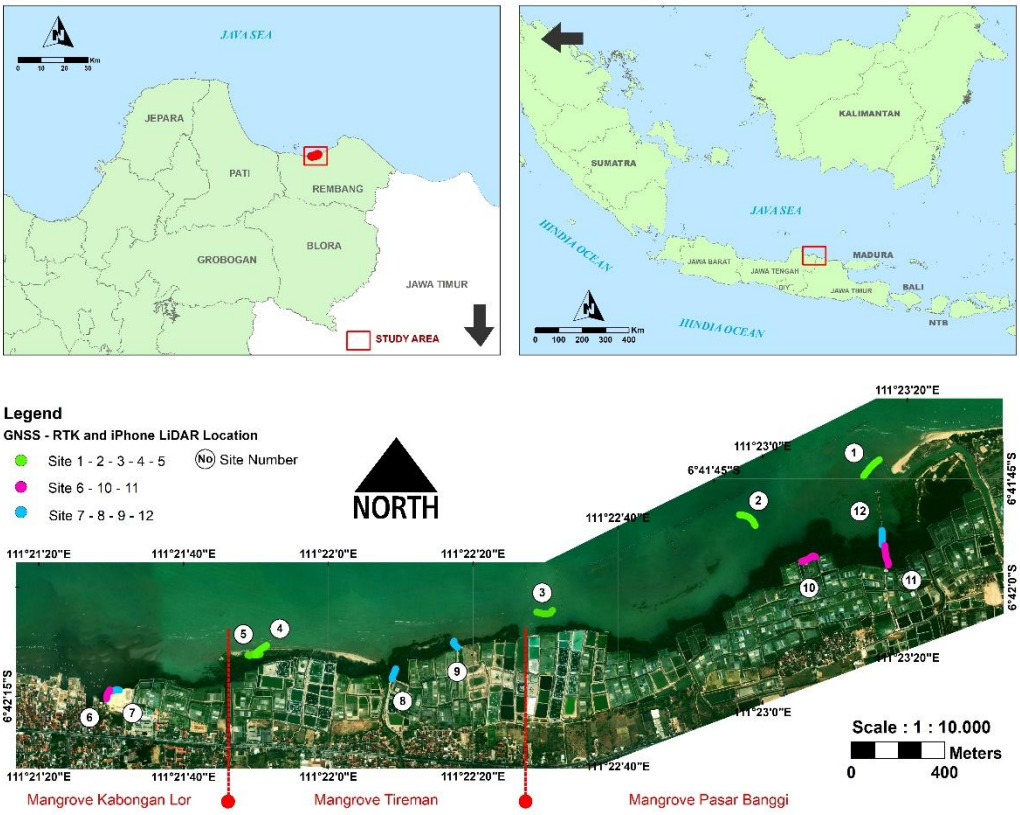


Fig. 1. Research location in Pasarbanggi, Tireman, and Kabonganlor, this site study 1-2-3-4-5 around the sand beach when the sea low tide, 6-10-11 in Dense mangrove canopy and 7-8-9-12 in Thin mangrove canopy.

This region is ever evolving and features a combination of sandy beaches, mudflats, rehabilitated mangrove forests, aquaculture ponds, and adjacent industrial facilities (Iryanthony, et al., 2025). The mangrove region comprises six primary tree species: Rhizophora apiculata, R. mucronata, R. stylosa, Avicennia marina, Excoecaria agallocha, Sonneratia. R. apiculata and R. mucronata are the predominant species, indicating the efficacy of the region's conservation initiatives (Iryanthony, et al., 2025; Iryanthony, et al., 2025; Soeprobowati et al., 2024).

The region comprises four distinct zones: the ocean, sandy shoreline, mangrove salt ponds, and populated areas, exemplifying a complex and diverse coastal environment (Bagas et al., 2024; Mustofa et al., 2023). The data collecting process occurred from October 11 to 14, 2024. The tidal dynamics in the coastal region of Rembang Regency indicated a rising tide began at 01:03 WIB, peaking at 04:22 WIB, followed by the ebb phase initiating at approximately 07:45 WIB and attaining the lowest tide point at 11:18 WIB. This tidal pattern is a component of the daily cycle shaped by the gravitational affects of the moon and sun, along with the local coastal topography. The northern section of the research site is a sandy beach plain, whereas the southern area consists of a mudflat that transitions into a mangrove forest. Beyond the mangroves are salt ponds and intense shrimp farms. Measurements in the open area were performed on the seashore plain, a highly exposed site devoid of vegetation and human settlements. The research site and the arrangement of sample sites are illustrated in **Fig 1**.

3. DATA AND METHODS

This section outlines a cohesive methodological framework aimed at maintaining consistency across data gathering, processing, and validation phases. The workflow is organized in a sequential manner, beginning with mobile LiDAR surface data collection, proceeding to high-precision GNSS measurements, and culminating in database integration and statistical validation. In this context, the iPhone 12 Pro LiDAR functions as the primary source of high-resolution elevation data, supplying the essential dataset for further studies. All resulting datasets were carefully aligned via georeferencing, ground control integration, and GIS-based processing to facilitate rigorous cross-comparison, uncertainty evaluation, and quantitative accuracy assessment.

3.1. iPhone 12 Pro LiDAR

The iPhone 12 Pro and iPhone 12 Pro Max feature a LiDAR (Light Detection and Ranging) sensor that improves depth-sensing functionality. The iPhone 12 Pro features a 12 MP camera system including three distinct cameras (1x telephoto, 1x wide, and 1x ultrawide), a flashlight, and a LiDAR sensor on the rear of the device (Kottner et al., 2023). The iPhone 12 Pro's rear camera assembly contains an iLiDAR module featuring a vertical cavity surface-emitting laser (VCSEL) as the emitter and a single-photon avalanche diode (SPAD) sensor integrated with a complementary metal-oxide semiconductor (CMOS) for signal detection (Gollob et al., 2021b; Mikalai et al., 2022; Vogt et al., 2021b). The VCSEL operates in the near-infrared (NIR) spectrum, at approximately 800 nm, generating a measuring array comprising 576 points, 12 x 12 dot matrix (Kottner et al., 2023) or 24 $\times$ 24 points per photon burst (King et al., 2023; Luetzenburg et al., 2021). The point density of this array adheres to a linear trajectory on a logarithmic scale, indicating that uncertainty increases with distance (7225 points per m^2 at 0.25 m, decreasing to 150 points per m^2 at 2.5 m) (Luetzenburg et al., 2021). In adequately illuminated environments, the iLiDAR module can measure distances up to 5 meters, possesses an instantaneous field of view (IFOV) of 90 degrees, and exhibits an average deviation of approximately 10 millimeters from the actual depth measurement (King et al., 2022, 2023).

The current investigation utilized LiDAR scanning with the 3D Scanner App (version 2.1.3) on iOS 18.2.1, obtained from the iOS App Store, consistent with a prior study (King et al., 2023b; Luetzenburg et al., 2021). Data acquisition was conducted at a scanning height of approximately 1–1.2 meters to guarantee uniform coverage throughout the surveyed region. The LiDAR point cloud

acquisition was set up with automated texturing, processing of small models, automatic orientation for diminutive items, and GPS-tagged scans to improve spatial referencing. GPS tagging was essential for enabling georeferencing corrections, given that the positional accuracy of field-acquired data fluctuated between 3 and 5 meters, as demonstrated by the 3D Scanner output in LAS format. The acquired high-density point cloud data were subsequently transferred into CloudCompare, an open-source LiDAR processing application (Kottner et al., 2023). In CloudCompare, Ground Control Points (GCPs) were implemented to enhance spatial precision, and the LAS point cloud was transformed into a 3D mesh representation (Luetzenburg et al., 2021). The processed data were ultimately exported in GeoTIFF format for subsequent spatial analysis and incorporation into Geographic Information System (GIS) procedures. This methodological approach guarantees superior terrain reconstruction, enhancing the capabilities of mobile LiDAR technology for accurate topographic mapping and geospatial analysis.

3.2. Real Time Kinematic (RTK) survey

The present investigation achieved precise coordinate collection using the Global Navigation Satellite System (GNSS) Geomate SG7 receiver. To enhance positional accuracy, the study utilized Network Real-Time Kinematic (NRTK) corrections (Nik Azhan Hakim et al., 2023; Zeybek et al., 2023; Zvirgzds & Celms, 2020), implementing a Continuously Operating Reference Station (CORS) within a 2‑6 km Line of Sight (LOS) for optimal performance (Ji et al., 2022; Yurdakul & Kalaycı, 2022). To ensure optimal performance, a stable internet or mobile network connection was maintained throughout the survey. The GNSS data (**Fig. 2)** was acquired while stationary, employing the Geomate SG7 NRTK method, which yielded highly precise measurements with a horizontal precision of 8 mm (Kanellopoulos et al., 2019; Pepe, 2018) and a vertical accuracy ranging from 15 mm to 25 mm for distances under 10 km (Bernstein & Janssen, 2022; Yurdakul & Kalaycı, 2022).

The NRTK approach facilitated swift location determination, attaining a fixed answer in roughly 5 seconds in unobstructed environments. Data collecting beneath dense mangrove canopies necessitated prolonged processing durations owing to signal attenuation. The research was carried out in three different environmental settings: sandy open fields, moderately dense canopy, and totally dense mangrove canopy. Each surveyed site consisted of 55 measurement points, with three identified as Ground Control Points (GCPs) at strategically chosen locations (samples 1, 23, and 55). This stringent process guaranteed precise geospatial data acquisition, facilitating dependable integration with LiDAR-derived datasets for high-resolution topographic assessment (**Table 1**).

Table 1.

The report provides a summary of the RTK survey's (mean) elevation in orthometric terms, sample size, standard deviation, standard error, and canopy cover classifications, as well as their typical locations and preparation guidelines for the survey.

Site condition	NDVI Class	Canopy	Site	N	Mean (m)	SD (m)
Coastal Sand Beach	-1 to 0,32	No	1	55	0,912	0,049
Coastal Sand Beach	-1 to 0,32	No	2	55	-0,224	0,053
Coastal Sand Beach	-1 to 0,32	No	3	55	-0,168	0,020
Coastal Sand Beach	-1 to 0,32	No	4	55	0,222	0,106
Coastal Sand Beach	-1 to 0,32	No	5	55	0,636	0,144
Thin mangrove canopy	0,43 to 1	High	6	55	1,002	0,398
Dense mangrove canopy	0,33 to 042	Mid	7	55	1,556	0,201
Dense mangrove canopy	0,43 to 1	High	8	55	0,327	0,121
Dense mangrove canopy	0,33 to 042	Mid	9	55	0,285	0,282
Thin mangrove canopy	0,33 to 042	Mid	10	55	0,953	0,387
Thin mangrove canopy	0,43 to 1	High	11	55	0,040	0,208
Dense mangrove canopy	0,43 to 1	High	12	55	1,212	0,920

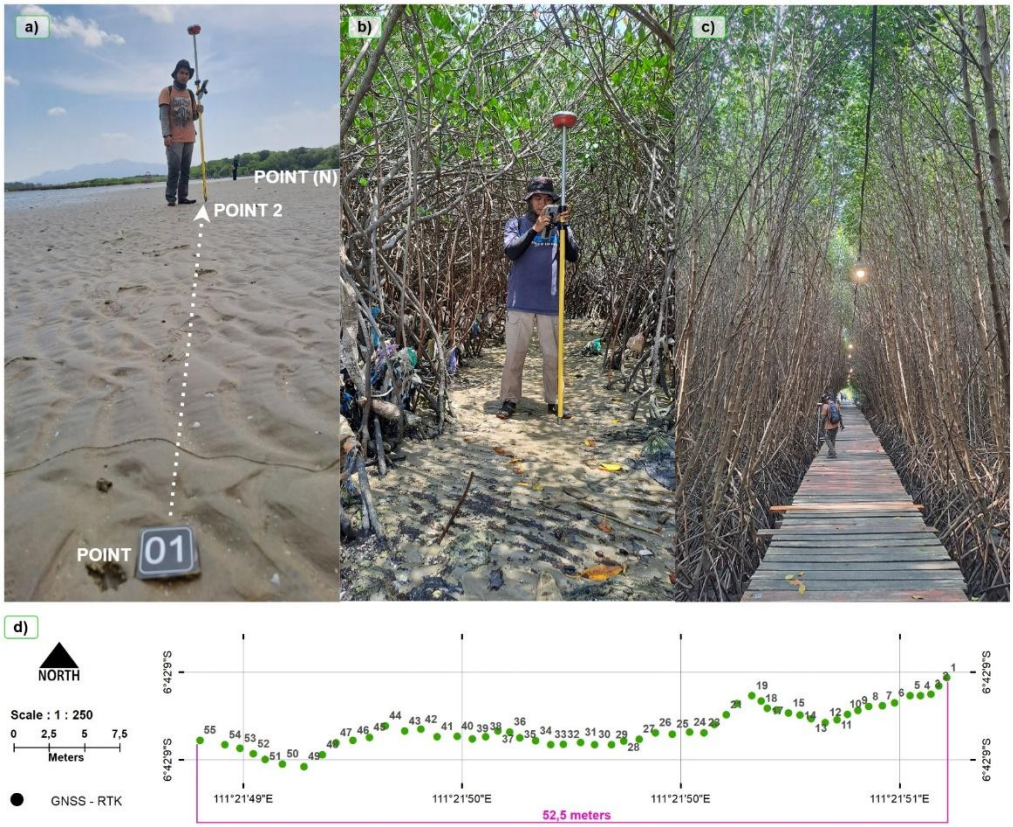


Fig. 2. (a) RTK data collecting was performed in an open sandy beach setting, encompassing points 1 to 55, (b) RTK point capture conducted in sparse canopy circumstances, demonstrating difficulties associated with partial vegetative cover, (c) Dense canopy conditions required the use of a bridge to get ground control points in obstructed locations, (d) Summary of a location where 55 RTK points were effectively obtained, illustrating diverse topography and vegetation cover conditions.

3.3. LIDAR-derived DTM accuracy assessment

The 3D Scanner application on an iPhone 12 Pro was utilized to gather LiDAR-based field data for this research. The application stored georeferenced information in an XYZ format. Ground Control Points (GCPs) in CloudCompare, an open-source LiDAR processing software, were utilized to calibrate the raw data and ensure excellent spatial accuracy. Upon meticulous rectification, the dataset was converted into a raster format, facilitating the extraction of precise pixel values essential for constructing a robust Digital Terrain Model (DTM). The subsequent phase involved integrating Real-Time Kinematic (RTK) survey points with the LiDAR-generated Digital Terrain Model (DTM) utilizing ArcGIS Pro. This facilitated a comprehensive comparison. The meticulously structured dataset in Excel provided the basis for extensive statistical studies. A comprehensive accuracy assessment and error analysis were conducted in Excel to ensure the reliability and precision of the elevation data obtained from the LiDAR device. This multi-step strategy enables the use of consumer-grade devices for high-accuracy topographic mapping in challenging field situations by integrating modern mobile sensor technology with meticulous data processing and validation techniques.

This study meticulously assessed the accuracy of the Digital Elevation Model (DEM) obtained by LiDAR by comparing GNSS survey data with LiDAR measurements collected via an iPhone across a 55-point cross-section comprising 12 distinct locations (**Fig. 3**). We employed significant statistical metrics to ascertain the accuracy of the outcomes.

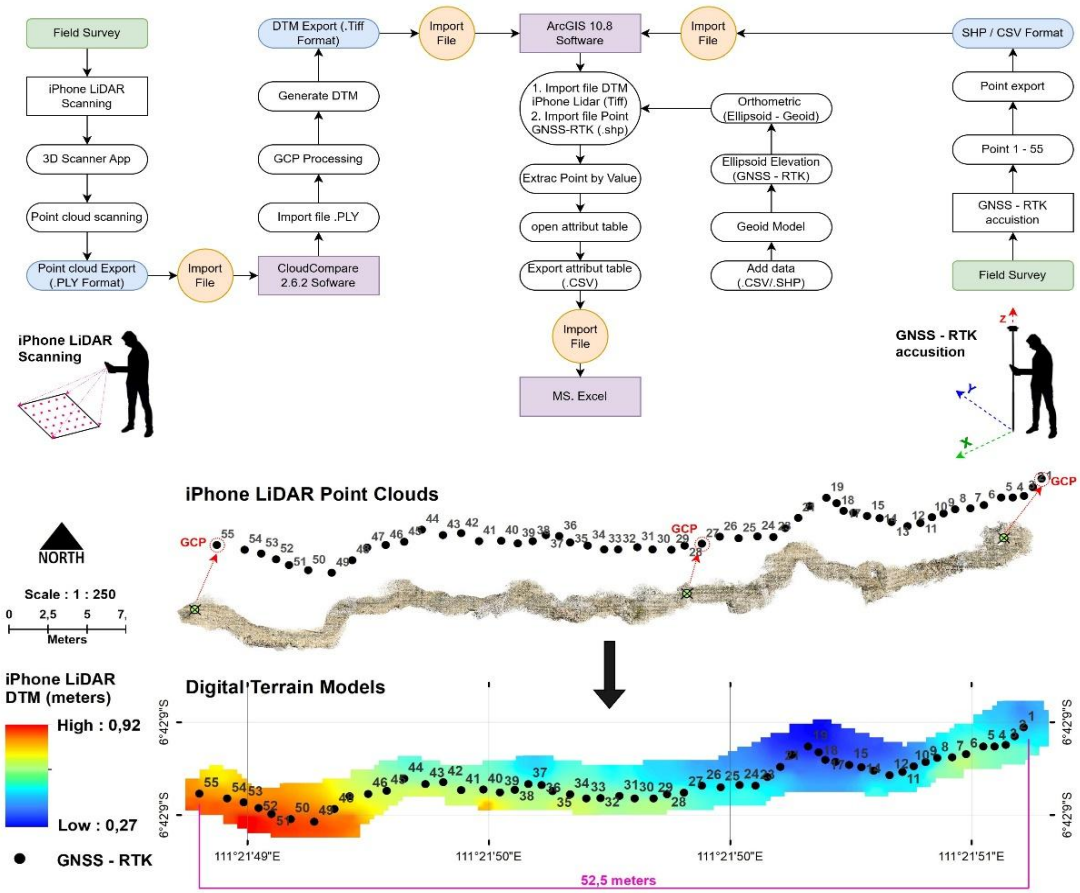


Fig. 3. The process includes building a DTM utilizing the iPhone 12 Pro LiDAR, corroborating it with GNSS-RTK data, and subsequently producing CSV data for Excel importation.

The metrics considered are Root Mean Square mistake (RMSE) (Gollob et al., 2021b), which assesses the magnitude of the overall mistake; Mean Absolute Error (MAE), which evaluates the average absolute deviation; and Bias (King et al., 2022, 2023; Kottner et al., 2023), which identifies systematic bias in elevation estimations. The Pearson Correlation Coefficient (r) was utilized to determine the strength and direction of the linear relationship between GNSS and LiDAR-derived elevations. Confidence Intervals (CI) of 95% were computed for each error metric to enhance the reliability evaluation (King et al., 2023b; B. Song et al., 2023). Confidence intervals are an effective method for quantifying uncertainty. This comprehensive validation methodology ensures the accuracy of the LiDAR-derived DEM, enabling its application in high-resolution topographic mapping. This enhances the use of mobile LiDAR technology in geospatial analysis. While a box plot does not explicitly present the standard deviation (B. Song et al., 2023; Vogt et al., 2021), it facilitates its estimation and offers valuable insights into the data distribution, variability, and potential outliers.

$$MAE = (1/n)\sum(i = 1)^{n}|y_i - \hat{y}_i| \quad (1)$$

where y_i denotes the observed value, $\hat{y}_i$ represents the predicted value, and n indicates the total number of observations.

$$Bias = (1/n)\sum(i = 1)^{n}(y_i - \hat{y}_i) \quad (2)$$

where y_i is the observed value, $\hat{y}_i$ is the predicted value, and n denotes the total number of observations.

$$RMSE = \sqrt{(1/n)\sum(i=1)^n(y_i - \hat{y}_i)^2} \quad (3)$$

where y_i represents observed values, $\hat{y}_i$ denotes predicted values, and n is the number of observations.

$$r = [\, n\sum(xy) - (\sum x)(\sum y)\,] / \sqrt{[n\sum x^2 - (\sum x)^2][n\sum y^2 - (\sum y)^2]} \quad (4)$$

where x *and* y are paired observed and predicted values, respectively, and n is the sample size.

4. RESULTS AND DISCUSSIONS

4.1. Positional Accuracy of iPhone 12 Pro Across Varying Vegetation Densities

The findings indicate that the positional accuracy of the iPhone 12 Pro, when adjusted with three Ground Control Points (GCPs) per location, is significantly affected by canopy cover environments. In unobstructed environments, the device operates at peak efficiency, providing a low mean absolute error (MAE < 0.1 m), a strong correlation with GNSS RTK data (up to r = 0.989), and negligible bias and RMSE−especially at Locations 3, 4, and 5−indicating accuracy to GNSS RTK in clear settings. Nonetheless, precision diminishes beneath medium-density canopy cover. Some places, such as Location 9, exhibit a robust correlation (r = 0.918) and a low mean absolute error (MAE) of 0.086 m, whereas others, like Location 10, demonstrate considerable deterioration, with an MAE of 0.381 m, a root mean square error (RMSE) of 0.482 m, and a weak correlation (r = 0.329). Performance is least effective in densely canopied regions, where errors significantly increase (e.g., Location 6: MAE = 1.064 m, bias = 0.928 m), and correlation may become negative (e.g., Location 12: r = -0.078), suggesting positional estimates are inconsistent with real movement or location. The findings indicate that the iPhone 12 Pro is inadequate for high-precision mapping in densely vegetated areas, while it demonstrates significant promise for accurate placement in open or semi-open regions (**Table 2**).

Table 2.
Summary statistics of GNSS RTK and iPhone 12 Pro location estimates at each site under different canopy conditions, including their mean values for the entire observation.

Canopy criteria	Site	MAE (meters)	Bias (meters)	Pearson Correlation Coefficient (r)	RMSE (m)	Bias (m)
No canopy covered	1	0,137	0,137	0,579	0,156	-0,137
	2	0,166	-0,164	0,693	0,190	0,164
	3	0,039	-0,035	0,782	0,045	0,035
	4	0,058	0,058	0,982	0,061	-0,058
	5	0,082	0,082	0,989	0,085	-0,082
medium-density canopy-covered	7	0,154	-0,028	0,514	0,168	0,028
	9	0,086	-0,011	0,918	0,107	0,012
	10	0,381	0,232	0,329	0,482	0,232
dense canopy covered	6	1,064	0,928	0,726	0,963	0,928
	8	0,121	0,077	0,092	0,276	-0,077
	11	0,234	-0,138	0,307	0,371	-0,138
	12	0,345	0,240	-0,078	0,489	-0,249

Elevation analysis of the Coastal Sand Beach and mangrove canopy zones indicates differing accuracy levels between the DTM_IP12 model and GNSS-RTK readings, significantly affected by topographic and surface features. In flat, unobstructed beach regions (e.g., Site 1 and Site 3), DTM_IP12 demonstrates great consistency and negligible variation from RTK data (median differences <0.05 m), signifying robust model reliability. Discrepancies arise in regions characterized by micro-topographic complexity or transitional surfaces (e.g., Site 2 and Site 5), where DTM_IP12 frequently overestimates or underestimates elevations by as much as ±0.2 m. In low-canopy mangrove areas, precision fluctuates with surface roughness and flora diversity. Sites 7 and 9 provide strong concordance, however Site 10 shows a significant overestimation (~±0.3 m), presumably attributable to residual canopy interference despite thin categorization. Under dense mangrove cover, performance markedly deteriorates, exhibiting increased vertical spreads and outliers in DTM outputs (e.g., Site 6 and Site 12), attributable to signal distortion caused by dense vegetation. Nonetheless, several locations (e.g., Site 8) have a strong correlation between methodologies, underscoring localized effectiveness in areas where vegetation and topography are generally homogeneous. The accuracy of DTM_IP12 is significantly dependent on vegetation density and surface complexity, with model performance diminishing in diverse or densely vegetated areas (**Fig. 4**).

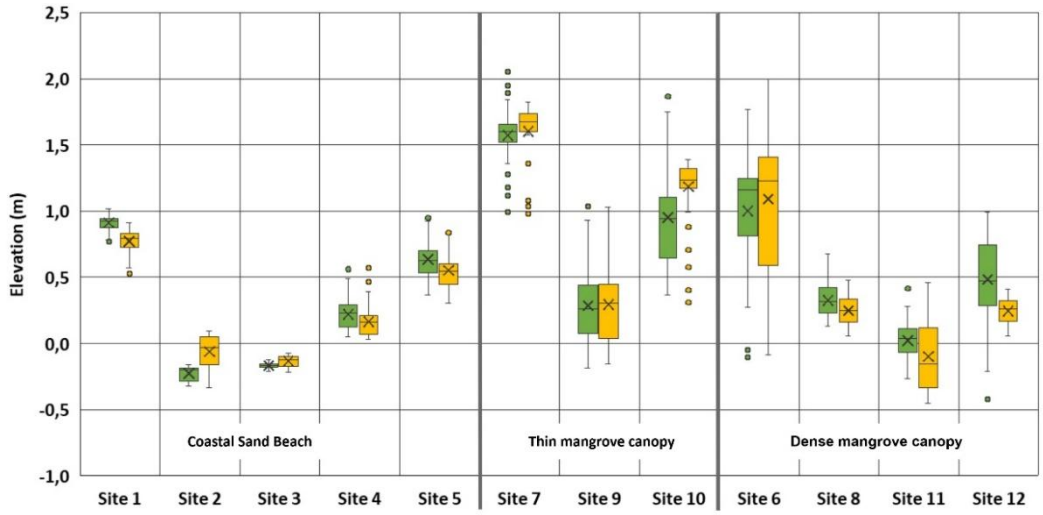


Fig. 4. Performance Comparison of Elevation RTK (green) and iPhone 12 (yellow) Models Across Coastal Sand Beach, thin mangrove canopy, and dense mangrove canopy in Microtopography.

4.2. Interplay Between Canopy Density and UAV-Derived Horizontal and Vertical Accuracy

In open field circumstances (**Fig. 5**, sites 1 to 5), the horizontal accuracy regularly exceeds that of dense mangrove areas, indicating enhanced positioning precision where canopy interference is limited. Nonetheless, the vertical precision in these broad fields poses issues, since minor topographic discrepancies occur more frequently than in thick mangrove areas. For example, Site 1 shows a little vertical variation of 0.5 meters between datasets utilizing Ground Control Network (GCN) and those lacking Ground Control Points (GCPs), while presenting a substantial horizontal disagreement of 11 meters. Conversely, Site 9, distinguished by minimal canopy cover, exhibits a vertical discrepancy of 3.1 meters and a horizontal error of 1.5 meters, signifying a significant influence of vegetation on positional precision. Site 11, characterized by a dense mangrove canopy, exhibits the greatest vertical variation of 4.2 meters, while displaying a comparatively minimal horizontal variance of 1 meter. These findings highlight the intricate relationship between canopy density and the location precision gained from UAVs. Although broad fields enhance horizontal accuracy, vertical precision is uneven due to variations in terrain.

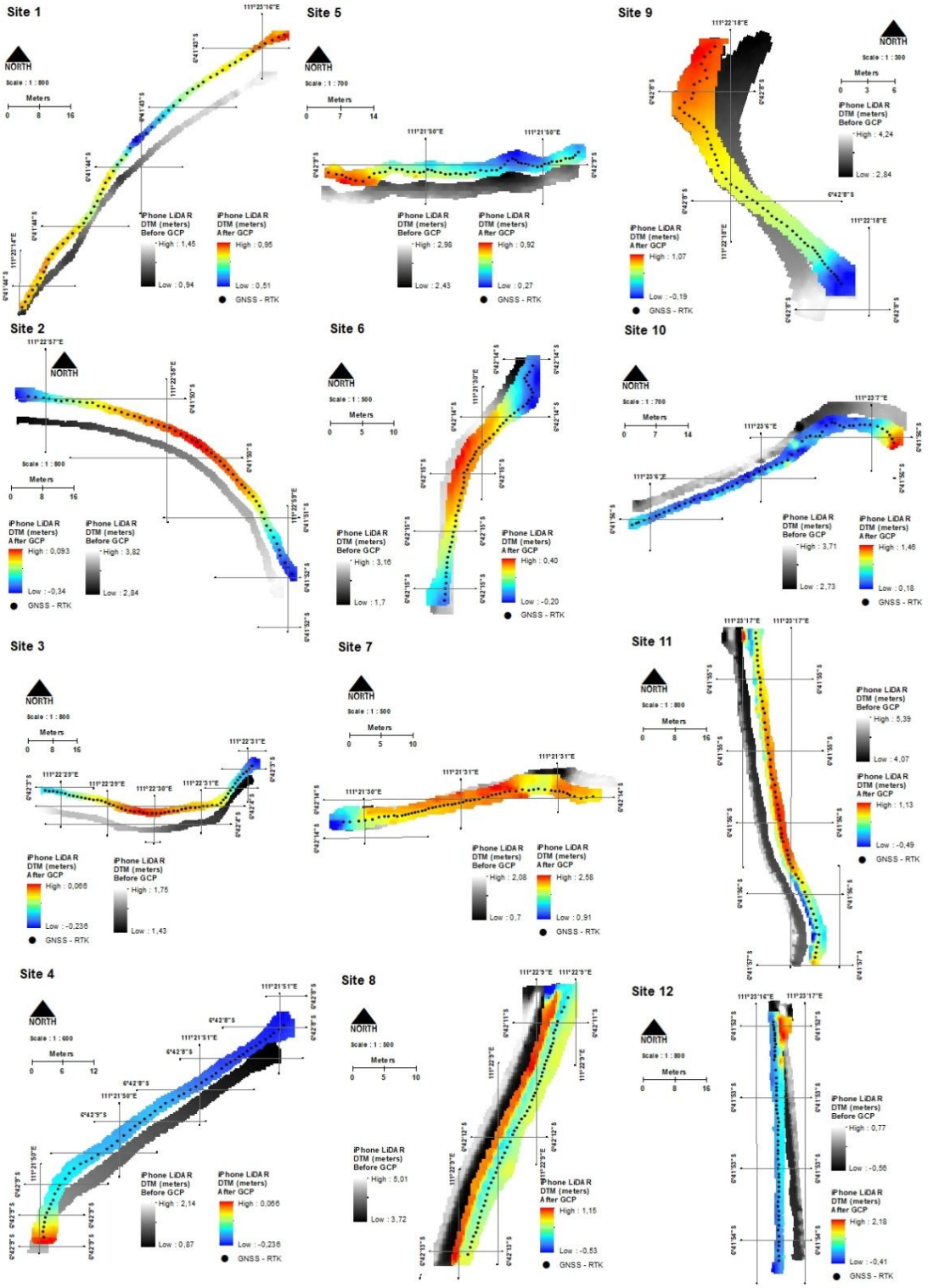


Fig. 5. The LiDAR-generated point cloud from the iPhone, including XYZ correction in CloudCompare (CC), produces a Digital Terrain Model (DTM) prior to Ground Control Point (GCP) correction (white to black) and subsequent to GCP correction (red to blue), with the DTM matching with RTK data.

In contrast, dense canopies present considerable vertical obstacles but may mitigate horizontal drift owing to their uniform construction. These results are essential for enhancing UAV data collection methodologies in diverse coastal settings. **Fig. 6** delineates the discrepancies in elevation measurements between the DTM iPhone GCP - No GCP and the RTK survey.

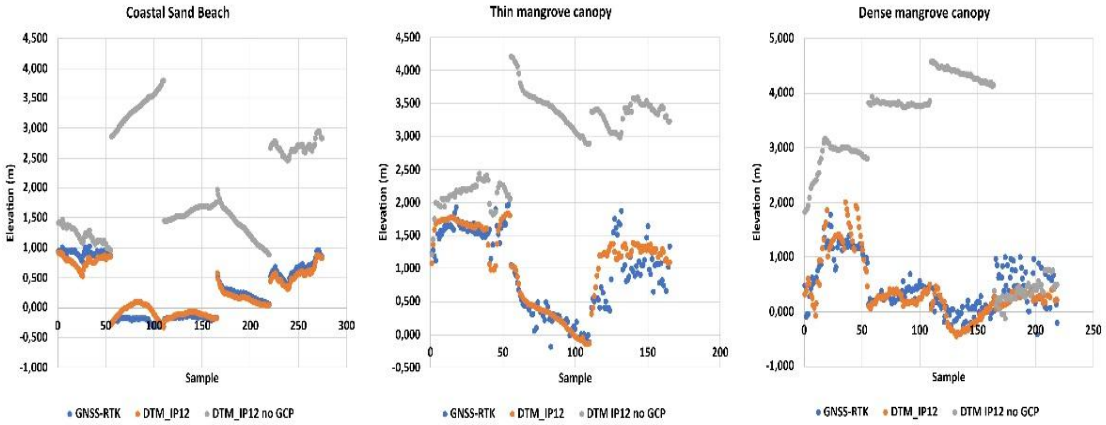


Fig. 6. The elevation value is assessed under three scenarios: open, sparse, and dense mangrove canopy; data conditions include RTK, DTM iPhone with GCP correction, and DTM iPhone without GCP.

4.3. Development and Application of Correction Models for iPhone LiDAR Elevation Data Across Varying Vegetation Densities

The elevation data acquired by iPhone LiDAR were juxtaposed with high-precision GNSS-RTK measurements to assess accuracy across three land cover categories: open fields, sparse mangrove canopies, and dense mangrove canopies. Linear regression analysis yielded correction formula tailored to each situation, demonstrating a substantial association in open areas ($R^2 = 0.956$), a moderate correlation in thin canopies ($R^2 = 0.7991$), and a weaker correlation in dense canopies ($R^2 = 0.663$). These correction models enable the proper calibration of iPhone LiDAR elevation data to achieve RTK-level precision (**Fig. 7**). This method improves the functionality of mobile LiDAR sensors, especially in coastal and mangrove regions where dense foliage might affect measurement accuracy. Utilizing these methods, researchers can conduct swift and reasonably precise elevation evaluations without requiring cumbersome or costly apparatus. Furthermore, including these models into data pipelines or mobile applications provides a pragmatic, scalable approach for conducting field surveys in intricate and dynamic settings, hence enhancing comprehensive environmental monitoring initiatives.

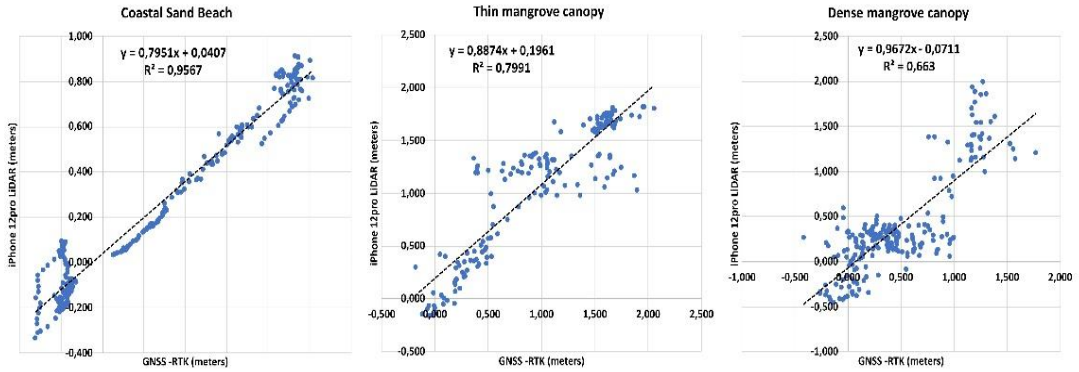


Fig. 7. Scatterplots showing elevation correction equations derived from iPhone LiDAR and GNSS-RTK data across open fields, thin mangrove canopy, and dense canopy conditions.

5. DISCUSSION

Creating a Digital Terrain Model (DTM) in mangrove ecosystems presents considerable difficulties for traditional techniques like GNSS, photogrammetry, and total stations, owing to the dense canopy and challenging topography (Basyuni, Amelia, et al., 2025; Basyuni et al., 2023; Basyuni, Mubaraq, et al., 2025; Wirasatriya et al., 2022). Although drone photogrammetry is effective for surface mapping, it frequently yields biased elevation data (Basyuni, Mubaraq, et al., 2025; Wirasatriya et al., 2022). LiDAR provides excellent precision; yet, it is expensive and presents dangers to equipment in saline conditions (Grottoli et al., 2021; Rogers et al., 2020; Zhang & Zhu, 2023). An option is iPhone-based LiDAR scanning, offering a cost-effective, efficient, and low-risk method that captures topography data (King et al., 2022, 2023b; Luetzenburg et al., 2021) over distances of 25 to 150 meters each scan. Its portability and compatibility with waterproof casings render it appropriate for mangrove environments, presenting significant potential for DTM creation. Scatter plot-derived linear regression equations ($Y = aX + b$) serve as an effective calibration function to adjust iPhone LiDAR elevation (Z) data in relation to GNSS-RTK standards.

The coefficient of determination (R^2) measures the strength of the association, revealing a high correlation in open areas ($R^2 = 0.956$), a moderate correlation in sparse mangrove canopies ($R^2 = 0.7991$), and a lesser correlation beneath dense canopies ($R^2 = 0.663$). The fluctuations indicate that vegetation density influences LiDAR accuracy. The regression equations provide a robust correction strategy, particularly in open and semi-obstructed situations, enhancing the applicability of smartphone-based LiDAR for forthcoming elevation research in various coastal contexts. This linear regression model can be advanced into an allometric model contingent upon land circumstances (NDVI, canopy density, automatic classification), facilitating economical and rapid topographic mapping utilizing mobile LiDAR. This methodology can function as a foundation for calibrating image-based machine learning and mobile elevation data.

In difficult site conditions characterized by steep slopes and deep forest, the full-waveform Riegl LMS-Q560 LiDAR, affixed to a DA42 MPP aircraft, achieved robust DTM accuracy (RMSE 0.15–0.62 m), Notwithstanding diminished point densities, effective interpolation techniques (NN, TPS) maintained model accuracy, confirming LiDAR's dependability for ecological and forestry purposes (Cățeanu & Ciubotaru, 2021). Although LiDAR and UAS photogrammetry exhibit similar vertical accuracy in unobstructed environments (±0.03 to ±0.06 m RMSE) (Rogers et al., 2020), this study's results indicate a systematic escalation in error beneath vegetative cover, with average RMSE values of 0.107 m in open regions, 0.252 m under medium-density canopies, and 0.525 m under dense canopies, highlighting the substantial influence of vegetation complexity on DSM accuracy.

In alignment with the results of (Luetzenburg et al., 2021), our research similarly indicates that the LiDAR sensor of the iPhone 12 Pro attains a remarkable RMSE of ±1 cm for small objects (side length > 10 cm) and ±10 cm for larger models (130 × 15 × 10 m), thereby reinforcing its viability as a cost-efficient substitute for conventional remote sensing methods in geoscientific applications. (King et al., 2023b) illustrate that the iPhone 12 Pro LiDAR (iLiDAR) mounted on a DJI Phantom 4 quadcopter offers a viable low-cost solution for snow depth estimation, attaining a root mean square error (RMSE) of 3 cm and an absolute mean error of 2.5 cm relative to conventional snow ruler measurements, underscoring its potential for accurate and economical snow monitoring. (King et al., 2022) further validated its high precision (RMSE ~6 mm), indicating its applicability for citizen research initiatives.

The findings of this investigation corroborate and enhance existing knowledge regarding the reliability of consumer-grade Apple LiDAR systems, while also demonstrating their applicability in creating Digital Terrain Models (DTMs) of mangroves with varying canopy densities. Previous studies have consistently shown that iPhone and iPad LiDAR achieve centimetric to sub-centimetric accuracy in both controlled and open settings, with inaccuracies increasing during dynamic data collection and extensive spatial coverage due to cumulative pose and SLAM-related drift (Luetzenburg et al., 2021; Teo & Yang, 2023). Significant accuracy has been recorded in various

applications, such as snow depth estimation, forensic documentation, anthropometry, and rapid environmental monitoring, with biases and RMSE values typically remaining under 1 cm (King et al., 2022; Kottner et al., 2023; Mikalai et al., 2022). The method by which applications handle data is the paramount aspect influencing the ultimate quality of the metrics. Applications such as PIX4DCatch and SiteScape, which exhibit robust drift control and global orientation, consistently outperform their counterparts. Conversely, the 3D Scanner App and EveryPoint are more prone to errors due to noise and orientation during extended scans (Corradetti et al., 2022; Teppati Losè et al., 2022).

The present results align with these tendencies, indicating enhanced DTM accuracy in open mangrove areas, intermediate precision under sparse canopies, and considerable decline in dense vegetation due to occlusion, signal attenuation, and vertical bias. These constraints illustrate the challenges of employing mobile LiDAR in wetlands with intricate structures, although they also indicate potential improvements through enhanced acquisition techniques and allometric correction. While professional LiDAR remains superior in dense canopies, the iPhone 12 Pro LiDAR presents a robust, cost-effective alternative for high-resolution Digital Terrain Model mapping in mangrove regions characterized by sparse to moderate vegetation. It additionally facilitates scalable and accessible MRV applications.

6. CONCLUSIONS

This research demonstrates that iPhone LiDAR can generate dependable and accurate Digital Terrain Models (DTMs), especially when supplemented by GNSS-RTK Ground Control Points (GCPs). In dense canopy conditions, GNSS signals often deteriorate, leading to possible inaccuracies and vertical bias. Nonetheless, iPhone LiDAR ensures data consistency across diverse contexts, particularly in aquatic and exceptionally dark circumstances. The robust correlation (R^2) seen in open field circumstances indicates that these locations can be relied upon to rectify iPhone LiDAR-generated DTMs. Moreover, employing allometric equations presents a viable alternative for rectifying terrain data in the absence of GNSS-based ground control points, offering a cost-effective method to enhance survey accuracy without compromising data integrity. This method possesses considerable promise for extensive environmental mapping and monitoring applications, particularly in financially limited or logistically difficult regions.

ACKNOWLEDGEMENT

This research is supported by Faculty of Fisheries and Marine Science, Diponegoro University with contract number: 20/UN7.F10/PP/VII/2025.

REFERENCES

Alongi, D. M. (2022). Impacts of Climate Change on Blue Carbon Stocks and Fluxes in Mangrove Forests. Forests, 13(2), 149. https://doi.org/10.3390/f13020149

Amelia, R., Basyuni, M., Alfinsyahri, A., Sulistiyono, N., Slamet, B., Bimantara, Y., Harahap, S. S. H., Harahap, M., Harahap, I. M., Al Mustaniroh, S. S., Sasmito, S. D., & Arifanti, V. B. (2023). Evaluation of Plant Growth and Potential of Carbon Storage in the Restored Mangrove of an Abandoned Pond in Lubuk Kertang, North Sumatra, Indonesia. Forests, 14(1). https://doi.org/10.3390/f14010158

Amuyou, U. A., Wang, Y., Ebuta, B. F., Iheaturu, C. J., & Antonarakis, A. S. (2022). Quantification of Above-Ground Biomass over the Cross-River State, Nigeria, Using Sentinel-2 Data. Remote Sensing, 14(22). https://doi.org/10.3390/rs14225741

Arifanti, V. B., Kauffman, J. B., Subarno, J. B., Ilman, M., Tosiani, A., & Novita, N. (2022). Contributions of mangrove conservation and restoration to climate change mitigation in Indonesia. Global Change Biology, 28(15), 4523‑4538. https://doi.org/10.1111/gcb.16216

Arnaud, M., Krause, S., Norby, R. J., Dang, T. H., Acil, N., Kettridge, N., Gauci, V., & Ullah, S. (2023). Global mangrove root production, its controls and roles in the blue carbon budget of mangroves. In Global Change Biology (Vol. 29, Issue 12, pp. 3256‑3270). John Wiley and Sons Inc. https://doi.org/10.1111/gcb.16701

Bagas, A., Trinida, P., Muskananfola, M. R., Febrianto, S., & Ayuningrum, D. (2024). Analysis of shoreline change along the coast of Rembang, Indonesia, using digital shoreline analysis system. In Songklanakarin J. Sci. Technol (Vol. 46, Issue 5).

Basyuni, M., Amelia, R., Aznawi, A. A., Wirasatriya, A., Iryanthony, S. B., Slamet, B., Al Mustaniroh, S. S., Rahmania, R., Rahmila, Y. I., Sumarga, E., Larekeng, S. H., Salmo, S., Kajita, T., Sivaipram, I., & Ali, H. M. (2025). Reduction of mangrove carbon stock ecosystems due to illegal logging using a combination of unmanned aerial vehicle imagery and field surveys. Global Journal of Environmental Science and Management, 11(1), 225‑242. https://doi.org/10.22034/gjesm.2025.01.14

Basyuni, M., Mubaraq, A., Amelia, R., Wirasatriya, A., Iryanthony, S. B., Slamet, B., Al Mustaniroh, S. S., Pradisty, N. A., Sidik, F., Hanintyo, R., Sumarga, E., Larekeng, S. H., Salmo, S. G., Kajita, T., Ali, H. M., Sakti, A. D., & Arifanti, V. B. (2025). Mangrove aboveground biomass estimation using UAV imagery and a constructed height model in Budeng‑Perancak, Bali, Indonesia. Ecological Informatics, 86. https://doi.org/10.1016/j.ecoinf.2025.103037

Basyuni, M., Wirasatriya, A., Iryanthony, S. B., Amelia, R., Slamet, B., Sulistiyono, N., Pribadi, R., Sumarga, E., Eddy, S., Al Mustaniroh, S. S., Sasmito, S. D., Sidik, F., Kajita, T., Ali, H. M., Macklin, P. A., & Arifanti, V. B. (2023). Aboveground biomass and carbon stock estimation using UAV photogrammetry in Indonesian mangroves and other competing land uses. Ecological Informatics, 77. https://doi.org/10.1016/j.ecoinf.2023.102227

Bernstein, T., & Janssen, V. (2022). Determining Positional Uncertainty of NRTK Observations for Inclusion in the GDA2020 State Adjustment. In New South Wales.

Bimrah, K., Dasgupta, R., Hashimoto, S., Saizen, I., & Dhyani, S. (2022). Ecosystem Services of Mangroves: A Systematic Review and Synthesis of Contemporary Scientific Literature. In Sustainability (Switzerland) (Vol. 14, Issue 19). MDPI. https://doi.org/10.3390/su141912051

Cățeanu, M., & Ciubotaru, A. (2021). The effect of lidar sampling density on dtm accuracy for areas with heavy forest cover. Forests, 12(3), 1‑20. https://doi.org/10.3390/f12030265

Chan, E. P. Y., Fung, T., & Wong, F. K. K. (2021). Estimating above-ground biomass of subtropical forest using airborne LiDAR in Hong Kong. Scientific Reports, 11(1). https://doi.org/10.1038/s41598-021-81267-8

Corradetti, A., Seers, T., Mercuri, M., Calligaris, C., Busetti, A., & Zini, L. (2022). Benchmarking Different SfM-MVS Photogrammetric and iOS LiDAR Acquisition Methods for the Digital Preservation of a Short-Lived Excavation: A Case Study from an Area of Sinkhole Related Subsidence. Remote Sensing, 14(20). https://doi.org/10.3390/rs14205187

Di Stefano, F., Chiappini, S., Gorreja, A., Balestra, M., & Pierdicca, R. (2021). Mobile 3D scan LiDAR: a literature review. In Geomatics, Natural Hazards and Risk (Vol. 12, Issue 1, pp. 2387‑2429). Taylor and Francis Ltd. https://doi.org/10.1080/19475705.2021.1964617

Donato, D.C.; Kauffman, J.B.; Murdiyarso, D.; Kurnianto, S.; Stidham, M.; Kanninen, M. (2011) Mangroves among the most carbon-rich forests in the tropics. Nature Geoscience, 4 (5), 293‑297. http://dx.doi.org/10.1038/ngeo1123

Donato, D.C.; Kauffman, J.B.; Mackenzie, R.A.; Ainsworth, A.; Pfleeger, A.Z. (2012) Whole-island carbon stocks in the tropical Pacific: Implications for mangrove conservation and upland restoration. Journal of Environmental Management, 97 (1), 89‑96. http://dx.doi.org/10.1016/j.jenvman.2011.12.004

Feng, T., Chen, S., Feng, Z., Shen, C., & Tian, Y. (2021). Effects of canopy and multi-epoch observations on single-point positioning errors of a GNSS in coniferous and broadleaved forests. Remote Sensing, 13(12). https://doi.org/10.3390/rs13122325

Friess Daniel A, Kerrylee Rogers, Catherine E. Lovelock, Ken W. Krauss, Stuart E. Hamilton, Shing Yip Lee, Richard Lucas, Jurgenne Primavera, Anusha Rajkaran, & Suhua Shi. (2019). Daniel A. Friess_2019_compressed. Annual Reviews, 44, 89‑115. https://doi.org/https://doi.org/10.1146/annurev-environ-101718-033302

Gao, L., Chai, G., & Zhang, X. (2022). Above-Ground Biomass Estimation of Plantation with Different Tree Species Using Airborne LiDAR and Hyperspectral Data. Remote Sensing, 14(11). https://doi.org/10.3390/rs14112568

Giri, C., Ochieng, E., Tieszen, L. L., Zhu, Z., Singh, A., Loveland, T., Masek, J., & Duke, N. (2011). Status and distribution of mangrove forests of the world using earth observation satellite data. Global Ecology and Biogeography, 20(1), 154‐159. https://doi.org/10.1111/j.1466-8238.2010.00584.x

Gollob, C., Ritter, T., Kraßnitzer, R., Tockner, A., & Nothdurft, A. (2021a). Measurement of forest inventory parameters with apple ipad pro and integrated lidar technology. Remote Sensing, 13(16). https://doi.org/10.3390/rs13163129

Gollob, C., Ritter, T., Kraßnitzer, R., Tockner, A., & Nothdurft, A. (2021b). Measurement of forest inventory parameters with apple ipad pro and integrated lidar technology. Remote Sensing, 13(16). https://doi.org/10.3390/rs13163129

Grottoli, E., Biausque, M., Rogers, D., Jackson, D. W. T., & Cooper, J. A. G. (2021). Structure-from-motion-derived digital surface models from historical aerial photographs: A new 3d application for coastal dune monitoring. Remote Sensing, 13(1), 1‐22. https://doi.org/10.3390/rs13010095

Hu, T., Zhang, Y. Y., Su, Y., Zheng, Y., Lin, G., & Guo, Q. (2020). Mapping the global mangrove forest aboveground biomass using multisource remote sensing data. Remote Sensing, 12(10). https://doi.org/10.3390/rs12101690

Iryanthony, S. B., Wirasatriya, A., Pribadi, R., Purnomo, P. W., Muchtar, E., Basyuni, M., & Wijayanto, D. (2025). High-resolution Unmanned Aerial Vehicles (UAV) imagery for estimating above and below-ground biomass in mangroves of Rembang, Central Java, Indonesia. Biodiversitas, 26(5), 2065‐2078. https://doi.org/10.13057/biodiv/d260505

Iryanthony, S. B., Wirasatriya, A., Pribadi, R., Wahyu Purnomo, P., Mukhtar, E., Basyuni, M., & Wijayanto, D. (2025). High-Resolution UAV-Based Mapping and Species Identification of Mangroves in Pasar Banggi, Rembang, Central Java. IOP Conference Series: Earth and Environmental Science, 1496(1). https://doi.org/10.1088/1755-1315/1496/1/012012

Ji, S., Liu, G., Weng, D., Wang, Z., He, K., & Chen, W. (2022). Single-Epoch Ambiguity Resolution of a Large-Scale CORS Network with Multi-Frequency and Multi-Constellation GNSS. Remote Sensing, 14(15). https://doi.org/10.3390/rs14153819

Jurado, J. M., Ramos, M. I., Enríquez, C., & Feito, F. R. (2020). The impact of canopy reflectance on the 3D structure of individual trees in a Mediterranean Forest. Remote Sensing, 12(9). https://doi.org/10.3390/RS12091430

Kauffman, J.B.; Bernardino, A.B.; Ferreira, T.O.; Giovannoni, L.R.; Gomes, L.E.O.; Romero, D.J.; Jimenez, L.C.Z.; Ruiz, F. (2018) Carbon stocks of mangroves and salt marshes of the Amazon region, Brazil. Biology Lettters, 20180208. http://dx.doi.org/10.1098/rsbl.2018.0208

Kanellopoulos, N., Pantazis, G., & Lambrou, E. (2019). Distance Limitations when using CORS Networks and GNSS Receivers for Deformation Monitoring.

King, F., Kelly, R., & Fletcher, C. G. (2022). Evaluation of LiDAR-Derived Snow Depth Estimates From the iPhone 12 Pro. IEEE Geoscience and Remote Sensing Letters, 19. https://doi.org/10.1109/LGRS.2022.3166665

King, F., Kelly, R., & Fletcher, C. G. (2023a). New opportunities for low-cost LiDAR-derived snow depth estimates from a consumer drone-mounted smartphone. Cold Regions Science and Technology, 207. https://doi.org/10.1016/j.coldregions.2022.103757

King, F., Kelly, R., & Fletcher, C. G. (2023b). New opportunities for low-cost LiDAR-derived snow depth estimates from a consumer drone-mounted smartphone. Cold Regions Science and Technology, 207. https://doi.org/10.1016/j.coldregions.2022.103757

Kottner, S., Thali, M. J., & Gascho, D. (2023). Using the iPhone’s LiDAR technology to capture 3D forensic data at crime and crash scenes. Forensic Imaging, 32. https://doi.org/10.1016/j.fri.2023.200535

Krause, S., Sanders, T. G. M., Mund, J. P., & Greve, K. (2019). UAV-based photogrammetric tree height measurement for intensive forest monitoring. Remote Sensing, 11(7). https://doi.org/10.3390/rs11070758

Li, Z., Lu, T., Yu, K., & Wang, J. (2023). Interpolation of GNSS Position Time Series Using GBDT, XGBoost, and RF Machine Learning Algorithms and Models Error Analysis. Remote Sensing, 15(18). https://doi.org/10.3390/rs15184374

Lovelock, C. E., Barbier, E., & Duarte, C. M. (2022). Tackling the mangrove restoration challenge. PLoS Biology, 20(10). https://doi.org/10.1371/journal.pbio.3001836

Luetzenburg, G., Kroon, A., & Bjørk, A. A. (2021). Evaluation of the Apple iPhone 12 Pro LiDAR for an Application in Geosciences. Scientific Reports, 11(1). https://doi.org/10.1038/s41598-021-01763-9

Lynch, J. C., Winn, N., Kovalenko, K., & Guntenspergen, G. (2024). Comparing Wetland Elevation Change Using a Surface Elevation Table, Digital Level, and Total Station. Estuaries and Coasts, 47(7), 2071‐2079. https://doi.org/10.1007/s12237-023-01263-1

Mcleod, E.; Chmura, G.L.; Bouillon, S.; Salm, R.; Björk, M.; Duarte, C.M.; Lovelock, C.E.; Schlesinger, W.H.; Silliman, B.R. (2011) A blueprint for blue carbon: Toward an improved understanding of the role of vegetated coastal habitats in sequestering CO2. Frontiers in Ecology and the Environment, 9, 552-560. https://doi.org/10.1890/110004

Mêda, P., Calvetti, D., & Sousa, H. (2023). Exploring the Potential of iPad-LiDAR Technology for Building Renovation Diagnosis: A Case Study. Buildings, 13(2). https://doi.org/10.3390/buildings13020456

Mikalai, Z., Andrey, D., Hawas, H. S., Tetiana, H., & Oleksandr, S. (2022). Human body measurement with the iPhone 12 Pro LiDAR scanner. AIP Conference Proceedings, 2430. https://doi.org/10.1063/5.0078310

Murtiyoso, A., Grussenmeyer, P., Landes, T., & Macher, H. (2021). First assessments into the use of commercial-grade solid state lidar for low cost heritage documentation. International Archives of the Photogrammetry, Remote Sensing and Spatial Information Sciences - ISPRS Archives, 43(B2-2021), 599‑604. https://doi.org/10.5194/isprs-archives-XLIII-B2-2021-599-2021

Mustofa, V. M., Soenardjo, N., & Pratikto, I. (2023). Analisis Tekstur Sedimen terhadap Kelimpahan Gastropoda di Ekosistem Mangrove Desa Pasar Banggi, Rembang. Journal of Marine Research, 12(1), 137‑143. https://doi.org/10.14710/jmr.v12i1.35003

Nik Azhan Hakim, N. N. A., Razali, R., Mohd Said, M. S., Muhamad, M. A. H., Abdul Rahim, H., & Mokhtar, M. A. (2023). Accuracy Assessment on Detail Survey Plan Using iPhone 13 Pro Max LiDAR Sensor. International Journal of Geoinformatics, 19(5), 79‑86. https://doi.org/10.52939/ijg.v19i5.2665

Paul, S., Siddiqua, F., & Tayung, K. (2023). Exploration of Mangroves Associated Microbes for Bioactive Metabolites. INTERNATIONAL JOURNAL OF PLANT AND ENVIRONMENT, 9(03), 202‑209. https://doi.org/10.18811/ijpen.v9i03.03

Pepe, M. (2018). Cors architecture and evaluation of positioning by low-cost gnss receiver. Geodesy and Cartography, 44(2), 36‑44. https://doi.org/10.3846/gac.2018.1255

Raza, by M., Hassan, A., Khan, M., Emad, M., Saki, S., & Raza, M. (2023). A critical comparison of interpolation techniques for digital terrain modelling in mining Correspondence to: Dates: How to cite: ORCID. The Journal of the Southern African Institute of Mining and Metallurgy, 123(2), 53‑62. https://doi.org/10.17159/2411

Razali, M. I., Idris, A. N., Razali, M. H., & Syafuan, W. M. (2022). Quality Assessment of 3D Point Clouds on the Different Surface Materials Generated from iPhone LiDAR Sensor. International Journal of Geoinformatics, 18(4), 51‑58. https://doi.org/10.52939/ijg.v18i4.2259

Rogers, S. R., Manning, I., & Livingstone, W. (2020). Comparing the spatial accuracy of digital surface models from four unoccupied aerial systems: Photogrammetry versus lidar. Remote Sensing, 12(17), 1‑17. https://doi.org/10.3390/rs12172806

Sasmito, S. D., Basyuni, M., Kridalaksana, A., Saragi-Sasmito, M. F., Lovelock, C. E., & Murdiyarso, D. (2023). Challenges and opportunities for achieving Sustainable Development Goals through restoration of Indonesia ' s mangroves. Nature Ecology and Evolution, 7(1), 62‑70. https://doi.org/10.1038/s41559-022-01926-5

Shapiro, A. (2024). Mangroves. In Cloud-Based Remote Sensing with Google Earth Engine (pp. 1023‑1043). Springer International Publishing. https://doi.org/10.1007/978-3-031-26588-4_47

Soeprobowati, T. R., Sularto, R. B., Hadiyanto, H., Puryono, S., Rahim, A., Jumari, J., & Gell, P. (2024). The carbon stock potential of the restored mangrove ecosystem of Pasarbanggi, Rembang, Central Java. Marine Environmental Research, 193. https://doi.org/10.1016/j.marenvres.2023.106257

Song, B., Kim, J., Kwon, H., Kim, S., Oh, S. H., Ha, Y., & Song, S. H. (2023). Smartphone-Based LiDAR Application for Easy and Accurate Wound Size Measurement. Journal of Clinical Medicine, 12(18). https://doi.org/10.3390/jcm12186042

Song, S., Ding, Y., Li, W., Meng, Y., Zhou, J., Gou, R., Zhang, C., Ye, S., Saintilan, N., Krauss, K. W., Crooks, S., Lv, S., & Lin, G. (2023). Mangrove reforestation provides greater blue carbon benefit than afforestation for mitigating global climate change. Nature Communications, 14(1). https://doi.org/10.1038/s41467-023-36477-1

Suwa, R., Rollon, R., Sharma, S., Yoshikai, M., Albano, G. M. G., Ono, K., Adi, N. S., Ati, R. N. A., Kusumaningtyas, M. A., Kepel, T. L., Maliao, R. J., Primavera-Tirol, Y. H., Blanco, A. C., & Nadaoka, K. (2021). Mangrove biomass estimation using canopy height and wood density in the South East and East Asian regions. Estuarine, Coastal and Shelf Science, 248. https://doi.org/10.1016/j.ecss.2020.106937

Teo, T. A., & Yang, C. C. (2023). Evaluating the accuracy and quality of an iPad Pro ' s built-in lidar for 3D indoor mapping. Developments in the Built Environment, 14. https://doi.org/10.1016/j.dibe.2023.100169

Teppati Losè, L., Spreafico, A., Chiabrando, F., & Giulio Tonolo, F. (2022). Apple LiDAR Sensor for 3D Surveying: Tests and Results in the Cultural Heritage Domain. Remote Sensing, 14(17). https://doi.org/10.3390/rs14174157

Tian, Y., Huang, H., Zhou, G., Zhang, Q., Xie, X., Ou, J., Zhang, Y., Tao, J., & Lin, J. (2023). Mangrove Biodiversity Assessment Using UAV Lidar and Hyperspectral Data in China's Pinglu Canal Estuary. In Remote Sensing (Vol. 15, Issue 10). https://doi.org/10.3390/rs15102622

Tomaštík, J., & Everett, T. (2023). Static Positioning under Tree Canopy Using Low-Cost GNSS Receivers and Adapted RTKLIB Software. Sensors, 23(6). https://doi.org/10.3390/s23063136

Tong, P., Yang, X., Yang, Y., Liu, W., & Wu, P. (2023). Multi-UAV Collaborative Absolute Vision Positioning and Navigation: A Survey and Discussion. Drones, 7(4). https://doi.org/10.3390/drones7040261

Vogt, M., Rips, A., & Emmelmann, C. (2021a). Comparison of iPad Pro®'s LiDAR and TrueDepth Capabilities with an Industrial 3D Scanning Solution. Technologies, 9(2). https://doi.org/10.3390/technologies9020025

Vogt, M., Rips, A., & Emmelmann, C. (2021b). Comparison of iPad Pro®'s LiDAR and TrueDepth Capabilities with an Industrial 3D Scanning Solution. Technologies, 9(2). https://doi.org/10.3390/technologies9020025

Wainwright, B. J., Millar, T., Bowen, L., Semon, L., Hickman, K. J. E., Lee, J. N., Yeo, Z. Y., & Zahn, G. (2023). The core mangrove microbiome reveals shared taxa potentially involved in nutrient cycling and promoting host survival. Environmental Microbiome, 18(1), 1‑12. https://doi.org/10.1186/s40793-023-00499-5

Wirasatriya, A., Pribadi, R., Iryanthony, S. B., Maslukah, L., Sugianto, D. N., Helmi, M., Ananta, R. R., Adi, N. S., Kepel, T. L., Ati, R. N. A., Kusumaningtyas, M. A., Suwa, R., Ray, R., Nakamura, T., & Nadaoka, K. (2022). Mangrove Above-Ground Biomass and Carbon Stock in the Karimunjawa-Kemujan Islands Estimated from Unmanned Aerial Vehicle-Imagery. Sustainability (Switzerland), 14(2). https://doi.org/10.3390/su14020706

Yang, W., Liu, Y., & Liu, F. (2020). An improved relative gnss tracking method utilizing single frequency receivers. Sensors (Switzerland), 20(15), 1‑19. https://doi.org/10.3390/s20154073

Yurdakul, Ö., & Kalaycı, İ. (2022). The effect of GLONASS on position accuracy in CORS-TR measurements at different baseline distances. International Journal of Engineering and Geosciences, 7(3), 229‑246. https://doi.org/10.26833/ijeg.975204

Zeybek, M., Taşkaya, S., Elkhrachy, I., & Tarolli, P. (2023). Improving the Spatial Accuracy of UAV Platforms Using Direct Georeferencing Methods: An Application for Steep Slopes. Remote Sensing, 15(10). https://doi.org/10.3390/rs15102700

Zhang, Z., & Zhu, L. (2023). A Review on Unmanned Aerial Vehicle Remote Sensing: Platforms, Sensors, Data Processing Methods, and Applications. In Drones (Vol. 7, Issue 6). MDPI. https://doi.org/10.3390/drones7060398

Zvirgzds, J., & Celms, A. (2020). GNSS RTK Performance Improvements using Galileo Satellite Signal. Latvian Journal of Physics and Technical Sciences, 57(1‑2), 78‑84. https://doi.org/10.2478/lpts-2020-0010

ASSESSMENT AND CHARACTERIZATION OF WATER QUALITY AND POLLUTION IN THE COASTAL ENVIRONMENT OF PEKALONGAN, CENTRAL JAVA, INDONESIA

Muhammad ZAINURI [1*,3], Anindita Rahma CANDRASEKAR [2,3], Kunarso KUNARSO [1], Baskoro ROCHADDI [1], Lilin BUDIATI [4], Salma Ayu SASMITA [1], Asshifa Poetri FEBRIYANTI [1]& Anik SUSILOWATI [1]

DOI: 10.21163/GT_2026.211.19

ABSTRACT

Coastal waters are complex ecosystems essential to environmental, economic, and social sustainability. The dynamic characteristics of the Pekalongan coast are shaped by both natural processes and human activities. This study analyzes pollution characteristics at the Loji and Sengkarang estuaries. In-situ sampling was conducted to measure pH, temperature, salinity, and dissolved oxygen (DO), while ex-situ laboratory analysis was used to examine BOD, COD, TSS, nitrate, phosphate, and total coliform levels. The overall water quality was assessed using the Pollution Index and visualized through a geospatial approach. Results show that pollution indices in Pekalongan's coastal waters fall into the "slightly polluted" to "heavily polluted" category, with varying scores at different stations. The Loji Estuary exhibited higher pollution levels than the Sengkarang Estuary. Coastal areas were generally more polluted than open sea areas. The primary sources of pollution are human activities, including industry, fishing, port operations, agriculture, and residential settlements. A multidisciplinary approach is recommended to foster effective dialogue among researchers, environmental advocates, and stakeholders for the sustainable management of coastal ecosystems.

Keywords: *Water quality; Pollution; Coastal environment; Pekalongan; Anthropogenic.*

1. INTRODUCTION

Coastal waters are complex ecosystems that play a vital role in maintaining environmental, economic, and social sustainability. The Pekalongan coast is one of Central Java's most promising coastal areas and contributes significantly to the fisheries sector. This is supported by the presence of the Pekalongan Nusantara Fisheries Port at the mouth of the Loji River, with marine fisheries

[1]*Universitas Diponegoro, Department of Oceanography, Semarang, Indonesia.* [*]*Corresponding author muhammadzainuri@lecturer.undip.ac.id (MZ); kunarso@lecturer.undip.ac.id (KK); rochaddi@ymail.com (BR); salmaasasmita@gmail.com (SAS); asshifapoetri0204@gmail.com (APF); aniksusilowati099@gmail.com (AS).*

[2] *Universitas Diponegoro, Department of Marine Science, Semarang, Indonesia, sekarahma@students.undip.ac.id (ARC).*

[3] *Universitas Diponegoro, Center for Coastal Rehabilitation and Disaster Mitigation Studies, Semarang, Indonesia, muhammadzainuri@lecturer.undip.ac.id (MZ), sekarahma@students.undip.ac.id (ARC).*

[4] *Universitas Diponegoro, Department of Urban Planning, School of Vocational, Semarang, Indonesia, lilinbudiati@lecturer.undip.ac.id (LB).*

production reaching 9,635.5 tons (a 7.05% increase) in 2024, and by fish auction sites located near the Loji and Sengkarang Rivers (BPS Statistics of Pekalongan Municipality, 2025). The dynamic nature of the Pekalongan coast is largely influenced by environmental variations driven by both natural processes and human activities. Intensive land-based human activities have significantly increased the flow of chemical elements into estuaries via river discharge (Maslukah et al., 2023).

In Indonesia, coastal pollution is primarily caused by high levels of nutrients and organic matter from household wastewater, industrial operations, agriculture, aquaculture, and solid waste (Adyasari et al., 2021). Pekalongan is known as an industrial city with diverse anthropogenic activities. It has a population of 321,095, around 2,894 industrial businesses, 1,407 hectares of agricultural land, 207 aquaculture enterprises, and tourism destinations such as Mangrove Park, Pasir Kencana Beach, Slamaran Indah Beach, and the Batik Museum (BPS Statistics of Pekalongan Municipality, 2025). This broad range of activities raises concerns about water quality degradation and its impact on marine ecosystems due to poorly managed waste. Environmental changes in coastal areas can lead to habitat destruction, biodiversity loss, and a long-term decline in the ecological health of coastal waters (Senarathna Atapaththu et al., 2025).

Previous studies on water quality in Pekalongan have been conducted by (Maslukah et al., 2019) and (Zainuri et al., 2022). Research by (Maslukah et al., 2019) examined the relationship between water quality—particularly phosphate levels—and chlorophyll-a concentrations at the Sragi River estuary. In 2022, (Zainuri et al., 2022) conducted an analysis of flood inundation as part of a disaster mitigation analysis and changes in nutrient distribution patterns. This study demonstrated that these distribution patterns had changed due to hydro-oceanographic factors, weather, and increasing pollution loads due to densely populated settlements, particularly the massive input of poorly managed Batik waste into river ecosystems. The embankment construction process was carried out in stages, resulting in varying inundation patterns and periods (Zainuri et al., 2024; Helmi et al., 2025). This paper's novelty lies in the assumption that seawall construction will continue to evolve following national long-term development policies. Based on this assumption, this research forms part of a sustainable long-term management plan to address disasters resulting from the impacts of seawall development. Research in these areas is essential, as intense human activity may lead to water pollution and a decline in marine ecosystem quality.

One of the mitigation measures implemented is pollution index analysis. Some advantages of using an index include the ability to determine water quality status with only a single sampling and the absence of a time series (Swandani et al., 2023). This reduces the cost and time required. This consideration provides a second novelty that will later be compared through temporal analysis of results from previous years. Therefore, this study aims to characterize pollution in the Loji and Sengkarang estuaries. The findings can serve as a reference for preliminary observations on how different human activities affect estuarine conditions. Water quality directly influences the health of organisms in the region. Thus, it is urgent to control and reduce pollution in coastal waters through regular assessments and a deeper understanding of variations in estuarine water quality.

2. STUDY AREA

This study was conducted in two river estuaries: the Loji River Estuary (stations A1–A7, located at coordinates 109°41'9.56"–109°42'6.80" E and 6°50'43.15"–6°51'45.25" S) and the Sengkarang River Estuary (stations B1–B7, at coordinates 109°39'6.98"–109°40'2.35" E and 6°50'7.98"–6°51'15.84" S). The research locations are shown in **Fig. 1**. Sampling sites were selected using a purposive sampling method to represent river, coastal, and open sea areas. Each estuary was divided into seven stations with the following designations: station 1 in the river, station 3 at the river mouth, stations 2 and 4 in coastal waters, and stations 5 to 7 in the open sea. Differences in station characteristics, determined using a spatial approach, are presented in **Table 1**. In situ data sampling was conducted on 15 May 2025 to represent Transitional Season I, between 06:00 and 12:00 Western Indonesian Time (WIB), when the tide transitioned from high to low.

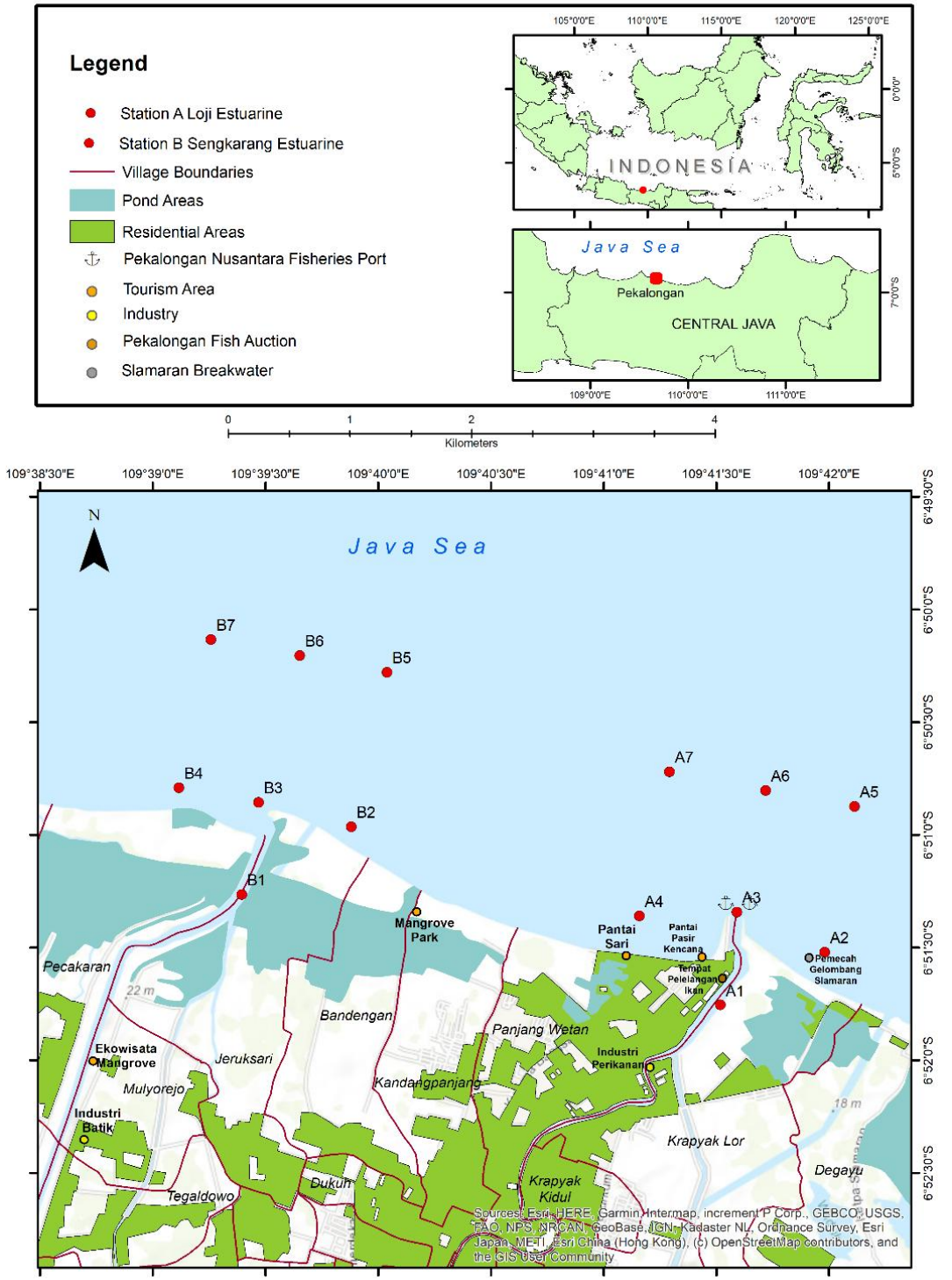


Fig. 1. Sampling location.

Table 1.

Characteristics of the sampling sites (spatial approach).

Location	Station	Characteristics	Ordinate	
			Longitude	Latitude
Loji Estuarine	A1	Loji River, near Pekalongan Fish Auction, settlements, ponds, fish industry	109°41'31.09"E	6°51'45.25"S
	A2	Coastal, near Slamaran Beach and pond areas	109°41'58.85"E	6°51'31.25"S
	A3	River mouth, near Pekalongan Nusantara Fisheries Port	109°41'35.52"E	6°51'20.56"S
	A4	Coastal, near Sari Beach and settlement areas	109°41'9.56"E	6°51'21.56"S
	A5	Open sea area	109°42'6.80"E	6°50'52.44"S
	A6		109°41'43.15"E	6°50'48.16"S
	A7		109°41'17.56"E	6°50'43.15"S
Sengkarang Estuarine	B1	Sengkarang river	109°39'23.69"E	6°51'15.84"S
	B2	Coastal, near Pekalongan Mangrove Park	109°39'52.85"E	6°50'57.80"S
	B3	River mouth, near mangrove forest	109°39'28.19"E	6°50'51.32"S
	B4	Coastal, near mangrove forest	109°39'6.98"E	6°50'47.47"S
	B5	Open sea area	109°40'2.35"E	6°50'16.69"S
	B6		109°39'39.17"E	6°50'12.23"S
	B7		109°39'15.52"E	6°50'7.98"S

3. DATA AND METHODS

3.1. Data Collection and Laboratory Analysis

Water samples were collected from the sea surface at each sampling coordinate and stored in sample containers for laboratory analysis. Temperature and pH were measured in situ using a pH meter, while dissolved oxygen (DO) and salinity were measured using a DO meter and a refractometer, respectively. Water quality parameters were assessed using both in situ and ex-situ approaches. In situ measurements, conducted directly at the sampling sites, were used to evaluate parameters that change rapidly, such as pH, temperature, salinity, and DO. Ex-situ analysis, conducted in the laboratory, measured Biological Oxygen Demand (BOD), Chemical Oxygen Demand (COD), Total Suspended Solids (TSS), nitrate (NO_3^-), phosphate (PO_4^-), and total coliforms. The results of ex-situ tests and laboratory evaluations were compiled in tabular format and analyzed descriptively, supported by a review of relevant literature.

TSS and total coliforms were the primary physical and biological parameters analyzed in the laboratory. TSS was evaluated using the gravimetric method, which involves weighing the sample before and after isolating suspended solids (Alaerts & Santika, 1987). Total coliform analysis employed the Most Probable Number (MPN) method. The presence of fecal coliforms is indicated by metallic green colonies on Eosin Methylene Blue Agar (EMBA) media, while pink colonies indicate non-fecal coliform bacteria (APHA 9221 B.C., 2022) The analysis in this study included laboratory testing of nitrate, phosphate, BOD, and COD parameters. Nitrate concentrations were determined using the cadmium reduction method, where nitrate compounds are reduced to nitrite by cadmium (Cd) coated with copper in a column. The sample was then analyzed using a UV-Vis spectrophotometer at a wavelength of 543 nm (Parsons et al., 1984). Phosphate concentrations were analyzed using the molybdenum blue method, with absorbance measured at 885 nm using a UV-Vis

spectrophotometer (Strickland & Parsons, 1968). BOD_5 was measured using the 5-day BOD method, which quantifies the oxygen consumed during a 5-day incubation period. This includes the oxygen required for the biochemical decomposition of organic substances (carbonaceous demand), oxidation of inorganic compounds such as sulfides and ferrous iron, and oxidation of reduced nitrogen compounds (nitrogenous demand) (APHA 5210 B, 2022a). COD was determined using the closed reflux colorimetric method for water and wastewater samples. In this method, most organic matter in the sample is oxidized by a boiling mixture of chromic and sulfuric acids in the presence of excess potassium dichromate ($K_2Cr_2O_7$). After refluxing, the remaining dichromate is titrated with ferrous ammonium sulfate (FAS), and the color change indicates the end of the reaction (APHA 5220 D, 2022).

3.2. Pollution Index Calculation

The Pollution Index (PI) calculation involved several steps. First, water quality data from each sampling point were entered into a spreadsheet. For each parameter, the ratio between the measured concentration (Ci) and the corresponding water quality standard (Lij) was calculated. For parameters that have an inverse relationship with water quality, such as DO, the ratio was calculated using a special calculation. The maximum ratio was defined as the highest individual parameter ratio between Ci and Lij at each station, while the average ratio was calculated as the arithmetic mean of all parameter ratios. These two values were then combined using Equation (1) to obtain the final PI value for each sampling location. All parameters were given equal weight, and no additional normalization was applied beyond the regulatory formulation. This index can inform decision-makers when water quality declines due to pollutant presence and prompt necessary actions. The overall water quality index for coastal Pekalongan was calculated based on the Ministry of Environment and Forestry Regulation No. 27 of 2021 (Appendix I: Environmental Quality Index), which provides the basis for the PI method. The formula used is shown in Equation (1). A GIS desktop software was employed to visualize the spatial distribution of PI scores and land use in the study area.

The pollution index (PI) was calculated separately for river and coastal waters using parameter sets and reference standards appropriate to each environment. Although several physicochemical parameters were standard to both calculations, the final parameter selection was guided by the respective regulatory water quality criteria. As a result, the type of parameters included in the PI calculation was not identical for river and coastal stations. Instead, PI values were used to evaluate pollution status relative to the designated water quality standards within each aquatic system. In contrast, spatial patterns and qualitative trends were used to infer land–sea interactions. This approach ensures regulatory consistency while avoiding misleading cross-system quantitative comparisons.

$$PI = \sqrt{\frac{\left(\frac{Ci}{Lij}\right)^2 Max + \left(\frac{Ci}{Lij}\right)^2 Avg}{2}} \quad (1)$$

where:
L_{ij}: Standard concentration for water usage (j)
C_i: Sample concentration of water quality parameter (i)
PI: Pollution Index for specific usage
(C_i/L_{ij}) Max: Maximum value of C_i/L_{ij}
(C_i/L_{ij}) Avg: Average value of C_i/L_{ij}

The interpretation of the PI is as follows:

$0 \leq PI \leq 1$ = meets the standard (good condition)
$1 < PI < 5$ = slightly polluted
$5 < PI \leq 10$ = moderately polluted
$PI > 10$ = heavily polluted

4. RESULTS AND DISCUSSIONS

4.1. Assessment of Water Quality at Loji Estuary

This study evaluates river water quality based on temperature, TSS, COD, pH, BOD, DO, phosphate, nitrate, and total coliform levels. The assessment follows Government Regulation No. 22 of 2021, Appendix VI, which provides water quality standards for rivers. **Table 2** presents the results of water quality testing at the Loji and Sengkarang Rivers, based on the standards for class 2 river water. This classification includes activities such as recreation, freshwater aquaculture, livestock, and irrigation—uses consistent with those of the Loji River. Based on the analysis, the PI for the Loji River was 12.2604, categorizing it as heavily polluted.

Table 2.

Water Quality Measurements in the Loji and Sengkarang Rivers.

Water Quality Variable	Unit	Sampling Station (River)		Permitted Level
		A1 (Loji)	B1 (Sengkarang)	
Physical				
Temperature	C	**31.6**	28.85	Dev 3 (23-29)
TSS	mg/L	**73.9**	34.4	50
Chemical				
COD	mg/L	**38.02**	23.15	25
pH		7.93	7.65	6 - 9
BOD	mg/L	2.881	**7.317**	3
DO	mg/L	**0.61**	6.44	4
Phosphate	mg/L	**3.419**	**0.515**	0.2
Nitrate	mg/L	0.420	0.412	10
Biological				
Total Coliform	MPN/ 100 mL	240	49	5000
PI Score		**12.2604**	**2.18113**	
Water Quality Status		**Heavily Polluted**	**Slightly Polluted**	

Permitted level source: National Regulation of the Republic of Indonesia No. 22/2021, Appendix VI.

Based on tests conducted in the Loji River area (A1), all physical parameters, including temperature and total suspended solids (TSS), exceeded the class II river water quality standards. Elevated TSS levels may result from the densely populated settlements surrounding the river, which reduce groundwater absorption. This disrupts the natural soil layer, leading to erosion, runoff, and sedimentation in the river (Istomi et al., 2025). In addition to residential areas, the Loji River is located near the fishing industry, a known source of domestic waste (**Table 1**). The discharge of solid and liquid waste into the river contributes to increased TSS concentrations (Ciupa et al., 2021).

High water temperatures in the Loji River are likely caused by limited vegetation along the riverbanks, allowing direct sunlight to reach the water surface (Pandiangan et al., 2023). Elevated temperatures stimulate microbial activity that breaks down organic matter, increasing oxygen consumption. As a result, DO levels decrease (Anh et al., 2023). The DO value in the Loji River was recorded at 0.61, below the minimum acceptable threshold. Low DO levels can harm aquatic organisms, as oxygen is essential for respiration and metabolic processes. A drop in DO can also increase the toxicity in the water.

In addition to dissolved oxygen (DO), other chemical parameters that exceed designated quality standards include Chemical Oxygen Demand (COD) and phosphate levels in Loji River (A1). These elevated COD and phosphate values are suspected to stem from the careless disposal of Batik dye waste into the river. Based on data from the Pekalongan City Environmental Agency, there are approximately 600 active Batik industries, of which 75% of Batik waste is not adequately processed (Dinas Lingkungan Hidup Kota Pekalongan, 2025). High COD levels in Batik wastewater are

typically attributed to the considerable amount of organic compounds generated during fabric processing, such as starch, oils, and residues from the wax rolling process. Consequently, the river water often appears black and emits an unpleasant odor. Additional organic compounds arise from detergents and caustic soda used during the washing of Batik cloth, contributing to increased phosphate content, which further degrades water quality (Agustina et al., 2025; Safamaura & Afany, 2025). Meanwhile, other parameters—such as pH, BOD, nitrate, and total coliform—remained within the acceptable limits. However, total coliform levels in the Loji River were significantly higher than those in the Sengkarang River, indicating substantial waste contamination, particularly from human or warm-blooded animal sources (Ismanto et al., 2024).

Estuary water quality assessment using the PI method at six sampling points is presented in **Table 3.** Parameters include temperature, TSS, salinity, pH, BOD, DO, phosphate, nitrate, and total coliform. Based on these results, the Loji estuary was categorized as moderately polluted at points A2 and A3 and lightly polluted at other points, with PI values varying at each station (**Fig. 2**). Pollution levels in the coastal area (stations A2, A3, and A4) were higher, with PI scores ranging from 4.89 to 6.88, compared to the offshore stations (A5, A6, and A7), which ranged from 1.72 to 4.69. This pattern is likely due to the coastal area's proximity to human activities on land, which increase pollutant discharge into the estuary via river flow (Indrayanti et al., 2022).

Table 3.

Water Quality Measurements in the Loji Estuary.

Water Quality Variable	Unit	Sampling Station (Loji Estuary)						Permitted Level
		A2	A3	A4	A5	A6	A7	
Physical								
Temperature	C	31.3	31.3	31.1	30.8	31	31	28-32
TSS	mg/L	**80.9**	72.9	**88.7**	60.6	73.4	77.8	80
Chemical								
Salinity	‰	30	23	31	19	30	30	34
pH		8.26	8.18	**8.53**	8.295	8.175	8.27	7-8.5
BOD	mg/L	2.301	2.02	1.778	1.746	1.201	5.21	20
DO	mg/L	6.315	5.435	6.4	6.735	7.025	6.915	5
Phosphate	mg/L	**0.258**	**0.756**	**0.206**	**0.137**	**0.189**	**0.017**	0.015
Nitrate	mg/L	**0.419**	**0.415**	**0.410**	**0.254**	**0.140**	**0.110**	0.06
Biological								
Total Coliform	MPN/ 100 mL	17	49	23	49	14	33	1000
PI Score Water Quality Status		***5.231365 Moderately Polluted***	***6.881005 Moderately Polluted***	***4.8943966 Slightly Polluted***	***4.22408 Slightly Polluted***	***4.69812 Slightly Polluted***	***1.72791 Slightly Polluted***	

Permitted level source: National Regulation of the Republic of Indonesia No. 22/2021, Appendix VIII.

Based on the assessment of the coastal areas (A2-A4), several parameters—namely TSS, nitrate, and phosphate—exceeded the quality standards, as shown in **Table 3**. The increase in TSS levels is believed to be influenced by nearby artificial structures. At sampling point A2, the Slamaran breakwater traps sediment carried by currents, leading to accumulation in that area. At point A4, elevated TSS levels are likely caused by sediment buildup due to the current obstruction from the Pekalongan Nusantara Fisheries Port located to the east. This aligns with the findings of (Senarathna Atapaththu et al., 2025), which stated that coastal construction projects such as ports, seawalls, and breakwaters can disrupt natural water flow and alter tidal patterns. These disruptions can affect water circulation, concentrating pollutants in specific areas and leading to erosion or sediment accumulation that impacts surrounding ecosystems. However, TSS levels at point A2 were lower than those recorded at point A4.

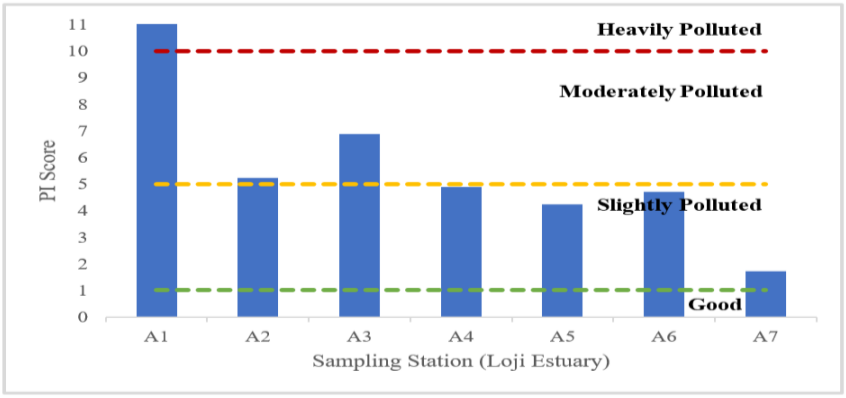


Fig. 2. Classification Ranges of PI Scores at Loji Estuary

In addition, nitrate and phosphate levels in coastal areas exceeded established standards. These nutrients are likely carried by river currents after waste decomposition into organic matter (Maslukah et al., 2023). Beyond river runoff, coastal aquaculture also contributes to nutrient loading. The area of ponds in North Pekalongan sub-district reaches 474.8 hectares (BPS Statistics of Pekalongan Municipality, 2025). Pond activities release organic waste through uneaten or undigested feed and fish excretion, which decomposes and increases nitrogen and phosphorus levels in nearby waters (Edwards et al., 2024). Elevated nitrate and phosphate concentrations were also observed in all open sea locations, likely due to the offshore transport of nutrients by tidal currents.

4.2. Assessment of Water Quality at Sengkarang Estuary

This assessment is based on Government Regulation No. 22 of 2021, Appendix VI, which outlines class II river water quality standards. This classification covers uses such as freshwater aquaculture and irrigation, consistent with the function of the Sengkarang River. Based on the evaluation, the pollution index for the Sengkarang River is 2.18113, indicating a slightly polluted status. Among the tested parameters, only BOD and phosphate exceeded the standard. The BOD value recorded was 7.317 mg/L, while the permissible limit is 3 mg/L (see **Table 2**). BOD refers to the amount of oxygen required by microorganisms to decompose organic matter in water. A high BOD level suggests a significant presence of organic pollutants, likely originating from household waste and decaying vegetation along the river (Anh et al., 2023). This elevated BOD indicates that bacteria are consuming large amounts of oxygen to break down the organic material. Agricultural activities—including the use of pesticides, fertilizers, compost, and manure—also contribute to higher BOD through surface runoff from residential and farming areas (Istomi et al., 2025; Lee et al., 2020). Meanwhile, the recorded phosphate concentration in the Sengkarang River was measured at 0.515 mg/L, which surpasses the permissible limit of 0.2 mg/L (refer to Table 2). This elevation in phosphate levels can be attributed to the multitude of anthropogenic and industrial activities in the vicinity of the river. Furthermore, the Sengkarang River functions as a transit route for local fishermen and is utilized for various activities, including bathing, washing, and recreational white-water rafting. Such practices can significantly contribute to the increased influx of phosphate into the aquatic environment, thereby amplifying concerns regarding water quality and its ecological implications (Damayanti et al., 2022).

Water quality in the Sengkarang estuary was assessed using the PI method at six sampling points, as shown in **Table 4**. Based on the results, the estuary is categorized as slightly to moderately polluted, with varying PI scores at each location (**Fig. 3**). Pollution levels were higher in coastal areas (stations B2, B3, and B4), with PI values ranging from 4.75 to 5.19, compared to the open sea stations (B5, B6, and B7), which ranged from 3.47 to 4.82. Similar to the Loji estuary, this trend is likely due to human activity near coastal areas, which introduces more pollutants into the estuary through river flow.

Table 4.

Water Quality Measurements in the Sengkarang Estuary.

Water Quality Variable	Unit	Sampling Station (Sengkarang Estuary)						Permitted Level
		B2	**B3**	**B4**	**B5**	**B6**	**B7**	
Physical								
Temperature	°C	31.45	29.3	30.4	30.92	30.35	31.35	28-32
TSS	mg/L	**83.3**	40.8	47.9	78.4	53.7	58.4	80
Chemical								
Salinity	‰	26.5	14	25	25	24.5	25	34
pH		8.48	7.915	8.325	8.505	8.435	8.43	7-8.5
BOD	mg/L	1.838	1.206	2.067	1.298	1.672	1.617	20
DO	mg/L	6.86	6.68	6.84	6.995	7.195	7.085	5
Phosphate	mg/L	**0.189**	**0.206**	**0.258**	**0.206**	**0.155**	**0.086**	0.015
Nitrate	mg/L	**0.387**	**0.356**	**0.347**	**0.099**	**0.094**	**0.085**	0.06
Biological								
Total Coliform	MPN/ 100 mL	13	27	33	7.8	4.5	6.8	1000
PI Score		***4.75334***	***4.84556***	***5.19692***	***4.82457***	***4.37327***	***3.47375***	
Water Quality Status		***Slightly Polluted***	***Slightly Polluted***	***Moderately Polluted***	***Slightly Polluted***	***Slightly Polluted***	***Slightly Polluted***	

Permitted level source: National Regulation of the Republic of Indonesia No. 22/2021, Appendix VIII.

In the coastal area (B2–B4), several parameters exceeded the quality standards, including TSS, nitrate, and phosphate (see **Table 4**). Elevated TSS at station B2 is likely influenced by the nearby lagoon. The lagoon's sedimentary basin traps sediments transported by currents, increasing the solubility of suspended solid pollutants due to contributions from the mainland and estuary, along with current-induced movement (Erfando et al., 2023). This disruption in water circulation can lead to erosion or sediment accumulation, which affects the surrounding ecosystem. Increased nitrate and phosphate levels in coastal stations are likely caused by decomposing waste carried by river flow. The continuous release of organic waste contributes to nutrient buildup in the coastal areas (B2, B3, and B4), with concentrations decreasing toward the open sea (Indrayanti et al., 2022). This is consistent with (Feng et al., 2024), who noted that nutrient levels are typically higher near land due to terrestrial influences such as agricultural runoff, domestic waste, and industrial activity. Agriculture and residential settlements are the primary sources of pollution in the Sengkarang River.

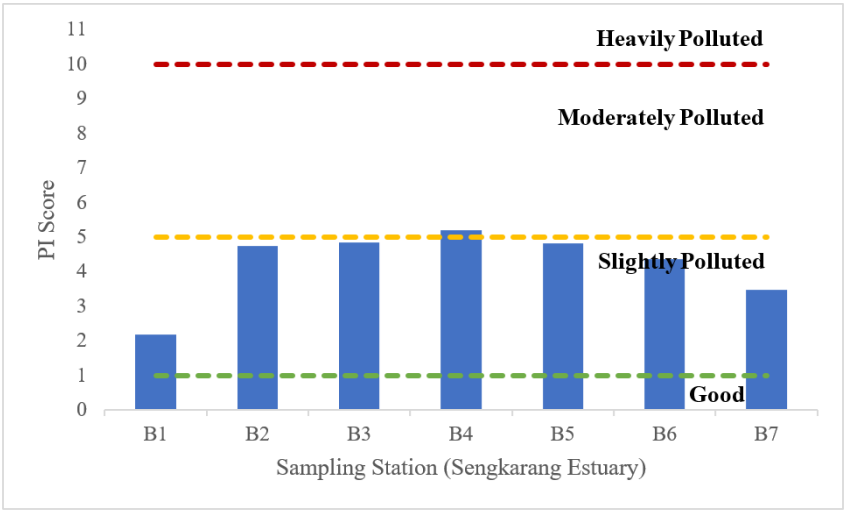


Fig. 3. Classification Ranges of PI Scores at Sengkarang Estuary.

4.3. Characterization and Evaluation of Water Pollution

4.3.1. Comparative Analysis of Pollution Index Between Estuaries

Water quality and pollution profiles were analyzed using several parameters: TSS, COD, BOD, DO, pH, salinity, phosphate, nitrate, and total coliform. The PI provides a single value summarizing water quality by integrating multiple parameters measured at a specific time and location. The coastal water quality assessment using the PI method for the Loji and Sengkarang estuaries is illustrated in **Fig. 4**. The results indicate that both estuaries fall into the "slightly polluted" to "heavily polluted" category, with varying PI scores across sampling points. The Loji Estuary shows higher pollution levels than the Sengkarang Estuary. This is attributed to various anthropogenic activities, including industrial discharge, domestic waste, and port operations, that heavily influence the Loji River mouth. According to data from the Environmental Agency of Pekalongan City, the amount of wastewater generated from domestic activities is 30,549.22 m³/day, corresponding to a population of 318,221 in 2024 (Dinas Lingkungan Hidup Kota Pekalongan, 2025). The estuary is also located near the Pekalongan Nusantara Fisheries Port, which functions as a boat mooring site and fish auction center and receives waste from fish processing activities. Intensive port activities can increase wastewater containing dissolved organic matter, nitrates, and phosphates.

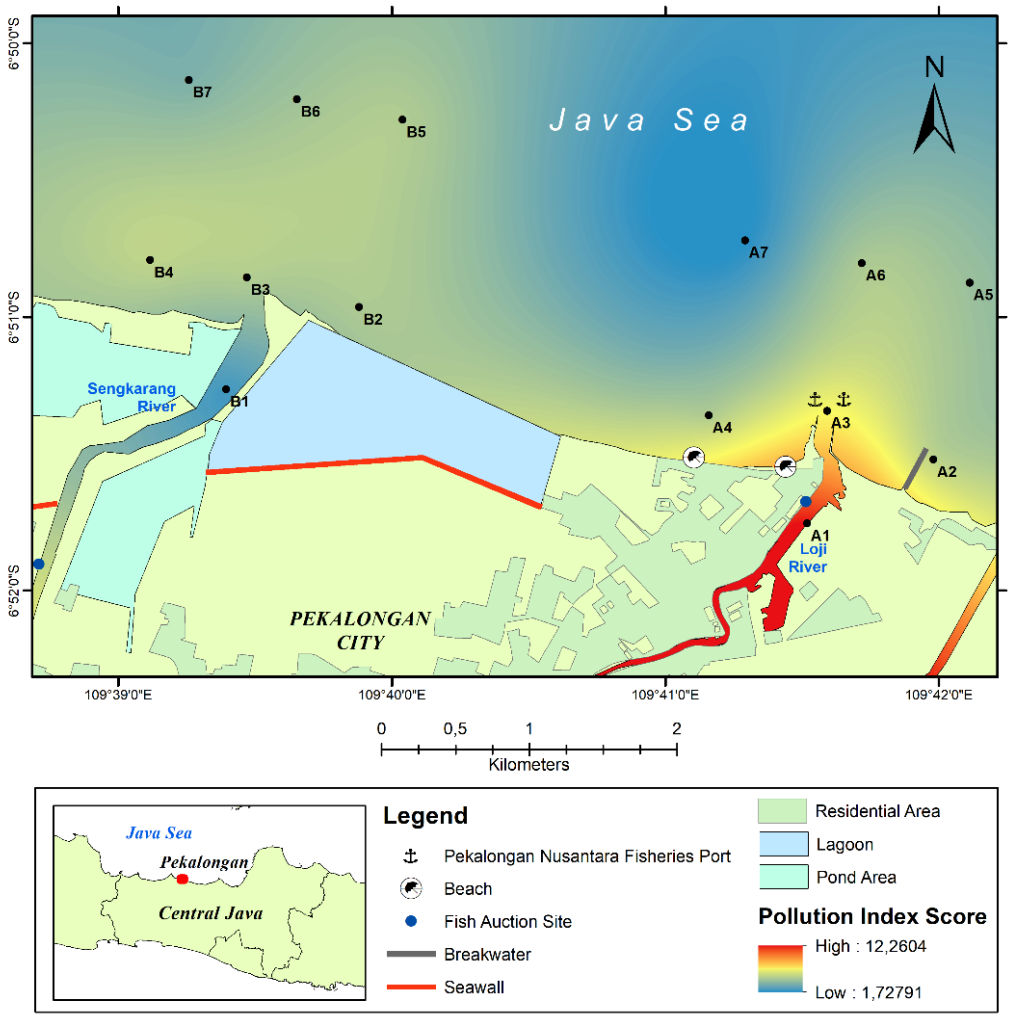


Fig. 4. Spatial distribution of Pollution Index for Loji and Sengkarang Estuaries.

Additionally, pollution input is amplified by household, agricultural, and industrial activities along the river that discharge waste into the estuary (Wardani et al., 2024). According to (I Patty et al., 2019), villages, ports, industrial areas, and river systems significantly contribute to marine waste, making the surrounding waters highly susceptible to pollution and water quality degradation.

4.3.2. Influence of Hydrodinamic Factors on Pollution Distribution

Pollutant distribution is also influenced by tides, which result from differences in gravitational forces arising from the Moon and Sun's changing positions relative to Earth's surface. The coastal area of Pekalongan has a mixed tidal type, consistent with the general tidal pattern on the north coast of Java (Windupranata et al., 2024). The highest high tide was 2.48 m, and the lowest low tide was 1.44 m. The tidal pattern is shown in **Fig. 5,** where the high-tide-to-low-tide transition dominates sampling. Under these conditions, river flow exceeds sea flow, resulting in the accumulation of organic matter in the estuary, which then moves offshore.

Tidal patterns can alter current direction. Based on modeling results, the current direction at the time of sampling was predominantly northwest, southwest, and southeast. Current speeds at high and low tide were lower than those between low and high tide, a phenomenon known as the slack-water effect (Shidqirrohman et al., 2024). As seen in **Fig. 6**, current speeds initially peaked northwestward during low tide to high tide, then decreased at 8:00 a.m. Western Indonesian Time (WIB), when the highest tide occurred, and the current direction turned landward. Subsequently, current speeds increased southeastward, affecting pollutant transport in the waters. This hydrodynamic condition plays a crucial role in shaping the spatial distribution of Pollution Index (PI) values across the study area. Higher PI values observed at coastal stations (A2-A4 and B2-B4) compared to open sea stations (A5-A7 and B5-B7) can be attributed to the proximity of these coastal sites to land-based pollution sources, including river discharge and anthropogenic activities. As the ebb tide progresses, pollutants accumulated in estuarine and nearshore zones are transported offshore by seaward-directed currents, leading to a gradual dilution effect with increasing distance from the coast, which is reflected in the lower PI values at offshore stations. This pattern also influenced pollutant distributions in offshore waters, with elevated levels at eastern stations such as A5, A6, and B5.

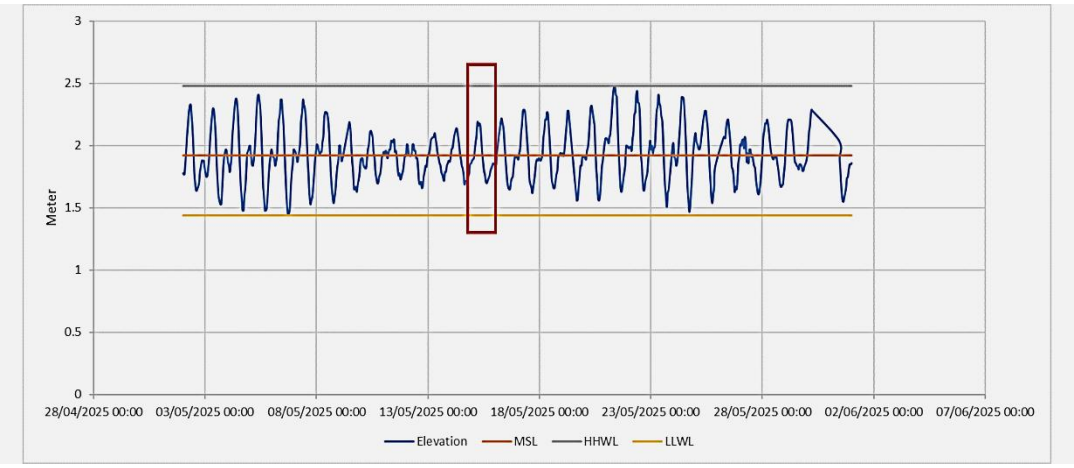


Fig. 5. Tidal Graph of Pekalongan Waters.

In addition to tides and currents, rainfall indirectly affects coastal water pollution through runoff and the transport of materials from upstream areas to estuaries and coastal waters. Stations located near river mouths, particularly A3 and B3, exhibited relatively elevated PI values, which may be influenced by antecedent rainfall prior to sampling. Rainfall can enhance surface runoff and mobilize pollutants from upstream catchments, subsequently increasing pollutant loads entering the estuarine environment. Rainfall levels several days before sampling are shown in **Fig. 7**.

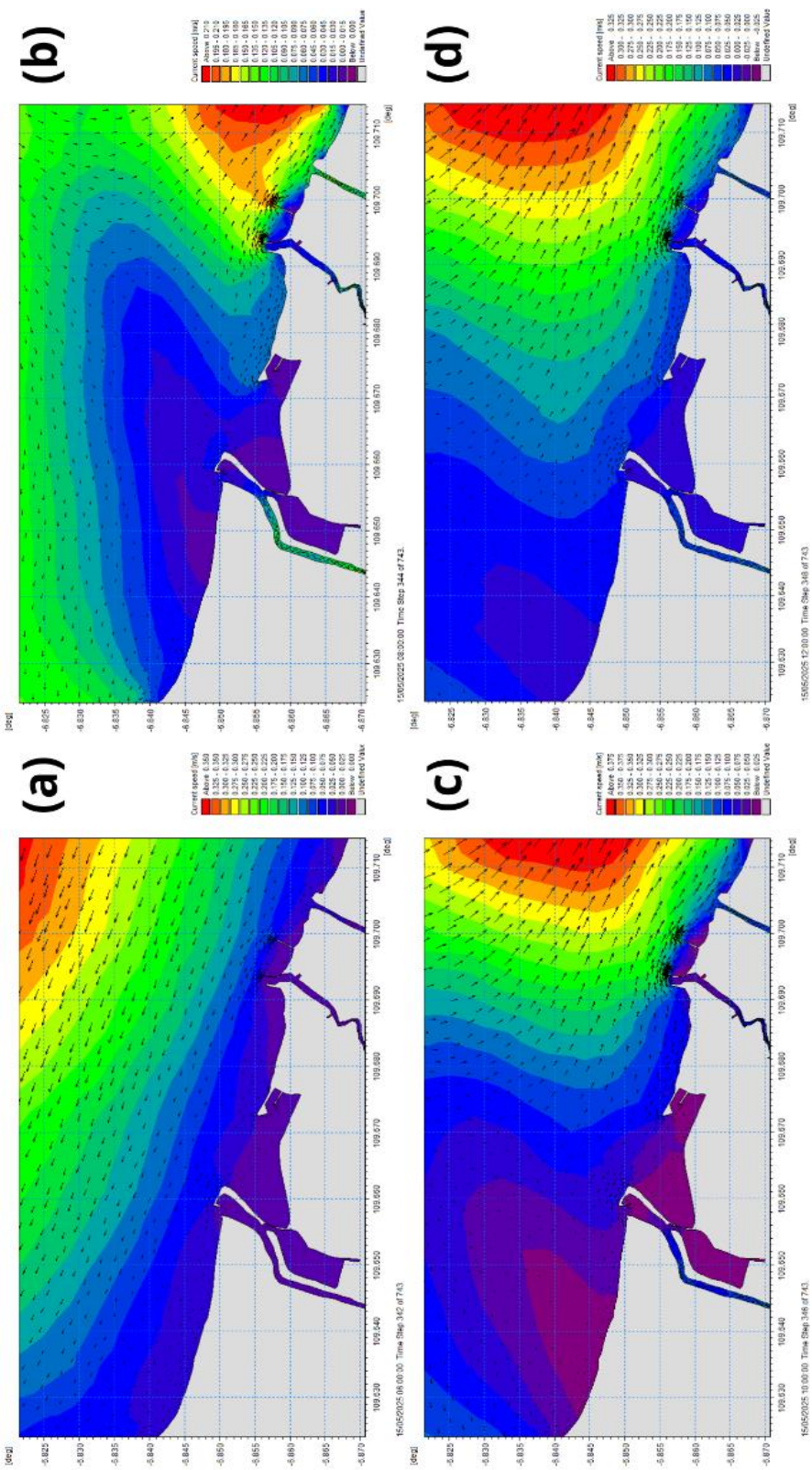


Fig. 6. Surface Current Patterns (a) 06.00 WIB, (b) 08.00 WIB, (c) 10.00 WIB, (d) 12.00 WIB.

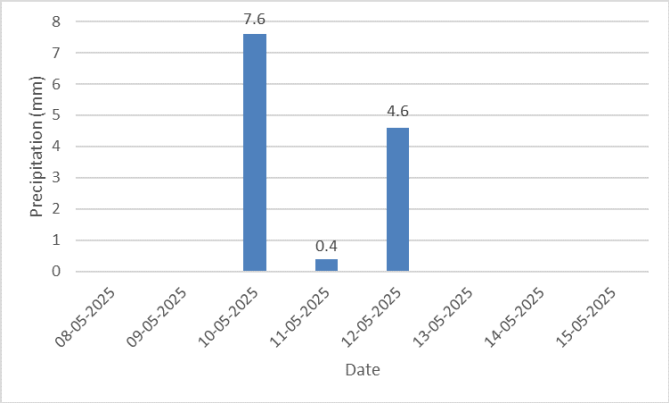


Fig. 7 Rainfall Levels Before the Sampling Period.

Even at relatively low intensities, rainfall events can dissolve and transport pollutants accumulated on land surfaces, in drainage channels, and in river bodies. This process is accumulative and has a time lag, so the impact of rainfall is not always immediately detectable on the day of the incident. Still, it may appear several days later in coastal areas. Furthermore, hydrodynamic conditions, such as relatively weak tides and currents during the transitional season, can slow dispersion, allowing pollutants carried from land to accumulate along the coast and increase pollution levels in that area. The combined effects of rainfall-driven inputs and tidal current transport therefore explain the observed spatial variability in PI values, highlighting the strong coupling between hydrodynamic processes and water quality conditions in the study area.

4.3.3. Key Pollution Parameters and Sources

In this study, the parameters TSS, phosphate, and nitrate exceeded coastal water quality standards. Elevated TSS levels are attributed to coastal development projects, such as ports, embankments, and breakwaters, which disrupt natural water flow and tidal movements, leading to sediment accumulation in nearby areas. Phosphate levels were consistently high across all locations. This increase is primarily caused by river runoff carrying organic waste−including detergents, human waste, and household cleaners−into the sea. These substances are major sources of phosphate and initiate biogeochemical processes involving the breakdown of organic matter. Nitrate levels also rose due to similar processes. The bacterial decomposition of organic matter in wastewater results in the formation of nitrate molecules. This process, referred to as nitrate output, contributes to water quality indices. The presence and activity of bacteria significantly influence nitrate concentrations, which are also linked to organic matter and sediment in the water. While biogeochemical processes are simplified in water quality calculations, they are more complex under natural conditions and vary by location and time.

Across all stations, nitrate concentrations were higher in coastal areas than in the open sea. Typically, nitrate levels are greatest near land and decrease with distance from shore (Adnina et al., 2023). This pattern reflects the influence of tides, currents, and bathymetry, which facilitate nitrate accumulation in coastal zones (Patanda et al., 2024; Zainuri et al., 2022). Nitrate distribution generally mirrors pollution patterns, with coastal areas exhibiting higher levels of both. The pollution pattern is highly concentrated in the coastal area and then decreases in the open sea following the current. In marine environments, nitrate is often the primary limiting nutrient in the nitrogen-to-phosphorus (N:P) ratio, a key indicator of algal bloom potential (Feng et al., 2024). While elevated nutrient levels can enhance phytoplankton growth and fish production, they also pose risks, including oxygen depletion and the proliferation of harmful algal blooms.

4.3.4. Regional Comparison and Study Limitations

The novelty found in this study is the distributions of all variables were concentrated in the coastal area and decreased in the land during the sea level rise (high tidal flood) compared to the (Zainuri et al., 2022) result. These previous studies demonstrated a distribution related to the land elevation which are not limited by the presence of embankment. The limitation of pollution distribution identified by the application of the pollution index and resulting a narrow scale of the pollution values. A significant limitation of this study is the reliance on a single sampling campaign conducted in May 2025. Water quality in estuarine and coastal environments exhibits pronounced seasonal variability, driven by changes in rainfall and hydrodynamic conditions. May represents a transitional period between the wet and dry seasons in Indonesia, which may not fully capture annual water quality conditions. Future studies incorporating multi-seasonal sampling and relevant meteorological and hydrological data, with emphasis on precipitation rate and period, are recommended to improve the robustness of the conclusions. Another limitation of this study is the lack of quantitative data on wastewater discharge volumes and pollutant loads from each source, such as fishing ports, agriculture, and aquaculture. The absence of sector-specific discharge data limits the applicability of quantitative source-identification analyses. Consequently, pollution sources are discussed qualitatively, drawing on land-use information, spatial patterns in water-quality parameters, and supporting evidence from prior research. Future studies that integrate discharge measurements, pollutant load estimation, and source identification modeling are recommended to strengthen causal attribution.

High pollution levels are not unique to the Pekalongan coast but are also observed in various areas surrounding the Java Sea. To place the findings of this study in a broader national context, **Table 5** presents pollution levels reported for several Indonesian coastal regions. It should be noted that the pollution levels presented in Table 5 were derived from different studies that employed varying sets of water quality parameters, pollution index formulations, and reference standards. Differences in study periods, seasonal conditions, sampling times, and spatial coverage may also influence the reported pollution status. Therefore, the comparison in **Table 5** is intended to provide a qualitative overview of pollution conditions in several Indonesian coastal areas rather than a direct quantitative comparison.

Pollution levels are reported using the original methodologies and reference standards employed in each study and are qualitatively compared to illustrate general pollution patterns across Indonesian coastal regions. In general, these areas experience pollution primarily due to human activities such as industrial operations, fishing, port activity, agriculture, and residential development. Inadequate waste management significantly contributes to rising pollution levels (Tosepu & Umu Nasibah, 2025). Additionally, climate change-related factors—such as sea level rise and marine heatwaves—further increase the vulnerability of coastal waters (Senarathna Atapaththu et al., 2025). Pollution in coastal areas endangers both the marine ecosystem and the well-being of the surrounding communities. Without effective mitigation, this ongoing pollution poses serious risks to coastal ecosystems and may lead to long-term environmental degradation. A multidisciplinary approach is recommended to foster effective dialogue among researchers, environmental advocates, and stakeholders for the sustainable management of coastal ecosystems.

Table 5

Pollution Levels in Several Coastal Regions of Indonesia.

Study Sites	Pollution Level	Sources
West Java, North Bekasi, and Indramayu Coasts	Slightly polluted	(Patanda et al., 2024)
Banten, Banten Bay	Slightly to moderately polluted	(Adnina et al., 2023; Dafitri et al., 2025; Rahmania et al., 2024)
Lampung, Ketapang Beach	Moderately polluted	(Delis et al., 2024)
South Kalimantan, Kusan Estuary	Moderately polluted	(Zainudin et al., 2024)

5. CONCLUSIONS

The PI values for the Loji and Sengkarang estuaries indicate that both fall into the polluted category, with varying scores across sampling points. Pollution levels in the Loji Estuary are generally higher than those in the Sengkarang Estuary, primarily due to anthropogenic influences such as industrial discharge, household waste, and port-related activities. Coastal areas also show higher pollution levels compared to open sea zones. Similar patterns are observed in other coastal regions around the Java Sea. Pollution in these areas largely originates from human activities, including industrial operations, fishing, port infrastructure, agriculture, and residential development. The findings of this study provide valuable insights for stakeholders to recognize the environmental impact of industries located near water bodies that discharge waste into rivers and, ultimately, the ocean. This study serves as a baseline assessment, highlighting the need for more extensive future studies to explore additional influencing factors. A comprehensive and cooperative approach is essential for fostering a healthy and sustainable coastal ecosystem.

ACKNOWLEDGEMENTS

This research was supported by a Research Grant from the Faculty of Fisheries and Marine Sciences, Universitas Diponegoro, and funded by the State Budget under No. 16/UN7.F10/PP/III/2025, dated 17 March 2025.

REFERENCES

Adnina, G. S. N., Rastina, & Sulistiono. (2023). Water pollution index based on physical-chemical parameters in Bojonegara Coastal Waters of Banten Bay, Indonesia. *IOP Conference Series: Earth and Environmental Science*, *1251*(1). https://doi.org/10.1088/1755-1315/1251/1/012023

Adyasari, D., Pratama, M. A., Teguh, N. A., Sabdaningsih, A., Kusumaningtyas, M. A., & Dimova, N. (2021). Anthropogenic impact on Indonesian coastal water and ecosystems: Current status and future opportunities. *Marine Pollution Bulletin*, *171*, 112689. https://doi.org/10.1016/j.marpolbul.2021.112689

Agustina, E. B., Lestiyanti, Y., Tachriri, Y. I., & Ulfiya, N. (2025). Analisis Pengaruh Limbah Cair terhadap Kualitas Air Sungai di Kota Pekalongan. *INSOLOGI: Jurnal Sains Dan Teknologi*, *4*(2), 230–239. https://doi.org/10.55123/insologi.v4i2.5117

Alaerts, G., & Santika, S. S. (1987). *Water Research Method*. Usaha Nasional.

American Public Health Association (APHA). (2022). *Standard Method for The Examination of Water and Wastewater: Vol. 5210 B* (24th ed.). American Public Health Association (APHA).

American Public Health Association (APHA). (2022). *Standard Method for The Examination of Water and Wastewater: Vol. 5220 D* (24th ed.). American Public Health Association (APHA).

American Public Health Association (APHA). (2022). *Standard Method for The Examination of Water and Wastewater: Vol. 9221 B.C.* (24th ed.). American Public Health Association (APHA).

Anh, N. T., Can, L. D., Nhan, N. T., Schmalz, B., & Luu, T. Le. (2023). Influences of key factors on river water quality in urban and rural areas: A review. *Case Studies in Chemical and Environmental Engineering*, *8*, 100424. https://doi.org/10.1016/j.cscee.2023.100424

BPS Statistics of Pekalongan Municipality. (2025). *Pekalongan Municipality in Figures* (Vol. 30). BPS Statistics of Pekalongan Municipality. [Online] Available from: https://pekalongankota.bps.go.id/id/publication/2025/02/28/d4aa7ac234f2a4426bfde31d/kota-pekalongan-dalam-angka-2025.html [Accessed 18th September 2025].

Delis, P., Yuliana, D., & Kartini, N. (2024). Study of Water Quality and Pollution Level at Ketapang Beach, Pesawaran Regency, Lampung. In *AQUASAINS Jurnal Ilmu Perikanan dan Sumberdaya Perairan*, *12*(3). https://doi.org/10.23960/aqs.v12i3.p1563-1574

Ciupa, T., Suligowski, R., & Wałek, G. (2021). Impact of an urban area on the dynamics and features of suspended solids transport in a small catchment during floods. *Ecohydrology & Hydrobiology*, *21*(4), 595–603. https://doi.org/10.1016/j.ecohyd.2020.11.006

Dafitri, E., Hariyadi, S., Sulistiono, S., Putri, A. W., Supriyono, E., Puspito, G., Prihatiningsih, I., Supyan, S., & Sarasati, W. (2025). Water Quality Status in Margagiri-Grenyang Coastal Waters, Banten Bay. *BIO Web of Conferences*, *176*. https://doi.org/10.1051/bioconf/202517601018

Damayanti, T. R., Ismanto, A., Indrayanti, E., Zainuri, M., & Maslukah, L. (2022). Distribution of Phosphate Concentration in the Sengkarang River Estuary with a 2-Dimensional Mathematical Model Approach. *Indonesian Journal of Oceanography*, *4*(1), 12–22. [in Bahasa] https://doi.org/10.14710/ijoce.v4i1.12691

Dinas Lingkungan Hidup Kota Pekalongan. (2025). Executive summary: Environmental management performance information document (DIKPLHD) of Pekalongan City, 2025 [in Bahasa]. Kota Pekalongan: Dinas Lingkungan Hidup Kota Pekalongan. [Online] Available from: https://dlh.pekalongankota.go.id//upload/file/file_20251008032355.pdf [Accessed 15th December 2025].

Edwards, T. M., Puglis, H. J., Kent, D. B., Durán, J. L., Bradshaw, L. M., & Farag, A. M. (2024). Ammonia and aquatic ecosystems – A review of global sources, biogeochemical cycling, and effects on fish. *Science of The Total Environment*, *907*, 167911. https://doi.org/10.1016/j.scitotenv.2023.167911

Erfando, W., & Ismanto dan Sri Yulina Wulandari, A. (2023). Distribution of Suspended Solid Material in Pekalongan Waters Lagoon. *Indonesian Journal of Oceanography*, *05*(03), 158–164. [in Bahasa] https://doi.org/10.14710/ijoce.v5i3.19042

Feng, M., Li, W., Huang, X., Hou, W., & Yu, J. (2024). Distribution Characteristics and Driving Factors of Chlorophyll a and Pollutants in the Liugu Estuary. *Water, Air, & Soil Pollution*, *235*(8), 490. https://doi.org/10.1007/s11270-024-07290-3

Helmi, M., Sugianto, D. N., Widyani, A. P., Candrasekar, A. R., Zainuri, M., Ferdian, R. A., Widada, S., Rochaddi, B., Rofiqoh, F. N., Sitanggang, M. M. N., Durhan, Y. Z., Ratu, K. A. S., & Jihadi, M. S. (2025). Influence of Embankment Construction on Oceanographic Parameters and Emerging Pollutant Dynamics in Pekalongan Waters, Central Java. *Environmental Quality Management*, *35*(1). https://doi.org/10.1002/tqem.70125

I Patty, S., Pandu Rizki, M., Rifai, H., & Akbar, N. (2019). Study of Water Quality and Marine Water Pollution Index in Manado Bay Reviewed from the Physico-Chemical Parameters of Sea Water. *Jurnal Ilmu Kelautan Kepulauan*, *2*(2), 1–13. [in Bahasa] https://doi.org/10.33387/jikk.v2i2.1387

Indrayanti, E., Maslukah, L., Astariningrum, M., & Zainuri, M. (2022). Impact of Nutrients and Suspended Particulate Matter on Phytoplankton Chlorophyll-a Biomass, in the Estuary of Kendal, Indonesia. *Ecological Engineering & Environmental Technology*, *23*(4), 212–218. https://doi.org/10.12912/27197050/150635

Ismanto, A., Zainuri, M., Sugianto, D. N., Rochaddi, B., Widada, S., Atmodjo, W., Satriadi, A., Siagian, H., Ridarto, A. K. Y., Anindita, M. A., Sibero, M. T., & Hadibarata, T. (2024). Tidal Current-Driven Coliform Bacteria Distribution in Pekalongan Waters and Estuaries, Indonesia. *Environmental Quality Management*, *34*(2). https://doi.org/10.1002/tqem.70016

Istomi, A. R., Suharso, Buhani, Tugiyono, Satria, H., Artika, E., & Zulaicha, A. S. (2025). Study of water pollution parameters in the dry and rainy seasons on the pollution index of the Mesuji River, Lampung, Indonesia. *Results in Chemistry*, *13*, 101906. https://doi.org/10.1016/j.rechem.2024.101906

Lee, J.-W., Lee, S.-W., An, K.-J., Hwang, S.-J., & Kim, N.-Y. (2020). An Estimated Structural Equation Model to Assess the Effects of Land Use on Water Quality and Benthic Macroinvertebrates in Streams of the Nam-Han River System, South Korea. *International Journal of Environmental Research and Public Health*, *17*(6), 2116. https://doi.org/10.3390/ijerph17062116

Maslukah, L., Handoyo, G., Wulandari, S., Sihite, C. B., & Sarjito, S. (2023). The Chlorophyll-a Response of Phytoplankton to Ratio N/P in Different Coastal Waters. *Ecological Engineering & Environmental Technology*, *24*(9), 121–129. https://doi.org/10.12912/27197050/172292

Maslukah, L., Zainuri, M., Wirasatriya, A., & Salma, U. (2019). Spatial Distribution of Chlorophyll-a and Its Relationship with Dissolved Inorganic Phosphate Influenced by Rivers in the North Coast of Java. *Journal of Ecological Engineering*, *20*(7), 18–25. https://doi.org/10.12911/22998993/108700

Pandiangan, Y. S., Zulaikha, S., Warto, W., & Yudo, S. (2023). Ciliwung River Water Quality Status Based on Online Monitoring in the DKI Jakarta Region Reviewed from Temperature, pH, TDS, DO, DHL, and Turbidity Parameters. *Jurnal Teknologi Lingkungan*, *24*(2), 176–182. [in Bahasa] https://doi.org/10.55981/jtl.2023.1003

Parsons, T. R., Maita, Y., & Lalli, C. M. (1984). *A Manual of Chemical and Biological Methods for Seawater Analysis*. Pergamon Press.

Patanda, M., Ernaningsih, D., & Limbong, M. (2024). Mapping West Java Northern waters quality using sea water quality standards. *Depik*, *13*(3), 439–446. https://doi.org/10.13170/depik.13.3.40641

Rahmania, A., Iswantari, A., & Sulistiono. (2024). Pollution level in Domas coastal waters based on some water quality parameters. *BIO Web of Conferences*, *106*. https://doi.org/10.1051/bioconf/202410602009

Safamaura, R. S., & Afany, M. R. (2025). The Effect of Batik Industry Liquid Waste on the Water Quality of the Loji River in Pekalongan. *Jurnal Tanah Dan Sumberdaya Lahan*, *12*(1), 153–158. [in Bahasa] https://doi.org/10.21776/ub.jtsl.2025.012.1.15

Senarathna Atapaththu, K. S., Herath, S. S., Subramaniam, G., Ajith Lalith Weerasinghe Yapa, Y. M., Shirani Manel Kumari, W. G., Masakorala, K., Kolita Kamal Jinadasa, B. K., & Wu, M. (2025). Challenges in coastal ecosystem Sustainability: Drivers of water quality degradation and their ecological impact. *Marine Environmental Research*, *209*, 107194. https://doi.org/10.1016/j.marenvres.2025.107194

Shidqirrohman, N., Handoyo, G., & Ismanto, A. (2024). Study of Current Patterns in the Banger River Estuary Area, Pekalongan City, Central Java. *Indonesian Journal of Oceanography, 6*(1), 39-48. [in Bahasa] https://ejournal2.undip.ac.id/index.php/ijoce

Strickland, J. D. H., & Parsons, T. R. (1968). *A Practical Handbook of Sea Water Analysis*. Fisheries Research Board of Canada.

Swandani PA, Yuliani E, & Haribowo R. (2023). View of Study of Determining Water Quality Status Using the STORET Method, Pollution Index, and CCME-WQI in the Metro River, Malang City, East Java. *Jurnal Teknologi dan Rekayasa Sumber Daya Air*, *3*(2), 780. [in Bahasa] https://doi.org/10.21776/ub.jtresda.2023.003.02.066

Tosepu, R., & Umu Nasibah, S. (2025). *Impact of Environmental Pollution in Coastal Areas: A Review*. 2(1), 80-90. https://stikbar.org/ycabpublisher/index.php/jhsp/article/view/1171/500

Wardani, A. E., Zainuri, M., Wulandari, S. Y., & Rochaddi, B. (2024). Distribution of Chlorophyll-a and Total Suspended Solids (TSS) in the Loji River Estuary, Pekalongan. *Indonesian Journal of Oceanography*, *6*(3), 229–238. [in Bahasa] https://doi.org/10.14710/ijoce.v6i3.18194

Windupranata, W., Nusantara, C. A. D. S., & Nuraghnia, A. (2024). Spatial Variation of Tidal Characteristics in the Java Sea Based on the TPXO9v5 Global Tide Model. *Buletin Oseanografi Marina*, *13*(2), 239–249. [in Bahasa] https://doi.org/10.14710/buloma.v13i2.59689

Zainudin, M., Nursalam, N., & Amri, U. (2024). Analysis of Water Quality Pollution Levels Using the Pollution Index (IP) Method in the Kusan River Estuary, Tanah Bumbu Regency. *Marine Coastal and Small Islands Journal - Jurnal Ilmu Kelautan*, *4*(1), 1. [in Bahasa] https://doi.org/10.20527/m.v4i1.11779

Zainuri, M., Helmi, M., Novita, M. G. A., Pancasakti Kusumaningrum, H., & Koch, M. (2022). An Improve Performance of Geospatial Model to Access the Tidal Flood Impact on Land Use by Evaluating Sea Level Rise and Land Subsidence Parameters. *Journal of Ecological Engineering*, *23*(2), 1–11. https://doi.org/10.12911/22998993/144785

Zainuri, M., Suryani, O. G. A., Ismanto, A., Handoyo, G., Rifai, A., Rochaddi, B., Endrawati, H., Kusumaningrum, H. P., Jihadi, M. S., & Hadibarata, T. (2024). Geospatial Modeling of the Nitrate Distribution as an Indicator of Aquatic Fertility in the Lagoon Waters of the Mangrove Information Center (PIM), Pekalongan. *Jurnal Kelautan Tropis*, *27*(3), 401–407. https://doi.org/10.14710/jkt.v27i3.24081

DEVELOPMENT OF FLOOD RISK MAPS USING AN INTEGRATED HYDRODYNAMIC MODEL AND FAHP IN THE LOWER NAM PHONG BASIN, THAILAND

Chalermchai PAWATTANA[1], Phaisarn JEEFOO [2*], Chaiwiwat VANSAROCHANA[3] & Satit POOPIWKHAM [4]

DOI: 10.21163/GT_2026.211.20

ABSTRACT

Flooding frequently affects rivers and low-lying areas of the Phong River, making flood risk assessment essential for mitigation and loss reduction. This study developed flood risk maps for the Lower Nam Phong basin using a fuzzy analytic hierarchy process (FAHP) integrated with GIS. Hazard (flood depth, slope, soil drainage) and vulnerability (land use) weights were derived through FAHP. Results show that under baseline conditions, 19.44% of Nong Bua, Bung Nium, and Khok Sri Sub-Districts were classified as high risk, consistent with historical flood records. Future scenarios indicate downstream expansion of high-risk zones: 10.45% under RCP 4.5 (Representative Concentration Pathways) and 12.00% under RCP 8.5, particularly in Bung Nium and Khok Sri. Across all scenarios, medium-risk areas dominated (8.13, 36.45, and 72.67 km^2 for baseline, RCP 4.5, and RCP 8.5, respectively). The maps provide actionable insights for flood management and planning in the basin.

Keywords: *Climate change; Representative Concentration Pathways (RCP); Flood risk; Fuzzy analytic hierarchy process (FAHP); GIS; Lower Nam Phong basin;*

1. INTRODUCTION

Floods are among Thailand's most destructive hazards (Singkran, 2017), repeatedly affecting the Lower Nam Phong basin (Nut et al., 2013). The 2011 flood, driven by extreme rainfall and tropical storms, caused widespread damage to agriculture, infrastructure, and livelihoods, highlighting the basin's vulnerability (Promchote et al., 2016). Despite this history, basin-specific flood risk maps that integrate physically based hydrodynamic modeling with transparent vulnerability weighting remain scarce. Previous studies often relied on single hazard indices or heuristic scoring, with limited validation against observed events, leaving a gap in reliable tools for local flood management (Arianti et al., 2023; Maranzoni et al., 2023; Bokhari et al., 2024).

Flood risk is commonly defined as the interaction of hazard and vulnerability (Vojinovic et al., 2016; Hagos et al., 2022; Edamo et al., 2023). Hazard factors such as flood depth, slope, and soil drainage determine physical exposure (Hu et al., 2017), while land use strongly influences socioeconomic vulnerability (Lai et al., 2015; Cikmaz et al., 2023).

[1]*Sustainable Infrastructure Research and Development Center, Department of Civil Engineering, Faculty of Engineering, Khon Kaen University, Thailand, chapaw@kku.ac.th (CP).*
[2*] *Geographic Information Science, School of Information and Communication Technology, University of Phayao, Thailand. Corresponding author phaisarn.je@up.ac.th (PJ).*
[3]*Department of Natural Resources and Environment, Faculty of Agriculture Natural Resources and Environment, Naresuan University, Thailand, chaiwiwatv@nu.ac.th (CV).*
[4]*Department of Highways, Khon Kaen 3 Ban Phai Highway District, Thailand, satit_tue@hotmail.co.th (SP).*

Multi-criteria decision-making methods, particularly the analytic hierarchy process (AHP), have been widely applied to flood risk assessment (Liu et al., 2020). However, conventional AHP struggles with uncertainty in expert judgment. The fuzzy analytic hierarchy process (FAHP) extends AHP by incorporating fuzzy numbers, improving robustness under subjective evaluations (Baalousha et al., 2023). Coupling FAHP with hydrodynamic simulation and GIS provides a systematic framework for spatial risk mapping (Ahmad et al., 2022; Cikmaz et al., 2023).

This study develops an integrated SWAT‑MIKE‑FAHP‑GIS framework tailored to the Lower Nam Phong basin. Hydrologic and hydrodynamic models simulate flood depths under baseline and climate scenarios (RCP 4.5 and 8.5), while FAHP weights hazard and vulnerability indicators based on expert input. Validation combines satellite-derived inundation, historical flood records, and community insights. The research addresses three questions: (i) How do baseline and climate scenarios translate into flood depths and extents? (ii) How do FAHP-derived weights influence spatial risk patterns? (iii) What uncertainties affect interpretation and operational use? By answering these, the study contributes reproducible methods and actionable maps to support zoning, preparedness, and mitigation planning in a flood-prone Thai basin.

2. STUDY AREA

The Phong River basin in northeastern Thailand consists of two sub-basins: the Upper Nam Phong (12,253 km^2) and the Lower Nam Phong (2,937 km^2) (**Fig. 1**). The study focuses on the Lower Nam Phong, located between 16°30′0″ N to 17°30′0″ N and 102°0′0″ E to 103°0′0″ E, which has repeatedly experienced damaging floods, including the 2011 event. Average annual rainfall is 1,130 mm (1986-2018), with extreme 3-day totals ranging from 50 to 177 mm that have triggered inundation downstream.

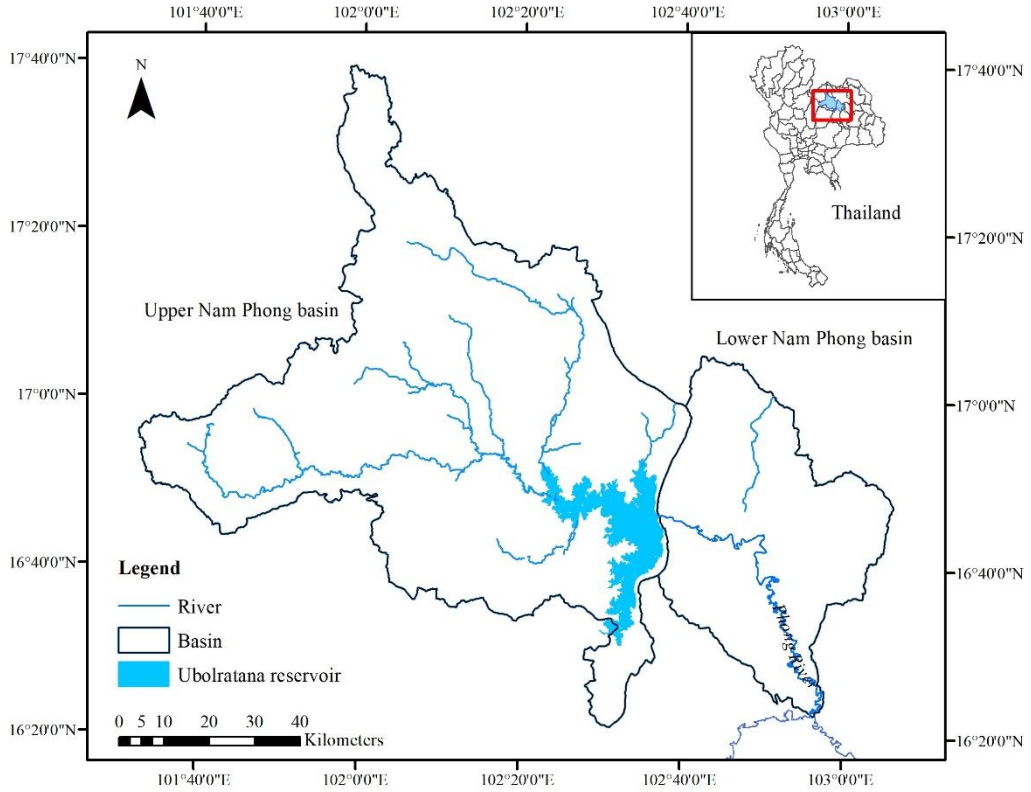


Fig. 1. Location map of the study area.

The Upper basin contains the Ubolratana Dam, with a storage capacity of 2,400 MCM and average inflow of 2,515 MCM (1986-2018), ranging from 567 to 5,425 MCM (Pawattana et al., 2021). Reservoir operations influence downstream hydrology, making the Lower basin particularly vulnerable to flood hazards. For this study, rainfall and temperature time series, a 30 m SRTM DEM (WGS84, Zone 48N), soil drainage and land-use data (the Land Development Department (LDD) of Thailand, 2016), and RADARSAT-1 imagery (21 September 2011) were compiled. All spatial datasets were harmonized to a 30 m grid for integration with hydrologic-hydrodynamic modeling and FAHP analysis. These inputs provide the basis for simulating flood depths and assessing risk under baseline and climate scenarios.

3. DATA AND METHODS

3.1. Fuzzy analytic hierarchy process

Flood risk assessment requires systematic weighting of hazard and vulnerability factors. Conventional AHP is widely used but limited in handling uncertainty in expert judgment (Hategekimana et al., 2018; Putra et al., 2018). FAHP extends AHP by incorporating triangular fuzzy numbers (TFNs), which better capture ambiguity in pairwise comparisons (Yang et al., 2013; Emrouznejad & Ho, 2018; Peng et al., 2021). In this study, six experts with backgrounds in hydrology, GIS, and disaster management provided judgments. Divergent opinions were averaged, and consistency was checked (CR < 0.1) to ensure reliability. The following are the processes of FAHP (Parsian et al., 2021; Yodying et al., 2022).

Table 1.

Fuzzy scale for pairwise comparison.

Definition	Crisp scale	Fuzzy scale
Equal importance	1	(1, 1, 1)
Somewhat more important	3	(2, 3, 4)
Much more important	5	(4, 5 ,6)
Very much more important	7	(6, 7, 8)
Absolutely more important	9	(8, 9, 9)
Intermediate values	2, 4, 6, 8	(x-1, x, x+1)

Step 1. Hierarchical structure development: The primary and secondary criteria are established in accordance with the overarching objectives.

Step 2. Calculation of the fuzzified pairwise comparison matrix: Eq. 1 contains the pairwise comparison, where M_{gij} (i = 1, 2, ..., n and j = 1, 2, ..., m) are TFNs (Yodying et al., 2022).

$$\left(M_{gi}^{j}\right)_{nxm}=\begin{bmatrix} M_{g1}^{1} & M_{g1}^{2} & \cdots & M_{g1}^{m} \\ M_{g2}^{1} & M_{g2}^{2} & \cdots & M_{g2}^{m} \\ \vdots & \vdots & & \vdots \\ M_{gn}^{1} & M_{gn}^{2} & \cdots & M_{gn}^{m} \end{bmatrix}=\begin{bmatrix} (1,1,1) & \left(l_{1_2},m_{1_2},u_{1_2}\right) & \cdots & \left(l_{1_m},m_{1_m},u_{1_m}\right) \\ \left(l_{2_1},m_{2_1},u_{2_1}\right) & (1,1,1) & \cdots & \left(l_{2_m},m_{2_m},u_{2_m}\right) \\ \vdots & \vdots & \vdots & \vdots \\ \left(\frac{1}{u_{n_1}},\frac{1}{m_{n_1}},\frac{1}{l_{n_1}}\right) & \left(\frac{1}{u_{n_2}},\frac{1}{m_{n_2}},\frac{1}{l_{n_2}}\right) & \cdots & (1,1,1) \end{bmatrix} \quad (1)$$

Step 3: Calculation of the imprecise synthetic extent: This phase is computed using Eq. 2.

$$S_i = \sum_{j=1}^{m} M_{gi}^{j} \times \left[\sum_{i=1}^{n} \sum_{j=1}^{m} M_{gi}^{j} \right] \tag{2}$$

where S_i is the synthetic extent value of the pairwise comparison and $\sum_{j=1}^{m} M_{gi}^{j}$ is the total number of TFNs. Additional information is provided in Eqs. 3 to 5, correspondingly.

$$\sum_{j=1}^{m} M_{gi}^{j} = \left[\sum_{j=1}^{m} l_j, \sum_{j=1}^{m} m_j, \sum_{j=1}^{m} u_j \right] \tag{3}$$

$$\sum_{i=1}^{n} \sum_{j=1}^{m} M_{gi}^{j} = \left(\sum_{i=1}^{n} l_i, \sum_{i=1}^{n} m_i \sum_{i=1}^{n} u_i \right) \tag{4}$$

$$\left[\sum_{i=1}^{n} \sum_{j=1}^{m} M_{g}^{j} \right]^{-1} = \left(\frac{1}{\sum_{i=1}^{n} l_i}, \frac{1}{\sum_{i=1}^{n} m_i}, \frac{1}{\sum_{i=1}^{n} u_i} \right) \tag{5}$$

Step 4. Utilize the equation below to determine the degree of probability.

$$V\left(S_i \geq S_j\right) = \begin{cases} 1 & m_i \geq m_j \\ 0 & if \quad l_j \geq u_i \\ \dfrac{l_j - u_i}{\left(m_i - u_i\right) - \left(m_j - l_j\right)} & otherwise \end{cases} \tag{6}$$

In the case of S_i is greater than S_j, then $V\left(S_i \geq S_j \,|\, j = 1, 2, ..., m; \neq j\right) = \min V\left(S_i \geq S_j \mid j = 1, 2, ..., m; \neq j\right)$.

Step 5. Determine the weight vector: The definition of a weight vector is as follows:

$$W_i^{'} = \min V\left(S_i \geq S_j \,|\, j = 1, 2, ..., i \neq j\right) \tag{7}$$

$$W_i = \frac{w_i^{'}}{\sum_{i=1}^{n} w_i^{'}} \tag{8}$$

where the term W, is defined as $(w_1, w_2, ..., w_n)^T$, is a weight vector that has been normalized. The non-fuzzy number (w_i) for each weight will be derived then.

Step 6. Consistency determination: The comparison matrix is established by the consistency of the evaluation, as indicated by the expert decision. Eq. 9 is applied to calculate the consistency index (*CI*), which is used to determine the degree of consistency.

$$CI = \frac{\lambda_{\max} - n}{n - 1} \tag{9}$$

where λ_{max} and n are the maximum eigenvector derived from the calculation of pairwise comparison matrix and the number of factors. The consistency ratio (CR) is computed using Eq. 10 to certify the acceptance of the degree of consistency.

$$CR = \frac{CI}{RI} \tag{10}$$

where RI is the random inconsistency which depends on the number of factors. The consistency of the judgment matrix is satisfactory, as indicated by $CR < 0.1$. The consistency of the judgment matrix must be reevaluated when CR is greater than or equal to 0.1 (Peng et al., 2021).

3.2. Evaluation of flood risk

Flood risk was defined as the product of hazard and vulnerability (Risk = Hazard × Vulnerability) (Vojinovic et al., 2016). Hazard scores were derived from hydrologic-hydrodynamic simulations of flood depth, slope, and soil drainage, while vulnerability scores were based on land use. FAHP weights were applied to each factor, and risk scores were computed in GIS. Raster layers (30 m resolution) were classified into low, medium, and high risk using the standard deviation method, chosen for its suitability in continuous hazard data and comparability across scenarios. Referring **Fig. 2**, the flowchart depicts the processes to derive the flood risk maps using FAHP and GIS database.

Furthermore, flood risk scores (FRS) are generated by multiplying the flood hazard score (FHS) and flood vulnerability score (FVS) (Eq. 11).

$$FRS = FHS \times FVS \tag{11}$$

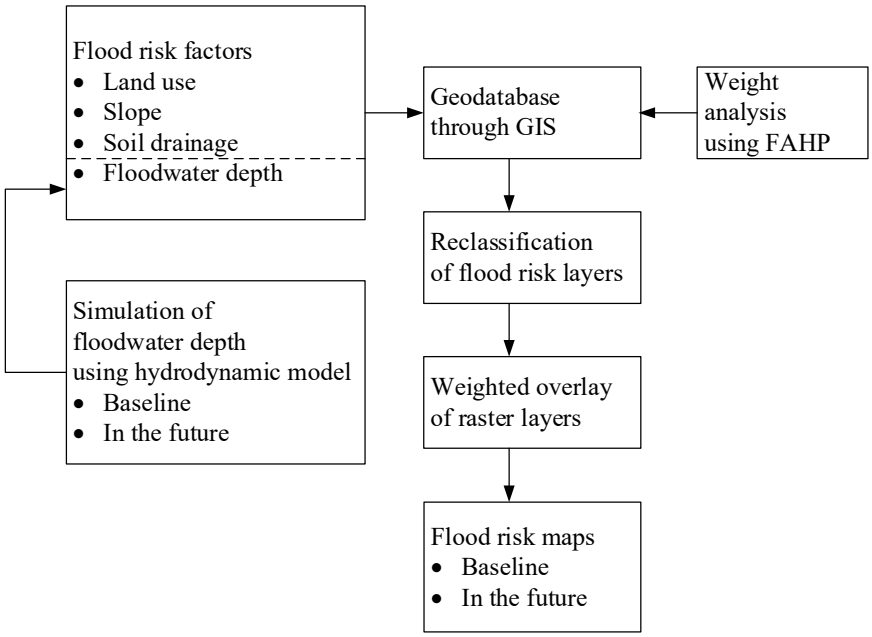


Fig. 2. Work flow of flood risk map development.

The flood hazard score is calculated by

$$FHS = wm_{Fd} \times wsub_{Fd} + wm_{Sl} \times wsub_{Sl} + wm_{Sd} \times wsub_{Sd} \quad (12)$$

where wm_{Fd}, wm_{Sl}, and wm_{Sd} are the weights of main-criteria for floodwater depth, slope, and soil drainage, respectively. $wsub_{Fd}$, $wsub_{Sl,}$ $wsub_{Sd}$ indicate the weights of each. The score of vulnerability is computed from Eq. 13.

$$FVS = wm_{Lu} \times wsub_{Lu} \quad (13)$$

where wm_{Lu} and $wsub_{Lu}$ stand for the weights of main and sub-criteria for land use.

Then, the weight values were input into the risk factors through GIS database. According to the utilization of Eqs. 12 and 13 to compute *FHS* and *FVS* and the process of reclassification, the risk layers in the vector format were converted into the raster format with the resolution of 30x30 m^2. Finally, the weighted overlay of raster layer using Eq. 11 was employed to calculate *FRS* and classified by the standard deviation method into low-, medium-, and high-level to derive the flood risk maps (Gigovic' et al., 2017).

3.3. Flood risk factors

3.3.1. Slope

The digital elevation data of the NASA Shuttle Radar Topographic Mission (SRTM) from USGS EarthExplorer (https://earthexplorer.usgs.gov/) has provided the digital elevation model (DEM) with resolution of 30x30 m^2. Positions of elevation data are a WGS84 horizontal datum with zone 48 N. The selection of 54 references elevation data was used to test the accuracy of DEM with R-square value of 0.78. The slope was generated directly from the DEM data by ArcGIS version 10.8 software and classified into five levels such as 0-5%, 5-12%, 12-20%, 20-35%, and more than 35%, respectively (**Fig. 3 (a)**).

3.3.2. Soil drainage

The sort of soil particle characteristics of year 2005 present in this study is indicated in **Fig. 3 (b)**, which has significant impact on the likelihood of flooding. The information was gathered from the LDD of Thailand. According to soil series and performance of permeability existing in the original GIS database, soil drainage layer was reclassified as very poor drainage, poor drainage, moderate drainage, good drainage, and very good drainage (Poopiwkham, 2018).

3.3.3. Land use

The different types of land use of year 2016 was collected from the LDD of Thailand. Many kinds of land use were classified into agriculture, forest, urban, and village (**Fig. 3 (c)**) (Poopiwkham, 2018; Hussain et al., 2021). The agricultural area consists of mostly irrigated rice areas and rainfed rice fields. The forest area comprises dry evergreen forest, mixed forest, and forest plantation. Urban area contains city and commercial areas, government office, and industrial areas. Village area comprises rural villages rely on their homes. Water body consists of water sources and natural water sources.

3.3.4. Floodwater depth

Simulated using hydrodynamic models for baseline (1989-2018) and future scenarios (2020-2049). The 3-day 50-year rainfall was derived from frequency analysis of annual maxima (1989-2018). Future rainfall inputs (RCP 4.5 and 8.5) were obtained from CNRM-CM5 projections downscaled via CORDEX and bias-corrected using quantile mapping (Anuthaman et al., 2023; Satriagasa et al., 2023). RCP 4.5 represents moderate stabilization, while RCP 8.5 reflects high-emission futures, bracketing plausible climate impacts. MIKE-11 was applied to simulate 1D unsteady flow along the Phong River, while MIKE-21 modeled 2D floodplain inundation. These outputs provided flood depth, velocity, and extent for risk assessment.

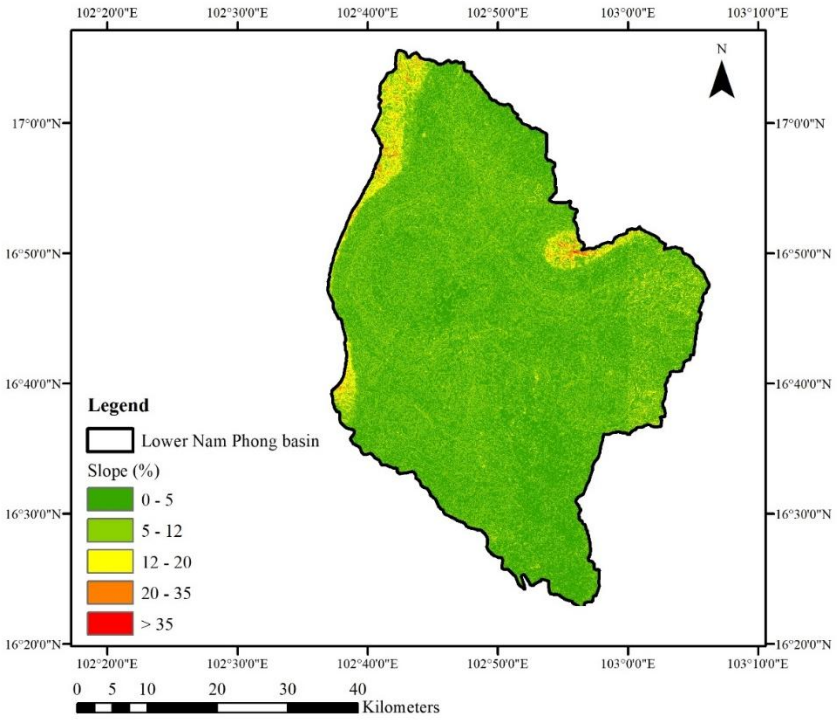


Fig. 3 (a) Slope.

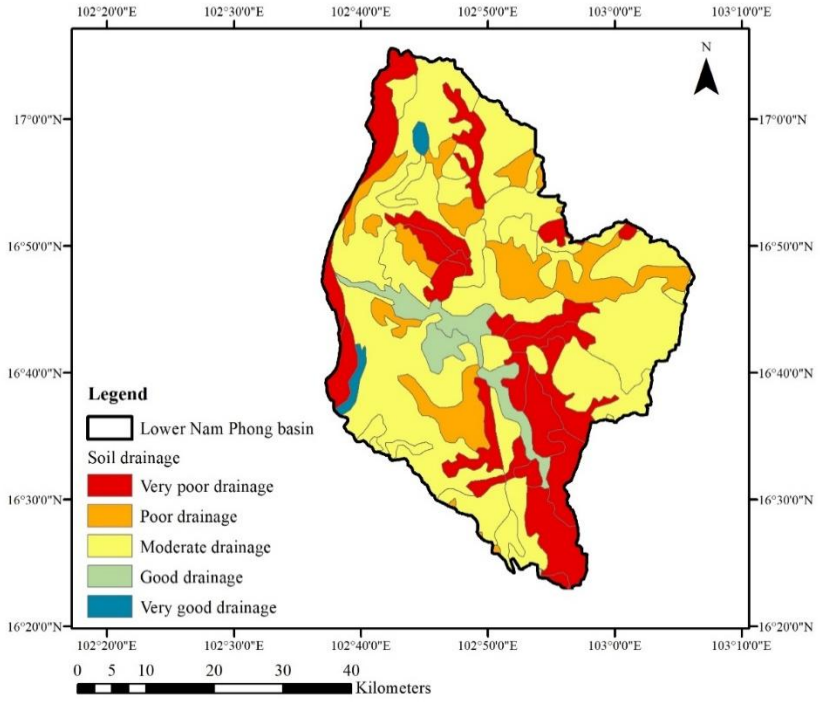


Fig. 3 (b) Soil drainage.

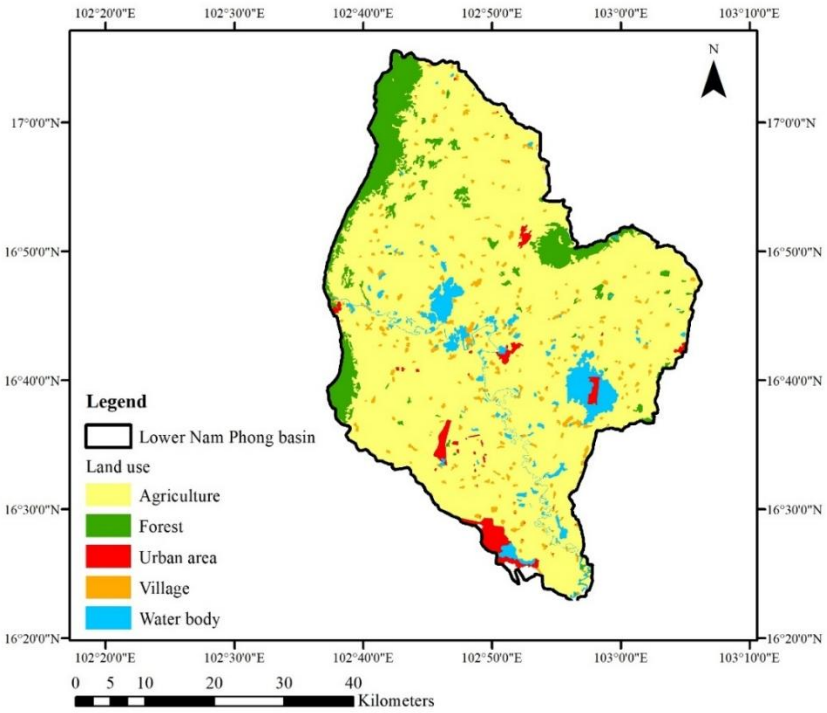


Fig. 3 (c) Land use.

Fig. 3. Maps of slope, soil drainage, and land use.

3.4. Hydrologic and Hydrodynamic Models

The Soil and Water Assessment Tool (SWAT) model was used to simulate runoff and lateral inflows (Li & Fang, 2021; M′Barek et al., 2021). Sub-basins and hydrologic response units (HRUs) were delineated using DEM, soil, and land-use inputs. Runoff was calculated using the SCS-CN method, infiltration by Green–Ampt, and streamflow calibrated (2005-2011) and validated (2012-2014) with NSE and R^2 metrics.

MIKE-11 simulated 1D unsteady flow along the Phong River using Saint-Venant equations, with Manning's n = 0.025-0.040 for channels and floodplains. MIKE-21 modeled 2D floodplain routing and inundation, including the 21 September 2011 flood event. Mesh resolution and stability were checked, and inundation extents compared with RADARSAT-1 imagery (76% overlap), confirming model reliability.

3.5. Performance and Uncertainty

Model performance was evaluated using R^2 and Nash‑Sutcliffe Efficiency (NSE), both yielding satisfactory values for calibration and validation (Parhi et al., 2012; Swagatika et al., 2022). Uncertainty arises from parameter sensitivity, input data accuracy, expert judgment variability, and climate projection assumptions. These limitations were acknowledged, and future work will incorporate probabilistic inundation modeling, expanded hazard indicators, and broader stakeholder engagement to strengthen robustness. The two indices are expressed mathematically in the following Eqs. 14 and 15, respectively.

$$R^2 = \left[\frac{\sum_{i=1}^{n} \left(y_i^{obs} - y_{mean}^{obs} \right) \left(y_i^{sim} - y_{mean}^{sim} \right)}{\sqrt{\sum_{i=1}^{n} \left(y_i^{obs} - y_{mean}^{obs} \right)^2} \sqrt{\sum_{i=1}^{n} \left(y_i^{sim} - y_{mean}^{sim} \right)^2}} \right]^2 \quad (14)$$

$$NSE = 1 - \left[\frac{\sum_{i=1}^{n} \left(y_i^{obs} - y_i^{sim} \right)^2}{\sum_{i=1}^{n} \left(y_i^{obs} - y_{mean}^{obs} \right)^2} \right] \quad (15)$$

where, y_i^{obs} and y_i^{sim} are the ith observed and simulated data. y_{mean}^{obs} and y_{mean}^{sim} are the mean observed and simulated data, and n is the total number of observations.

4. RESULTS AND DISCUSSIONS

4.1. Flood depth simulation

The SWAT model successfully simulated lateral inflows to the Phong River for both baseline (1989–2018) and future scenarios (2020-2049). Calibration (2005-2011) achieved NSE = 0.68 and R^2 = 0.70, while validation (2012-2014) yielded NSE = 0.79 and R^2 = 0.81, indicating satisfactory performance. These inflows were used as boundary conditions for MIKE hydrodynamic models.

MIKE-11 reproduced 1D unsteady flow with NSE and R^2 values above 0.75, while MIKE-21 simulated 2D floodplain inundation. Comparison with RADARSAT-1 imagery (21 September 2011) showed 76% spatial overlap, confirming credible hazard representation. The maximum 3-day rainfall of 177 mm (August 1991) produced 10.7 km^2 inundation under baseline conditions. Future scenarios projected 387 mm (RCP 4.5) and 468 mm (RCP 8.5), resulting in 43.35 km^2 and 89.05 km^2 inundation, respectively.

4.2. Weight analysis

FAHP weighting emphasized land use as the dominant vulnerability factor, reflecting the economic importance of irrigated rice fields. Hierarchical structure of flood risk depending on hazard and vulnerability is illustrated in **Fig. 4**.

Flood depth >2.75 m received the highest hazard weight, consistent with severe crop losses. Slope (0–5% irrigated, 5–12% rainfed) and poor soil drainage further increased vulnerability. Six experts contributed to pairwise comparisons; consistency ratios (CR < 0.1) confirmed reliability.

The **Table 2** shows the pairwise comparisons among the four main criteria (floodwater depth, slope, soil drainage, and land use). Land use received the highest weight, reflecting its dominant role in vulnerability. Consistency ratio (CR = 0.063) indicates reliable judgments.

The matrix (**Table 3**) presents expert comparisons of five soil drainage classes, from very poor to very good. Poorly drained soils were weighted highest, consistent with their strong influence on flood hazard. CR = 0.070 confirms acceptable consistency.

Slope categories (0-5%, 5-12%, 12-20%, 20-35%, >35%) were compared (**Table 4**). Gentle slopes (0-5%) received the highest weight, reflecting their greater susceptibility to inundation. CR = 0.077 indicates satisfactory consistency.

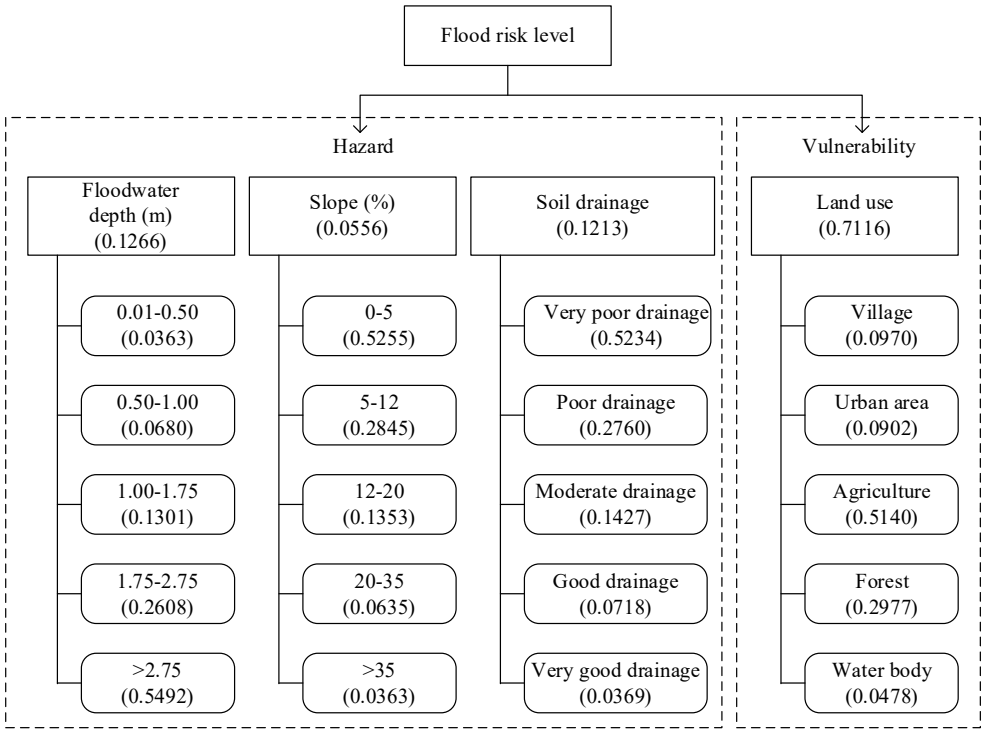


Fig. 4. Hierarchical structure of flood risk in Lower Nam Phong basin.

Table 2.

Main-criteria judgment matrix.

Main-criteria	Floodwater depth	Slope	Soil drainage	Land use
Floodwater depth	1,1,1	2,3,4	1,1,1	1/8,1/7,1/6
Slope	1/4,1/3,1/2	1,1,1	1/4,1/3,1/2	1/9,1/9/1/8
Soil drainage	1,1,1	2,3,4	1,1,1	1/9,1/9/1/8
Land use	6,7,8	8,9,9	8,9,9	1,1,1
λ_{max} = 4.17, *CI* = 0.056, *RI* = 0.89, *CR* = 0.063				

Table 3.

Sub-criteria judgment matrix of soil drainage.

Sub-criteria of soil drainage	Very poor drainage	Poor drainage	Moderate drainage	Good drainage	Very good drainage
Very poor drainage	1,1,1	2,3,4	4,5,6	6,7,8	8,9,9
Poor drainage	1/4,1/3,1/2	1,1,1	2,3,4	4,5,6	6,7,8
Moderate drainage	1/6,1/5,1/4	1/4,1/3,1/2	1,1,1	2,3,4	4,5,6
Good drainage	1/8,1/7,1/6	1/6,1/5,1/4	1/4,1/3,1/2	1,1,1	2,3,4
Very good drainage	1/9,1/9,1/8	1/8,1/7,1/6	1/6,1/5,1/4	1/4,1/3,1/2	1,1,1
λ_{max} = 5.31, CI = 0.078, RI = 1.11, CR = 0.070					

Table 4.

Sub-criteria judgment matrix of slope.

Sub-criteria of slope	0-5%	5-12%	12-20%	20-35%	>35%
0-5%	1,1,1	2,3,4	4,5,6	8,9,9	8,9,9
5-12%	1/4,1/3,1/2	1,1,1	2,3,4	6,7,8	6,7,8
12-20%	1/6,1/5,1/4	1/4,1/3,1/2	1,1,1	2,3,4	4,5,6
20-35%	1/9,1/9,1/8	1/8,1/7,1/6	1/4,1/3,1/2	1,1,1	2,3,4
>35%	1/9,1/9,1/8	1/8,1/7,1/6	1/6,1/5,1/4	1/4,1/3,1/2	1,1,1
λ_{max} = 5.34, *CI* = 0.086, *RI* = 1.11, *CR* = 0.077					

Table 5.

Sub-criteria judgment matrix of floodwater depth.

Sub-criteria of floodwater depth	0.01-0.50 m	0.50-1.00 m	1.00-1.75 m	1.75-2.75 m	>2.75 m
0.01-0.50 m	1,1,1	1/4,1/3,1/2	1/6,1/5,1/4	1/8,1/7,1/6	1/9,1/9,1/8
0.50-1.00 m	2,3,4	1,1,1	1/4,1/3,1/2	1/6,1/5,1/4	1/9,1/8,1/7
1.00-1.75 m	4,5,6	2,3,4	1,1,1	1/4,1/3,1/2	1/8,1/7,1/6
1.75-2.75 m	6,7,8	4,5,6	2,3,4	1,1,1	1/4,1/3,1/2
>2.75 m	8,9,9	7,8,9	6,7,8	2,3,4	1,1,1
λ_{max} = 5.35, *CI* = 0.089, *RI* = 1.11, *CR* = 0.080					

Flood depth ranges (0.01-0.50 m to >2.75 m) were evaluated. Depths exceeding 2.75 m obtained the highest weight, consistent with severe crop losses. CR = 0.080 demonstrates reliable expert agreement (**Table 5**).

Table 6.

Sub-criteria judgment matrix of land use.

Sub-criteria of land use	Village	Urban area	Agriculture	Forest	Water body
Village	1,1,1	1,1,1	1/6,1/5,1/4	1/6,1/5,1/4	2,3,4
Urban area	1,1,1	1,1,1	1/8,1/7,1/6	1/6,1/5,1/4	2,3,4
Agriculture	4,5,6	6,7,8	1,1,1	2,3,4	6,7,8
Forest	4,5,6	4,5,6	1/4,1/3,1/2	1,1,1	4,5,6
Water body	1/4,1/3,1/2	1/4,1/3,1/2	1/8,1/7,1/6	1/6,1/5,1/4	1,1,1
λ_{max} = 5.34, *CI* = 0.084, *RI* = 1.11, *CR* = 0.076					

Land use types (village, urban, agriculture, forest, water body) were compared (**Table 6**). Agriculture was assigned the highest weight due to its economic importance and vulnerability to flooding. CR = 0.076 confirms consistency of expert judgments.

4.3. Flood risk assessment

Risk maps (**Figs. 5-7**) classified areas into low, medium, and high risk using the standard deviation method. **Table 7** summarizes scenario differences:

- Baseline (1991 event): 19.44% high risk, concentrated in Nong Bua, Bung Nium, and Khok Sri.
- RCP 4.5: High risk reduced to 10.45%, but medium risk expanded to 36.45 km^2, covering downstream and midstream zones.
- RCP 8.5: High risk increased to 12.00%, with medium risk dominating (72.67 km^2), particularly in Bung Nium, Khok Sri, and Tha Kraserm.

This comparative presentation highlights the downstream expansion of risk under climate change, with irrigated rice fields consistently most vulnerable.

Fig. 5 presents flood risk map of the Lower Nam Phong basin for the baseline (1991 event). High-risk zones (19.44%) are concentrated in Nong Bua, Bung Nium, and Khok Sri, while medium-risk areas (76.98%) dominate across downstream and midstream sub-districts. Low-risk zones (3.58%) are scattered in Nong Bua, Khu Thong, Bung Nium, Khok Sri, Si La, and Muang Yarn.

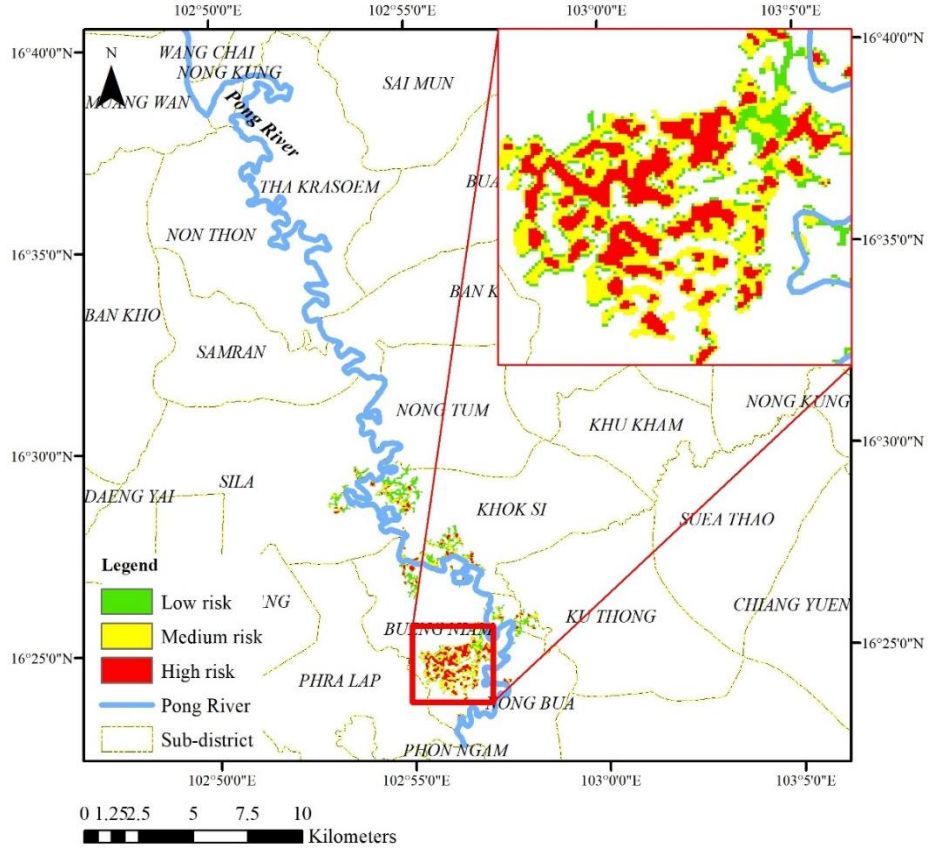


Fig. 5. Flood risk map of the Lower Nam Phong basin for baseline.

Fig. 6 presents flood risk map of the Lower Nam Phong basin under RCP 4.5 scenario (2020-2049). High-risk zones decrease to 10.45%, mainly in downstream areas (Nong Bua, Bung Nium, Pra Lab, Khu Thong, Khok Sri). Medium-risk zones expand to 36.45 km^2 (84.08%), covering downstream, midstream, and parts of upstream. Low-risk zones (5.47%) are distributed across Khok Sri, Si La, Non Thon, Tha Kraserm, Bung Nium, and Sai Mun.

Fig. 7 illustrates flood risk map of the Lower Nam Phong basin under RCP 8.5 scenario (2020-2049). High-risk zones increase to 12.00%, concentrated in Bung Nium and Khok Sri. Medium-risk zones dominate (72.67 km^2, 81.61%), particularly in Bung Nium, Khok Sri, Si La, Non Thon, and Tha Kraserm. Low-risk zones (6.39%) are scattered in Khok Sri, Si La, Non Thon, Tha Kraserm, and Ban Kham.

Table 7 illustrates areas (km^2) of flood risk levels under baseline and future scenarios. This table compares the extent of low-risk, medium-risk, and high-risk zones across baseline (1991 event), RCP 4.5, and RCP 8.5 scenarios. Results show that medium-risk areas expand substantially under climate change (36.45 km^2 in RCP 4.5 and 72.67 km^2 in RCP 8.5), while high-risk zones decrease under RCP 4.5 (4.53 km^2) but increase again under RCP 8.5 (11.57 km^2). The comparative values highlight the downstream expansion of flood risk and the growing vulnerability of agricultural land under future climate conditions.

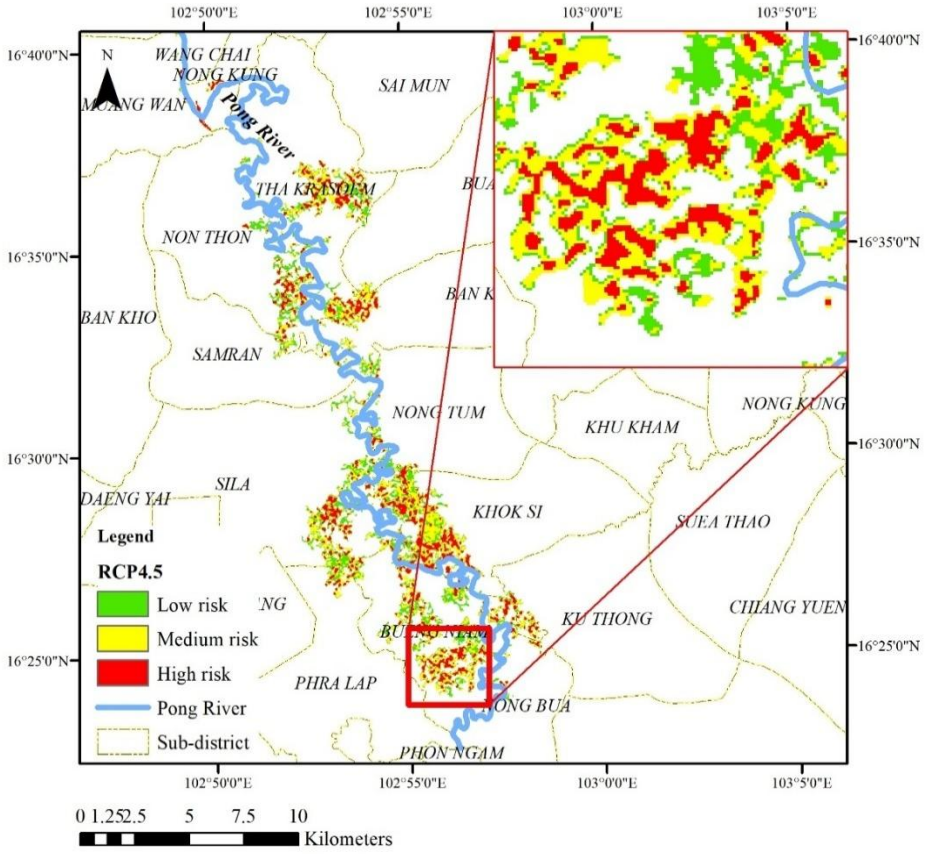


Fig. 6. Flood risk map of the Lower Nam Phong basin for RCP 4.5.

Table 7.
Areas (km^2) of various risk levels in the Lower Nam Phong basin.

Risk level / Scenario	Low-risk	Medium-risk	High-risk
Baseline	0.49	8.13	2.08
RCP 4.5	2.37	36.45	4.53
RCP 8.5	4.82	72.67	11.57

4.4. Validation of flood risk map

Validation combined multiple approaches:

- Historical comparison: High-risk zones matched flood events in 2011, 2017, and 2022 (Typhoon Noru).
- Community insights: Interviews confirmed prolonged inundation in rice fields, supporting land use weighting.
- Satellite overlap: 76% agreement between MIKE-21 outputs and RADARSAT-1 imagery.
- Model performance: NSE and R^2 values exceeded 0.75, supporting robustness.

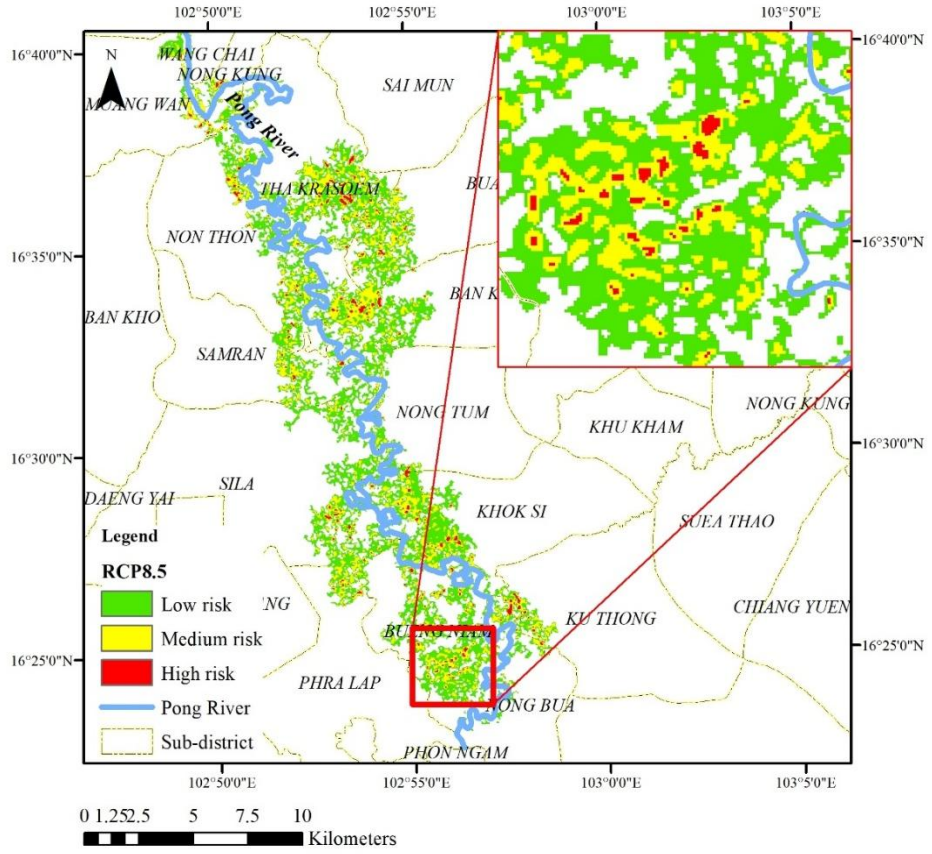


Fig. 7. Flood risk map of the Lower Nam Phong basin for RCP 8.5.

4.5. Uncertainty and Practical Relevance

Uncertainty arises from hydrodynamic parameters, expert judgment variability, limited flood events, and climate projection assumptions. While FAHP improves handling of subjective input, averaging expert scores may introduce bias. Future work should incorporate sensitivity analysis, probabilistic inundation modeling, and expanded datasets.

Practically, the maps provide actionable guidance for zoning, prioritizing structural and non-structural measures, and agricultural planning. The methodology is transferable to other flood-prone basins, offering a reproducible framework for climate-informed risk management.

5. CONCLUSIONS

This study developed and validated an integrated SWAT‑MIKE‑FAHP‑GIS framework for climate-informed flood risk mapping in the Lower Nam Phong basin. Validation against satellite imagery and historical floods confirmed credible hazard representation, while FAHP weighting highlighted land use particularly irrigated rice fields as the dominant vulnerability factor. Risk maps revealed medium risk zones across much of the basin, with high-risk areas clustering downstream and expanding under RCP 8.5, underscoring the influence of climate change on future flood exposure.

Key limitations include parameter and projection uncertainties, reliance on six expert judgments, and restricted flood event samples. The use of standard deviation for classification, while suitable for continuous hazard data, may yield different spatial outcomes under alternative schemes. Future work should incorporate additional hazard and vulnerability indicators, higher-resolution datasets, probabilistic inundation modeling, and broader stakeholder engagement. Explicit treatment of climate projection uncertainty and sensitivity analysis of hydrodynamic parameters would further strengthen robustness.

The developed maps provide a practical foundation for flood management, supporting zoning, prioritization of structural and non-structural measures, and agricultural planning. Beyond the Lower Nam Phong basin, the methodology is transferable to other flood prone basins where integrated hydrodynamic modeling and FAHP can enhance decision-making under uncertainty. Real-world implementation will require institutional readiness, long-term monitoring, and sustained collaboration among local authorities, communities, and researchers. Overall, the framework offers a replicable approach for climate-informed flood risk management.

ACKNOWLEDGEMENTS

Authors would like to acknowledge Department of Civil Engineering, Faculty of Engineering, Khon Kaen University for supporting the research budget. We would like to deliver special thanks to Nongwai Irrigation Project and Ubonratana dam for providing essential data.

REFERENCES

Ahmad, I., Wang, X., Waseem, M., Zaman, M., Aziz, F., Khan, R.Z.N. & Ashraf, M. (2022) Flood management, characterization and vulnerability analysis using an integrated RS-GIS and 2D hydrodynamic modelling approach: The case of Deg Nullah, Pakistan. *Remote Sensing,* 14 (2138), 1-19. https://doi.org/10.3390/rs14092138.

Anuthaman, S.N., Ramasamy, S., Ramasubbu, B. & Lakshminarayanan, B. (2023) Modelling and forecasting of urban flood under changing climate and land use land cover. *Journal of Water and Climate Change,* 14 (12), 4314-4335. http://dx.doi.org/10.2166/wcc.2023.164.

Arianti, I., Rafani, M., Fitriani, N. & Nizar. (2023) Spatial modeling of flood vulnerability as basic data for flood mitigation. *Civil Engineering Journal,* 9 (4), 787-798. https://doi.org/10.28991/CEJ-2023-09-04-02.

Baalousha, H.M., Younes, A., Yassin, M.A. & Fahs, M. (2023) Comparison of the fuzzy analytic hierarchy process (F-AHP) and fuzzy logic for flood exposure risk assessment in arid regions. Hydrology. 10(136), 1-22. https://doi.org/10.3390/hydrology10070136.

Bokhari, B.F., Tawabini, B. & Baalousha, H.M. (2024) A fuzzy analytical hierarchy process ‑GIS approach to flood susceptibility mapping in Neom, Saudi Arabia. *Frontiers in Water,* 6 (1388003), 1-14. https://doi.org/10.3389/frwa.2024.1388003 .

Cikmaz, B.A., Yildirim, E. & Demir, I. (2023) Flood susceptibility mapping using fuzzy analytical hierarchy process for Cedar Rapids, Iowa. *International Journal of River Basin Management*, 23, 1-13. https://doi.org/10.1080/15715124.2023.2216936.

Edamo, M.L., Hatiye, S.D. & Minda, T.T. (2023) Flood inundation and risk mapping under climate change scenarios in the Lower Bilate Catchment, Ethiopia. *Natural Hazards,* 118, 2199-2226. https://doi.org/10.1007/s11069-023-06101-y.

Emrouznejad, A. & Ho, W. (2018) Fuzzy analytic hierarchy process. Boca Raton, Florida. CRC Press.

Gigovic', L., Pamučar, D., Bajic', Z. & Drobnjak, S. (2017) Application of GIS-interval rough AHP methodology for flood mapping in urban areas. *Water,* 9 (360), 1-26. https://doi.org/10.3390/w9060360.

Hagos, Y.G., Andualem, T.G., Yibeltal, M. & Mengie, M.A. (2022) Flood hazard assessment and mapping using GIS integrated with multi-criteria decision analysis in Upper Awash River Basin, Ethiopia. *Applied Water Science,* 12 (148), 1-18. https://doi.org/10.1007/s13201-022-01674-8.

Hategekimana, Y., Yu, L., Nie, Y., Zhu, J., Liu, F. & Guo F. (2018) Integration of multi-parametric fuzzy analytic hierarchy process and GIS along the UNESCO world heritage: A flood hazard index, Mombasa Country, Kenya. *Natural Hazards,* 92 (2), 1137-1153. https://doi.org/10.1007/s11069-018-3244-9.

Hu, S., Cheng, X., Zhou, D. & Zhang, H. (2017) GIS-based flood risk assessment in suburban areas: A case study of the Fangshan District, Beijing. *Natural Hazards,* 87, 1525-1543. https://doi.org/10.1007/s11069-017-2828-0.

Hussain, M., Tayyab, M., Zhang, J., Shah, A.A., Ullah, K., Mehmood, U. & Al-Shaibah, B. (2021) GIS-based multi-criteria approach for flood vulnerability assessment and mapping in District Shangla: Khyber Pakhtunkhwa, Pakistan. *Sustainability,* 13 (3126), 1-29. https://doi.org/10.3390/su13063126.

Lai, C., Chen, X., Chen, X., Wang, Z., Wu, X. & Zhao, S. (2015) A fuzzy comprehensive evaluation model for flood risk based on the combination weight of game theory. *Natural Hazards,* 77 (2), 1243-1259. http://dx.doi.org/10.1007/s11069-015-1645-6.

Li, C. & Fang, H. (2021) Assessment of climate change impacts on the streamflow for the Mun River in Mekong Basin, Southeast Asia: using SWAT model. *Catena,* 201, 1-13. http://dx.doi.org/10.1016/j.catena.2021.105199.

Liu, Y., Eckert, C.M. & Earl, C. (2020) A review of fuzzy AHP methods for decision making with subjective judgements. *Expert System with Applications,* 161 (113738), 1-30. https://doi.org/10.1016/j.eswa.2020.113738.

M′Barek, S., Rochdi, A., Bouslihim, Y. & Miftan A. (2021) Multi-site calibration and validation of SWAT model for hydrologic modeling and soil erosion estimation: A case study in El Grou Watershed, Morocco. *Ecological Engineering and Environmental Technology,* 22 (6), 45-52. http://dx.doi.org/10.12912/27197050/141593.

Maranzoni, A., D'Oria, M. & Rizzo, C. (2023) Quantitative flood hazard assessment methods: a review. *Journal of Flood Risk Management,* 16 (1), 1-31. https://doi.org/10.1111/jfr3.12855.

Nut, N. & Plermkamon, V. (2013) Estimation of flood damages on Nam Phong River by HEC-RAS. In: The 6th International Conference, SWE-04, 179-86.

Parhi, P.K., Sankhua, R.N. & Roy, G.P. (2012) Calibration of channel roughness for Mahanadi River, (India) using HEC-RAS model. *Journal of Water Resource and Protection,* 4 (10), 847-850. http://dx.doi.org/10.4236/jwarp.2012.410098.

Parsian, S., Amani, M., Moghimi, A., Ghorbanian, A. & Mahdavi, S. (2021) Flood hazard mapping using fuzzy logic, analytical hierarchy process, and multi-source geospatial datasets. *Remote Sensing,* 13 (23), 4761-4783. https://doi.org/10.3390/rs13234761.

Pawattana, C., Panasoontorn, S., Poopiwkham, S. & Ikhwali, F. (2021) Assessment of water shortage situations in Lower Nam Pong Basin under climate change. *Naresuan University Journal: Science and Technology,* 29 (4), 52-6. https://doi.org/10.14456/nujst.2021.35.

Peng, G., Han, L., Liu, Z., Guo, Y., Yan, J. & Jia, X. (2021) An application of fuzzy analytic hierarchy process in risk evaluation model. *Frontiers in Psychology,* 12, 1-12. https://doi.org/10.3389/fpsyg.2021.715003.

Poopiwkham, S. (2018) Development of potential flood maps using fuzzy logic due to climate change in Pong River Basin [Thesis]. Department of Civil Engineering: Khon Kaen University.

Promchote, P., Wang S.Y.S., & Johnson, P.G. (2016) The 2011 great flood in Thailand: Climate diagnostics and implications from climate change. *Journal of Climate,* 29 (1), 367-79.

Putra, M.S.D., Andryana, S., Fauziah, K. & Gunaryati, A. (2018) Fuzzy analytical hierarchy process method to determine the quality of gemstones. *Advance in Fuzzy System,* 2018, 1-6. https://doi.org/10.1155/2018/9094380.

Satriagasa, C., Tongdeenok, P. & Kaewjampa, N. (2023) Assessing the implication of climate change to forecast future flood using SWAT and HEC-RAS model under CMIP5 climate projection in Upper Nan Watershed, Thailand. Sustainability. 15(5276), 1-21. https://doi.org/10.3390/su15065276.

Singkran, N. (2017) Flood risk management in Thailand: Shifting from a passive to a progressive paradigm. *International Journal of Disaster Risk Reduction,* 25, 92-100.

Swagatika, S., Paul, J.C., Sahu, A.P., Das, D.M. & Patra, A.K. (2022) Streamflow Simulation of Brahmani River Basin using SWAT model. *Biological Forum,* 14 (3), 1707-1714.

Vojinovic, Z., Hammond, M., Golub, D., Hirunsalee, S., Weesakul, S., Meesuk, V., Medina, N., Sanchez, A., Kumara, S. & Abbott, M. (2016) Holistic approach to flood risk assessment in areas with cultural heritage: A practical application in Ayutthaya, Thailand. *Natural Hazards,* 81, 589-616. https://doi.org/10.1007/s11069-015-2098-7.

Yang, X., Ding, J. & Hou, H. (2013) Application of a triangular fuzzy AHP approach for flood risk evaluation and response measures analysis. *Natural Hazards.,* 68, 657-674. http://dx.doi.org/10.1007/s11069-013-0642-x.

Yodying, A., Mahavik, N., Tantanee, S., Kongmuang, C., Keteku, A.K., Chidburee P, Seejata, K. & Chatsudarat, S. (2022) A fuzzy AHP approach to assess flood hazard for area of Bang Rakam model 60 project in Yom River Basin, Northern Thailand. *Applied Environmental Research,* 44 (1), 108-125. https://doi.org/10.35762/AER.2021.44.1.9.

RIVERBED DYNAMICS OF SUCEAVA RIVER AT THE TRANSITION BETWEEN THE CARPATHIANS AND THE EASTERN LOWLANDS

Diana ISTRATE [1], ***Domenic Raul BECICA*** [1], ***Mihai BARBACARIU*** [1], ***Ionela GRĂDINARU*** [2] ***& Marcel MÎNDRESCU*** [1*]

DOI: 10.21163/GT_2026.211.21

ABSTRACT

This study examines the morphological evolution of the mountain riverbed reach of Suceava river over a span of more than 150 years using historical maps, orthophotos, and satellite imagery. Key morphological parameters, including sinuosity and braiding indices, as well as variations in active river area and floodplain width, were analysed from 1869 to 2021. The findings reveal periods of increased river dynamics, marked by active meandering and braiding, alternating with phases of stabilization of the riverbed. Both natural processes and anthropogenic interventions have contributed to these adjustments, interfering with regional flood risks, sediment transport, and habitat development along the watercourse. This analysis underscores the need for adaptive management strategies to promote sustainable river management in the context of ongoing hydrological and environmental changes.

Keywords: *Braiding; Evolutionary trend; Morphology; Riverbed dynamics; Suceava river*

1. INTRODUCTION

Rivers are dynamic geomorphological systems which play a crucial role in shaping landscapes, ecosystems, and human settlements through processes like erosion, sediment transport, and deposition (Leopold et al., 1964; Schumm, 1977). Watercourse behaviour results from the interaction between climatic variability and human intervention, which underscores their importance for studies focused on water resource management, flood risk mitigation, and environmental conservation (Knighton, 1998; Foley et al., 2005; Langat et al., 2019; de Musso et al., 2020; Korjenić et al., 2021).

At the global scale, long-term trends in river discharge remain difficult to generalize, as regional signals often outweigh any overarching trend (Eyring et al., 2021). At the European level, however, analyses covering the second half of the twentieth century reveal pronounced spatial contrasts, including declining streamflow in southern regions, mixed responses in central areas, and increasing discharge in the north (Caretta et al., 2022). Against this background, the investigation of river channel dynamics over the last 150 years has become a central component of river management. Long-term reconstructions allow past adjustments to be placed in context and provide a framework for interpreting present-day channel behaviour and potential future trajectories (Mandarino et al., 2019; Mandarino, 2022).

Recent methodological approaches increasingly use historical cartographic sources and remote sensing data to trace channel adjustments across multiple temporal scales. The integration of old maps, aerial photographs, and satellite imagery supports both qualitative interpretations and quantitative assessments of planform and morphological change in river systems worldwide (Harmar & Clifford, 2006; Schwenk et al., 2017; Batalla et al., 2018; Langat et al., 2019; Vercruysse & Grabowski, 2021).

---

[1] *Department of Geography, Stefan cel Mare University, Suceava, Romania.*
diana.istrate27@gmail.com (DI); rauldomenic@gmail.com (DRB); mihaimihai464si@gmail.com (MB);
**Corresponding author: mindrescu@atlas.usv.ro (MM)*
[2] *Geoconcept Association of Applied Geography, Cârlibaba, Romania, ionela.gradinaru@gmail.com (IG).*

A growing body of research has examined the evolution of European rivers over the past two centuries, emphasizing the interplay between natural processes and human pressures. Studies from Italy indicate that many channels underwent a prolonged phase of narrowing and bed incision beginning in the late nineteenth century, followed more recently by partial widening and local bed stabilization. These trends are mainly associated with sediment extraction, engineering works and dam construction, which altered sediment supply more strongly than discharge regimes (Surian et al., 2009; Mandarino et al., 2019; de Musso et al., 2020). Evidence from other Southern European catchments, including rivers in Spain, points to wider planform reorganization under the combined influence of hydrological variability and human disturbance (Baena-Escudero et al., 2019; Llena et al., 2020). Similar multi-decadal adjustments are reported in Albania, where satellite-based reconstructions document high planform variability and active channel reconfiguration in response to sustained anthropogenic pressure (Spada et al., 2018). In Slovenia, recorded channel changes are linked primarily to land-use shifts, especially agricultural abandonment and reforestation, which reduced sediment yield and flood peaks and were followed by incision and bar stabilization (Keesstra et al., 2005). For Croatia, Pavlek and Faivre (2020) highlight progressive channel contraction, reduction of bar surfaces, and island growth associated with dam building and hydropower development.

Western European examples from Scotland and France reveal how channelization, flood protection, and flow regulation have transformed previously mobile multi-thread reaches into more confined channels (Winterbottom, 2000; Bulteau et al., 2022; Jautzy et al., 2022). Central European case studies describe river systems under sustained human pressure, where narrowing, incision, and planform simplification are frequently reported. Evidence comes from Germany (Eschbach et al., 2018), Austria (Hohensinner et al., 2004), and Poland (Rinaldi et al., 2005; Zawiejska & Wyżga, 2010; Hajdukiewicz & Wyżga, 2023). Hungarian rivers display regulated meander adjustment (Amissah et al., 2018; Kiss & Blanka, 2012), while Slovak mountain channels preserve active braided-wandering sectors (Kidová et al., 2016); comparable transformations have also been observed in the Czech Republic (Škarpich et al., 2013). In Eastern Europe recent studies from Ukraine, combining historical topographic maps with satellite imagery and GIS analysis, reconstruct long-term channel deformation patterns, including lateral migration and width variability (Burshtynska et al., 2024). Research on major Russian rivers indicates that channel boundary changes and pattern adjustments reflect both large-scale human regulation (especially reservoir construction) and natural controls, depending on basin and reach characteristics (Alexeevsky et al., 2013).

Romanian rivers generally align with the broader European tendency of channel adjustment, although several studies point to a slower tempo of geomorphic change and a delayed response to sustained anthropogenic pressures (Bălteanu et al., 2012; Rădoane et al., 2017). Compared with rivers from Italy, France, or Germany, where incision, narrowing, and planform shifts often developed earlier under similar disturbances, many Romanian systems show more progressive, cumulative adjustments. Research carried out in Romania addresses both vertical and planform dynamics across multiple temporal scales. Early investigations examined the long-term evolution of longitudinal profiles in the Carpathians (Rădoane et al., 2003), while more recent work documents shorter-term changes such as bed incision, aggradation, and flood-related threshold responses (Rădoane et al., 2010; Rădoane et al., 2013; Ioana-Toroimac et al., 2020; Dumitriu, 2021). These results indicate that channel morphology reflects the combined effects of hydrological variability, engineering works, sediment extraction, and land-use change.

Channel geometry has been reconstructed mainly through the comparison of historical maps, aerial photographs, and satellite imagery, allowing the tracking of sinuosity changes, braiding structure, and lateral migration over roughly the last 150 years (Cristea, 2011; Perșoiu & Rădoane, 2011; Chiriloaei, 2012; Chiriloaei & Rădoane, 2015). The integration of older cartographic sources with modern remote sensing data improves the detection of long term channel shifts.

Case studies further show that structural modifications of river corridors (including dams, bank consolidation and embankments, and floodplain reclamation) alter sediment transfer and channel behaviour, as documented for Suceava river (Romanescu, 2013), the Prahova river (Ioana Toroimac

et al., 2010; Armaș et al., 2013), the Prut river (Rădoane et al., 2008), the Siret river (Salit et al., 2015), the Ialomița river (Radu & Comănescu, 2025), and the Danube corridor (Grecu et al., 2017). At national scale, the dominant tendency points toward channel simplification and stabilization, with notable differences in timing and magnitude between basins.

Previous investigations (e.g., Ujvari, 1972; Romanescu, 2003; Horodnic, 2023) describe the Suceava River in north-eastern Romania as a representative example of a channel system that has undergone substantial morphological transformation. These changes are linked to the combined effects of hydrological processes and human pressures, including deforestation, agricultural expansion, and urban development. Within this context, analysing multi-decadal shifts in channel sinuosity, braiding, and width provides valuable insight into the mechanisms through which multiple drivers have interacted over time to reshape the river corridor.

The present study examines the Suceava river valley at the contact between the Obcinele Bucovinei mountain sector and the Moldavian Plateau lowlands. The objective is to identify the main geomorphic and hydrological changes recorded in this sector over time. Since the late nineteenth century, the morphology of the Suceava river valley has undergone notable transformations, as evidenced by historical maps, orthophotographs, and satellite imagery. These records reveal alternating phases of heightened fluvial activity (characterized by shifts in channel width, sinuosity, and braiding), followed by intervals of relative stability associated with both hydrological variability and human intervention. Gaining a better understanding of these dynamics is important for developing effective river management strategies, particularly as fluvial systems face increasing pressure from climate change and human activity (Diaconu, 1999). Accordingly, this study analyses key parameters of morphological evolution, including the width of the active river area (ARA), as well as sinuosity and braiding indices over more than a century, in order to clarify how the Suceava river has responded to natural controls and anthropogenic forcing.

2. MATERIALS AND METHODS

2.1. Selecting the study area

Covering approximately 391 km², the study area follows the course of the Suceava River within the Rădăuți Depression. In this extra Carpathian sector, the river flows for about 113 km along its main channel, from Straja at the Carpathian margin to the area upstream of Dornești. The region marks the transition between the Eastern Carpathians (characterized by low mountains generally ranging from 500 to 1000 m a.s.l.) and the adjacent hilly landscape of the Moldavian Plateau (as detailed by Oprea, 2014), which includes piedmonts and depressions situated between 320 and 500 m a.s.l. (**Fig. 1**).

To delineate the investigated sector, we integrated historical cartographic materials with high resolution LiDAR data (**Fig. 2**). This dataset enabled the identification of fine geomorphological features, including paleo-meanders, channel displacements, and subtle morphological adjustments that are difficult to detect using conventional DEM products.

Similar methodological frameworks have been successfully applied in north-eastern Romania. Stoleriu et al. (2020) and Huțanu et al. (2020) demonstrated that integrating dense LiDAR point clouds with HEC-RAS modelling significantly enhances the accuracy of flood hazard assessments by allowing a more precise representation of channel morphology and flood prone areas.

2.2. Data collection and preparation

Channel planform dynamics were analysed using a diverse set of cartographic materials, aerial photographs and complementary historical sources, following established approaches in fluvial geomorphology (Kondolf & Piégay, 2003; Perșoiu, 2010) and based on the cartographic assemblage illustrated in **Fig. 3**. The dataset includes historical maps from multiple survey stages, beginning with Austro-Hungarian editions and continuing with later Romanian series, obtained from archives, libraries and specialized cartographic collections.

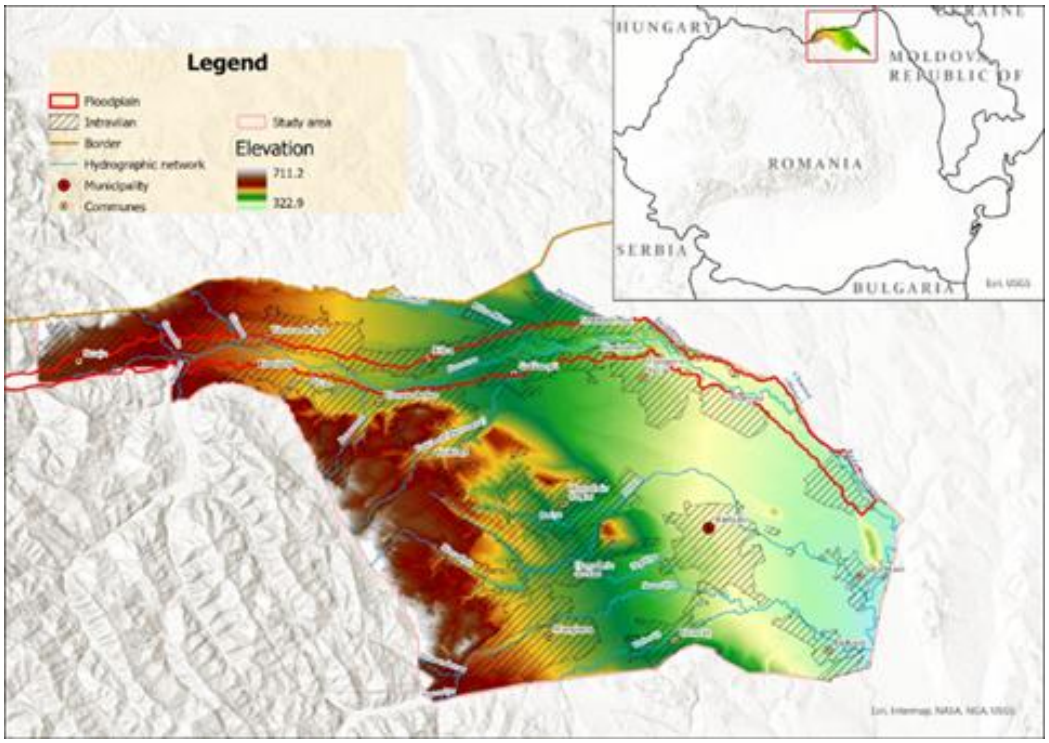


Fig. 1. Location of the study area in Romania and the regional setting.

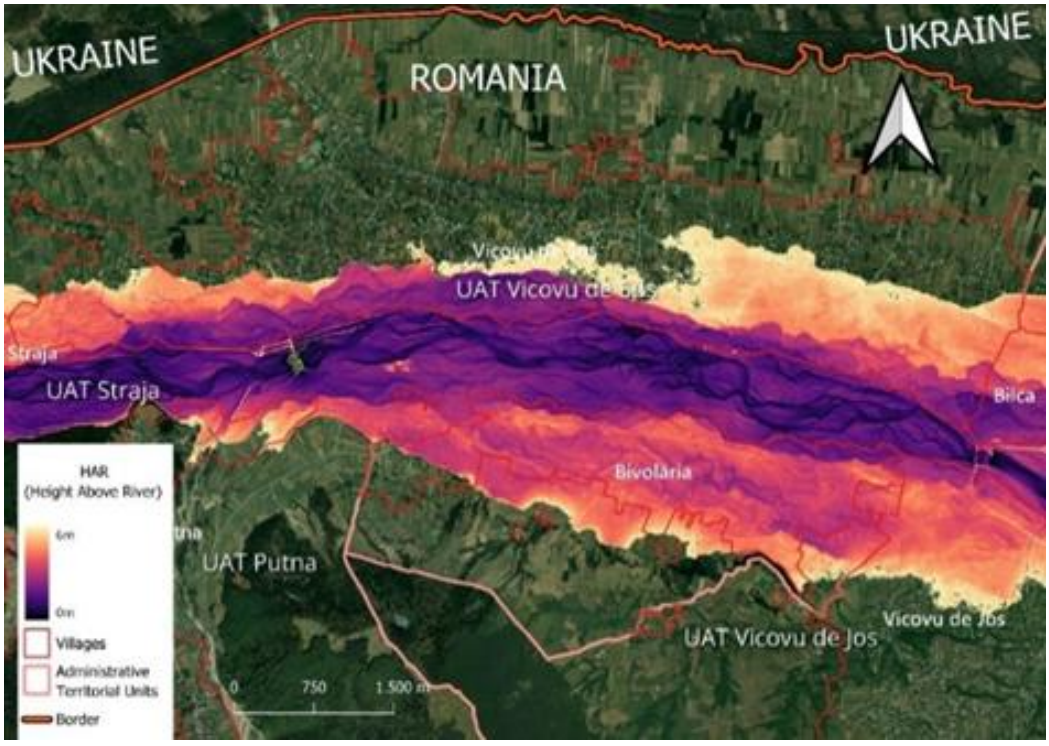


Fig. 2. Study area delimitation based on LiDAR-derived imagery.

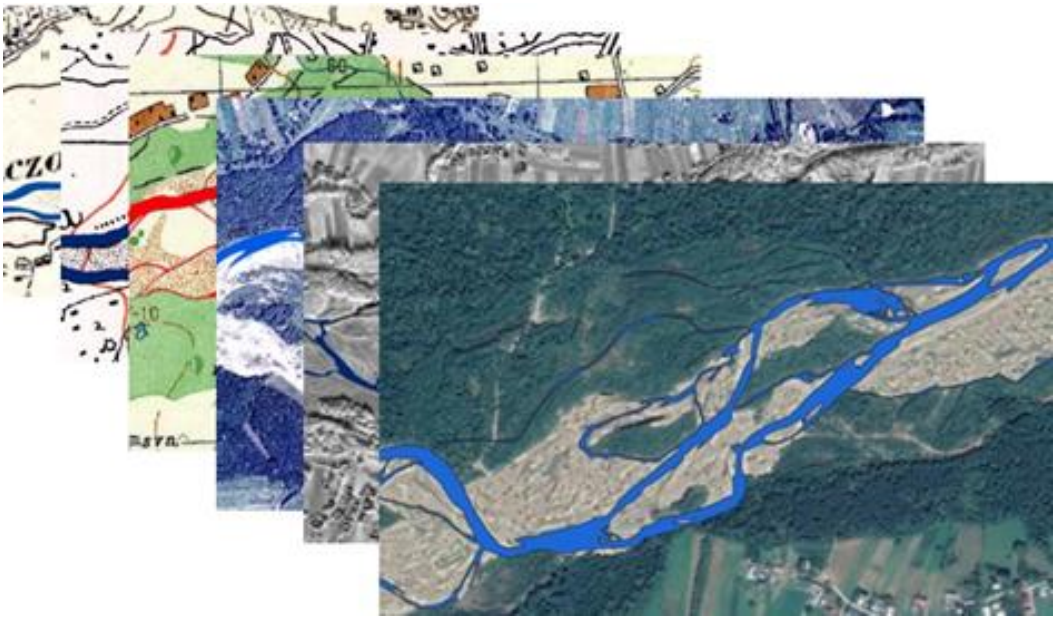


Fig. 3. Historical and modern cartographic sources supporting the analysis of channel planform changes.

High resolution orthophotos from 2006 and 2011 were acquired from national geospatial providers (ANCPI) and dedicated platforms such as www.geospatial.org, ensuring an accurate representation of the river corridor and adjacent landscape. Together, these sources supported the construction of a spatial database covering more than 150 years of channel evolution, from late nineteenth century surveys to recent satellite imagery, for the extra-Carpathian sector of the Suceava river.

2.3. Vectorization process

Historical maps, orthophotos and satellite imagery were digitized in ArcGIS Pro 3.2. River features identifiable in both historical and recent cartographic sources were manually traced and vectorized. To maintain consistency and reduce operator-related variability, the digitization was performed by a single analyst using a uniform workflow, as recommended in comparable multi temporal channel studies (see, for example, Mandarino et al., 2019).

2.4. Cross-section generation and reach subdivision

Cross-sections were generated along the river valley at regular 400 m intervals using GIS-based tools. These profiles, oriented perpendicular to the channel, captured the main features of valley morphology and planform variability. The study reach was divided into nine subsections, each comprising 11 measurement transects.

The digitized river morphology and cross sectional data were integrated into a comprehensive spatial database, which was used for the subsequent analysis, enabling an in-depth assessment of the morphological characteristics and shifts of the riverbed. Additionally, the results obtained using this approach provide a reliable data source for future studies on fluvial dynamics, water resource management, and environmental conservation strategies in Suceava drainage basin.

2.5. Extraction of the geomorphological database from cartographic documents (1869-1884, 1897-1902, 1977, 2006, 2011, 2021)

To characterize the morphology of Suceava river channel, a detailed morphometric database was created based on a collection of cartographic sources (**Tab. 1**), focusing on identifying the features of

the floodplain, which is relatively recent in origin, and is subject to rapid changes due to more intense fluvial processes compared to other areas.

Table 1.

Summary of cartographic materials used in the study.

Name of the map	Timeframe of completion	Year(s) of publication	Scale	Projection	Data
Third Austro-Hungarian Survey	1869 - 1884	1890 - 1910	1:25,000	Stereographic projection of Tg. Mureș on the Bessel 1841 ellipsoid	Institute of Military Geography, Vienna
"Plan Director de Tragere"	1897 - 1902	Different years of printing	1:20,000	Lambert Projection	Serviciul Geografic al Armatei Române
Topographic maps	1977	1978 - 1979	1:25,000	Gauss - Krüger Pulkovo, Cylindrical Projection 1942	IGFCOT
Orthophotos	2004 - 2006	-	1:5,000	Stereographic projection Stereo70 ellipsoid Krasovschi	ANCPI
Orthophotos	2011	-	1:5,000	Stereographic projection Stereo70 ellipsoid Krasovschi	ANCPI
Satellite Imagery	2021	-	1:20,000	WGS 84	Google Earth

The construction of the database was based on the careful definition and measurement of morphometric parameters, following the cross-sectional valley methodology (**Fig. 4**) as outlined by Rapp & Abbey (2003), and Rădoane et al. (2008).

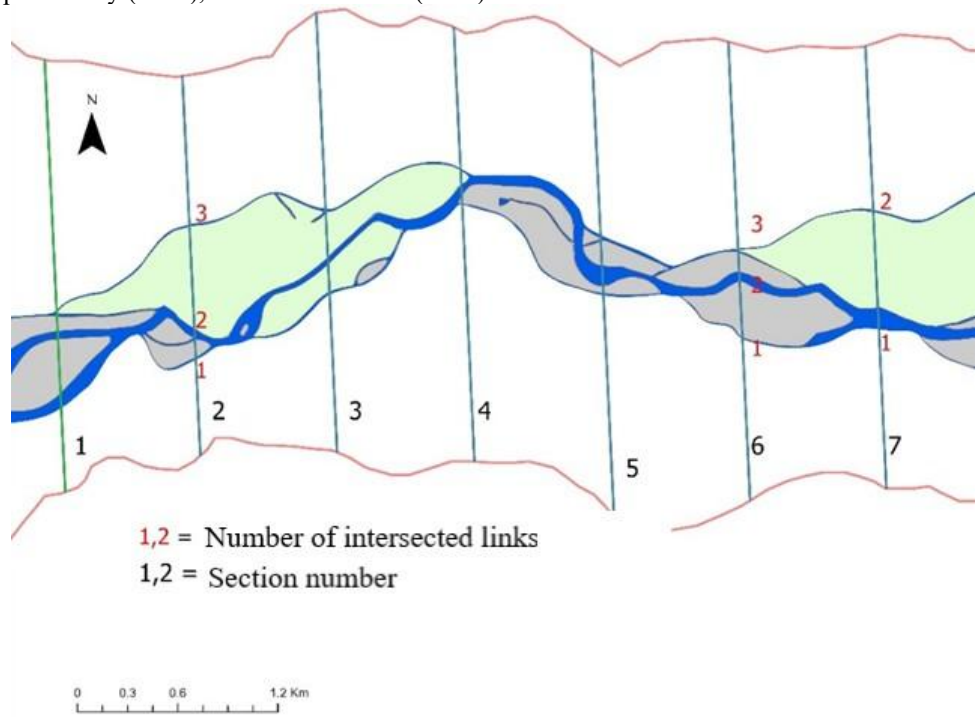


Fig. 4. River braiding index calculation according to Ashmore (1991) with cross-sections along Suceava river.

Morphometric measurements were conducted on the valley bed, which includes the floodplain - an area situated on either side of Suceava river channel, with relatively low elevations, of up to 5-7 meters in height above the channel. The floodplain consists of the active river area (ARA), representing the free migration zone of the river, and the terraces situated at 2 meters, 4 meters, and 5-7 meters above the channel level. On the surface of the floodplain, traces of the old river channels can be observed in the form of abandoned river branches. The integration of these data into a comprehensive spatial database allowed for a detailed assessment of the morphological characteristics of Suceava river, providing a consistent foundation for further studies on river dynamics in this region.

2.6. Definition and classification of riverbed morphology

In the investigation stage dedicated to defining and establishing the riverbed morphology (**Fig. 5**), the primary objective was to fully understand its current physical characteristics and behaviour. This analysis relies on gathering essential data, such as the natural (including climatic) attributes of the surrounding environment, the degree of constraint affecting the river channel (whether influenced by natural terrain morphology or man-made structures), and critical metrics such as the sinuosity index, which measures the extent of meandering along the river course. Additionally, parameters such as the braiding index, which indicates the complexity and number of channels in the riverbed, and the anastomosis index, quantifying the branching degree of the channels, are essential in this assessment.

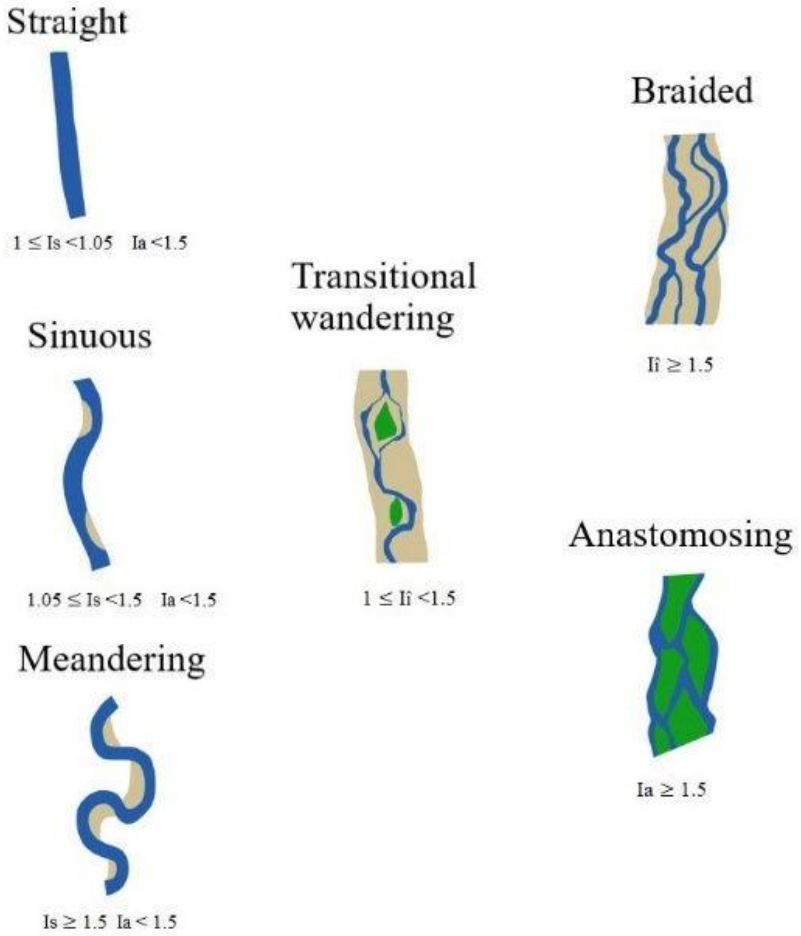


Fig. 5. Fluvial morphology scheme and variability ranges of the main planimetric indices: Si, sinuosity index; Bi, braiding index; Ai, anastomosis index (adapted from Brice, 1975).

- **Straight channels**: Are characterized by a single, relatively unaltered course, with a braiding index close to 1 and sinuosity index below 1.05. These are rare in natural environments, as emphasized by Brice (1975), Malavoi & Bravard (2010), and Rinaldi et al. (2011).

- **Sinuous channels**: Are defined by a sinuosity index greater than 1.05. According to Brice (1984), channels with a sinuosity index of up to 1.25 are slightly sinuous, while those exceeding this value are highly sinuous or meandering. Leopold & Wolman (1957) suggest that the transition to meandering occurs at a sinuosity index of 1.5.

- **Meandering channels**: Occur when the sinuosity index exceeds 1.5 (Leopold & Wolman, 1957) or, according to alternative classifications, 1.3 (Chang, 1979).

- **Transitional channel types**: Exhibit intermediate characteristics between sinuous, meandering, braided, and anastomosing forms.

- **Wandering transitional channels**: Are defined by a diffuse braiding index greater than 1, but lower than 1.5. The term wandering has no precise equivalent in Romanian, where specialized literature uses *vagabond* or *divagant* (Brice, 1975; Rinaldi, 2003).

- **Sinuous Transitional Channels with Alternating Arms**: Are characterized by a single, strongly sinuous channel with braiding index values close to 1 and a sinuosity between 1.05 and 1.45 (according to Rinaldi, 2003). A distinctive feature is the continuous and alternating presence of lateral bars, which has led some authors to refer to this type as "pseudo - meandering."

- **Braided**: These channels have multiple arms separated by islands, with a braiding index above 1.5 (**Fig. 5**).

- **Anastomosing**: Characterized by multiple channels separated by vegetated islands, and described by the anastomosing index.

2.7. Braiding index according to Brice (1964) and Ashmore (1991)

The braiding index is commonly used to quantify the degree of channel subdivision in multi thread rivers. A synthesis of the main calculation approaches was provided by Thorne (1997), who discussed, among the most widely applied formulations, those introduced by Brice (1964) and Ashmore (1991).

Brice (1964) defined the braiding index using a length-based formulation (Eq. (1)):

$$Bi = \frac{2\times(\textit{sum of the lengths of the branches or channels})}{\textit{length of the sector measured across the channel}} \quad (1)$$

Ashmore (1991) later proposed an alternative approach based on the number of channel branches intersected by cross-sections (Eq. (2)):

$$Bi = \frac{\textit{number of intersected branches (average values obtained)}}{\textit{number of considered sections}} \quad (2)$$

For the present dataset, we assessed the suitability of both formulations and selected the Ashmore (1991) method as more appropriate for the cross-section based analysis used here. Its implementation is illustrated in **Fig. 4**.

2.8. Sinuosity index

Channel sinuosity was calculated for each defined river sector as the ratio between channel length and the corresponding distance measured along the valley axis (Eq. (3)).

$$Si = \frac{la}{lv_1+lv_2+lv_3+lv_4} \quad (3)$$

Sinuosity may be measured along reaches of different lengths, but segments must be sufficiently long to yield meaningful values. A commonly accepted reference scale corresponds to distances of

about 10-14 channel widths, which provides a representative measure of channel curvature (Thorne, 1997). This procedure supports the evaluation of channel curvature and planform complexity, both relevant for interpreting fluvial dynamics and channel evolution.

2.9. Data analysis and interpretation

The resulting dataset was organized in Microsoft Excel, where all calculated indicators were recorded in a consistent format. We used graphical outputs to examine temporal and spatial variation in the indices and to identify patterns in channel behaviour. Reaches with higher sinuosity were generally more prone to bank erosion and sediment accumulation, whereas sectors with higher braiding values showed uneven flow distribution and more frequent bar development.

In order to ensure that the results we obtained were reliable, we applied strict quality checks at every stage. We compared our findings with field data to validate the digitized river features and cross-sectional profiles, and we ran sensitivity analyses to test the robustness of the calculated indices. These steps helped confirm both the accuracy and the consistency of our results.

3. RESULTS AND DISCUSSION

3.1. Active river area (ARA) width variation

For the morphological analysis of Suceava river valley, several relevant periods and years were identified in order to structure the temporal record and capture the distinct phases of channel dynamics. The multi-year periods (1869-1884, 1897-1902) were selected because they correspond to blocks of historical cartographic materials with comparable coverage and consistency (topographic/cadastral maps), allowing robust cross-sector comparisons. Furthermore, the individual years (1977, 2006, 2011, 2021) were chosen as methodological and data milestones which coincide with aerial photogrammetric campaigns, orthophotos, or the transition to high-resolution remote sensing and LiDAR. These timeframes reflect key hydrological or anthropogenic moments, such as flow regime changes, engineering works, land use modifications etc., which could explain abrupt shifts or thresholds in channel width (**Fig. 6**). This combined approach leverages the advantages of multi-annual windows (sensitive to long-term trends) and reference years (sensitive to episodic or geomorphic thresholds).

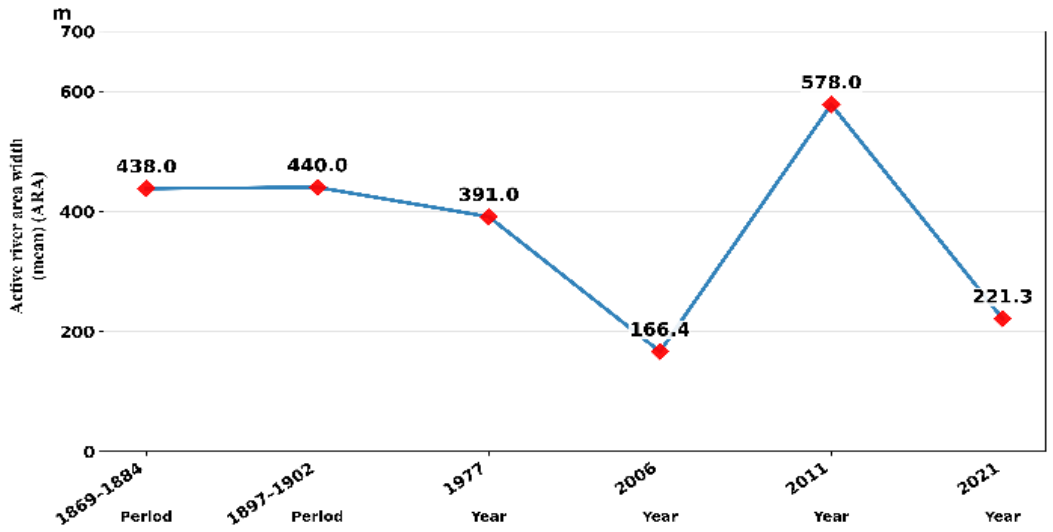


Fig. 6. Width of the mean active river area (ARA).

1869-1884: The active river area (ARA) width varied significantly across sectors, with Sector 1 ranging from 108.42 m to 78.48 m, Sector 2 from 542 m to 287 m, Sector 3 from 526.64 m to 105 m, and Sector 4 from 718 m to just 142.11 m. These variations reflect local factors and prevailing hydrological conditions.

1897-1902: ARA width continued to vary notably. Sector 1 ranged from 55.26 m to 203.66 m, Sector 2 from 396.15 m to 431 m, Sector 3 increased from 344.11 m to 600.96 m, and Sector 4 ranged from 518.85 m to 302.78 m, indicating responsiveness to changes in flow regime and major hydrological events.

The ample variations in ARA morphology during these intervals could be related to large-scale changes in the landscape occurring from 1790 to 1864, when a total area of ca. 1085 km^2 was affected by major land use/landcover shifts, accounting for 39.2% of the area of Suceava drainage basin (Horodnic, 2023). By 1964, just 48% of the drainage basin area was covered by forest, compared to approx. 65% in 1790, indicating a severe drop in the protective function of vegetation and increased erosion. Subsequently, between 1864 and 1985, significant land use/landcover changes affected ca. 35.84% of the drainage basin. Additionally, during the same period exceptional amounts of precipitation were recorded in the Suceava region in 1837, 1846, 1850, 1893-1897, 1900-1901. In 1897 the annual volume of precipitation at Slatina (in the plateau area) exceeded by approx. 185% the mean annual amount of 645 mm. Of the total 1844 mm of precipitation recorded in 1897, 1574 mm fell between April and June, surpassing by 570% the average amount of the rainy season. The abundant precipitation has likely contributed to ARA width adjustments in the upper and mid-course of Suceava river, particularly considering the large-scale deforestation of mountain and hill slopes occurring at a fast pace in the drainage basin.

1977: Significant variability was observed. Sector 1 varied from 40 m to 286.59 m, Sector 2 from 211 m to 288.38 m, Sector 3 from 344 m to 758 m, and Sector 4 from 292 m to 994 m in width, suggesting considerable changes due to river flow modifications and human interventions.

Prior to this year, considerable precipitation amounts were recorded in the upper basin of Suceava river in 1970 and 1975, possibly contributing to the dynamics of the river channel as reflected by ARA width changes. Moreover, additional human intervention occurred in the basin, in the form of small embankments (e.g. on Putna river at confluence in 1959, and on Suceava river at Dornești in 1970), while agricultural lands expanded to the detriment of forests, which accounted for just 39.2% of the total drainage basin in 1985 (Horodnic, 2023), distributed mainly in the montane sector.

2006: Width variability remained significant. Sector 1 ranged from 13.5 m to 199.9 m, Sector 2 from 27.25 m to 248.96 m, Sector 3 from 105.55 m to 508.93 m, and Sector 4 from 65.73 m to 464.85 m, likely influenced by local factors such as flow variations and anthropogenic activities.

2011: Notable variations persisted. Sector 1 ranged from 17.18 m to 175.25 m in width, Sector 2 from 16.13 m to 315.88 m, Sector 3 from 28 m to 472.8 m, and Sector 4 from 22.24 m to 445.25 m, reflecting changes in flow regimes following recent floods. The entire 2005-2010 period was exceptionally rainy, with high precipitation occurring in 2005, 2006, 2008 and 2010, typically ensued by historic levels of Suceava river and tributaries, particularly during the major 2008 and 2010 flood events. During this timeframe the annual precipitation and the peak streamflow discharge reached record values: at Țibeni gauging station (in Rădăuți Depression) the measured discharge was as high as 200 m^3/s on 26 July 2008, compared to the mean discharge of 14,3 m^3/s.

2021: Significant variability continued, with Sector 1 ranging from 65.67 m to 245.97 m, Sector 2 from 126.85 m to 431 m, Sector 3 from 73.27 m to 473 m, and Sector 4 from 56.95 m to 232.52 m, indicating active fluvial dynamics driven by both hydrological changes and human interventions.

From 2011 to 2021 changes in the land use/landcover were not as significant, with the exception of forest fragmentation which continued as large portions of forests were reclaimed by private owners and logging became a major source of income for the population inhabiting the mountainous part of Suceava drainage basin. This timeframe has also coincided with a period of marked climate changes in north-eastern Romania, including an increase in temperature (by 0,36°C per decade, according to Piticar, 2013) and extreme precipitation events, both in terms of amount per event, intensity and frequency.

As regards other man-made structures which interfere to a significant degree with the dynamics of the river channel, additional embankments were installed along Suceava watercourse at Straja, Vicovu de Sus, Bilca, Frătăuții Noi, Costișa, Frătăuții Vechi, Măneuți etc. (**Fig. 7**), as well as some of its main tributaries at: Putna and Gura Putnei (on Putna river), Voitinel (on Voitinel river), and Horodnic de Jos (on Pozen river). Donati et al. (2019) demonstrated that rivers where such structures exist are potentially exposed to degradation, as shown in the case of rivers in metropolitan France.

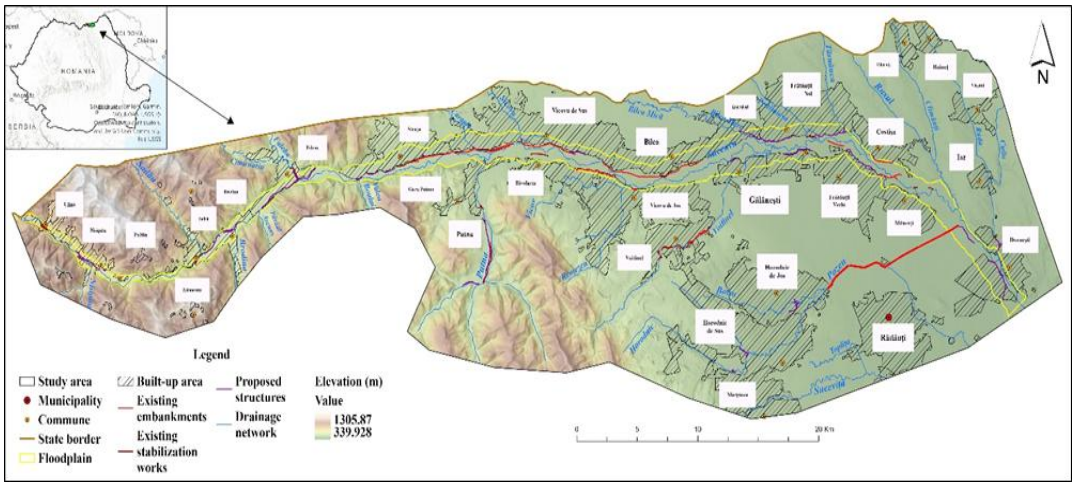


Fig. 7. Location of embankments (marked in red) and stabilization works (marked in purple) in Suceava drainage basin.

3.2. Variation in floodplain width

The data analysis focusing on the floodplain width (**Fig. 8**) reveals considerable variability along the river course, reflecting a dynamic fluvial landscape influenced by geomorphological, hydrological, and anthropogenic factors.

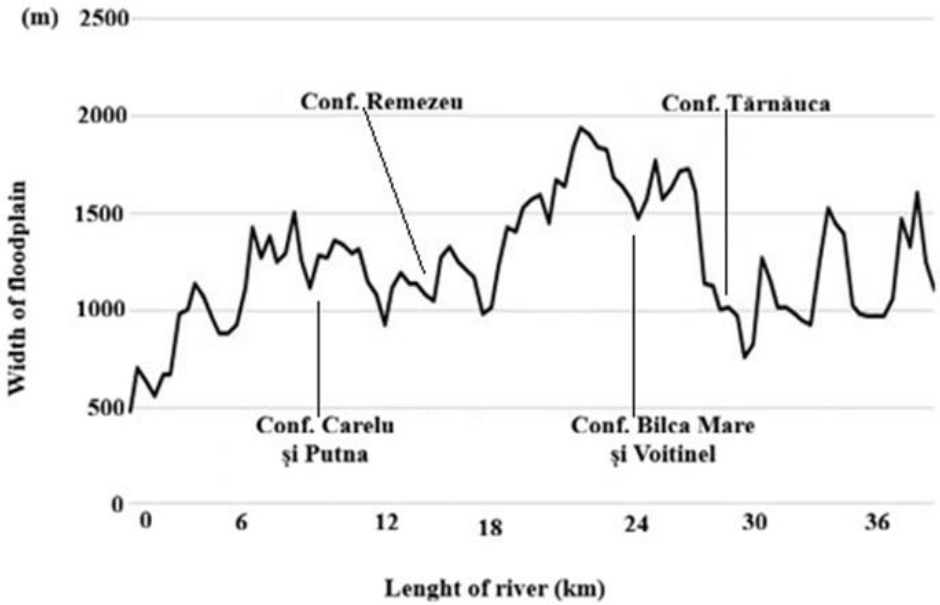


Fig. 8. Variation in floodplain width.

The floodplain width ranges from minimum values around 700 meters to maximum values exceeding 1900 meters. This variability indicates the presence of sections with intense lateral erosion and significant sediment deposition. For instance, the channel width increases significantly in the 8-12 km and 18-24 km reaches, suggesting areas with active sedimentation processes and extensive floodplain formation.

In certain sectors the floodplain narrows, potentially reflecting areas of intense lateral erosion or anthropogenic interventions (Fig. 8). For example, the width decreases to below 1000 meters at kilometres 2, 4, 8, 18, and 28. These narrower zones are influenced by topographical constraints, such as rocky slopes or anthropogenic infrastructure like embankments or bridges. Conversely, wider zones, such as the reaches between 22-24 km and 38-39 km, indicate regions with significant sediment deposition and the potential for formation of extensive floodplain (with widths between 1500 and 1900 m).

3.3. Braiding index (Bi)

The braiding index of Suceava river (**Fig. 9**) has been analysed throughout six timeframes: 1869-1884, 1897-1902, 1977, 2006, 2011, and 2021, across nine reaches. This index assesses the complexity of the braided river channel and is influenced by water levels and geomorphological changes.

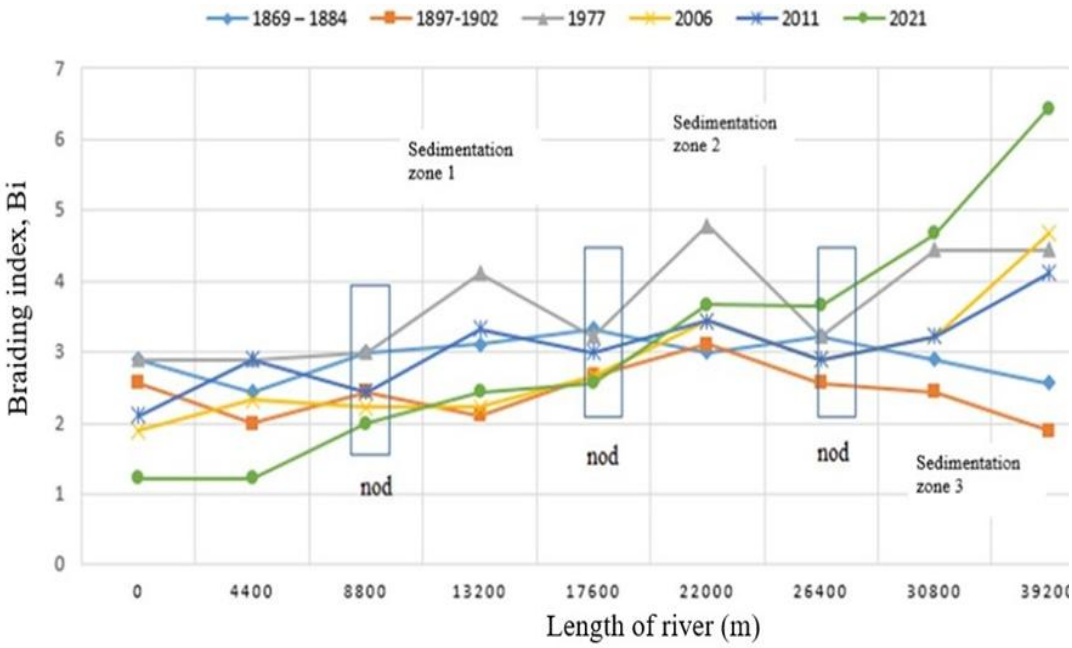


Fig. 9. Variation in braiding index (Bi) and sedimentation zones.

1869-1884: The braiding index values ranged from 2.44 to 3.33, indicating moderate to high channel complexity. Higher values (3.33) denote more dynamic and complex patterns, while lower values (2.44) suggest greater stability.

1897-1902: The index varied from 1.89 to 3.11. Lower values (1.89) in sectors 9 and 10 indicate increased stability, while the higher values reflect moderate fluvial activity.

1977: A notable increase was observed in this period, with values ranging from 2.89 to 4.78. Sectors 9 and 10 showed the highest values (up to 4.78), thus indicating intense fluvial activity and significant morphological changes.

2006: Index values ranged from 1.89 to 4.67, with sectors 8 and 9 showing the highest values (4.67), suggesting high geomorphic activity in these reaches, while lower values indicated more stable regions.

2011: The index fluctuated between 2.11 and 4.11. Again, the most dynamic sectors were 8 and 9, with values of up to 4.11, while partial stabilization occurred in other areas.

2021: Values ranged widely from 1.22 to 6.44. The highest values of the braiding index (6.44) pertained to sectors 8 and 9, indicating very active dynamics and instability, while reaches with lower values (1.22) appeared more stable.

Over time, coarse sediment accumulated in "sedimentation zones" separated by nodal points (**Fig. 9**). While the length of these zones has remained relatively constant, their width has significantly decreased.

3.4. Sinuosity index (Si)

The analysis of sinuosity indices for Suceava river across the specified periods revealed significant variations in river morphology (**Fig. 10**).

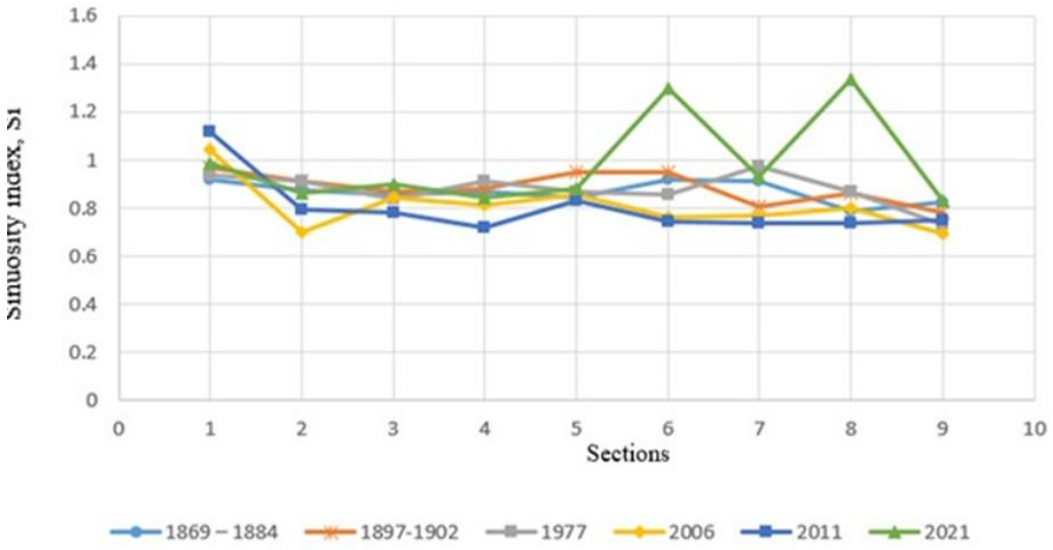


Fig. 10. Sinuosity index variations.

1869-1884: Sinuosity indices ranged from 0.78 to 0.92, indicating a relatively straight course, while sectors 1 (0.92), 6 (0.92), and 7 (0.91) are moderately sinuous.

1897-1902: Indices varied between 0.77 and 0.96, with sector 1 (0.96) showing the highest degree of sinuosity, followed by sectors 5 (0.949) and 6 (0.950).

1977: The index ranged from 0.73 to 0.97, with sector 6 (0.97) being the most sinuous.

2006: Values fluctuated between 0.692 and 1.041, with sector 1 (1.041) exhibiting clear sinuosity.

2011: Indices ranged from 0.72 to 1.11, with sector 1 (1.11) showing pronounced sinuosity.

Compared to earlier periods, in **2021** a general trend towards increased sinuosity became apparent in sectors 6 (1.29) and 8 (1.33).

Sectors with indices above 1 indicate a significant evolution towards more pronounced sinuosity. This trend may be influenced by natural factors such as erosion and sedimentation processes, as well as human interventions, including hydraulic works or changes in land use in the area adjacent to the river.

4. CONCLUSIONS

The analysis of morphological changes along the Suceava River over the 1869-2021 interval shows how channel form has evolved under the combined influence of natural processes and human interventions. Using historical maps, aerial imagery, and recent geospatial datasets, the study reconstructs more than a century and a half of channel adjustments and outlines the main directions of long-term change. The results point to a progressive reorganization of channel pattern and geometry, with a gradual increase in structural complexity compared to the earliest mapped conditions.

The quantified indicators confirm a clear intensification of channel complexity over time. In the earliest surveys (1869-1884), the braiding index generally ranged between 2 and 3, whereas the most recent measurements show values reaching about 4.5 5.5, indicating a higher degree of multi-thread development. A similar upward shift is visible for sinuosity, which increased from roughly 1.1-1.5 at the beginning of the record to about 1.6-2 in the latest stage (2021), reflecting stronger channel curvature and lateral development.

The active river area (ARA) exhibited substantial variability, expanding from 28-311 m (1869-1884) to a peak of 508 m in 2006, followed by a contraction to 65-245 m in 2021. This pattern reflects alternating phases of channel expansion, relative stability, and subsequent adjustment. Similarly, floodplain width increased from 86-594 m to over 1000 m by 1977, before narrowing to 65-245 m in recent decades, pointing to a dynamic interaction between the channel and its floodplain.

Hydrological records from 2014 to 2022 at Brodina in the mountain basin reveal pronounced seasonal contrasts. Mean streamflow discharge typically ranges between 0.2-0.9 m^3/s in winter months (January - February, November - December) and 1.0-3.5 m^3/s in spring-summer (April-June), with occasional peaks above 5 m^3/s. Minimum discharge frequently falls below 0.2 m^3/s, especially in late summer and winter, highlighting drought sensitivity. Inter-annual variability is evident: for instance, in 2015-2017 the seasonal regimes were relatively stable, with mean values between 0.3-1.0 m^3/s, while in 2019-2020 higher oscillations were documented, with monthly averages reaching 3-5 m^3/s, followed by a decline in 2021-2022, when values generally remained below 1.0 m^3/s.

This variability corresponds with precipitation data from the same period, where monthly totals at Brodina ranged from less than 1 mm in dry months to more than 70-80 mm in wet months, outlining the role of short but intense rainfall events in driving flood events. Data from the Brodina hydrometric station (on Suceava river) show an increase in mean annual temperature from around 7.50°C (2015-2021) to 8.59°C in 2023, indicating a rise of more than 1°C over the course of less than one decade, accompanied by increasing inter-annual oscillations which could have an effect on the development of fluvial processes.

Along with climate variability, the drivers of changes in riverbed morphology are likely linked to anthropogenic impacts relating mainly to large-scale land use/landcover shifts in the river basin. Landscape changes relied on deforestation and massive expansion of arable land from 1790 to 2020: while forested areas decreased by more than 42% (660 km^2) at an annual rate of ca. 3 km^2/yr in the entire basin (6 km^2/yr in the montane region) and natural pastures diminished by 33%, arable land and built-up areas increased by ca. 210% (450 km^2) and 310% (300 km^2), respectively (Horodnic, 2023).

The geomorphic effects of recent environmental changes and anthropogenic impacts have also been documented by the analysis of lake sediments in NE Romania, with findings from lacustrine sites demonstrating that sediment accumulation rates have predominantly increased over the last 150-year period (e.g. at lakes Știol and Buhăescu Mare in Rodna Mts and Sfânta Ana in Harghita Mts). Moreover, sediment yield and accumulation rates in lowland and mid-elevation lake basins were strongly influenced by the socialist land-use regime, which promoted intensive agriculture and large-scale deforestation

Therefore, the combination of human-induced land use/landcover changes and climate shifts has likely contributed to enhancing channel braiding and sinuosity, and increased hydrological variability, thus amplifying the vulnerability of Eastern Carpathian rivers.

The dynamics of Suceava river valley mirrors the trends observed in other Romanian rivers, with channels displaying delayed but cumulative responses to long-term anthropogenic pressures, including hydrotechnical works, land use changes, and floodplain reclamation. This evolution is in line with the shift toward more complex fluvial patterns under combined climatic and human drivers documented by several multi-decadal studies across Europe.

Sector-specific analysis showed that sectors 8 and 9 are particularly dynamic, aligning with findings indicating that localized reaches often concentrate migration and braiding activity (Brice, 1975; Rinaldi, 2003). The observed increase in sinuosity and braiding points to greater sediment mobility and a tendency toward instability, which directly influences erosion, flood risk and land use/landcover planning across the basin.

The dynamic of Suceava river valley throughout the last 150 years exemplifies the sensitivity of rivers in the NE region of Romania to both natural and anthropogenic drivers. The adjustments observed in the river evolution closely resemble those determined for the neighbouring Moldova river basin, where braided to meandering transitions and pronounced channel metamorphosis have been documented during the last century (Chiriloaei, 2012; Chiriloaei & Rădoane, 2015). Such parallels outline that although each river responds to local hydrological and geomorphic settings, the broader pattern of increased complexity and instability under human and climatic pressures is consistent across the region.

The results obtained through this detailed analysis of riverbed dynamics in the past 150 years along Suceava river at the transition between the mountainous area and the eastern lowlands can be utilized for establishing science-based river management strategies. Priority should be given to dynamic sectors such as 8 and 9, where intensified braiding and sinuosity raise concerns for bank erosion, flood risk, and infrastructure vulnerability.

Based on the data yielded by this study, further research in the area could link morphological adjustments with hydrological records and climate variability and projections, exploring sediment budgets in dynamic sectors. Future studies should expand monitoring efforts by incorporating high-resolution UAV surveys, repeated LiDAR scans, and automatic image analysis to capture short-term morphological adjustments that complement the long-term perspective derived from historical cartography. Such an approach would support the development of adaptive management strategies and contribute to enhancing resilience in Suceava basin, while also providing data for comparative studies of fluvial dynamics across Romania and Europe. Adaptive strategies could include buffer zones, controlled floodplain reconnection, and eco-geomorphological restoration measures, aligning with European directives on river basin management. Moreover, multi-river studies including NE Romanian rivers such as Moldova, Prut, and Siret, would provide a stronger empirical basis for anticipating future changes under projected climate scenarios and increasing human pressure.

REFERENCES

Alexeevsky, N.I., Chalov, R.S., Berkovich, K.M. & Chalov, S.R. (2013) Channel changes in largest Russian rivers: Natural and anthropogenic effects. *International Journal of River Basin Management*, 11(2), 175-191. DOI: 10.1080/15715124.2013.814660

Amissah, G.J., Kiss, T. & Fiala, K. (2018) Morphological evolution of the lower Tisza River (Hungary) in the 20th century in response to human interventions. *Water*, 10, 884. DOI: 10.3390/w10070884

Armaș, I., Gogoașe Nistoran, D., Osaci-Costache, G. & Brașoveanu, L. (2013) Morpho-dynamic evolution patterns of Subcarpathian Prahova River (Romania). *CATENA*, 100, 83-99. DOI: 10.1016/j.catena.2012.08.001

Ashmore, P.E. (1991) How do gravel-bed rivers braid?. *Canadian Journal of Earth Sciences*, 28(3), 326-341. DOI: 10.1139/e91-030

Baena-Escudero, R., Rinaldi, M., García-Martínez, B., Guerrero-Amador, I.C. & Nardi, L. (2019) Channel adjustments in the lower Guadalquivir River (Southern Spain) over the last 250 years. *Geomorphology*, 337, 15-30. DOI: 10.1016/j.geomorph.2019.03.027

Bălteanu, D., Jurchescu, M., Surdeanu, V., Ioniță, I., Goran, C., Urdea, P., Rădoane, M., Rădoane, N. & Sima, M. (2012) Recent landform evolution in the Romanian Carpathians and Pericarpathian regions. In: Lóczy, D., Stankoviansky, M. & Kotarba, A. (eds.) *Recent Landform Evolution: The Carpatho-Balkan-Dinaric Region*. Springer Geography, Dordrecht, The Netherlands, 249-286. DOI: 10.1007/978-94-007-2448-8_10

Batalla, R.J., Iroumé, A., Hernández, M., Llena, M., Mazzorana, B. & Vericat, D. (2018) Recent geomorphological evolution of a natural river channel in a Mediterranean Chilean basin. *Geomorphology*, 303, 322-337. DOI: 10.1016/j.geomorph.2017.12.006

Brice, J.C. (1964) Channel patterns and terraces of the Loup Rivers in Nebraska. *US Geological Survey Professional Paper*, 422-D, 1-41. DOI: 10.3133/pp422D

Brice, J. C. (1975) *Airphoto Interpretation of the Form and Behavior of Alluvial Rivers.* Final Report to the Army Research Office, Washington University, St. Louis.

Brice, J.C. (1984) Planform properties of meandering rivers. In: Elliott, C.M. (ed.) *River Meandering*: *Proceedings of the Conference Rivers '83*, *New Orleans, Louisiana, U.S.A.* ASCE, New York, 1-15.

Bulteau, T., Batalla, R.J., Chapron, E., Valette, P. & Piégay, H. (2022) Geomorphic effects of a run of the-river dam in a multi-driver context: The case of the upper Garonne (Central Pyrenees). *Geomorphology*, 408, 108243. DOI: 10.1016/j.geomorph.2022.108243

Burshtynska, K., Hrytskiv, N., Zayats, I., Babiy, L., Fijałkowska, A. & Bakuła, K. (2024) Monitoring of channel deformations of the lower Dniester using topographic maps and satellite imagery with the implementation of GIS technologies. *Water*, 16, 2148. DOI: 10.3390/w16152148

Caretta, M.A., Mukherji, A., Arfanuzzaman, M., Betts, R. A., Gelfan, A., Hirabayashi, Y., Lissner, T. K., Liu, J., Lopez Gunn, E., Morgan, R., Mwanga, S. & Supratid, S. (2022) Water. In: Pörtner, H.-O., Roberts, D.C., Tignor, M., Poloczanska, E.S., Mintenbeck, K., Alegría, A., Craig, M., Langsdorf, S., Löschke, S., Möller, V., Okem, A. & Rama, B. (eds.) *Climate Change 2022: Impacts, Adaptation and Vulnerability.* Contribution of Working Group II to the Sixth Assessment Report of the Intergovernmental Panel on Climate Change. Cambridge University Press, UK, pp. 551-712. DOI: 10.1017/9781009325844.006

Chang, H. H. (1979) Minimum stream power and river channel patterns. *Journal of Hydrology*, 41(3-4), 303-327. DOI: 10.1016/0022-1694(79)90068-4

Chiriloaei, F. & Rădoane, M. (2015) The Metamorphosis of a Braided River Channel during the Last 100 Years: Moldova River as a Case Study. *Revista de Geomorfologie*, 17, 19-28.

Chiriloaei, F.A. (2012) *Quantitative analysis of the channel changes of the Moldova River in the extra-Carpathian sector.* PhD Thesis, Alexandru Ioan Cuza University, Iași, Romania (in Romanian).

Cristea, I. (2011) *Geomorphological study of the Putna Vrânceană Valley*. PhD Thesis, Ștefan cel Mare University, Suceava, Romania (in Romanian).

de Musso, N. M., Capolongo, D., Caldara, M., Surian, N. & Pennetta, L. (2020) Channel changes and controlling factors over the past 150 years in the Basento River (Southern Italy). *Water,* 12(1), 307. DOI: 10.3390/w12010307

Diaconu, C. (1999) *Hydrology of Romania*. Bucharest, Technical Press.

Donati, F., Touchart, L., Bartout, P. (2019) *Do rivers upstream weirs have lotics or lentics characteristics?* Geographia Technica, 14 (2):1-9. DOI: 10.21163/GT_2019.142.01

Dumitriu, D. (2021) Flood Events as Geomorphic Thresholds for Channel Bed Level Change. *Carpathian Journal of Earth and Environmental Sciences*, 16, 77-92. DOI: 10.26471/cjees/2021/016/157

Eschbach, D., Schmitt, L., Imfeld, G., May, J.-H., Payraudeau, S., Preusser, F., Trauerstein, M. & Skupinski, G. (2018) Long-term temporal trajectories to enhance restoration efficiency and sustainability on large rivers: An interdisciplinary study. *Hydrology and Earth System Sciences*, 22, 2717-2737. DOI: 10.5194/hess-22-2717-2018

Eyring, V., Gillett, N. P., Achuta Rao, K. M., Barimalala, R., Barreiro Parrillo, M., Bellouin, N., Cassou, C., Durack, P. J., Kosaka, Y., McGregor, S., Min, S., Morgenstern, O. & Sun, Y. (2021) Human Influence on the Climate System. In Masson-Delmotte, V., Zhai, P. Pirani, A., Connors, S.L., Péan, C., Berger, S., Caud, N., Chen, Y., Goldfarb, L., Gomis, M. I., Huang, M., Leitzell, K., Lonnoy, E., Matthews, J.B.R., Maycock, T.K., Waterfield, T., Yelekçi, O., Yu, R. & Zhou, B. (eds.) *Climate Change 2021: The Physical Science Basis.* Contribution of Working Group I to the Sixth Assessment Report of the Intergovernmental Panel on Climate Change. Cambridge University Press, Cambridge, United Kingdom, 423-552, DOI:10.1017/9781009157896.005

Foley, J.A., DeFries, R., Asner, G.P., Barford, C., Bonan, G., Carpenter, S.R., Chapin, F.S., Coe, M.T., Daily, G.C., Gibbs, H.K., Helkowski, J.H., Holloway, T., Howard, E.A., Kucharik, C.J., Monfreda, C., Patz, J.A., Prentice, I.C., Ramankutty, N. & Snyder, P.K. (2005) Global consequences of land use. *Science*, 309, 570-574. DOI:10.1126/science.1111772

Grecu, F., Grigore, S., Ioana-Toroimac, G. & Ghiță, C. (2017) The Dynamics of the Danube Channel over the Last 150 Years (Giurgiu–Călărași Sector. Preliminary Data). In: *Proceedings of the Romanian Geomorphology Symposium, 33rd edition, 11-14 May 2017, Iași, Romania.* DOI: 10.15551/prgs.2017.56

Hajdukiewicz, H. & Wyżga, B. (2023) Analysis of historical changes in planform geometry of a mountain river to inform design of erodible river corridor. *Ecological Engineering*, 186, 106821. DOI: 10.1016/j.ecoleng.2022.106821

Harmar, O.P. & Clifford, N.J. (2006) Planform dynamics of the lower Mississippi River. *Earth Surface Processes and Landforms*, 31(7), 825-843. DOI: 10.1002/esp.1294

Hohensinner, S., Habersack, H., Jungwirth, M. & Zauner, G. (2004) Reconstruction of the characteristics of a natural alluvial river floodplain system and hydromorphological changes following human modifications: The Danube River (1812-1991). *River Research and Applications*, 20(1), 25-41. DOI: 10.1002/rra.719

Horodnic, V. (2023) *Land use and landscape change in the Suceava River basin*. PhD Thesis, Ștefan cel Mare University, Suceava, Romania (in Romanian).

Huțanu, E., Stoleriu, C., Romanescu, G., Enea, A. & Sandu, I. (2020) High-resolution LiDAR data and HEC-RAS modeling for flood risk analysis in NE Romania (Moldavian Plateau). *Natural Hazards*, 104, 1969-1991. DOI: 10.1007/s11069-020-04245-y

Ioana-Toroimac, G., Robert, D. & Grecu, F. (2010) Evolution 2D de la bande active de la Haute Prahova (Roumanie) durant les 150 dernières années. *Géomorphologie: Relief, Processus, Environnement*, 16, 275-286. DOI: 10.4000/geomorphologie.7945

Ioana-Toroimac, G., Zaharia, L., Neculau, G. & Minea, G. (2020) Impact of Channel Incision on Floods: A Case Study in the South-Eastern Subcarpathians (Romania). *Geography, Environment, Sustainability*, 13, 17-24. DOI: 10.24057/2071-9388-2019-177

Jautzy, T., Schmitt, L. & Rixhon, G. (2022) Historical geomorphological adjustments of an Upper Rhine sub-tributary over the two last centuries (Bruche River, France). *Géomorphologie: Relief, Processus, Environnement,* 28(1), 53-72. DOI: 10.4000/geomorphologie.16661

Keesstra, S. D., Van Huissteden, J., Vandenberghe, J., Van Dam, O., De Gier, J. & Pleizier, I. D. (2005) Evolution of the morphology of the river Dragonja (SW Slovenia) due to land-use changes. *Geomorphology*, 69(1-4), 191-207. DOI: 10.1016/j.geomorph.2005.01.004

Kidová, A., Lehotský, M. & Rusnák, M. (2016) Geomorphic diversity in the braided-wandering Belá River, Slovak Carpathians, as a response to flood variability and environmental changes. *Geomorphology*, 272, 137-149. DOI: 10.1016/j.geomorph.2016.01.002

Kiss, T. & Blanka, V. (2012) River channel response to climate and human-induced hydrological changes: Case study on the meandering Hernád River, Hungary. *Geomorphology,* 175-176, 115-125. DOI: 10.1016/j.geomorph.2012.07.003

Knighton, D. (1998) *Fluvial Forms and Processes: A New Perspective*. Oxford, Oxford University Press, 383 p. ISBN 0-340-66313-8.

Kondolf, G.M. & Piégay, H. (2003) *Tools in Fluvial Geomorphology*. Chichester, U. K., John Wiley & Sons.

Korjenić, A., Hrelja, E., Sivac, A., Banda, A. (2021) *Application of GIS in the assessment of flood risk and river characteristics*. Geographia Technica, 16 (2): 80-94. DOI: 10.21163/GT_2021.162.07

Langat, P.K., Kumar, L. & Koech, R. (2019) Monitoring river channel dynamics using remote sensing and GIS techniques. *Geomorphology*, 325, 92-102. DOI: 10.1016/j.geomorph.2018.10.007

Leopold, L. B. & Wolman, M. G. (1957) River channel patterns: Braided, meandering, and straight. *U.S. Geological Survey Professional Paper*, 282, 39-84. DOI: 10.3133/PP282B

Leopold, L.B., Wolman, M.G. & Miller, J.P. (1964) *Fluvial Processes in Geomorphology*. San Francisco, W.H. Freeman and Company.

Llena, M., Vericat, D., Martínez-Casasnovas, J.A. & Smith, M.W. (2020) Geomorphic adjustments to multi-scale disturbances in a mountain river: A century of observations. *CATENA*, 192, 104584. DOI: 10.1016/j.catena.2020.104584

Malavoi, J.R. & Bravard, J.P. (2010) *Éléments d'hydromorphologie fluviale*. ONEMA, Paris, France.

Mandarino, A. (2022) Morphological adjustments of the lower Orba River (NW Italy) since the mid-nineteenth century. *Geomorphology*, 410 (Special Issue 1), 108280. DOI: 10.1016/j.geomorph.2022.108280

Mandarino, A., Maerker, M. & Firpo, M. (2019) Channel planform changes along the Scrivia River floodplain reach in northwest Italy from 1878 to 2016. *Quaternary Research*, 91 (2), 620-637. DOI: 10.1017/qua.2018.67

Oprea, D. (2014) *The Suceava Valley. A geomorphological study*. PhD Thesis, Ștefan cel Mare University, Suceava, Romania (in Romanian).

Pavlek, K. & Faivre, S. (2020) Geomorphological changes of the Cetina River channels since the end of the nineteenth century, natural vs anthropogenic impacts (the Dinarides, Croatia). *Environmental Earth Sciences,* 79, 482. DOI: 10.1007/s12665-020-09213-x

Perșoiu, I. & Rădoane, M. (2011) Spatial and Temporal Controls on Historical Channel Responses-Study of an Atypical Case: Someșul Mic River, Romania. *Earth Surface Processes and Landforms,* 36, 1391-1409. DOI: 10.1002/esp.2169

Perșoiu, I. (2010) *Geomorphological and hydrological evolution of karst areas in the Apuseni Mountains, Romania.* PhD Thesis, Babeș-Bolyai University, Cluj-Napoca, Romania.

Piticar, A. (2013) *Studies on recent climate change in northeastern Romania.* PhD Thesis, Babeș-Bolyai University, Cluj-Napoca, Romania (in Romanian).

Radu, A. & Comănescu, L. (2025) Historical evolution and future trends of riverbed dynamics under anthropogenic impact and climatic change: a case study of the Ialomita River (Romania). *Water,* 17, 2151. DOI: 10.3390/w17142151

Rădoane, M., Obreja, F., Cristea, I. & Mihăilă, D. (2013) Changes in the channel-bed level of the eastern Carpathian rivers: Climatic vs. human control over the last 50 years. *Geomorphology*, 193, 91-111. DOI: 10.1016/j.geomorph.2013.04.008

Rădoane, M., Pandi, G. & Rădoane N. (2010) Contemporary Bed Elevation Changes from the Eastern Carpathians. *Carpathian Journal of Earth and Environmental Sciences*, 5(2), 49-60. https://www.cjees.ro/viewTopic.php?topicId=90

Rădoane, M., Perșoiu, I., Chiriloaei, F., Cristea, I. & Robu, D. (2017) Styles of Channel Adjustments in the Last 150 Years. In: Rădoane, M., Vespremeanu-Stroe, A. (eds.) *Landform Dynamics and Evolution in Romania.* Springer Geography, Cham, Switzerland, 489-518. DOI: 10.1007/978-3-319-32589-7_21

Rădoane, M., Rădoane, N., Cristea, I. & Dinu, O. (2008) Evaluarea modificărilor contemporane alealbiei râului Prut pe granița românească. *Revista de Geomorfologie,* 10, 57-71. https://revistadegeomorfologie.ro/geo/index.php/revista/issue/view/10/13

Rădoane, M., Rădoane, N. & Dumitriu, D. (2003) Geomorphological Evolution of Longitudinal River Profiles in the Carpathians. *Geomorphology*, 50, 293-306. DOI: 10.1016/S0169-555X(02)00194-0

Rapp, A. & Abbey, D.G. (2003) Geomorphology, Human Impact, and River Channel Change. In: Gregory, K.J.& Benito, G. (eds.) *Geomorphological Processes and Human Impacts in River Basins*. Wiley, Chichester, UK, 75-94. ISBN: 978-1901502282

Rinaldi, M. (2003) Recent channel adjustments in alluvial rivers of Tuscany, Central Italy. *Earth Surface Processes and Landforms,* 28(6), 587-608. DOI: 10.1002/esp.464

Rinaldi, M., Surian, N. & Comiti, F. (2005) Geomorphic response of rivers to human disturbances: A review. *Geomorphology*, 71(1-2), 71-86. DOI: 10.1016/j.geomorph.2005.02.010

Rinaldi, M., Piégay, H. & Surian, N. (2011) Geomorphological approaches for river management and restoration in Italian and French rivers. In: *Stream restoration in dynamic fluvial systems: scientific approaches, analyses and tools*, American Geophysical Union, Geophysical Monograph Series 194, 95-113. DOI: 10.1029/2010GM000984

Romanescu, G. (2003) *Hydrogeomorphological study of the Siret River Basin*. „Al. I. Cuza" University Press, Iași, Romania.

Romanescu, G. (2013) Floods in the Siret and Pruth Basins. In: *Geomorphological impacts of extreme weather: Case studies from central and eastern Europe*, 99-120, Dordrecht, Springer Netherlands. DOI: 10.1007/978-94-007-6301-2_7

Salit, F., Arnaud-Fassetta, G., Zaharia, L., Madelin, M. & Beltrando, G. (2015) The Influence of River Training on Channel Changes During the 20th Century in the Lower Siret River (Romania). *Géomorphologie: Relief, Processus, Environnement*, 21, 175-188. DOI: 10.4000/geomorphologie.11002

Schumm, S.A. (1977) *The Fluvial System*. Wiley Interscience, New York.

Schwenk, J., Khandelwal, A., Fratkin, M., Kumar, V. & Foufoula-Georgiou, E. (2017) High spatio-temporal resolution of river planform dynamics from Landsat: The RivMAP toolbox and results from the Ucayali River. *Earth and Space Science*, 4(2), 46-75. DOI: 10.1002/2016EA000196

Škarpich, V., Hradecký, J. & Dušek, R. (2013) Complex transformation of the geomorphic regime of channels in the forefield of the Moravskoslezské Beskydy Mts.: Case study of the Morávka River (Czech Republic). *CATENA*, 111, 25-40. DOI: 10.1016/j.catena.2013.06.028

Spada, D., Molinari, P., Bertoldi, W., Vitti, A. & Zolezzi, G. (2018) Multi-temporal image analysis for fluvial morphological characterization with application to Albanian rivers. *ISPRS International Journal of Geo-Information,* 7(8), 314. DOI: 10.3390/ijgi7080314

Stoleriu, C., Romanescu, G., Enea, A., Huțanu, E. & Sandu, I. (2020) Flood hazard mapping using high-density LiDAR data and HEC-RAS modeling: A case study from NE Romania. *Water,* 12(4), 1165. DOI: https://doi.org/10.3390/w12041165

Surian, N., Rinaldi, M., Pellegrini, L., Audisio, C., Maraga, F., Teruggi, L., Turitto, O. & Ziliani, L. (2009) Channel adjustments in northern and central Italy over the last 200 years. G*eological Society of America Special Papers*, 451, 83-95. DOI: 10.1130/2009.2451(05)

Thorne, C.R. (1997) Channel types and morphological classification. In: Thorne, C.R., Hey, R.D. & Newson, M.D. (eds.) *Applied Fluvial Geomorphology for River Engineering and Management.* Wiley, Chichester, 175-222.

Ujvari, I. (1972) *Geografia apelor României*, Bucureşti, Editura Științifică.

Vercruysse, K. & Grabowski, R.C. (2021) Human impact on river planform within the context of multi-timescale river channel dynamics in a Himalayan river system. *Geomorphology*, 381, 107659. DOI: 10.1016/j.geomorph.2021.107659

Winterbottom, S.J. (2000) Medium and short-term channel planform changes on the Rivers Tay and Tummel, Scotland. *Geomorphology,* 34(3-4), 195-208. DOI: 10.1016/S0169-555X(00)00007-6

Zawiejska, J. & Wyżga, B. (2010) Twentieth-century channel change on the Dunajec River, southern Poland: Patterns, causes and controls. *Geomorphology,* 117(3-4), 234-246. DOI: 10.1016/j.geomorph.2009.01.014

Aims and Scope

Geographia Technica is a journal devoted to the publication of all papers on all aspects of the use of technical and quantitative methods in geographical research. It aims at presenting its readers with the latest developments in G.I.S technology, mathematical methods applicable to any field of geography, territorial micro-scalar and laboratory experiments, and the latest developments induced by the measurement techniques to the geographical research.

Geographia Technica is dedicated to all those who understand that nowadays every field of geography can only be described by specific numerical values, variables both oftime and space which require the sort of numerical analysis only possible with the aid of technical and quantitative methods offered by powerful computers and dedicated software.

Our understanding of ***Geographia Technica*** expands the concept of technical methods applied to geography to its broadest sense and for that, papers of different interests such as: G.I.S, Spatial Analysis, Remote Sensing, Cartography or Geostatistics as well as papers which, by promoting the above mentioned directions bring a technical approach in the fields of hydrology, climatology, geomorphology, human geography territorial planning are more than welcomed provided they are of sufficient wide interest and relevance.

Targeted readers:

The publication intends to serve workers in academia, industry and government.
Students, teachers, researchers and practitioners should benefit from the ideas in the journal.

Guide for Authors

Submission

Articles and proposals for articles are accepted for consideration on the understanding that they are not being submitted elsewhere.

The publication proposals that satisfy the conditions for originality, relevance for the new technical geography domain and editorial requirements, will be sent by email to the address editorial-secretary@technicalgeography.org.

This page can be accessed to see the requirements for editing an article, and also the articles from the journal archive found on www.technicalgeography.org can be used as a guide.

Content

In addition to full-length research contributions, the journal also publishes Short Notes, Book reviews, Software Reviews, Letters of the Editor. However the editors wish to point out that the views expressed in the book reviews are the personal opinion of the reviewer and do not necessarily reflect the views of the publishers.

Each year two volumes are scheduled for publication. Papers in English or French are accepted. The articles are printed in full color. A part of the articles are available as full text on the www.technicalgeography.org website. The link between the author and reviewers is mediated by the Editor.

Peer Review Process

The papers submitted for publication to the Editor undergo an anonymous peer review process, necessary for assessing the quality of scientific information, the relevance to the technical geography field and the publishing requirements of our journal.

The contents are reviewed by two members of the Editorial Board or other reviewers on a simple blind review system. The reviewer's comments for the improvement of the paper will be sent to the corresponding author by the editor. After the author changes the paper according to the comments, the article is published in the next number of the journal.

Eventual paper rejections will have solid arguments, but sending the paper only to receive the comments of the reviewers is discouraged. Authors are notified by e-mail about the status of the submitted articles and the whole process takes about 3-4 months from the date of the article submission.

Indexed by: **CLARIVATE ANALYTICS**
SCOPUS
GEOBASE
EBSCO
SJR
CABELL

ISSN: 1842 - 5135 (Print)
ISSN: 2065 - 4421 (Online)



